SPACE
SYSTEMS

Document No. 69SD4372

March 31, 1970

GRAVITY GRADIENT STABILIZATION SYSTEM

for the

APPLICATIONS TECHNOLOGY SATELLITE

FINAL TECHNICAL REPORT

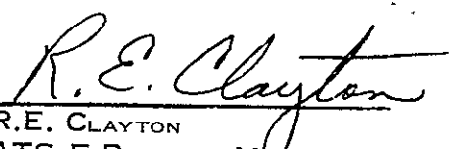System Software and Analysis

VOLUME I

GENERAL ⊕ ELECTRIC

FINAL REPORT

FOR THE

APPLICATIONS TECHNOLOGY SATELLITE
GRAVITY GRADIENT
STABILIZATION SYSTEM

VOLUME I

SYSTEM SOFTWARE AND ANALYSIS

CONTRACT NO. NAS 5-9042

FOR THE

NATIONAL AERONAUTICS AND SPACE ADMINISTRATION
R.J. WIRTH
ATS TECHNICAL OFFICER

APPROVED BY: *R.E. Clayton*

R.E. CLAYTON
ATS-E PROGRAM MANAGER

GENERAL ⚙ ELECTRIC

SPACE SYSTEMS ORGANIZATION
Valley Forge Space Center
P. O. Box 8555 • Philadelphia, Penna 19101

SYSTEM REQUIREMENTS AND ANALYSIS

TABLE OF CONTENTS

TABLE OF CONTENTS (Cont'd)

TABLE OF CONTENTS (Cont'd)

TABLE OF CONTENTS (Cont'd)

vi

LIST OF ILLUSTRATIONS

LIST OF ILLUSTRATIONS (Cont'd)

LIST OF ILLUSTRATIONS (Cont'd)

LIST OF TABLES

LIST OF TABLES (Cont)

SECTION 1

INTRODUCTION

SECTION 1

INTRODUCTION

1.1 PROGRAM SUMMARY

Under Contract NAS 5-9042, the Space Systems Organization of the General Electric Company provided the NASA Goddard Space Flight Center with gravity gradient stabilization systems for three Applications Technology Satellites and provided flight analysis and data reduction support when each system was flown. One system (ATS-A) was designed for flight in a 6,000 nautical mile (nm) circular orbit, inclined $28\frac{1}{2}$ degrees to the earth's equatorial plane. The other two (ATS-D and ATS-E) were designed for flight in synchronous altitude, equatorial orbits. ATS-A was designed for direct orbit insertion by the Atlas SLV-3/Agena D launch vehicle system, but ATS-D and E required an on-board apogee motor to circularize the orbit at synchronous altitude. Injection into the $5\frac{1}{2}$-hour transfer orbit was accomplished by the Atlas SLV-3/Centaur system. All launches were from the Eastern Test Range. ATS-D and E required an intermediate spin stabilization mode for the period from Centaur separation, through apogee motor burn and orbit station-positioning, to the final yo-yo despin maneuver on station. Each gravity gradient system included a set of motor-driven, extendable/retractable primary booms and tip masses which could be "scissored" in orbit to change the geometry of the deployed-boom configuration.

The booms and tip masses provided the required design flexibility for achievement of the required moments of inertia. The gravity gradient orienting torques tend to align the axis of minimum moment of inertia with the local vertical. After the local vertical has been established, orbital rate appears on the spacecraft and the maximum moment of inertia tends to align with the orbit plane normal, thereby producing three-axis control. The orienting torques are all proportional to the differences in the spacecraft moments of inertia and the rods and tip masses are sized to provide torques of sufficient magnitude for attitude stability. The ability to extend and retract (as well as scissor) the primary booms provided the capability for a steady-state experiment on the sensitivity of gravity-gradient systems to basic configuration parameters. Also included was a combination passive damper which provided the capability for in-orbit selection of either of two technically competitive damping

schemes: eddy-current damping or magnetic hysteresis damping. Both schemes were designed to dissipate spacecraft librational energy through the use of permanent magnets only. The eddy current damper was diamagnetically suspended and utilized a crescent of very thin ferromagnetic material to provide the torsional restraint. The hysteresis damper was suspended by a torsion wire which inherently provided its own torsional restraint. Attached to the damping axis was a self-deployable damper boom system which was "detuned" from the frequency characteristics of the primary system to ensure relative motion through the damper for all but ideal steady-state conditions. Damping of spacecraft motion in all axe was achieved with a single-axis damper by taking advantage of the inherent cross coupling between axes, a characteristic of this particular configuration. The basic configuration parameters (spring constant, damping coefficient, rod lengths and tip masses, etc.) were selected as a result of an interchange of ideas and information between NASA/Ames and the General Electric Company and adopted for use on the Application Technology Satellite progra by NASA/Goddard.

A TV camera system was provided to observe motion of targets fastened to the tips of the primary booms. This was primarily for the purpose of obtaining data on in-orbit boom dynamics and thermal bending. A distributed solar aspect sensing system was provided to work in conjunction with an earth IR sensor (GFE), or antenna polarization angle (POLANG), to provide sufficient data for a determination of three-axis spacecraft attitude. A power control unit provided the electronics interface with the spacecraft's telemetry, command and power systems. Two sets of ground test equipment were also furnished. Software developments included an ATS Mathematical Model computer simulation program, an Attitude Determination/Data Reduction/Data Analysis program for reduction and processing of PCM data recorded on magnetic tape, and a "quick look" data system for quick turnaround processing of PCM data bursts received by NASCOM teletype. The in-orbit spacecraft configuration is depicted in Figure 1-1.

The first system (ATS-A) was launched 6 April 1967. Failure of the orbit-circularizing Agena second burn left the spacecraft stranded in a highly elliptical (e = 0.454) orbit. This prevented achievement of earth-pointing stability and, despite the fact that all gravity gradient
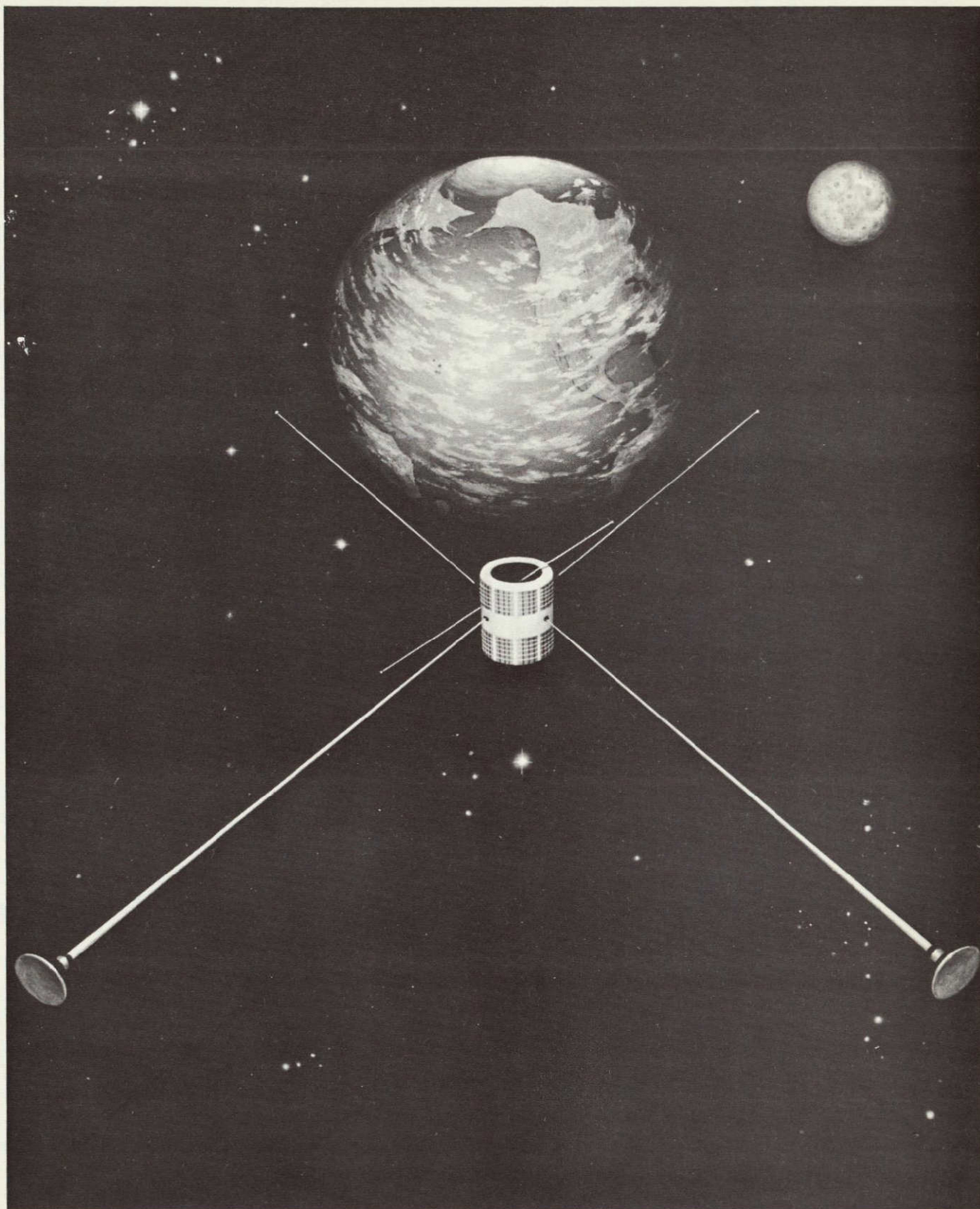
Figure 1-1. Spacecraft Configuration

systems were deployed and functioned normally, the prime gravity gradient experiments could not be accomplished.

The second system (ATS-D) was launched 10 August 1968. Failure of the Centaur second burn left the spacecraft stranded in a low altitude parking orbit and prevented separation of the spacecraft from either the Centaur or the spacecraft apogee engine. The gravity gradient hardware was successfully exercised, but no gravity gradient experimentation could be performed. The system reentered the earth's atmosphere on 17 October 1968.

The third system (ATS-E) was launched 12 August 1969. Shortly after synchronous orbit injection, and while still in the intermediate spin-stabilized mode, the spacecraft developed uncontrollable nutations which precipitated a fall over into a flat tumbling mode. Subsequent separation of the apogee motor casing caused the spacecraft to revert to a spin mode, but in the wrong direction for system despin using the yo-yo despin system. Consequently, the spacecraft cannot be despun and the gravity gradient system cannot be deployed without catastrophic consequences. Hence, again, the gravity gradient experiment can not be performed.

In spite of the inability to perform or initiate the gravity gradient experiments, GE provided active support to the ATS Operations Control Center and the GSFC Project Office during each of the three periods of post-launch contingency operations. Under separate contract, GE continues to provide support in the development of techniques for salvaging data from the ATS-E magnetometer experiment.

1.2 SCOPE AND ORGANIZATION OF REPORT

This report provides a technical summary of the design, development, test and flight analysis for each gravity gradient stabilization system. The time period is from 29 June 1964 (contract inception) through 31 December 1969 (initiation of contract closeout). An overall schedule of activities during this period is presented in Table 1-1. The report is dividied into two volumes: Volume I, System Software and Analysis, and Volume II, Hardware Development and Test. Volume I contains the background analysis which established the

Table 1-1. NAS5-9042 Composite Schedule

	1964	1965	1966	1967	1968	1969

Program Definition (Phase I)
  Work Statement, Program Plans and
  Schedules, Integrated Test Plan,
  Component and System Specs, Spacecraft
  Interface Specs, Drawing Tree, Initial
  Breadboards, Subcontract Selection, etc.

Program Implementation (Phase II)
  Definitive Test Planning & Documentation
  Component Thermal & Dynamic Models
  AGE Console Development and Checkout
  Engineering Design and Development
  Engineering Unit Testing
  Subsystem Prototype Testing (GE)
  Subsystem Flight Unit Testing (GE)   } ATS-A
  System Prototype Testing (HAC)
  System Flight Acceptance Testing (HAC)
  Launch (ATS-A)
  Subsystem Prototype and Flight Unit
      Testing, Storage & Special Tests   } ATS-D&E
      at GE (Flights D & E)
  Launch (ATS-D)
  Launch (ATS-E)
  Flight Support & Analysis
      ATS-A
      ATS-D
      ATS-E
  Software Development and Checkout
      (Attitude Determination Programs,
      Quick-Look Data System & ATS Math Model)
  Performance Simulation and Orbit Test Planning

▲(ATS-A)   ▲(ATS-D)   ▲(ATS-E)

basic hardware parameters and performance estimates and provided estimates of performance variations due to a variety of necessary design modifications. Also included in Volume I is a descriptive summary of software developments. Volume II contains a comprehensive summary of the engineering effort associated with the development and test of each subsystem and includes a description of the hardware requirements and assumptions.

SECTION 2

GRAVITY GRADIENT EXPERIMENT

SECTION 2

GRAVITY GRADIENT EXPERIMENT

2.1 EXPERIMENT OBJECTIVES

The basic objectives of the ATS gravity gradient stabilization system experiment were to:

1. Demonstrate operational feasibility at medium and synchronous orbit altitudes

2. Demonstrate compatibility with stabilization requirements of long-life, applications-type satellite missions

3. Obtain flight data for design performance evaluation and subsequent application to the design of gravity gradient stabilization systems for compatible future programs.

These objectives, delineated further in Table 2-1 and as follows, dictated the fundamental system requirements for the stabilization system hardware and software. Gravity gradient experiment orbit test and flight evaluation plans, prepared for each of the gravity gradient flights, delineated the specific tests to be performed in orbit and provided all pertinent data required for efficient on-orbit operations. References to these documents will be found in Section 6.

Table 2-1. Gravity Gradient Mission Objectives

Mission Objectives	Orbit Tests
I. Operational Feasibility	1 Initial Capture 2 Transient Damping 3 Steady-State Performance 4 Pitch Inversion 5 Yaw Inversion
II. Mission Compatibility	1 System Response to Impulse Functions 2 Operational Tests by ATS Experimenters 3 Life Test
III. Design Performance Evaluation	1 Performance Sensitivity – Moment of Inertia Ratios and Magnitudes 2 Boom Thermal Bending and Boom Dynamics Effects 3 TV and POLANG for Attitude Determination 4 Evaluation of Mathematical Model

2.1.1 OPERATIONAL FEASIBILITY

To demonstrate the operational feasibility of gravity gradient stabilization, it must be shown that the time to capture and settle to steady-state (and the subsequent steady-state performance) are compatible with the mission requirements of programs which would typically utilize such systems. "Capture" was defined to be the point at which pitch and roll tumbling have ceased (yaw tumbling, by definition, was allowed to continue beyond the point of capture). Due to the bi-stable characteristics of gravity gradient systems, spacecraft motion was described as tumbling in pitch, roll or yaw if the attitude excursions about the respective axes exceeded 90 degrees. With increasing altitude, capture without an initial period of tumbling is increasingly difficult. This is primarily due to the increased sensitivity of capture stability to body axis rates at the time of initiation of the gravity gradient mode. Initial rates result typically from launch vehicle separation rates (ATS-A) or yo-yo despin residual rates (ATS-D and E) depending upon whether or not an intermediate spin stabilization mode is required. These residual rates, coupled with spacecraft moment of inertia properties, produce a level of initial angular momentum which must be controlled in order to achieve capture. This becomes more difficult with increased altitude due to the weakening of the gravity field gradient. For ATS-A, at an altitude of 6,000 nautical miles (nm), little or no tumbling was expected for initial rates of up to 1 degree/second about all axes. For ATS-D and E, however, an initial period of tumbling would not have been unexpected. To avoid potential tumbling periods of 400 hours or more, operational procedures were developed (and recommended in the Gravity Gradient Orbit Test Plans for ATS-D and E) to achieve boom deployment in the vicinity of the local vertical. These procedures were expected to minimize the initial capture problems on ATS-D and E and produce an initial period of little or no tumbling for these flights also. The mechanical sequence of capture necessitated a properly timed deployment of the primary booms followed by deployment of the damper booms and "scissoring" of the primary boom system from an initial deployment scissor angle of 19 degrees to a nominal, steady-state scissor angle of 25 degrees. The "scissor angle" was defined as half the acute angle of the X formed by the fully deployed booms. Following the "scissor" maneuver, the Combination Passive Damper was to be uncaged – initially in the eddy current mode. Transient damping characteristics of the eddy current damper were thereby to be obtained during the initial period of capture and

damping to steady state. The design goal for achievement of steady state was 15 orbit periods from the point of capture. This corresponded to 4 days for ATS-A and 15 days for ATS-D and E. Transient damping data for the hysteresis damper was to be obtained during subsequent tests requiring large angle perturbations by the pitch inversion thrusters. This would nominally have been accomplished as a direct corollary to the results of the pitch inversion experiments.

Once steady-state was achieved, the gravity gradient tests were to be concerned primarily with Mission Objectives II and III. However, as a part of Objective I, sufficient data was required at proper times in the orbit and at proper times of the year to evaluate the effects on steady-state of:

1. Sun in the orbit plane

2. Sun at maximum inclination to orbit plane

3. Eddy-current damping versus passive hysteresis damping

4. Stationkeeping thrusters, including frequency and duration of pulses

5. Combinations of Items 1 through 4.

During the initial capture period, if capture without an initial period of tumbling were achieved, the spacecraft would have reached steady-state in an upright orientation. Unfortunately, unless optimum initial rates were obtained and attitude sensing techniques were utilized to ensure timely deployment of the primary booms, the more probable situation would have been a brief initial period of tumbling. Since the system was stable in either an upright or an inverted orientation, a finite probability of inverted capture existed. If capture was inverted, an early operational requirement to turn the spacecraft over would have arisen. This could have been done in either of two ways:

1. Subliming rocket thruster inversion

2. Boom retraction and extension inversion

The first system would probably have been the safest but offered the least assurance of success on the first try due to uncertainties in the thrust levels of the inversion thrusters. The second system offered a more certain systems approach but was probably a little riskier because of the catastrophic consequences of a failure in the boom system during the retraction and extension phases. The recommendation was for the thruster system to be utilized and, if necessary, the attempts be repeated until a successful inversion was obtained. Since some form of an inversion system will be required on all earth-seeking operational spacecraft (unless redundant payloads are utilized), the pitch inversion tests on ATS were considered to be some of the most significant of the gravity gradient tests.

In addition to being bi-stable in pitch, the ATS gravity gradient spacecraft was bi-stable in yaw. Although no ATS requirements existed for "forward" versus "backward" flight, future missions may involve such requirements. Hence, as an additional gravity gradient test, a controlled yaw inversion attempt was planned. The main effort was to have been concerned with the establishment of the sensitivity of the yaw transient to initial pitch displacements. There is a notable general tendency for a yaw inversion to occur as a characteristic of the attitude dynamics associated with large pitch displacements. If the pitch inversion techniques previously discussed could be utilized to obtain a pitch displacement of just sufficient amplitude to cause one inversion in yaw (as the spacecraft settles back to steady-state), the techniques could then be utilized not only for pitch inversion but for yaw inversion as well.

2.1.2 MISSION COMPATIBILITY

The second mission objective was aimed at demonstrating compatibility with mission requirements of long-life, applications-type satellites. The most significant measure of success, for this particular objective, would have been the compatibility of steady-state attitude dynamics with other attitude sensitive ATS experiments. Gravity gradient attitude data (provided NASA by GE) was to have been added to the ATS World Map (at NASA/GSFC) for distribution to all ATS experimenters for use in the evaluation of their own particular experiments. One expected result of this evaluation would have been an assessment of the compatibility of gravity gradient stabilization with the mission requirements of the various

applications-oriented experiments. One particular measure of compatibility would have been the spacecraft response, if any, to the torque impulses produced each time the tape recorder in the ATS-A meteorological experiment package was turned on or off. The characteristics of these impulses were known in advance and the start and stop times would have been available via telemetry from the spacecraft. The spacecraft reaction to these impulses would have been sought in the resultant attitude determined from telemetered attitude sensor data.

Finally, since long-life in orbit is one of the prime advantages of passive stabilization, a life test was to have been performed. This test, essentially, called for a periodic monitoring of spacecraft performance for the life of the telemetry and attitude-sensing subsystem. The end objective was to detect any long-term performance changes (such as might occur through degradation of surface properties with an associated unbalancing of solar pressure torques) and establish the ultimate cause of failure.

2.1.3 DESIGN PERFORMANCE EVALUATION

The biggest uncertainty in predicting the performance of gravity gradient satellites is the effect of boom thermal bending and boom dynamics. Full scale ground simulation and testing is not practical. ATS provided the first opportunity for direct observation of these phenomena in orbit.

Boom thermal bending results from the temperature gradient induced in the booms through solar heating on one side of the boom and radiative cooling on the opposing side. The expansion of material on the "hot" side and contraction of material on the "cold" side cause the booms to bend in much the same manner as a bi-metallic strip. The proper choice of materials and surface coatings can minimize this effect but not completely eliminate it. The ATS booms were silver-plated beryllium copper. The bending phenomena is complicated (for the case of the overlapped configuration used on ATS) by the fact that the maximum temperature gradient is not necessarily across the boom diameter. The "skewed" temperature gradient results in stresses which produce bending in a plane other than that containing the sun vector.

Mathematical simulation of this phenomenon was the subject of considerable effort at GE and included both test and analysis. The results of these efforts were formulated in semi-empirical equation form and incorporated into the ATS Mathematical Model. The empirical nature of the formulation was embodied in the coefficients of the individual terms of the thermal bending equations and were specified, along with optical surface properties, as inputs to the computer program. This allowed sufficient flexibility in the thermal bending model for updates based on data obtained from orbit via the gravity gradient television system.

The television data was to be recorded by 35 mm photography of the TV monitors at the ground stations. The processed film was then to be transmitted to GE-Valley Forge for analysis. Nine-inch diameter targets, designed to optimize reflected lighting conditions over the widest possible range of solar incidence angles, were mounted on each of the primary boom tips. Reduced TV data, for correlation with the empirical thermal bending equation in the Mathematical Model, would have been in the form of boom tip deflections relative to fixed spacecraft body coordinates. To get a "zero" point for these deflections (representing the contribution of initial curvature to the observed total deflection due to initial curvature plus thermal bending), television pictures were required at the point of exit from a solar eclipse region. This required a combination of ground station coverage (preferably Rosman, N.C.) and orbit-eclipse conditions which, for ATS-A, may have been difficult to achieve. Conditions would have been beyond control (other than from a data acquisition scheduling viewpoint) once the orbit was established. In addition, it was required that the time in eclipse preceding the exit point be sufficiently long for the transient dynamic effects (due to thermal "twang") to be damped out before emergence from the eclipse region. Thermal bending data was to be analyzed under a variety of solar incidence angles in an attempt to obtain complete environmental coverage. The results were to be correlated with predictions based on the thermal bending formulation within the Mathematical Model and, if the quality of the data warranted, used to update the analytical model of the thermal bending.

The thermal "twang" phenomena was an example of the boom dynamics effects to be studied. The thermal time constant of the ATS booms was estimated to be about 40 seconds. The fundamental period of mechanical motion of the booms, however, was about 500 seconds. Hence, as the spacecraft entered an eclipse region with the booms thermally bent, the temperature gradient would have been removed from the booms faster than the booms could mechanically respond to the resultant stresses of bending. The result would have been comparable to the effect of deflecting and releasing the tip of a cantilever spring. This phenomena is usually referred to as the thermal "twang" effect. It was not expected to produce an appreciable effect on the attitude of the central body but its observance, via the gravity gradient television system, could have resulted in a significant contribution to the body of knowledge required for confident design of gravity gradient boom systems. The observance of this effect, however, imposed an even tighter constraint on ground-station coverage and orbit-eclipse conditions. It was required that the eclipse period be long enough to ensure significant thermal cooling but short enough to preclude structural damping from reducing the resultant boom oscillations to a point where they were no longer observable. This type condition can be achieved only at the beginning or end of a continuous sunlight period as the satellite passes through the edge of the eclipse region. This constraint, plus the requirement for continuous thermal bending data throughout an orbital period (without interference from the thermal twang effect) produced basic requirements for a period of continuous sunlight. ATS-A requirements could be satisfied only through proper constraints on launch and orbit injection conditions. These constraints were specified in the Gravity Gradient Orbit Test Plan for ATS-A.

Other boom dynamics phenomena planned for observation with the gravity gradient television system included scissoring of the booms, retraction and extension of the booms, the effect of thruster torques during pitch-up maneuvers and the deflection response of the booms during spacecraft inversion.

The primary boom system scissoring capability was included as a means for ground control of one of the key design parameters affecting spacecraft steady state performance. As previously defined, the scissor angle is half the acute angle formed by the X of the fully

deployed rods. This angle could be varied by ground command and used to introduce variations in the spacecraft moment-of-inertia ratios. The angle could be varied over a range of from 11 degrees to 31 degrees, with 25 degrees representing the nominal design point for optimum performance. Off-nominal scissor angles would have, most noticeably, introduced a bias in yaw attitude called the "crab" angle. For ATS-D, with the sun out of the orbit plane, this crab angle could have approached 20 degrees at a scissor angle of 11 degrees. Comparative evaluation of the two damping schemes (eddy-current damping and passive hysteresis damping) was to be performed at selected values of the scissor angle. This would have included a steady-state performance evaluation, as well as a transient performance evaluation. Transient performance data would have been obtained through pitch displacements to approximately 30 degrees using short burns of the inversion thrusters. The resultant time to settle to steady-state would have been established as a function of the scissor angle. The whole procedure was to be repeated at shorter boom lengths giving the added parametric effect of changing the moment-of-inertia magnitudes. The main objective of these tests was to evaluate the performance sensitivity to variations in moment-of-inertia properties for subsequent correlation with predictions of the ATS Mathematical Model.

A Boom System Failure Mode Simulation test was proposed for much the same reason. The objective was to scissor, for example, one pair of booms to 11 degrees and the other pair to 31 degrees. This would have introduced a significant shift in the system center of radiation pressure. The result would have represented an exaggerated off-nominal condition for correlation of performance data with Math Model prediction. A second example was the case of shortening one pair of booms to, for example, 50 feet while leaving the remaining pair of booms at their fully-deployed length. This condition would have come closer to a true simulation of a failure mode than the antisymmetric scissoring test. (Normally, scissoring capability would not be included in a gravity stabilized system; however, full deployment on one set of booms and partial deployment on another set of booms is a potential mode of failure on most gravity gradient systems.) Because of the hazards associated with this test, it was not scheduled until the latter part of the orbit test period.

The gravity gradient television system, designed primarily for observations of boom thermal bending and boom dynamics phenomena, also offered the potential of a back-up attitude sensing device. Its value, for real-time assessment of attitude, is unquestionable: if the earth is in the field of view and remains there for any period of time, a real-time visual proof of steady-state operation is obtained. It also provides the capability for estimating attitude rate if the earth is seen to pass through the field of view. Although not planned for use on ATS, templates and overlays could easily have been designed for direct computation of attitude from the visual evidence presented on the TV monitors at the ground stations. Plans for evaluation of the TV as an attitude sensor depended on data analysis of the films produced by photographing the TV monitors. The angle between the local vertical and the spacecraft's yaw axis could have been determined if a sufficiently large section of the earth had appeared in the presentation for establishment of the direction of the radius of curvature. Once this was known, knowledge of the size of the earth from the altitude at which the pictures were taken would have been sufficient information to compute the attitude angle in question. If the earth's terminator (the division between the sunlit and night portions of the earth) was clearly enough identified, or if land masses could have been identified, there was the possibility of establishing yaw attitude. Once this was known, complete 3-axis attitude determination would have been a matter of routine. Attitude determined in this manner would have been correlated with attitude determined from the solar aspect and earth IR sensors to assess the accuracy of attitude determination using the TV system.

POLANG, an acronym for polarization angle, was also planned for use in attitude determination. The polarization angle defined the orientation of the incoming linearly polarized E-vector radiated from the spacecraft's antenna system. POLANG, measured at the ground stations, was to be transmitted to NASA/GSFC for corrections related to antenna errors and Faraday rotation which occur at passage of the E-vector through the earth's ionosphere. The corected POLANG was then to be transmitted to GE, along with the sun sensor and earth sensor data for the computation of attitude. The corrected POLANG data would have provided significant information on the orientation of the spacecraft's pitch axis.

.Finally, the last item under Mission Objective III was the evaluation of the ATS Mathematical Model. The design of gravity gradient systems (especially two-body coupled systems such as ATS) is heavily dependent upon the use of the computer as a design evaluation tool. The systems problems are too complex and interrelated to evaluate in any other manner. Computer programs, however, can be no better than the assumptions and mathematical modeling techniques used in generating them. One of the basic gravity gradient experiment objectives, therefore, was to check the ATS Mathematical Model against real data to establish the confidence necessary for the commitment of future ATS-type programs to its use. The plan for accomplishing this objective is discussed further in Section 2.2.2.

The distinction between test plans for ATS-A and ATS-D/E was a matter of emphasis. The emphasis on ATS-D/E, however, was to have been primarily in terms of time to capture and achieve steady-state and the compatibility of steady state and stationkeeping requirements. Spacecraft inversion, for example, was to have been attempted on ATS-D/E only if required to achieve an upright orientation. Experiments with scissoring were to be much more restrictive. Simulation of boom failure modes and attempts at yaw inversion were to have been eliminated. Thus, the original test plan for ATS-D/E was, in general, to be a simplified version of the plan for ATS-A, with emphasis placed on mission compatibility rather than gravity gradient experimentation. This philosophy changed somewhat after the failure of ATS-A and ATS-D to achieve acceptable orbits.

2.2 MATHEMATICAL MODEL

2.2.1 DESCRIPTION

The ATS Mathematical Model is a digital computer program designed to simulate the orbital behavior of the two-body gravity gradient configuration used for the Applications Technology Satellites A, D and E. The gravity gradient orienting torques are, for small angle deviations, linear with attitude error. As a consequence, the spacecraft behaves in a manner characteristic of a spring-mass system, and will oscillate as a result of external disturbances. The minimum error (peak of the sine wave) achieved by the spacecraft is defined to be the steady state error. The value of steady state error is a function of the magnitude

and frequency of the external disturbances as related to the magnitude of the orienting torques and the frequency response of the spacecraft. The Mathematical Model simulates the disturbances, as well as they are known, and by integrating Euler's dynamical equations, provides a time history of the performance which can be used to determine the steady state error. The program is not limited to small angles, however, and large angle transient behavior can also be evaluated. A brief discussion of the simulated disturbance torques is provided herein. The equations contained in the program, as well as the limitations, are discussed in GE Document No. 66SD4214, <u>Attitude Equations for the Applications Technology Satellite</u>, June 1, 1966.

2.2.1.1 Magnetic Errors

A source of attitude error at any altitude is the torque due to a residual magnetic dipole within the central body. Most spacecraft have electric circuits, ferromagnetic materials, etc., which combine to create a magnetic dipole moment. This dipole moment interacts with the earth's magnetic field and torques the spacecraft. The magnitude of the torque is a function of the spacecraft magnetic moment (orientation and magnitude) and the local value of the earth's magnetic field strength. The local value of the earth's magnetic field strength is, of course, dependent upon the location of the spacecraft within the magnetic field. The altitude, latitude and longitude of the spacecraft all change as the satellite revolves about the earth, and as the earth rotates. Hence, an accurate orbit model is required. At synchronous and near-synchronous altitudes, the magnetic field is distorted by the sun on both a continuous (solar wind effects) and intermittent (solar storms) basis. This distortion is a function primarily of the earth's position with respect to the sun. Hence, an accurate model of the geomagnetic field with solar effect modifications is required. These effects have all been considered in the Mathematical Model. The magnetic field model is described in GE Document No. 66SD4567, <u>Geomagnetic Field Simulation for the ATS</u>, March 15, 1967.

2.2.1.2 Orbit Effects

The satellite is assumed to be in orbit about the earth and changing position relative to the earth in accordance with orbit dynamics. In this connection, the secular precession of the

orbit line of apsides, and the secular regression of the orbit line of nodes is included in the calculation of spacecraft position. Orbital dynamics are assumed independent of the attitude motions, except for the effect of an eccentric orbit. The radius vector of an eccentric orbit does not rotate at a constant rate, and the variation in rate causes a gravity gradient torque to appear on the spacecraft pitch axis. For eccentricities up to about 0.1, the resulting errors are directly proportional to the magnitude of the eccentricity, being on the order of 1.2 degrees (pitch) per 0.01 eccentricity. The original version of the Math Model limited eccentricity to 0.1 for simplicity. After the troubles with ATS-A, however, the capability was expanded into the non-linear range of eccentricities up to about 0.5. It was then possible to demonstrate orbit-eccentricity-induced tumbling modes.

2.2.1.3 Solar Torque

A significant disturbance at high altitude is solar torque. The solar pressure of the sun creates a force on the spacecraft as long as the spacecraft is in sunlight. If this solar force vector does not pass through the system center of mass, a torque will appear. This solar torque is a function of satellite shape, rod and satellite reflectivity and orbit position relative to the sun. From the solar torque standpoint, the central body is represented as a cylinder divided into three sections with end effects considered. The gravity gradient rods may either be straight, as an option, or curved due to thermal bending. For a symmetrical spacecraft, the greatest source of solar torque are variations in gravity gradient rod reflectivity, central body reflectivity variations, center of mass offsets, etc. In addition, shadowing of the gravity gradient rods by the central body will cause solar torques. All of these factors, as well as modeling of the earth's umbra (no sunlight) and penumbra (reduced sunlight) are included in the Mathematical Model.

2.2.1.4 Thermal Bending

Thermal bending is a phenomenon associated with solar heating of gravity gradient rods. Heating of one side of the rod and cooling of the opposite side of the rod creates a temperature gradient across the rod diameter. The gradient causes the rod to bend because of differential thermal expansion, much like a bi-metallic strip. Thermal bending has three effects:

1.   It creates a solar torque because the symmetry of the vehicle is destroyed.

2.   It causes a shift in the center of mass.

3.   It rotates the principal axes.

The last effects are primarily the result of the tip mass being displaced by the bent rod, and are completely dependent on the nature of the gravity gradient rod. The Mathematical Model simulates, as realistically as possible the behavior of the open section, overlapped rods used on ATS. These are difficult rods to model, however, and simpler rods may be simulated for comparison runs by appropriate selection of input. The effect of movement of the center of mass as a result of thermal bending has been considered both in the solar torque calculation (along with the curved rod effect) and the stationkeeping torque.

2.2.1.5 Stationkeeping

The synchronous gravity-gradient stabilized ATS carries a thruster to act as a station-keeper. If the thrust vector does not pass through the spacecraft center of mass, the system will be torqued. Thermal bending will cause the center of mass to wander, but nominal misalignments of the gravity gradient rods, thruster misalignments, and uncertainty in the nominal center of mass will also cause the center of mass to be other than the predicted value. All of these effects can be included in the Mathematical Model.

2.2.1.6 Maneuvers

In addition to the external disturbance torques, several specialized spacecraft maneuvers must be simulated. The maneuver with the widest applicability is rod retraction and extension. The gravity gradient rods are extendible, and are stowed during launch. Deployment occurs shortly after separation from the booster on ATS-A and after spacecraft despin on ATS-D and E. During deployment, the moment of inertia of the spacecraft rapidly changes, and this change must be considered in order to determine the initial rates and positions for capture of the earth (i.e., the attainment of near orbital rate) and the ensuing transient. In addition, retraction of the rods followed by re-extension of the rods after a short wait has been used to invert a spacecraft that has stabilized upside down. The principle

of conservation of momentum is utilized. Retraction of the rods causes the vehicle to speed up its rate of rotation. When sufficient speed has been obtained, the spacecraft is allowed to coast until it is nearly rightside up. At this point the rods are re-extended. This re-extension captures the spacecraft in the correct attitude. The maneuver has been successfully demonstrated in orbit and can be simulated in the Mathematical Model. The Model can then be used to determine the inversion timing sequence. The Mathematical Model also contains the capability for simulating spacecraft inversion by application of thruster torques. The thrusters are mounted so that their thrust vectors do not pass through the system center of mass. The torque produced by each thruster is enough to invert the spacecraft. A retro thruster is provided to stop the vehicle after it has inverted. The rise and decay times of these thrusters are considered to be exponential. Another Math Model routine provides the capability for simulating performance before and after damper boom unclamping. During launch, the damper boom assembly is rigidly mounted to the spacecraft. After spacecraft deployment, the damper boom is uncaged and begins to operate. Before this uncaging, the spacecraft acts as a rigid body. The ability to perform this unclamping maneuver has been included in the Mathematical Model. Damping of the transient motion of the spacecraft after damper boom deployment is achieved either by rate damping (eddy current damper) or amplitude damping (hysteresis damper). The actual spacecraft can physically have only one damper engaged at a time, but in the Mathematical Model simultaneous combinations of both are possible.

2.2.2 EVALUATION PLAN

The ATS Mathematical Model was developed primarily for use in system design evaluation, but its potential value as an operational device for time extrapolation of attitude and performance data was an important element in plans for Math Model evaluation. The degree of correlation between measured satellite performance and predicted satellite performance was to have been the measure of success in the accomplishement of the Math Model goals. Unfortunately, poor correlation could have been obtained through no fault of the Math Model and carefully considered judgements would have been required at each step of the way to ensure that deviations labeled as being due to Math Model imperfections were real Math

Model imperfections and not simple errors in input. Measured satellite performance would have been represented by the output from GE's ATS Attitude Determination Program (ADP) and would have contained (as inherent measurement system inaccuracies) errors due to both hardware and software tolerances in the data loop from the spacecraft attitude sensors through spacecraft telemetry, ground recording and processing, to final computation of attitude. Predicted satellite performance would have been a direct output of the ATS Mathematical Model computer program but would have contained (as inherent performance prediction uncertainties) errors due to the inability to exactly simulate the spacecraft or its environment or to specify exact initial performance conditions. The combined effect of measurement system inaccuracies and performance prediction uncertainties would have influenced and modified the conclusions of the evaluation effort. To minimize differences due to these effects, predicted satellite performance was to have been based on a final set of performance predictions made after establishment of the orbit and measurement (via telemetry and attitude determination) of initial conditions associated with the various phases of the Orbital Operations Plan. If observed deviations between measured and predicted data had been judged to be attributable primarily to uncertainties in hardware parameters, initial conditions, or the effect of orbit eccentricity, a valid argument for verification of the Math Model system design evaluation capability could and would have been presented. On the other hand, if deviations were explainable only in terms of basic flaws in the mathematical modeling, recommendations for Math Model improvements and/or studies to delineate modification requirements would have been made. Specific correlation parameters for use in this endeavor were to be transient decay time and steady-state performance envelope. Transient decay time was defined as the time from a 30-degree or larger pitch displacement angle (negligible roll and yaw displacements) to steady-state. The steady-state performance envelope was defined to be a statement of pitch, roll, yaw and pointing angle bias and oxcillatory components encompassing the excursions of the respective axes for a period of three or more orbits.

As a secondary objective, the capabilities of the Math Model were to be examined in terms of the basic feasibility and accuracy of time extrapolation of attitude and performance data. The potential application to the problem of missing data (for example) was to be investigated

by generating Math Model extrapolations through an area of no data and comparing the continuance of predicted data with measured data in the next coverage period. If feasible, time-extrapolated attitude and performance data had application to the advanced planning of attitude sensitive experiments and/or operations. One of the criteria of feasibility for such applications was the sensitivity of time-extrapolated data to variations and/or uncertainties in the specification of Math Model initial conditions. The specific correlation parameters for use in this endeavor were:

1. Amplitude

2. Frequency

3. Phase shift.

Only steady-state conditions were to be considered and the sensitivity of initial conditions was to be established by a limited series of iterative runs, varying initial attitudes and rates over the range of prevailing uncertainties. This effort was to have continued only as long as engineering judgement suggested that reasonable progress towards an assessment of time extrapolation feasibility was being made.

The general task of Math Model evaluation required performance simulation runs and was organized on an experiment package basis to ensure compatibility between evaluation requirements and measured data availability. For example, evaluation of Math Model capability for prediction of initial capture performance would have awaited completion of all flight analysis associated with initial capture.

The sequence of tasks associated with each experiment package was as follows:

1. Establish requirements for the performance simulation run(s) necessary to the evaluation of Math Model capability in the experiment package category under consideration. This will be based primarily on a review of available measured data and will ensure the adequacy of measured data for a reasonable correlation effort with predicted data. The adequacy of data for specification of realistic initial conditions in performance simulation runs will also be considered.

2. Generate required performance simulation runs and plot results.

3. Extract from simulation runs and measured data listings or plots, the parameters for comparative evaluation.

4. Provide quantitative and/or qualitative assessment (as the data warrants) of the Math Model's applicability to the stated application goals.

Additional tasks associated with Math Model evaluation were an assessment of the validity of the thermal bending model (employed as a subroutine of the Math Model computer program) and an assessment of the validity of the assumption that boom dynamics can be safely considered as a separate and distinct phenomena in the simulation of spacecraft system performance. This latter assumption was to be examined, primarily, in terms of the presence or absence of "high" frequency (greater than 0.003 cycle/second) components in measured attitude data. Of special interest was data to be taken at entry and exit from solar eclipse regions for evaluation in conjunction with television data on dynamics of boom tip motion.

2.3 GRAVITY GRADIENT DATA SYSTEMS

2.3.1 "QUICK-LOOK" SYSTEM

The Quick-Look data system was established for the express purpose of providing a near-to-real-time data link between GE-Valley Forge, the ATS Operations Control Center (ATSOCC) at NASA/GSFC and the ATS ground stations. The basic intent of the system was to support operations at ATSOCC through a rapid determination of attitude performance and an assessment of gravity gradient system health. This was accomplished by utilizing the existing NASCOM teletype communications network and interfacing with the GE Desk Side Computer Service (DSCS) at GE-Penn Park. The general flow of data is illustrated in Figure 2.3-1. Data for action and/or information, GE/VFSTC, is originated at the appropriate ATS ground tracking station in response to requests from the ATS Operations Control Center (ATSOCC) at NASA/GSFC. Data messages are routed through the Communications Control Center at GSFC and may take either of two forms -- the form to be specified by ATSOCC at time of request: (1) the "GE Special" Message or (2) Gravity Gradient Class II data. The

TELEMETRY FROM SPACECRAFT

GROUND STATIONS

SDS 910

SDS 910

SDS 91(

NASA GSFC

NASCOM
490
SWITCHING AND
ROUTING COMPUTER

ATS
OPERATIONS
CONTROL CENTER

FULL DUPLEX NASCOM TERMINAL

GE DESK SIDE COMPUTER

GENERAL ELECTRIC COMPANY SPACE SYSTEMS (VALLEY FORGE, PA.)

DATA NET 30
HANDLING SYSTEM

GE 235 COMPUTER
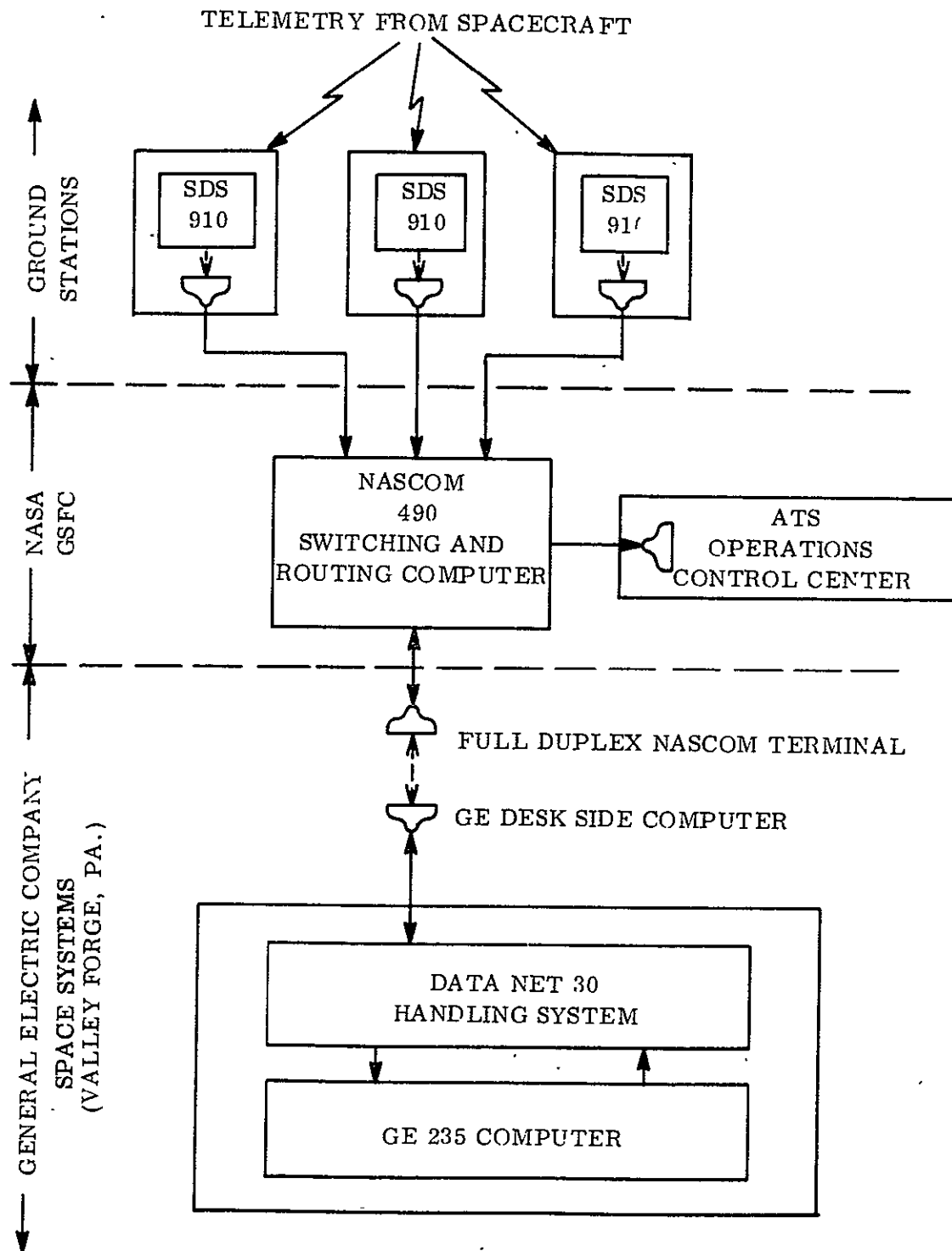
Figure 2.3-1.   Quick Look System Hardware Configuration

"GE Special" message required a response by GE as soon as possible after receipt. The Gravity Gradient Class II message was for information only and required no response. All quick-look data except POLANG was in octal format.

The "GE Special" Message contained the telemetry data necessary to the calculation of spacecraft attitude and included an antenna polarization word and X, Y data for antenna coordinate corrections when available. For consistency with TTY transmission rate constraints, only every third frame of available spacecraft telemetry data was actually sent. Thus, one complete data frame was to be received each 9 seconds, approximately, after initiation of special message transmission. No more than 5 orbit-minutes of data were to be sent in any given "burst." Upon notification by ATSOCC of a forthcoming GE special message, GE was to prepare for receipt. Following receipt of the special message, GE was to respond with a statement of gravity gradient attitude including computed values for PITCH, ROLL, YAW and GAMA. (GAMA was the angle of rotation of the damper boom.) If data smoothing was used (i.e., more than one frame of data per attitude point), both means and standard deviations of PITCH, ROLL, and YAW were to be provided. After sufficient accumulation of data, rates were to be derived manually from hand-plots and added to the quick-look attitude format.

Damper boom angles and rates were to be based on manual conversion and computation. The system was to provide one of the few techniques available for an early assessment of initial capture performance and would have proven invaluable during dynamic operations required by the Gravity Gradient Orbit Test Plan. It was to be used extensively as a means of verifying steady-state operation at completion and initiation of gravity gradient orbital experiments. It actually was used extensively on ATS-4 and ATS-5 in a manner not visualized before the launches. Quick modifications to a variety of peripheral deskside computer programs allowed direct support of ATSOCC operations in the determination of spacecraft spin attitude and rate using data from the gravity gradient system's solar aspect sensor. These activities are fully reported in the final flight reports referenced in Section 6.

The Gravity Gradient Class II Message consisted of three lines of 16 words each including most of the data pertinent to a gravity gradient status and/or "health" assessment. Class II messages are distinguished from Class I and Class III messages as follows:

Class I - Data displayed in real time at tracking stations

Class II - Data transmitted in real time to ATSOCC (by teletype)

Class III - Data recorded on magnetic tape for processing and shipment with no critical time requirement

The "GE Special" Message was also a Class II message but was referenced in a different manner because of its unique characterics and requirements. POLANG data, though not required in real time was transmitted as a Class II message. The Gravity Gradient Class II message was to be received by GE at each new ground station acquisition on ATS-A and once per orbit on ATS-D and E. Programs were developed at GE for the automatic conversion of the Gravity Gradient Class II data messages from actual data to engineering units.

2.3.2 "LONG-TERM" SYSTEM

The remainder of the GE data was handled as Class III data. All PCM data received at ATS ground stations was recorded on magnetic tape and shipped airmail to NASA/GSFC. The GE data was stripped and formatted, at GSFC, to produce the GE Raw Telemetry Data Tape (RTDT). POLANG data was provided GE on a GE-POLANG tape which was also produced at GSFC. These two tapes were 556 characters per inch, high density magnetic data tapes and were provided at weekly intervals for what was referred to as "long-term" data processing using the GE-developed Attitude Determination Program. The ATS Attitude Determination Program (ADP) is a generic title used to reference a group of large-scale digital computer programs developed for ATS attitude computations and smoothing; preliminary processing of "raw" PCM telemetry data and merger with data relative to spacecraft antenna polarization, reduction and computation of statistical parameters associated with diagnostic data, reduction and processing of data extracted from filmed television

pictures, production of data lists for selected gravity gradient telemetry functions, production of summary data reports, and finally the production of spacecraft attitude and raw data plots.

Along with the RTDT and POLANG tapes, GE was to receive the week's accumulation of developed TV data film strips. Figure 2.3-2 illustrates the procedure that was to be followed upon receipt of this data. The RTDT and POLANG tapes were first merged to produce two new tapes, the Telemetry Data Tape (TDT) and the Data Analysis Module Telemetry/POLANG tape (DAMTP). In the process of merging the RTDT and POLANG tapes, special data list reports, attitude sensor plots, and summary printouts were to be generated. This preliminary processing pass also converted all "raw" telemetry data into appropriate engineering units. The DAMTP was then to be used in the computation of spacecraft attitude and the subsequent production of attitude plots, the NASA Attitude Data Tape (NADT) and the GE Attitude Data Tape (GEADT). The NADT was to be transmitted
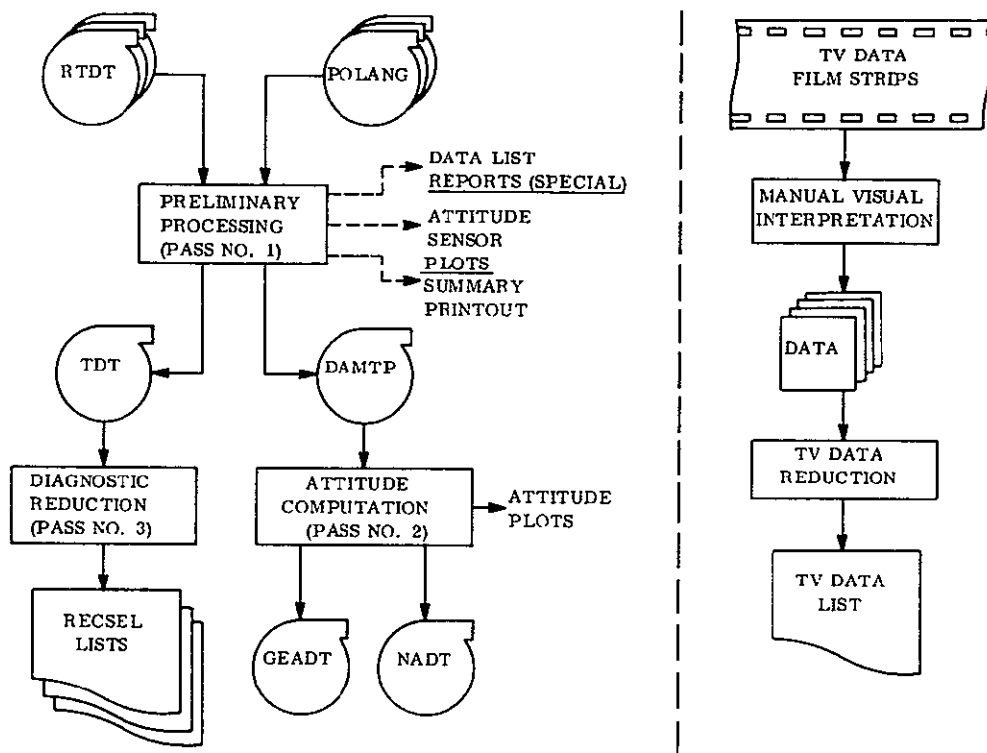
Figure 2.3-2. ATS Data System

to GSFC on a 24-hour turnaround basis. Computed values for spacecraft pitch, roll, yaw, body-axis rates and damper boom angle and rate were to be provided at 5-minute intervals. Data from the spacecraft sun sensors, earth IR sensors and antenna polarization measurements provided the necessary inputs for computation of these parameters. The GEADT was to contain data at 1-minute intervals for use in GE flight analysis activities.

The data provided NASA was to be incorporated into a NASA world map program for subsequent distribution to all ATS experimenters. It was from this data that the ATS experimenter would have obtained the time history of orbital position and attitude for his particular experiment. Following production of the NADT and GEADT, the TDT was to be utilized in the generation of summary reports providing event conditions, event levels, mean and standard deviations of selected functions, and point-by-point listings of selected functions. The television data was to be utilized in the evaluation of boom thermal bending and boom dynamics phenomena, as well as a separate and distinct method of computing spacecraft attitude. Plots of the NADT and/or GEADT were to be utilized in analyses associated with the verification of the ATS Mathematical Model. Needless to say, due to the successive failures to achieve an orbital condition compatible with the gravity gradient experiment requirements, there was no real opportunity to exercise or prove out the capabilities of these programs. Developmental efforts on the programs are fully reported in the references of Section 6 and a descriptive summary of the programs is contained in Section 4.

SECTION 3

SYSTEM ANALYSIS

SECTION 3

SYSTEM ANALYSIS

The stabilization subsystem for ATS A, D, and E, is a three-axis passive stabilization subsystem employing gravity gradient torques as control torques. The stabilization subsystem consists of six major components: two rod deployment mechanisms (each of which has two gravity gradient rods), a combination passive damper (including two secondary rod deployment mechanisms), two inversion thrusters, and a power control unit. Stabilization is provided by the four gravity gradient rods and their tip masses, with damping of the spacecraft provided by the combination passive damper. The performance of the stabilization subsystem is largely determined by the characteristics of these components. The inversion thrusters provide spacecraft inversion capability and the power control unit acts as an electronics interface between the attitude stabilization subsystem and the spacecraft's power, telemetry and command subsystems.

Selection of the stabilization subsystem parameters required analysis and optimization of the gravity gradient subsystem. This section describes the analyses and studies performed to select the spacecraft, determine its performance, and evaluate and select specialized maneuvers. Section 3.1 describes the fundamentals of gravity gradient stabilization and the logic behind the design. The equations of motion are not presented in detail; the discussion is primarily qualitative with only occasional use of basic equations to illustrate or emphasize. The complete equations are available in open literature and can also be found in the Attitude Equations for the Applications Technology Satellite, GE Document No. 66SD4214, 1 June 1966.

The general parameters which affect the spacecraft design and the general nature of the external torques are discussed in Section 3.2, and the procedure which was used to obtain the optimum spacecraft presented. Again, the discussion is primarily qualitative, with detailed analyses contained in the appendixes. Results of the analyses, particularly where they affect spacecraft selection are, of course, presented.

The analysis of capture (sometimes called acquisition) is presented in Section 3.3. Because capture involves large angular motions of the spacecraft, the equations of motion are transcendental and typically require computer simulation. Most of the results were obtained using a General Electric computer simulation, available at the start of the analysis, and the ATS Mathematical Model, a computer program developed for NASA by GE as a part of the ATS contract. The results of the simulations are typically presented as time histories of the motion of the spacecraft.

Section 3.4 contains inversion analyses of the spacecraft. A gravity gradient spacecraft is stable rightside up or upside down (Section 3.1) and ATS is required to be rightside up. Consequently, inversion maneuvers were developed and specified in the event of inverted capture. The maneuvers calculated were a rod retraction/extension inversion maneuver and a microthruster inversion maneuver. The evaluation was done both analytically and by computer simulation because spacecraft inversion is nonlinear in nature.

Section 3.5 contains performance estimates and error analyses of the actual spacecraft. These are used to predict pointing and stabilization capability as accurately as possible. Both analysis and simulation were employed.

Section 3.6 is a "catch-all" section containing analyses and studies performed for ATS, but not falling directly into any of the categories specified earlier. The individual analyses are contained under separate subheadings.

3.1 GRAVITY GRADIENT STABILIZATION THEORY

A gravitational field of a solid body is a conservative force field, and can be represented by a potential function of the form

$$V = -\frac{\mu M}{r} \qquad\qquad 3.1\text{-}1$$

where r is the distance from the center of the body, and μ is the gravitational constant and M is the mass of the body.

The gradient of the potential field is

$$\vec{f} = -\ \vec{\text{grad}}\ V = -\ \frac{\mu M}{r^2}\ \vec{r}_\mu \qquad\qquad\qquad 3.1\text{-}2$$

where $\vec{r}_\mu$ is the unit vector along a line radially away from the primary body, and $\vec{f}$ is the force per unit mass. The expression indicates that the force per unit mass acting on an object in the potential field is a function of distance from the origin and changes smoothly with the distance. Along a local radius (from the primary body), the differential force is

$$dF = 2\frac{\mu M}{r^3}\ dr \qquad\qquad\qquad 3.1\text{-}3$$

Hence, two identical point masses separated by even a small distance, dr, along the local radius will have slightly different gravitational forces. For a general analysis, Equation 3.1-2 is put in differential form by substituting $\dfrac{d\vec{F}}{dm}$ for $\vec{f}$

$$d\vec{F} = -\ \frac{\mu M}{r^2}\ dm\ \vec{r}_\mu \qquad\qquad\qquad 3.1\text{-}4$$

The gravity gradient torques are obtained from Equation 3.1-4 by calculating the differential torque about the spacecraft center of mass (caused by the force on the differential mass) and integrating over the entire mass.

The torques can be visualized by referring to Figure 3.1-1 which illustrates a spacecraft consisting of two point masses separated by a weightless rod (a dumbbell configuration). The center of mass of the spacecraft is at a distance r from the center of the earth, and each tip mass is a distance dr from the support. Assuming the gravity field to be parallel (not radial) and assuming dr is small compared to r, differential calculus may be applied and the differential force calculated. Because of the symmetry of the dumbbell, the sum of the differential forces is zero, but the torque about the center of mass is not.

Using the geometry of the vehicle, as shown in Figure 3.1-1, the torque for a parallel gravity field is calculated to be

$$T = \frac{4}{2} \left(\frac{K}{r^3} \right) (ml^2) \, \text{Sin } 2\theta \qquad\qquad 3.1\text{-}5$$

Where K = gravitational constant multiplied by the mass of the earth

m = tip mass

1 = half rod length

θ = angle between local vertical and the rod

For the configuration presented, $2\,ml^2$ is the moment of inertia of the dumbbell indicating a relationship between gravity gradient torque and moments of inertia. The exact gravity gradient torques must be calculated for a continuous body in a radial gravitational field, rather than a parallel field; but the torques are similarly dependent upon the moments of inertia of the spacecraft.

$$F \pm dF \approx \frac{KM}{r^2} - 2KM \, \frac{dr}{r^3}$$

$$\text{TOTAL FORCE} = 2F \approx \frac{2KM}{r^2}$$
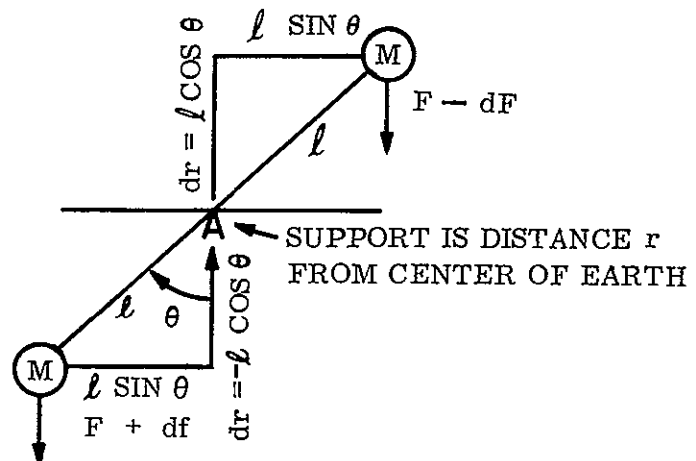
TOTAL TORQUE

$$T = (F + dF)\,l \, \text{SIN } \theta - (F - dF)\,l \, \text{SIN } \theta$$

$$T = 2\,(dF)\,l \, \text{SIN } \theta = 2l \, \text{SIN } \theta \left(\frac{-2KM}{r^3} \, (l \, \text{COS } \theta) \right)$$

$$T = -\frac{4}{2} \, \frac{K}{r^3} \, (Ml^2) \, \text{SIN } 2\theta$$

Figure 3.1-1. Origin of Gravity Gradient Torques

The direction of the exact gravity gradient torques is such that they tend to align the space-craft's axis of minimum moment of inertia with the local vertical, as indicated in Equation 3.1-5. For small departures from this orientation, the torques are proportional to the sine of the angle between the minimum axes of inertia and the local vertical, and to the differences in the moments of inertia.

The spacecraft coordinate system is shown in Figure 3.1-2, and the torque equations are shown in approximate form in Figure 3.1-3. Gravity gradient provides pitch and roll control torques, but there is no torque about yaw (for small angle motions of pitch and roll). Gravity gradient torques will not provide direct yaw control.

Yaw control is obtained for a gravity gradient stabilized spacecraft through dynamic coupling. With proper spacecraft configuration (and damping), pitch and roll control will be maintained and the axis of minimum moment of inertia of the spacecraft will orient to the local vertical at all times. The spacecraft will, therefore, make one rotation in inertial space for every
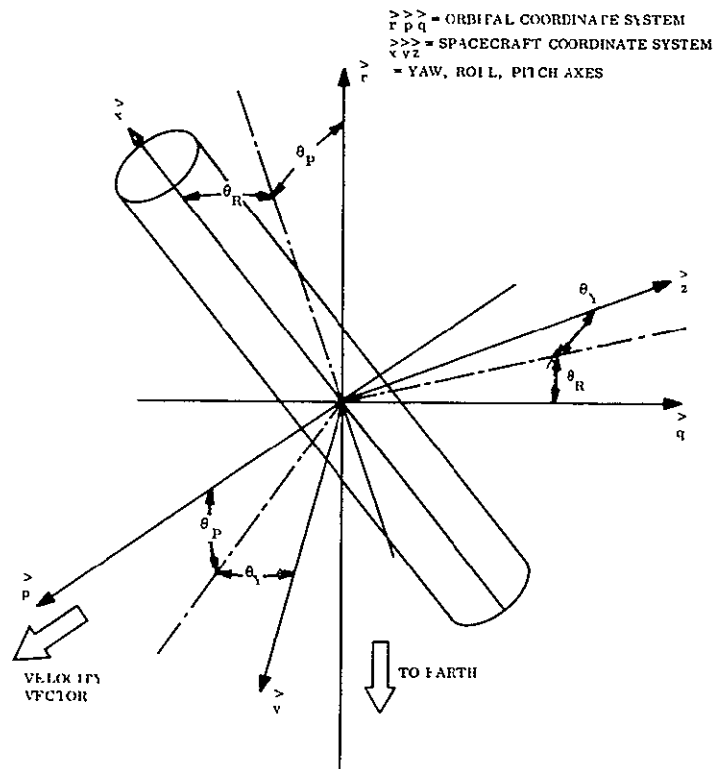
Figure 3.1-2. Spacecraft Coordinate System

$$T_P \approx \frac{3}{2} \frac{K}{r^3} (I_R - I_Y) \text{ SIN } 2\ \theta_P$$

$$T_R \approx \frac{3}{2} \frac{K}{r^3} (I_P - I_Y) \text{ SIN } 2\ \theta_R$$

$$T_Y \approx 0$$

I_R = SPACECRAFT ROLL MOMENT OF INERTIA

I_P = SPACECRAFT PITCH MOMENT OF INERTIA

I_Y = SPACECRAFT YAW MOMENT OF INERTIA

Figure 3.1-3. Simplified Gravity Gradient Torques

orbit revolution. This rotation is always about an axis normal to the orbit plane. Because the spacecraft is rotating at orbital rate, it will assume characteristics similar to those of a spinning spacecraft, and will prefer to spin about its axis of maximum moment of inertia. With effective pitch and roll control, the spacecraft is forced to spin about the normal to the orbit plane, and will therefore attempt to orient its axis of maximum moment of inertia with that axis. This preference provides the yaw control characteristics of three-axis gravity gradient stabilized spacecraft.

In addition to providing yaw control, dynamic coupling improves roll control, because the "preference" attempts to align a spacecraft axis (nominally the pitch axis) with the orbit normal which is two-axis control (roll-yaw).

The linearized equations of motion for a single rigid body spacecraft operating in a gravity gradient mode are shown in Figure 3.1-4 and derived in appendix A. The orbit is assumed to be nearly circular, and the parameter k is replaced by ω_o^2 (from orbit dynamic

$$
\begin{array}{lll}
\text{(1) YAW} & I_Y \ddot{\theta}_Y + & \boxed{\theta_R \omega_o (I_P - I_R - I_Y)} + \boxed{\omega_o^2 (I_P - I_R) \theta_Y} = \boxed{T_Y} \\[2mm]
\text{(2) ROLL} & I_R \ddot{\theta}_R + & \boxed{\dot{\theta}_Y \omega_o (I_R + I_Y - I_P)} + \boxed{4\omega_o^2 (I_P - I_Y) \theta_R} = \boxed{T_R} \\[2mm]
\text{(3) PITCH} & I_P \ddot{\theta}_P + & \boxed{} \quad \boxed{3\omega_o^2 (I_R - I_Y) \theta_P} = \boxed{T_P}
\end{array}
$$

COUPLING TORQUES — RESTORING TORQUE — DISTURBANCE TORQUES

LIMITATIONS ON MOMENT OF INERTIA

$$I_P \leq I_R + I_Y$$

Figure 3.1-4. Rigid Body Equations of Motion (Linearlized and Small Angles, Undamaged)

considerations) and added to Eulers dynamical equations. The equations of Figure 3.1-4 have been divided into four sets of terms. The first terms are the acceleration terms and need no further explanation. The second terms are the coupling torques which arise because of the rotation of spacecraft at orbital rate (i.e., one rotation per revolution). Note that a yaw term appears whenever the roll axis is moving and vice versa. As a consequence, sinusoidal oscillations in roll produce sinusoidal oscillations in yaw, even though there is no externally applied torque on yaw. Pitch, however, is not affected by, nor does it affect roll and yaw, and is said to be "decoupled."

The restoring torques, as mentioned earlier, are the combined gravity gradient and dynamical torques. Because the "gravity gradient torques" are linear with angular displacement, a gravity gradient spacecraft behaves as a spring mass system. The system will therefore oscillate under the influence of disturbance torques (the last set of terms in Figure 3.1-4). The magnitude of the oscillation is dependent upon the magnitude and frequency of

the disturbance torques, the natural frequencies of the spacecraft, and the damping characteristics of the spacecraft.

For stability and proper control, the momemts of inertia must have the relationship $I_p > I_R > I_y$. Thus, I_y must be the minimum moment of inertia and will orient along the local vertical. Similarly I_p must be the maximum moment of inertia, and will orient along the orbit normal. These observations are, of course, obvious from discussions presented earlier.

To obtain good pointing accuracy, it is necessary to obtain the proper relationship of all the factors. Typically, this requires low disturbance torques and large restoring torques. The restoring torques are made large by providing the spacecraft with large amounts moments of inertia. Even with large moments of inertia, however, the orienting torques are extremely small. At 500 nm (altitude) for example, a spacecraft with $I_p = 1000$ slug-ft^2, $I_r = 900$ slug-ft^2, and $I_y = 200$ slug-ft^2, will have a torque on the pitch axis of 3.57×10^{-5} lb-ft for a 1 degree attitude error. At higher altitudes, the gravity gradient torques are even smaller because the torques are proportional to the inverse cube of the orbit radius (or the square of the orbital rate). At synchronous altitude, for example, the gravity gradient torque is reduced by a factor of nearly 200 below that obtained at 500 nm.

As indicated by the equations in Figure 3.1-4, the restoring torques are not all equal. Roll has the highest coefficient (four) in the equations, and because pitch has the largest moment of inertia, and yaw the smallest, the difference of the two will be greater than any of the other moment of inertia differences. The result is that roll has the largest restoring torque.

The smallest restoring torque is on yaw, which has one as a coefficient, and depends upon the difference between the largest and intermediate (roll) moment of inertia. Because of natural physical constraints, the maximum difference between pitch and roll is the yaw moment of inertia itself (this type configuration is defined as a planar configuration). A quick perusal of the equations indicates that if the vehicle were a planar configuration, the coupling terms would vanish, and the roll and yaw restoring torques would be maximized.

However, a calculation of the natural frequencies shows that under these conditions, the yaw axis has a natural frequency of orbital. Since yaw is forced by a large number of orbital frequency external torques, the resonant condition would cause large oscillations, rendering the satellite useless. To avoid this condition, the difference between the pitch and roll moments of inertia is made to be less than yaw which "detunes" the axis, but reduces its strength. In general, it is more difficult to obtain good performance on the yaw axis than any other axis.

Adjusting the natural frequencies of the spacecraft is another approach to improving the performance of the spacecraft. The spacecraft behaves as a three-axis spring mass system, and has three natural frequencies. Because the disturbance torques which cause pointing errors typically occur at frequencies which are harmonics of orbital, resonant conditions on the spacecraft can be avoided only if the spacecraft natural frequencies are not integral values of orbital frequency. Hence the moment of inertia relationships of the spacecraft must be selected to provide non-integral values of natural frequency.

The natural frequencies of the spacecraft are constrained, however, by the moment of inertia relationships discussed earlier and fall within very narrow limits. These limits can be approximately determined from the equations in Figure 3.1-4 by applying

$$\omega_n = \sqrt{\frac{K}{I}}$$

where K = spring restoring torque

I = moment of inertia

Using this equation, the absolute moments of inertia disappear and the frequencies become dependent only upon moment of inertia relationships and orbital rate. From the physical limitations on moments of inertia (indicated on Figure 3.1-4), the pitch natural frequency is equal to or less than $3\omega_o$, the roll natural frequency is equal to or less than $2\omega_o$, and the yaw natural frequency is equal or less than ω_o.

A third way of obtaining good overall pointing accuracy is to reduce the magnitude of the external torques. The nature of the disturbance torques, as well as the methods of reducing their magnitude is discussed in Section 3.2.2.1. In general, minimization of the external torques is essential for good pointing accuracy, and is practiced during the design phase of most gravity gradient spacecraft.

The remaining parameter to be determined is the damping parameter. The achievement of this damping defines the gravity gradient configuration. The damping approach which has been favored by a large number of agencies is "dividing" the spacecraft into several bodies, hinged with respect to each other through a spring and damper. The underlying principle of operation of these "multi-body" configurations is to make each body gravity gradient controlled, but adjust the frequencies so that each body has a different frequency (within the limits of gravity gradient natural frequencies). By damping the relative motion between the bodies, the stabilization subsystem as a whole is damped.

There are several multi-body gravity gradient stabilization subsystems in operation, all of which have the same general characteristics and design approaches. The orientation of the spacecraft, for example, is determined by the principal moments of inertia of the combined bodies when they are in the nominal position. Therefore, it is possible to utilize the gravity gradient torques of all the bodies for stabilization and control. All the bodies are controlled by gravity gradient, but one (or more) of the secondary bodies (i.e., the bodies which do not contain the spacecraft and payload) is usually placed in the unstable gravity gradient equilibrium and stabilized by a spring. The spring is sized to induce large secondary body oscillations for small primary body oscillations, thereby damping the complete system rapidly. Too "stiff" a spring or damper would cause the system to "lock up" and prevent good system damping. A light spring would be unstable (because of gravity gradient), and light damping would require a long time for the system to damp. Part of the design study for these vehicles is to select the proper spring and damper.

The gravity gradient stabilization subsystem of ATS-A, D, and E spacecraft is of the multi-body type, but consists of only two bodies. The configuration is shown in Figure 3.1-5, and
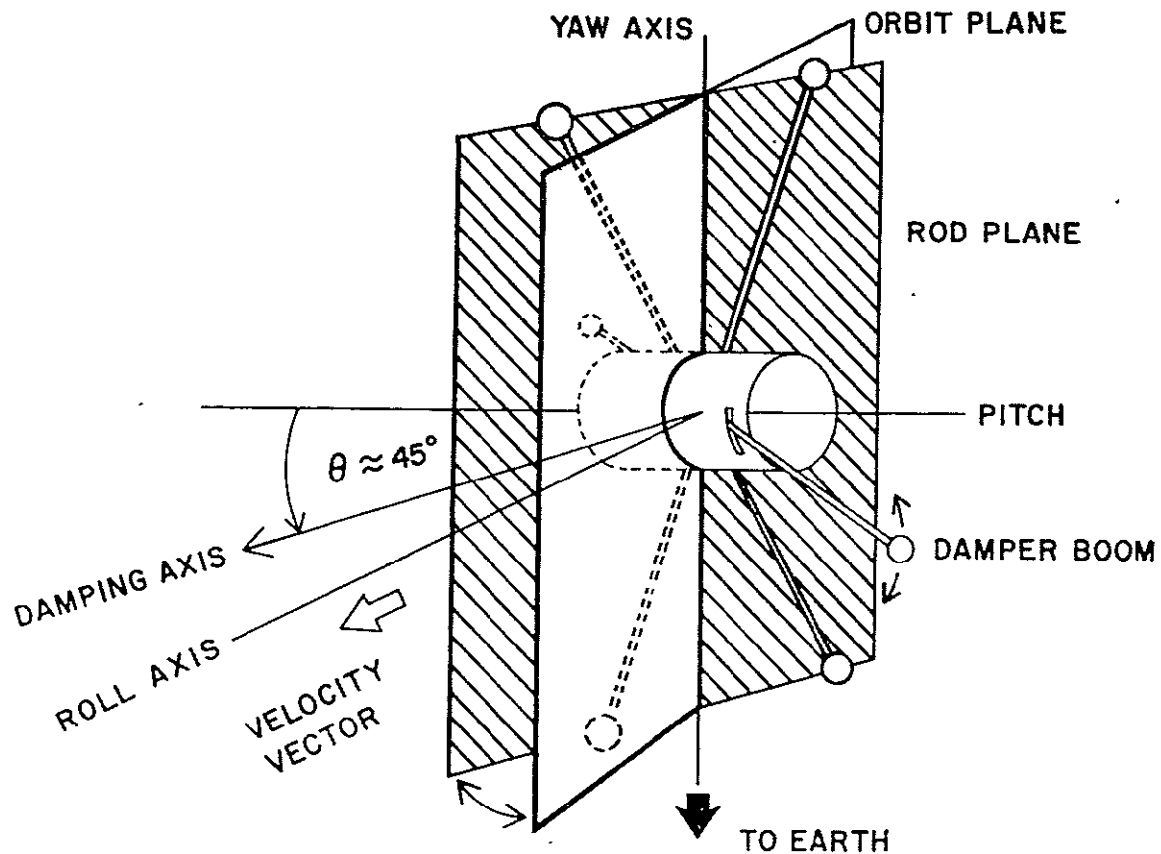
Figure 3.1-5. ATS Configuration

the optimization of the design is discussed in Section 3.2. Basically, the primary body provides the majority of the orienting torques for control, and the secondary body provides damping and assists in adjusting the spacecraft natural frequency.

One facet of gravity gradient stabilization which must be mentioned is the uncertainty associated with nominal orientation. Because moments of inertia have an axis but no direction (i.e., they are not vectors), the spacecraft can be rotated 180 degrees in any direction without altering the torques. Consequently, the vehicle is bi-stable and may orient rightside up or upside down, and forwards or backwards. Because rightside up orientation is required for ATS, inversion maneuvers must be performed or some method of assuring rightside up capture used. The methods are discussed in Section 3.4.

3.2 DESIGN OPTIMIZATION

Optimization of the Applications Technology Satellite gravity gradient stabilization subsystem was performed in two distinct phases:

1. Optimization of the transient damping characteristics

2. Optimization of the steady state performance

Ideally, only one optimization, which simultaneously optimizes steady state performance and transient damping, should be required, but such an optimization appears to be beyond the state of the art, and was well beyond the scope of the optimization analysis performed for ATS. Consequently, the optimization was performed in two stages.

3.2.1 OPTIMIZATION FOR MAXIMUM DAMPING

The Applications Technology Satellite gravity gradient stabilization subsystem is shown in general form in Figure 3.1-5. It consists of a primary body, with three different moments of inertia to which the spacecraft proper (central body) is attached, and secondary body consisting largely of two gravity gradient rods and tip masses rigidly connected to each other. The secondary body is spring mounted, with rate damping, to the primary body. The secondary body (also called the damper boom) is free to pivot about one axis (the damping axis) which is perpendicular to the damper boom and nominally in the horizontal plane. It is constrained to follow the spacecraft in the other two axes.

The orientation of the damping axis with respect to the primary body was selected to provide damping in all three spacecraft axes. To do this with a single-axis damper, the damping axis must be oriented such that the damper boom is sensitive to primary body motions about the pitch and roll or yaw axes. Roll and yaw are dynamically coupled (as discussed for a rigid body in Section 3.1) and damping of one axis automatically damps the other. Pitch, however, is decoupled from the roll and yaw axes, and must be damped separately. The approach taken, as indicated in Figure 3.1-5. was to position the damping axis of the secondary body at an angle to the pitch axis of the spacecraft so that components of the damping torque appeared on both pitch and roll. Consequently, both axes are damped and the yaw axis is damped through dynamic coupling.

"Skewing" of the damping axis provides complete subsystem damping but changes the dynamics of the stabilization subsystem and couples all axes. Motion of the primary body in pitch is "sensed" by the damper boom which reacts to motion. In responding to the pitch motion, the damper couples its motion into the roll and yaw axes, and causes them to oscillate. As a consequence, oscillations on any axis are sensed by every other axis, and they respond as a function of their coupling "gains." Oscillations of the damper due to external torques applied directly to the damper also excite the spacecraft. Hence, analysis of the ATS gravity gradient subsystem requires that all axes, including the "damping axis," be analyzed simultaneously. The original optimization on the ATS type configuration was performed and published by B. Tinling and V. Merrick of NASA/Ames. Subsequent analyses by General Electric confirmed their results.

Optimization for maximum damping is a mathematical technique which makes use of the linearized (in this case) equations of motion. The ATS stabilization subsystem consists fundamentally of two bodies each of which has three degrees of freedom (maximum). Translation of the center of mass of the spacecraft and secondary body is ignored in this type analysis and the three "extra" degrees of freedom associated with translation can be ignored. Each rotational degree of freedom requires a second order differential equation, and initially there are six equations. The damper boom is constrained in two axes on the spacecraft, however, and by using the equations of constraint, assuming a rigid connection to the spacecraft in two axes, two of the equations can be eliminated. Hence, only four dynamic equations of motion need be considered. These equations linearized for small angles are derived in Appendix B and shown in Figure 3.2-1, and the coordinate systems are shown in Figure 3.1-2.

Solution to these equations is straightforward, but because of the number (four) and order (i.e., second) it cannot be solved in general form. Hence, numerical techniques are required. The problem is essentially an eigenvalue problem which can be solved easily on a digital computer. Since there are four second order equations, there will be eight eigenvalues. In general, the eigenvalues will be four sets of complex conjugates which correspond to the natural frequencies and time constants of the stabilization subsystem. The time constant of particular concern in the optimization procedure is the longest one, since oscillations which have this time constant will persist after the other oscillation modes have disappeared. It

is necessary to identify this mode (numerically) and adjust the spacecraft parameters in order to reduce this time constant to the lowest possible value. The numerical approach is usually to obtain the partial derivatives of the longest time constant with respect to the subsystem parameters, and change the parameters in the direction to cause the greatest change in time constant (the method of steepest descent). When the partial derivatives are zero, the optimum has been reached.

For the ATS analysis, optimums can be reached without the partial derivatives being zero. The parameter being optimized is the longest time constant, which is a parameter defined in terms of the problem, not a specific mathematical parameter.

As a consequence, the longest time constant is not associated with any one particular frequency. Hence, at one point in the optimization, the longest time constant may be associated with one frequency, and at a different point with another frequency. Therefore it is possible to obtain an optimum damping which is a "spike" due to the longest time constant changing frequency. A generalized presentation of a spike is shown in Figure 3.2-2. The difficulty with this spike type of optimum is the sensitivity of the damping time constant to variations in subsystem parameters. The actual ATS gravity gradient stabilization subsystem has this type optimum.

The number of spacecraft parameters which must be varied in order to obtain an optimum is seven; the pitch, roll and yaw moments of inertia of the primary body, the moment of inertia of the damper boom, the orientation of the damping axis, the spring constant, and the damping coefficient. It is possible to nondimensionalize the parameters to six, however, as shown in Figure 3.2-3. This makes the results useful for all altitudes, and removes the absolute moment of inertia from the problem.

The nature of the configurations under consideration allows one additional parameter to be removed in the final optimization analysis. The moment of inertia of the ATS spacecraft proper is small compared to the moment of inertia of the deployed stabilization subsystem. Because all four primary rods are in the same plane, the configuration is essentially planar, and the relationship
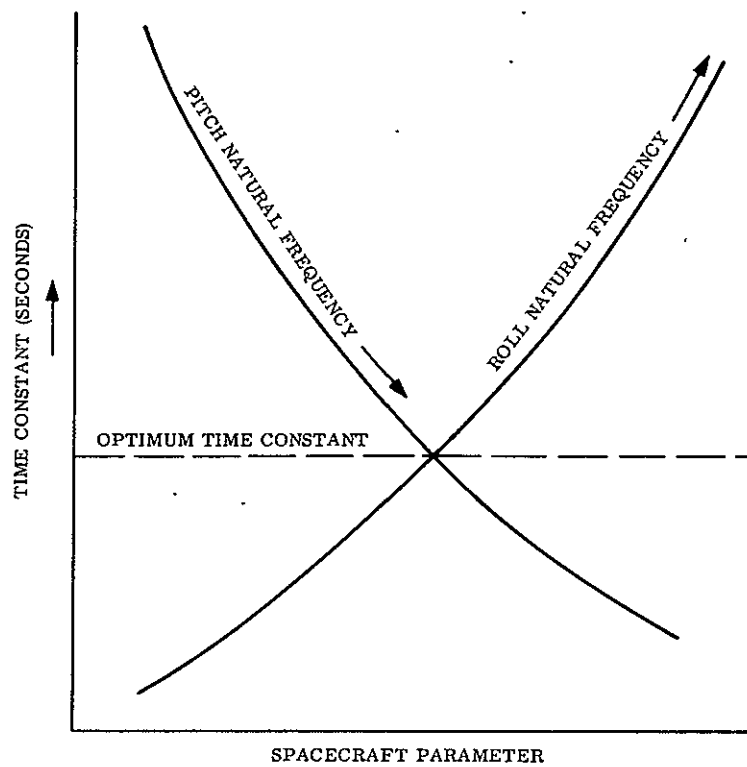
Figure 3.2-2. "Spike" Optimum, Generalized Representation

PARAMETERS TO BE OPTIMIZED

I_P b (DAMPING CONSTANT)

I_R K (SPRING CONSTANT)

I_Y ϕ (ANGLE BETWEEN PRIMARY AND
          SECONDARY BODY)

I_D

NON-DIMENSIONAL PARAMETERS

$$\frac{I_D}{I_P}, \ \frac{I_R}{I_P}, \ \frac{I_Y}{I_P}, \ \frac{b}{I_D \omega_O}, \ \frac{K}{I_D \omega_O^2}, \ \phi$$

Figure 3.2-3. Optimization Parameters

$$I_Y = I_P - I_R \qquad\qquad . \; 3.2\text{-}1$$

is reached. Rearranging,

$$\frac{I_Y}{I_P} = 1 - \frac{I_R}{I_P} \qquad\qquad 3.2\text{-}2$$

As a convenience in the nondimensionalization, the half angle between the yaw axis and the rod axis (symmetry is assumed for the rods), denoted as ξ, was selected. With this parameter

$$\frac{I_Y}{I_P} = \mathrm{Sin}^2 \, \xi \qquad\qquad 3.2\text{-}3$$

$$\frac{I_R}{I_P} = \mathrm{Cos}^2 \, \xi \qquad\qquad 3.2\text{-}4$$

The angle ξ is the physical mounting angle of the rods. Note that for a rigid body, this arrangement would be resonant in yaw at orbital frequency, as discussed in Section 3.1. The presence of the damper and damper boom alters the yaw natural frequency, however, and prevents the resonance from occurring.

Optimization performed strictly on the basis of damping would be performed by allowing all six parameters to be varied. Configurations derived in this manner, however, typically exhbit very poor steady state performance and are generally unsatisfactory from an overall performance standpoint. As a consequence, optimization of subsystem damping must be performed with some knowledge of the steady state characteristics · and restrictions on specific parameters of the proposed configuration. For the ATS damping optimization, this was achieved by selecting a standard configuration (rod lengths, tip masses, etc.), and a standard set of disturbances (see Section 3.2.2.1) for each "damping configuration" and

simulating the performance of the spacecraft. The simulation was a GE digital computer program developed for simulating gravity gradient stabilized spacecraft. The standard values used for the simulation are shown in Table 3.2-1 and were developed jointly by GE and Ames Research Center.

Table 3.2-1. Standard Configuration Values

1. The magnetic dipole (Section 3.2.2.1.1) of the spacecraft is assumed to be 1,000 pole centimeters located along the spacecraft roll axis.

2. The center of solar pressure/center of mass offset (see Section 3.2.2.1.2) of the entire spacecraft assuming the basic rod straightness tolerances (due to manufacturing only) will be within a 1-inch radius circle of uncertainty. (Assume rigid body.)

3. The center of mass/center of thrust misalignment will be assumed to be 1/2-inch and the stationkeeping thruster (see Section 3.2.2.1.5) will have a continuous thrust of $1/2 \times 10^{-5}$ pounds.

4. NASA will use a thermal bending (see Section 3.2.2.1.3) radius of curvature of 1,825 feet. GE will continue to input basic rod parameters into their computer program, with an absorptivity (α) of 0.15.

5. The present nominal ATS configuration will be used with the 100-foot primary rods and 2.5 pound tip weights for the ATS-A and 10.0-pound tip weights for ATS-D/E. The diameter of the primary rods is 0.500 ± 0.020 inch, and weighs 0.01565 pound/foot.

6. The present nominal damper rod length is 45-feet, root to tip, with 1.9-pound tip weights for ATS-A and 7.15-pound tip weights for ATS-D/E. For the optimization study the 45-foot length will be considered as fixed, and the minimum tip weight will be 1.1 pounds each. If the damper boom moment of inertia had to be reduced further than the above minimums, the boom length would be changed. The nominal damper rod diameter is 0.560 ± 0.020-inch, and weighs 0.01565 pound/foot. The radius of curvature of the damper boom is 1630 feet. The damping axis will be assumed to pass through the center of mass of the spacecraft, and the distance from the damper boom center line to the spacecraft center or mass is 30.2 inches.

7. The orbit eccentricity (see Section 3.2.2.1.4) for the ATS-A satellite is considered to be 0.01.

As a starting point in the optimization, the configuration originally developed by Tinling and Merrick and suggested by NASA/Goddard was selected. The nondimensional parameters of this system are shown in Table 3.2-2 and the standard "dimensional" parameters are shown in Table 3.2-1. The results of simulations and analyses using these parameters were combined into an error budget which is shown for ATS-A in Table 3.2-3, and ATS-D on Table 3.2-4. For convenience, the error sources have been broken down into bias errors and oscillation errors. Bias errors are those which are relatively fixed in time and do not change appreciably in one orbit. Sinusoidal errors are those which are sinusoidal at near orbital frequencies, and the peak amplitudes are shown on the table irrespective of the presence of multiple frequencies. Direct addition of the two error types should produce a complete error estimate. The total error shown in the chart was obtained by computer simulation with the torques phased to produce the worst attitude errors. Combining the individual errors to produce an overall error estimate is also a method of calculating total error, but the manner in which the errors should be combined is uncertain. Direct addition is one possibility, as is root sum squaring, or possibly a combination of the two. From the Table, it is not obvious, however, that either of these approaches would have produced the same results as the computer simulation which included all the disturbance torques.

From the error budgets, it is evident that ATS-A has different problems than ATS-D, and the error breakdowns are much different. The difference in orbit altitude (6,000 nm for ATS-A versus synchronous for ATS-D) and the stationkeeping requirement on ATS-D are largely responsible for the performance differences. Ideally, the subsystem should be optimized for each altitude, but a "commonality" requirement was placed on the spacecraft and a set of nondimensional parameters adequate for both spaecraft was required.

The primary difficulty with the configuration shown in Tables 3.2-3 and 3.2-4 was the stationkeeping error on ATS-D. To reduce this error, it was necessary to increase the stiffness of the yaw axis, which is done (in this case) by decreasing the roll moment of inertia. Hence the parameter ξ, which affects the roll to pitch moment of inertia ratio had to be increased. Several larger values of ξ were selected and additional optimum damping configurations obtained both by GE and Ames Research Center. Their steady state performance was

evaluated using the standard configuration. The configuration which indicated the best over-all performance was obtained by Ames Research Center. The non-dimensional parameters for this configuration are shown in Table 3.2-5 and the error budgets are shown in Tables 3.2-6 and 3.2-7 for ATS-A and ATS-D, respectively.

Table 3.2-2. Non-Dimensional Parameters for Initial Configuration

$$\frac{I_p}{I_R} = 1.08$$

$$\frac{I_Y}{I_R} = 0.08$$

$$\frac{I_D}{I_R} = 1.12$$

$$\frac{b}{I_D \omega_o} = 1.5455$$

$$\frac{k}{I_D \omega_o^2} = 4.538$$

$$\phi = 62.6$$

where:

I_p, I_R, I_Y = Pitch, roll and yaw moments of inertia of the X-booms about their own coordinate system – slug-ft^2

I_D = Damper boom moment of inertia about the damper axis – slug-ft^2

b = Damping constant – lb-sec

k = Damper spring constant –lb-ft/rad

ϕ = Angle between the nominal damper boom position and the plane of the X-booms

ω_o = Orbital rate – rad/sec

Table 3.2-3. Performance Comparison Chart, GSFC Configuration, ATS-A

APPLICATIONS TECHNOLOGY SATELLITE

GSFC CONFIGURATION ATS - A	SUN 28° TO ORBIT PLANE						Sun in Orbit Plane					
	Pitch		Roll		Yaw		Pitch		Roll		Yaw	
	Bias	Osc	Bias	Osc	Bias	Osc	Bias	Osc	Bias	Osc	Bias	Osc
Thermal Bending and Rod Solar Torque	0	0.3	0	0.4	0.4	0.4	0	0.3	0	0.3	0.4	0.3
Magnetics	0	0.3	0	0	1.9	0.7	0	0.3	0	0	1.9	0.7
Central Body Solar Torque												
Eccentricity	0	1.1	0	0.1	0.5	2.3	0	1.1	0	0.1	0.5	2.3
Rod Alignment	0.2	0	0.2	0	0.4	0	0.2	0	0.2	0	0.4	0
Curved Booms												
Principal Axis Shift	0.2	0	0.2	0	0.5	0	0.2	0	0.2	0	0.5	0
Solar Torque	0	0	0	0	0	0.1	0	0	0	0	0	0.1
Total Performance	0.1	1.0	0	0.4	3.1	2.4	0.2	1.2	0	0.2	3.1	3.0

$b/I_D \omega_o$	$k/I_D \omega_o^2$	I_Y/I_R	I_D/I_R	ϕ	α	δ	ξ
1.5455	4.5379	.12	.08	62.62	41.87	20.75	19

X Rods

Damper Boom

α δ ϕ

Table 3.2-4. Performance Comparison Chart, GSFC Configuration, ATS-D

APPLICATIONS TECHNOLOGY SATELLITE

GSFC CONFIGURATION ATS-D	SUM 23.45° TO ORBIT PLANE						Sun in Orbit Plane					
	Pitch		Roll		Yaw		Pitch		Roll		Yaw	
	Bias	Osc	Bias	Osc	Bias	Osc	Bias	Osc	Bias	Osc	Bias	Osc
Thermal Bending and Rod Solar Torque												
Magnetics	0	0	0	0	0.3	0	0	0	0	0	0.3	0
Central Body Solar Torque	0	0	0	0.1	0.1	0.2						
Rod Alignment	0.2	0	0.2	0	0.4	0	0.2	0	0.2	0	0.4	0
Curved Booms												
Principal Axis Shift	0.2	0	0.2	0	0.5	0	0.2	0	0.2	0	0.5	0
Solar Torque	0	0.1	0	0.1	0.6	0.2	0	0.1	0	0.1	0	0.4
Total Performance												
Without Thruster	0.2	0.9	0	1.0	0.7	2.5	0.2	1.1	0	1.1	0.6	3 8
With Pulsed Thruster	0.3	1.8	0.2	1.6	7.2	12.6	0	1.5	0.2	1.1	4.3	2.0
With Constant Thruster	0.1	1.1	0	0.9	6.9	1.2	0.1	1.2	0	1.1	2.3	2.8

$b/I_D \omega'_o$	$K/I_D \omega_o$	I_Y/I_R	I_D/I_R	ϕ	α	δ	ξ
1.5455	4.5379	0.08	0.12	62.62	41.87	20.75	19

X Rods

Damper Boom
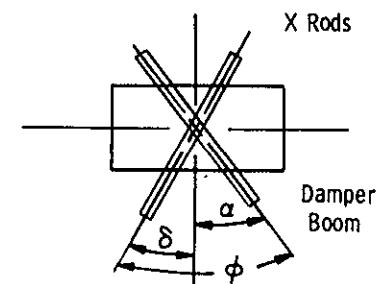
Table 3.2-5. Non-Dimensional Parameters for Optimum Configuration

$$\frac{I_p}{I_R} = 1.2308$$

$$\frac{I_Y}{I_R} = 0.2308$$

$$\frac{I_D}{I_R} = 0.04$$

$$\frac{b}{I_D \omega_o} = 1.0588$$

$$\frac{k}{I_D \omega_o^2} = 5.1504$$

$$\phi = 58.2^o$$

There is a larger pitch error on ATS-A with the new configuration than with the old, but the yaw improvement for ATS-D was felt to more than compensate for the slight ATS-A degradation. The non-dimensional paramters shown on Table 3.2-5 were therefore taken for the nominal configuration.

3.2.2 OPTIMIZATION FOR STEADY STATE

It was pointed out in Section 3.1 that a gravity gradient subsystem behaves as a spring mass system, and responds to external torques by oscillating at an amplitude dependent upon the frequency and magnitude of the external torques. The absolute magnitude of the external torques is of less importance than the magnitude of these torques compared to the magnitude of the gravity gradient torques. From the nondimensionalization procedure of Section 3.2.1, used to facilitate optimization, a nondimensional torque term appears in the form

$$T/I_p \omega_o^2 \qquad\qquad\qquad\qquad 3.2-5$$

Table 3.2-6. Performance Comparison Chart, Optimum Configuration, ATS-A

APPLICATIONS TECHNOLOGY SATELLITE

TM-2 CONFIGURATION ATS-A	SUN 28° TO ORBIT PLANE						Sun in Orbit Plane					
	Pitch		Roll		Yaw		Pitch		Roll		Yaw	
	Bias	Osc	Bias	Osc	Bias	Osc	Bias	Osc	Bias	Osc	Bias	Osc
Thermal Bending and Rod Solar Torque							0	0.4	0	0.2	0.1	0.7
Magnetics	0	0.3	0	0	1.0	0.7	0	0.3	0	0	1.0	0.7
Central Body Solar Torque												
Eccentricity	0	1.5	0	0.1	0	2.0	0	1.5	0	0.1	0	2.0
Rod Alignment	0.2	0	0.2	0	0.4	0	0.2	0	0.2	0	0.4	0
Curved Booms												
Principal Axis Shift	0.2	0	0.2	0	0.5	0	0 2	0	0.2	0	0.5	0
Solar Torque	0	0	0	0	0	0.1	0	0	0	0	0	0.1
Total Performance	0	2.0	0	0.2	1.0	2.5	0.1	1.9	0	0.4	1.1	3.3

$b/I_D\omega_o$	$K/I_D\omega_o$	I_Y/I_R	I_D/I_R	ϕ	α	δ	ξ
1.0588	5.1504	0.2308	0.04	58.2	53.4	4.8	25.65

Table 3.2-7. Performance Comparison Chart, Optimum Configuration, ATS-D

APPLICATIONS TECHNOLOGY SATELLITE

TM-2 CONFIGURATION ATS-D	SUN 23.45° TO ORBIT PLANE						Sun in Orbit Plane					
	Pitch		Roll		Yaw		Pitch		Roll		Yaw	
	Bias	Osc	Bias	Osc	Bias	Osc	Bias	Osc	Bias	Osc	Bias	Osc
Thermal Bending and Rod Solar Torque	0	1.0	0	0.7	0.3	1.6	0.1	1.0	0	1.1	0.4	3.6
Magnetics	0	0	0	0	0.4	0	0	0	0	0	0.4	0
Central Body Solar Torque												
Rod Alignment	0.2	0	0 2	0	0.4	0	0.2	0	0.2	0	0.4	0
Curved Booms												
Principal Axis Shift	0.2	0	0.2	0	0.5	0	0.2	0	0.2	0	0.5	0
Solar Torque	0	0.1	0	0.1	0.3	0.3	0	0.1	0	0.1	0	0.4
Total Performance												
Without Thruster	0	1.4	0	0.5	0.4	1.1	0.1	1 4	0	0.8	0.4	2.5
With Pulsed Thruster												
With Constant Thruster	0	1.3	0	0 7	3.7	1.2	0	1.3	0	0.9	1.7	2.9

$b/I_D\omega_o$	$K/I_D\omega_o^2$	I_Y/I_R	I_D/I_R	ϕ	α	δ	ξ
1 0588	5 1504	0.04	0.2308	58.2	53.4	4 8	25.65

X Rods

Damper Boom

3-27

where

T = any external torque

I_p = pitch moment of inertia

ω_o = orbital rate

Hence, the attitude error is proportional to the ratio of the external torques to the pitch moment of inertia (or any other convenient moment of inertia). The frequency of the disturbance torque is also of importance, because the gravity gradient subsystem has gains which are dependent upon frequency. The gain can be found from the linear equations of motion by rewriting them in operator notation (or Laplace notation with no initiation conditions) and using Cramers rule to solve for the variable. By substituting frequencies in the form of $j\omega$, the gain and phase at a particular frequency can be determined. Because the ATS gravity gradient subsystem is coupled in all axes (see Section 3.2.1) a torque about one axis will produce errors in all axes; hence, there will be four outputs (pitch, roll, yaw and damper) for every input. Figures 3.2-4, 3.2-5, 3.2-6 and 3.2-7 show these outputs as a function of frequency for torques applied on each axis. For convencience, the non-dimensional torque terms contain the moment of inertia of the axis being torqued.

Once the frequency response of the subsystem has been determined, the equations indicate that by increasing the moment of inertia of the spacecraft any desired pointing accuracy can be achieved. Although this is true in general, the approach assumes that the disturbance torques are unaffected by the manner in which the required gravity gradient configuration is achieved. For the Application's Technology Satellite, whose moment of inertia is inadequate for gravity gradient control, the required moments of inertia are achieved by the use of long rods and tip masses. The rods are extendable and are generally known as gravity gradient rods because they are used extensively in the design of gravity gradient subsystems. The rods and tip masses do provide the required moments of inertia, but also introduce disturbance torques, particularly solar torque (Section 3.2.2.1.2) and thermal bending (Section 3.2.2.1.3). Hence, an optimization study is required to determine the best combination of rod length and
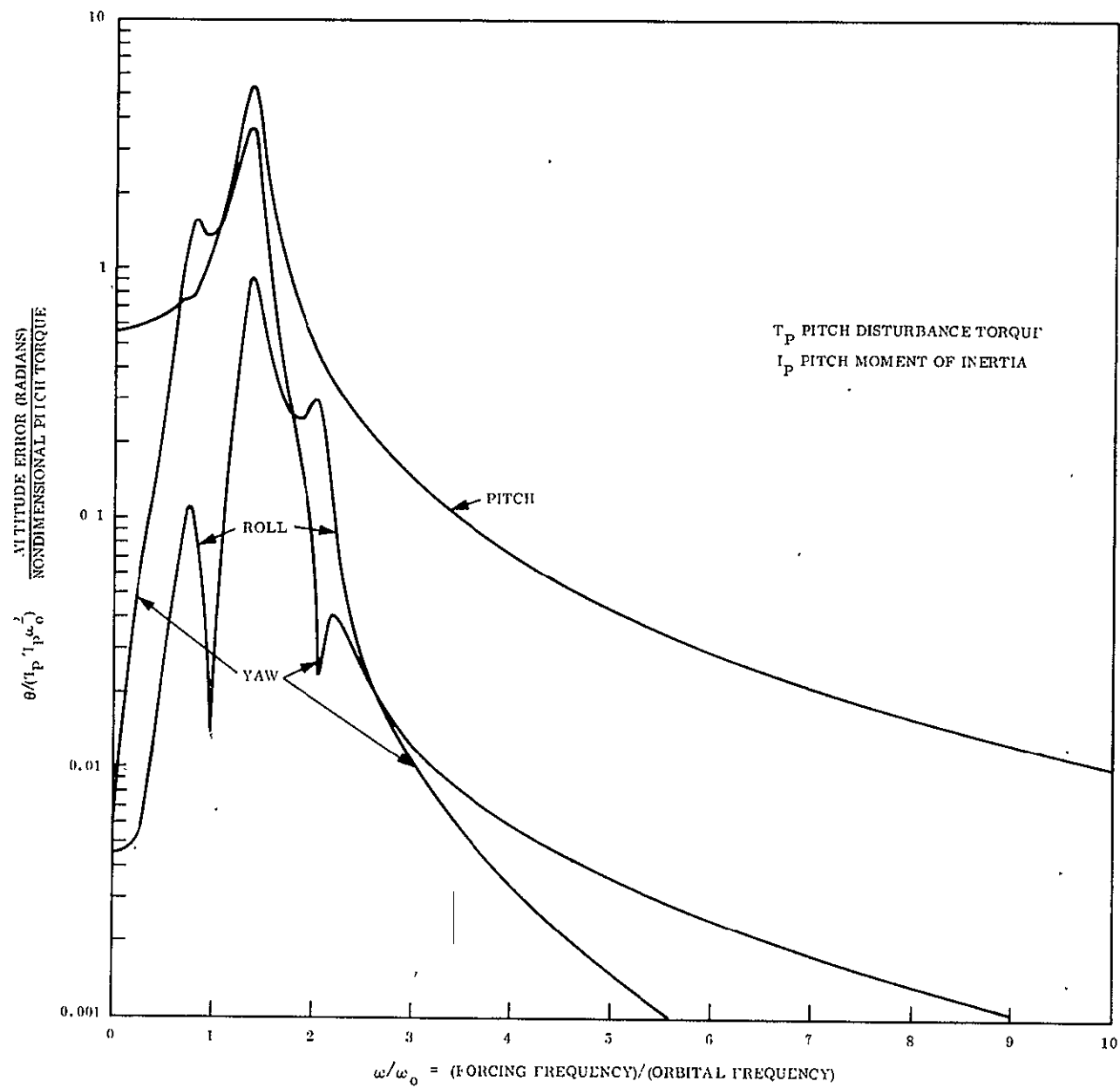
Figure 3.2-4. ATS Spacecraft Response to Pitch Excitation

The y-axis is labeled: $\dfrac{\text{ATTITUDE ERROR (RADIANS)}}{\text{NONDIMENSIONAL PITCH TORQUE}}$, $\theta / (T_p / I_p \omega_o^2)$

T_p PITCH DISTURBANCE TORQUE

I_p PITCH MOMENT OF INERTIA

PITCH

ROLL

YAW

ω / ω_o = (FORCING FREQUENCY)/(ORBITAL FREQUENCY)
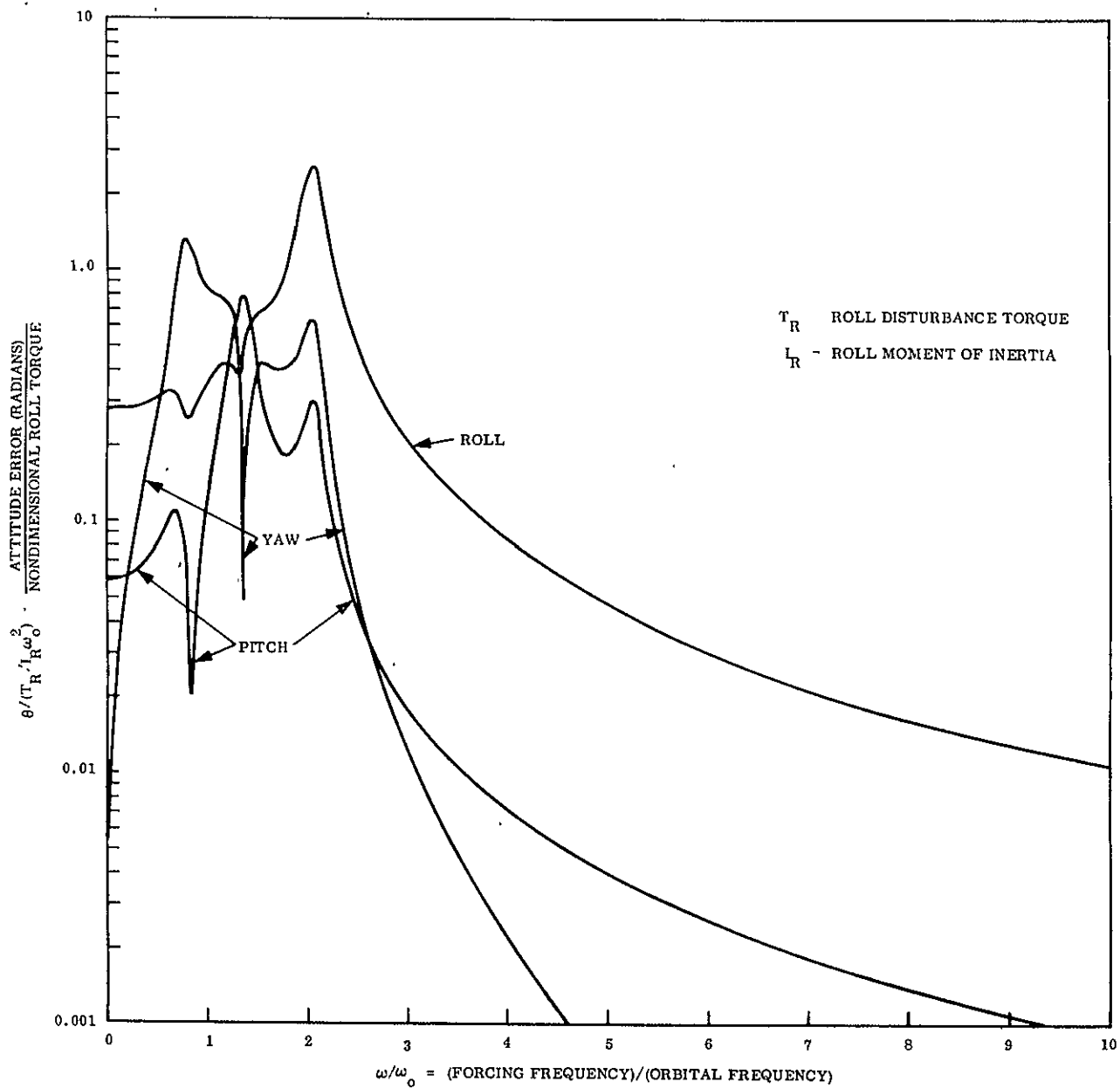
Figure 3.2-5. ATS Spacecraft Response to Roll Excitation
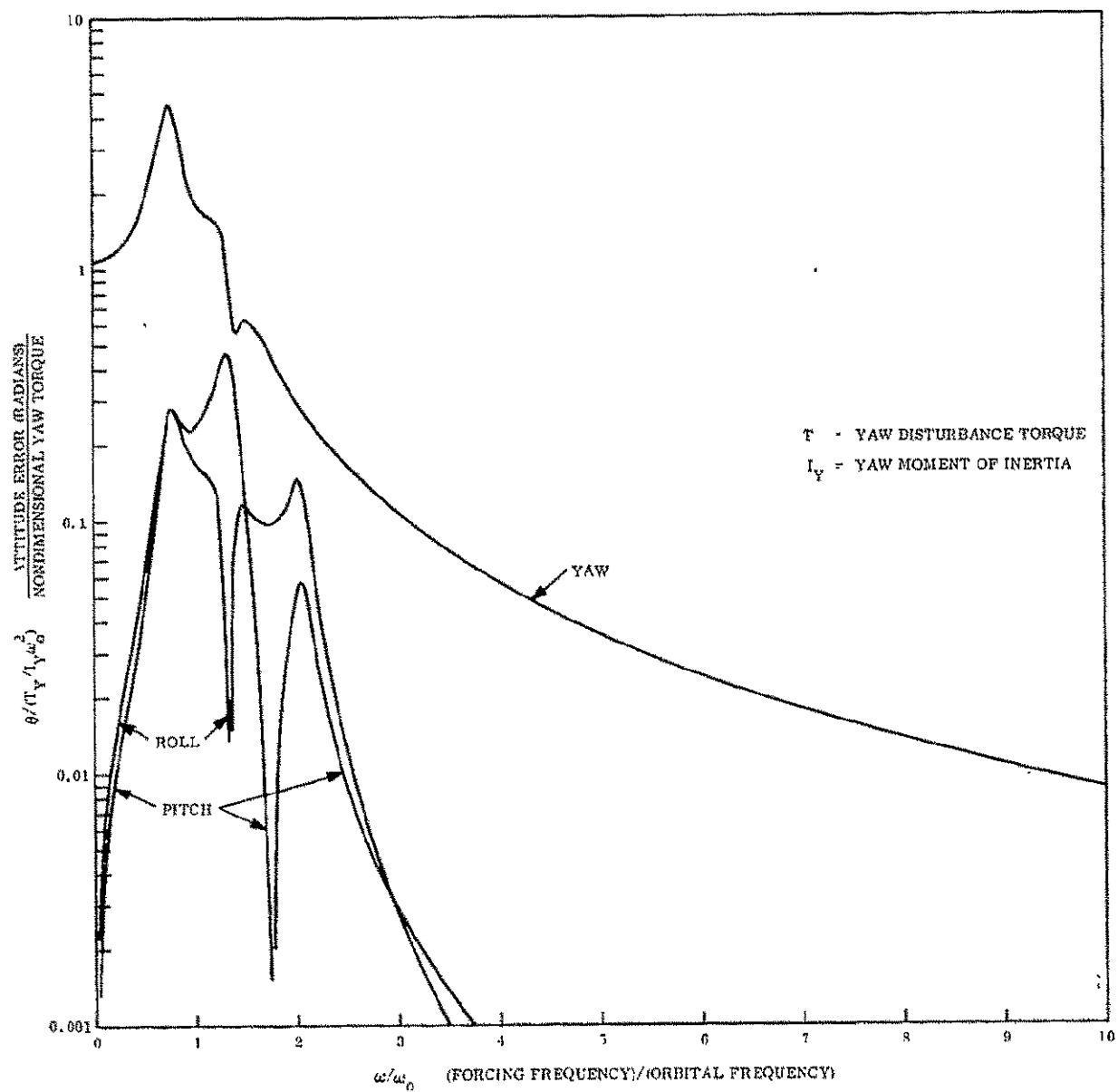
Figure 3.2-6. ATS Spacecraft Response to Yaw Excitation

The axes and labels of the figure:

- Vertical axis: $\dfrac{\text{ATTITUDE ERROR (RADIANS)}}{\text{NONDIMENSIONAL YAW TORQUE}}$, with $\theta / (T_Y / I_Y \omega_0^2)$, scale from 0.001 to 10.
- Horizontal axis: ω/ω_0 (FORCING FREQUENCY)/(ORBITAL FREQUENCY), scale from 0 to 10.
- Curves labeled ROLL, PITCH, YAW.

T = YAW DISTURBANCE TORQUE

I_Y = YAW MOMENT OF INERTIA
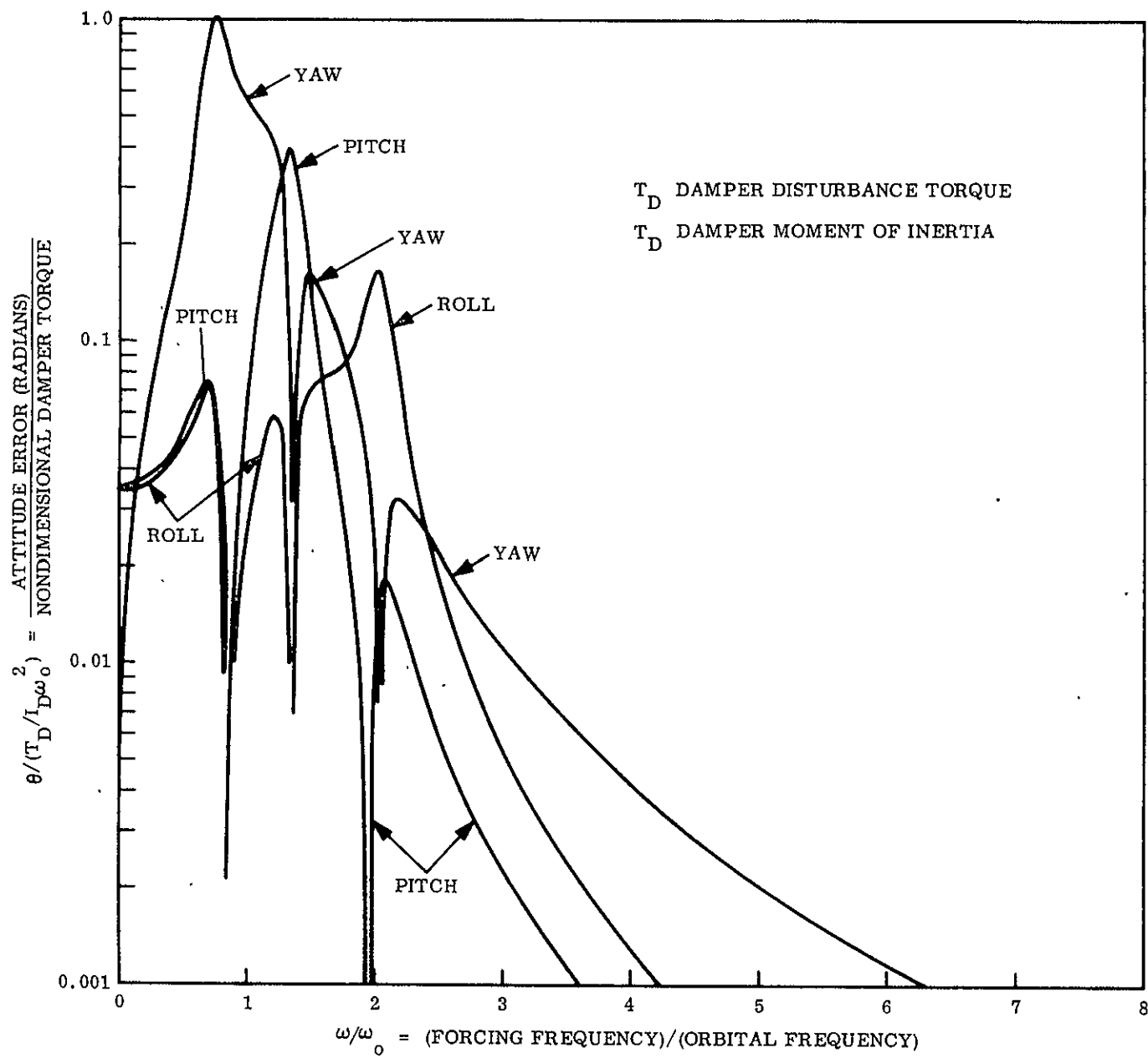
Figure 3.2-7. ATS Spacecraft Response to Damper Excitation

tip mass to minimize pointing error. This is the second optimization mentioned in the opening paragraph of Section 3.2.

3.2.2.1 Disturbance Torques and Error Sources

To optimize effectively, all the disturbance torques which affect the spacecraft must be identified and analyzed. For convenience, a brief description of the disturbance torques and their effect on the spacecraft is presented in the following paragraphs. The analytical approach used for the error calculations was a simple scaling procedure derived from a knowledge of the external distrubances and a reference point obtained from the computer simulation. This technique is not the type normally employed for optimization, but is equally good, although not as comprehensive, as the standard technique. Its advantage is speed, and the optimization was completed within a short period of time.

The key to scaling is the parameter $T/I_p \omega_o^2$. From the non-dimensional analysis of Section 3.1, a relationship of the form

$$\theta \sim T/I_p \, \omega_o^2 \qquad\qquad\qquad 3.2\text{-}6$$

where θ = attitude error.

can be derived. This can be rewritten as

$$\theta = K \frac{T}{I_p} \qquad\qquad\qquad 3.2\text{-}7$$

where K is a constant dependent upon the nature of the disturbance torque and the orbital angular rate. Ignoring offsets of the base of the rod which exist on the actual spacecraft, the pitch moment of inertia is dependent upon the length of the rods and the tip masses. Hence

$$I_p = 4 (M\ell^2 + \frac{1}{3} \rho \ell^3) \qquad\qquad\qquad 3.2\text{-}8$$

, where

M = mass of the primary rod tip weights

ℓ = primary rod length

ρ = rod mass per unit length = 0.000485 slug/ft.

The attitude error can therefore be determined by

$$\theta = K_1 \left[\frac{T}{M\ell^2 + 1/3 \, p\ell^3} \right] \qquad 3.2\text{-}9$$

Scaling is done by determining the nature of T from analysis, and K_1 (plus other multiplier constants) from the computer simulation. The optimization of the configuration is presented in Section 3.2.2.2.

3.2.2.1.1 Magnetic Torques

The earth possesses not only a gravitational field but a magnetic field. Any magnetic dipole, caused by magnetic materials or electrical "loops" contained within the spacecraft, will attempt to align itself with the earth's magnetic field and will torque the spacecraft. The magnitude of the torque is proportional to the strength of the magnetic dipole moment, the orientation of the dipole within the spacecraft, and the location of the spacecraft with respect to the earth. The magnetic field strength decreases with the cube of the orbit radius (exactly the same as gravity gradient), and is twice as strong at the poles (north and south) as at the equator. Hence a spacecraft in a high inclination orbit has more torque on it than a spacecraft in a low inclination orbit. A spacecraft at a high altitude has less torque on it than a spacecraft in a low altitude orbit, but it has correspondingly less gravity gradient torque by exactly the same ratio. The attitude error resulting from magnetics is therefore, virtually, independent of altitude. The exception to this is at near-synchronous altitudes the magnetic field is significantly affected by the sun, and earth's field can be reinforced or replaced by magnetic fields created by sun-generated

atomic particles interacting with the earth's field. The effect is on the order of a five to one increase in magnitude, and a change in the stationary characteristic (when viewed from the spacecraft) of the field. This information was not available at the time of the optimization, and only the "stationary" earth's field was considered. The effect of field variation is not severe for ATS-D/E, however.

At high inclinations and low altitudes, the local magnetic field changes as the spacecraft moves in orbit. As a consequence, the magnetic torque changes as a function of time. For orbit periods short compared to earth's period, the torques (pitch, roll and yaw) are largely constant (zero frequency) and sinusoidal at orbital frequency. At high altitudes, the differences between earth's rate and orbital rate must be evaluated in conjunction with the inclination. As previously mentioned at synchronous altitude, the field is stationary because the difference in rates and the inclination is zero.

Because the altitude is not a factor in the magnetic attitude errors, the non-dimensional error term indicates that the attitude error is dependent only upon the strength of the magnetic dipole compared to the spacecraft pitch moment of inertia. Hence, a small magnetic moment and a large pitch moment of inertia are required for small attitude errors. Neither the gravity gradient rods nor the tip masses (if properly designed) have magnetic moments. The moment of inertia can therefore be increased without increasing the disturbance torques. As a consequence, the magnetic attitude errors decrease with increasing rod length and tip mass.

From the computer simulation, the expressions for the error due to the magnetic moment on ATS-A are:

$$\theta_{YAW} = \frac{1500}{M\ell^2 + 1.61 \times 10^{-4}\ell^3} \qquad\qquad 3.2\text{-}10$$

$$\theta_{PITCH} = \frac{300}{M\ell^2 + 1.64 \times 10^{-4}\ell^3} \qquad\qquad 3.2\text{-}11$$

Similarly for ATS-D,

$$\theta_{YAW} = \frac{1305}{M \ell^2 + 0.1452 \times 10^{-6} \ell^3} \qquad 3.2\text{-}12$$

$$\theta_{PITCH} = 0$$

The roll error has not been considered here, nor will it be considered for the other disturbance torques because its amplitude of oscillation is usually very low. Pitch and yaw are the two axes of greatest concern.

The effect on ATS-A is shown in Figures 3.2-8 and 3.2-9, and the effect on ATS-D is shown in Figure 3.2-10. The attitude error curves decrease rapidly with rod length because moment of inertia increases as the square of the rod length (and directly with tip mass).

3.2.2.1.2 Solar Torques

Sunlight striking a body exerts a pressure on that body of 9.6×10^{-8} lb/ft^2. The total force exerted on the body as well as its direction is a function of the total area of the body, the surface shape, and the surface characteristics. If the surface has purely specular reflection (i.e., a perfect mirror), the force can be as much as double that of pressure multiplied by cross sectional area. A diffusely reflecting surface (white like a piece of paper, but no image) can also increase the force above pressure times area. For a spacecraft in orbit, the total force is the result of the aggregate of all the surfaces which comprise the spacecraft (including the gravity gradient rods). If the total force does not pass through the spacecraft center of mass, a torque will be exerted on the spacecraft. The magnitude of this torque is a function of the total force on the spacecraft and the misalign ment between the solar force vector and the center of mass. The nominal design of the ATS spacecraft is such that the center of mass and center or pressure are coincident. However, tolerances and uncertainties on the spacecraft prevents the two from being coincident. To allow for this, the nominal center of pressure/center of mass offset was
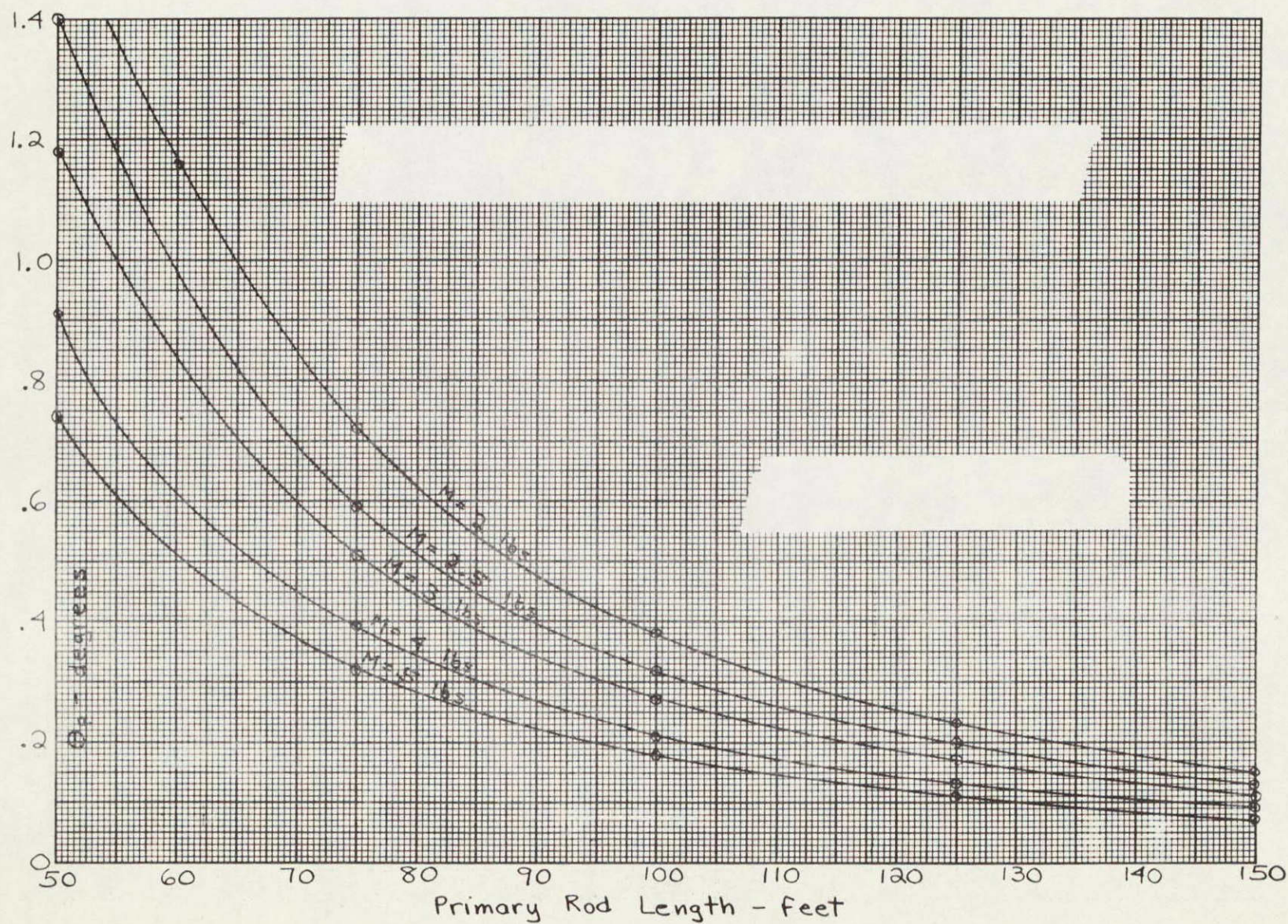
Figure 3.2-8. Effect of Primary Rod Length and Tip Mass Weight on ATS-A Pitch Error Caused by 1000 Pole-Cm Dipole Along the Roll Axis
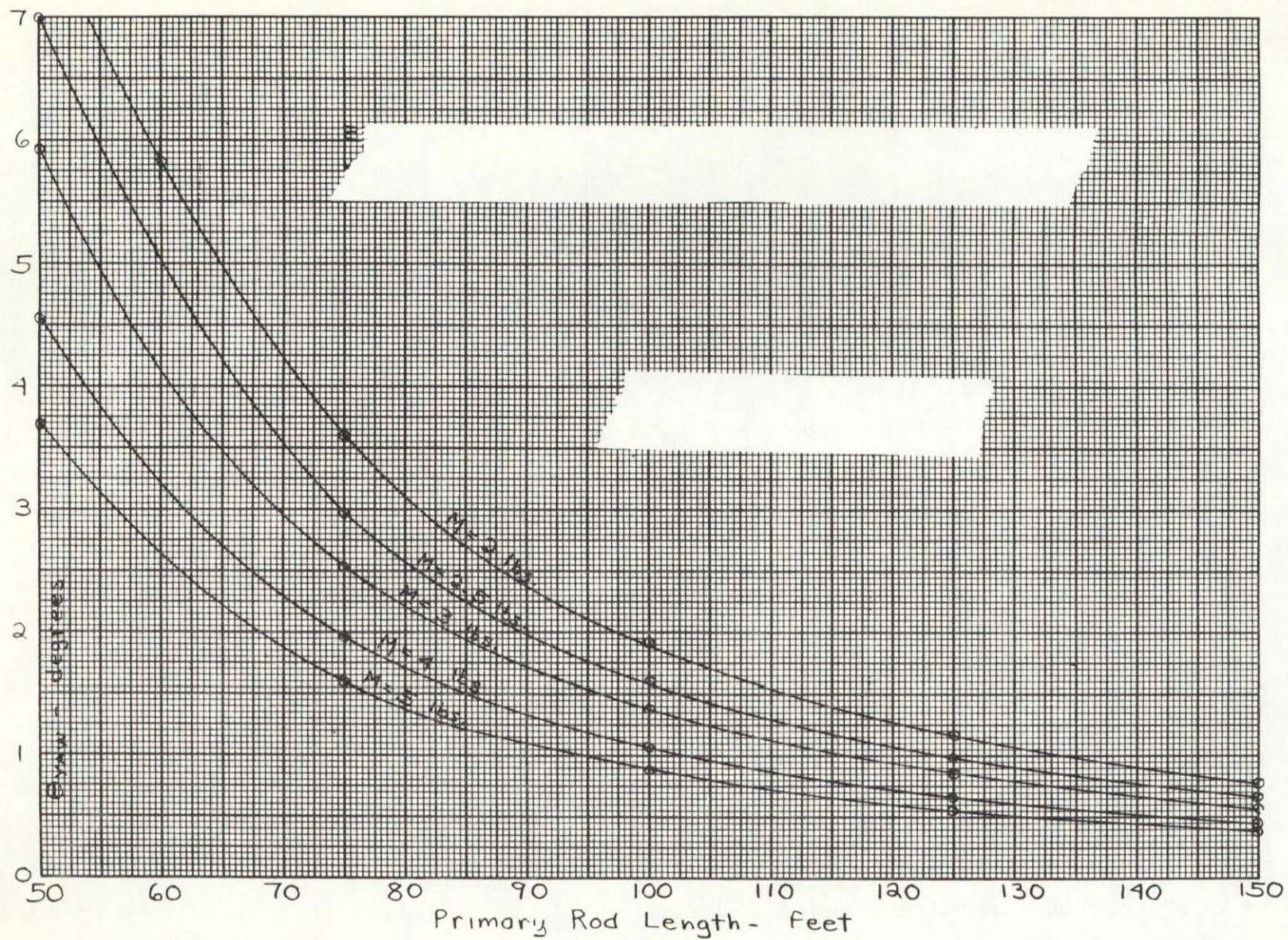
Figure 3.2-9.   Effect of Primary Rod Length and Tip Mass Weight on ATS-A Yaw Error Caused by 1000 Pole-Cm Dipole Along the Roll Axis

The graph shows curves labeled M = 5 (165.), M = 6, M = 7, M = 8, M = 9, M = 10. The vertical axis is labeled "Θ_Y — degrees" with values 0, .5, 1, 1.5, 2, 2.5. The horizontal axis is labeled "Primary Rod Length — feet" with values 50, 60, 70, 80, 90, 100, 110, 120, 130, 140, 150. A note reads "Subsatellite point is located at 100° w. long."
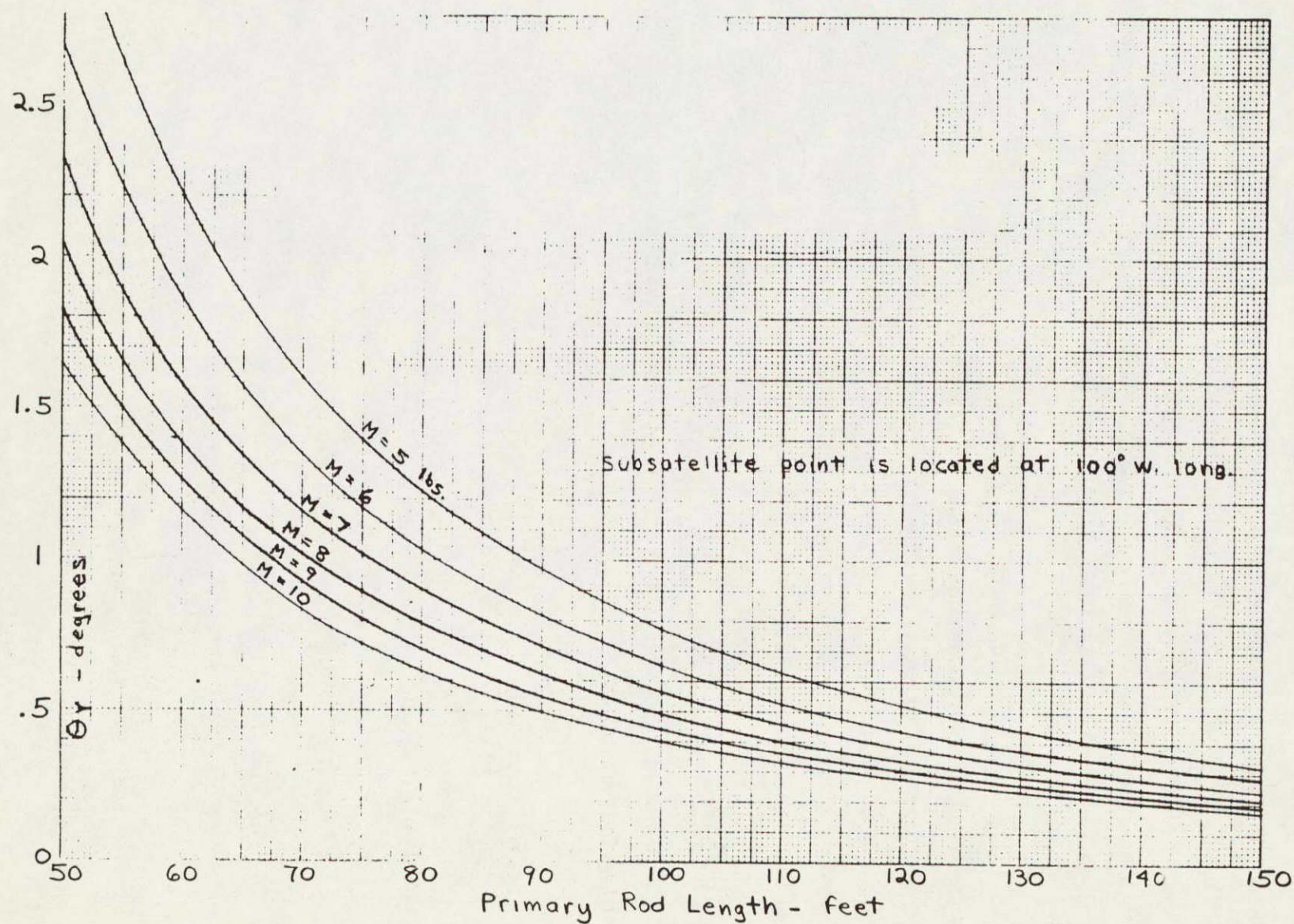
Figure 3.2-10.   Effect of Primary Rod Length on Yaw Error Caused by 1000 Pole-Cm Dipole Along the Roll Axis, ATS-D Spacecraft

estimated to be 1 inch. Because the rods are nominally symmetrical, they do not contribute to the solar torque (except for rod reflectivity variations which are discussed in Section 3.5.1.2.2.2) and the solar torque error would decrease with increasing rod length. A chart for solar torque has not been included for this variation since thermal bending (Section 3.2.2.1.3) contributes a similar center of mass/center of pressure misalignment and the overall effect is included with thermal bending.

3.2.2.1.3 Thermal Bending Torques

Thermal bending is a phenomenon peculiar to gravity gradient rods. The sun shining on the gravity gradient rod heats the side of the rod facing the sun to a temperature higher than that of the shaded side, and the rod bends due to differential thermal expansion. For a closed tube, the rod would form roughly a "horseshoe" shape, which is symmetrical about the sun line. For short rod lengths (short is defined later), the rod can be assumed to bend along an arc of a circle. The radius of the circle depends upon the reflectivity of the rod, the amount of heat that can be conducted from the sunlit side to the shaded side, and the coefficient of expansion of the material. The radius of curvature can be approximated by the expression

$$R = \frac{2\,k}{443\,(\mu\,\alpha\,r)} \left(\frac{1}{\sin\lambda}\right) \qquad\qquad 3.2\text{-}14$$

for silver plated beryllium-copper rods

$\mu \quad = 9.9 \times 10^{-6} \; \frac{\text{ft/ft}}{{}^{\circ}\text{F}} \quad = $ Coefficient of thermal expansion

$\alpha \quad = 0.15 = $ rod absorbitivity

$k \quad = 75 \; \frac{\text{Btu/ft}^2}{{}^{\circ}\text{F/ft}} \quad = $ thermal conductivity of rod material

$\tau \quad = 1.66 \times 10^{-4}$ feet $= $ thickness of rod wall

$443 = $ solar flux

$\lambda \quad = $ rod to solar flux angle of incidence

For the original analysis, the rods were estimated to have an 1800-foot radius of curvature (based on the characteristics of beryllium copper and the reflectivity of silver). By definition, therefore, a short rod length is a rod which is short compared to the thermal radius of curvature.

Thermal bending has three effects on the spacecraft.

1. It destroys the basic symmetry of the spacecraft and produces a solar torque.

2. It rotates the principal axes of the configuration causing a gravity gradient torque.

3. It causes the center of mass to wander resulting in a station keeper error (if applicable).

The second effect shown above is relatively minor for a symmetrical spacecraft and is not considered herein. The third effect is considered in the section discussing stationkeeping (Section 3.2.2.1.6) and is also not discussed herein. The first effect is significant for high altitude spacecraft, particularly in pitch and yaw. Solar pressure does not change with altitude; whereas, the gravity gradient torque decreases with increasing altitude. Consequently, the error for a given solar torque increases with increasing altitude. ATS-D is therefore more sensitive to this type disturbance than ATS-A. Solar torque caused by thermal bending is proportional to the cube of the rod length. The cubic relationship between thermal bending solar torque and rod length is relatively easy to visualize. Referring to Figure 3.2-11, the deflection of any point on a rod thermally bending along an arc of a circle is proportional to the square of the rod length. The total area of the rod, and hence its total solar force is proportional to its length. The overall solar torque is proportional to the force multiplied by its leverage, and is, therefore, proportional to the cube of the rod length. As with the other error sources the proportionality factor was determined from a computer simulation. For ATS-A, the errors were calculated from

$$\theta_{YAW} = \frac{6.56 \times 10^{-4} \ell^3}{M \ell^2 + 1.64 \times 10^{-4} \ell^3}$$
<div align="right">3.2-15</div>

$$\theta_{PITCH} = \frac{3.75 \times 10^{-4} \, \ell^3}{M \, \ell^2 + 1.64 \times 10^{-4} \, \ell^3} \qquad 3.2\text{-}16$$

And for ATS-D, with the sun in the orbit plane (Equinox)

$$\theta_{YAW} = \frac{13.1 \times 10^{-3} \, \ell^3}{M \, \ell^2 + 1.64 \times 10^{-4} \, \ell^3} \qquad 3.2\text{-}17$$

$$\theta_{PITCH} = \frac{36.0 \times 10^{-4} \, \ell^3}{M \, \ell^2 + 1.64 \times 10^{-4} \, \ell^3} \qquad 3.2\text{-}18$$

For ATS-D with the sun inclined 23.45 degrees to the orbit plane (solstice)

$$\theta_{YAW} + \frac{6.22 \times 10^{-3} \, \ell^3}{M \, \ell^2 + 1.64 \times 10^{-4} \, \ell^3} \qquad 3.2\text{-}19$$

$$\theta_{PITCH} = \frac{32.7 \times 10^{-4} \, \ell^3}{M \, \ell^2 + 1.64 \times 10^{-4} \, \ell^3} \qquad 3.2\text{-}20$$

The effect of orbit position with respect to the sunline is important because it changes the magnitude and frequency of the heat input. For ATS-A, however, the overall effect of thermal bending is small and only one orbit position (sun in the orbit plane) was considered. For ATS-D, the effect is large, and the two extremes of sun position (solstice and equinox) were considered.

The results of the analytical studies and scaling are shown for ATS-A in Figures 3.2-12 and 3.2-13, and for ATS-D in Figures 3.2-14, 3.2-15, 3.2-16 and 3.2-17. As indicated in the figures, the attitude error from thermal bending increases linearly with rod length and decreases with increasing tip mass. As indicated earlier, the errors for ATS-D are higher than those of ATS-A.
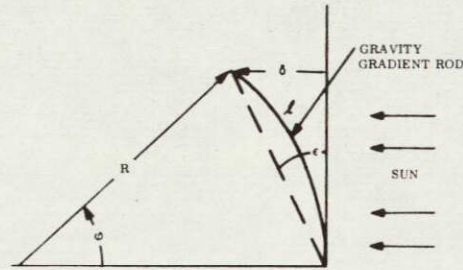
ASSUMING THE ROD BENDS ALONG AN ARC OF RADIUS R.
THE ANGLE ϕ IS

$$\phi = \frac{\ell}{R}$$

WHERE ℓ - ROD LENGTH

THE DISTANCE δ IS

$$\delta = R - R \cos \phi$$

FOR ϕ SMALL,

$$\cos \phi \approx 1 - \frac{\phi^2}{2}$$

HENCE

$$\delta = R \frac{\phi^2}{2} = \frac{\ell^2}{2R}$$

AND

$$\epsilon = \frac{\delta}{\ell} = \frac{\ell}{2R}$$

Figure 3.2-11. Thermal Bending

3.2.2.1.4 Orbit Eccentricity Torques

One of the characteristics of a circular orbit is the constant rate of rotation of the radius vector (a vector from the center of the primary body to the orbiting body). For a spherical earth, the radius vector is parallel to the local vertical, and a gravity gradient spacecraft will align itself with the local vertical and acquire the average rate of rotation.

The rate of rotation of the radius vector is not uniform for an eccentric orbit, however, but varies from a minimum at apogee to a maximum at perigee. The spacecraft will therefore acquire the average rate of rotation of the orbit, but will be torqued by gravity gradient due to offsets between the axis of the minimum moment of inertia and the local vertical. Because the disturbance torque is a gravity gradient torque, moment of inertia scaling is irrelevant, and the non-dimensional torque parameter reduces to a constant depending upon moment of inertia relationships. Consequently, the response of the spacecraft to an eccentric orbit is determined solely by the non-dimensional spacecraft parameters, without regard to rod length
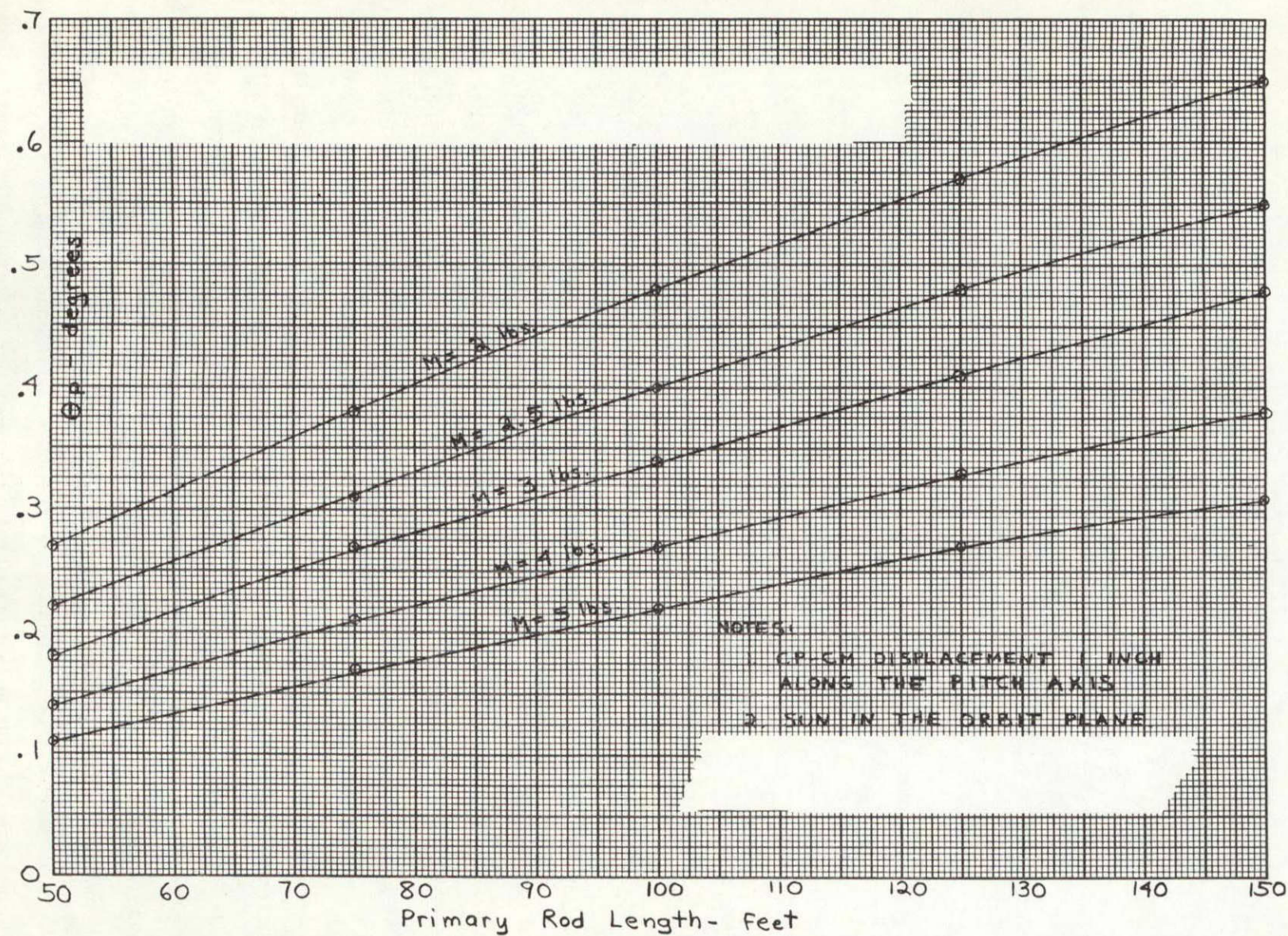
Figure 3.2-12. Effect of Primary Rod Length and Tip Mass Weight on ATS-A Pitch Error Caused by Rod Thermal Bending and Solar Pressure Torque
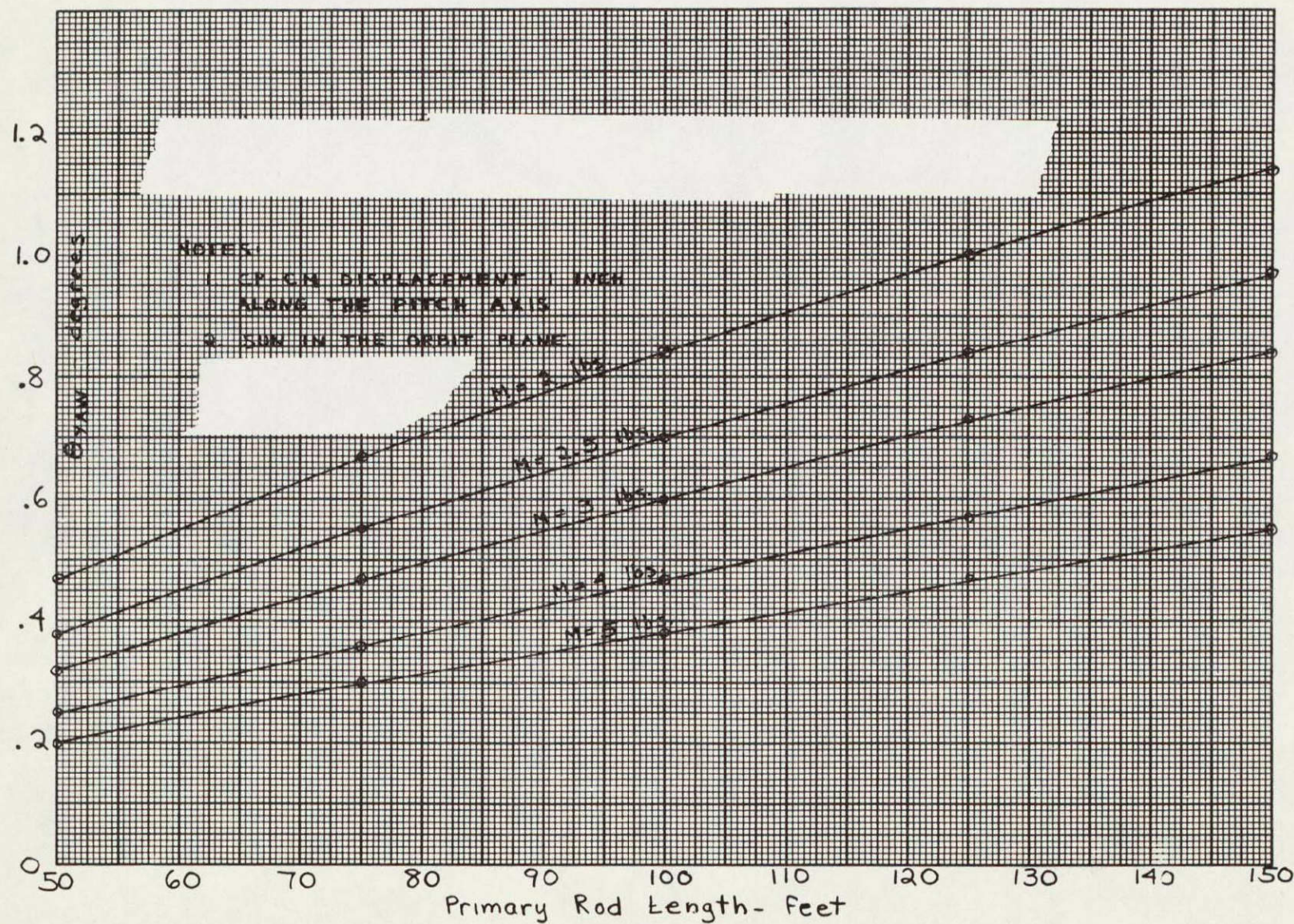
Figure 3.2-13. Effect of Primary Rod Length and Tip Mass Weight on ATS-A Yaw Error
Caused by Rod Thermal Bending and Solar Pressure Torque
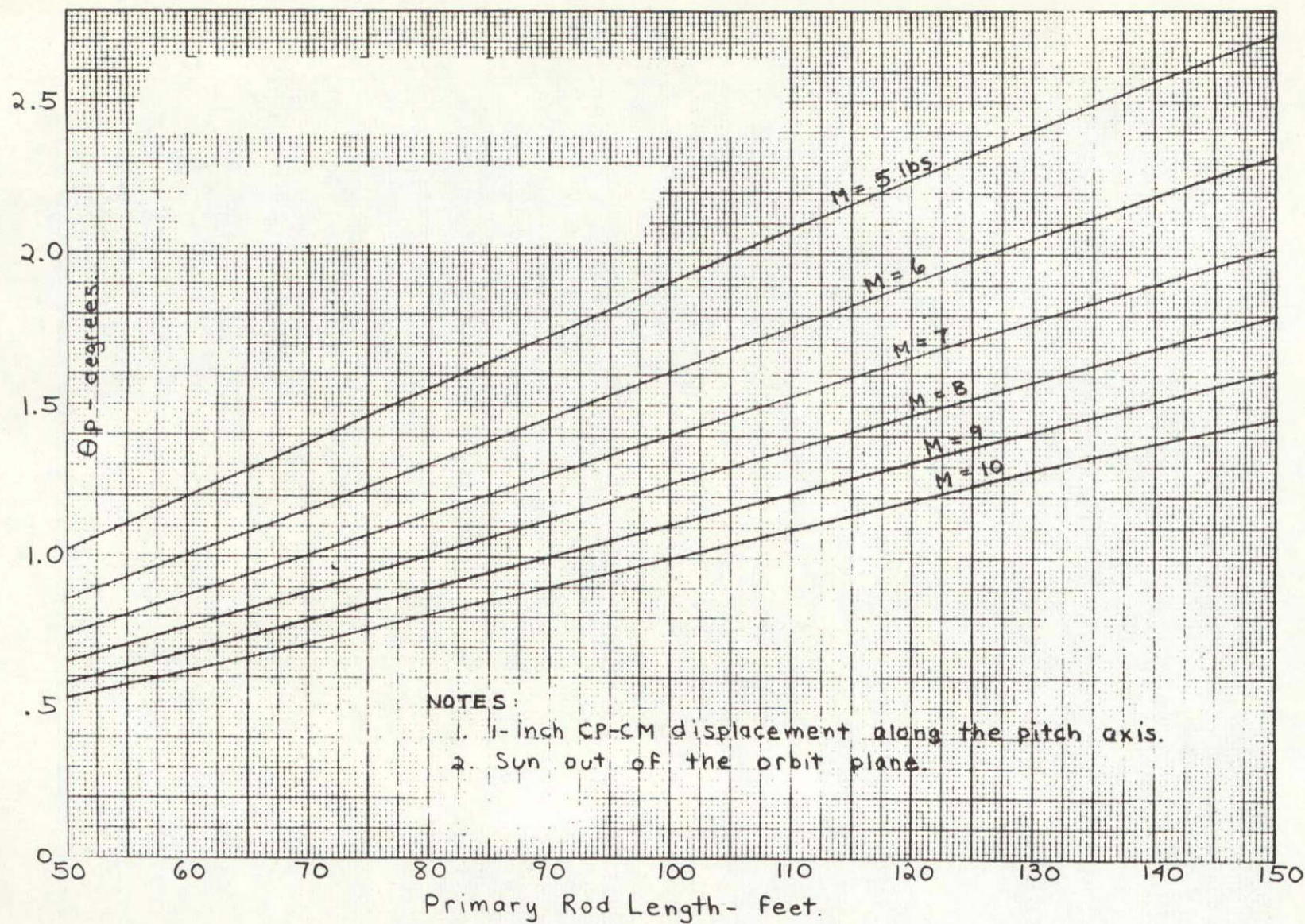
Figure 3.2-14. Effect of Primary Rod Length on Pitch Error Caused by Rod Thermal Bending and Solar Pressure Torque, ATS-D Spacecraft
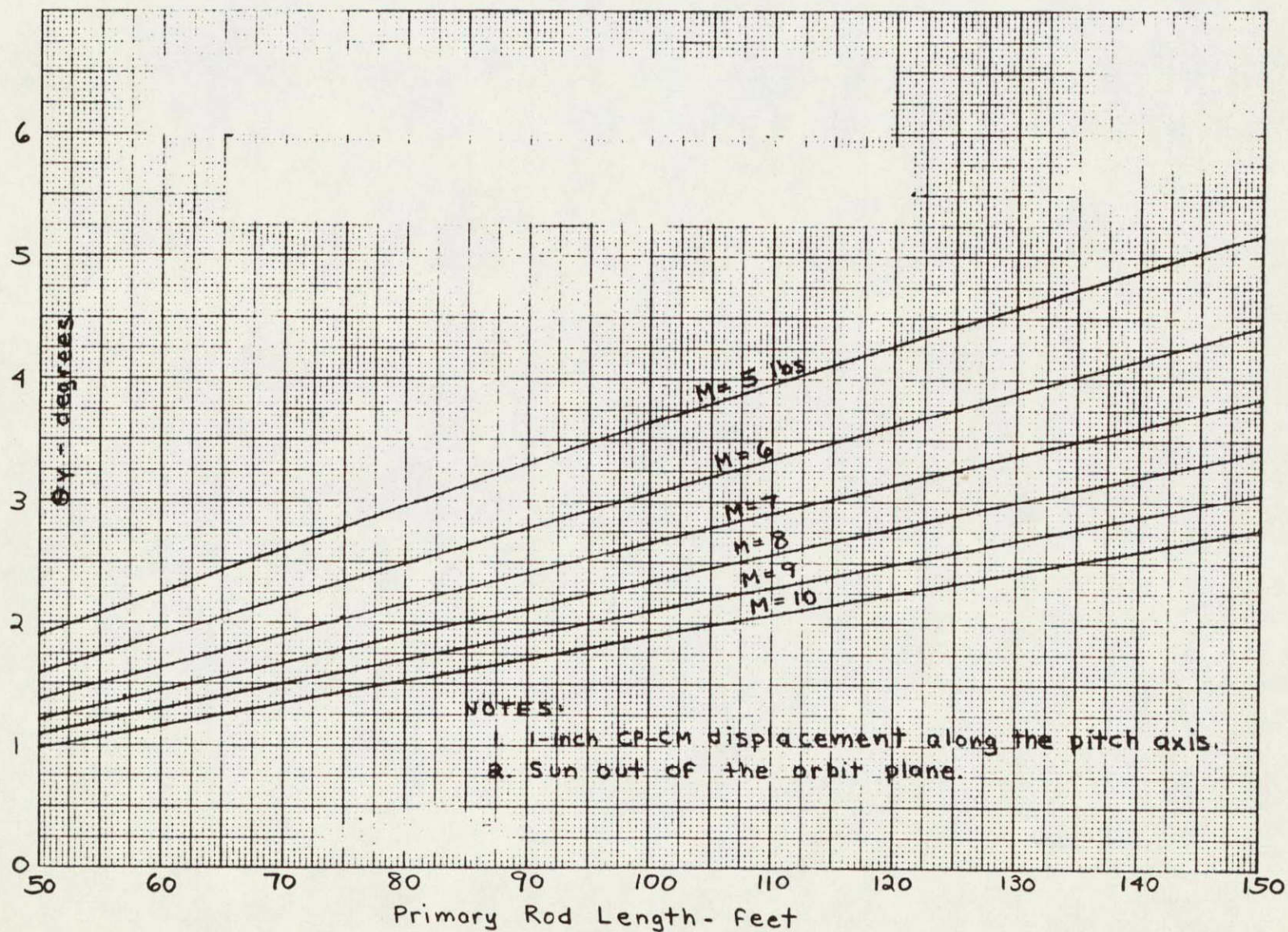
Figure 3.2-15. Effect of Primary Rod Length on Yaw Error Caused by Rod Thermal Bending and Solar Pressure, ATS-D Spacecraft
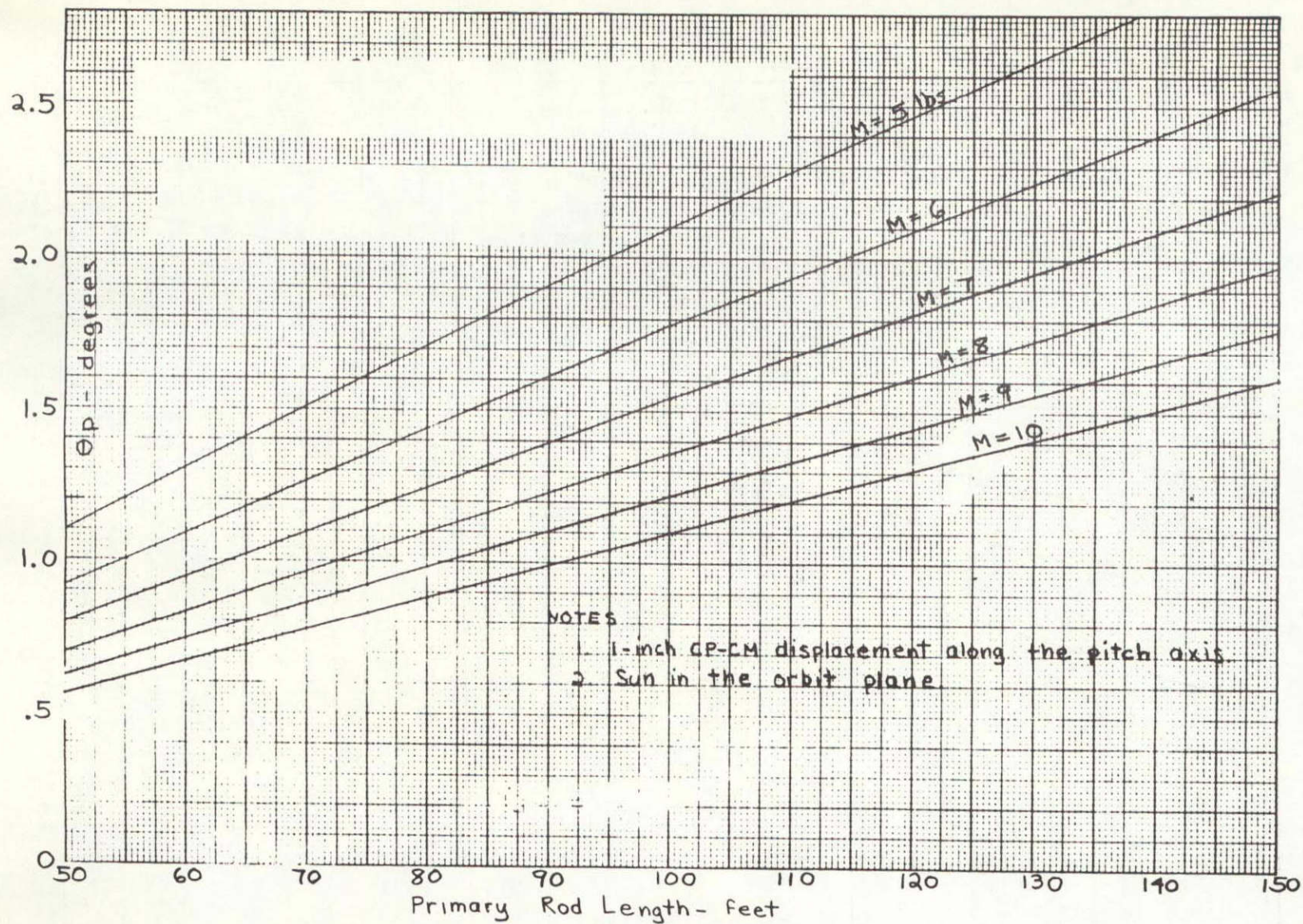
Figure 3.2-16. Effect of Rod Length on Pitch Error Caused by Rod Thermal Bending
and Solar Pressure Torque, ATS-D Spacecraft
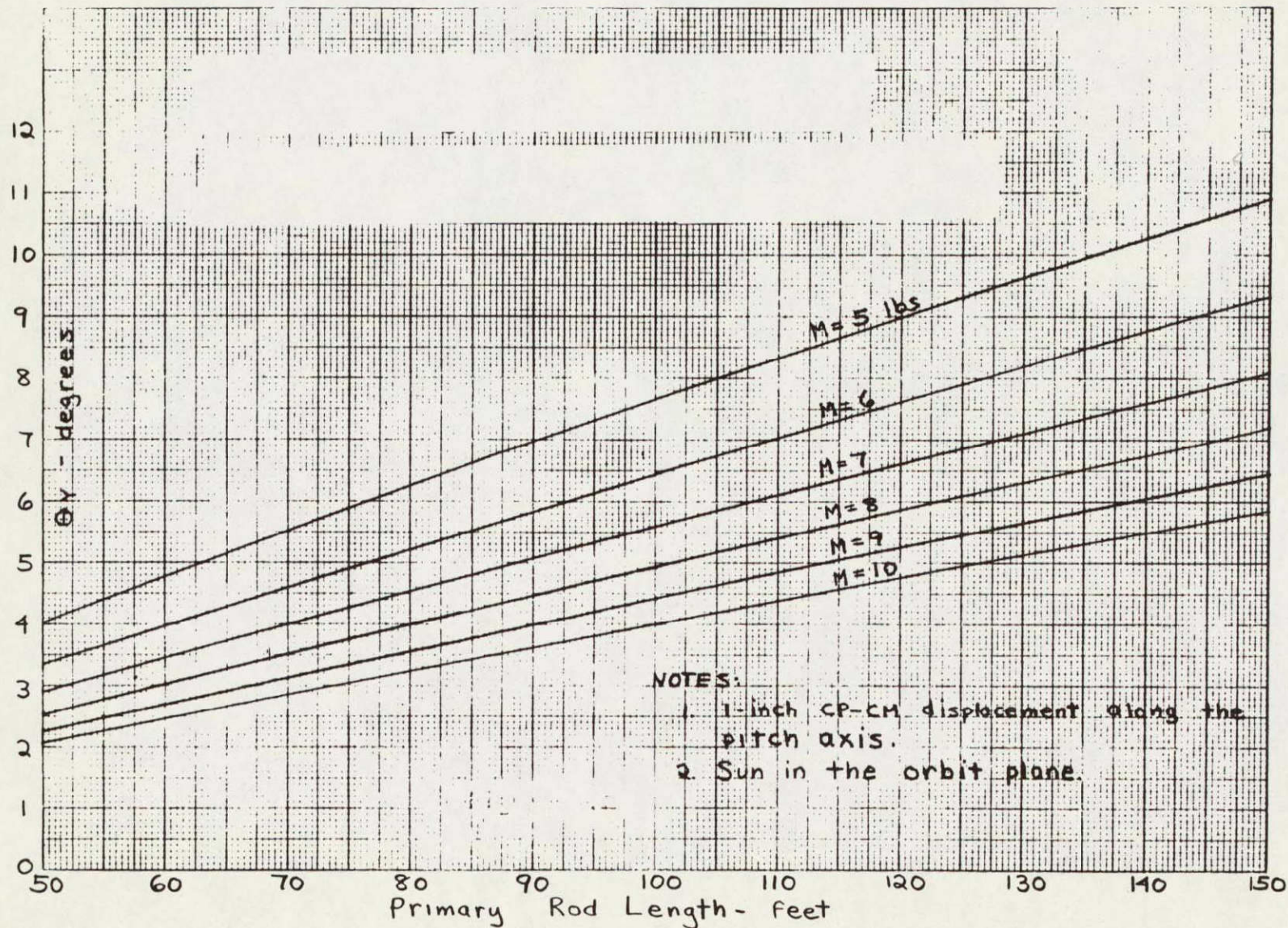
Figure 3.2-17. Effect of Primary Rod Length on Yaw Error Caused by Rod Thermal Bending and Solar Pressure Torque, ATS-D Spacecraft

and tip mass. It cannot, therefore, be optimized because these parameters have been selected. An indication of the effect of these parameters on the eccentricity response can be observed by noting the errors resulting from orbit eccentricity in Tables 3.2-3 and 3.2-5. For the optimum spacecraft design, the pitch eccentricity response is 1.5 degree, the roll response is 0.1 degree and the yaw response is 2.0 degree per 0.01 orbit eccentricity.

3.2.2.1.5 Stationkeeping Torques

ATS-D has a stationkeeping thruster on board to provide east-west stationkeeping. The thruster is a microthruster with a peak force output of 10^{-5} pounds. The thrust required for stationkeeping is approximately half that value, however, indicating a fifty percent duty cycle is required.

At the time of the optimization, the pulse rate of the microthruster had not been determined, and it was assumed for convenience that the pulsing frequency would be too fast for the spacecraft to respond to, and would appear to be a constant. For the optimization, therefore, the thrust level was assumed constant at 0.5×10^{-6} pounds.

The stationkeeping thruster is a large disturbance torque, and the effects of manufacturing misalignments and tolerances significantly affect the selection of rod length and tip mass. As a consequence, they were included in this portion of the design study.

The stationkeeping thruster creates a disturbance torque to the spacecraft only when the thrust vector does not pass through the spacecraft center of mass. For the ATS-D spacecraft, there are several reasons why this will be true. The primary reason is thermal bending, discussed in Section 3.2.2.1.3. The bending of the rod displaces the tip mass and causes the center of mass of the spacecraft to move. The torque created by the station-keeper is the force multipled by the center of mass offset. The expression for tip deflection as a function of thermal bending rod radius is shown in Figure 3.2-11. The expression for the radius of curvature of the rod is given by Equation 3.2-14. From system geometry presented in Figure 3.2-18, the maximum tip deflection occurs on the z axis when

$$\lambda = \sin \left[\cos^{-1} (\cos \xi \cos \lambda_o) \right] \qquad 3.2\text{-}21$$

where

ξ = half angle of rods-referred to X_1 axis

= 25.66^o

λ_o = angle between x_1 axis and solar flux with Sun in x_1, z_1 plane

= 23.45^o

For worst case (shortest radius)

$$R = \frac{+ 2 \tau k}{443 \mu \alpha r} \frac{1}{\sin \left[\cos^{-1} (\cos \xi \cos \lambda_o) \right]} \qquad 3.2\text{-}22$$

$$R = 3243.9 \text{ feet} \qquad 3.2\text{-}23$$

From Figure 3.2-11

$$\delta \approx \frac{\ell^2}{2R} \qquad 3.2\text{-}24$$

The center of mass offset is therefore proportional to the square of the rod length, and the tip mass. Hence, ignoring the weight of the rods

$$T = F \frac{4M\ell^2}{M_t 2R} \qquad 3.2\text{-}25$$

Where M_t = total spacecraft mass ≈ 18.2 slugs.
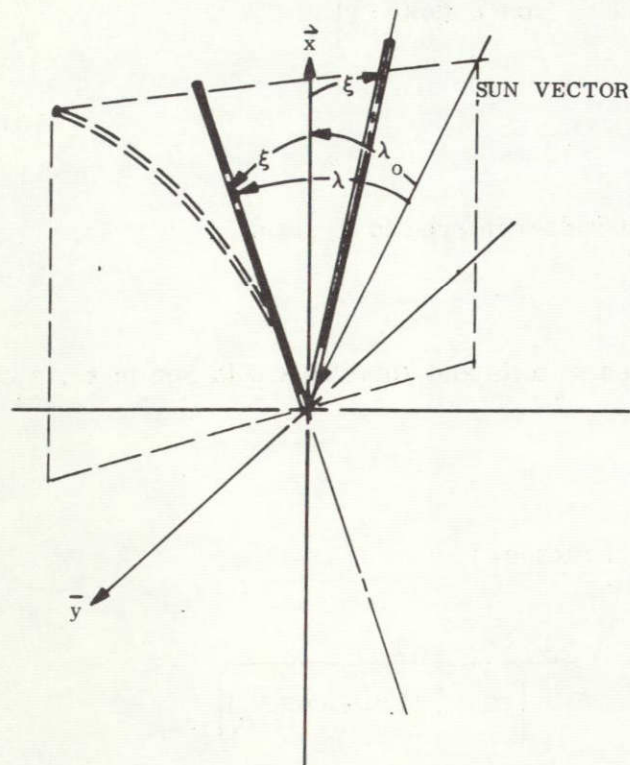
Figure 3.2-18.   Sun-Rod Geometry

Substituting into Equation 3.2-9 and dropping the second order ℓ^3 term from the denominator, the attitude error becomes a constant, independent of rod length or tip mass.   The constant is dependent upon the rod thermal characteristics, reflectivity, etc., and once the rod has been selected, represents the minimum possible error.   For ATS-D this error is 4.6 degrees.

At short rod lengths, secondary center of mass offsets due to manufacturing tolerances become important.   There are four tolerance effects which must be considered in the station-keeping analysis: rod straightness, rod alignment, thruster alignment, and spacecraft center of mass uncertainty.   All the error sources are obvious, except the rod straightness effect.   The gravity gradient rods are not straight when manufactured; and at the time of the optimization, there was not an effective means of straightening them.   As a result, an acceptance specification was placed on the rods which limited their allowable curvature.   The permissible rod envelope is shown in Figure 3.2-19, and was used to determine the attitude error. The remaining error sources were assumed to be a center of mass uncertainty of 0.3 inch, a rod misalignment of 0.5 degree, and a thrust vector misalignment of 1 degree.
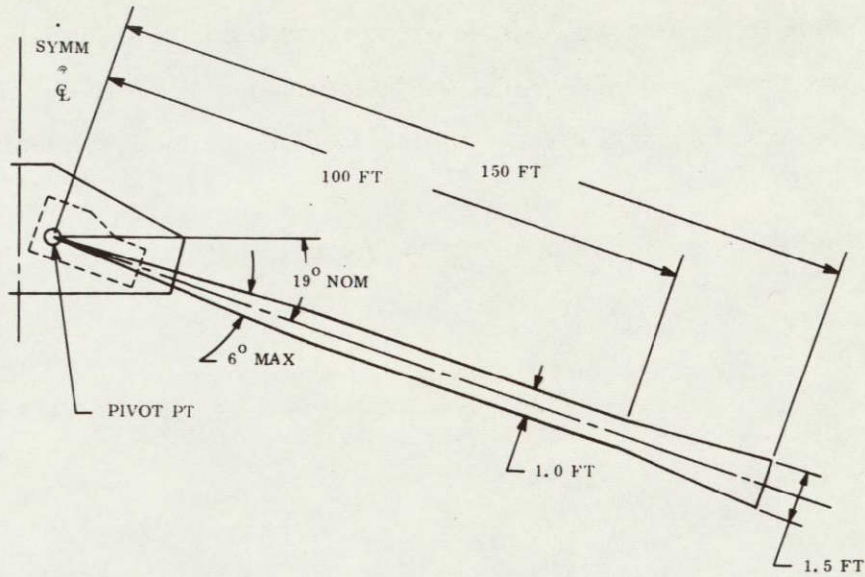
BE-CU 25
AG PLATED, POLISHED α - 0.1 TO 0.15
0.500 DIAMETER (98° OVERLAP-NOMINAL)
M/G -132.3 FT LENGTH, 0.002-INCH THICK
TIP MASS: ATS "A" - 2.50 LB
            ATS "D" AND "E" - 8.00 LB
ERECTION RATE - 1.5 TO 0.9 FT/SEC
SCISSORING RATE - 1/8°/SEC ± 1/16/SEC

Figure 3.2-19.   Primary Boom Envelope Specification

Of the four tolerances, the simplest source of torque to analyse is the center of mass uncertainty; the torque for the error equation is of the form

$$T = 0.025 \times F \qquad\qquad 3.2\text{-}26$$

where F is the thruster force. Since the torque is constant, the attitude error resulting from this torque will decrease with increasing rod length approximately as the inverse square of the rod length.

The torque resulting from the rod misalignment is

$$T = \frac{F}{M_t} \left[4 M \ell \, \mathrm{Sin}\, \nu + 4 \rho \frac{\ell^2}{2} \, \mathrm{Sin}\, \nu \right] \qquad\qquad 3.2\text{-}27$$

where ν = rod mounting error.

Substituting into Equation 3.2-9, the attitude error resulting from this disturbance torque will decrease approximately linearly as the length increases, because the numerator contains both linear and square length terms, similar to those in the denominator.

The torque resulting from rod curvature is of the form

$$T = \frac{F}{M_t} \left[4M(0.5 + 0.005 \, \ell') \right.$$

$$\left. + 4\rho \, \ell \, (0.5) \right]$$

3.2-28

where ℓ' = rod length in excess of 100 feet.

The ℓ' term is required because of the "break" in the rod envelope at 100 feet (see Figure 3.2-19). The effect is significant for the tip mass, but second order for the rod itself, and the rod was therefore ignored. The error resulting from this torque decreases generally as the square of the rod length, the term adding slightly at long rod lengths.

The final torque is the thruster misalignment torque, which is

$$T = F \times d \, Sin \, \xi$$

3.2-29

where

ξ = thruster misalignment = 1 degree

d = distance of thruster from geometric center.

The error resulting from this torque decreases as the inverse square of the rod length.

The total stationkeeper error is a function of all these torques acting simultaneously. As a worst case, the errors were assumed to be additive on the yaw axis (the weakest axis).

The results are shown in Figure 3.2-20. It is evident that the tolerance effects vanish quickly, and the thruster error becomes constant due entirely to thermal bending. There is some improvement associated with heavy tip masses, but it is limited to short rod lengths.
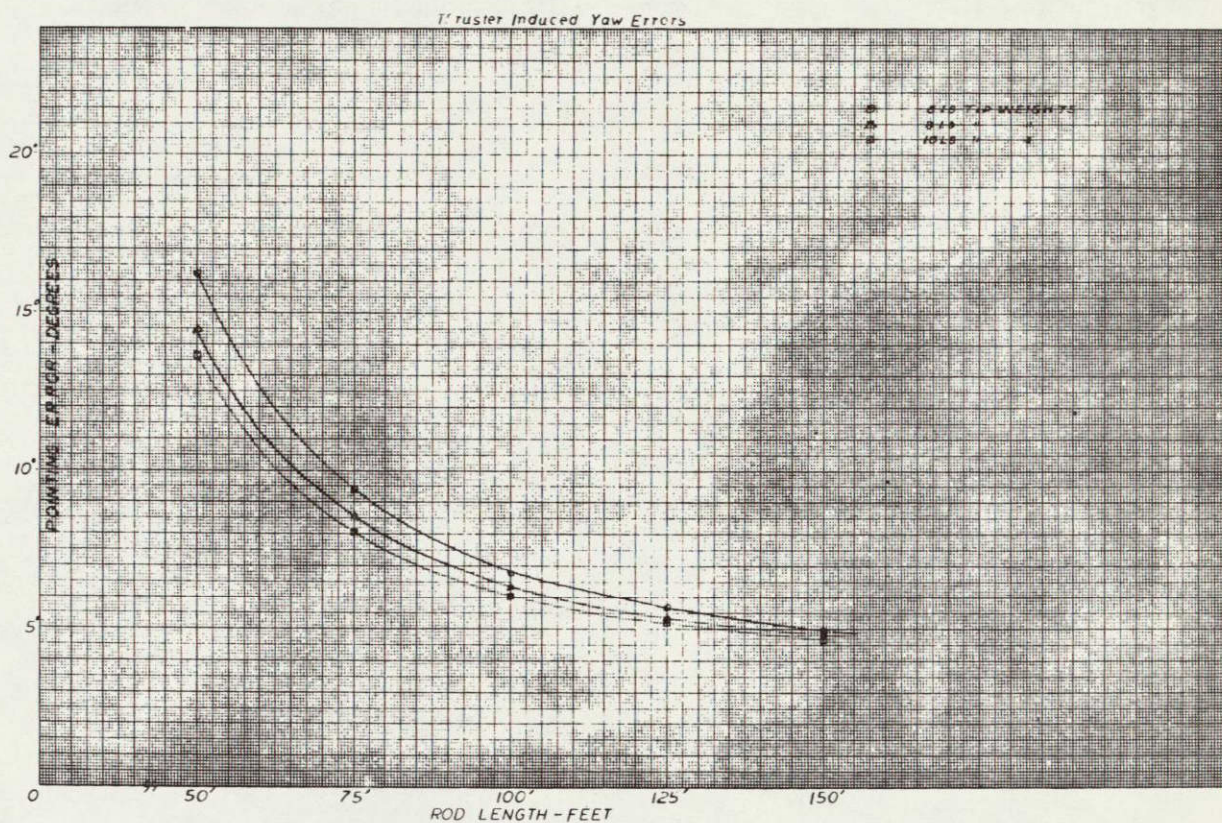
Figure 3.2-20. Thruster Induced Yaw Error

3.2.2.2 Optimization of Nominal Spacecraft

To determine the optimum spacecraft design, it is necessary to combine the errors produced by the disturbance torques and "pick-off" the point of minimum attitude error. One difficulty which arises when the errors are combined is the manner in which they should be combined. Because the phasing of the torques with respect to one another is arbitrary, and changes with time, direct addition appears to be pessimistic. On the other hand, root sum squaring has been shown in previous work to be optimistic. The actual case is undoubtely some place in between. For this optimization, the direct addition approach was taken, because it was convenient, and provided results which were known to be pessimistic.

3.2.2.2.1 ATS-A Optimization

The attitude errors resulting from solar torque and thermal bending (Figure 3.2-12 and 3.2-13) and magnetic (Figures 3.2-8 and 3.2-10) were combined into the two plots (pitch and yaw) shown in Figures 3.2-21 and 3.2-23. It is obvious from these graphs that long rod lengths and heavy tip masses produce good performance (note that orbit eccentricity error is not included since it cannot be optimized in this manner). It is a basic fact of
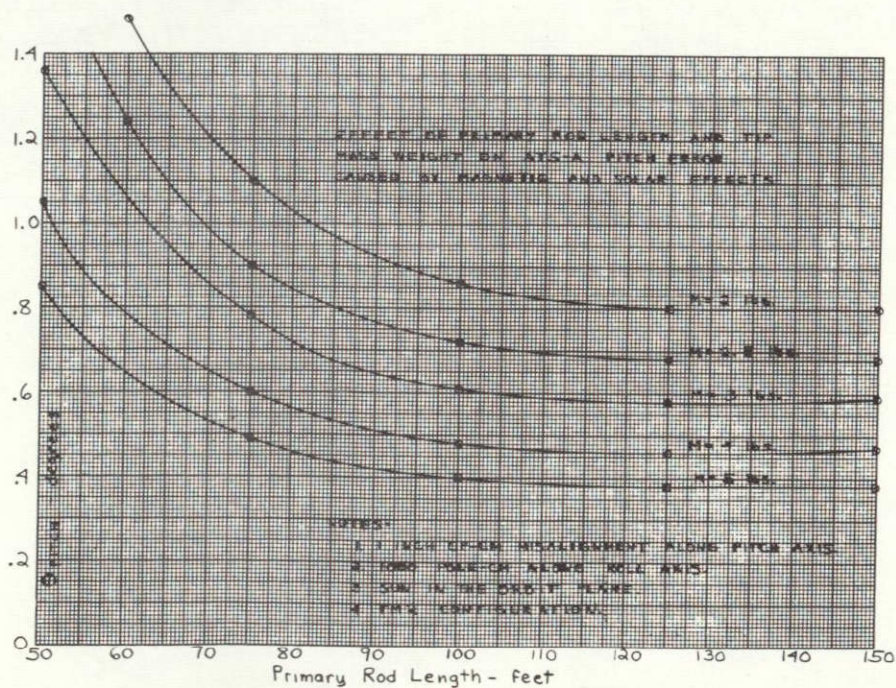
Figure 3.2-21.   Effect of Primary Rod Length and Tip Mass Weight
on ATS-A Pitch Error Caused by Magnetic and Solar Effects
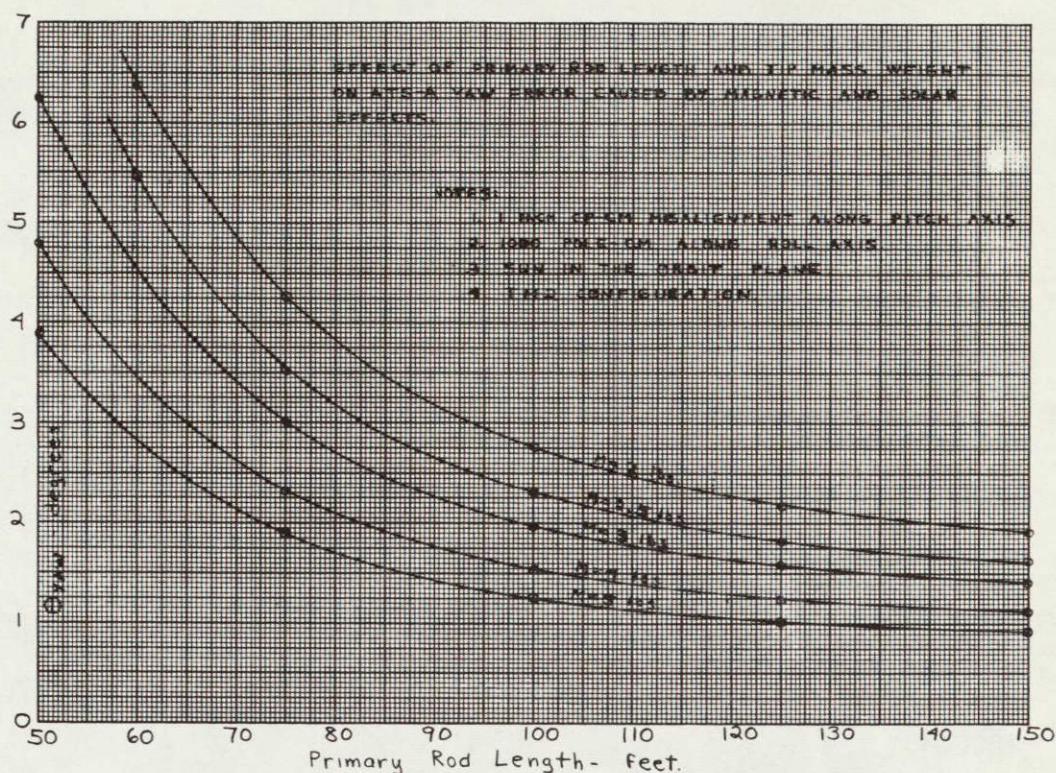
Figure 3.2-22. Effect of Primary Rod Length and Tip Mass Weight
on ATS-A Yaw Error Caused by Magnetic and Solar Effects

gravity gradient spacecraft that heavy tip masses, which provide large moments of inertia
with no disturbance torque, almost invariably provide good performance.

The choice of system parameters for ATS-A was strongly influenced by hardware designs,
program schedules, and budgets which existed at the time of optimization. The primary
limiting item was the spring constant of 21 dyne-cm/deg designed for the original ATS Con-
figuration. Increasing this constant would require a complete redesign of the damper
component, which was undesirable from the cost and schedule standpoint. With the spring
constant that existed at the time of optimization, the pitch moment of inertia (from the non-
dimensional parameters) had to be 7107 slug-ft^2, and the damping coefficient 15,800 dyne-
cm-sec. Since the change in damping coefficient could be achieved with only slight modifi-
cation, the pitch moment of inertia of 7107 slug-ft^2 was selected based primarily on the
spring constant.

Table 3.2-8 ATS-A Parameters

Parameter	Optimum Configuration
X Rod Length (ft)	133.75
Damper Rod Length (ft)	45.0
X Rod Tip Mass (lb)	2.50
Damper Rod Tip Mass (lb)	1.60
X Rod Half Angle (deg)	$\approx$26.0
Angle Between X Rod Plane and Roll Axis (deg)	4.8
Angle Between Damping Axis and Pitch Axis (deg)	53.4
Spring Constant (dyne-cm)/deg	21.0
Damping Constant $\frac{\text{(dyne-cm)}}{\text{(deg/sec)}}$	15,800.0
Moments of Inertial (slug-ft^2)	
Pitch	7,107.0
Roll	5,774.0
Yaw	1,333.0
Damper	231.0

Figure 3.2-23 is a plot of pitch moment of inertia as a function of rod length and tip mass. It is apparent that several combinations of rod length and tip weight can be selected to provide 7107 slug-ft^2. Figures 3.2-21 and 3.2-22 show that the best rod length is 150 feet and the best performance is obtained from the heaviest tip mass. While ATS-A did not have a weight problem, it was felt to be more profitable to utilize as much of the 150 feet of available rod length as possible. Because it was undesirable to reduce the tip masses below the level originally anticipated, the recommended system was primary rod lengths of 133.75 feet with 2.5-pound tip masses.

The damper rod is 45 feet with a 1.60-pound tip mass. The remaining parameters are shown in Table 3.2-8 and the hardware location and orientations are shown in Figure 3.2-24.

Two computer simulations were made to compare the recommended system with the previous standard configuration (Table 3.2-1 in Section 3.2.1). For each simulation, the orbit eccentricity was 0.01, the CP-CM displacement was 1 inch along the pitch axis, the magnetic dipole moment was 1000 pole-cm along the roll axis, and the sun was in the orbit plane. The other factors are as defined in Section 3.2.1. The improvement in performance shown in Table 3.2-9 agrees well with the values predicted by Figures 3.2-21 and 3.2-22. The simulations are shown in Figures 3.2-25 and 3.2-26.

Table 3.2-9. Performance Comparisons for ATS-A

	θ_P (deg)	θ_R (deg)	θ_Y (deg)
Previous Configuration	1.9	0.3	4.3
Recommended Configuration	1.8	0.3	3.3
Increase in Accuracy	0.1	---	1.0
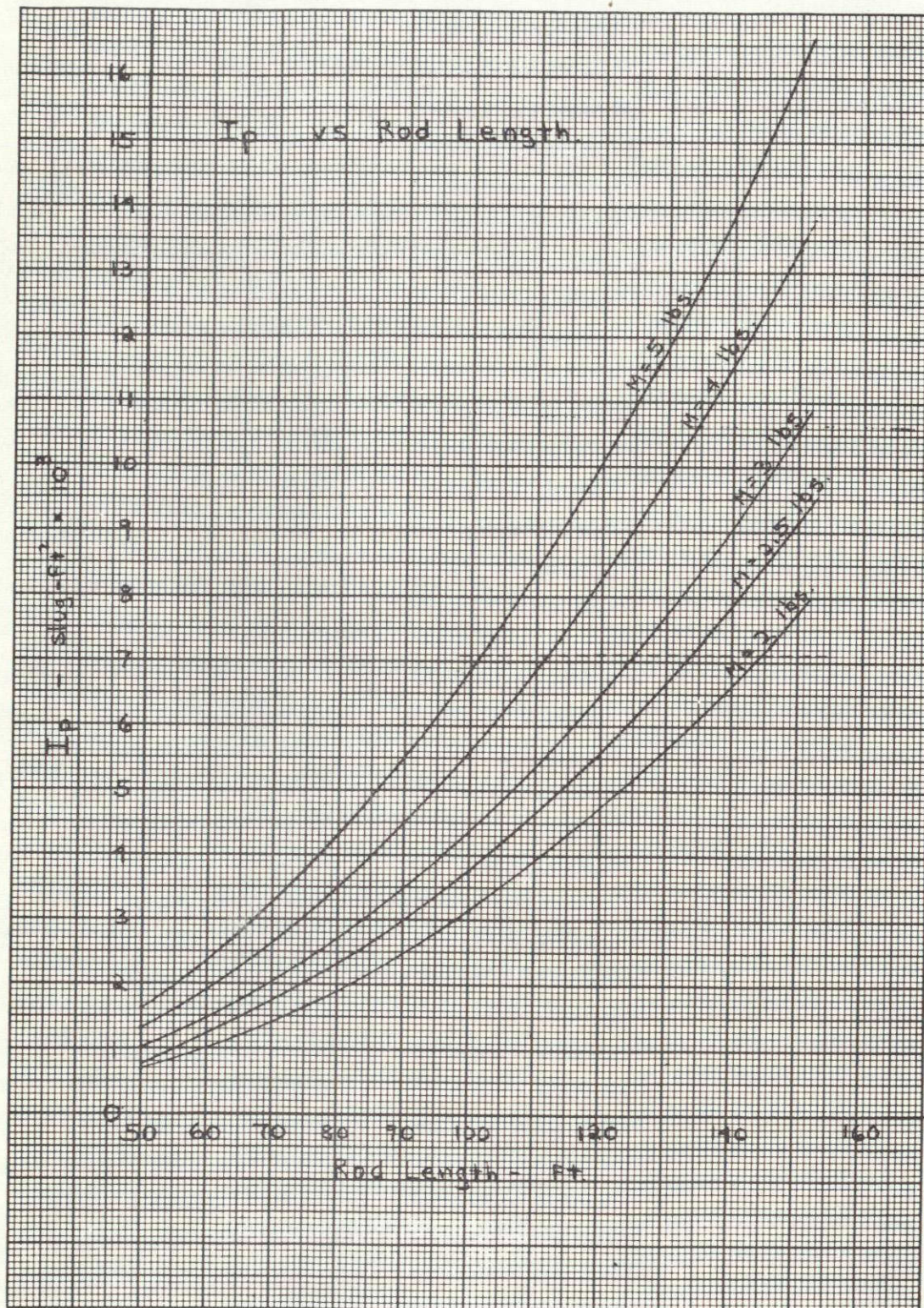
Figure 3.2-23. I_p vs Rod Length for ATS-A
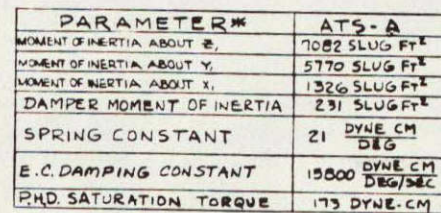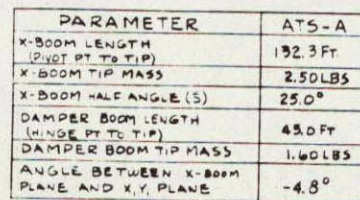
Figure 3.2-24. ATS-A Standard Configuration

PARAMETER	ATS-A
X-BOOM LENGTH (PIVOT PT. TO TIP)	132.3 FT.
X-BOOM TIP MASS	2.50 LBS
X-BOOM HALF ANGLE (S)	25.0°
DAMPER BOOM LENGTH (HINGE PT TO TIP)	45.0 FT
DAMPER BOOM TIP MASS	1.60 LBS
ANGLE BETWEEN X-BOOM PLANE AND X,Y, PLANE	-4.8°

PARAMETER *	ATS-A
MOMENT OF INERTIA ABOUT Z₁	7082 SLUG FT²
MOMENT OF INERTIA ABOUT Y₁	5770 SLUG FT²
MOMENT OF INERTIA ABOUT X₁	1326 SLUG FT²
DAMPER MOMENT OF INERTIA	231 SLUG FT²
SPRING CONSTANT	21 DYNE CM / DEG
E.C. DAMPING CONSTANT	15800 DYNE CM / DEG/SEC
P.H.D. SATURATION TORQUE	173 DYNE·CM

* MOMENTS OF INERTIA DO NOT INCLUDE CONTRIBUTIONS OF CENTRAL BODY OR DAMPER BOOMS

Figure 3.2-25. Performance of ATS-A Vehicle (Medium Altitude) with 100-Foot Primary Rods and 2.5-Pound Tip Weight
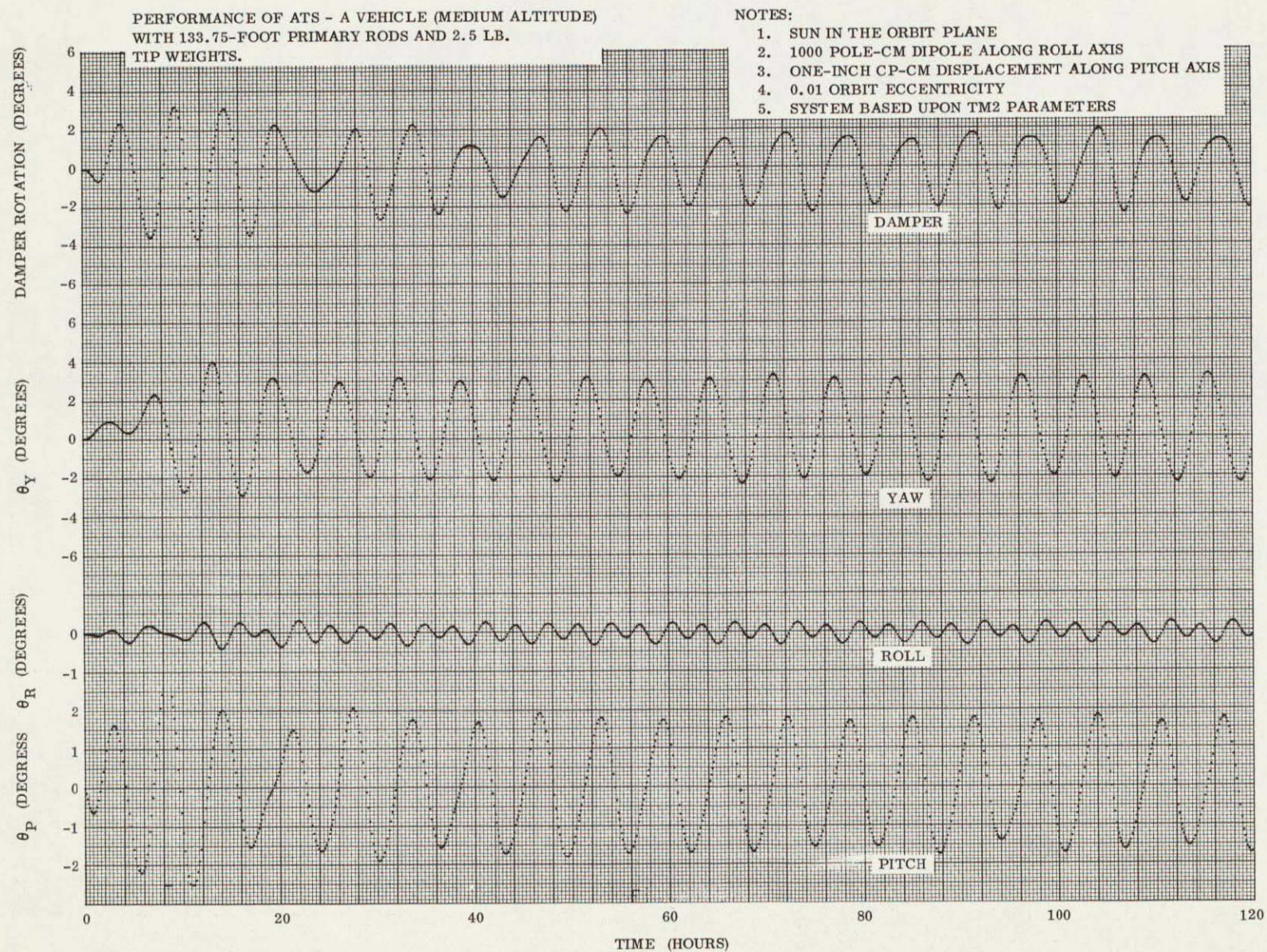
Figure 3-26.   Performance of ATS-A Vehicle (Mechanism Altitude) with 33.75-Foot
Primary Rod and 25 Tip Weighed

3.2.2.2.2 ATS-D/E Optimization

The yaw errors resulting from solar torque and thermal bending ((Figure 3.2-15), magnetic torques (Figure 3.2-10), and thruster torques (Figure 3.2-20) were combined into a single plot representing the yaw error as a function of rod length. Because the pitch axis has only one major disturbance torque, solar torque, a tradeoff plot for pitch, is not possible.

The resultant plot, Figure 3.2-27 indicates that long rod lengths are practical for ATS-D/E in order to obtain good pointing accuracy. As with ATS-A, heavy tip masses produce better performance than light tip masses, but the tip masses on ATS-D/E were already heavy (10 pounds) and additional weight was undesireable. The results of optimization (Figure 3.2-27) indicated that rod lengths in excess of 125 feet were not very beneficial in yaw. Since there is some degradation in pitch with increasing rod length (the primary error source in pitch is thermal bending), longer rod lengths should be avoided.

A limiting hardware item for ATS-D/E was the torsion wire of the hysteresis damper (Section 3.2.3). The originally specified 5 dyne-cm/deg required a large moment of inertia
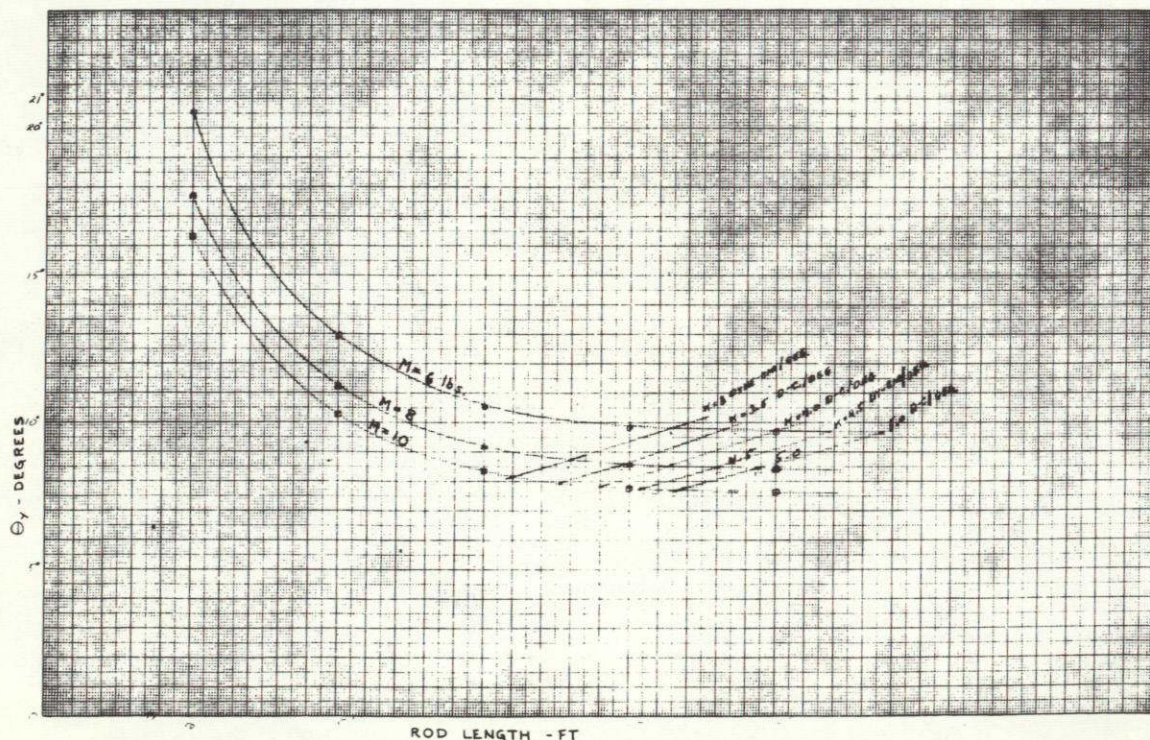
Figure 3.2-27. Total Pointing Error

system and virtually eliminated the possibility of reducing the attitude control weight. Discussions with TRW, the manufacturer of the hysteresis damper, indicated a probable lower limit of 3.5 dyne-cm/deg. This was used for the optimum spring constant and the system was sized accordingly. At a small sacrifice in performance, a weight savings of approximately 14 pounds (over the original configuration) was accomplished by reducing the tip masses. The resultant configuration utilizes 8-pound tip masses and 124.33-foot rods. Parameters selected are shown in Table 3.2-10. The hardware location and orientation is shown in Figure 3.2-28.

Four computer simulations were made to check the optimization. Two of these were for the standard comparison configurations with 100-foot rods and 10-pound tip weights, and two were for the new configuration. Cases with the sun in and out of the orbit plane were checked.

Figure 3.2-29 and 3.2-30 simulate the standard configuration and optimum configuration, respectively, at the summer solstice. In this orbit, a large large yaw bias error would be expected because the CM moves its greatest distance along the vehicle Z axis (pitch) due to thermal bending. The yaw bias is evident in both figures, but the new configuration has a smaller oscillation amplitude than the old configuration. This reduced amplitude results in a yaw performance improvement for the new configuration, as well as a weight improvement, although the other axes are slightly degraded. The performance results are summarized on Table 3.2-11.

At the time of the spacecraft optimization studies, no distinction was drawn between the ATS-D and ATS-E configurations. The term "ATS-D/E" was used to designate the fact that statements about either applied to both. However, as time progressed, there were more and more distinctions between the two. A new gravity-gradient boom system was developed for ATS-E (with half the deployment/retraction rate of those on ATS-D), new spacecraft experiments were added which had significant effects on central body moments of inertia and center of pressure/center of mass relationships, etc. These changes were reflected in revised performance estimates only (see Section 3.5). ATS-E characteristics are shown in Figure 3.2-31.

Table 3.2-10. ATS-D/E Parameters

Parameter	Optimum Configuration
X-Rod Length (ft)	124.33
Damper Rod Length (ft)	45.0
X-Rod Tip Mass (lbs)	8.0
Damper Rod Tip Mass (lbs)	4.06
X-Rod Half Angle (deg)	26.0
Angle Between X-Rod Plane and Roll Axis (deg)	4.8
Angle Between Damping Axis and Pitch Axis (deg)	53.4
Spring Constant $\frac{\text{(dyne-cm)}}{\text{deg}}$	3.5
Damping Constant $\frac{\text{(dyne-cm)}}{\text{deg/sec}}$	986.7
Moments of Inertia (slug-ft^2)	
Pitch	16,617.8
Roll	13,498.7
Yaw	3,115.5
Damper	540.2
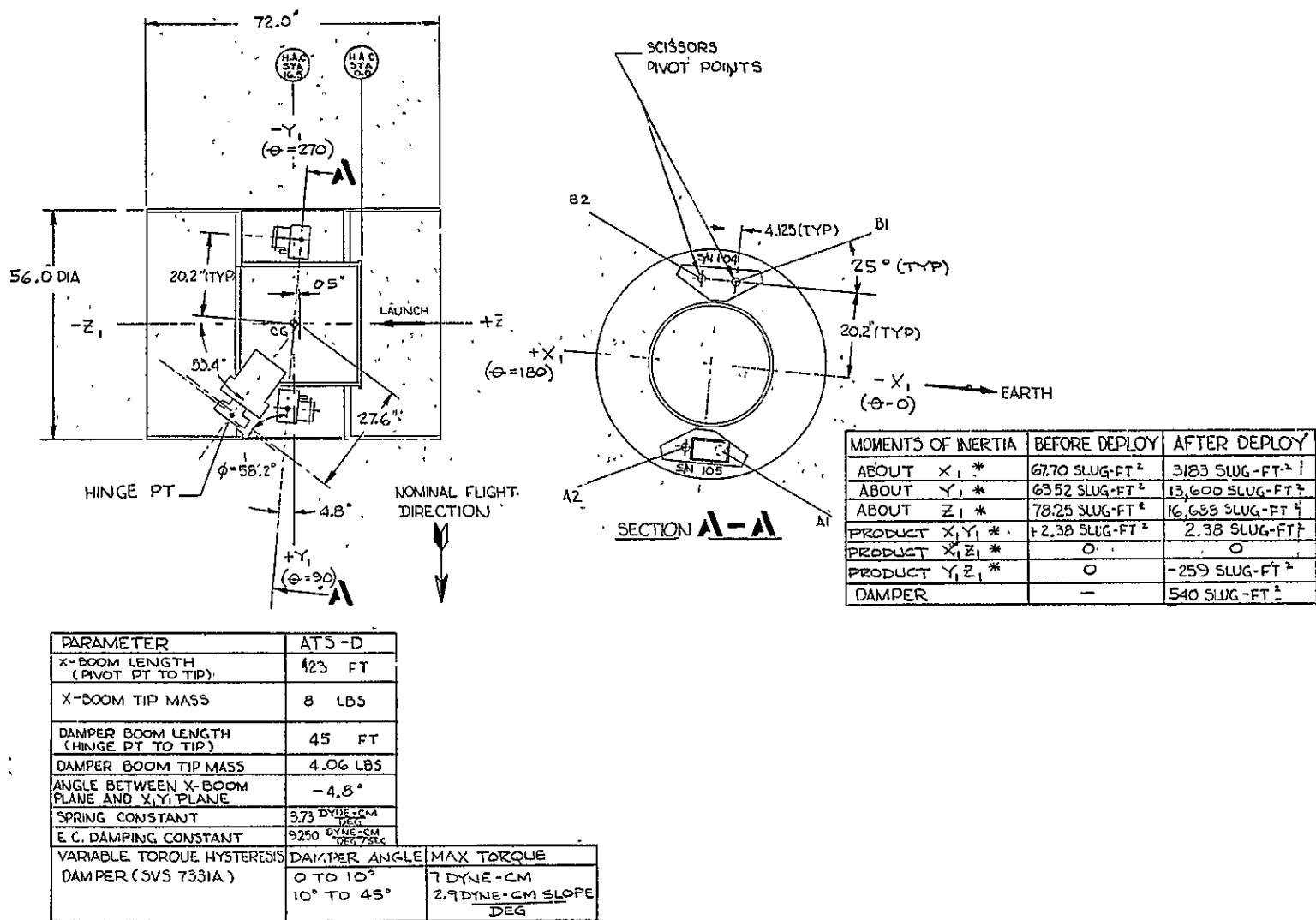
Figure 3.2-28. ATS-D Standard Configuration

MOMENTS OF INERTIA	BEFORE DEPLOY	AFTER DEPLOY
ABOUT X_1 *	67.70 SLUG-FT^2	3183 SLUG-FT^2
ABOUT Y_1 *	63.52 SLUG-FT^2	13,600 SLUG-FT^2
ABOUT Z_1 *	78.25 SLUG-FT^2	16,638 SLUG-FT^2
PRODUCT X_1Y_1 *	+2.38 SLUG-FT^2	2.38 SLUG-FT^2
PRODUCT X_1Z_1 *	O	O
PRODUCT Y_1Z_1 *	O	-259 SLUG-FT^2
DAMPER	—	540 SLUG-FT^2

PARAMETER	ATS-D	
X-BOOM LENGTH (PIVOT PT TO TIP)	123 FT	
X-BOOM TIP MASS	8 LBS	
DAMPER BOOM LENGTH (HINGE PT TO TIP)	45 FT	
DAMPER BOOM TIP MASS	4.06 LBS	
ANGLE BETWEEN X-BOOM PLANE AND X_1Y_1 PLANE	-4.8°	
SPRING CONSTANT	3.73 $\frac{DYNE-CM}{DEG}$	
E.C. DAMPING CONSTANT	9250 $\frac{DYNE-CM}{DEG/SEC}$	
VARIABLE TORQUE HYSTERESIS DAMPER (SVS 7331A)	DAMPER ANGLE	MAX TORQUE
	0 TO 10°	7 DYNE-CM
	10° TO 45°	2.9 $\frac{DYNE-CM SLOPE}{DEG}$

SECTION A-A

NOTES:

1. 1000 POLE-CM
   ALONG ROLL AXIS
2. 1.35 INCH CP-CM
   DISPLACEMENT
   ALONG PITCH AXIS
3. SUMMER SOLSTICE

Figure 3.2-29. ATS-D Reference Configuration

Figure 3.2-30. ATS-D Optimum Configuration

72.0"

H.A.C STA 16.5   H.A.C STA 0.0

−Y₁ (θ=270)

56.0 DIA

20.2"(TYP)

0.5°

−Z₁

CG

LAUNCH   +Z₁ (θ=180)

53.4°

φ=58.2°

HINGE PT

27.6"

−4.8°

+Y₁ (θ=90)

NOMINAL FLIGHT DIRECTION

SCISSORS PIVOT POINTS

A1 & B1 : "MASTER" DEPLOYERS
A2 & B2 : "SLAVE" DEPLOYERS

B2

SN 0002

4.125(TYP)   B1

25° (TYP)

20.2"(TYP)

+X₁ (θ=180)

−X₁ (θ=0)   EARTH

SN 0003   A1

A2

SECTION A-A

PARAMETER	ATS-E
X-BOOM LENGTH (PIVOT PT TO TIP)	121 FT
X-BOOM TIP MASS	8 LBS
DAMPER BOOM LENGTH (HINGE PT TO TIP)	45 FT
DAMPER BOOM TIP MASS	4.06 LBS
ANGLE BETWEEN X-BOOM PLANE AND X₁Y₁ PLANE	−4.8°
SPRING CONSTANT	4.11 DYNE-CM/DEG
E.C. DAMPING CONSTANT	11470 DYNE-CM/DEG/SEC

VARIABLE TORQUE HYSTERESIS DAMPER (SVS 7531A)	DAMPER ANGLE	MAX TORQUE
	0 TO 10°	14 DYNE-CM
	10° TO 45°	2.6 DYNE-CM SLOPE/DEG

MOMENTS OF INERTIA (SLUG-FT²)	BEFORE DEPLOYMENT	AFTER DEPLOYMENT *	
		WITH DAMPER	W/O DAMPER
ABOUT X₁	81.20	3554.1	3008.2
ABOUT Y₁	82.40	13142.5	12792.0
ABOUT Z₁	95.80	15887.0	15691.6
PRODUCT X₁Z₁	+ 2.382	0	0
PRODUCT X₁Z₁	0.0	0	0
PRODUCT Y₁Z₁	+ 1.046	+16.6	−243.5
DAMPER	—	540	—

* AFTER SCISSORING

Figure 3.2-31. ATS-E Nominal Configuration

Table 3.2-11. Performance Comparison for ATS-D/E

	θ_p (degree)	θ_R (degree)	ϑ_Y (degree)
Previous Configuration	1.0	1.5	7.8
Recommended Configuration	1.2	1.8	7.4
Increase in Accuracy	-0.2	-0.3	+0.4

3.2.3 OPTIMIZATION OF HYSTERESIS DAMPING

The ATS spacecraft, as originally conceived, was based upon rate damping in the damper. The use of rate damping facilitated the linear analysis and permitted the optimization of the non-dimensional parameters. From the standpoint of hardware implementation however, rate damping is cumbersome and heavy for this particular damper design. As a consequence, due to its light weight, magnetic hysteresis damping was considered and ultimately added as an experimental damping mechanism. Hysteresis damping is not a linear phonomenon however, and optimization using standard optimization techniques is not possible. To determine the optimum value of hysteresis torque, a computer study was undertaken. To provide the proper base for a computer study, an accurate model of the hysteresis phenomenon was necessary. No good theoretical models (of general form) exist, however, and an empirical relationship, based on data supplied by TRW, was derived. The data is shown in Figures 3.2-32 and 3.2-33, and uses the constant torque hysteresis damper. To effectively utilize this information, it was necessary to remove the spring constant which was included in the data. The "pure" hysteresis torques obtained from this data are shown in Figure 3.2-34.

For convenience in the following discussion, several terms will be defined.

1. Hysteresis torque is the torque exerted on the boom by the hysteresis damper and may be less than or equal to the saturation torque.

2. Saturation torque is the maximum hysteresis torque the damper is capable of producing.
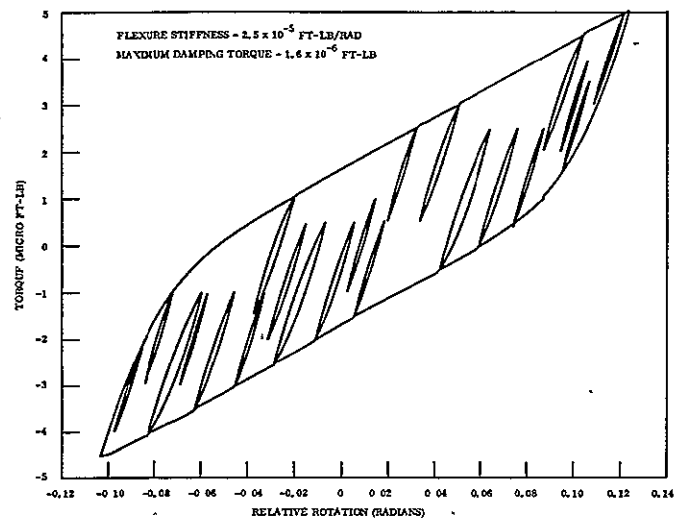
Figure 3.2-32. Torque vs Rotation for Laboratory Model Damper
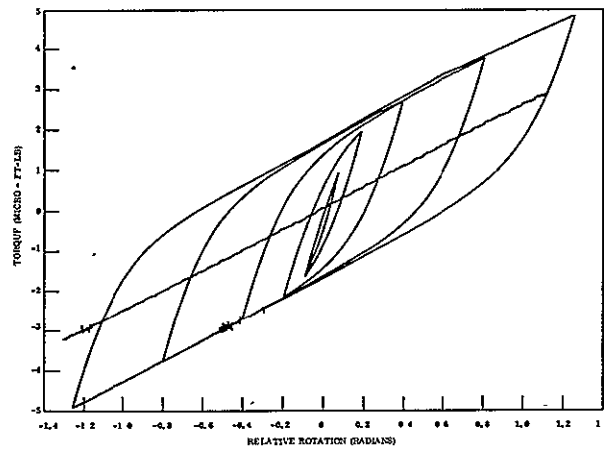
Figure 3.2-33. Magnetic Hysteresis Data
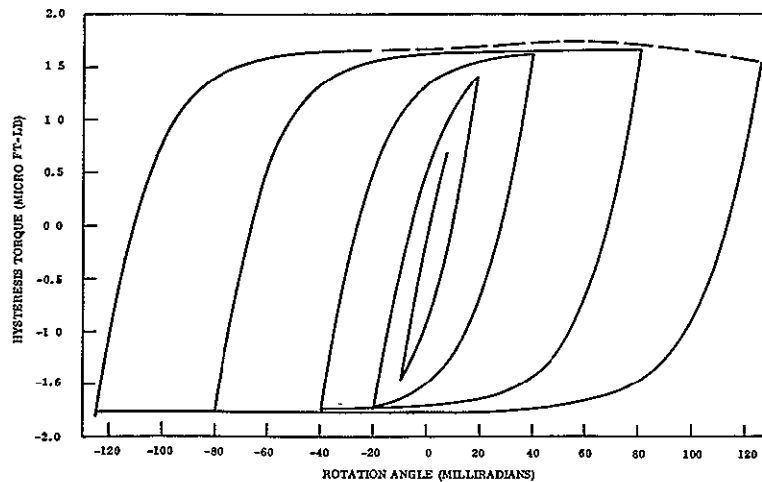
Figure 3.2-34. Magnetic Hysteresis Data

3. <u>Major loops</u> describe the curve of hysteresis torque versus angle when the torque starts from positive (or negative) saturation torque.

4. <u>Minor loops</u> are loops which do not start from saturation.

This terminology will be used throughout the section.

After several curve fitting attempts on Figure 3.2-34, it was found that an exponential curve would fit a major loop with good accuracy. Figure 3.2-35 is a plot of a major loop from the data of Figure 3.2-33 with an exponential curve of the form

$$T = T_o \left(1 - e^{\frac{\Delta\alpha}{\alpha_{rise}}} \right) \qquad \qquad 3.2-30$$

(indicated by dots) superimposed. For this plot, $1/\alpha_{rise} = 60$ and the exponential equation fits well within the limits of the reduction of the data. To ensure that this was not a chance fit, additional data (not presented) was obtained and another exponential fit attempted. The exponent of the equation had to be increased to 77, but the fit was as good as that of Figure 3.2-35. It is probable that manufacturing tolerances produce a slight difference in damper characteristic.

Minor loop simulation is also achieved by curve fitting. Theory and data indicate that after a reversal, the torque will change as a function of the angle from reversal in such a manner as to pass through a point of previous reversal. Figure 3.2-33 clearly shows this phenomenon in the appearance of the closed minor loops. After passing this point of reversal, the hysteresis torque changes in the same manner it was changing before the reversal occurred.

Figure 3.2-36 is a hypothetical case involving minor loop construction. At the start, the hysteresis torque is changing in a manner indicated by Curve 1. After reversing at point α, the torque follows Curve 2 which passes through the point of previous reversal (not shown). Reversing again at β produces Curve 3 which passes through reversal point α. If it passes point α, the torque reverts to Curve 1 and continues. This process is followed
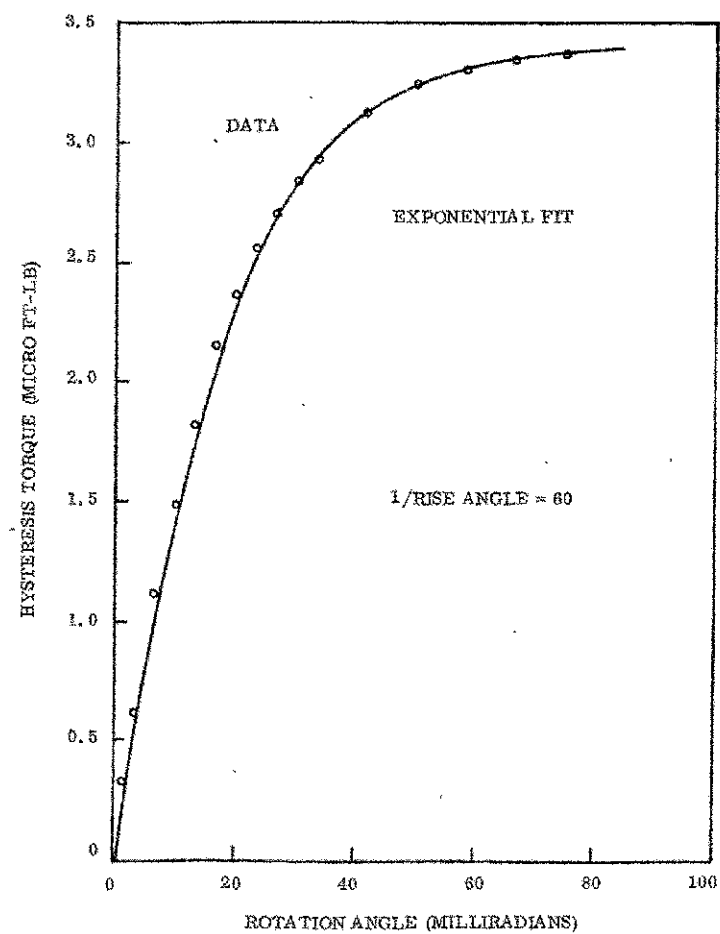
Figure 3.2-35. Exponatial Fits of Hysteresis Data
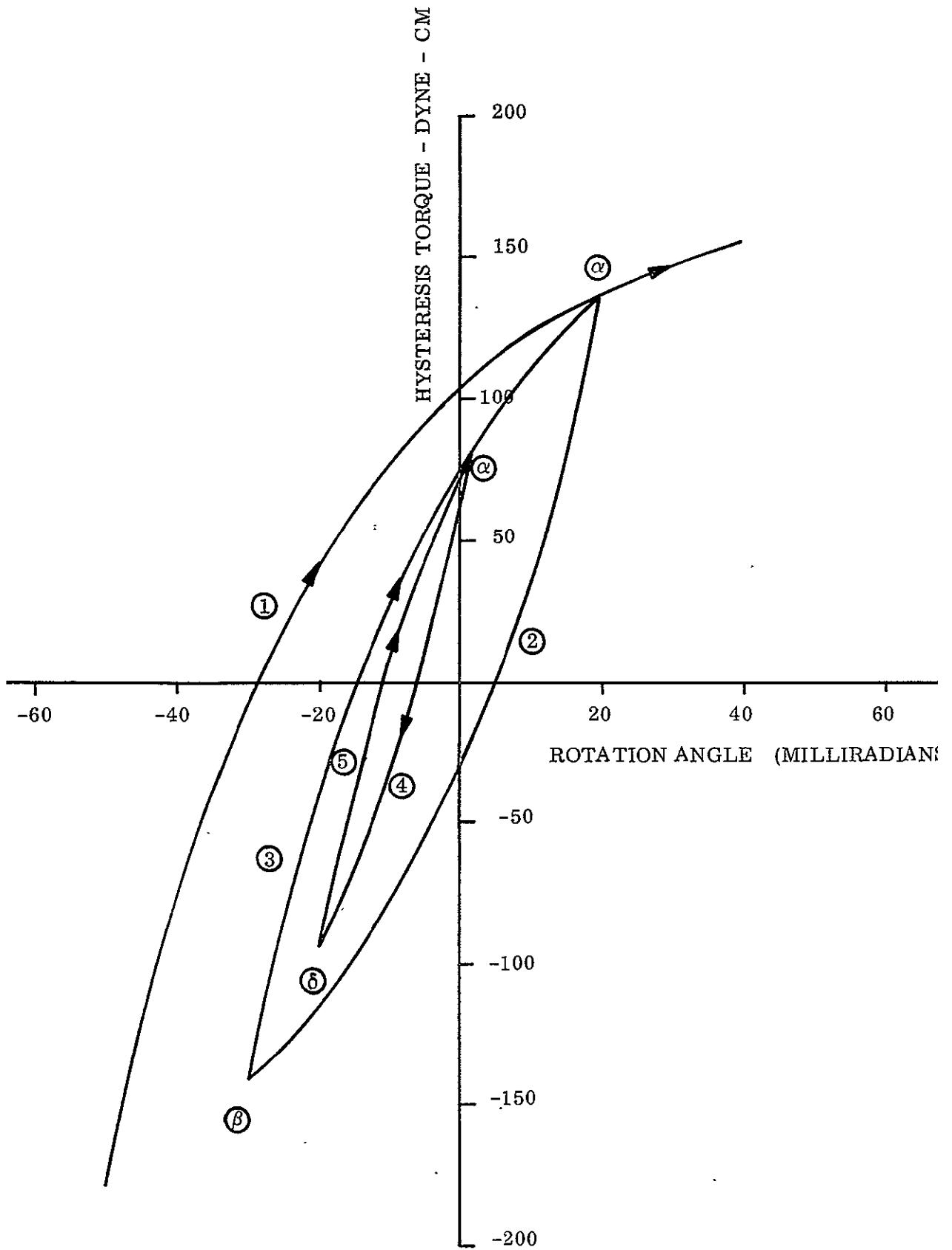
Figure 3.2-36. Theoretical Construction of Minor Loops

for all minor loops. The torque changing as shown on Curve 5, for example, would revert to the Curve 3 after passing reversal point γ and to Curve 1 after passing reversal point α.

Mathematical simulation of minor loops is achieved by using major loops which have their origin at the point of reversal. The results of this assumption are shown in Figure 3.2-37. Each major loop was initiated at the point of data reversal. Closer agreement could be obtained in most cases if the calculated curve was initiated at its calculated point of reversal (i.e., reversal would occur at the measured value of rotation angle, but the calculated value of hysteresis torque). However, correlation was good for the case show with the maximum percentage error less than 2.7 percent for the small loops.

This formulation of the minor loops and major loops was implemented within the digital simulation, and numerous simulations were made to determine the optimum hysteresis design. Two basic hysteresis designs were considered in the analysis, a constant torque hysteresis damper known as the passive hysteresis damper, (PHD), and a "bow tie" hysteresis damper known as the variable torque hysteresis damper (VTHD).

3.2.3.1 Passive Hysteresis Damper

In a hysteresis damped system utilizing a damper with a constant value of hysteresis satura tion torque, T_{SAT}, the optimum hysteresis value is selected based upon two factors. Fir; sufficient damping must be provided to minimize the time required to reduce the vehicle pointing error to a level where the vehicle can perform its mission. Second, T_{SAT} must be high enough to provide reasonable damping when the spacecraft is undergoing large oscillations. Steady-state pointing accuracy is virtually independent of T_{SAT}, and is not a factor in determining its value.

Figures 3.2-38 and 3.2-39 show the time required to settle to various levels of earth-pointing error as a function of T_{SAT} for the ATS-A and ATS-D spacecraft, respectively. These curves are based upon data obtained from a series of computer simulations.
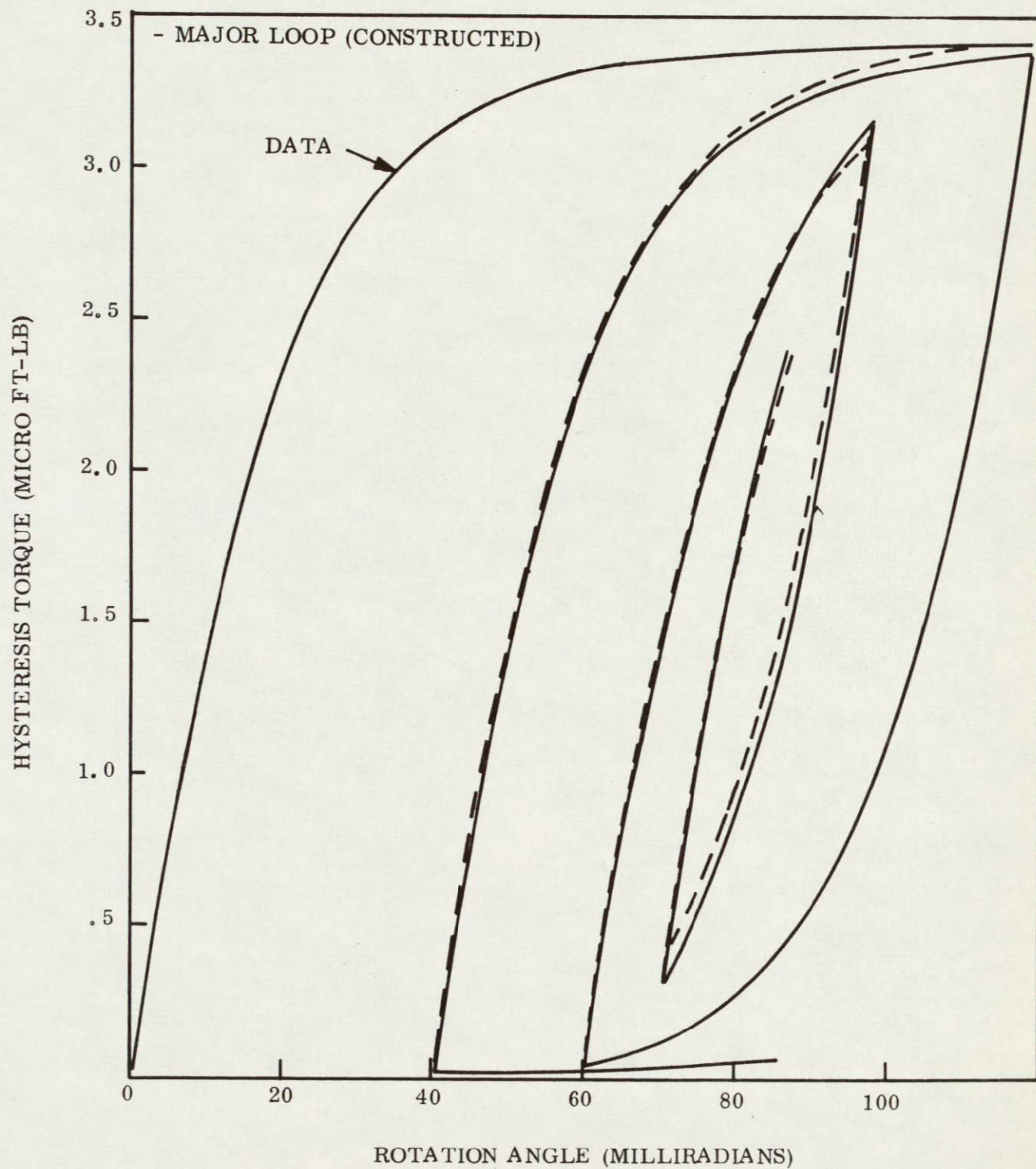
Figure 3.2-37. Minor Loop Simulation of Hysteresis Data Using Major Loop Shape
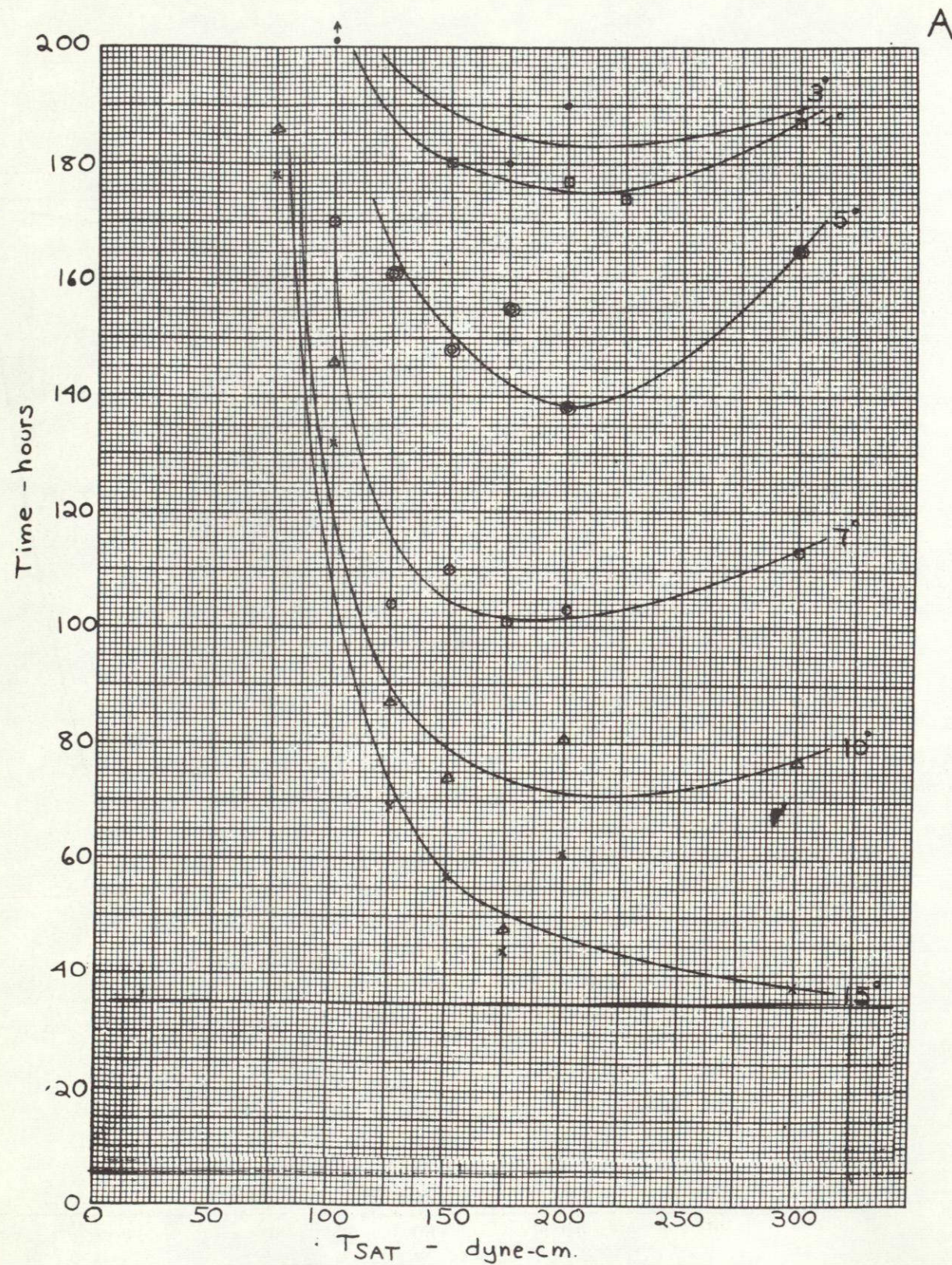
Figure 3.2-38. ATS-A with Constant Saturation Torque Hysteresis Damper Time to Damp Various Earth Pointing Errors as a Function of Hysteresis Saturation Torque
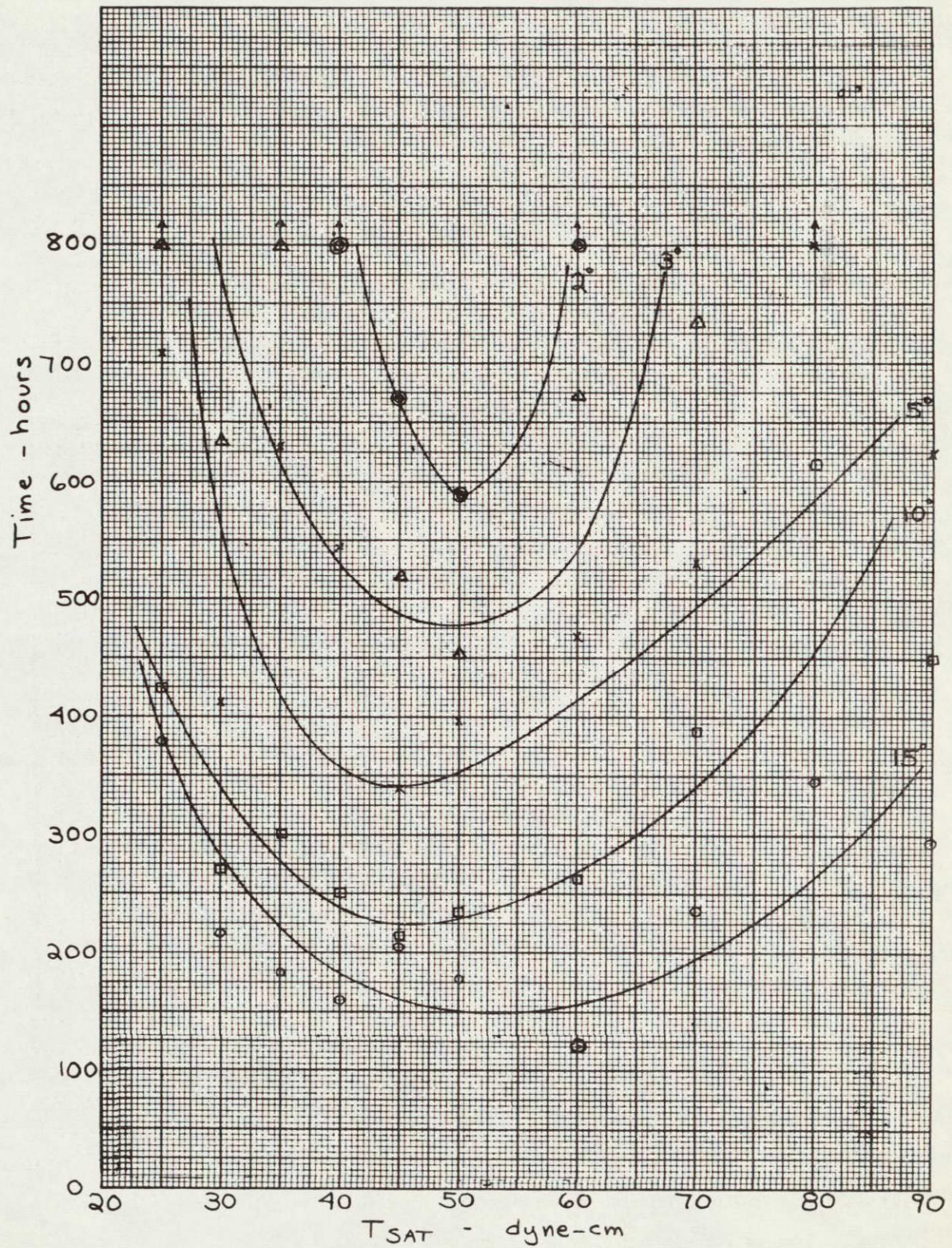
Figure 3.2-39. ATS-D with Constant Saturation Torque Hysteresis Damper Time to Damp Various Earth Pointing Errors as a Function of Hysteresis Saturation Torque

The spacecraft initial conditions listed in Table 3.2-12 define a standard transient which was used throughout the system analysis effort to provide meaningful comparisons of data. This standard transient was taken from an ATS-A capture study (Section 3.3.1) with the vehicle rates scaled down for use with ATS-D.

Table 3.2-12. Spacecraft Initial Conditions

	ATS-A	ATS-D
1. Vehicle initial attitude (Deg)		
Pitch	-35.9	-35.9
Roll	8.1	8.1
Yaw	180.5	180.5
Damper Room	0	0
2. Vehicle initial attitude rate $\frac{deg}{sec}$		
Pitch	- 0.0175	-0.00467
Roll	- 0.01408	-0.00376
Yaw	0.005993	0.0016
Damper Boom	0	0
3. Orbit Eccentricity	0.01	0
4. Magnetic Dipole Along Roll axis (pole-cm)	1000	1000
5. Solar Effects	None	None

Immediately evident in Figures 3.2-38 and 3.2-39 is the amount of scattering of the data. There are several reaons for this. Initially, the spacecraft is spinning in yaw. In some runs the spacecraft steady-state yaw angle is 0 degrees, in other runs it is 180 degrees. This difference in rotating through half a revolution will materially affect settling times.

Another factor that contributes to the data scatter in the Figures is the use of arbitrary levels of earth-pointing errors. For example, consider the following hypothetical case. At 150 hours, two runs yield the following data:

T_{SAT}	θ_E
150	4.9
175	5.1

The first run has already settled to 5 degrees. The second has not, and may not reach 5 degrees or less for another 30 or 40 hours. This yields scattered data points although it is apparent that these two runs are very similar.

Despite the data scatter there are obvious trends to be seen. Based upon this data, the following nominal values of T_{SAT} were chosen to minimize damping time to low values of pointing error.

ATS-A	ATS-D
175 dyne-cm	50 dyne-cm

These values were checked with additional digital simulations with solar effects included. For ATS-A, three 600-hour runs were made with T_{SAT} = 150, 173, and 200 dyne-cm. For ATS-D, three 2250-hour runs were made with T_{SAT} = 40, 50 and 60 dyne-cm. The resulting damping characteristics are plotted in Figures 3.2-40 and 3.2-41. Scattering of the data is not present in these curves because settling times to arbitrary values of error are not used. The curves shown are the envelopes of the earth-pointing error oscillations, and show similar damping performance for all the values of T_{SAT} used for each space-craft. As time increases the effect of the value of T_{SAT} on damping performance decreases. All the value used provide satisfactory damping performance, and this was used to select the tolerances values of ±25 dyne-cm for ATS-A and ±10 dyne-cm for ATS-D.
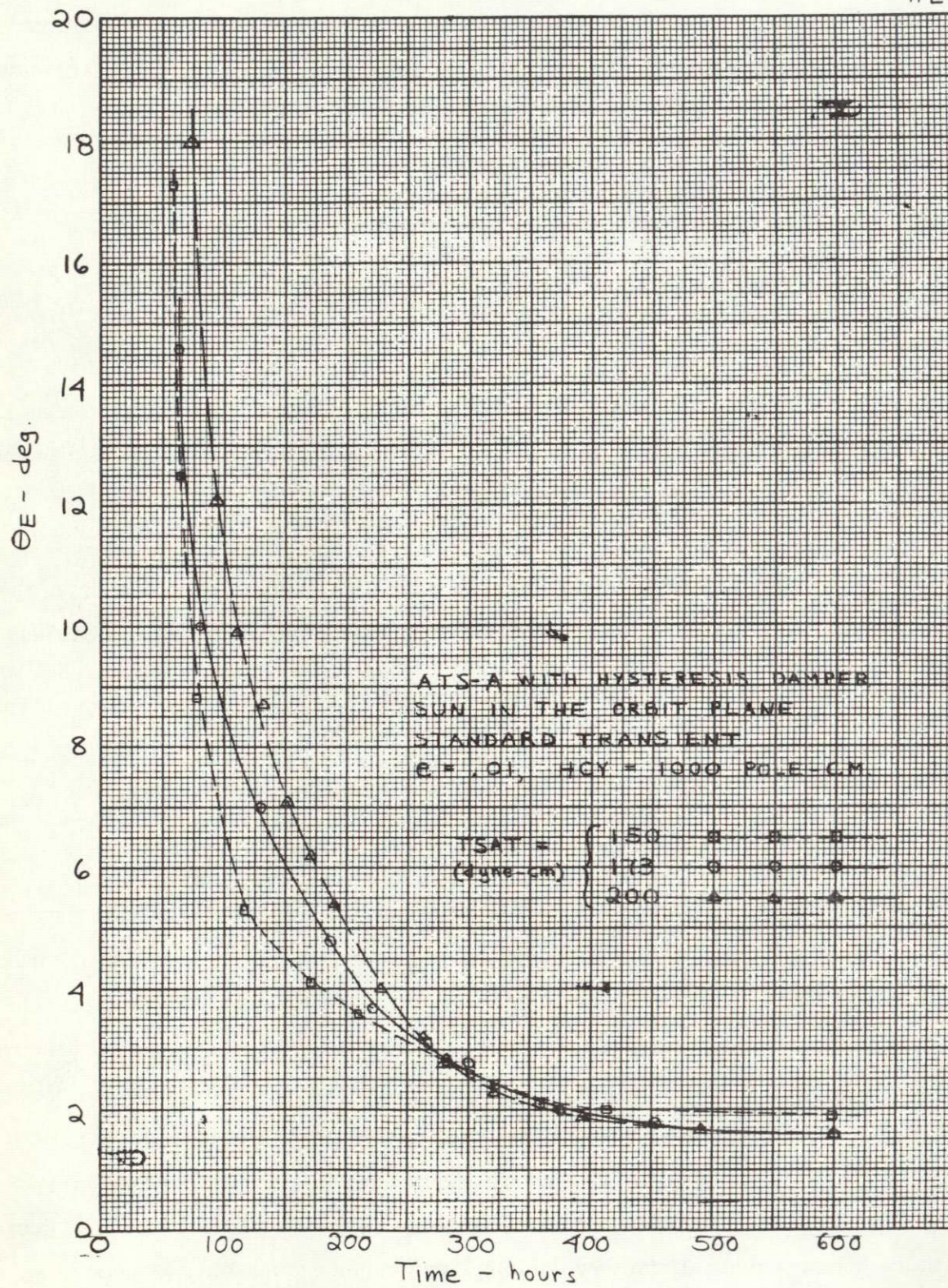
Figure 3.2-40. ATS-A Damping Performance
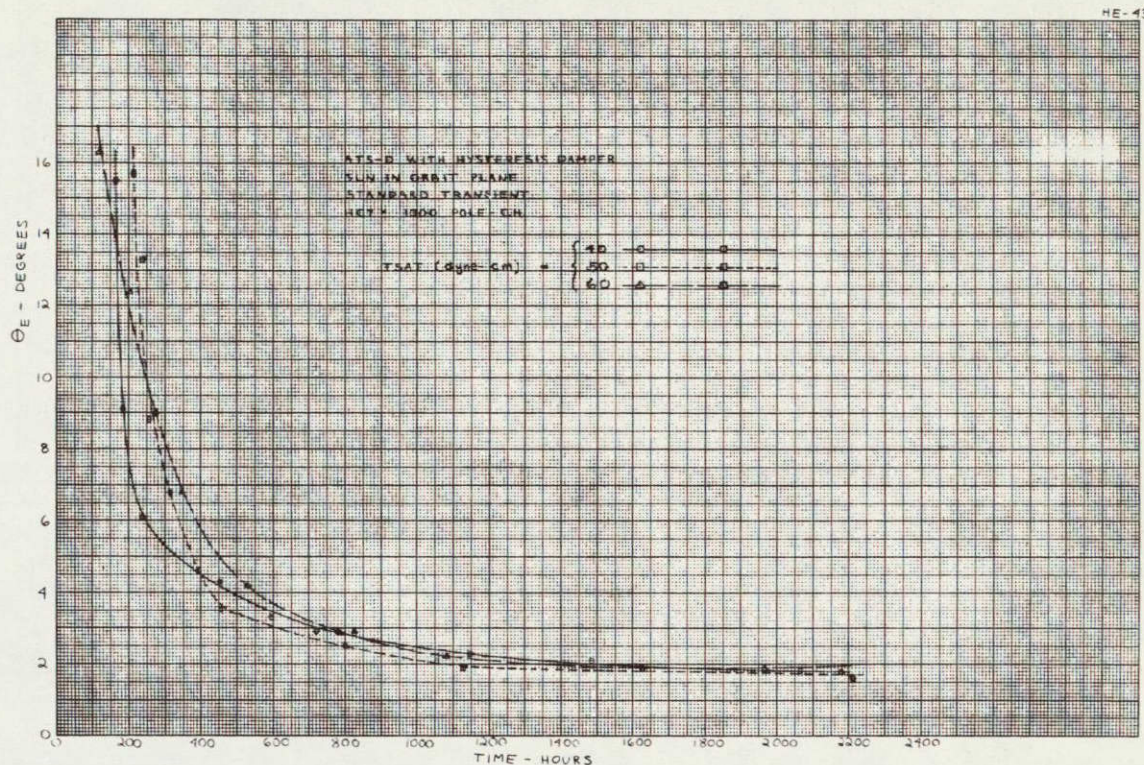
Figure 3.2-41.   ATS-D Damping Performance

Figures 3.2-42 through 3.2-45 show the performance with the nominal values of T_{SAT} for both ATS-A and ATS-D.   The 30-hour gap in the ATS-A curves between 190 and 220 hours was necessary to provide a convenient large scale plot for both transient and steady-state conditions.   Steady state performance is virtually identical to that achieved by the rate damper.

3.2.3.2   Variable Torque Hysteresis Damper

The passive hysteresis damper, even at its optimum, produces very long time constants as evidenced by Figures 3.2-42 and 3.2-43.   The problem is particularly severe for ATS-D, where steady state may not be reached for 1200 hours.   The value of T_{SAT} determined in Section 3.2.3.1 represents a compromise between good damping of large and small disturbances.   If T_{SAT} is high, there is good damping of large transients and the damper boom motion is not excessive.   However, when the disturbance errors are small the damper boom
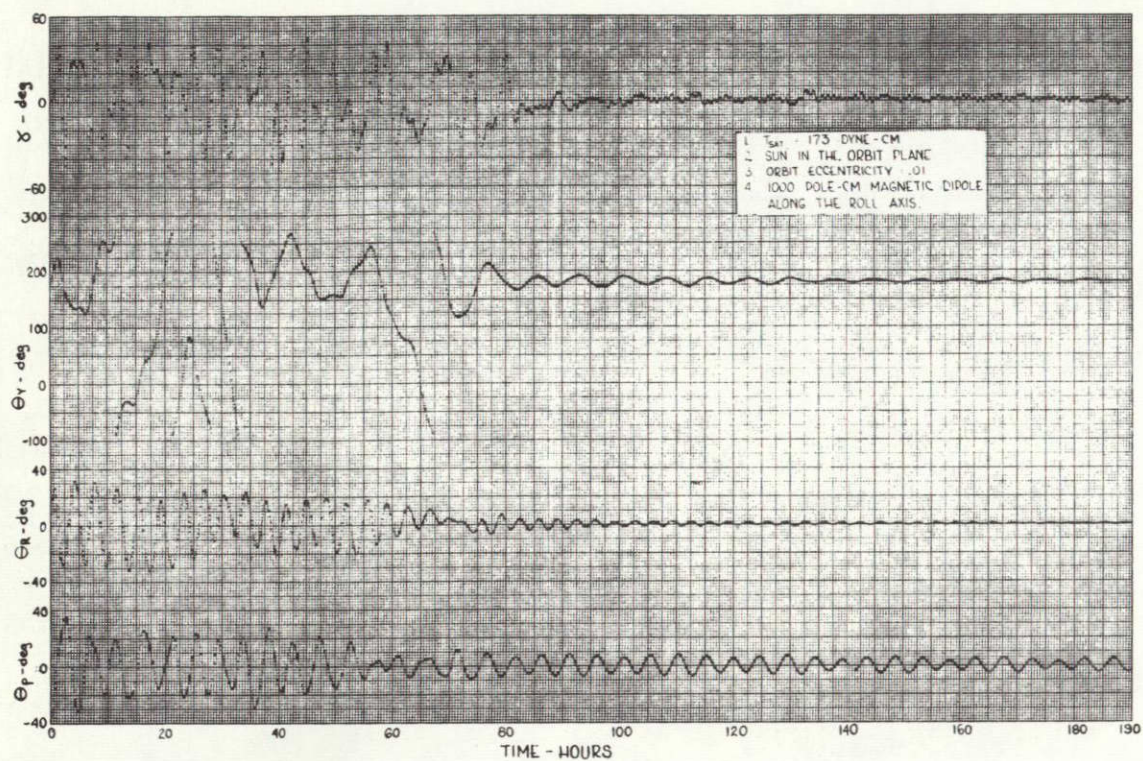
Figure 3.2-42.   ATS-A Dampint Performance
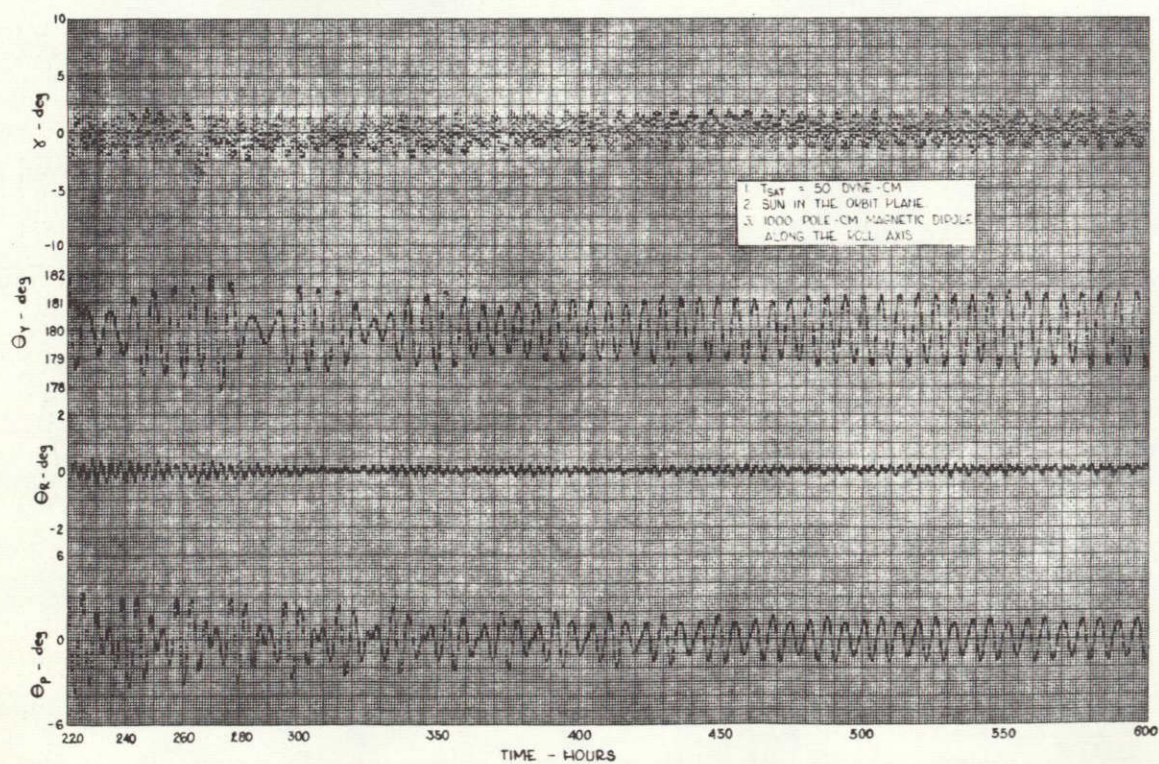
Figure 3.2-43.   ATS-A Damping Performance
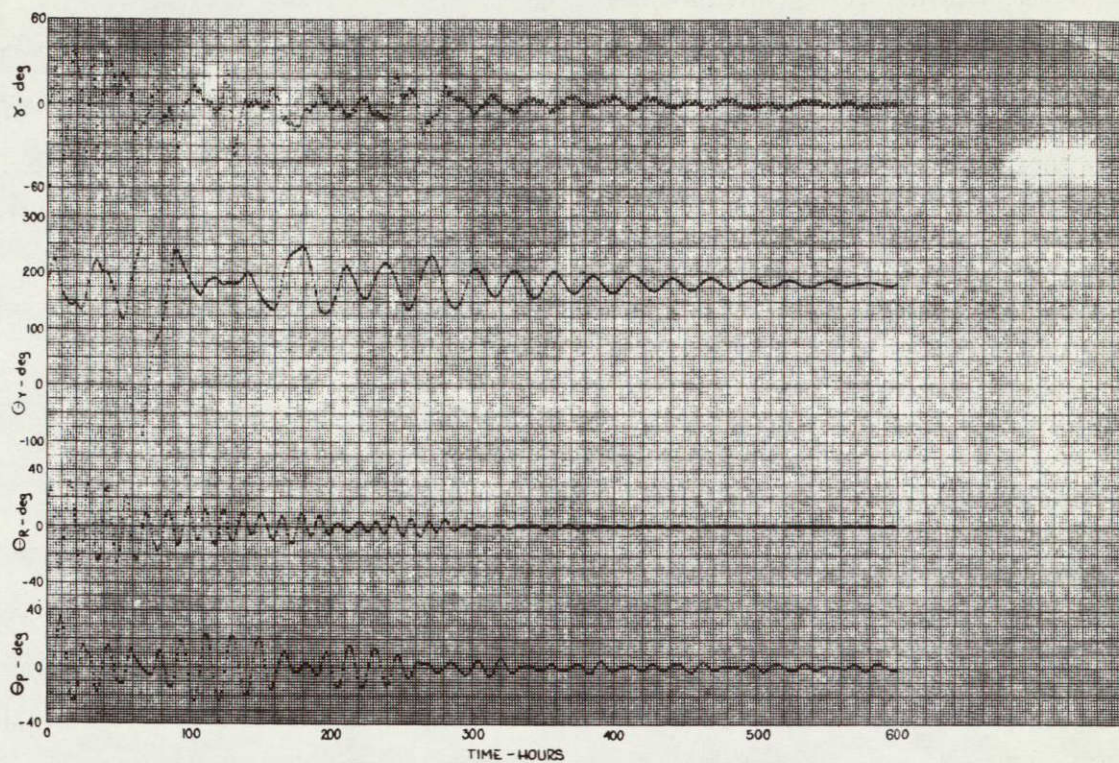
Figure 3.2-44.   ATS-D Damping Performance
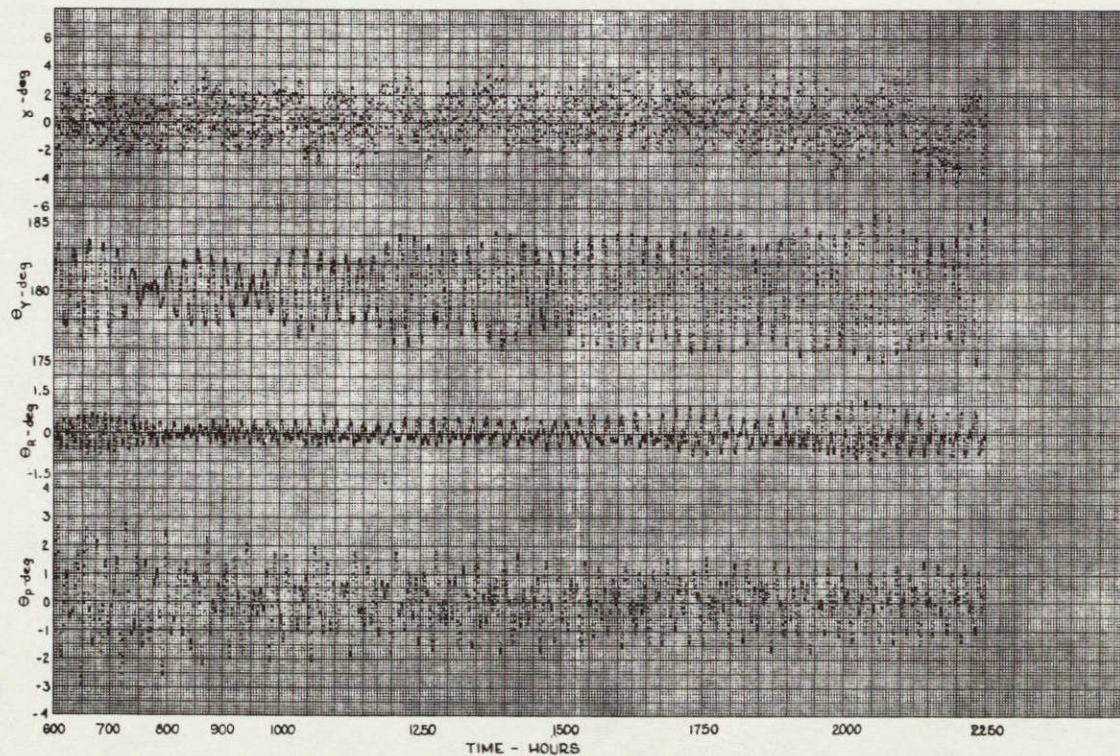
Figure 3.2-45.   ATS-D Damping Performance

motion is too limited to provide good damping. Conversely, low values of T_{SAT} provide good damping for small disturbances, but damping the presence of large disturbances is completely inadequate and damper boom motion is excessive. In an attempt to improve hysteresis damper performance, a damper was designed in which T_{SAT} is a function of damper boom angular rotation, γ. This has been called the "bowtie" concept. The approach permits the utilization of a small lightweight hysteresis damper without the penalty of long damping times.

To improve hysteresis damper performance, it is necessary to provide low values of T_{SAT} for small spacecraft disturbances, and large values for large disturbances. This is accomplished by making T_{SAT} a function of γ. The model used is shown in Figure 3.2-46 for the first quadrant. The other three quadrants are similar. To determine T_{MIN} a series of computer runs were made for a 5 degree pitch displacement of ATS-A and constant values of T_{SAT}. The time to damp to a 2.8 degree earth-pointing error as a function of T_{SAT} is shown in Figure 3.2-47. From this data T_{MIN} was chosen to be 20 dyne-cm (for ATS-A).

γ_1 was originally set at the value of the steady-state damper boom oscillation amplitude from the above runs. This was $\gamma_1 = 4$ degrees. Using $T_{MIN} = 20$ dyne-cm and $\gamma_1 = 4$ degrees, a series of runs was made with values of SLOPE 1 from 15 to 35 dyne-cm/deg. Initial conditions were a large transient taken from an ATS-A capture run (Section 3.3.1). This transient, often called the standard transient, has been used in many computer runs to permit meaningful comparisons of data. Its values are (from Table 3.2-12):

	Attitude (degrees)	Attitude Rate $\frac{deg}{sec}$
Pitch	-35.9	-0.0175
Roll	8.1	-0.01408
Yaw	180.5	0.005993
Damper Boom	0	0
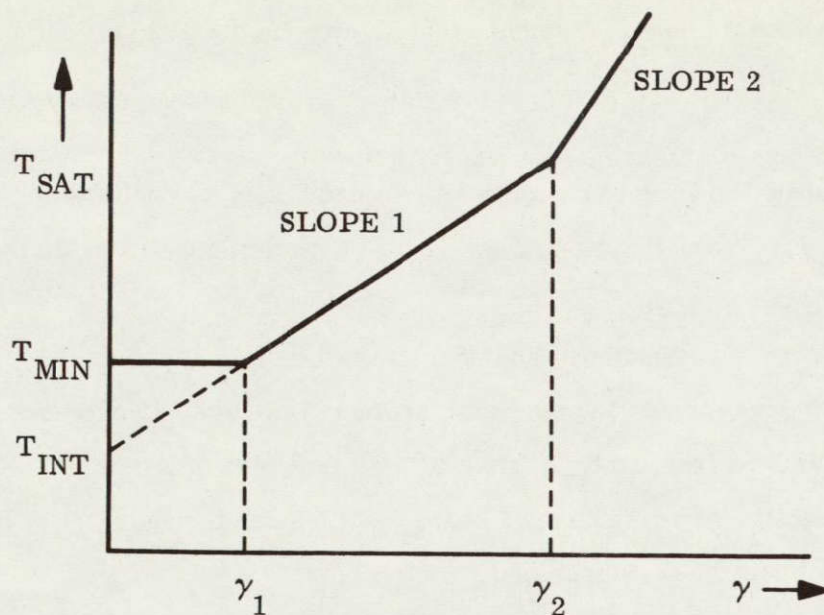
Figure 3.2-46. Typical "Bow Tie" Configuration for One Quadrant
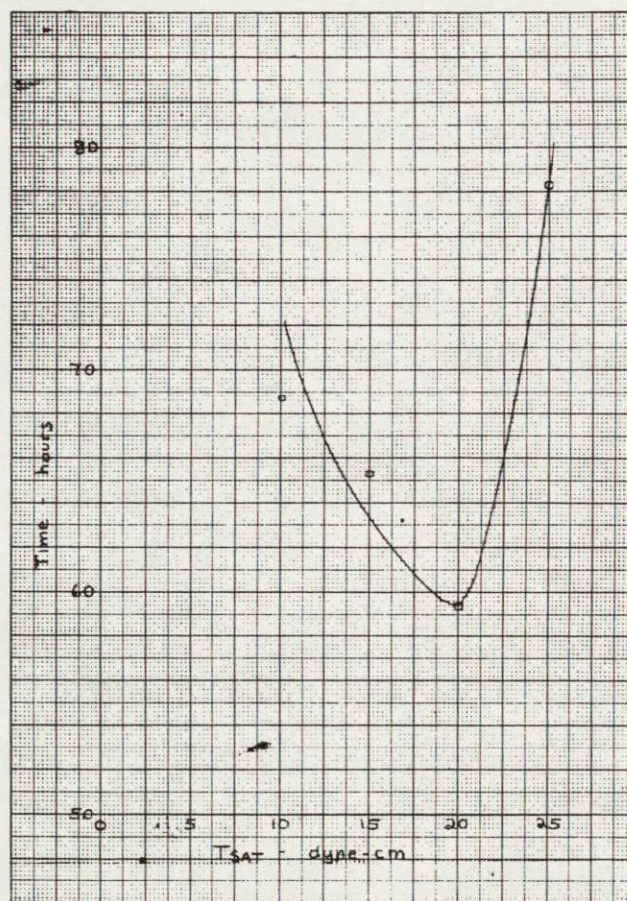
Figure 3.2-47. Time to Settle 2.8 Degrees from an Initial
5 Degree Pitch Error as a Function of T_{SAT} for ATS-A

Initial conditions also include 0.01 orbit eccentricity, and a 1000 pole-cm magnetic dipole along the vehicle roll axis.

Figure 3.2-48 shows the time to damp to an earth-pointing error of 4 degrees for various values of SLOPE 1. From Figure 3.2-48 SLOPE 1 was chosen to be 20 dyne-cm/deg.

Another series of runs was made to confirm the value of γ_1. Using T_{MIN} = 20 dyne-cm and SLOPE 1 = 20 dyne-cm/deg, values of γ_1 from 1-10 degrees were used. Initial conditions were the standard transient. Figure 3.2-49 is a plot of the earth-pointing error at 200 hours as a function of γ_1. There is some data scatter beyond $\gamma_1 = 5^O$ but a trend is evident. γ_1 was chosen to be 5 degrees.

This set of parameters provided relatively good damping for moderate and small disturbances. To improve large disturbance damping, SLOPE 2 was set at 30 dyne-cm/deg and γ_2 at 15 degrees. No additional runs were made to confirm these values. They were based upon the data already obtained, combined with engineering judgment.
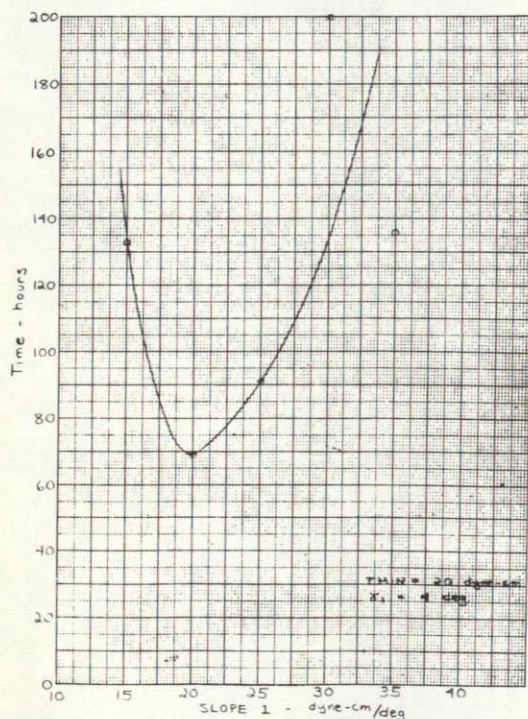
Figure 3.2-48. Time to Settle to 4 Degrees from the Standard Transient as a Function of Slope 1 for ATS-A
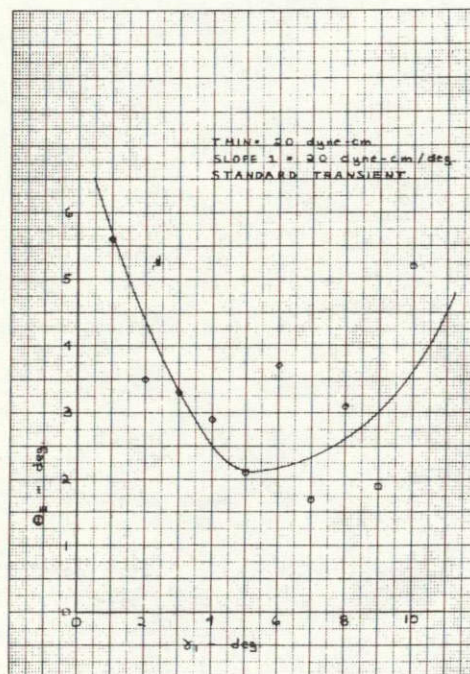
Figure 3.2-49. Maximum Earth-Pointing at 200 Hours as a Function of γ_1 for ATS-A

The recommended set of parameters and tolerances for ATS-A are listed below:

T_{MIN}	20 ± 5	dyne-cm
1	5 ± 1	deg
2	15	deg
SLOPE 1	20	dyne-cm/deg
SLOPE 2	30	dyne-cm/deg

Figure 3.2-50 is a plot of the ATS-A system response to the standard transient using the nominal hysteresis damper parameters, and including solar effects. Figure 3.2-51 shows the damping performance compared to the performance of: (1) the present hysteresis damper in ATS-A, in which T_{SAT} is constant at 175 dyne-cm, and (2) the present eddy current damper.
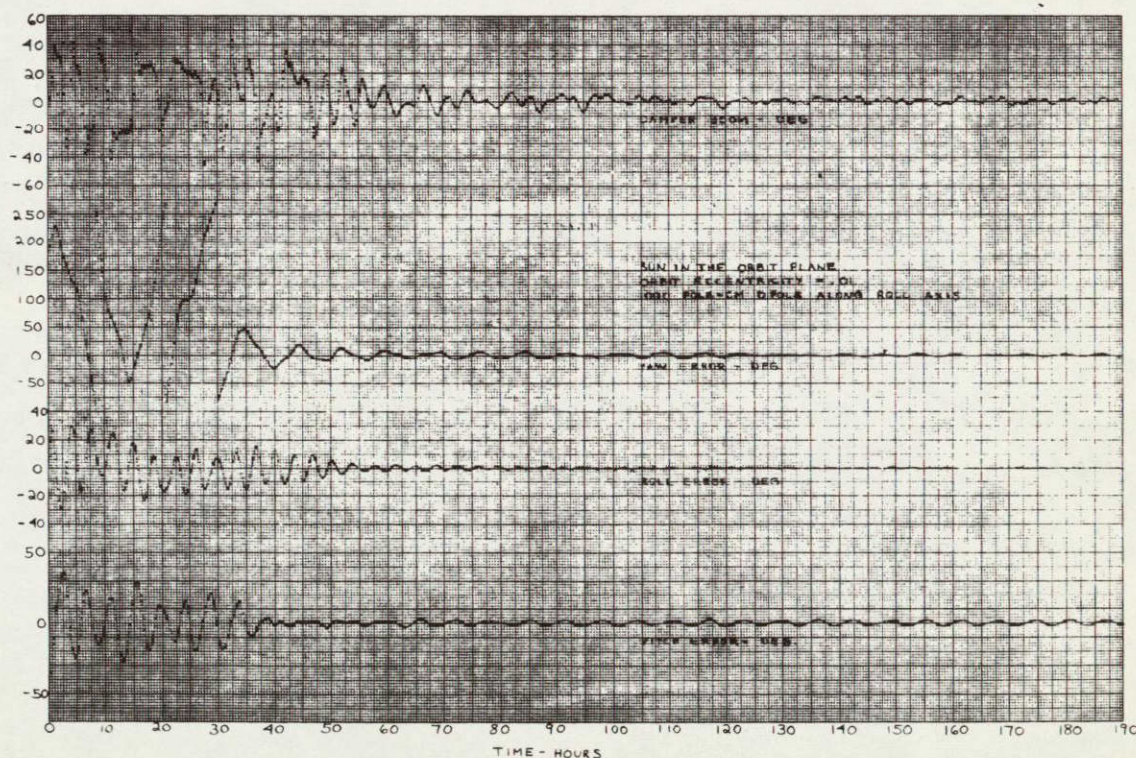
Figure 3.2-50. Response of ATS-A Vehicle with a "Bow Tie" Hysteresis Damper to the Standard Transient
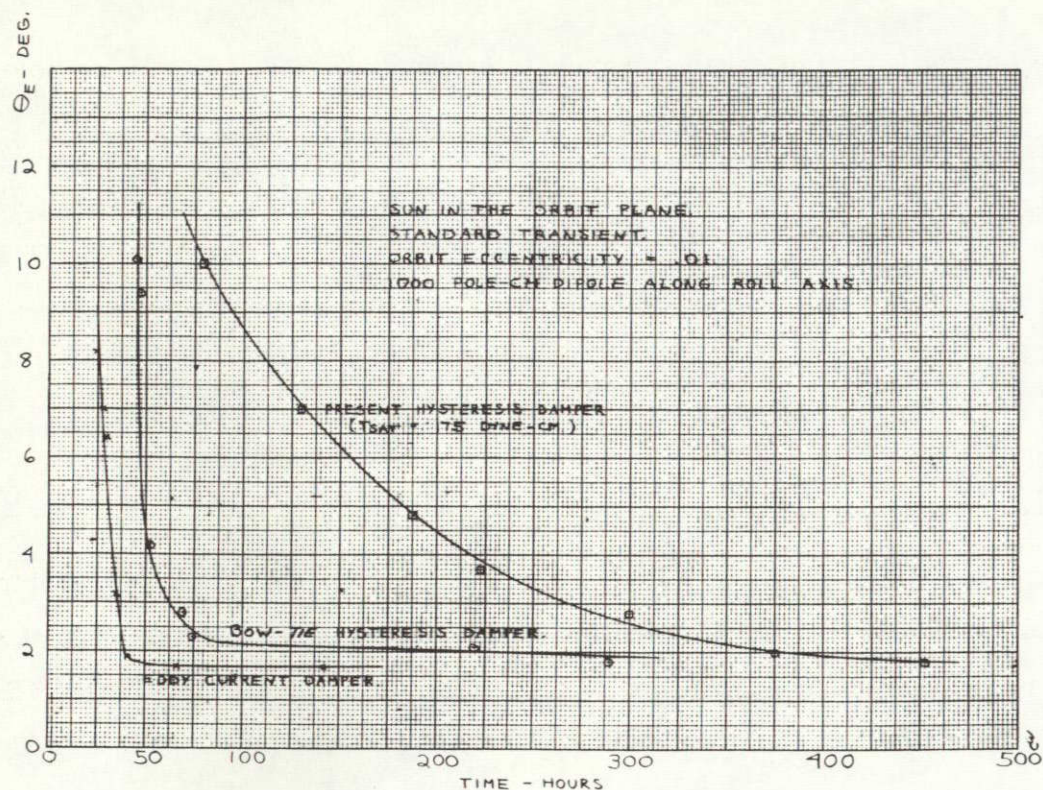
Figure 3.2-51. ATS-A Damping Characteristics

Several runs were made to determine the effects of the parameter tolerances. Figure 3.2-52 is a comparison of damping performance of the nominal hysteresis torque characteristic and the upper and lower boundary characteristics. The upper boundary is defined as the $T_{SAT} - \gamma$ curve in which T_{MIN}, SLOPE 1 and SLOPE 2 are at their upper limits. The lower boundary is defined in a corresponding manner.

The parameters for the ATS-D bow-tie hysteresis damper are scaled from the ATS-A values. The scale factor is:

$$\frac{\left(I_D \omega_o^2\right)_{ATS-A}}{\left(I_D \omega_o^2\right)_{ATS-D}} = 6.00 \qquad\qquad 3.2-31$$
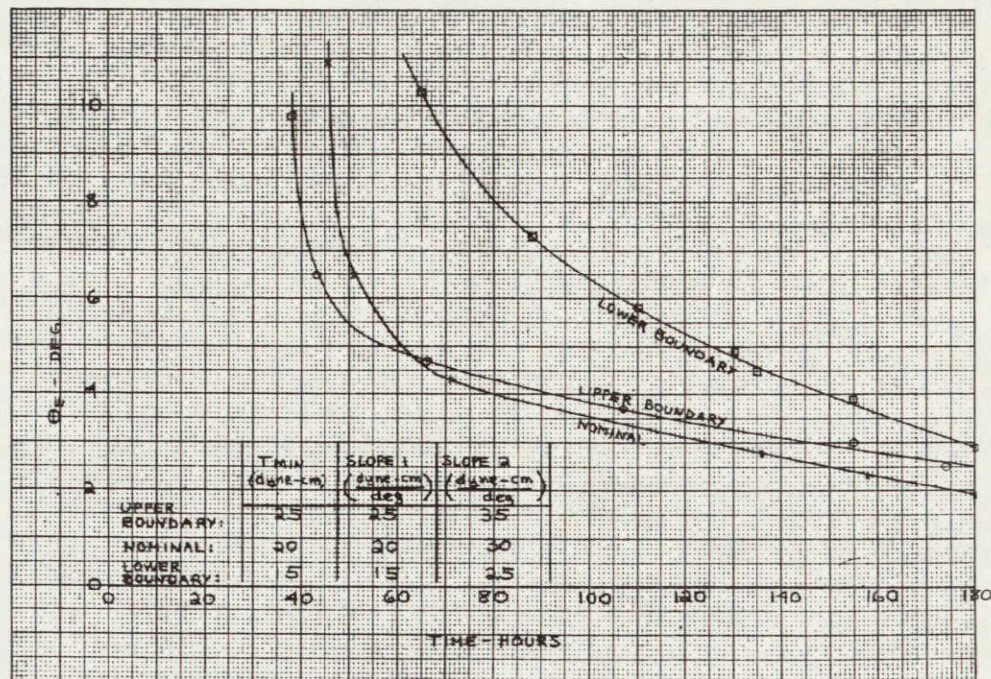
Figure 3.2-52. Effects of Parameter Tolerance of "Bow Tie" Hystersis Damper Upon Damping Performance

	T_{MIN} (dyne-cm)	SLOPE 1 $\left(\dfrac{\text{dyne-cm}}{\text{deg}}\right)$	SLOPE 2 $\left(\dfrac{\text{dyne-cm}}{\text{deg}}\right)$
UPPER BOUNDARY:	25	25	35
NOMINAL:	20	20	30
LOWER BOUNDARY:	5	15	25

where

I_D = damper moment of inertia

ω_o = orbital rate

T_{MIN}, SLOPE 1 and SLOPE 2 in ATS-A must be divided by 6.00 to obtain the equivalent values for ATS-D. γ_1 and γ_2 remain unchanged.

Studies on the problem of capture of ATS-D (see Section 3.3.2) have indicated that great care must be exercised in the selection of a hysteresis contour. The studies have shown that a significant increase in damping time can result if high separation rates are encountered. The cause of this phenomenon is the increased restriction of the boom at high spacecraft angular rates. It was felt, after completion of the capture study that a

high value of hysteresis torque such as that associated with the optimized hysteresis damper would result in even more restriction of the boom, and consequently less damping. To prevent this condition, a hysteresis contour was selected that had a low hysteresis value near the spring null, and a hysteresis torque that increased with damper angle, but always remained less than or equal to the spring torque (see Figure 3.2-53). The best contour within this range was estimated, and it was decided to evaluate the spacecraft performance for the limits of the range, and compare it to the results obtained using the constant torque hysteresis damper.

The initial conditions selected for the evaluation of the dampers were those originally selected for the capture study employing the eddy current damper (see Section 3.3.2). The conditions prior to rod extension are shown in Table 3.2-12.
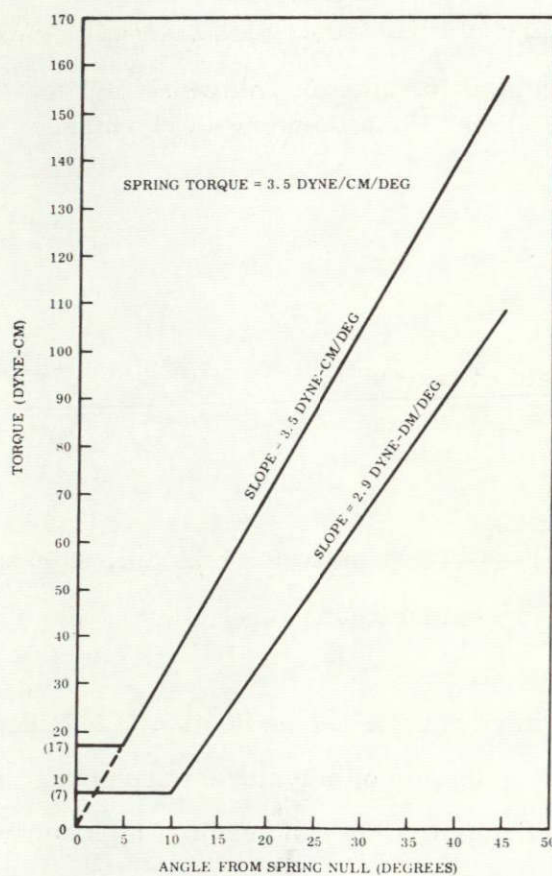
Figure 3.2-53. Range of Hysteresis Damping Torque for Varying Torque Hysteresis Damper ATS-D and E

Figures 3.2-54, 3.2-55, 3.2-56, 3.2-57, and 3.2-58 are the results of the computer simulations. Figure 3.2-54 is the first 160 hours of capture time with the constant hysteresis torque damper (50 dyne-cm). Figure 3.2-55 is an extension of this run to 400 hours plotted to a larger scale. The pitch, roll, and yaw errors are plotted, as well as the damper angle. Figures 3.2-5 and 3.2-57 are the same curves, but utilizing the minimum contour (Figure 3.2-53) of the varying torque hysteresis damper range. The improvement in damping time (and to some extent steady state) is clearly evident by the graphs. At the end of 400 hours, the constant torque hysteresis damper shows 10.7 degrees of pitch error, 7.0 degrees of roll error, and 8.4 degrees of yaw error. At the same time, the varying torque hysteresis damper shows 2.8 degrees of pitch error, 1.0 degrees of roll error, and 3.6 degrees of yaw error, indicating a significant improvement. Figure 3.2-53 is the first 160 hours of capture for the maximum contour of the varying torque hysteresis damper. At this point, the effective damping was less than that of the constant torque hysteresis damper and the run was terminated. As a consequence the minimum contour was selected as the nominal (Figure 3.2-53), with a permissible variation of ±10%.
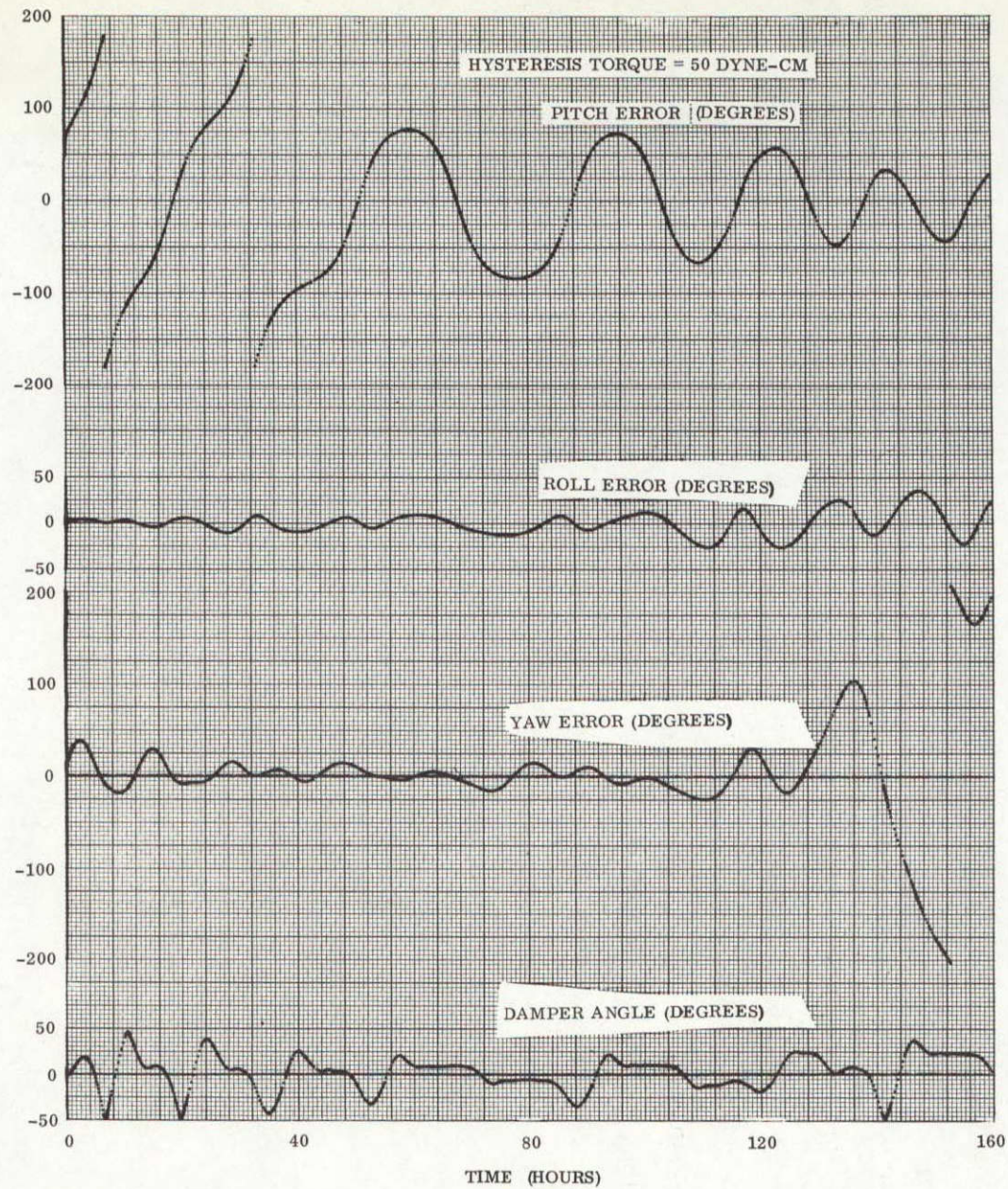
Figure 3.2-54. Nomiñal Constant Torque Hysteresis Damper for ATS-D and ATS-E
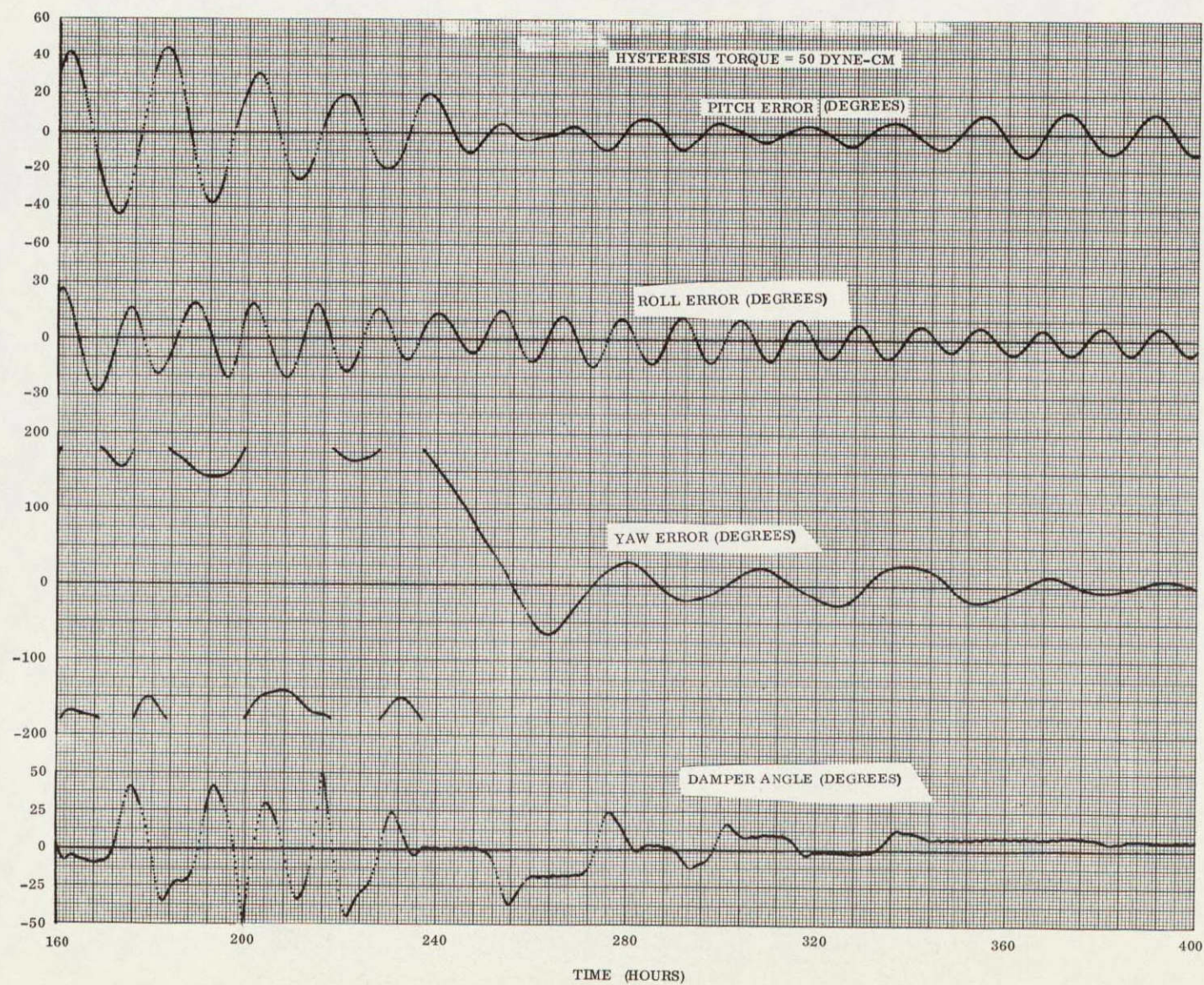
Figure 3.2-55. Nominal Constant Torque Hysteresis Damper for
ATS-D and ATS-E
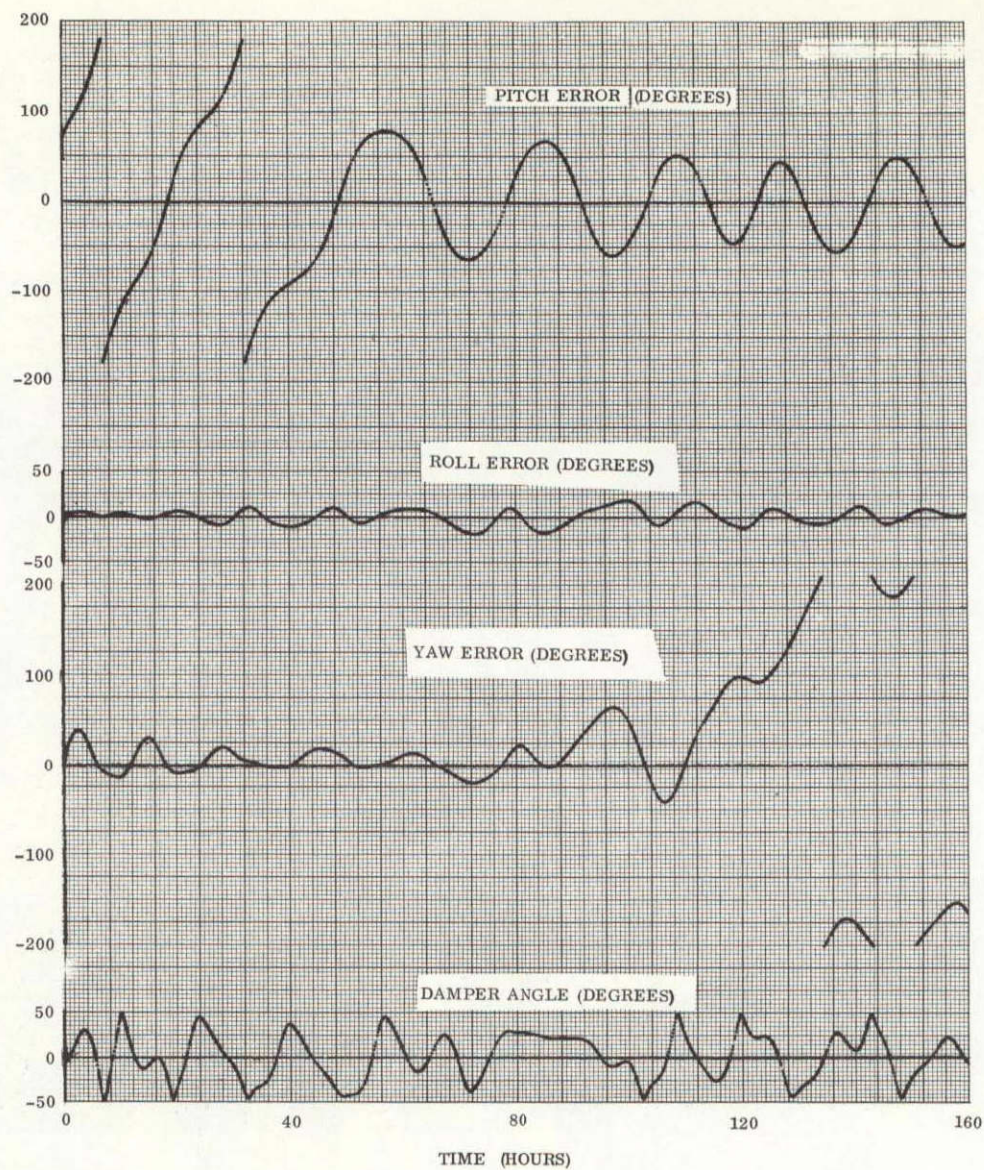
Figure 3.2-56. Varying Torque Hysteresis Damper for ATS-D and ATS-E

PITCH ERROR (DEGREES)

ROLL ERROR (DEGREES)

YAW ERROR (DEGREES)

DAMPER ANGLE (DEGREES)

TIME (HOURS)
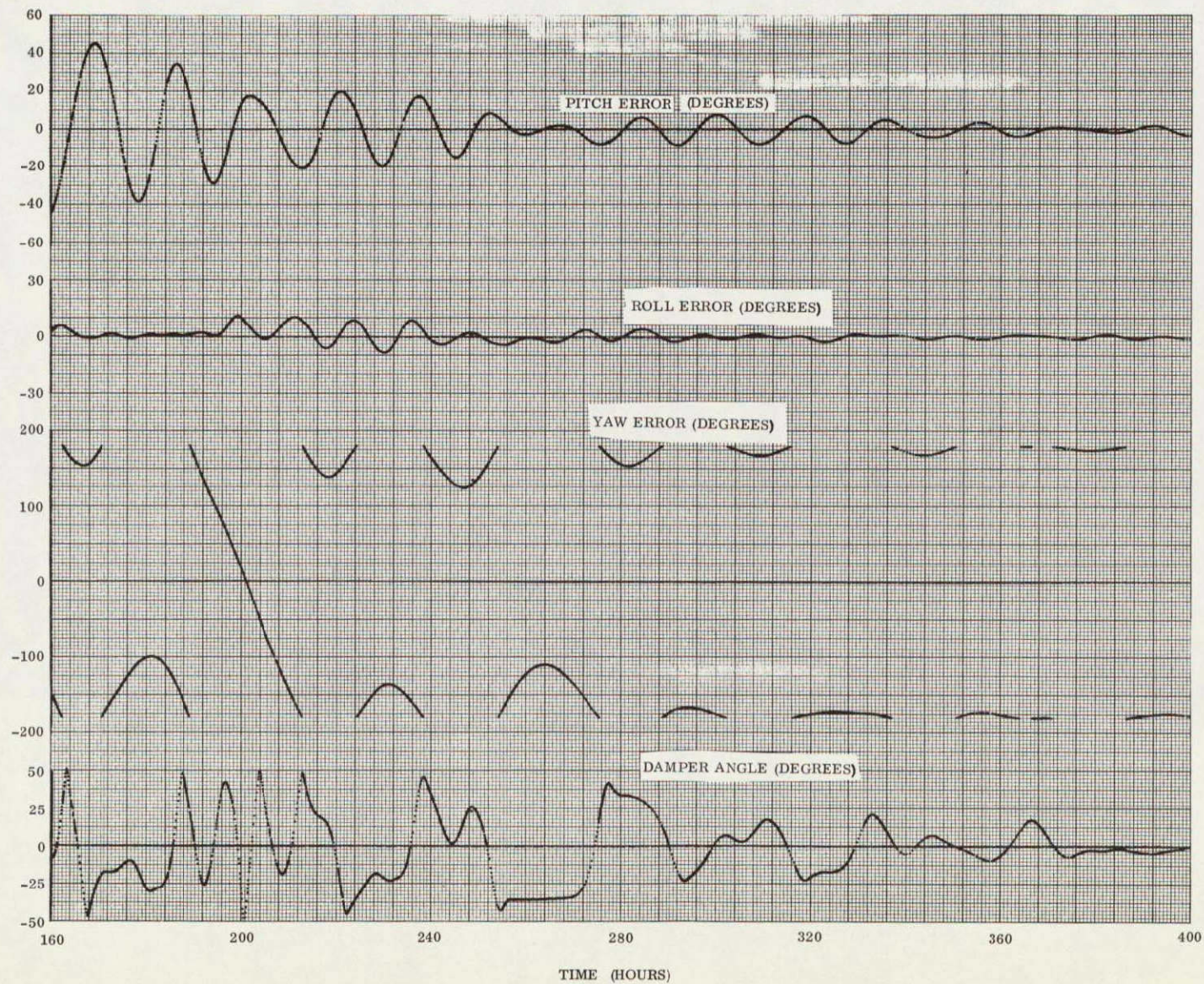
Figure 3.2-57.   Varying Torque Hysteresis Damper for ATS-D and ATS-E
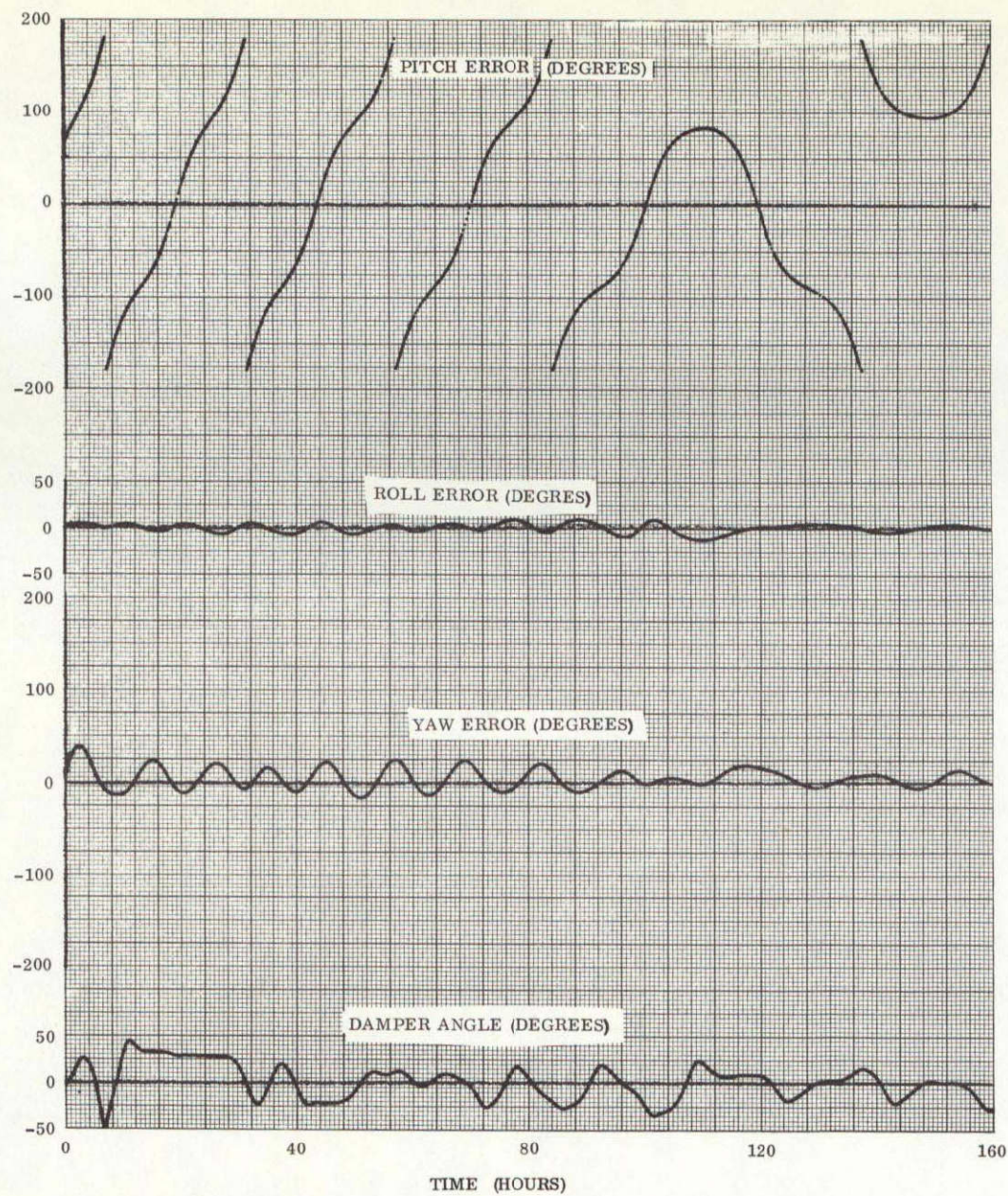
Figure 3.2-58. Varying Torque Hysteresis Damper for ATS-D and ATS-E

3.3 INITIAL CAPTURE ANALYSIS

The optimization analyses described in Section 3.2 were performed assuming small amplitude motion. Even the optimization for maximum damping was done on a linear small angle basis. In actual practice, however, the spacecrafts are rarely placed in orbit at the proper orientation with appropriately low rates. In this regard, ATS is no exception. ATS-A, for example, is separated from the booster stage with tip-off rates on the order of one degree per second. Residual rates as high as 2 degrees per second were considered possible for ATS-D and ATS-E. At the instant of separation (ATS-A) or completion of despin (ATS-D and ATS-E), the gravity gradient rods are in the stowed position, and the spacecraft moment of inertia is at its maximum. When the rods are deployed, the total moment of inertia of the spacecraft increases, and by conservation of angular momentum, the spacecraft angular rate decreases. The final spacecraft rate is a function of the initial rates, the axis the rates are on, the moment of inertia growth of the configuration, and to a lesser extent, the initial spacecraft orientation of rod deployment.

The spacecraft rates and position following rod deployment exert a considerable influence on the nature of the capture. If the initial spacecraft orientation is favorable, and the angular rates low enough, the spacecraft may not invert, and will quickly stabilize. When initial conditions are controllable, it is possible to attain a rightside up capture. This type capture is termed "upright capture" and, as indicated in Section 3.3.1, was a goal for ATS-A. With angular rates slightly higher than the maximum allowable for upright capture, the spacecraft will tumble until the damping reduces the angular rate below the tumble limit, and the spacecraft captures, and settles to steady state. In general, the final position for this mode of capture (i.e., rightside up or upside down) cannot be determined in advance with any degree of assurance. Capture, however, is usually achieved within a few orbits for low initial rates.

With initial rates much higher than the tumble limit, the capture problem becomes very complex, and the dynamic interaction between the spacecraft and the damper boom can result in the damper boom being "locked" in some position with very low amplitude oscillation. As a result, the effective damping is reduced and the tumble time prolonged. A dynamic analysis was performed which indicated that a critical rate exists about the

spacecraft y_1 (roll) and z_1 (pitch) axes, which will cause the damper to touch the stop. The analysis used to derive the equations of motion is given in Appendix C, and essentially parallels the work of T. Garber. The results of the analysis are given in Figures 3.3-1, 3.3-2, 3.3-3, and 3.3-4. Figure 3.3-1 represents the equilibrium position the damper will assume as a function of rates about the y_1 (roll) and z_1 (pitch) axes. This equilibrium position is the result of the "gyroscopic" torques (which tend to rotate the damper boom until it is along the x_1 axis) opposing the spring torque. At a samper deflection angle of 45 degrees the stop will be encountered and the basic equations no longer hold. As is shown by Figure 3.3-1, a motion rate of 3.54 times orbital about the pitch axis causes the damper to strike the stop. A similar motion rate of 4.77 times orbital about the roll axis has the same effect. In this condition, the damper is effective only for that half of the disturbance torque cycle which deflects the damper boom away from the stop. At rates higher than the critical rates, the gyroscopic torques tend to "push" the boom into the stop. Figure 3.3-2 is a plot of the dynamic torques holding the damper boom against the stop. The line at $T_D / I_D \omega_o^2$ equal to three is the gravity gradient torque acting on the damper boom. If the dynamical torques exceed this value the damper will probably remain stationary and, therefore, inoperative. In this condition, the vehicle will have a long period of tumbling before stabilization occurs. As a guideline, therefore, a maximum rate of five times orbital is placed on rates about the pitch and roll axis. In spite of the slight difference in approach, these results agree reasonably well with Garber.

There is no critical rate on the x_1 (yaw) axis because these rates tend to hold the damper on null. However, there is an increase in the effective spring constant due to yaw rates as shown in Figure 3.3-3. To estimate the effect of this spring constant, θ_p and θ_r were assumed small, and a linear time constant was calculated (by computer) as a function of spring constant. This allowed the representation shown in Figure 3.3-4. As an estimate, a maximum allowable rate of six orbital was permitted, corresponding to a time constant of 36 orbits. Note that each of the rates about the x_1, y_1 and z_1 axes is assumed independent on each other and thus the dynamics of the main body was ignored.
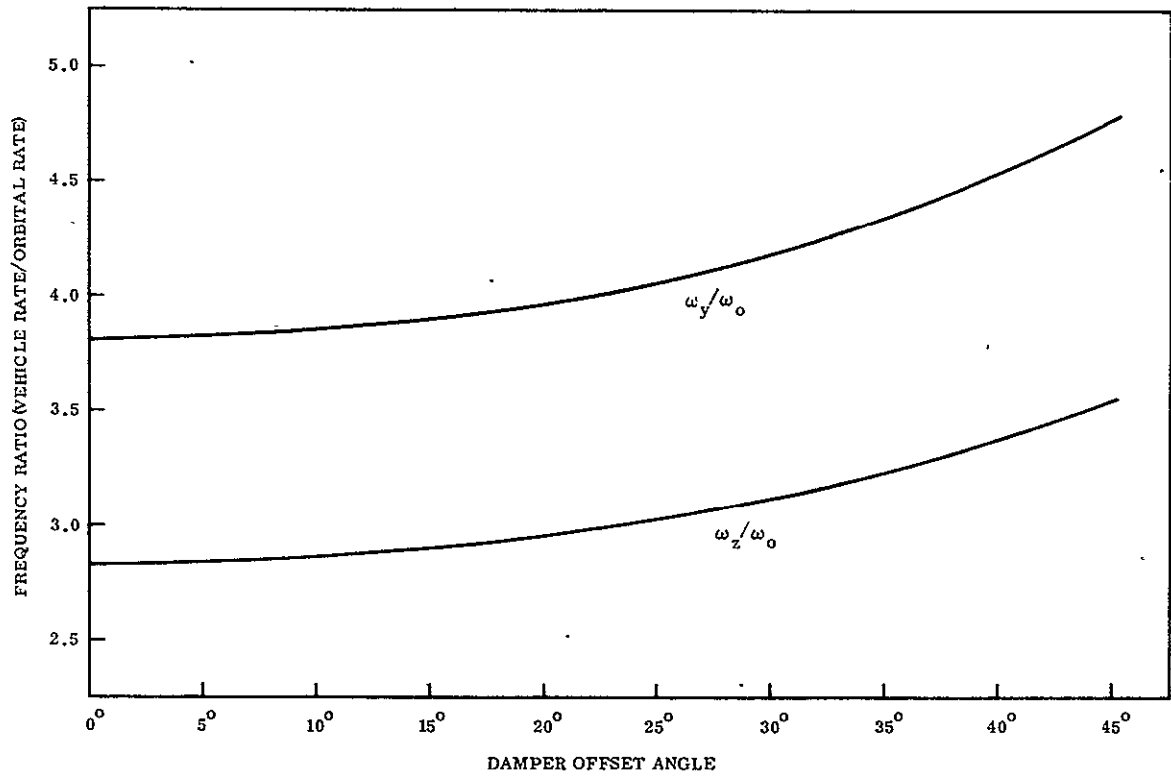
Figure 3.3-1. Stable Angle of Damper Versus Angular Rate of Vehicle
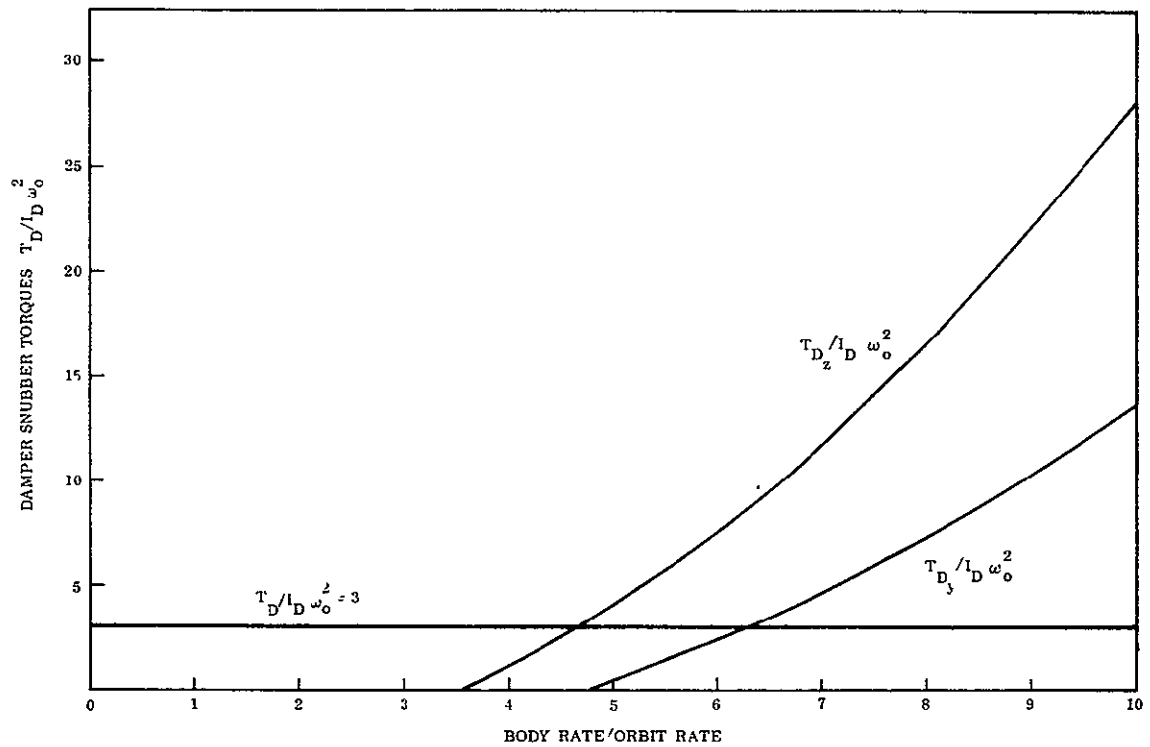
Figure 3.3-2. Damper Snubber Torques Versus Relative Body Rates
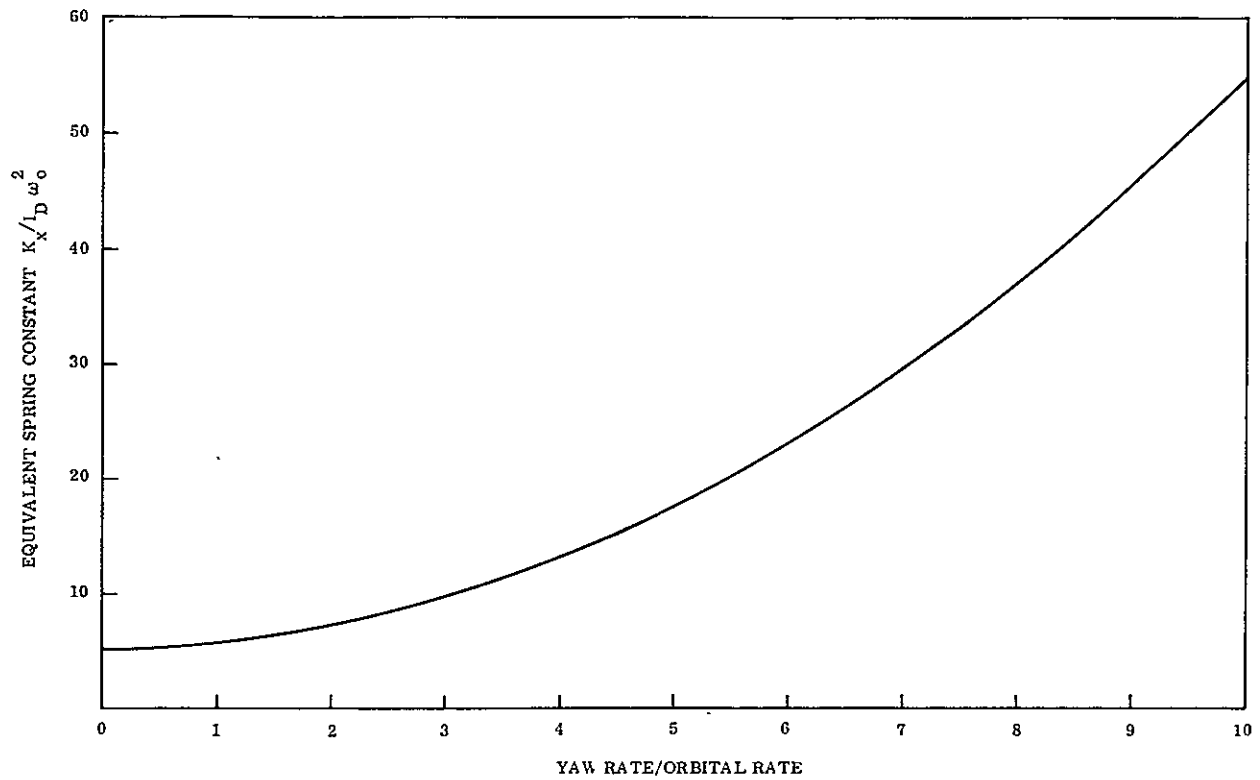
Figure 3.3-3.   Effective Damper Spring Constant Versus Vehicle Yaw Rate
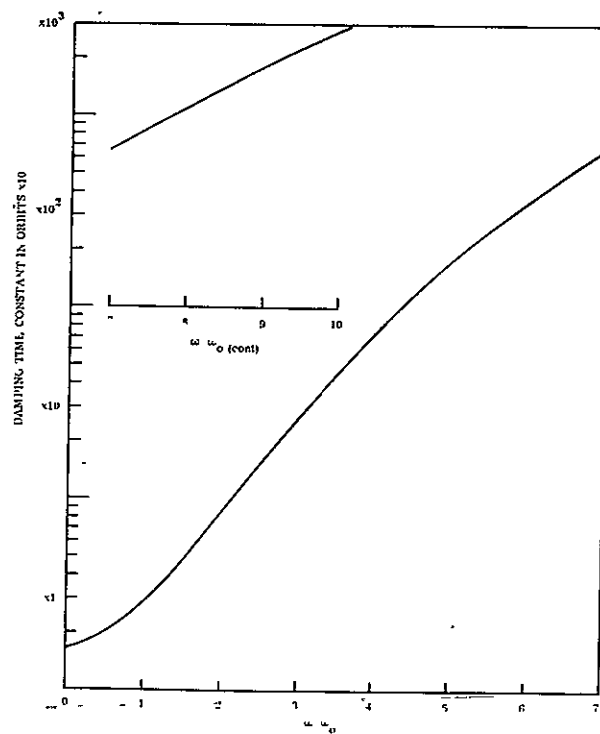
Figure 3.3-4.   Damping Time Constant Versus Body Rate Ratio

Because of the large angles and nonlinearities involved, capture is not readily amenable to analysis, except for the foregoing analysis and the problem of upright capture (see Section 3.3.1). Consequently, the time to capture, the behavior during large angle transients, and the time to damp to steady state were determined by digital simulation. In connection with the capture study, one aspect of the spacecraft must be mentioned. Much of the hardware for the gravity gradient subsystem was developed using the GSFC original parameters as guides. When the optimization was complete, the nominal half angle of the rods (Figures 3.2-24 and 3.2-28) was changed from the original 19 degrees to the optimum 25 degrees. The rod deployment units had variable rod angle capability (for in-flight experimentation) and were capable of accommodating the change, except during rod deployment. All initial rod deployments occur at rod angles of 19 degrees. "Scissoring" to 25 degrees can be performed anytime after the initial deployment (even if the rod length is only a few feet).

3.3.1 ATS-A CAPTURE

As a performance goal, ATS-A was required to capture rightside up. The orbital rate associated with a 6,000 nm orbit is high enough (0.0156 deg/sec), and separation tip off rates low enough (on the order of one degree per second) that with appropriate initial spacecraft orientation, upright capture can be achieved. The initial conditions required for upright capture can be determined analytically by employing conservation of energy approaches. The "gravity gradient field" is a conservative field, and the potential energy of the spacecraft is a function of its orientation only. The position of minimum energy is when the yaw axis (axis of minimum moment of inertia) is along the local vertical. The position of maximum potential energy is when the yaw axis is horizontal, and the yaw angle is 90 degrees. (The analysis deriving gravity gradient potential energy is found in Appendix D.) For upright capture, the total energy of the spacecraft (kinetic energy plus potential energy) must be less than the maximum gravity gradient potential energy. To be on the safe side, the maximum gravity gradient potential energy should be calculated for a yaw angle of zero degrees.

By definition, kinetic energy is calculated with respect to an inertial frame of reference. If the kinetic energy is used directly, it causes large variations in the total energy because oscillations about the local vertical are unsymmetrical in inertial space. For example, if the spacecraft is oscillating sinusoidally, the kinetic energy when the spacecraft is travelling in the plus pitch direction is

$$KE = 1/2 \left[I_{zz} \left(\omega_0 + \overset{o}{\theta} \right)^2 \right] \tag{3.3-1}$$

where

$$\omega_0 = \text{orbital rate}$$

$$\overset{o}{\theta} = \text{spacecraft angular rate with respect to the local vertical}$$

When the spacecraft is rotating in the negative direction, the kinetic energy is

$$KE = 1/2 \left[I_{zz} \left(\omega_0 - \overset{o}{\theta} \right)^2 \right] \tag{3.3-2}$$

and the total energy will be sinusoidal with time since the terms are not equal.

Whittaker, however, indicates that if the reference frame is rotating at a constant rate (orbital rate), and the rotational coordinate is ignorable (i.e., appears only as a rate), it can be removed from the kinetic energy (see Appendix E). A correction must be added to the potential energy, however, and Appendix D performs this analysis. When the total energy is calculated on this "relative" basis for a circular orbit, the energy will remain nearly constant during steady state oscillation, and will decrease during the decay of large oscillations.

With this relative approach, the equations indicate that upright capture is symmetrical about orbital rate (after rod deployment). The ideal situation, therefore, is when the initial conditions of the spacecraft are at zero attitude error, with orbital rate about pitch.

The position of ATS-A on the Agena booster was such that the pitch axis of the spacecraft was aligned with the roll axis of the Agena. The initial yaw error is therefore 90 degrees. The 3σ separation rate tolerance for the Agena was 1 degree/second on the Agena pitch and yaw axes, and 1/4 degree/second rate on the Agena roll axis. The calcula ions indicated that for an initial spacecraft moment of inertia of.67.5 slug-ft^2 (the value at the time of the analysis) and 100 -foot rod lengths (the original standard configuration), the spacecraft would tumble in pitch if the pitch rate were 1 degree/second in the negative pitch direction. To verify this conclusion a computer run was made with this condition, and the vehicle did tumble in pitch (Figure 3.3-5). Yaw also "tumbled", a condition which is normal and makes the "forward" capture of yaw virtually impossible. If the initial rate were forward in the pitch direction, the total energy is less than that required to tumble and the vehicle captures (Figure 3.3-6). The roll rate for both these runs was 1/4 deg/sec. Note that the time to erect the rod is short compared to the printout interval, and the vehicle appears to "jump" to an initial position.

If the separation rate occurs on the yaw axis, the final yaw rate will be high (because of the small moment of inertia growth), and the total energy content of the vehicle is greater than that required to tumble. Figure 3.3-7, however, indicates that the vehicle did not tumble, but is precessing about an axis slightly offset from the local vertical. It is expected that the introduction of the damper boom into this situation will cause significant oscillations, and tumble may occur. Damping has not previously been considered because it does not affect upright capture if the energy content is sufficiently low.

To circumvent the tumble problem indicated in Figure 3.3-5, two approaches were possible. The first approach required the Agena to be yawed 90 degrees such that the 1/4 deg/sec roll rate appears on the orbital pitch axis. This case should capture whether the rate is positive or negative, and Figures 3.3-8 and 3.3-9 indicate that capture does occur (note that the growth of the roll amplitude is accompanied by a decrease in pitch amplitude as would be expected from the conservation of energy law). As a result of this preliminary study, the Agena was programmed to execute a yaw maneuver of 90 degrees before spacecraft separation.

-1 DEG SEC PITCH RATE
1/4 DEG/SEC ROLL RATE
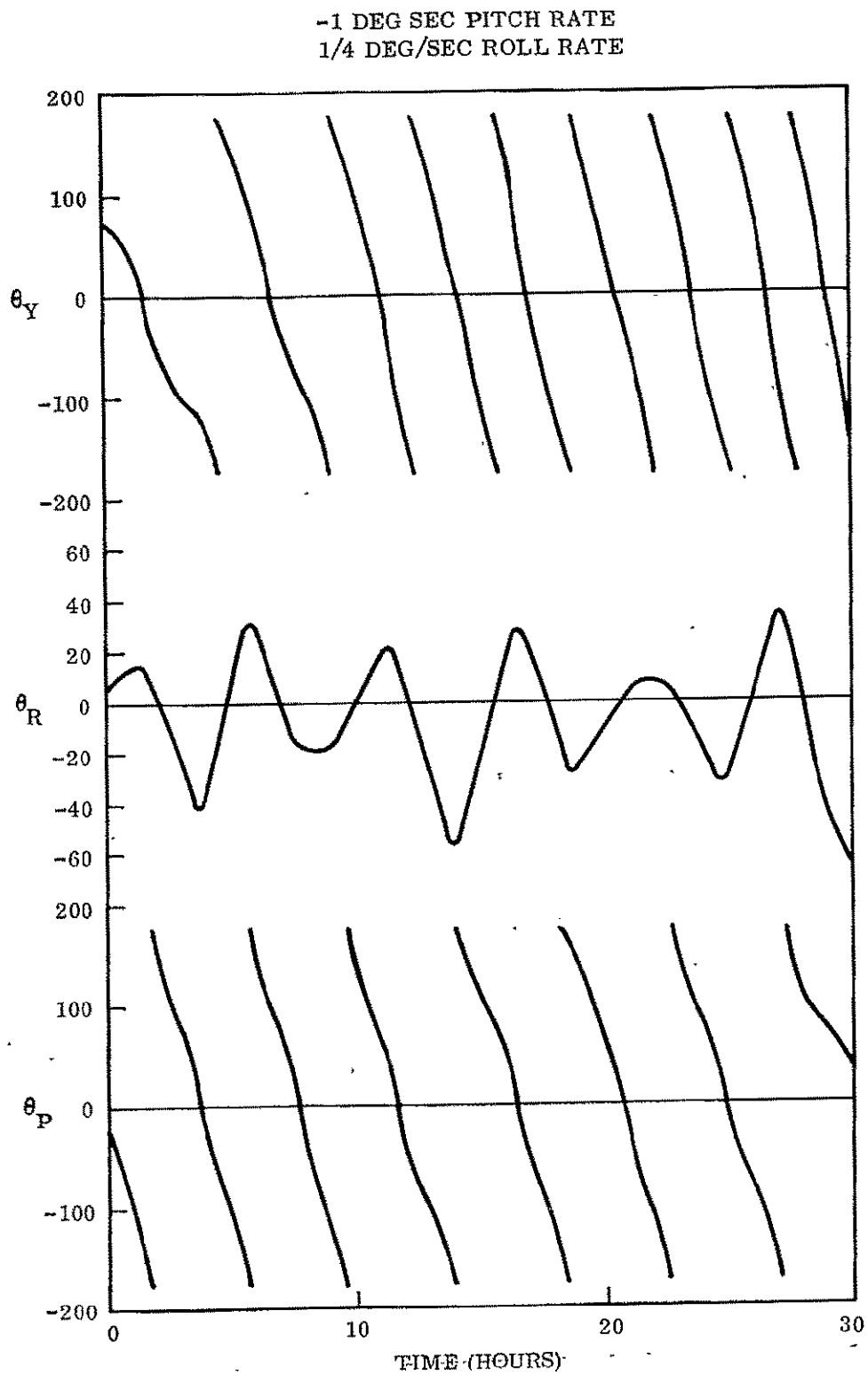
Figure 3.3-5. ATS Capture Phase, Normal Agena Position,
Negative Spacecraft Pitch Rate

1 DEG/SEC PITCH RATE
1/4 DEG/SEC ROLL RATE
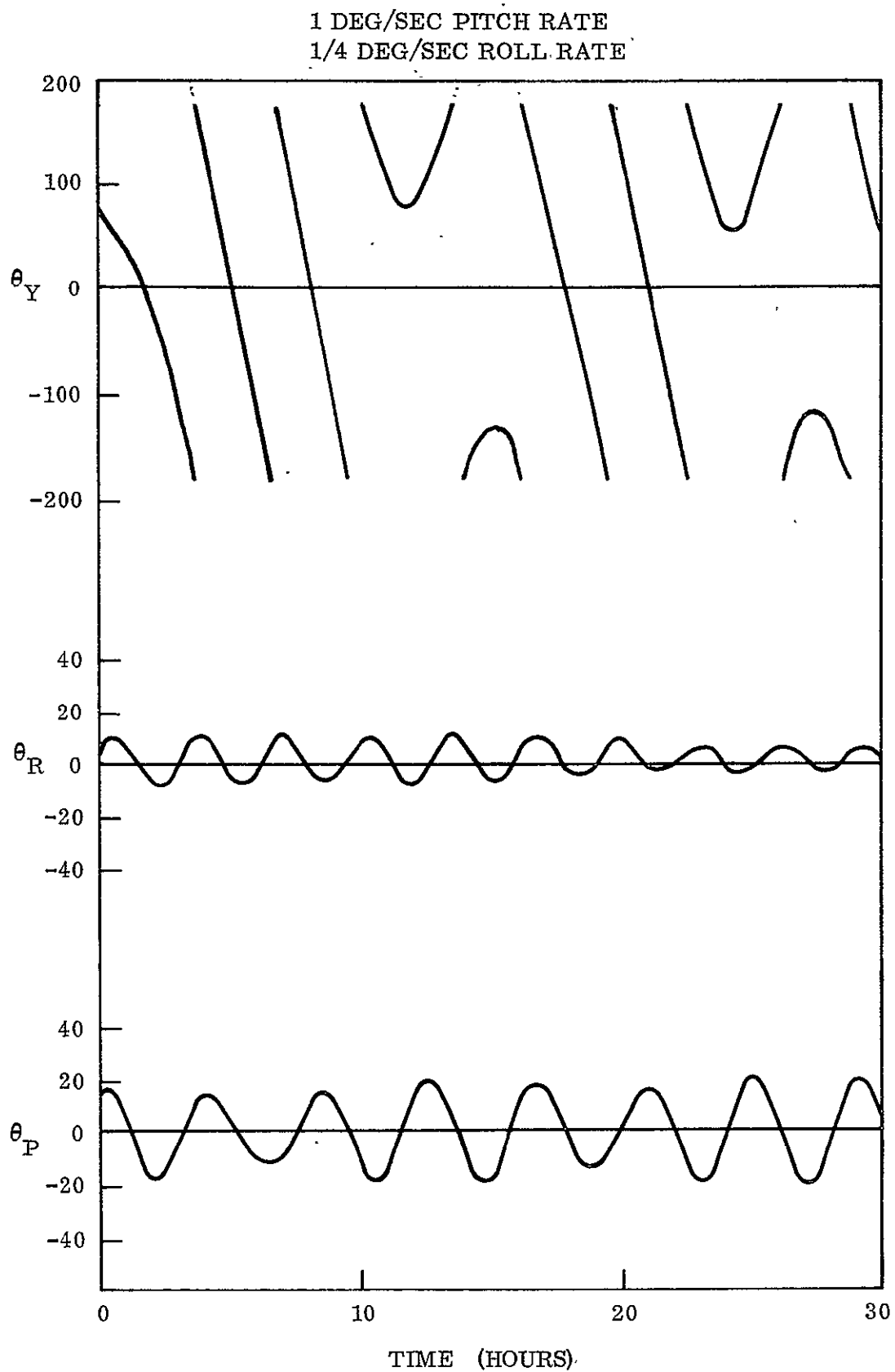
Figure 3.3-6. ATS Capture Phase, Normal Agena Position,
Positive Spacecraft Pitch Rate
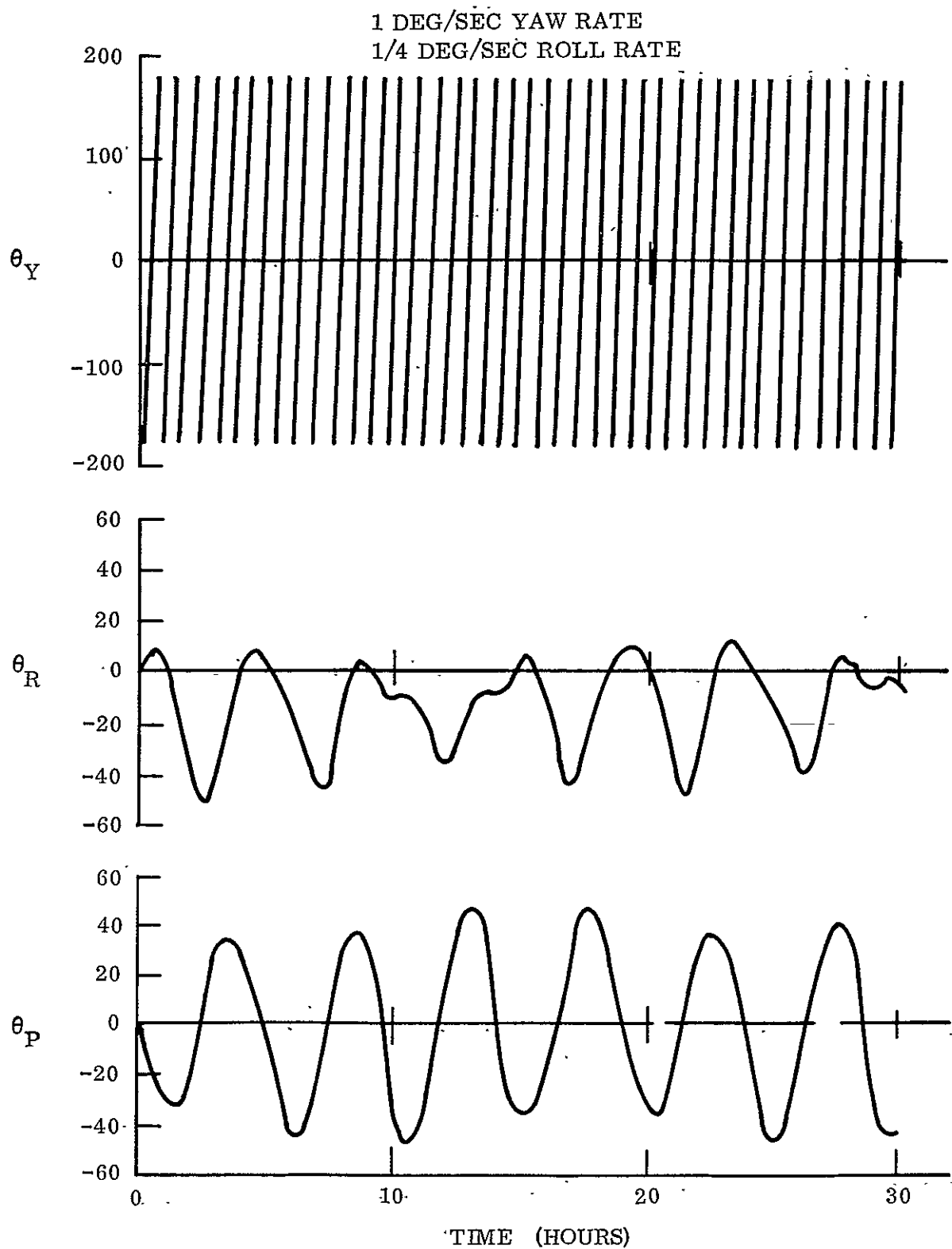
Figure 3.3-7. ATS Capture Phase, Normal Agena Position,
Separation Rate in Spacecraft Yaw
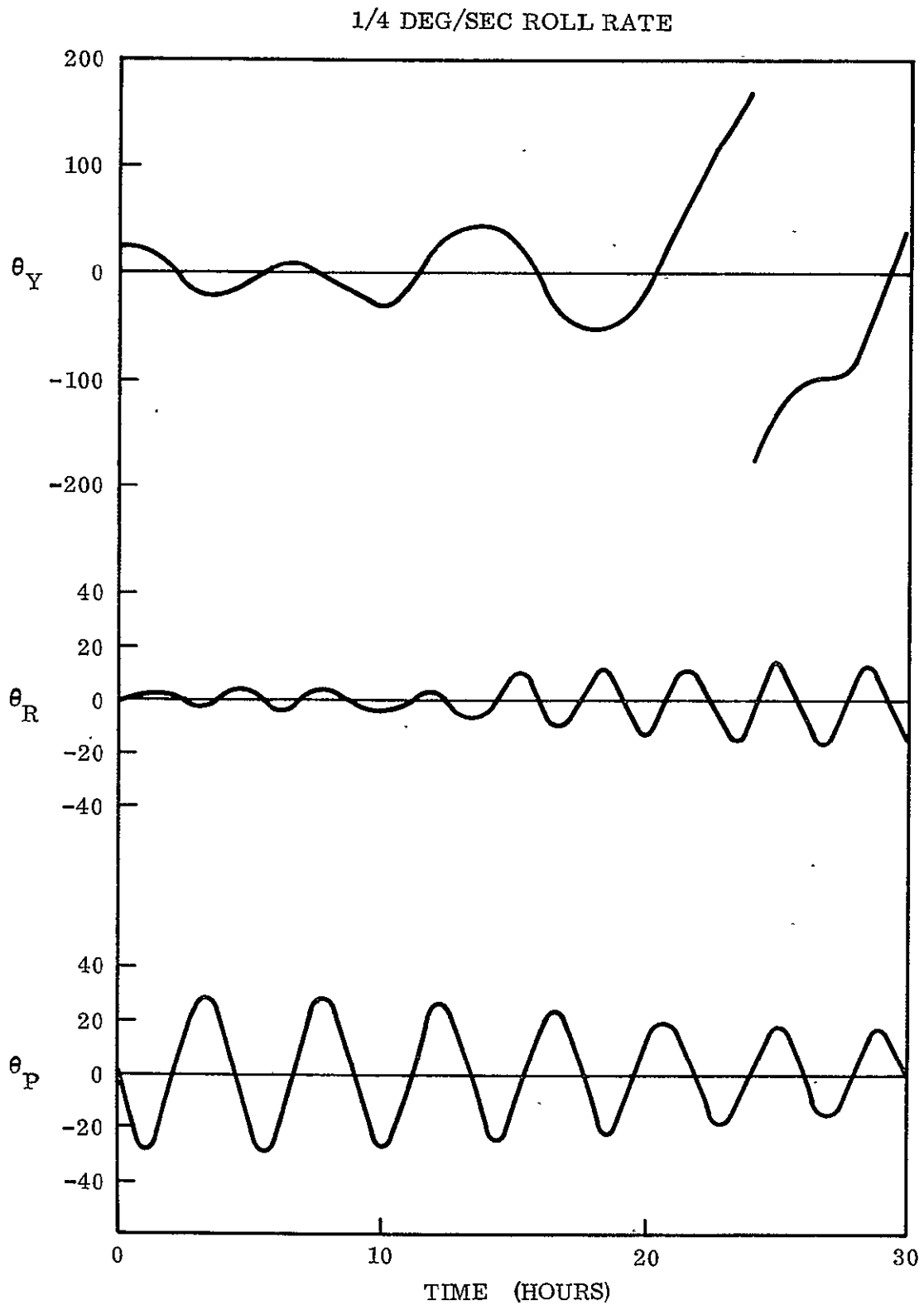
Figure 3.3-8.   ATS Capture Phase, 90-Degree Agena Yaw,
Positive Agena Roll Rate
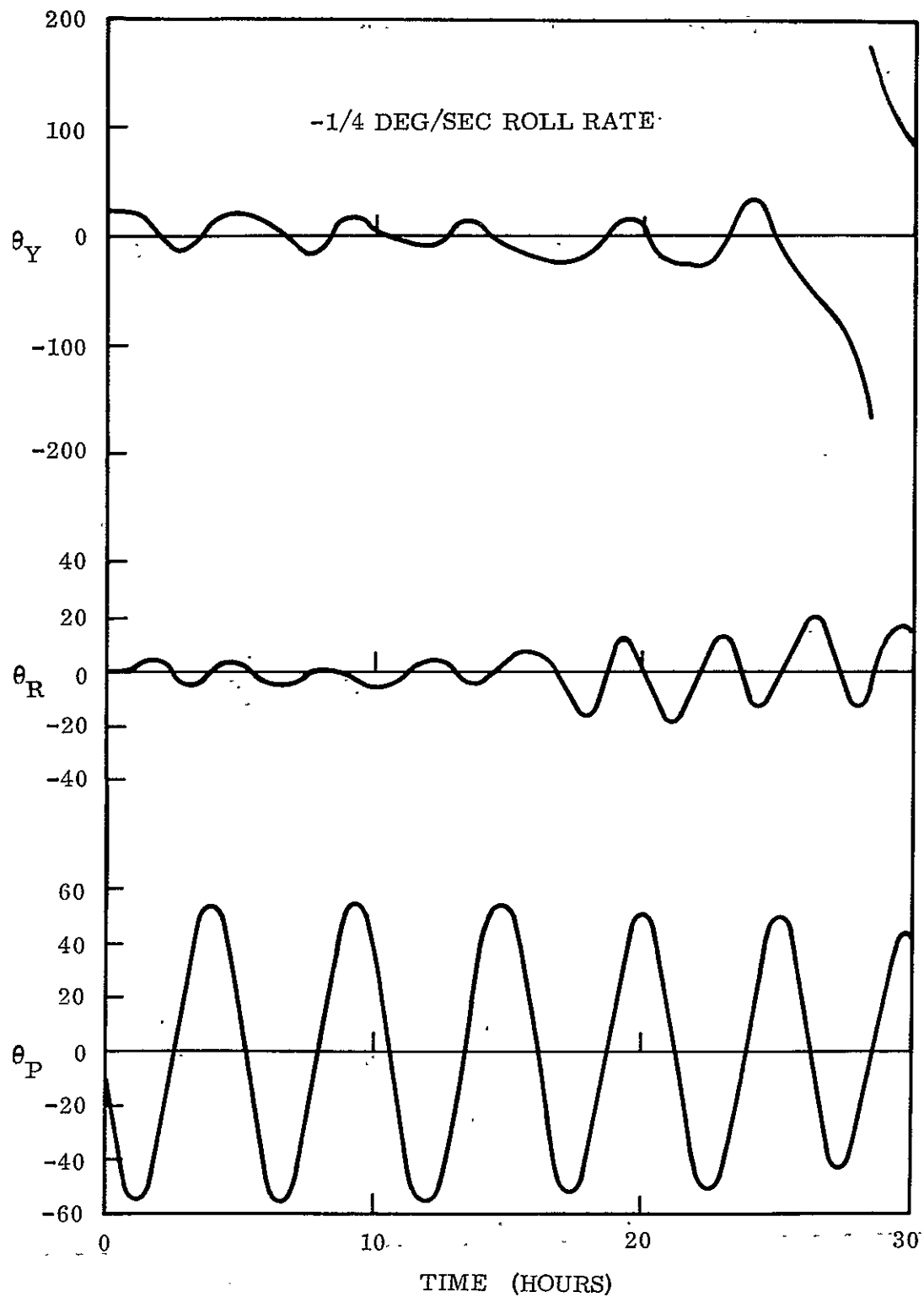
Figure 3.3-9. ATS Capture Phase, 90-Degree Agena Yaw,
Negative Agena Roll Rate

After the configuration was optimized (see Section 3.2), the rod length and moments of inertia changed, tolerances were specified, and additional Agena information was available. The factors used in the subsequent capture study are shown as follows:

1. The initial moments of inertia were:

    a. Roll (I_{zz}) 54.60 slug-ft^2 (Spacecraft Pitch Axis)

    b. Pitch (Maximum)   47.94 slug-ft^2 (Spacecraft Roll-Yaw Plane)

    c. Pitch (Minimum)   44.22 slug-ft^2 (Spacecraft Roll-Yaw Plane)

The maximum pitch moment of inertia was used as a conservative estimate.

2. The rod erection rates per Specification SVS 7316 were:

    a. X-Rods $2 \, {}^{+1}_{-1/2}$ ft/sec

    b. Damper Rod   4   ft/sec maximum

3. The separation rates (Agena plus tip-off rates) were:

    a. Roll Rate (After Separation) $\pm$ 1 degree/second

    b. Pitch Rate (After Separation) $\pm$ 0.4 degree/second

    c. Yaw Rate (After Separation) $\pm$ 1 degree/second

These are the satellite's separation rates about the satellite coordinate system.

4. Additional factors considered in the study were:

    a. Delay time of 3 seconds (maximum) before rod deployment.

    b. Tolerance on X-Rod Length   -2 feet maximum on two rods

    c. Initial Pitch and Roll $\pm$ 1 degree

         Position Error

    d. Agena Yaw Tolerance $\pm$ 5 degrees

5. Because the vehicle structure was designed to accommodate the rod erection when the half angle was 19 degrees, the half angle during capture must be 19 degrees in spite of its nominal value of 25 degrees.

Several series of computer simulations were made to determine the ability of ATS-A to capture upright under a variety of initial conditions and spacecraft parameters. The first series of simulations varied the initial rates and positions. Approximately eight simulations were made, two of which were considered to be worst case. The worst case conditions are defined to be:

1. Maximum negative initial pitch angle and pitch rate, and maximum values of roll and yaw attitudes and rates. The roll and yaw polarities have been assigned to maximize body rates about the X_1 and Z_1 axis on one simulation and the X_1 and Y_1 axis on the other. The nominal vehicle state is with zero angular errors, zero roll and yaw rates, and positive pitch rate equal to orbital rate. These conditions represent the maximum departure from nominal conditions.

2. Minimum rod extension rate. This provides the minimum rate of moment of inertia growth.

3. One rod in both rod pairs two feet short. This provides the minimum values of final moments of inertia.

The simulations are shown in Figures 3.3-10 and 3.3-11. The remainder of the simulations varied the rod extension rates within the limits imposed by the component, and varied the initial conditions with the Agena tolerances.

Right-side up capture was achieved in all the simulations. As expected, the maximum pitch and roll angles occurred in the worst-case runs. Also, the spacecraft was spinning in yaw because of the initial yaw rate (see Figures 3.3-10 and 3.3-11). To determine the spacecraft performance after the damper is uncaged, the final values of angles and rates from the first worst case condition were simulated. The plot of this run is shown in Figure 3.3-12. The 19-degree X-rod half angle was used in this simulation to duplicate the planned orbit conditions. It had the effect of reducing the subsystem damping, and
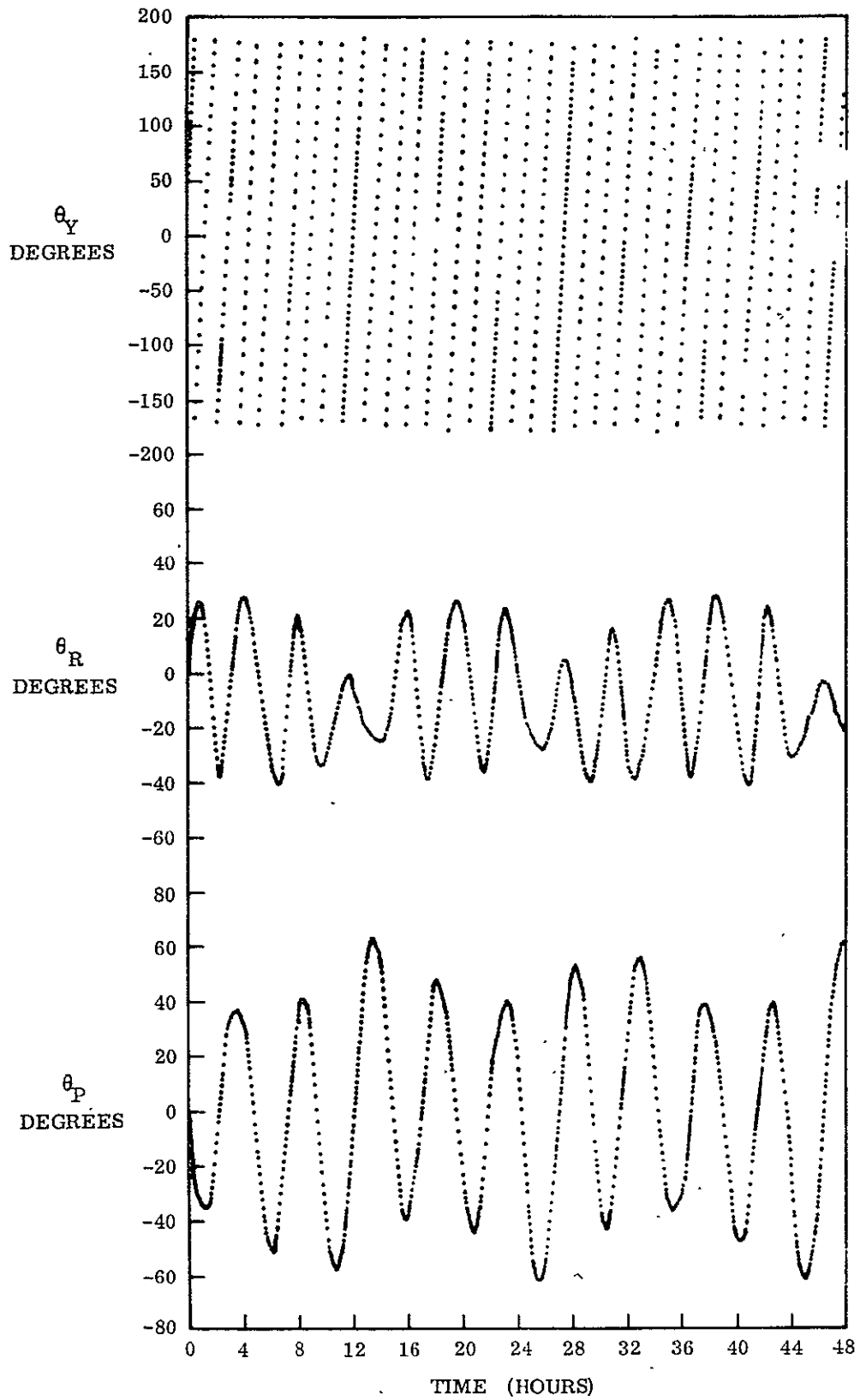
Figure 3.3-10. Computer Simulation.
ATS-A Capture (Worst Case I)
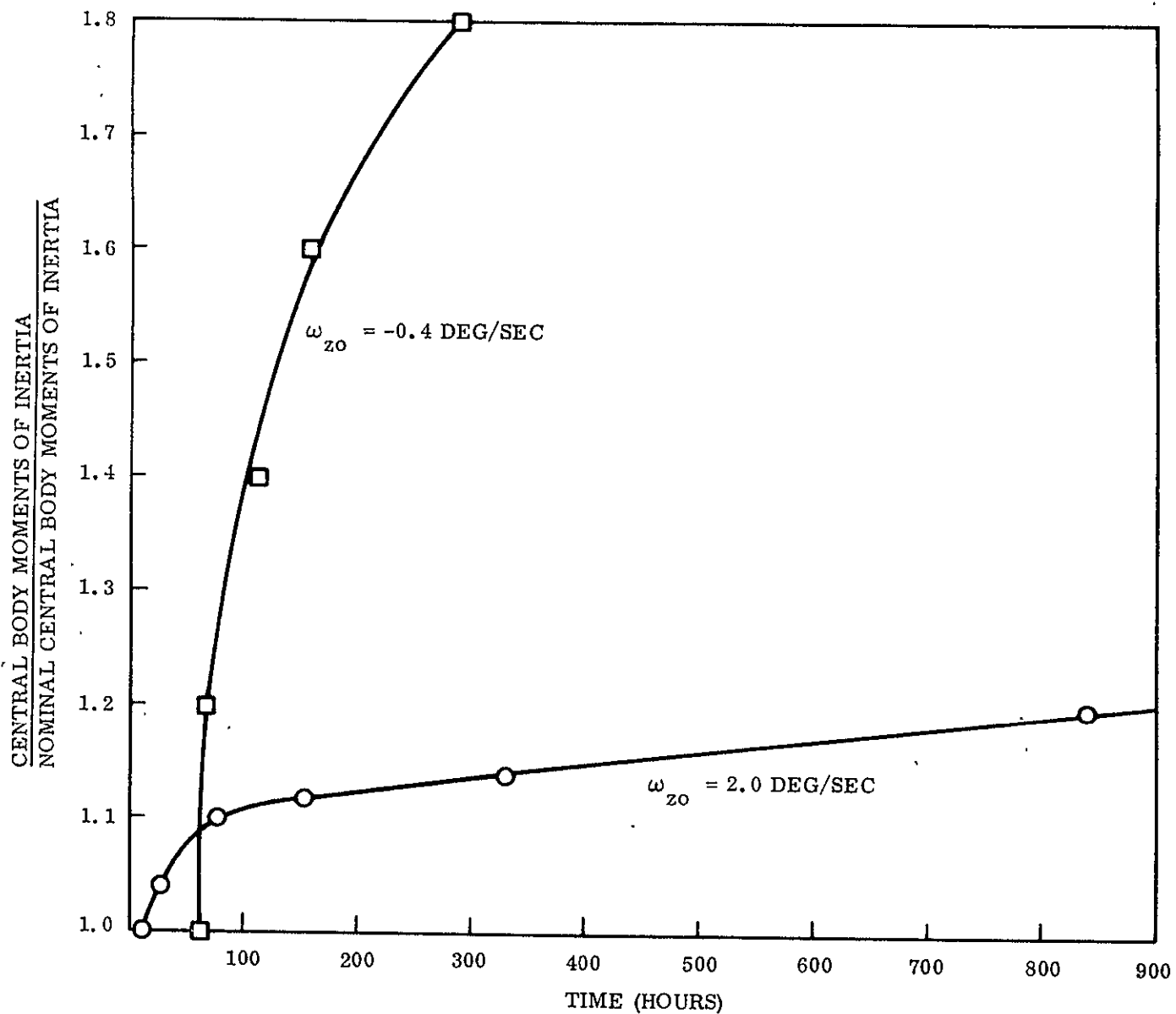
Figure 3.3-11. Computer Simulation, A TS-A Capture (Worst Case II)
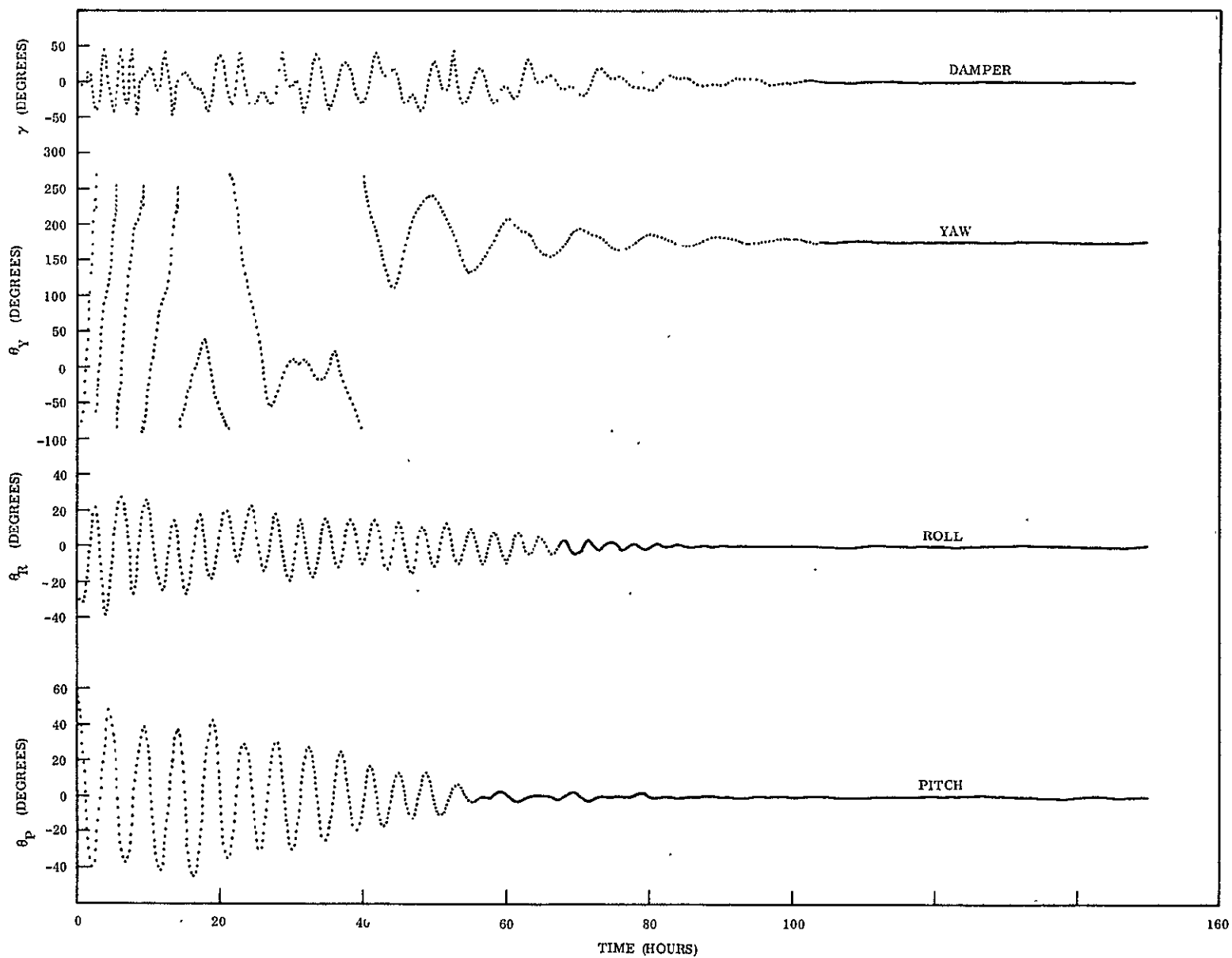
Figure 3.3-12. ATS-A Performance Following Initial Capture (Worst Case Conditions)

steady state conditions were not reached even after 150 hours of orbit time. This is not apparent on the plot because of the large scale used to accommodate the initial transient. It was recommended therefore, that the X-rod half angle be changed from 19 degrees to the nominal value of 25 degrees immediately after completing rod extension.

Three additional series of computer simulations were made. The first series was made to determine the minimum allowable rod extension rate, the second series was made to determine the allowable increase in moment of inertia of the central body, and the third series was made to determine the maximum allowable initial orientation. The first series consisted of sixteen simulations employing the worst case initial conditions (identical to those of Figure 3.3-10),but with rod extension rates of 0.5, 0.75, 0.8, 0.85, 0.9, 1.0 and 1.2 ft/sec.

The spacecraft tumbled when the rod extension rate was reduced to 0.75 ft/sec and the minimum value for rightside up capture was place at 0.80 ft/sec.

The second series consisted of sixteen simulations employing the worst case initial conditions, but gradually increasing the initial spacecraft moment of inertia. The spacecraft moment of inertia had been gradually increasing as time progressed, and by the time this series was performed, the moments of inertia were

1. I_{xx} = 51.99 slug-ft^2

2. I_{yy} = 56.86 slug-ft^2

3. I_{zz} = 65.51 slug-ft^2

Using these values as nominal, the simulations were performed and the results are shown in Table 3.3-1.

There is a significant amount of scatter in the data presented in Table 3.3-1. This is typical of capture runs made near the capture boundary. The results are extremely

Table 3.3-1. Spacecraft Moment of Inertia Simulations

Central Body Moment of Inertia Nominal Central Body Moment of Inertia	Upright Capture	Capture Time-hours
1.00	yes	
1.05	yes	
1.08	yes	
1.10	yes	
1.12		13.7
1.13		13.7
1.14	yes	
1.15		22.7
1.20		13.4
1.25	yes	
1.30	yes	
1.35	yes	
1.50		27.4
1.60	yes	
1.80		28.3
2.00		51.4

sensitive to initial conditions and modifications in the integration procedure. This effect is mentioned by D. M. Watson of NASA-Ames in his paper, "An Energy Approach to the Passive Gravity-Gradient Satellite Capture Problem." The only firm conclusion that can be drawn from Table 3.3-1 is that upright capture cannot be assured if the central body moments of inertia are increased 12 percent or more. In view of the repeated instances of upright capture for increases of 0 to 10 percent, it seems probable,but not certain,that upright capture is assured for increases up to 8 percent. The moment of inertia growth was therefore restricted to 10 percent for upright capture.

The last series was performed to determine the maximum angle between the spacecraft yaw axis and the local vertical at which upright capture could be assured. Again, the worst initial conditions were assumed, except that two yaw positions were evaluated: zero and 8.5 degrees. Also for these simulations, the damper boom was deployed, and the damper uncaged immediately following rod erection. Four simulations were made with an initial yaw attitude of zero: two had initial errors of 40 degrees (pitch and roll) and two had initial errors of 50 degrees. Of the two runs with 50 degrees initial attitude

errors, only the 50 degree roll error inverted (Figure 3.3-13). The 50 degree pitch error captured upright and damped (Figure 3.3-14). Neither of the simulations with 40 degree initial attitude errors tumbled. Verification simulations were made with the initial yaw error of 8.5 degrees, and initial roll errors of plus and minus 40 degrees. All four simulations successfully captured upright.

An additional simulation which scissored the rods from 19 degrees to 25 degrees was made to determine the effect of scissoring.

Capture was upright. An upper limit of 40 degrees between the local vertical and the yaw axis was therefore specified for upright capture.

3.3.2 ATS-D INITIAL CAPTURE

ATS-D is unlike ATS-A in that it does not separate from a stabilized booster, but is placed into a synchronous orbit in a spin stabilized mode. The entire orbit transfer from medium to synchronous attitude, as well as orbit circularization at synchronous altitude, is achieved while ATS-D is spinning. The high spin rate required for orbit transfer is reduced through the use of a two-stage yo-yo, when the orbit has been circularized and the spacecraft is on station. The angular rate remaining on the spacecraft after the yo-yo has been deployed is of great importance to the capture of ATS-D. Because of the nature of the spin mode, the orientation of the spacecraft when the rods are being deployed cannot be controlled, and it would only be by chance that it would be upright when the rods were deployed. At orientations other than zero (or 180 degrees), the potential energy associated with the "gravity gradient field" is not zero, and the potential energy must be added to the spacecraft kinetic energy to obtain the actual total energy. With low orbital rate, the total energy can easily be enough to tumble the spacecraft, and may be enough to cause prolonged tumble.
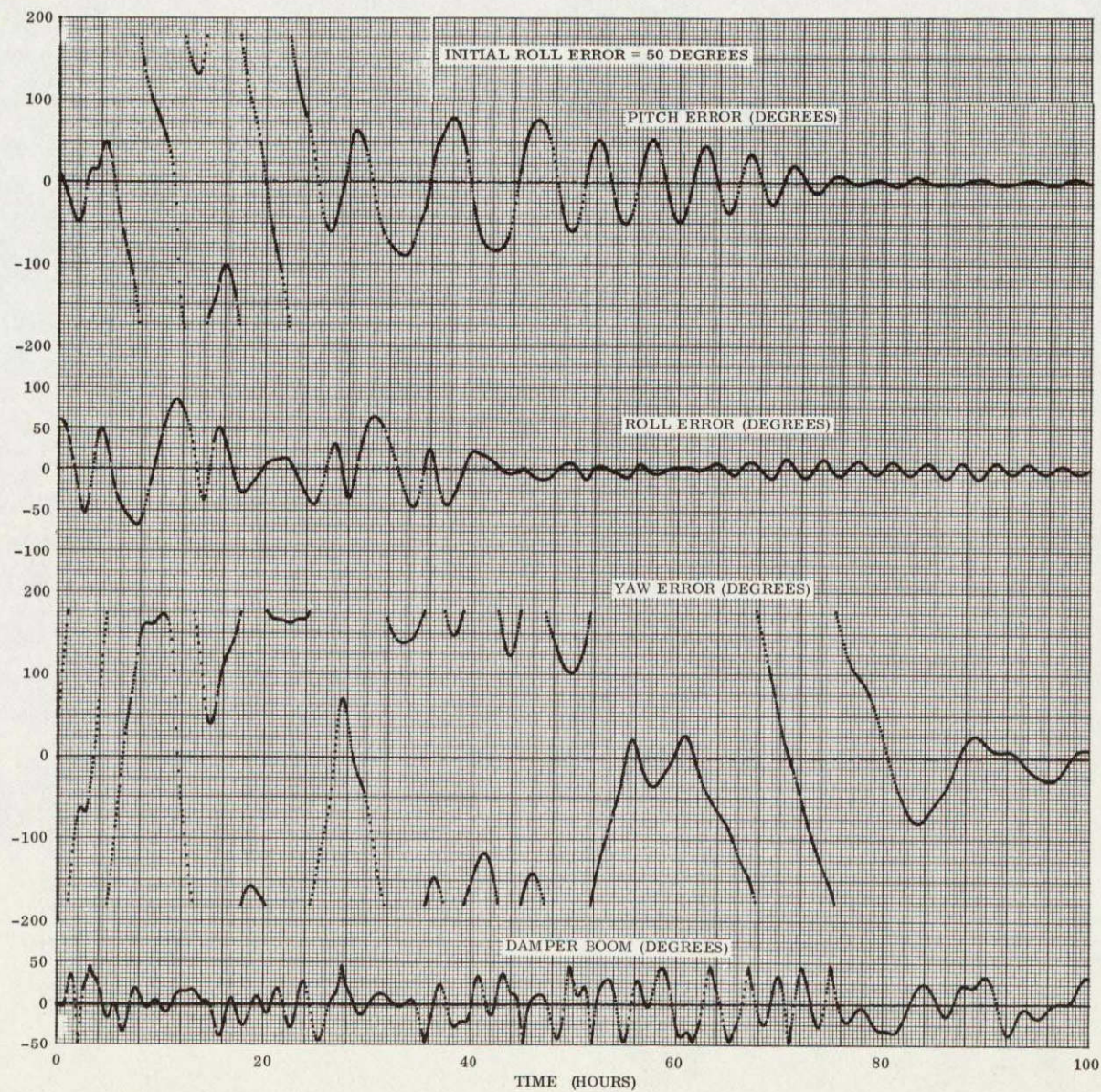
Figure 3.3-13. Capture of ATS-A With 19 Degree Scissor Angle
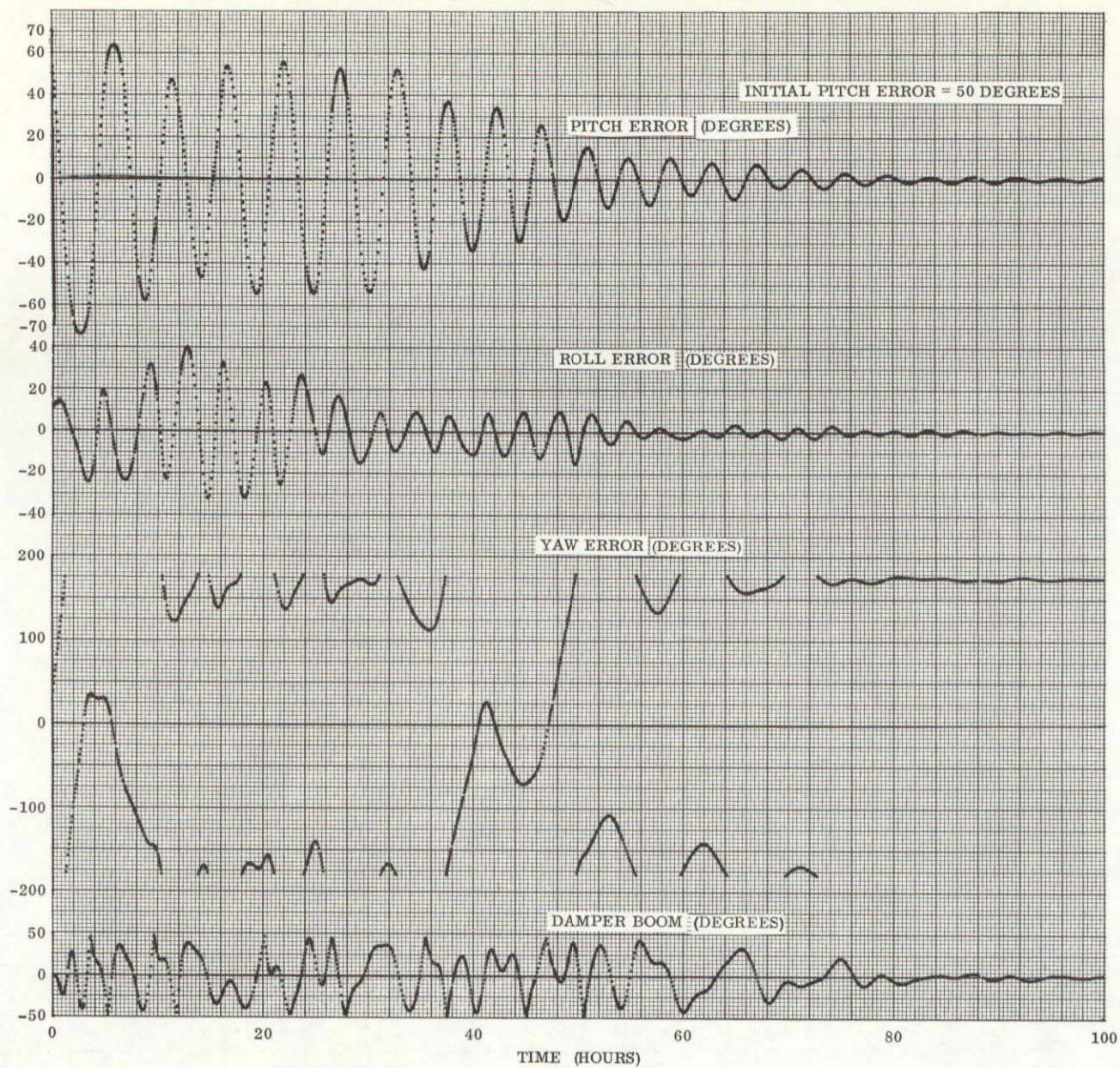
Figure 3.3-14.   Capture of ATS-A With 19 Degree Scissor Angle

3.3.2.1 <u>Single-Stage Rod Deployment</u>

The initial concept of rod deployment for ATS-D capture was to deploy the rods to full length immediately after despin. For this analysis, it was assumed that all the residual angular rate would be on the z axis. From the standpoint of capture, the worst initial orientation is with the spacecraft yaw axis perpendicular to the local vertical. This maximizes the potential energy content of the spacecraft, and to minimize the total energy of the spacecraft (which determines damping time), the initial rates must be very low.

A series of computer simulations was made to determine quantitatively the effect on capture of the initial spin rate on the z axis (ω_z). Two initial spacecraft positions were evaluated, one with the z axis parallel to orbital angular rate, and one with the z axis in the orbit plane. In both cases, the z axis was perpendicular to the local vertical. This approximates but is not quite a worst case (maximum) potential energy condition. The worst case condition occurs when the spacecraft is pitched 90 degrees at the conclusion of rod extension. For this study, however, the difference was felt to be minor.

The results of all the simulations were combined into "capture maps" which are shown in Figures 3.3-15 and 3.3-16, representing the two positions of the z axis. The two plots indicate the same general character, but Figure 3.3-15 shows the bias rate associated with orbital rate. At low initial rates, the ATS-D capture is symmetrical about orbit rate in the same manner as ATS-A (Section 3.3.1). The shaded area is there to indicate the sensitivity of capture time to initial conditions because there was a fair amount of scatter in the results of the simulation. A more accurate representation would be to replace the line with a wide brush mark.

From those plots, the conclusion was drawn that the ATS-D spacecraft can capture in less than 400 hours if the initial spin rate is less than 2.4 deg/sec and greater than -0.8 deg/sec when its z axis is along orbital angular rate. The nominal tolerance on the yo-yo despin, however, was ±1.2 degree/second which was too large on the negative side. The recommendation was, therefore, that a bias rate of 0.8 deg/sec be added to the yo-yo despin. The nominal tolerance of ±1.2 deg/sec is then satisfactory if the z axis is parallel to the direction of flight.

3-121
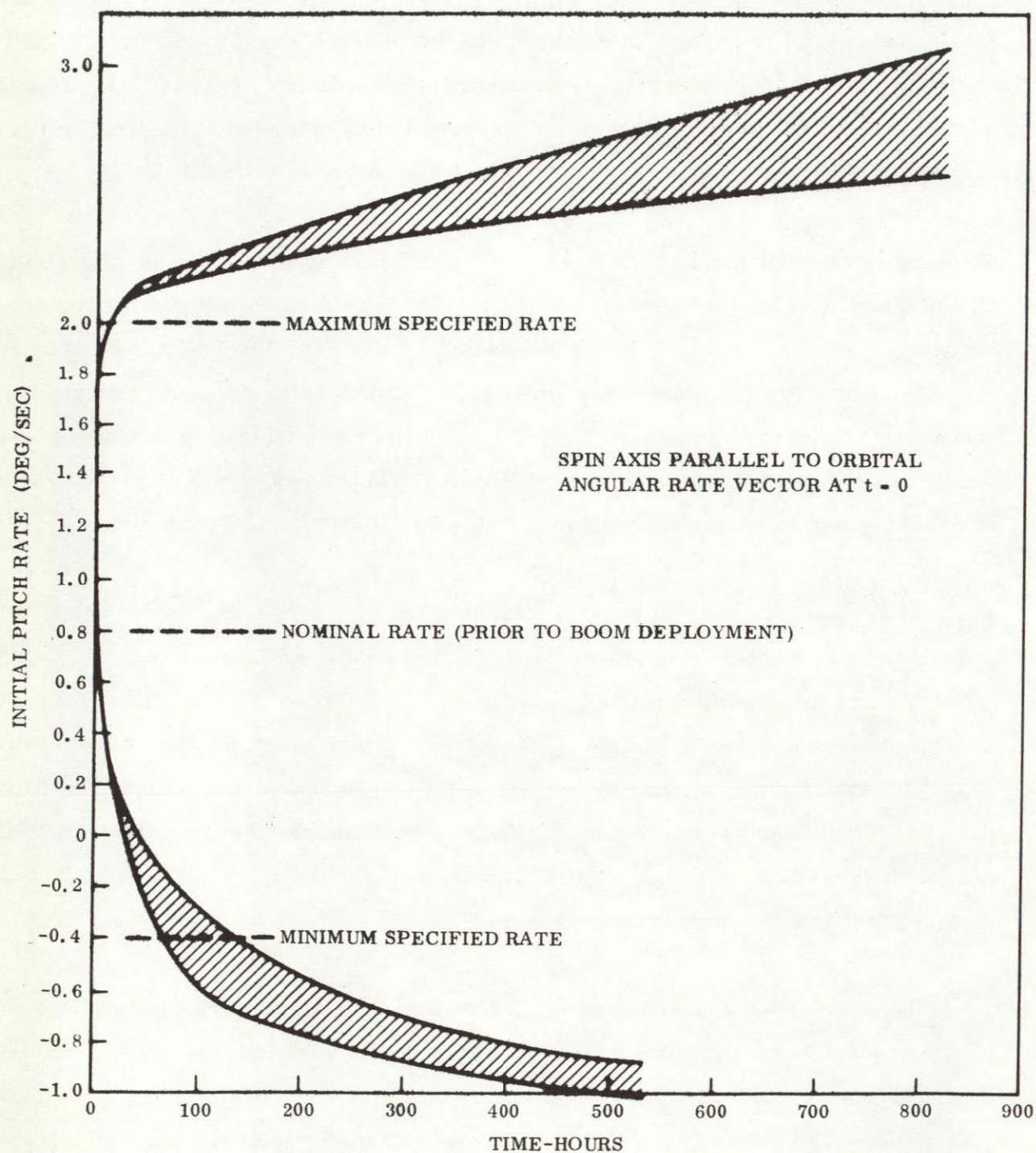
Figure 3.3-15. Capture Time Versus Pitch Rate Before Rod
Deployment For ATS-D
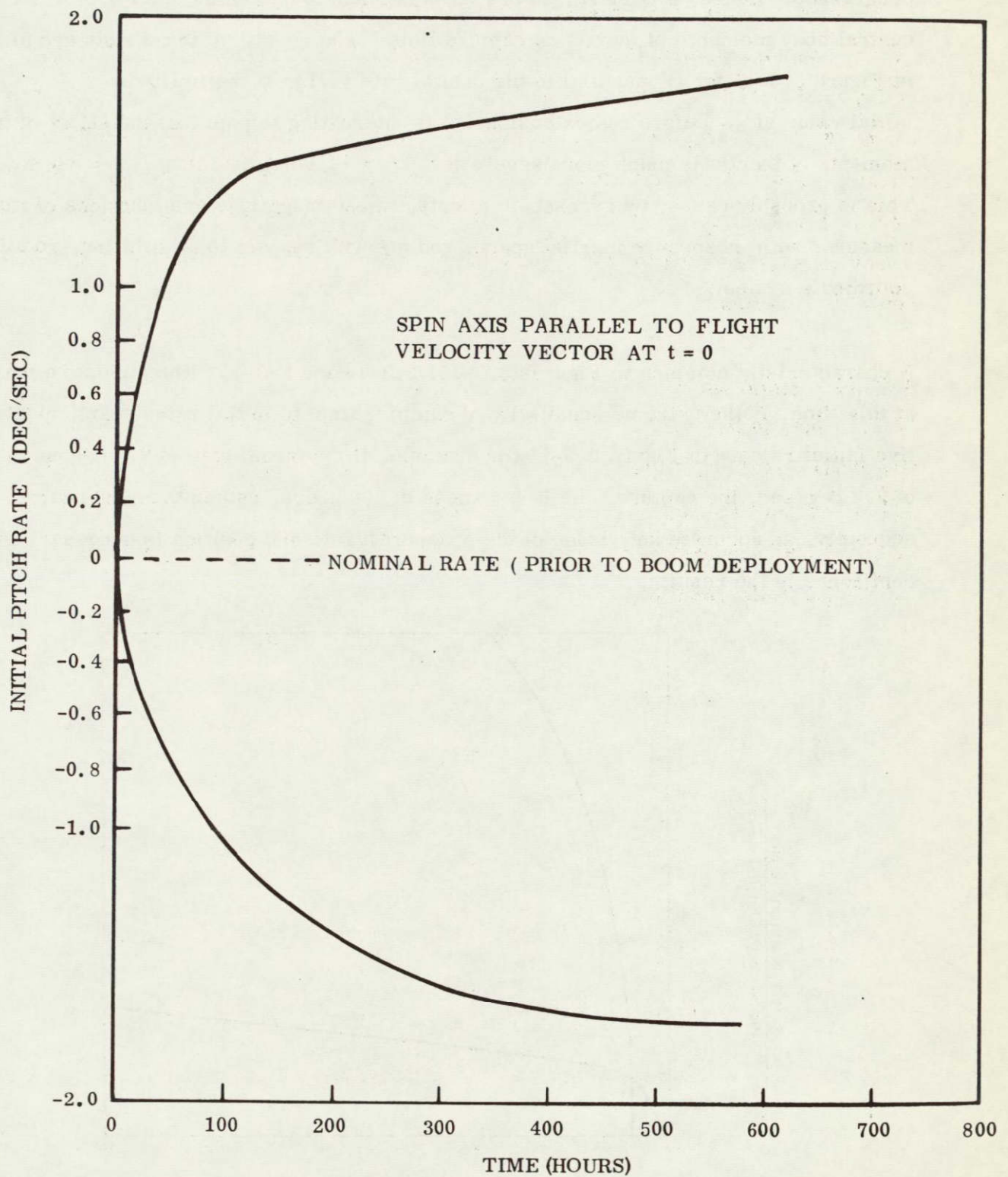
Figure 3.3-16. Capture Time Versus Pitch Rate Before Rod
Deployment For ATS-D

As with ATS-A, the moments of inertia of ATS-D tended to increase as the ATS program progressed. Hence, a later series of runs was made to determine the effect of increased central body moments of inertia on capture time. The results of these runs are plotted in Figure 3.3-17 for ω_z parallel to the orbital rate vector at the limits of ω_z. ω_{zo} is the initial value of ω_z before rod extension. It is interesting to note that the effect of increased moments of inertia is much more severe for $\omega_{zo} = +2.0$ deg/sec than $\omega_{zo} = -0.4$ deg/sec. This is probably caused by gyroscopic effects, whose magnitude are functions of rates measured with respect to inertial space, and not with respect to an orbiting, rotating coordinate system.

A characteristic common to Figures 3.3-15, 3.3-16 and 3.3-17, which must be mentioned at this time, is the extreme sensitivity of damping time to initial rates, particularly positive initial rates. In Figure 3.3-15 for example, if the initial rate is 2.6 deg/sec instead of 2.4 deg/sec, the capture time is in excess of 800 hours, rather than 400 hours. Consequently, an accurate knowledge of the spacecraft rate and position is necessary for confidence in the results.
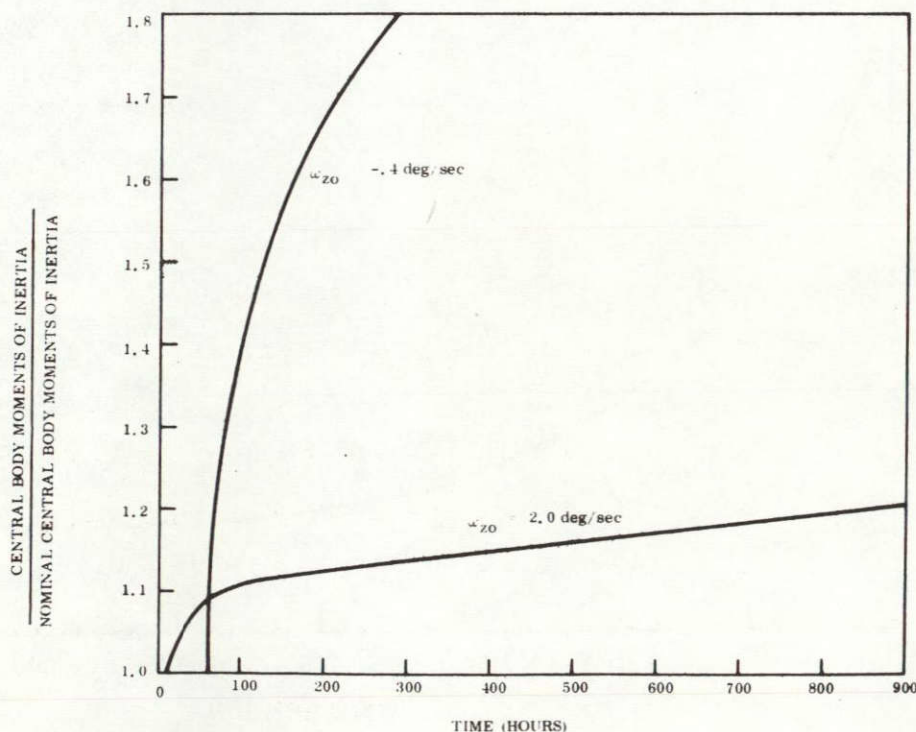
Figure 3.3-17. Effect of Central Body Moments of Inertia on ATS-D Capture Time

As a result of the foregoing analysis and its indication of extreme sensitivity, better definition of the yo-yo capabilities and the spacecraft moments of inertia were obtained and another capture study was undertaken. One of the purposes of this new study was to determine how significant the effect of initial position was, and what advantage could be obtained if the rods were deployed near the local vertical. The new initial conditions and parameters for the ATS-D spacecraft were:

1. Roll and yaw attitude at time of boom deployment are to be "worst case" for an angular momentum vector 5 degrees away from normal to the orbit plane, and 5 degrees away from the spacecraft's Z_1 axis.

2. Boom deployment rate = 1 ft/sec.

3. Magnitude of the angular momentum is to be based on "worst case" combination of the following:

    a. I_{xx} = 58.62 slug-ft^2

    b. I_{yy} = 55.60 slug-ft^2

    c. I_{zz} = 65.93 slug-ft^2

    d. $-0.40 \leq \omega_1 \leq 2.0$ degrees/second

Based upon previous studies that indicated high positive rate is most severe, the initial rates were selected to be 1.993 deg/sec about the pitch (z_1) axis, and 0.197 deg/sec about the yaw axis (x_1). The roll and yaw attitude errors were selected to be zero. The orbit was assumed to be circular to an altitude of 42,165,728 meters and at an inclination of zero. The sun is initially in the orbit plane with the earth located at the autumnal equinox. The spacecraft magnetic dipole is 1000 pole-cm along the positive roll axis.

The deployment sequence consisted of:

1. X-rod extension starting at t = 0.

2. Damper boom extension starting at t = 143.3 seconds.

3. Scissoring of the X rods from 19 degrees to 25 degrees starting at
   t = 174.6 seconds.

4. Unclamping the damper boom at t = 242.6 seconds.

The first computer run attempted was made with an initial pitch error of 30 degrees. This run indicated good capture time (see Figure 3.3-18) and it was decided to ignore the runs at smaller values of pitch error and concentrate on the effect of larger angles. Two additional runs were made, one at an initial pitch error of 50 degrees (see Figure 3.3-19), and one at 70 degrees (see Figure 3.3-20). It was evident from Figure 3.3-20 that an initial pitch error of 70 degrees is intolerable, resulting in long tumbling times. Because 50 degrees was satisfactory, it was decided to narrow down the "crossover line," and an additional computer run was made with an initial pitch error of 60 degrees (see Figure 3.3-21).

As shown, this initial condition results in tumbling for at least 400 hours. An initial pitch error of 50 degrees, therefore, appears to be the limit beyond which rod extension should not be initiated.

Several facets of Figures 3.3-20 and 3.3-21 should be noted. The most serious is the limited damper boom motion (please note difference in scale) when compared to Figures 3.3-18 and 3.3-19. This result is completely consistent with the previous result which is predicted both quantitatively and qualitatively (approximately) this phenomenon. The restricted motion greatly reduces the effectiveness of the damper. In spite of the reduced damper boom motion, however, damping is still taking place, as can be observed by comparing the slopes of the θ_p at the start of the run with those at the end of the run. The exact time of de-tumble cannot be determined with any degree of accuracy, however.

3.3.2.2 Double Stage Rod Deployment

As the ATS project progressed, and the spacecraft became better defined, the moments of inertia increased substantially (see Table 3.3-2) above those used in the previous capture studies. The increase was large enough (19 percent) to warrant a new capture study to determine if the spacecraft would successfully capture in less than 400 hours as had been originally specified.
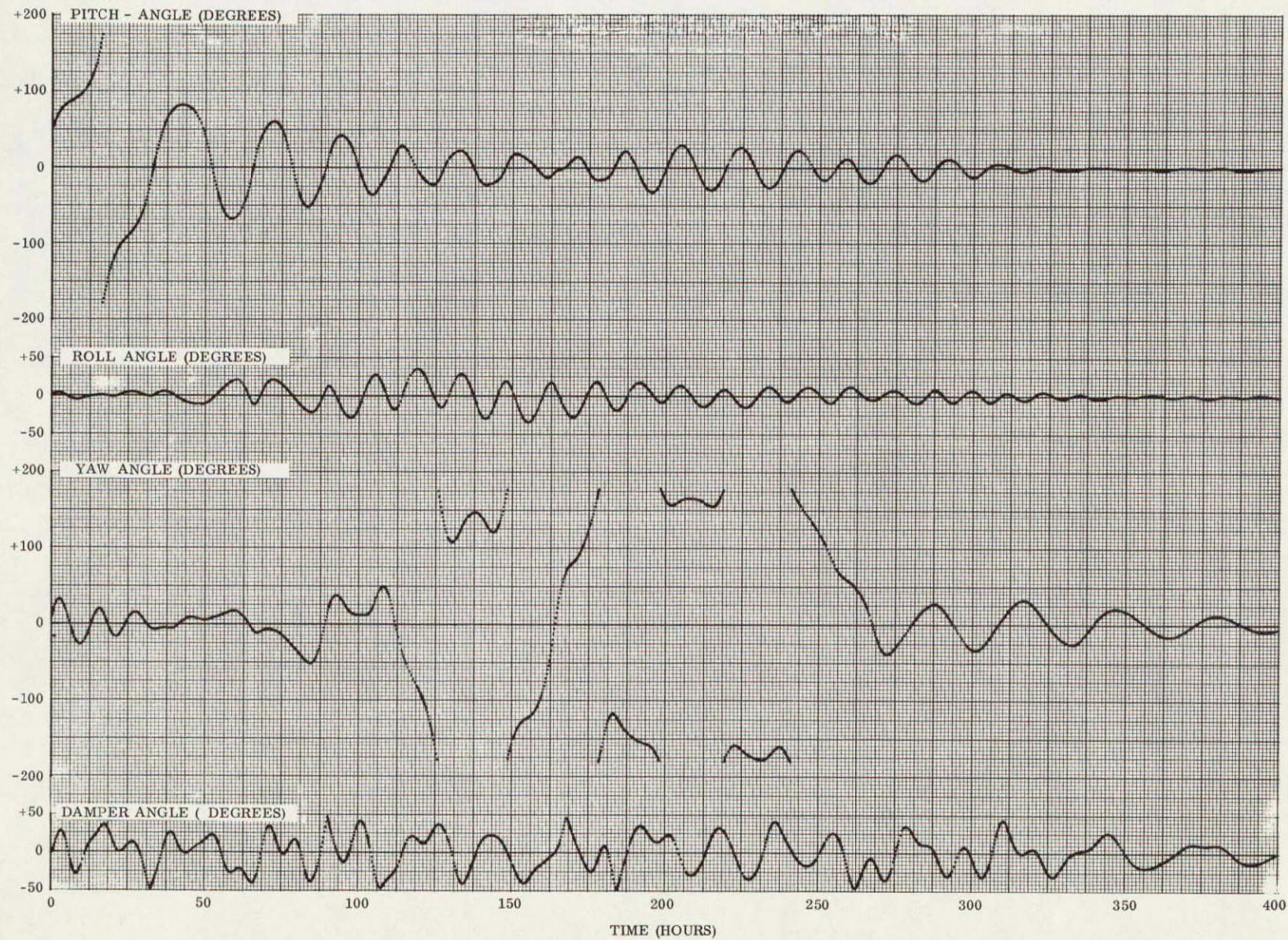
Figure 3.3-18. ATS-D Capture Study Damping Performance From Initial Pitch Error = 30 Degrees
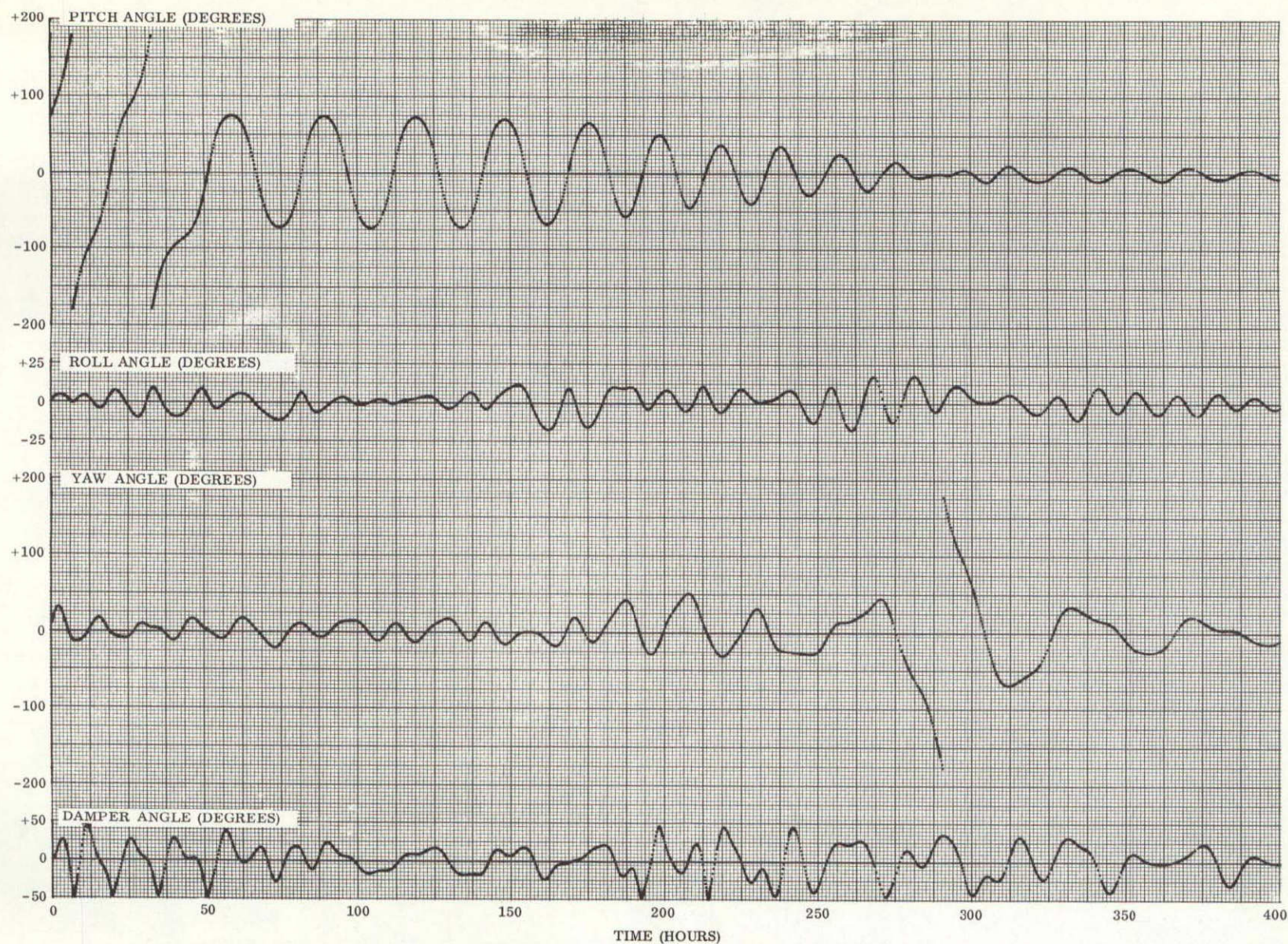
Figure 3.3-19.   ATS-D Capture Study Damping Performance From Initial Pitch Error = 50 Degrees
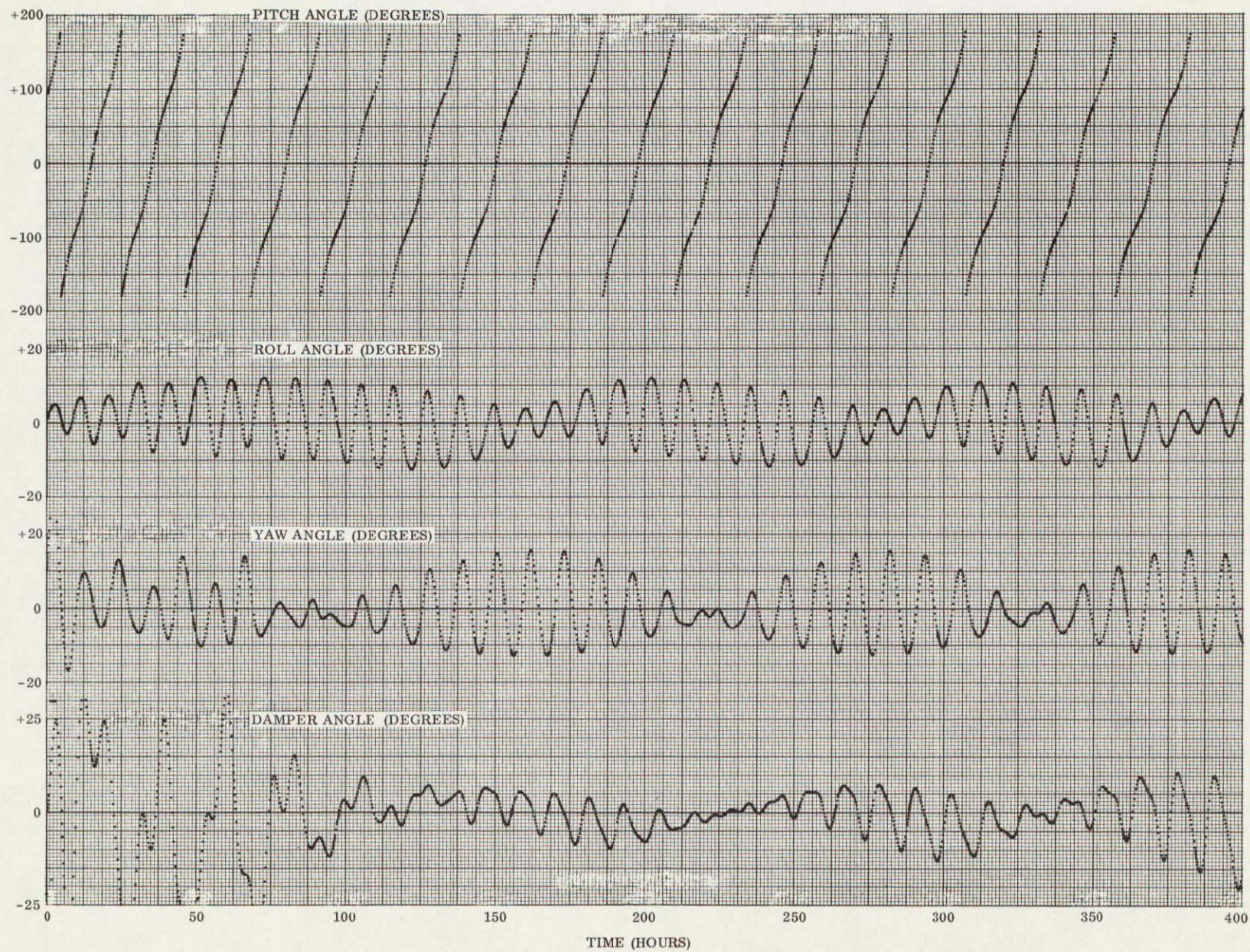
Figure 3.3-20. ATS-D Capture Study Damping Performance From Initial Pitch Error = 70 Degrees

3-129
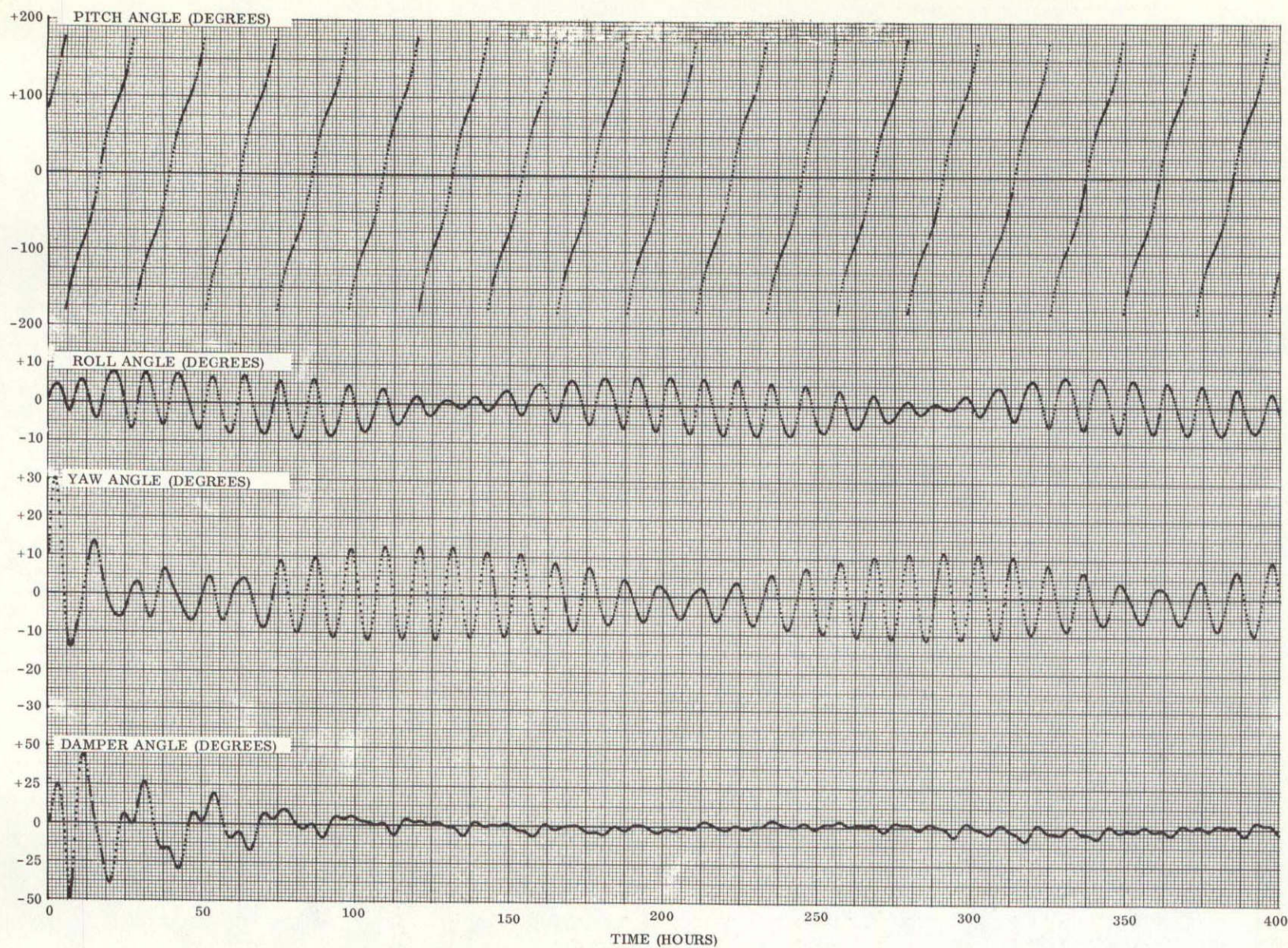
Figure 3.3-21. ATS-D Capture Study Damping Performance From Initial Pitch Error = 60 Degrees

Table 3.3-2. Moments of Inertia
(Slug-Ft^2)

| | Before Deployment | | After Deployment | |
	Previous	Current	70 Ft Rod*	123 Ft Rod**
About x_1	58.62	67.70	1229	3183
About y_1	55.60	63.52	5040	13,600
About z_1	65.93	78.25	5504	16,688
About $x_1 y_1$	1.73	2.38	2.38	2.38
About $x_1 z_1$*	0	0	0	0
About $y_1 z_1$*	0	0	+209	-259
Damper	-	-	540	540

*Including Damper
**Excluding Damper

The earlier studies (see Section 3.3.2.1) indicated that the pitch attitude could not exceed 50 degrees at the initiation of rod deployment or the spacecraft would tumble for more than 400 hours. As an estimate of the new pitch attitude limitations, 30 degrees was selected and a computer simulation made (see Figure 3.3-22) using the same sequence as the previous studies (Table 3.3-3). The results show the spacecraft tumbled for 150 hours before capturing. At the end of 400 hours, the spacecraft attitude errors are 7 degrees in pitch, 7 degrees in roll, and 40 degrees in yaw. The length of the tumble indicates that capture within 400 hours was extremely marginal, and 30 degrees was undoubtedly the maximum tolerable pitch error at rod deployment. As a consequence, no additional runs were made.

Successful capture of the ATS-D spacecraft using the deployment sequence shown in Table 3.3-3 requires that the telemetry data be obtained and processed and spacecraft attitude be determined in a short period of time. With initial tumble rates as high as two degrees per second, the spacecraft could pass through the deployment range in thirty seconds, suggesting that the attitude calculations be updated every ten seconds. Because
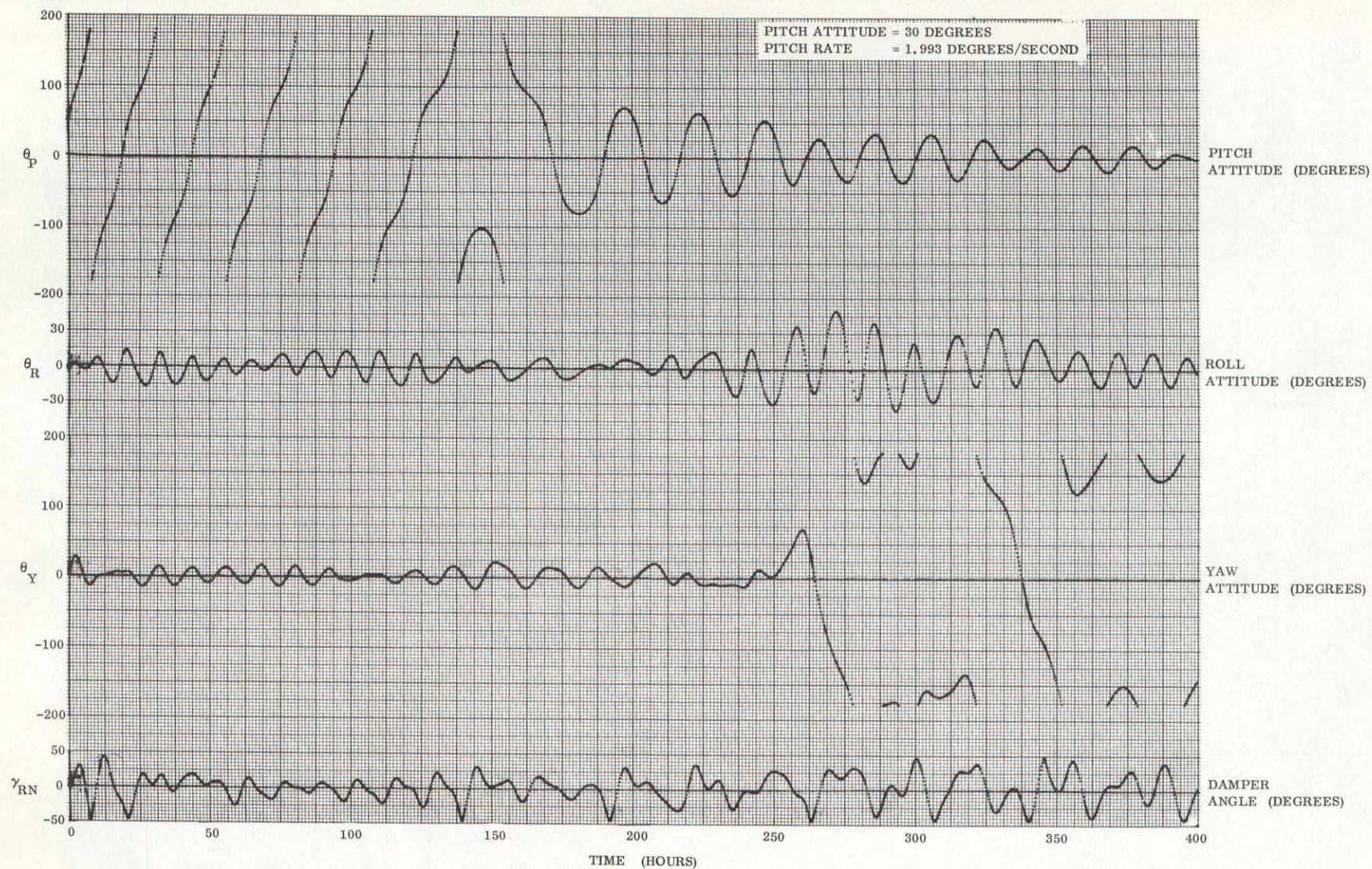
Figure 3.3-22. Single Deployment Sequence With Increased Moments of Inertia

of the multiple uncertainties in attitude computations at that rate, it was felt that there was little chance of "catching" the spacecraft when it was within the 60-degree band.

Table 3.3-3. Simulation Deployment Sequence

Single Stage Deployment Sequence	
Time (Seconds)	Operation
t + 0	Deploy Main Body Rods to 123 feet
t + 143.3	Deploy Damper Rods
t + 174.6	Scissor to 25 degrees
t + 242.6	Uncage Damper
Two Stage Deployment Sequence	
Time (Seconds)	Operation
t + 0	Deploy Main Body Rods to 70 feet
t + 143.3	Deploy Damper Rods
t + 242.6	Uncage Damper
t_1 + 0	Deploy Main Body Rods to 123 feet
t_1 + 75	Scissor to 25 degrees

The approach taken to solve the capture problem was a two stage development sequence, consisting of a rod deployment to less than full length, a hold period, and a second deployment of the rods to full length. The purpose of the first stage deployment is to slow the tumble to a point where reasonable position estimates can be made for one-half hour in advance. The attitude of the spacecraft will be monitored during the hold period, and estimates made as to when the spacecraft will be oriented closest to the local vertical. Because of the half-hour data processing time, the point of minimum local vertical error must be predicted at least one-half hour ahead. Under these conditions, the second stage rod deployment would have to be initiated immediately upon processing the most recent data point. A faster attitude data update, or a slower tumble rate of the spacecraft would allow an additional margin of time.

The second stage deployment would further reduce the tumble rate, and if executed when the spacecraft reaches a small angle to the local vertical, should prevent the spacecraft from tumbling more than 400 hours.

After evaluating the time limitations on attitude determination and the requirements for capture, a rod length of 70 feet was selected for the first stage deployment. The moments of inertia of this configuration are shown in Table 3.3-2. With a 5504 slug-ft^2 pitch moment of inertia, a two-degree per second initial rate will be reduced by a factor of 83.5 (to 0.024 deg/sec), approximately 6 times orbital at the end of the rod extension. Hence, in one-half hour, the spacecraft should not move more than 43 degrees, and should be reasonably predictable.

After considering the problems of deploying the spacecraft, it was decided to deploy the damper booms and uncage the damper after the first stage primary boom deployment. It was expected (and subsequently confirmed) that there would be little or no effective damping following the first stage rod deployment, in spite of the damper deployment. Scissoring was not to be performed until after the second stage deployment.

A computer simulation was made of the performance of the spacecraft with the same initial conditions as in Figure 3.3-22 (Table 3.3-4), but with an initial deployment to a rod length of 70 feet. The results were as anticipated (see Figure 3.3-23), and the spacecraft tumbled in pitch for the length of the simulation at approximately 0.024 degree per second (6 times orbital). The damper boom oscillated for a short period of time after deployment until it "jammed" against its limit, where it remained for the remainder of the simulation. There was very little damping after approximately 36 hours (when the damper boom stopped), and the spacecraft would probably have tumbled for considerably longer than 400 hours.

At this point, it was decided that if the two-stage capture sequence were to be effective, decisions regarding the time of second stage deployment would have to be made on the basis of past performance only. To simulate flight conditions, a procedure was set up whereby
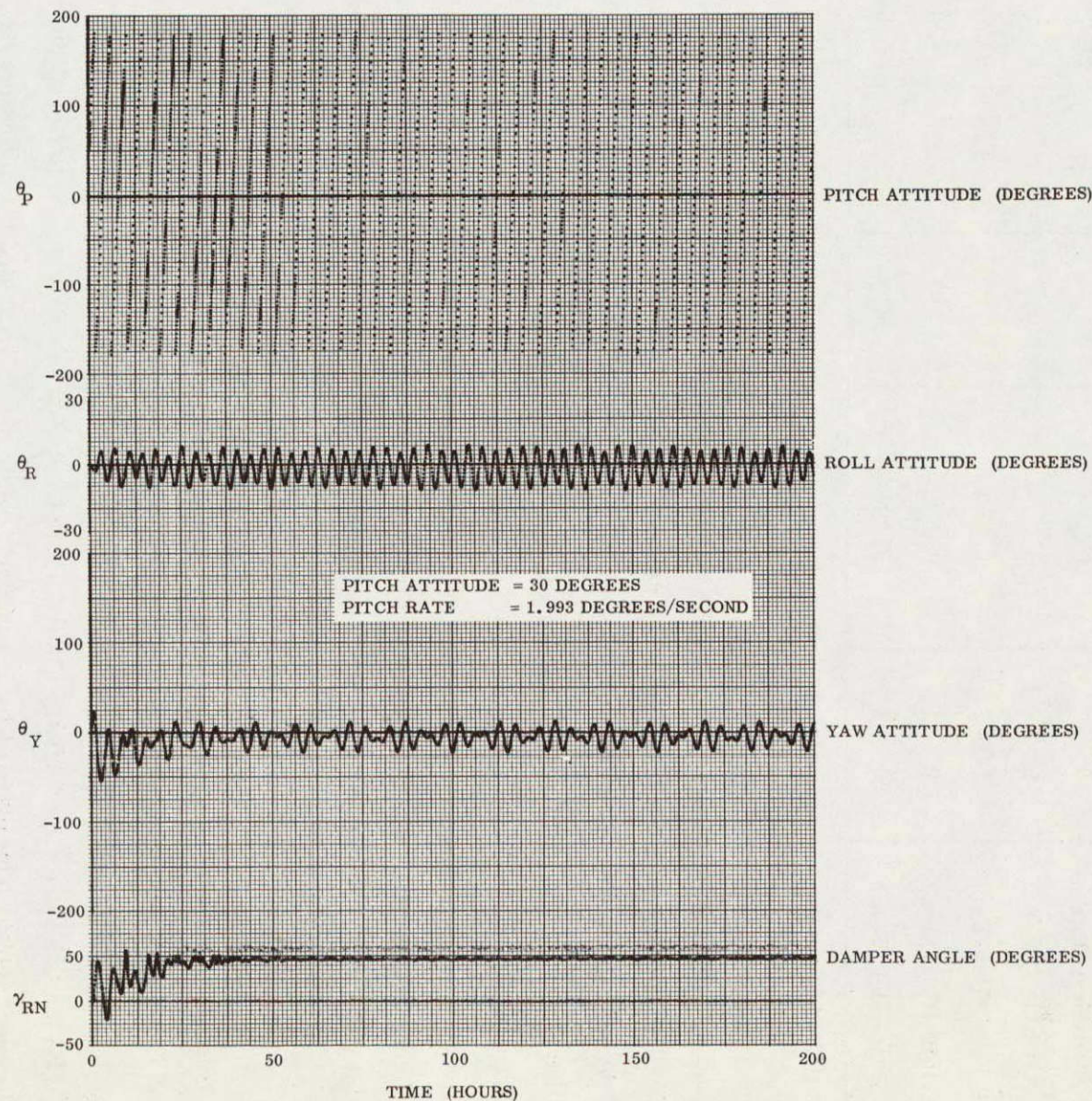
Figure 3.3-23. Initial Deployment To Rod Length Of 70 Feet

Table 3.3-4. Spacecraft Attitude and Rates Prior to Rod Deployment

	Previous Studies	Current Study Figures 3.3-22 and 3.3-23	Procedure Checkout		
			Figure 3.3-24	Figure 3.3-26	Figure 3.3-28
Pitch Attitude (Deg)	50	30	70	90	78
Roll Attitude (Deg)	0	0	0	0	36
Yaw Attitude (Deg)	0	0	0	0	34
Pitch Rate (Deg/Sec)*	1.993	1.993	1.993	-0.4	1.44
Roll Rate (Deg/Sec)*	0	0	0.197	0.197	0.374
Yaw Rate (Deg/Sec)*	0.197	0.197	0.197	0.197	0.243

*Inertial Rate

attitude (consisting of pitch, roll, yaw, pointing angle and damper angle) was available in approximately one-hour increments, with each increment being one-half hour old (i.e., the data point defining the spacecraft orientation at 1600 was not "available" until 1630). A small test group was formed consisting of Frank Kraus of the ATS Flight Analysis Group, Robert Clayton of the ATS Program Office, and Howard Foulke of Guidance and Control Subsystem Design. The points from the computer simulation were read off by H. Foulke at half-hour increments, and R. Clayton plotted local vertical pointing angle and F. Kraus plotted pitch and roll attitude (yaw attitude is essentially irrelevant) as a function of time. Three simulations were processed in this manner.

The first simulation evaluated is shown in Figure 3.3-24, and the initial conditions (prior to rod extension) are shown in Table 3.3-4. The simulation was limited to fifty hours when the additional ground rule was made that any action on the second stage deployment would be made before fifty hours. Figure 3.3-24, of course, was not available at the time of the processing. The plots of local vertical, pitch and roll attitude all indicated that deployment could be 3.00 hours after the start of the simulation, and the decision was made to deploy the rods. The actual time of deployment was 3.14 hours when a convenient
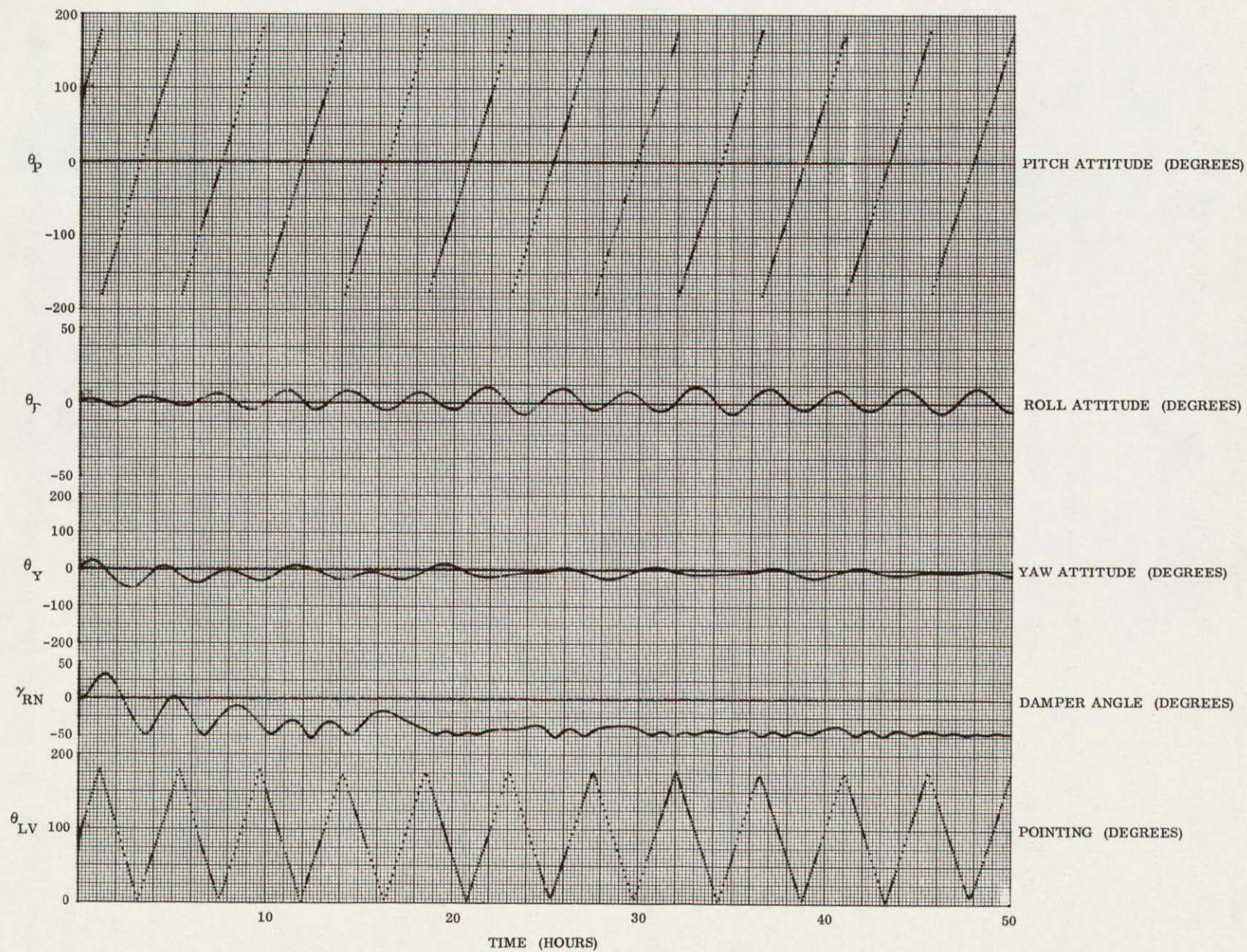
Figure 3.3-24.   First Stage Deployment For Pitch Rate = 2 Degree/Second

printout was available from which to pick initial conditions. The deployment time estimate was made after approximately two hours (orbit simulation time). As shown in Figure 3.3-24, 3.00 hours is nearly a minimum.

Figure 3.3-25 is in the follow-on simulation, which shows the performance of the spacecraft when the second stage rod deployment was initiated at the selected time. Capture was immediate and upright, and at the end of 400 hours, steady state had been achieved. Figure 3.3-24 does not, however, provide a good check on the data evaluation procedure because of the small roll error and the consequent regularity of the pitch motion. Pitch is tumbling at a constant rate, and it is relatively easy to predict when pitch will have a minimum value.

To provide a more general case, the second simulation used the negative extreme rate (-0.4 deg/sec) and is shown in Figure 3.3-26. At this lower pitch rate (Table 3.3-4) the spacecraft has little spin stability, and the gravity gradient torques alter the regular character. Again the attitude was plotted, and this time the estimate of the deployment time was 11.9 hours. The estimate was made well in advance of 11.4 hours since again the performance was still quite regular. The results of the follow-on simulations are shown in Figure 3.3-27. Capture was almost immediate, although the spacecraft did invert. Steady state was not quite reached in 400 hours since yaw did not settle until 250 hours.

The last simulation had arbitrary but feasible initial conditions and was selected to destroy as much as possible, the "clean" performance of the first two simulations, particularly in pitch. The initial conditions are shown on Table 3.3-4, and the simulation results are shown in Figure 3.3-28. The estimate of deployment time was slightly longer for this run and was finally selected to be 18.02 hours. The estimate was reasonable, although as shown in Figure 3.3-28, the best time would have been at 30.5 hours, where the pointing error was approximately five degrees (note that the motion is periodic). The follow-on run (Figure 3.3-29) indicates immediate and rightside up capture. Steady state was achieved by 400 hours.
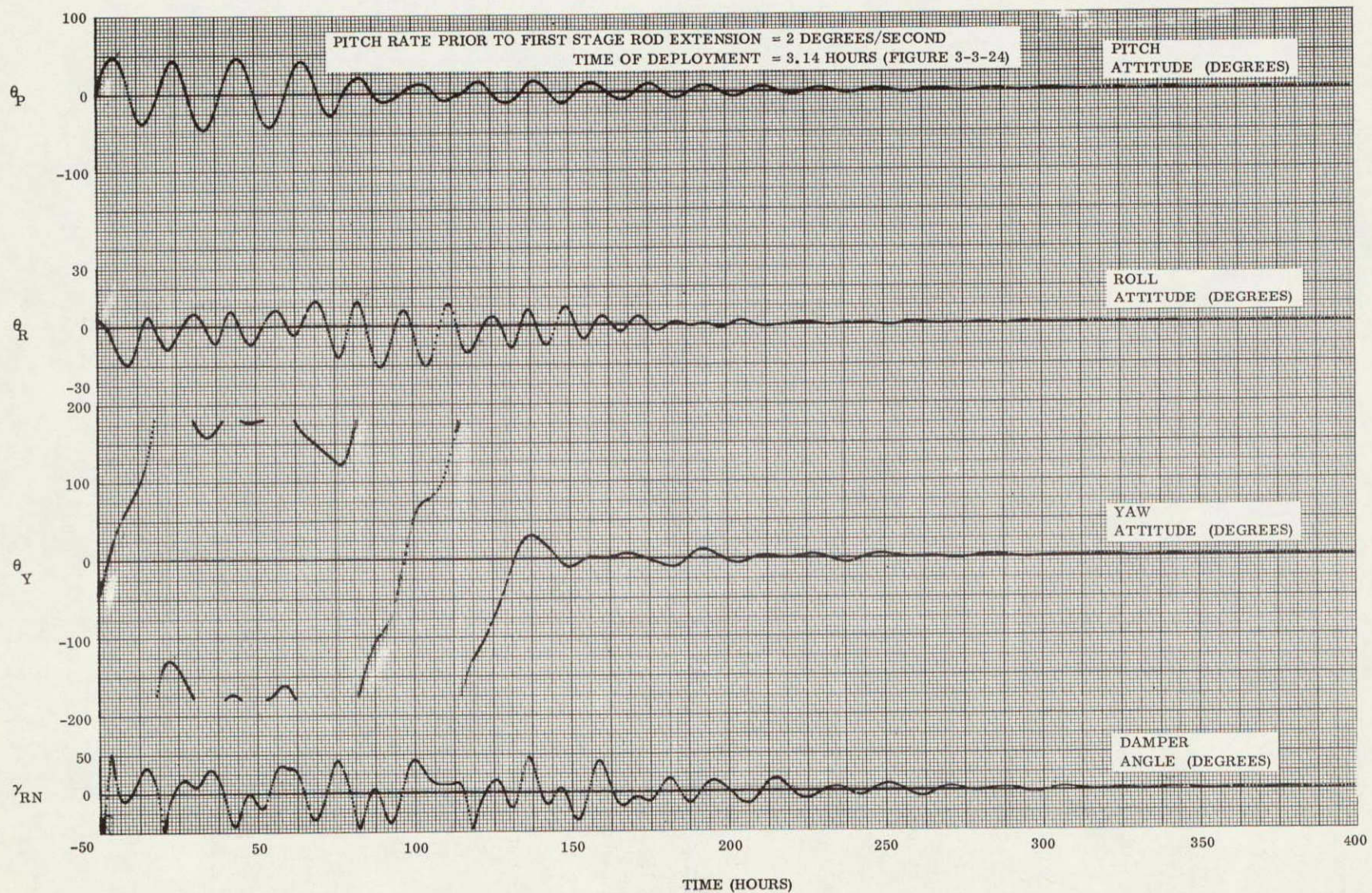
Figure 3.3-25. Second Stage Deployment From Rod Length Of 70 Feet To Rod Length Of 123 Feet
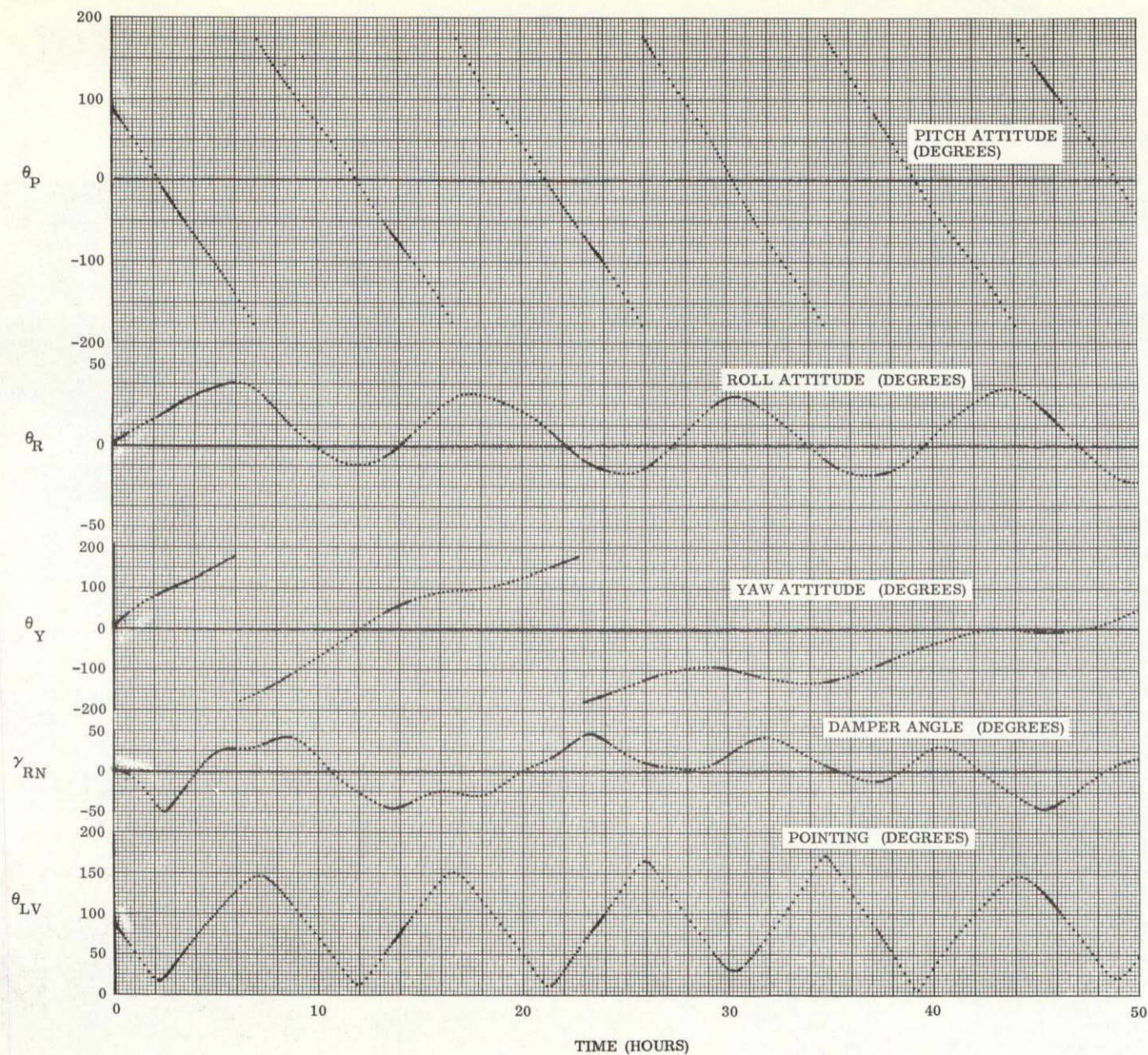
Figure 3.3-26. First Stage Rod Deployment For Pitch Rate = 0.4 Degree/Second

PITCH RATE PRIOR TO FIRST STAGE ROD EXTENSION = -.4 DEGREES/SECOND
TIME OF DEPLOYMENT = 11.9 HOURS (FIGURE 3.3-26)

PITCH ATTITUDE (DEGREES)

ROLL ATTITUDE (DEGREES)

YAW ATTITUDE (DEGREES)

DAMPER ANGLE (DEGREES)

TIME (HOURS)
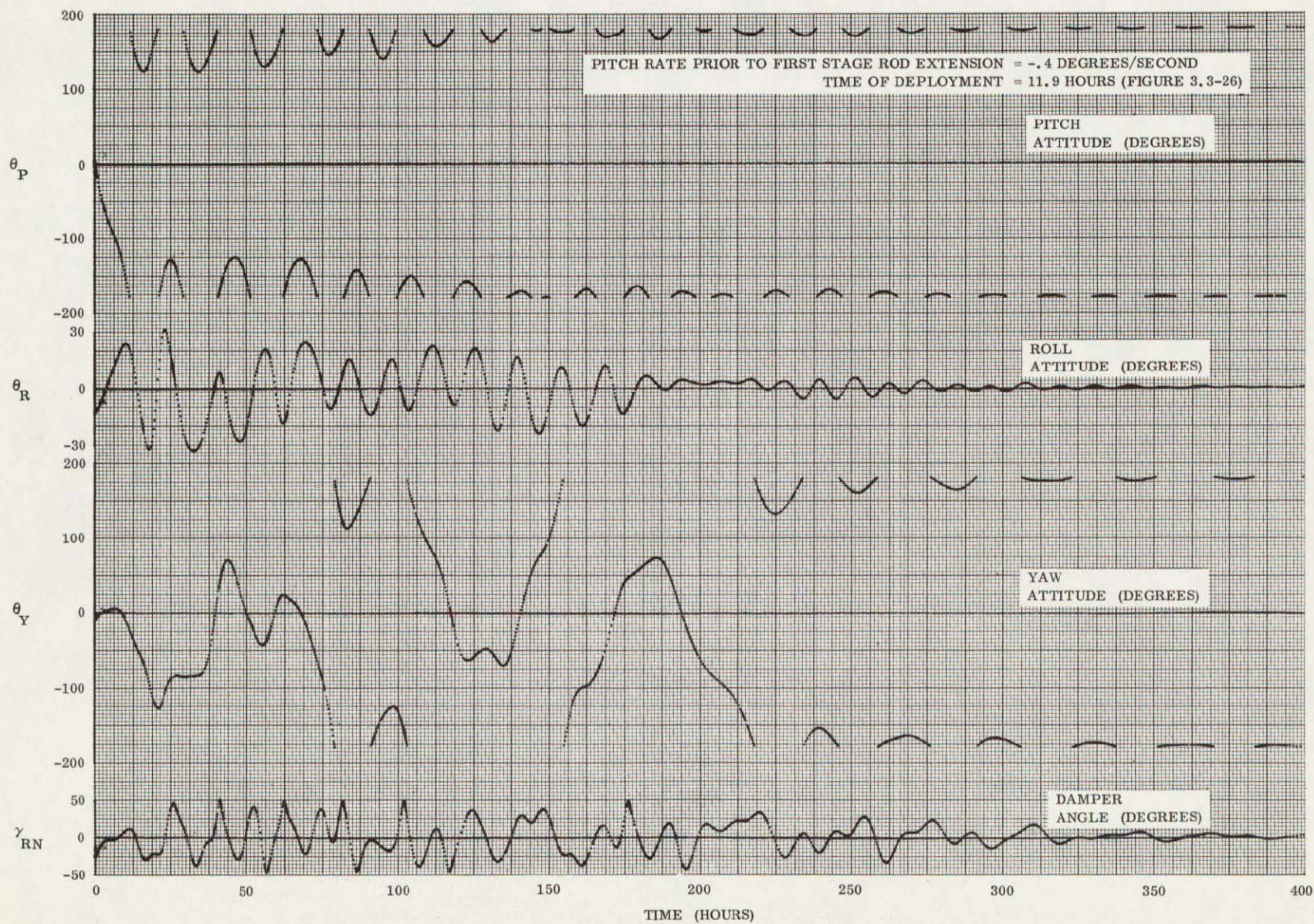
Figure 3.3-27. Second Stage Deployment From Rod Length Of 70 Feet To Rod Length of 123 Feet
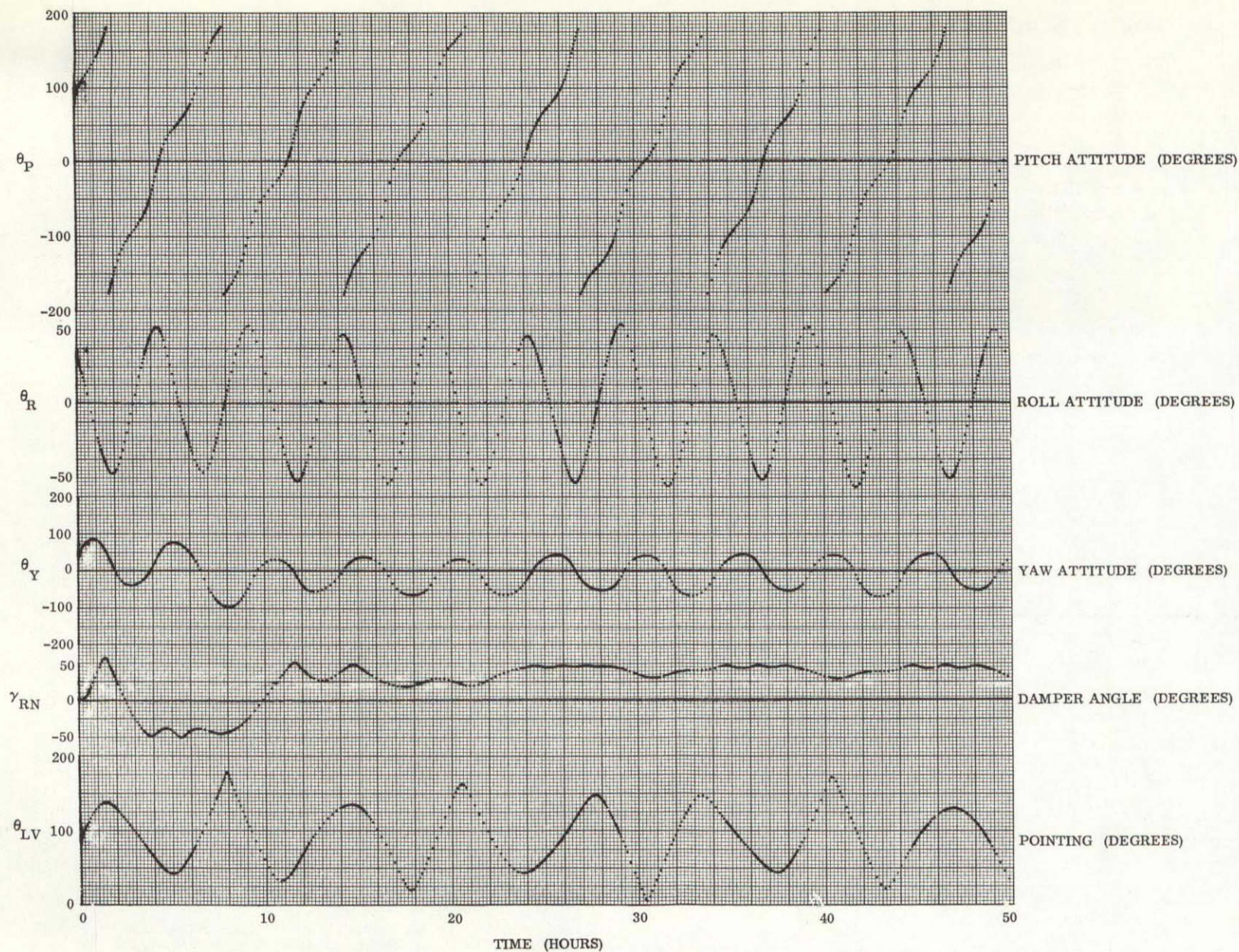
Figure 3.3-28. First Stage Rod Deployment For Pitch Rate = 1.44 Degrees/Second
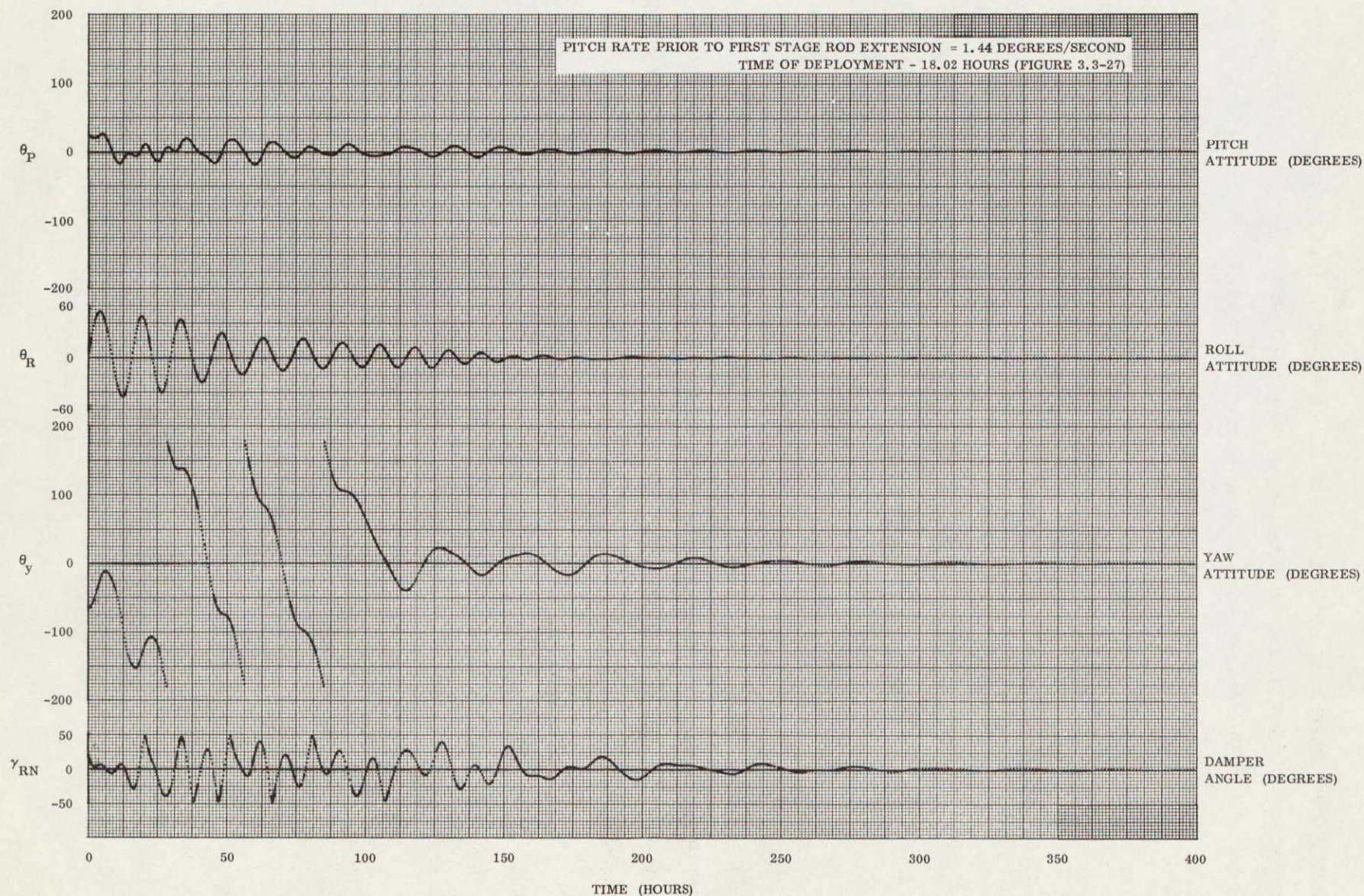
Figure 3.3-29. Second Stage Deployment From Rod Length Of 70 Feet To Rod Length Of 123 Feet
Pitch Rate Before First Stage Rod Extension = 1.44 Degrees/Second

As a result of these exercises, several things became evident. Plotting pitch, roll, and local vertical are all helpful, and all three should be plotted during the actual flight operation. Second, the tumble rate appears to be slow enough to predict reasonably well the performance of the spacecraft for short periods in advance, and periodic enough to make long term estimates about the approximate time when the pointing error will be minimum. Hence, intelligent estimates as to the best time to deploy can be made. Third, the chances of obtaining a rightside up capture are finite, although probability estimates cannot be made on the basis of three simulations. Fourth, with the two-stage deployment procedure the total time to steady state is likely to be nearly 400 hours, if the initial conditions are within the band specified (0.8 ± 1.2 deg/sec). Higher rates have not been simulated. Because of the structural limits on the rods, however, six degrees per second is the maximum rate at which this sequence would be employed.

3.3.2.3 Magnetic Damping

By late 1967, the moments of inertia of the spacecraft prior to rod deployment had increased to the point that capture using either the single- or two-stage rod deployment approach could not be assured. Consequently, an alternate approach to damping the spacecraft was required. The approach taken was a magnetic "Sample and Hold" technique similar to the one used successfully by the Applied Physics Laboratory of Johns Hopkins University on the DODGE spacecraft. The logic, in its simplest form, is to measure the earth's magnetic field and set the magnetic dipole of a set of electrical coils to be coincident with the field. As the spacecraft rotates, the magnetic torque attempts to restore the spacecraft to its original position and retards the motion. Continuous updating of the magnetic dipoles is required. This is performed by using magnetometers to measure the field, together with appropriate control logic or ground updating. Time did not permit a fully automatic version of the magnetic damping on ATS-D, and a ground operated technique was implemented. To determine the effectiveness of this approach, an analysis was performed. The analysis was divided into two sections, a detumble section which determined the procedure to be used when the spacecraft is tumbling, and an oscillation section which determined the procedure to be used when the spacecraft is oscillating. The latter approach is a backup to the damper boom.

3.3.2.3.1 Tumbling Spacecraft

In order to establish approximate detumble times for the ATS spacecraft when using a controlled magnetic dipole as a damping mechanism, a planar analysis was performed for various duty cycles and spacecraft tumble rates. The magnetic dipole generated by the controllable magnetics within the spacecraft will induce a body torque proportional to the sine of the angle between the magnet orientation and that of the earth's magnetic field direction. The equation is

$$T = M H_e \sin \theta \qquad \qquad (3.3\text{-}3)$$

where

T = Torque

M = Spacecraft magnetic dipole strength

H_e = Earth's magnetic field strength at the spacecraft's location

In the case of a tumbling spacecraft, the torque opposes the motion for one half revolution and aids the motion for the second half cycle. Therefore, the sample and hold technique must be applied during each one half revolution of the spacecraft, or if the dipole is to remain on continuously, its sign must be reversed at each half cycle.

The angular momentum removed from the system is the time integral of the torque:

$$\Delta H = \int_{t_1}^{t_2} T \, dt = \int_{t_1}^{t_2} M H_e \sin(\omega t) \, dt \qquad \qquad (3.3\text{-}4)$$

where t_1 is the turn-on time for the dipole, t_2 is the turn-off time of the dipole, and ω is the tumble rate of the spacecraft, as shown on the accompanying sketch.
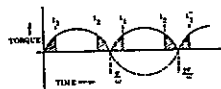
However, the off time between t_2 and π/ω may be utilized as the required off time for the second cycle (i.e. from π/ω to t_1), and thus the actual torque profile would be:
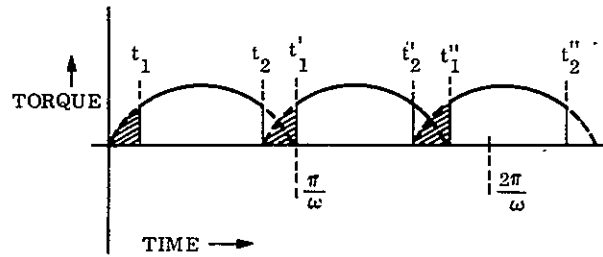
The period for one cycle is $2\pi/\omega$ and choosing $t_2 = (\frac{\pi}{\omega} - t_1)$

$$\Delta H = MH_e \left(\frac{1}{\omega}\right) \cos \omega t \Big|_{t_1}^{\pi/\omega - t_1} = -\frac{2MH_e}{\omega} \cos \omega t_1 \qquad (3.3\text{-}5)$$

This then is an expression for the total angular momentum removed per one half revolution of the spacecraft. The average period is t_2 which is $\frac{\pi}{\omega} - t_1$, hence the ΔH removed per unit is:

$$\left(\frac{\Delta H}{\Delta t}\right)_{avg} = \frac{\dfrac{2MH_e}{\omega} \cos \omega t_1}{\dfrac{\pi}{\omega} - t_1} \qquad (3.3\text{-}6)$$

$$= \frac{-2MH_e \cos \theta_1}{\pi - \theta_1} \qquad (3.3\text{-}7)$$

M = Dipole strength

H_e = Average magnetic field strength

θ_1 = Lag angle (ωt_1)

Realizing that the change in angular momentum requires a change in spacecraft tumble rate:

$$\Delta H = I \times \Delta \omega \qquad (3.3-8)$$

And combining the equation:

$$\Delta t = \cfrac{I \, (\Delta \omega)}{\left[\cfrac{2 \, MH_e \, \cos \theta_1}{\pi - \theta_1} \right]} \qquad (3.3-9)$$

This expression may be used to estimate the time required to reduce the spacecraft rate from the initial value to the approximate rate known to be necessary for capture. However, to this point, the motion of the spacecraft was assumed to be such that the angle between the dipole and the earth's magnetic field could vary from 0 to 90 degrees. If the motion is purely pitch and the orbit is equatorial, this range of angle cannot be realized without the addition of a more elaborate, self-contained, sensing and control system. With existing spacecraft capabilities, the scheme being recommended has a maximum angle of about 12 degrees. The average value of this angle, based upon the magnetic field model being used in the large angle computer simulations, is approximately 9 degrees. Therefore, the average magnetic torque opposing pitch motion is reduced by the sine of this angle (0.156) and predicted damping times are increased by the reciprocal of 0.156 or 6.4 times.

As indicated in Equation 3.3-9, the time required to remove a specified angular momentum is a function of lag angle. The relationship is shown in Figure 3.3-30, based on the following parameters:

Dipole Strength, M = 150,000 pole-cms

Average Magnetic Field, H_e = 1 x 10^{-3} oersteds x 0.156

Total Angular Momentum, $(I\omega)$ = 3 ft-lb-sec
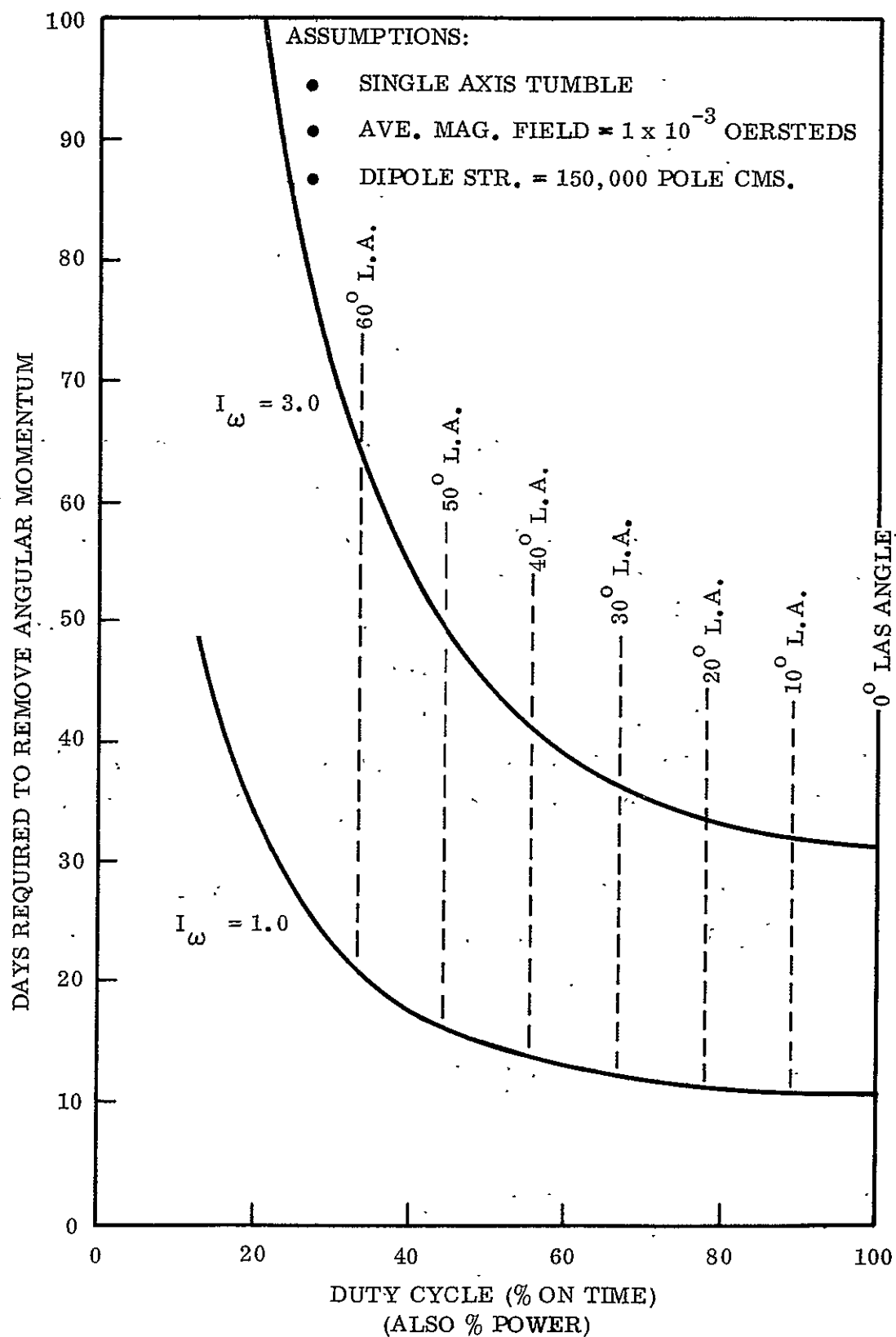
Figure 3.3-30. Detumble Time Versus Duty Cycle

A lag angle of 90 degrees produces the most rapid decay because the magnetic torque applied to the spacecraft is a maximum. This angle requires continuous update, however, which is operationally impossible because of limitations on the magnetometers and the magnetic coils.

The high dipole value of the magnetic coils significantly distorts the magnetic field and prevents a direct measurement of the field by the magnetometer. Consequently, the coils must be deactivated for a measurement to be made. Preliminary assessment of the length of time required to deactivate the coils, measure the magnetic field, transform the field into magnetic coil coordinates (the magnetometer axes are not aligned with the magnetic coil axes on the ATS-D/E spacecraft) and command the new dipole level, led to the selection of a 20 degree lag angle. The remaining analyses were conducted assuming that lag angle. With ATS-D moment of inertia of 16,638 slug-ft^2, the calculated value of tumble rate decay time is

$$\frac{\Delta t}{\Delta \omega} = 50 \text{ hours per } 0.001^{\circ}/\text{sec}$$

(3.3-10)

To look at a worst case example, if the ATS spacecraft is tumbling in pitch at 6 deg/sec before rod extension, the rate will be approximately 0.023 deg/sec after rod deployment. If the rate necessary for capture is between 0.007 and 0.008 deg/sec, then it will require approximately 32 days to realize capture.

Before specifying a sample and hold timing sequence for the tumbling phase, it was deemed advisable to analyze the case for the oscillating spacecraft and perform simulations for both.

3.3.2.3.2 Oscillating Spacecraft

The analysis of an oscillating spacecraft is quite different from that of a tumbling craft. In the case of tumble, the direction of the motion does not change and hence the sample and hold frequency is not nearly as critical as for the oscillatory case. With a changing direction of motion, ideally it is desirable to update the direction spacecraft dipole at each peak amplitude point. However, this would require either an on-board control system, not

presently available, or continuously monitored attitude data at the ground station to allow ground command control of the dipole. To avoid either of these requirements, this phase of study assumed no knowledge of spacecraft attitude information and concentrated on determining the existence of a practical sample and hold timing sequence. The sequence is required to produce effective damping regardless of the phase relationship between the dipole updating and the spacecraft oscillations.

The energy involved in the magnetic torquing is

$$E = \int T d\theta \qquad (3.3\text{-}11)$$

It can be shown that the total energy removed from the system while the torque exists is:

$$E = -MH \left[\cos (\theta_2 - \theta_M) - \cos (\theta_1 - \theta_M) \right] \qquad (3.3\text{-}12)$$

where:

$$\theta_1 = \theta_o \sin (\omega t_1)$$

$$\theta_2 = \theta_o \sin (\omega t_2)$$

θ_M = Angle of the magnetic field at time of sampling

θ_o = Peak amplitude of spacecraft oscillation

ω = Average spacecraft rate

t_1 = Time at which dipole is turned on

t_2 = Time at which dipole is turned off

The figure below helps describe the method used to evaluate the total energy removed from the system as a function of the number of sample and hold cycles per spacecraft oscillation.
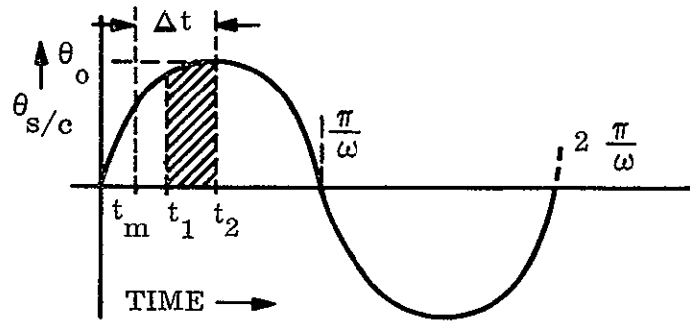
If N is defined as the number of sample and hold cycles per spacecraft oscillation and ω is specified as $(S \times \omega_o)$ where ω_o is orbital rate then:.

$$\Delta t = \frac{2\pi}{N (S\omega_o)} \tag{3.3-13}$$

If t_s is the dipole turn-on time for the first of the sample and hold cycles (allowing the process to start at any time relative to the spacecraft oscillation) and if C is the "duty cycle":

$$C = \frac{t_2 - t_1}{\Delta t} \tag{3.3-14}$$

then

$$t_1 = t_5 + (N-1) \Delta t \tag{3.3-15}$$

$$t_2 = t_1 + (C\Delta t) \tag{3.3-16}$$

$$t_m = t_2 - \Delta t \tag{3.3-17}$$

also

$$\theta_M = (t_2 - \Delta t) (S\omega_o)* \tag{3.3-18}$$

---

*Twice orbital rate is the maximum spacecraft frequency expected, therefore S = 2 is used in this analysis.

This then defines all terms necessary to solve the energy equation as a function of N, the number of sample and hold cycles per spacecraft oscillation, and also as a function of various values of t_s.

Certain deductions were evident prior to performing any mathematical evaluations:

1. The choice of one cycle per oscillation is of no use. It results in no effect since during one half of the spacecraft oscillation the magnetic torque is in the opposite direction to that desired and therefore cancels the desired effect of one-half cycle.

2. The other extreme, $N = \infty$, results in no induced magnetic torque, because the dipole follows the field exactly.

3. A third consideration limits the extent of choices for the values of N; i.e., a practical timing sequence in consideration of ground station requirements. It was decided to investigate values of N which result in ground station activity at intervals of no greater frequency than once every 2 hours. Since the highest expected spacecraft oscillation frequency is twice orbital rate (period = 12 hours), the maximum value of N is therefore 6.

Evaluation of the energy removal for values of $N = 2, 3, 4, 5$, and 6 and start times ranging from 0 to 12 hours (for each N) was done by computer. The results are shown in Figure 3.3-31 in terms of the average energy removed per spacecraft oscillation as a function of start time, t_s. Regardless of start time each problem extends for one full spacecraft oscillation. For the case $N = 2$, phasing of the sample and hold cycles with the spacecraft oscillation can be critical, as indicated at the near 0 and 6 hour points on the plot. As N is increased above 3, the average energy removed per spacecraft oscillation decreases until, as previously stated, no energy is removed as N approaches infinity (torque goes to zero). Figure 3.3-32 shows the minimum, maximum, and average energy as a function of N. At small values of N the energy removed is a random function of the phasing. However, the range between minimum and maximum energy narrows quickly with N for values greater than 3. For the remaining analyses and for large angle computer evaluations, emphasis was placed on the $N = 3$ case, which was the highest frequency of spacecraft oscillations expected to be encountered. $2 \omega_o$ corresponds to a sample and hold cycle of 4 hours duration (6 times per day).
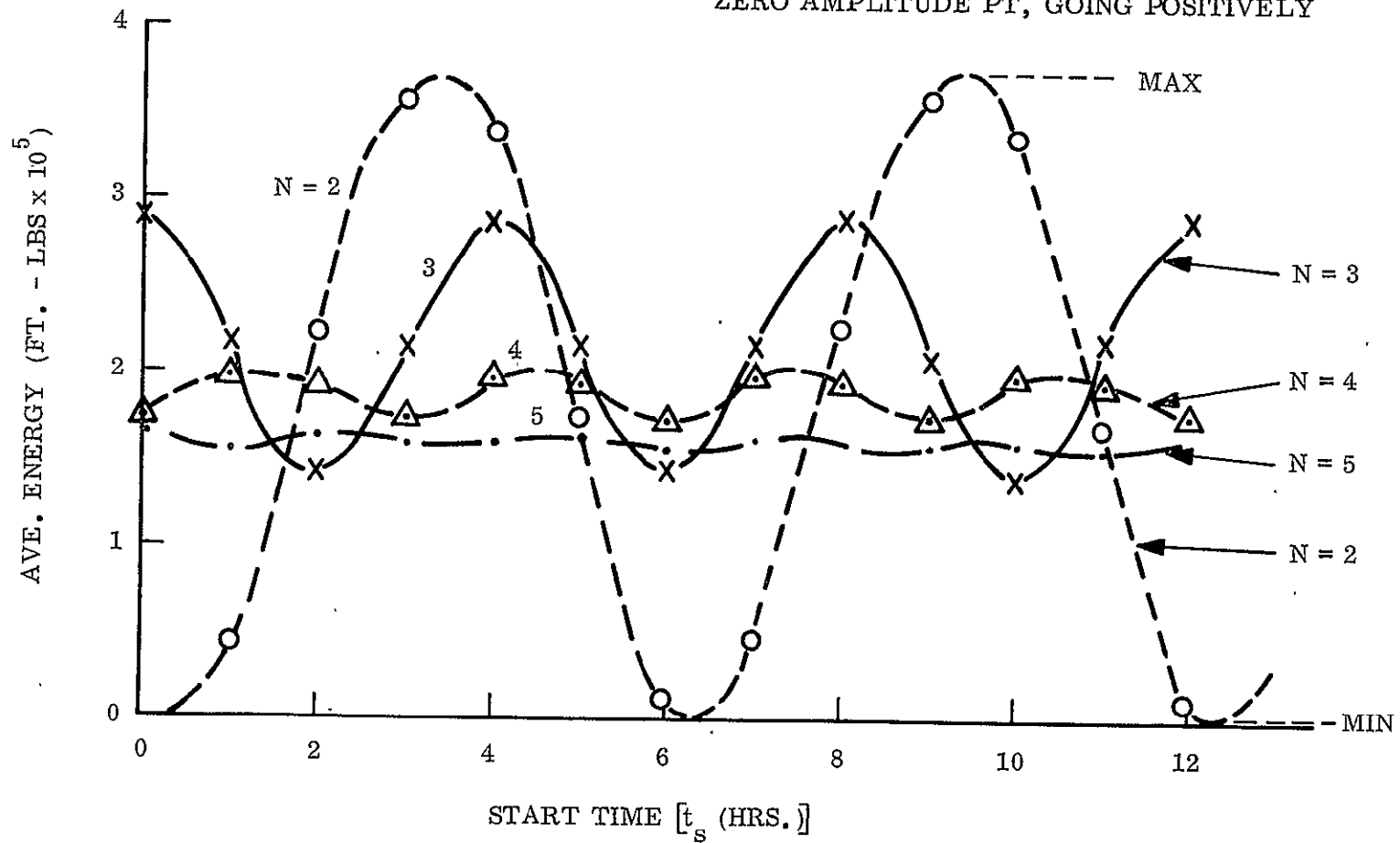
Figure 3.3-31. Average Energy Removed Per Oscillation Versus Short Time
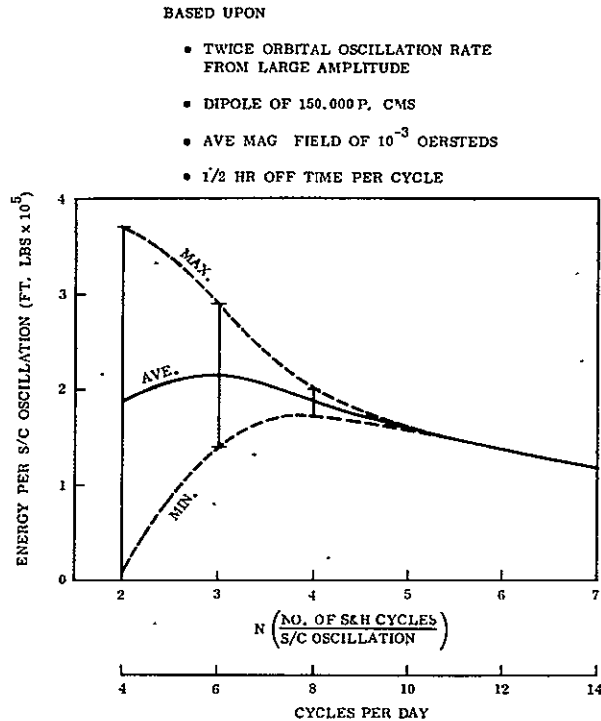
Figure 3.3-32.   Magnetic Damping Energy Versus Number of Sample and
Hold Cycles per Day

3.3.2.3.3 Simulations and Time Schedule

Three cases were simulated, using 4, 6, and 12 sample and hold cycles per day (i. e. ,

N = 2, 3 and 6, respectively, for a twice orbital oscillation rate). Other than the sample

and hold frequency, all evaluations were identical. Initial conditions were 2 deg/sec

tumble about pitch (0 deg/sec in roll and yaw) and the spacecraft pitched forward by +70

degrees from the desired orientation. Rod extension was initiated at the start of the

computer run and the damper boom unclamped at approximately 4 minutes after start.

The sample and hold process was not started until 2 orbits had been completed (48 hours).

The results of these runs are shown in terms of Euler angle time histories on Figure 3.3-33

through 3.3-35 for 4, 6, and 12 cycles per day, respectively. For each of these cases the

dipole "Off Time" was held constant at 30 minutes; therefore, the ratios of "On Time" to

"Off Time" are 11, 7 and 3, respectively.
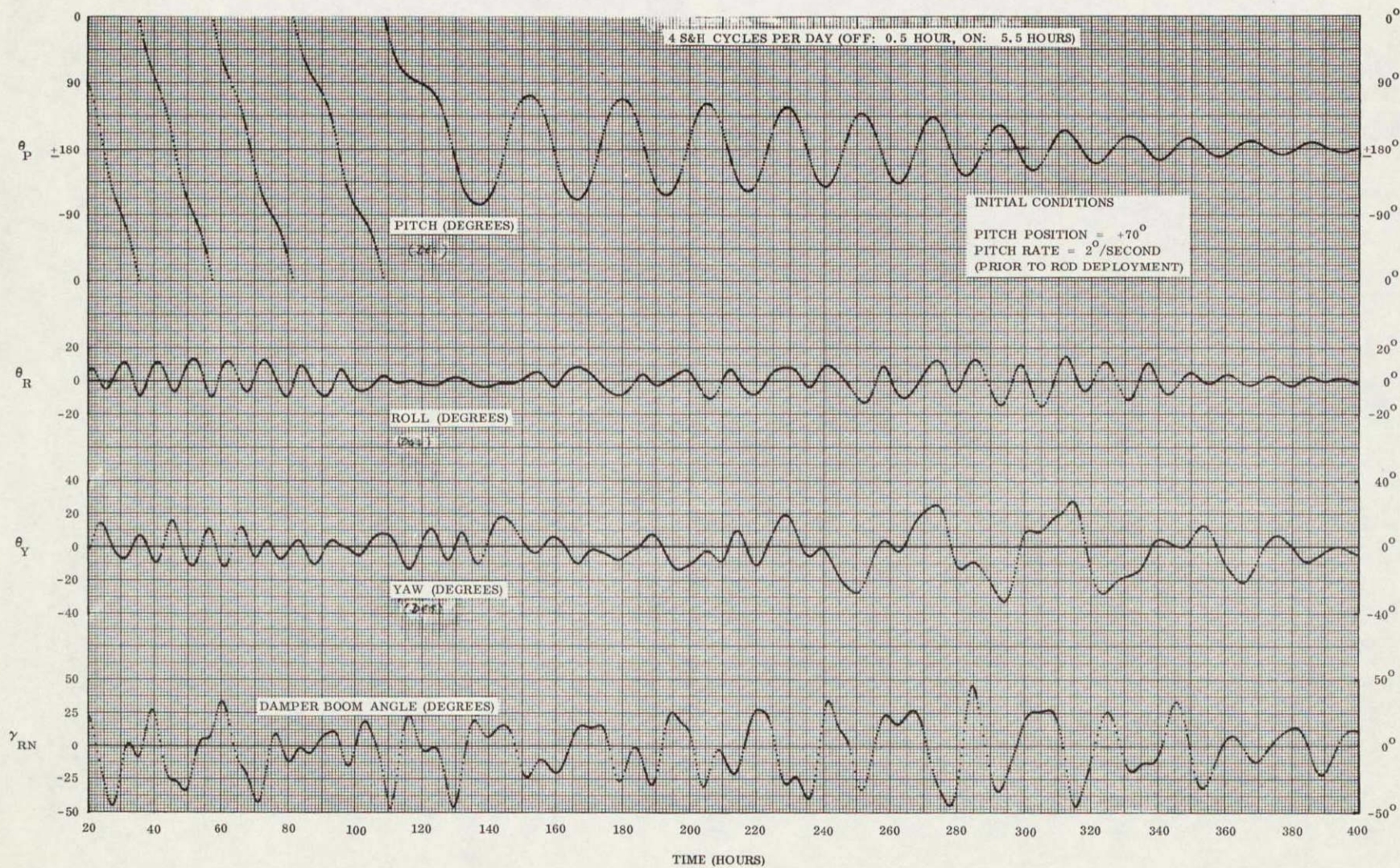
Figure 3.3-33. ATS-D Sample And Hold Simulation
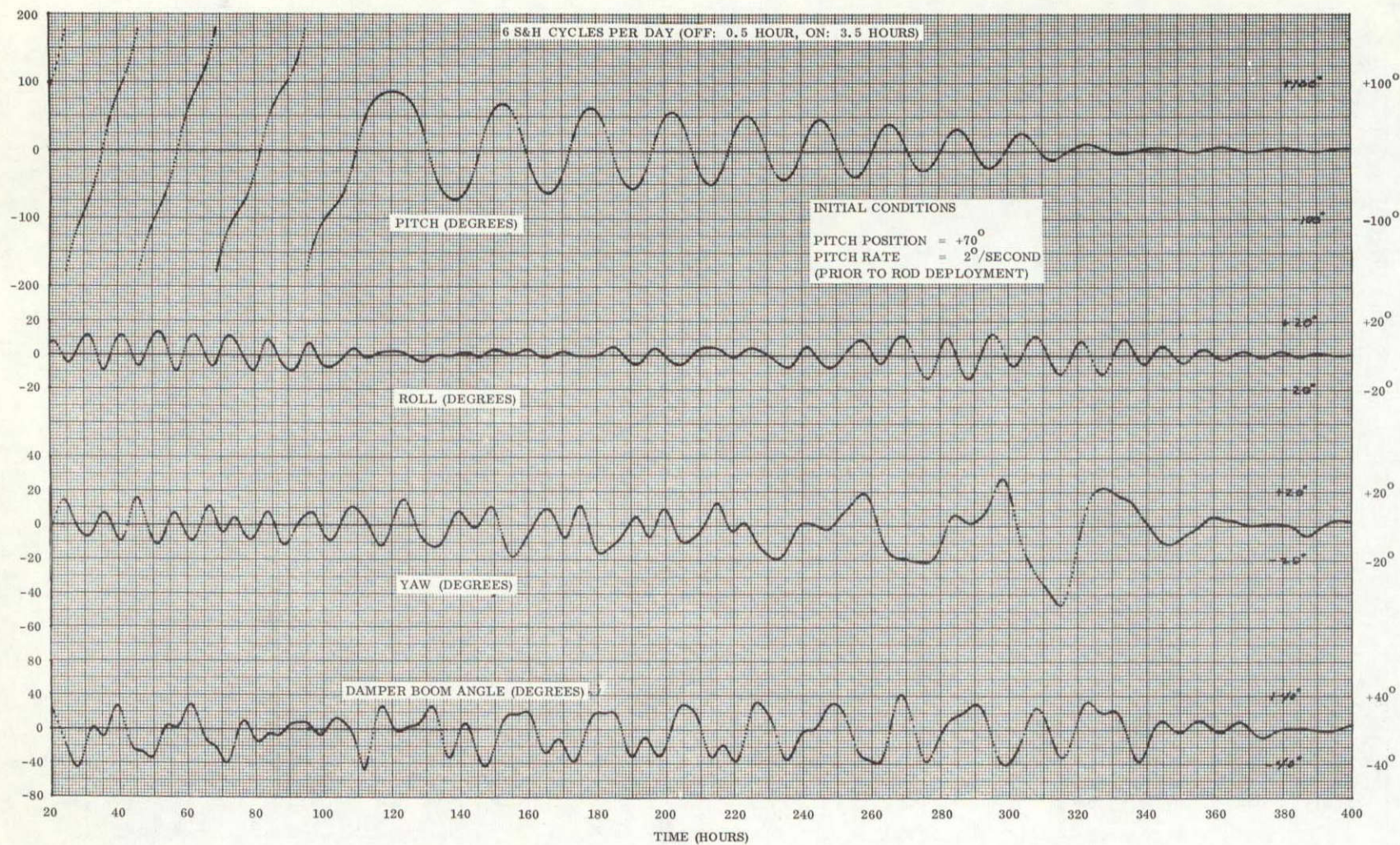
Figure 3.3-34. ATS-D Sample And Hold Simulation
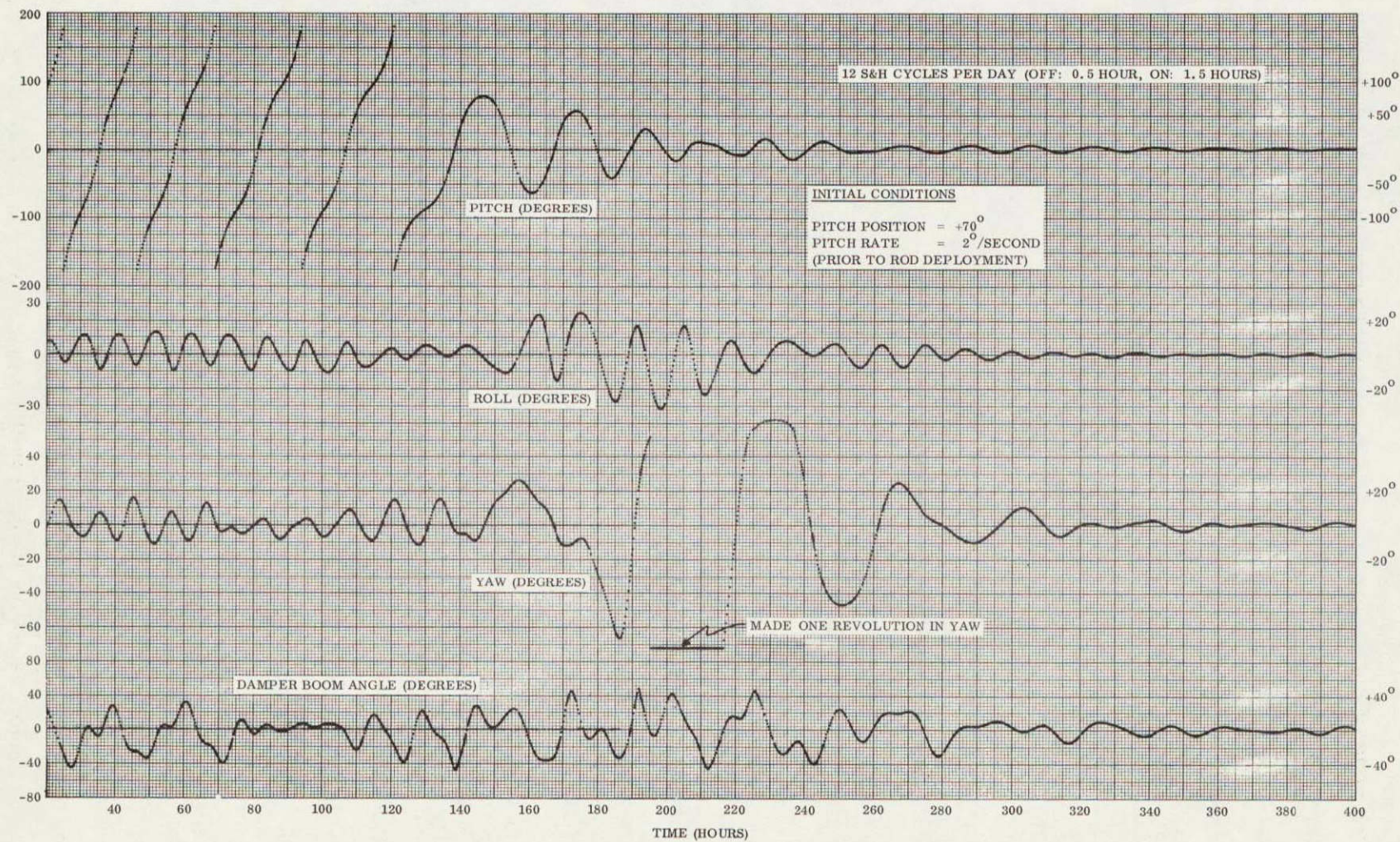
Figure 3.3-35. ATS-D Sample And Hold Simulation

3-157

Selecting the point of occurrence of the first reversal in direction of the pitch angle (θ_p) as the criteria for capture, the results are:

Sample and Hold Cycles Per Day	Time From Start to Capture	Time From Start of S & H Cycling to Capture
4	137 hrs	89 hrs
6	120 hrs	72 hrs
12	146 hrs	98 hrs

Comparing the performance after capture is a bit more difficult, since actual steady state as normally defined cannot be firmly verified for any of the runs.

S & H Cycles/Day	Time From Capture to $\pm$ 10 Degrees in Pitch
4	231 hrs
6	200 hrs
12	101 hrs

From the standpoint of capture, the optimum sequence is 6 cycles per day. Judging by the time for the pitch amplitude to reach the $\pm$ 10 degree point, 12 cycles per day appeared best. However, this particular simulation (Figure 3.3-35) involved a complete yaw around which did not occur on either of the other two runs. During such a maneuver, energy is transferred between axes due to coupling effects; in this case, energy was transferred from pitch to yaw; thus, pitch amplitudes are reduced. Also during a yaw-about, the damper boom is excited and more effective damping results. Performance of this nature is not always predictable; therefore, the beneficial results cannot be relied upon with any degree of certainty.

In order to ensure the reliability of this analysis, an additional simulation using nine cycles per day was evaluated. Capture times from the start of the run and the start of the sample

and hold process were practically the same as the 12 cycle per day case (specifically, 149 and 101 hours respectively), but in this case a yaw-around did not occur and the elapsed time from capture to the $\pm$ 10 degrees pitch amplitude point was 214 hours. This verifies the fact that under normal circumstances (no yaw-about), the 6 cycle per day sequence will result in earlier capture and faster damping.

A fourth simulation was made to verify the calculated value of 50 hours per 0.001 deg/sec decrease in tumble rate mentioned in Section 3.2.3.2.1. A computer simulation was made with the initial pitch rate set at 3 deg/sec and all other parameters identical to that of the six cycles per day case shown on Figure 3.3-34. These results appear on Figure 3.3-36. Capture took place at the 307 hour point which is 259 hours after the start of the sample and hold process. The average pitch rate during this tumble run is shown as a function of time on Figure 3.3-37. As may be observed the rate of change in tumble rate (average deceleration) is extremely close to the calculated value of 0.001 deg/sec per 50 hours.

Based upon the results of analyses, a timing sequence was derived as a function of space-craft rate prior to rod deployment and time after rod deployment. This "Time Schedule" is shown on Figure 3.3-38. It assumes no knowledge of the spacecraft attitude or motion other than the tumble rate prior to rod deployment, which would be necessary in any event in order to insure safe rod extension. Once the tumble rate prior to rod deployment is established, "hold" times may be read directly as a function of time from deployment. If the tumble rate could be determined more accurately than + 0.5/sec., the exact rate line could be sketched on the plot and used. After the elapsed hold time, the dipole would be turned on and left on for a period seven times longer than the hold time, at which time it would be turned off and the field direction again sampled and held. Hold times need not follow the curves exactly as plotted, but may be stepped in perhaps 50-hour increments. For example on the 6 deg/sec line the following schedule may be implemented:

6 S&H CYCLES PER DAY (OFF: 0.5 HOUR, ON: 3.5 HOURS)

PITCH (DEGREES)

INITIAL CONDITIONS

PITCH POSITION = +70°
PITCH RATE = 3°/SECOND
(PRIOR TO ROD DEPLOYMENT)

ROLL (DEGREES)

YAW (DEGREES)

DAMPER BOOM ANGLE (DEGREES)

TIME (HOURS)
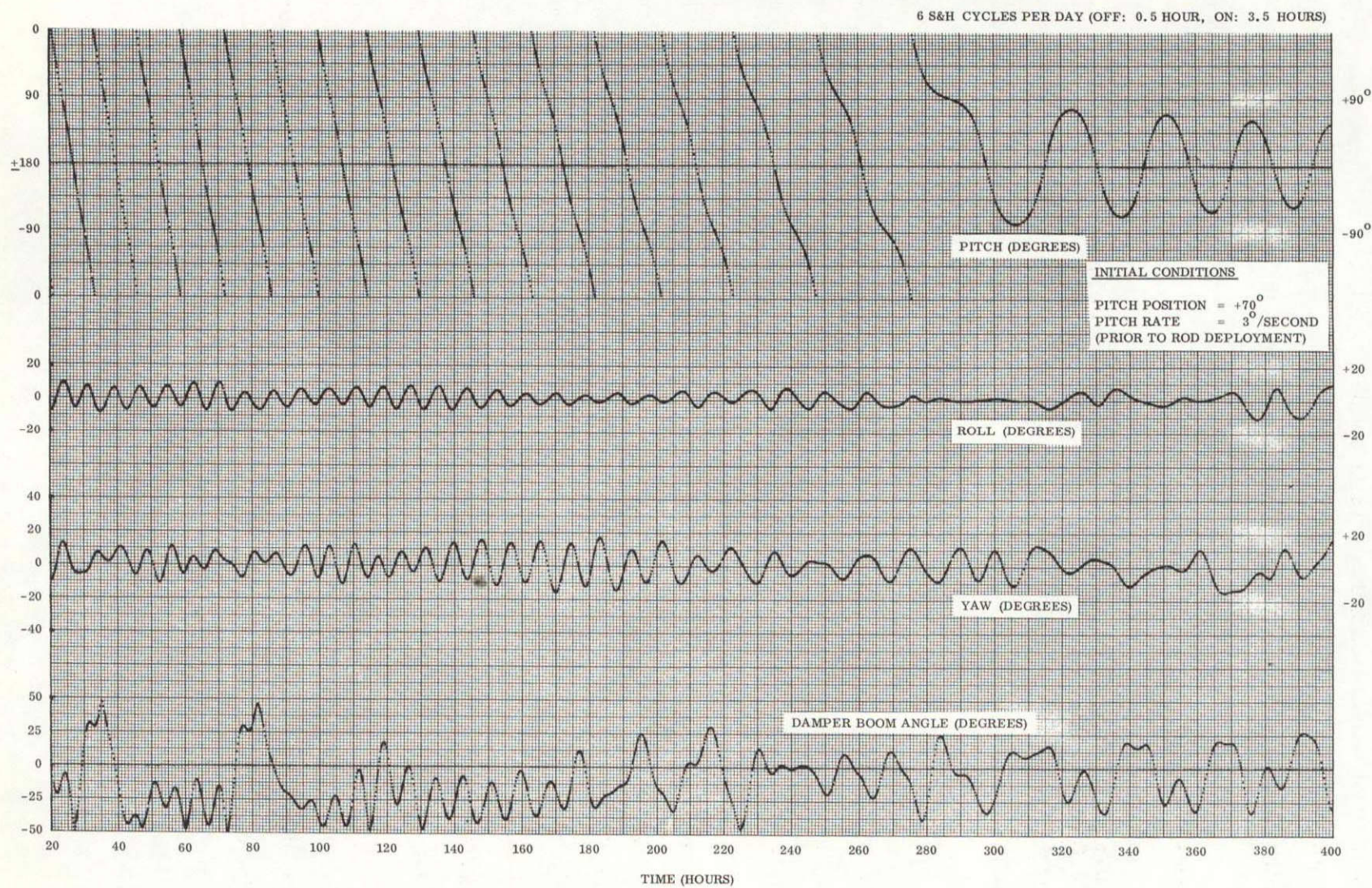
Figure 3.3-36.   ATS-D Sample And Hold Simulation
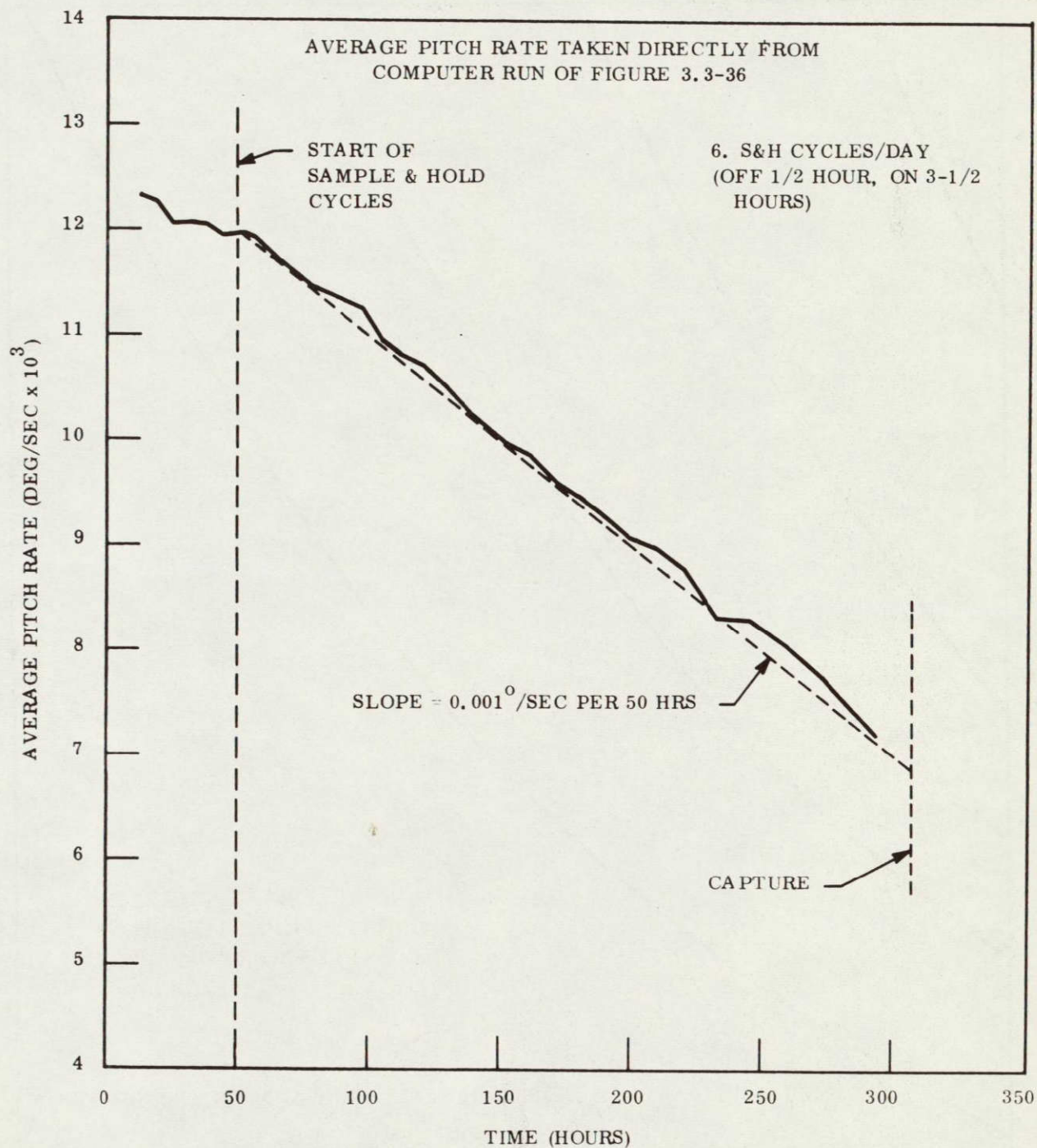
Figure 3.3-37. Tumble Rate Versus Time
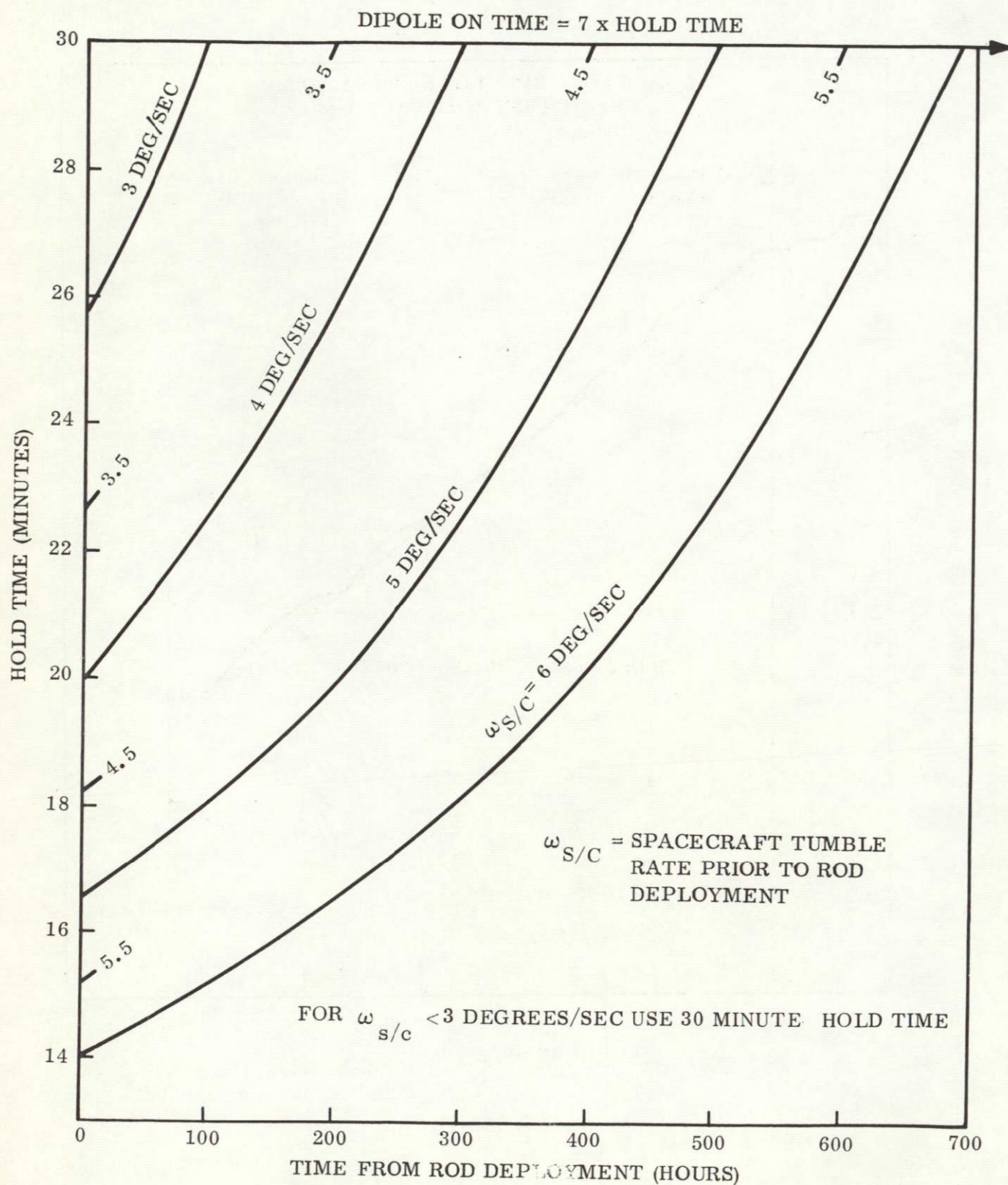
Figure 3.3-38. Sample And Hold Timing Sequence

Time From Deployment (hours)	Off Time (minutes)	On Time (minutes)
0 – 50	14.3	100
50 – 100	14.9	104
100 – 150	15.5	108
150 – 200	16.2	113
200 – 250	16.9	118
Etc.		

Regardless of which rate line is used, the time schedule should be followed until a 30 minute hold time is reached, at which point the cycle will be maintained at 30 minutes off followed by 3.5 hours on. This schedule (on Figure 3.3-38) is based upon the average tumble rate during each 24-hour period (orbital). However, during any one orbit the variation relative to the instantaneous local vertical will have a range equal to orbital rate.

In the event that tumble rate information is available, then the timing sequence shown on Figure 3.3-39 should be used exclusively. Hold times are strictly a function of the actual tumble rate.

To summarize the conclusions based upon these computer simulations –

1. The choice of 6 cycles per day appears justified.

2. From tumble rates (pre-deployment), of 2 deg/sec or less, capture will be realized within three days of the start of the sample and hold process.

3. Steady state should be reached within 8 to 9 days after capture.

The recommended timing sequence for a spacecraft tumbling at 2 deg/sec or less prior to rod deployment is one of:

WHEN TUMBLE RATE INFO IS AVAILABLE
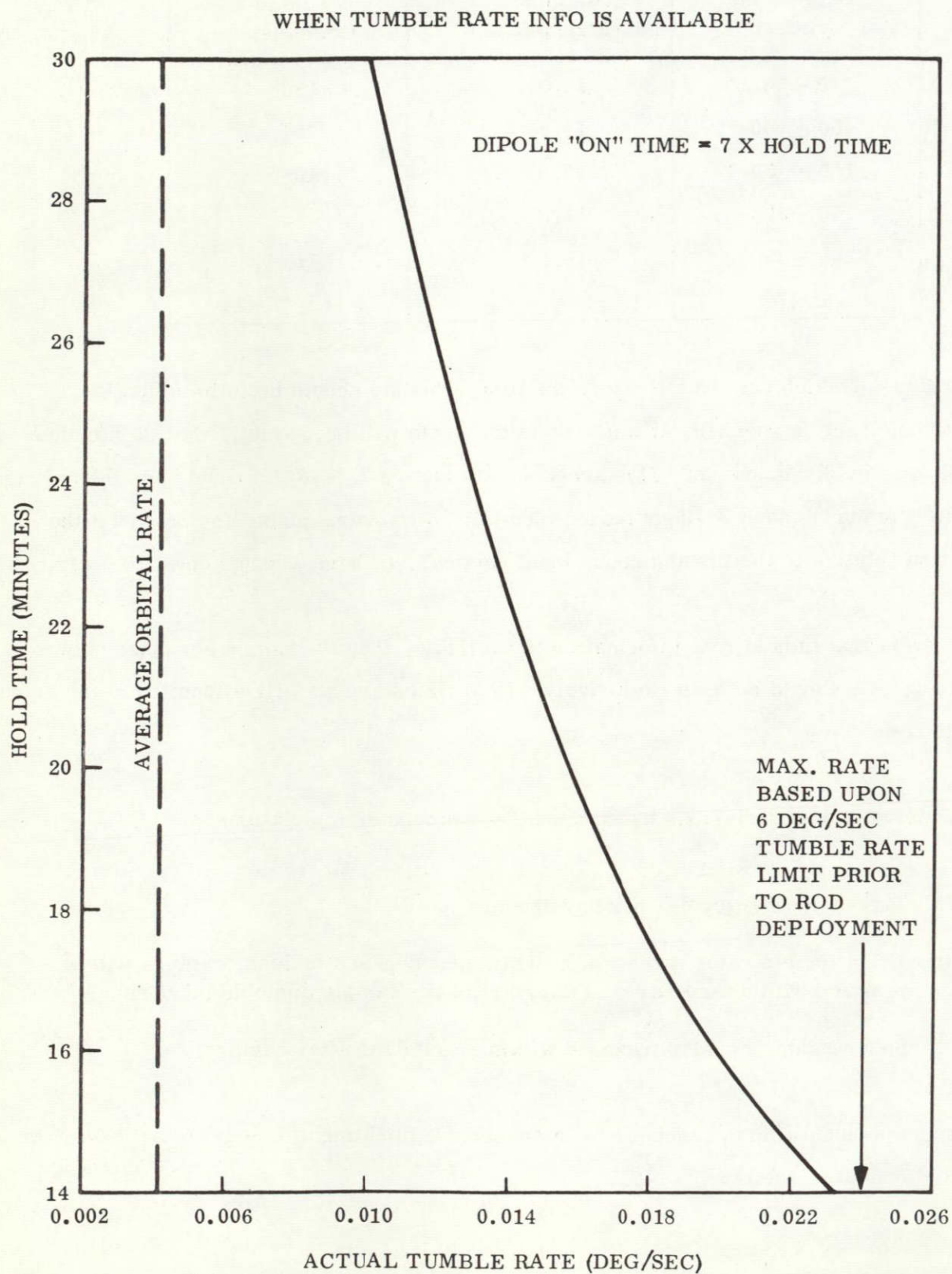
Figure 3.3-39. Sample And Hold Timing Sequence
When Tumble Rate Information Is Available

1. Sample magnetic field direction

2. After 30 minutes turn on dipole calculated from 1.

3. Leave dipole on for 3.5 hours, then turn off, sample field again, and continue this cycle.

This timing sequence may be started any time after rod deployment and continued through the capture phase until steady state conditions are verified.

The recommended timing sequence for a spacecraft tumbling at 6 deg/sec or less before rod deployment is dependent upon the availability of tumble rate information. If tumble rate is available, the sequence should be determined from Figure 3.3-39. If no tumble rate information is available, an "open loop" sequence can be determined from Figure 3.3-38.

3.3.3 ATS-E INITIAL CAPTURE

The ATS-E spacecraft launch configuration differed in several ways from the ATS-D configuration which was used in the early capture studies. The primary differences were:

1. Higher central body moments of inertia than ATS-D.

2. Use of Westinghouse X-boom rods, lighter and eventually shorter.

3. Primary rod extension/retraction rate approximately 1/2 of the value originally used.

Since it could not safely be assumed that these differences would not significantly affect the capture characteristics of the spacecraft, additional analysis and simulations were necessary.

The ATS-E capture study consisted of establishing capture times as a function of various initial conditions after all rods have been deployed, and verifying the results by means of complete capture simulations. This included primary rod deployment, damper boom deployment, scissoring, and damper boom unclamping with an appropriate timing sequence.

Table 3.3-5 lists the results of the computer simulations which start after all rods are deployed, but with various initial conditions imposed. All rates are normalized to orbital rate and the times are shown in hours from the start of the simulation until the point of the first pitch oscillation after which the spacecraft does not again tumble. This same information is plotted in Figure 3.3-40. Open symbols represent actual capture points from the dynamic simulations; solid symbols represent simulations which did not capture within 400 hours of orbit time.

Table 3.3-5. Time to Capture (Hours)

Initial Pitch Rate (ω_Z/ω_o)	Pitch Attitude: Roll Rate/ω_o Yaw Rate/ω_o	Other Initial Conditions			
		0° 0 0	90° 0 0	90° 0.425 0	90° 0 1.81
+3.00					
+2.75		>400			
+2.50		118			
+2.25		0			
+2.00		0			>400
+1.75			>400		
+1.50			46	108	51
+1.00 (Steady State)				0	0
+0.5				0	
0		0	86	0	
-0.50		44	196	145	184
-0.75			351	340	300
-1.00		134	>400		>400
-1.50		>400			
Figure 3.3-40 Symbols		⊙	⊡	△	▽

As may be observed, capture times are more sensitive to positive pitch rate than to negative rate, especially for shorter capture times. Also worth noting is the fact that when the final pitch angle is 90 degrees, the addition of roll or yaw rates do not appear to significantly affect capture time.

By means of the digital computer program, the entire deployment and capture phase of the mission was simulated.
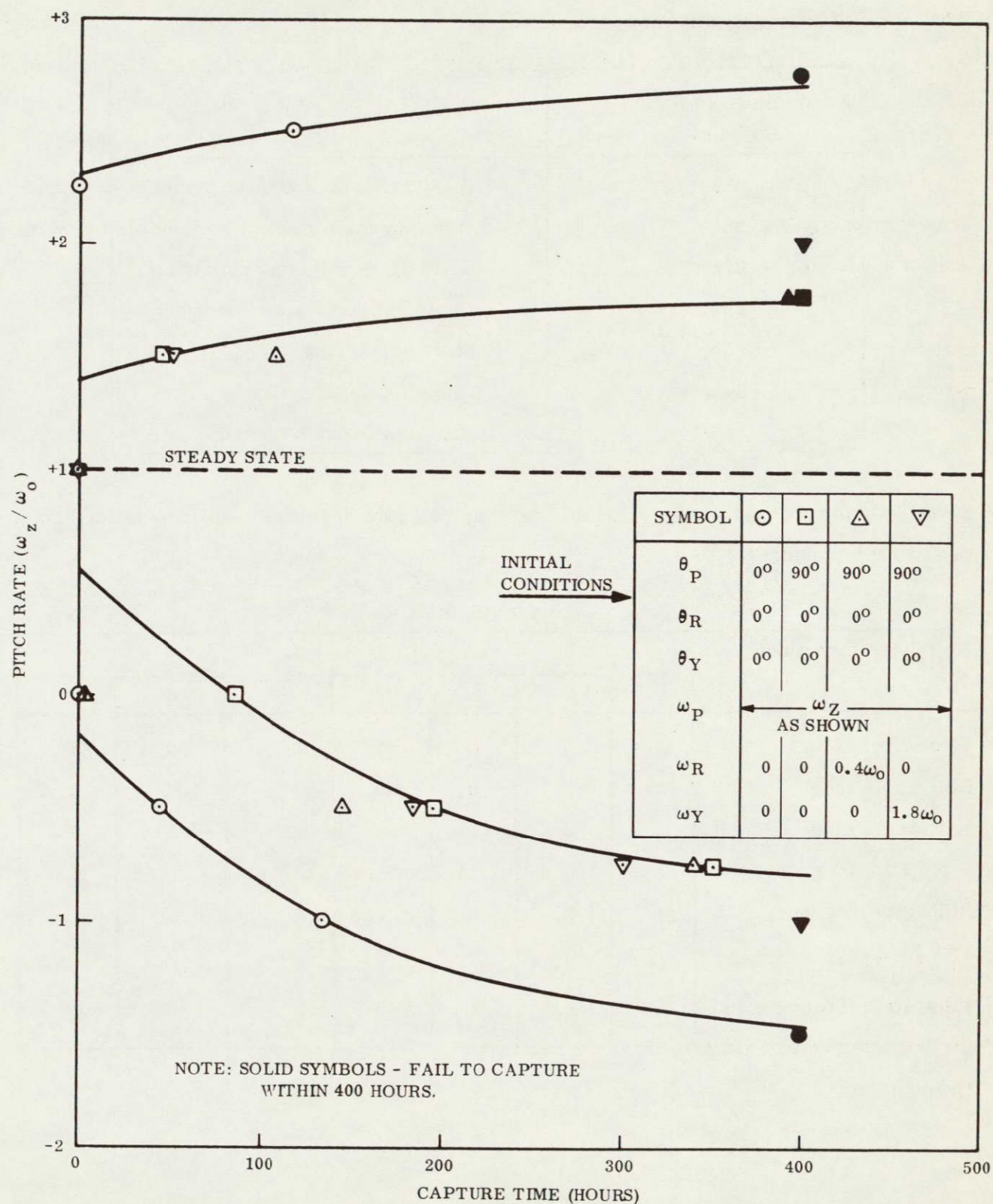
Figure 3.3-40.   ATS-E Capture Study Results

The order of events within the program were:

Time from Start (sec)	Event
1	Start primary booms extending
250	Primary booms fully extended
270	Start damper booms extending
295	Damper booms fully extended
300	Start scissoring
348	Complete scissoring
368	Unclamp damper booms

Seven individual cases were evaluated from various sets of initial conditions before start of rod deployment.

Complete Simulations

Initial Conditions	Case No.						
	1	2	3	4	5	6	7
Pitch Angle (deg)	0	0	0	90	90	90	90
Roll Angle (deg)	0	0	0	30	0	0	0
Yaw Angle (deg)	0	0	0	0	30	0	0
Pitch Rate (deg/sec)	0.29	0.66	1.03	1.03	1.03	1.03	1.03
Roll Rate (deg/sec)	0	0	0	1.0	0	0	0.6
Yaw Rate (deg/sec)	0	0	0	0	0.3	0.6	0
Time to Capture (Hours)	*	*	*	140	*	150	*

*Immediate

3-168

The first three of these runs were started with zero attitude errors and rates except pitch rate which was set to the minimum, nominal and maximum expected values. Each of these captured immediately without tumbling. These results are plotted in Figure 3.3-41 which shows the pitch angle history for the first 1200 seconds. Significant events during the capture sequence are noted at the appropriate times. The maximum pitch angle reached is 7, 17.5 and 33 degrees for the minimum, nominal and maximum initial pitch rates, respectively. These peak angles occur during the first orbit only, thereafter amplitudes decay as anticipated.

Simulations 4 through 7 assumed "worst-case-type" initial conditions on pitch, that is, maximum expected rate and 90 degrees attitude, combined with various rates and errors on roll and yaw. All the conditions investigated resulted in immediate or early capture (150 hours or less). Figure 3.3-42 is a duplicate of Figure 3.3-40, but with the complete deployment results noted at the appropriate pitch rate at the instant the deployment sequence is completed. General agreement with the steady state results are observed.

Cases 1, 2 and 3 (most readily predictable) capture immediately and at the expected pitch rates. Cases 5 and 7 also capture immediately even though roll or yaw rates are present. Cases 4 and 6 required approximately six orbits to capture. These points represent the worst conditions evaluated using the full deployment sequence, with the higher rates imposed on roll and yaw (i.e., 1 deg/sec and 0.6 deg/sec, respectively). It appears that 30 degrees attitude error on either roll or yaw is not particularly detrimental.

Capture times indicated on Figure 3.3-40 are accurate to no better than +1 orbit (+24 hours), due to the characteristics of the capture phenomenon itself. For example, even though a spacecraft is extremely close to capturing, if the pitch attitude is unfavorable at that instant, it may not capture; if not,then a complete orbit is usually required until it does. In one or two cases evaluated in this study, the spacecraft apparently captured; however two orbits later it tumbled once again before finally capturing and settling. This characteristic is the reason for the occasional inconsistency in some of the data shown in the plots.
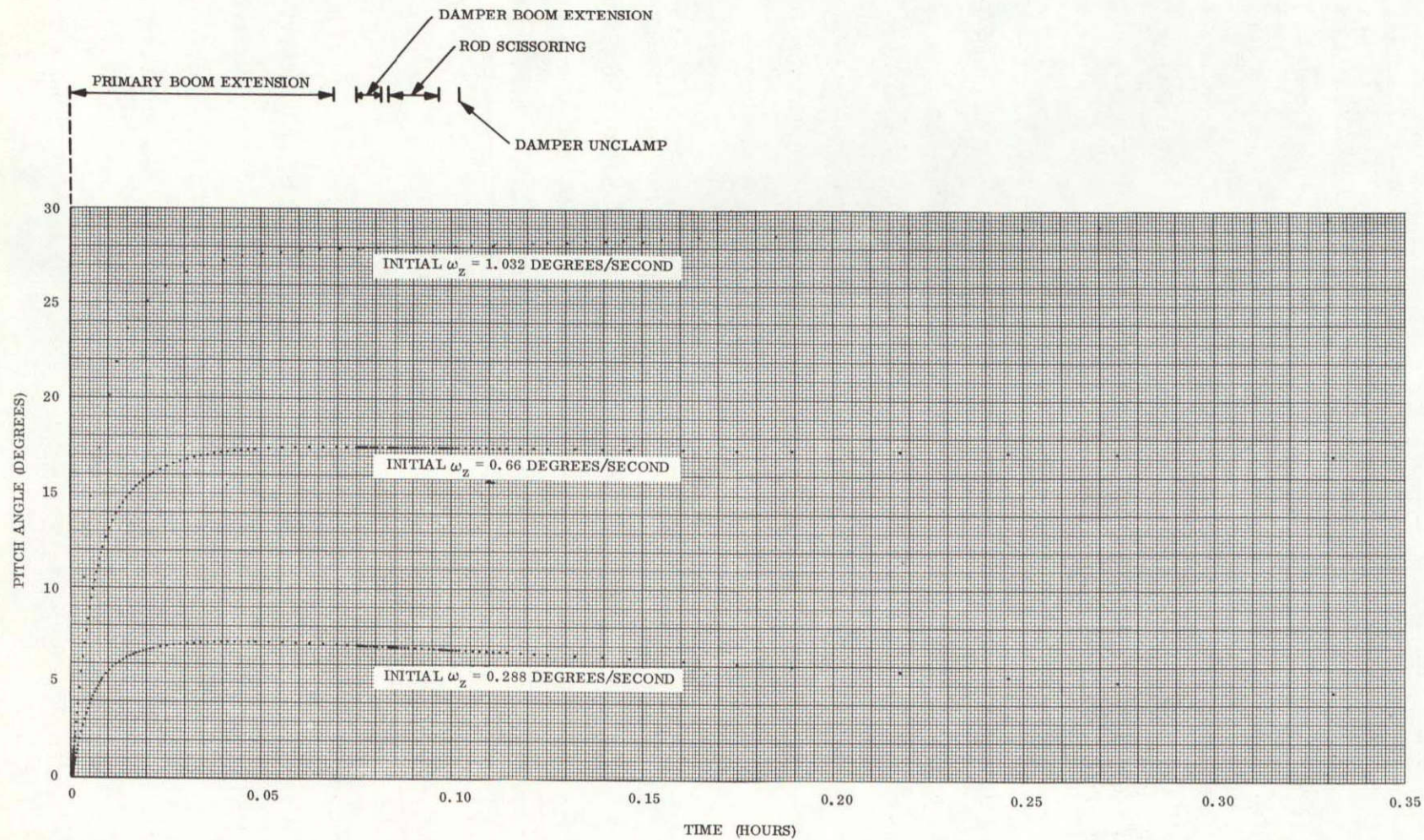
Figure 3.3-41. ATS-E Capture from Various Initial Pitch Rates
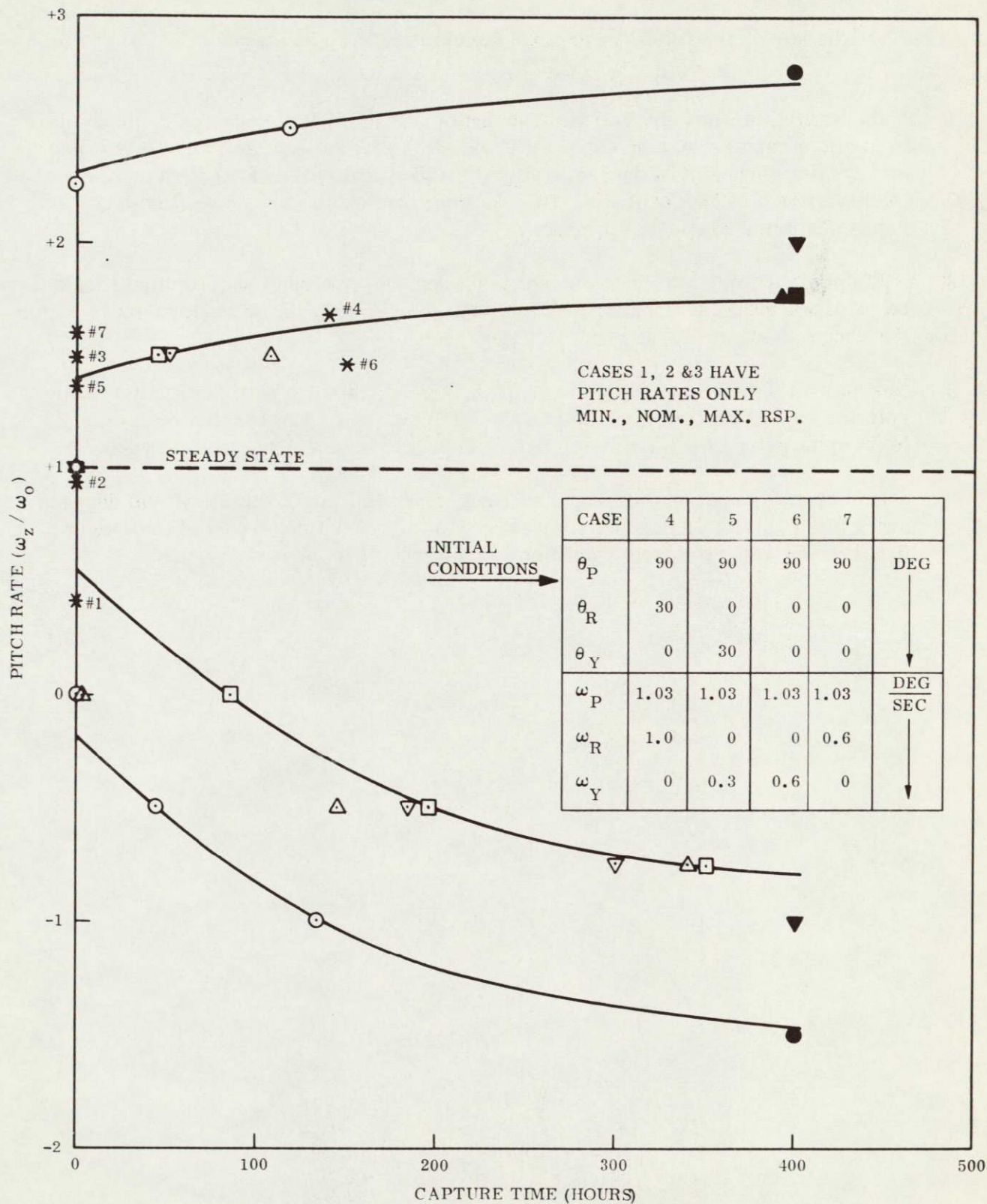
Figure 3.3-42. Full Deployment Cases Superimposed on Steady State Results

As a result of the study, the following general conclusions may be stated:

1. If the attitude errors and roll and yaw rates are small following rod deployment, immediate capture may be expected if the pitch rate is less than +0.005 deg/sec and greater than -0.004 deg/sec relative to the local vertical. Based upon an inertia growth of approximately 165, this corresponds to +1.48 deg/sec and 0 deg/sec prior to rod deployment.

2. If the pitch attitude after deployment is 90 degrees (worst case), capture should be realized within 400 hours, providing the pitch rate prior to deployment is within the range of -0.45 deg/sec and +1.2 deg/sec.

3. Based upon the steady state runs, capture times are not significantly affected by roll and yaw rates superimposed on the pitch rates cited in conclusion (2) (at least up to rates of 0.3 deg/sec, before deployment, on either roll or yaw).

4. Based upon the complete deployment runs, an initial pitch attitude of +90 degrees and a pitch rate of +1 deg/sec may exist with either a 1 deg/sec roll rate or a 0.6 deg/sec yaw rate; both conditions should result in an early capture.

3.4 PITCH INVERSION ANALYSIS

In Section 3.1 it was pointed out that the orientation of a gravity gradient spacecraft is determined by its principal axes. Moments of inertia have an axis, but no direction and the spacecraft can stabilize "rightside up or upside down." If no method of ensuring rightside up capture is available, the spacecraft must have the capability of being inverted after it has captured. There are several methods of achieving this, the most common being a rod retraction/extension maneuver, an approach which has been employed successfully in orbit. An alternate approach is to use thrusters to torque the spacecraft past 90 degrees and then retro to stop it. Both of these techniques were analyzed and implemented for ATS-A, D, and E.

3.4.1 MICROTHRUSTER INVERSION ANALYSIS

Inversion of a gravity gradient spacecraft is usually performed about the pitch axis of the spacecraft (as apposed to the roll axis). Because pitch is not as strongly coupled to roll and yaw, as roll and yaw are to each other, the inversion is generally smooth. A micro-thruster inversion analysis has been performed assuming planar motion.

The large amplitude planar equation of motion in pitch, with no applied torques, is:

$$ I_P \ddot{\theta}_P + \frac{3}{2} \omega_0^2 \left(I_R - I_Y \right) \sin 2\theta_P = 0 \qquad\qquad 3.4\text{-}1 $$

where

I = moment of inertia

ω_0 = orbital rate

θ_P = pitch attitude.

Changing the time base by setting $\tau = \omega_0 t$, equation (3.4-1) becomes:

$$ \ddot{\theta}_P + \frac{3}{2} \left(\frac{I_R - I_Y}{I_P} \right) \sin 2\theta_P = 0 \qquad\qquad 3.4\text{-}2 $$

Multiplying by $2 \dot{\theta}_P$:

$$2 \dot{\theta}_P \ddot{\theta}_P + 3 \dot{\theta}_P \left(\frac{I_R - I_Y}{I_P} \right) \sin 2 \theta_P = \qquad \text{3.4-3}$$

And integrating

$$\dot{\theta}_P^2 - \frac{3}{2} \left(\frac{I_R - I_Y}{I_P} \right) \cos 2 \theta_P = \qquad \text{3.4-4}$$

where

   C = constant, and represents the total vehicle energy.

For the spacecraft to invert successfully, the total spacecraft energy must equal or exceed the spacecraft potential energy at ninety degrees. The normalized potential energy is

$\frac{3}{2} \left(\frac{I_R - I_Y}{I_P} \right)$. Therefore:

$$C \geqq \frac{3}{2} \left(\frac{I_R - I_Y}{I_P} \right) = \frac{3}{2} \, \eta \left(\frac{I_R - I_Y}{I_P} \right) \qquad \text{3.4-5}$$

where η = multiple of total spacecraft energy required for inversion. Substituting Equation 3.4-5 into 3.4-4 and rearrangeing

$$\dot{\theta}_P^2 - \frac{3}{2} \left(\frac{I_R - I_Y}{I_P} \right) \left(\eta + \cos 2 \theta_P \right) = 0 \qquad \text{3.4-6}$$

During the first part of the inversion maneuver, the applied pitch torque is not zero but is equal to the inversion thruster torque, T. For this part of the maneuver Equation 3.4-1 is rewritten.

$$I_P \ddot{\theta}_P + \frac{3}{2} \omega_0^2 \left(I_R - I_Y \right) \sin 2\,\theta_P = T \qquad\qquad 3.4\text{-}7$$

Following the same procedure used for Equation 3.4-1 of changing the time base, muliplying by $2\,\dot{\theta}_P$, and integrating, the result is

$$\dot{\theta}_P^2 = \frac{3}{2} \left(\frac{I_R - I_Y}{I_P} \right) \cos 2\,\theta_P - \frac{2T\theta_P}{I_P \omega_0^2} = K \qquad\qquad 3.4\text{-}8$$

To evaluate K assume that at $\tau = 0$, $\theta_P = \dot{\theta}_P = 0$. Therefore,

$$K = -\frac{3}{2} \left(\frac{I_R - I_Y}{I_P} \right) \qquad\qquad 3.4\text{-}9$$

Substituting into equation 3.4-8:

$$\dot{\theta}_P^2 - \frac{3}{2} \left(\frac{I_R - I_Y}{I_P} \right) \left(\cos 2\,\theta_P - 1 \right) - \frac{2T\theta_P}{I_P \omega_0^2} = 0 \qquad\qquad 3.4\text{-}10$$

Equation 3.4-6 is the relationship between θ_P and $\dot{\theta}_P$ for a given value of η during a period of no applied torque. Equation 3.4-10 is the relationship between θ_P and $\dot{\theta}_P$ for a constant applied torque. When these equations are solved simultaneously, they result in an equation that relates torque to the cutoff angle for a given value of η. The cutoff angle is the value of θ_P at which the first inversion thruster is turned off. The equation is:

$$\frac{T}{I_P \omega_0^2} = \frac{3 \left(\eta + 1 \right)}{4\,\theta_P} \left(\frac{I_R}{I_P} - \frac{I_Y}{I_P} \right) \qquad\qquad 3.4\text{-}11$$

This equation is the basis of the analysis of ATS-A and D inversion sequences. It is possible to integrate Equation 3.4-11 with respect to time to obtain cutoff time, but the result can be only numerical, and not in closed form. It was felt that more accurate results would be obtained using ATS computer simulations. Individual studies were therefore undertaken for both ATS-A and ATS-D.

3.4.2 ATA-A MICROTHRUSTER INVERSION

The inversion of ATS-A was to be performed by two microthrusters, each with a nominal thrust level of 5.4×10^{-4} pounds and an effective moment of arm of 29 inches. The thrust uncertainty of the microthruster was quite large, however, due to the nature of the microthrusters, and thrusts as low as 2.8×10^{-4} pounds or as high as 7.9×10^{-4} pounds could be obtained. In addition, rise and decay times of the thrusters varied considerably, not only from thruster to thruster, but within each thruster. A general study was therefore undertaken.

Equation 3.4-11 is plotted in Figure 3.4-1 for a range of values of η. The maximum value of η for nominal thruster torque of 13.0×10^{-4} lb-ft is 7.25. This requires full thrust to $\theta_p = 90$ degrees and then full reverse thrust to $\theta_p = 180$ degrees with no coast phase.

Figure 3.4-2 is a plot of pitch attitude versus time for torque levels from 6.75 to 19×10^{-4} lb-ft which were obtained from computer simulations. Superimposed on this plot is the data from Figure 3.4-1 Thus, cutoff angle and the cutoff time can be determined for each value of T and η. Figure 3.4-3 is a cross plot of the data contained in Figure 3.4-2 and is used to find (for any preselected timing sequence) the minimum value of torque required to ensure initial inversion. This point is at the intersection of a horizontal line drawn through the operating point and the $\eta = 1$ curve.

A nominal timing sequence can be established for each value of η, assuming both inversion thrusters exert the nominal value of torque. This sequence requires firing the first thruster for its cutoff time, t_{co} (as given by Figure 3.4-2), allowing a coast time, t_{coast}, equal to twice the time required to reach $\theta_p = 90$ degrees following cutoff of the first thruster, and then firing the retro thruster for time t_{co}. This sequence is illustrated by the sketch in Figure 3.4-4. Note that inversion is accomplished by rotating in the negative direction. This reduces the spacecraft inertial pitch rate which in turn reduces cross axis coupling. This allows the maneuver to be completed more smoothly than if it had been done in the positive direction. Nominally, the spacecraft should invert and be left with little residual pitch rate.
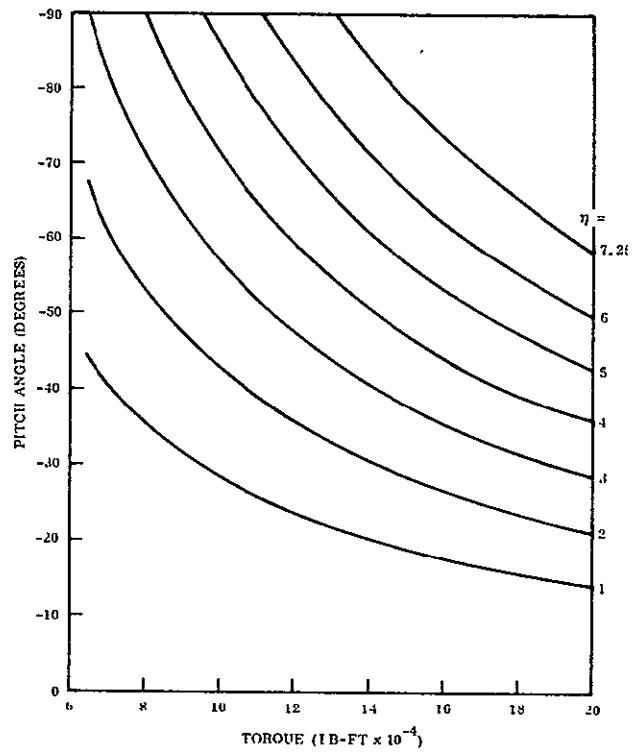
Figure 3.4-1. Cutoff Angle versus Inversion Thruster Torque for ATS-A
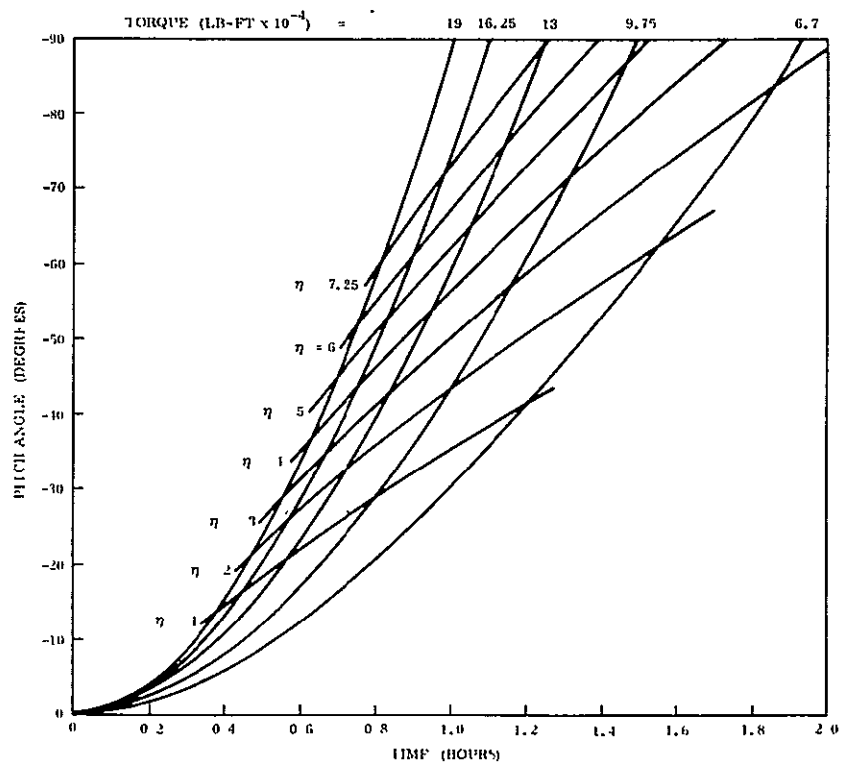
Figure 3.4-2. Response of ATS-A to Constant Thruster Torque
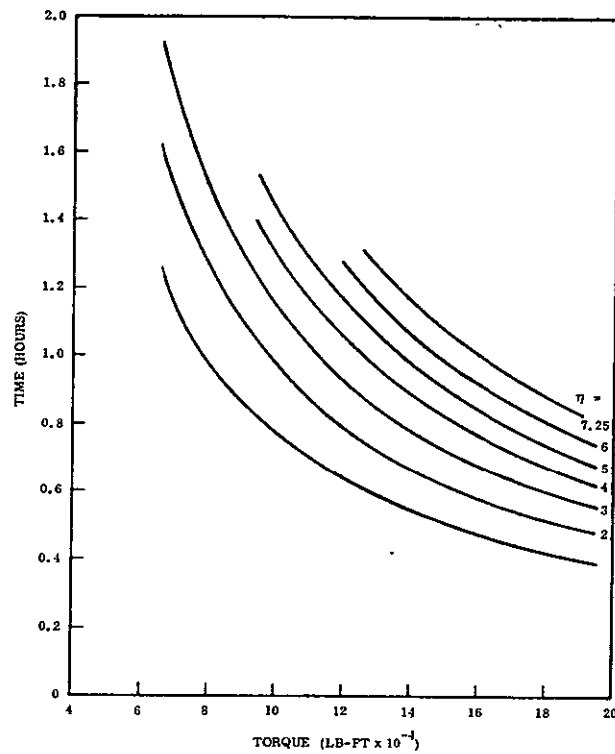
Figure 3.4-3. Cutoff Time versus Thruster Torque for ATS-A
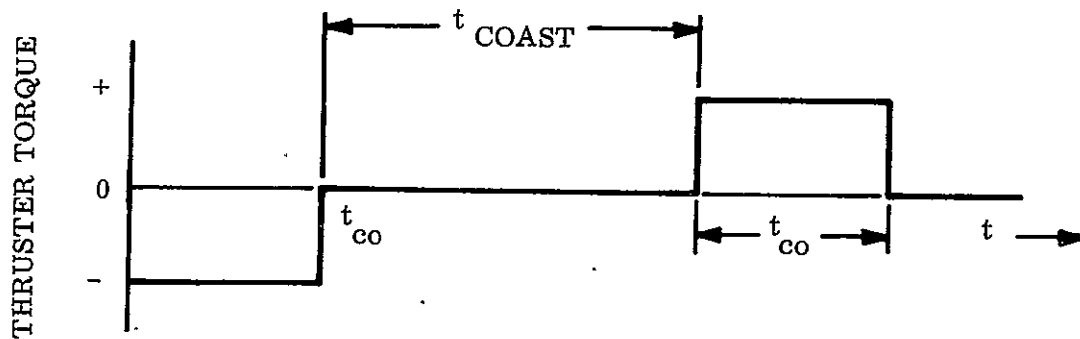
Figure 3.4-4. Inversion Sequence

The nominal timing sequences for ATS-A, as determined by computer simulations, in conjunction with Figure 3.4-1, are listed in Table 3.4-1.

Table 3.4-1. Nominal Timing Sequences for ATS-A Inversion Maneuver

η	First Thruster On-Time (minutes)	Coast Time (minutes)	Second Thruster On-Time (minutes)	Total Time (hours)
1.5	39.0	149.0	39.0	3.78
2.0	43.2	107.2	43.2	3.23
3.0	50.7	66.7	50.7	2.80
4.0	57.6	42.8	57.6	2.63
5.0	63.4	27.0	63.4	2.56
6.0	69.0	13.2	69.0	2.52
7.25	75.1	0	75.1	2.50

The computer simulations performed assumed the inversion thruster and the retrothruster were identical and nominal (13×10^{-4} lb-ft). However, an inversion maneuver based upon a specified timing sequence has several failure modes caused by thruster variations. The most severe of these are given in Table 3.4-2.

Table 3.4-2. Inversion Maneuver Failure Modes

First Thruster		Second Thruster	Failure Mode
1.	High	Low	Vehicle tumbles until damper removes energy.
2.	Low	High or Low	First thruster cannot invert the vehicle.
3.	Low	High	Vehicle inverts initially, but is returned to initial position by second thruster.

In the first two failure modes the timing sequence has little influence. However, in the third failure mode it is the primary factor. This is best illustrated by an example. Figure 3.4-5 is a plot of the time required to pitch 90 degrees versus the percentage decrease in torque of the first thruster. Note that at the lower values of η the function is extremely sensitive to torque variations. Assume $\eta = 1.5$, the first thruster is 8 percent low and the second thruster is nominal. Using the nominal timing sequence, the second thruster is fired at 3.13 hours. However, at this time the spacecraft pitch attitude is only −100 degrees. The result is the spacecraft is returned back towards zero attitude, resulting in an unsuccessful inversion. Figure 3.4-6 is a plot of this type situation taken from computer runs. If the firing of the second thruster had been delayed a proper amount, the inversion would have been successful.

To determine an appropriate timing sequence, both the inversion and retro thruster must be considered. Since the thrust level of the thrusters is uncertain, and each thruster is independent of the other, an infinite number of thrust combinations can exist. To reduce the inversion analysis to manageable proportions, two assumptions were made:

1. Thrust variations in both thrusters are equal

2. The first thruster has low thrust, the second has high thrust.

Under the assumption of equal thrust variations, the second assumption represents the worst case condition.

An additional mission constraint is that the inversion maneuver be completed in four hours.

A series of computer runs were made to determine the allowable thrust tolerance variation. The results are given in Figure 3.4-7. The maximum tolerance is 13 to 14 percent and occurs for η between 3 and 6. For values of η below 1.9, the tolerances are limited by the 4-hour time limit.
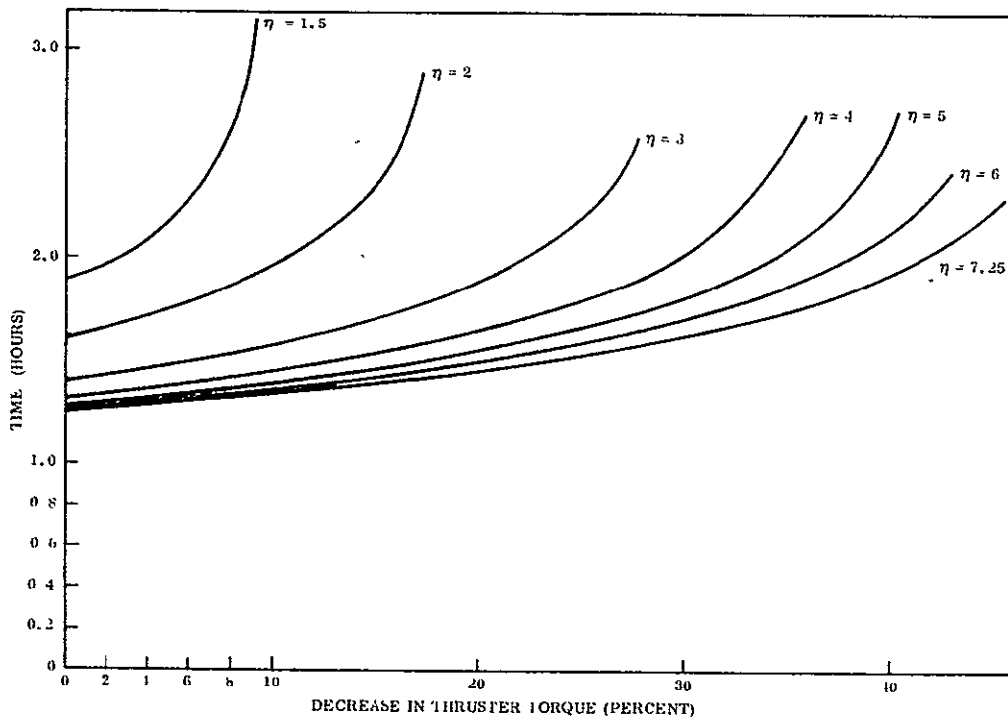
Figure 3.4-5. Time to Pitch 90 Degrees as a Function of Thruster Torque
Variation for ATS-A
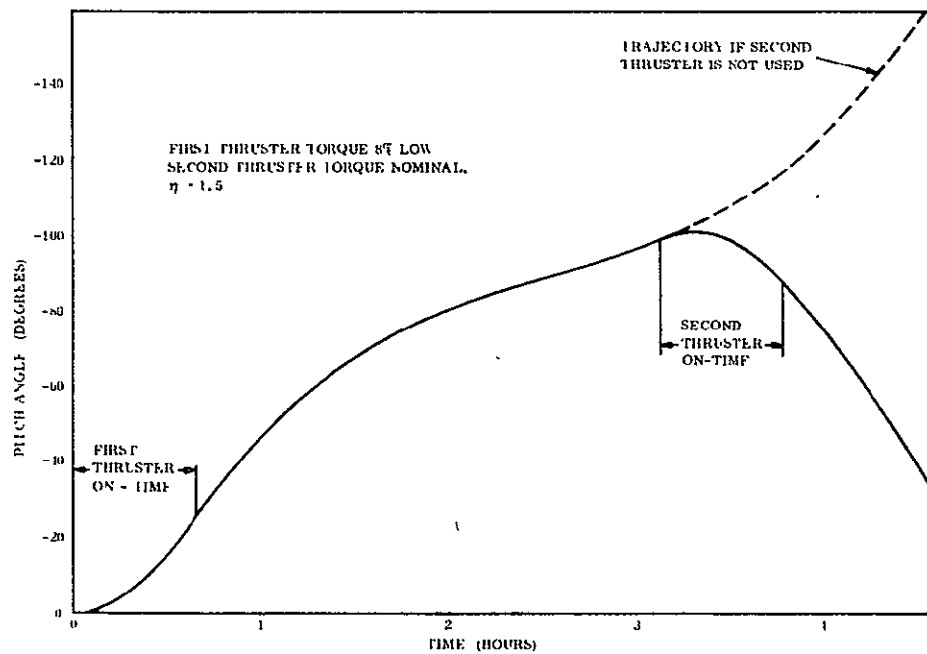
Figure 3.4-6. ATS-A Inversion Maneuver
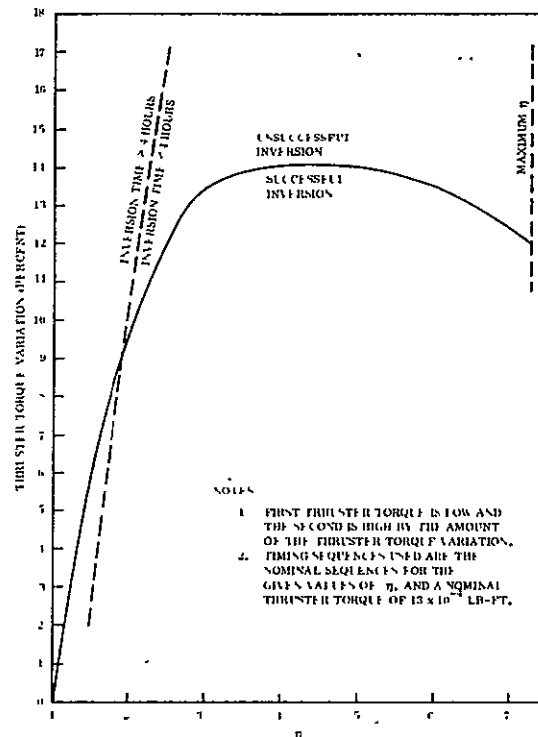
Figure 3.4-7. Effect of Thruster Torque Variation on Inversion Maneuver
Success for ATS-A

The effects of the disturbances upon allowable thrust tolerances were also studied and

in each case the disturbance was formulated to provide the worst case effect on inversio

The largest disturbance sources were:

1. Thruster misalignment. The CM is assumed located 1 inch along the $+X_1$ axis from the geometric center, and the thrust vector is rotated 1 degree in the $Y_1 X_1$ plane.

2. Short primary gravity gradient rods. One rod in each rod pair was assumed to be 1.76 feet shorter than the other.

3. Solar and magnetic effects. The sun was located in the orbit plane, and a 1,000 pole-cm dipole was placed along the Y_1 axis.

4. Initial attitudes and rates were for a circular orbit and for an eccentricity of 0. These were established from steady state computer runs, and are listed in the following:

3-182

	Eccentricity = 0	Eccentricity = 0.01
θ_P (deg)	0.2	0.0
θ_R (deg)	0.0	0.1
θ_Y (deg)	0.7 -0.3	2.6 -0.7
X (deg/sec)	3.302×10^{-5}	2.697×10^{-4}
Y (deg/sec)	3.073×10^{-4}	6.198×10^{-4}
Z (deg/sec)	1.583×10^{-2} 9.703×10^{-5}	1.640×10^{-2} 3.360×10^{-4}

The effects of these disturbances for values of $\eta = 3$, 4, 5, and 6 were studied. Short gravity-gradient rods, and solar and magnetic effects proved to have virtually no effect on allowable thruster tolerances. Figure 3.4-8 shows the effects of thruster misalignment and Figure 3.4-9 shows the effects of initial rates and attitudes. One series of runs was made combining thruster misalignment with the initial conditions for an eccentric orbit with an eccentricity of 0.01. The value of η was 3.

The results reduced the allowable thrust tolerance from 13 percent to 9 percent

The final choice of η, which determines the timing sequence, is a compromise between increasing thrust tolerances and decreasing fuel expenditure. Table 3.4-3 lists the pertinent data involved in this selection.

Table 3.4-3. Factors in the Selection of η

η	Total Firing Time For Inversion (minutes)	Allowable Thrust Tolerance With No Disturbances (percent)
2.0	86.4	9.6
3.0	101.4	13.5
4.0	115.2	14.0
5.0	126.8	14.0
6.0	138.0	13.5
7.25	150.2	12.0
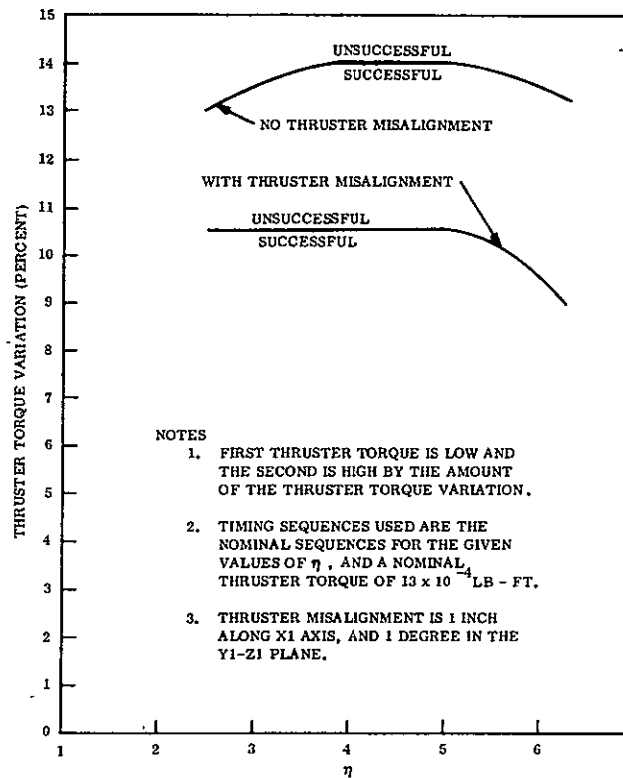
Figure 3.4-8. Effects of Thruster Torque Variation and Thruster Misalignment on Inversion Maneuver Success for ATS-A
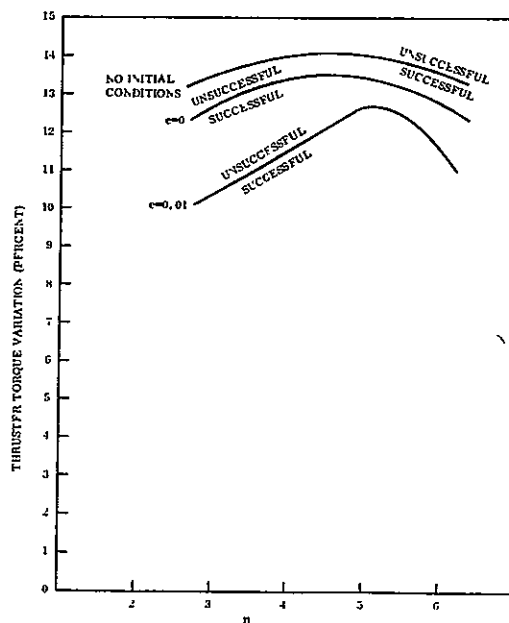
Figure 3.4-9. Effects of Thruster Torque Variation and Initial Attitudes and Rates on Inversion Maneuver Success for ATS-A

Based on these factors alone, it was recommended that a value of $\eta = 3$ be used. This gives the following timing sequence:

1. First Thruster On-Time   =   50.7 minutes

2. Coast Time   =   66.7 minutes

3. Second Thruster On-Time   =   50.7 minutes

The complete inversion maneuver would require 2.8 hours and the total firing time would be 1.69 hours. The allowable thrust variation is 9 percent.

3.4.2.1 ATS-D/E Microthruster Inversion

Two microthruster inversion analyses were performed for ATS D/E, an "open loop" inversion using a specified timing sequence, and a "closed loop" inversion where data was assumed available throughout the inversion. The latter approach is the more flexible and provides greater assurance of inversion, but is more complex operationally and is dependent upon attitude information being available on a real time basis.

3.4.2.1.1 ATS D/E Nominal Microthruster Inversion

The analysis required to establish the nominal timing sequences is identical to that included earlier in this section and need not be repeated here.

Figures 3.4-10 and 3.4-11 show the relationships between inversion thruster torque, cutoff time and pitch cutoff angle for a range of values for η for ATS-D/E. These plots were used to establish the nominal timing sequences listed in Table 3.4-4.
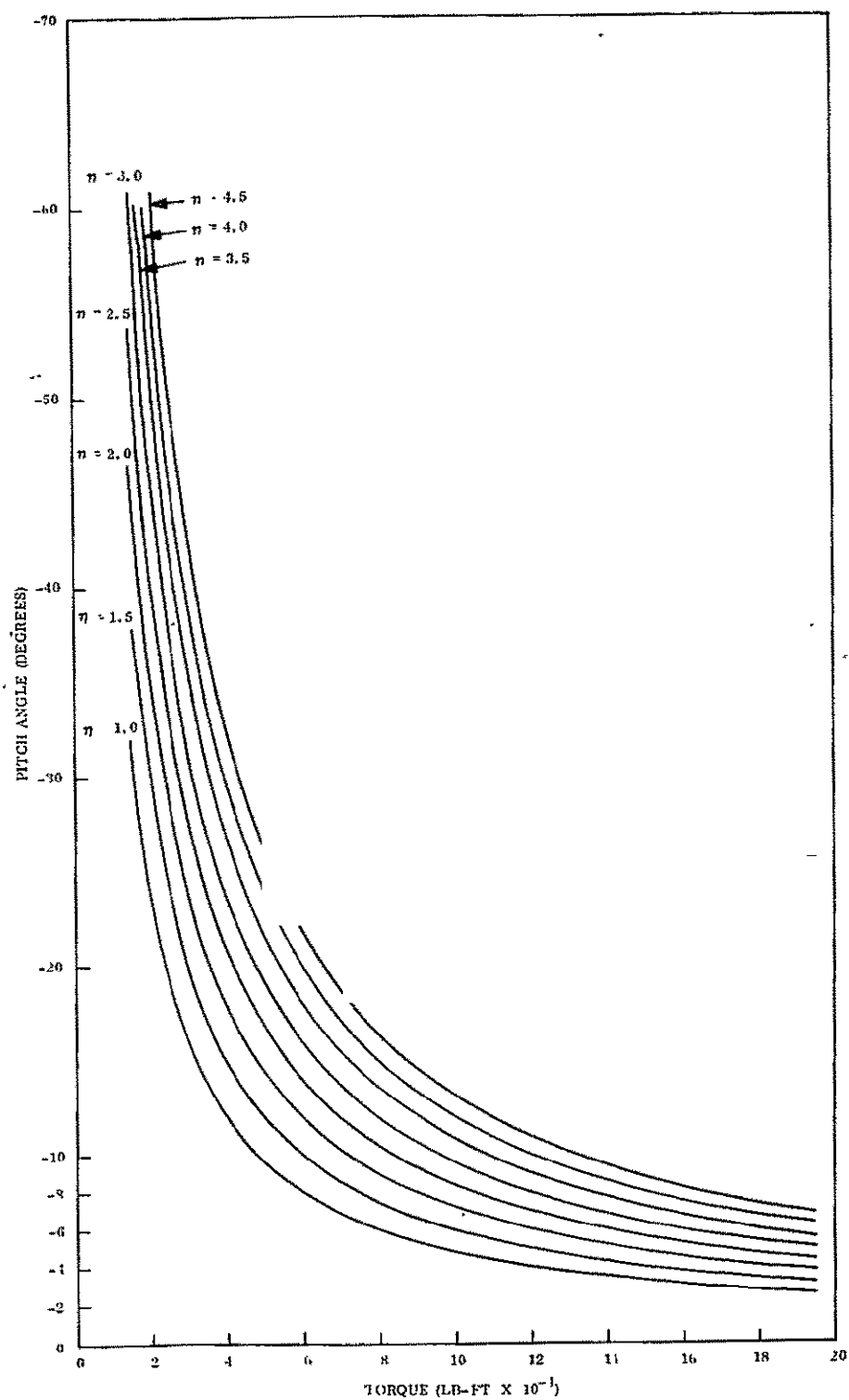
Figure 3.4-10. ATS-D Inversion Thruster Cutoff Angle

.3-186
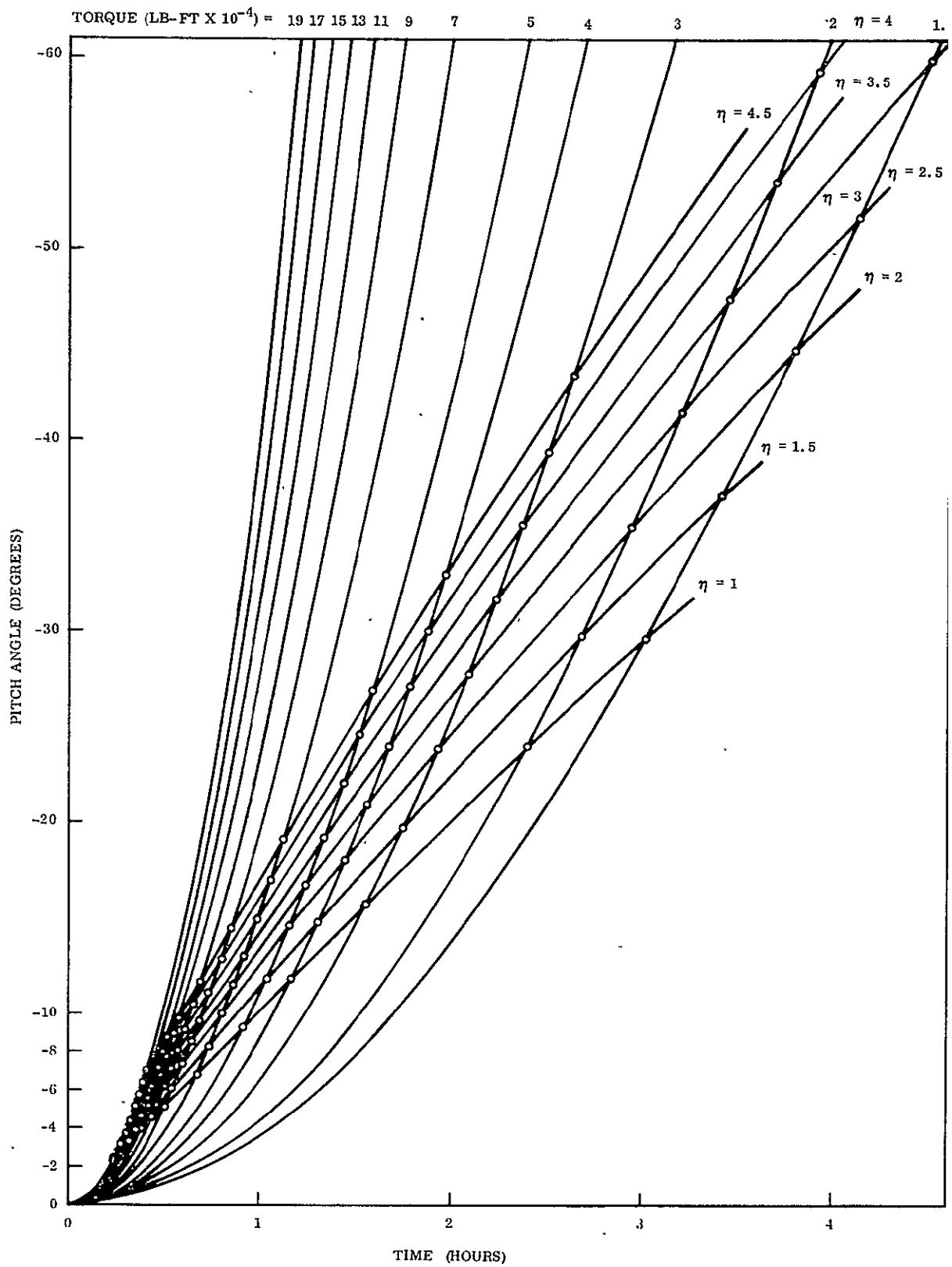
Figure 3.4-11. ATS-D Response to Constant Inversion Thruster Torque

Table 3.4-4. Nominal Timing Sequences for ATS-D/E Inversion Maneuver

η	Inversion Thruster On-Time (minutes)	Coast Time (minutes)	Retro Thruster On-Time (minutes)	Total Time (hours)
1.5	24.30	634.50	24.30	11.38
2.0	26.70	516.67	26.70	9.50
2.5	28.80	446.67	28.80	8.40
3.0	30.78	397.70	30.78	7.65
3.5	32.40	368.90	32.40	7.23
4.0	34.20	338.33	34.20	6.78
4.5	36.00	312.27	36.00	6.40

Section 3.4.1.1 concluded that the inversion thruster torque could not be allowed to vary more than +9 percent to assure a successful inversion based upon a specified timing sequence. The corresponding tolerance for ATS-D/E will not be significantly different, and it is unlikely that such low tolerances can be met. Therefore, the approach to the ATS-D/E inversion maneuver was to use a nominal timing sequence which was modified on the basis of spacecraft pitch attitude data as the maneuver progressed.

To modify the maneuver, the most obvious information required is pitch angle data. The pitch angle at which the inversion thruster is cut off is relatively low, however, and Figure 3.4-10 shows that it ranges from 3.7 to 10.1 degrees for values of η between 1.0 and 4.5. This does not allow sufficient time for modification of the initial firing time based on pitch attitude data. Therefore, it was decided to modify only the retro thruster timing. Because the initial thruster timing is to be fixed, it is necessary to choose a value of η sufficiently large to assure initial inversion even if the inversion thruster torque is low. The decision was made to provide for successful inversion even with an inversion thruster

torque of 7. 8 x 10^{-4} lb-ft, 40 percent below the nominal value. To accomplish this, η must be 4. 5 for the nominal torque of 13 x 10^{-4} lb-ft (see Figure 3. 4-12). This in turn determines the firing time of 36 minutes.

Figure 3. 4-13 contains trajectory plots for a range of inversion thruster torques and an inversion thruster cutoff time of 36. 0 minutes. These plots together with spacecraft attitude data can be used to determine the value of the inversion thruster torque.

When the inversion thruster torque is known, the timing sequence for the retro thruster can be obtained from Figure 3. 4-14 assuming that the retro thruster torque value is nominal.
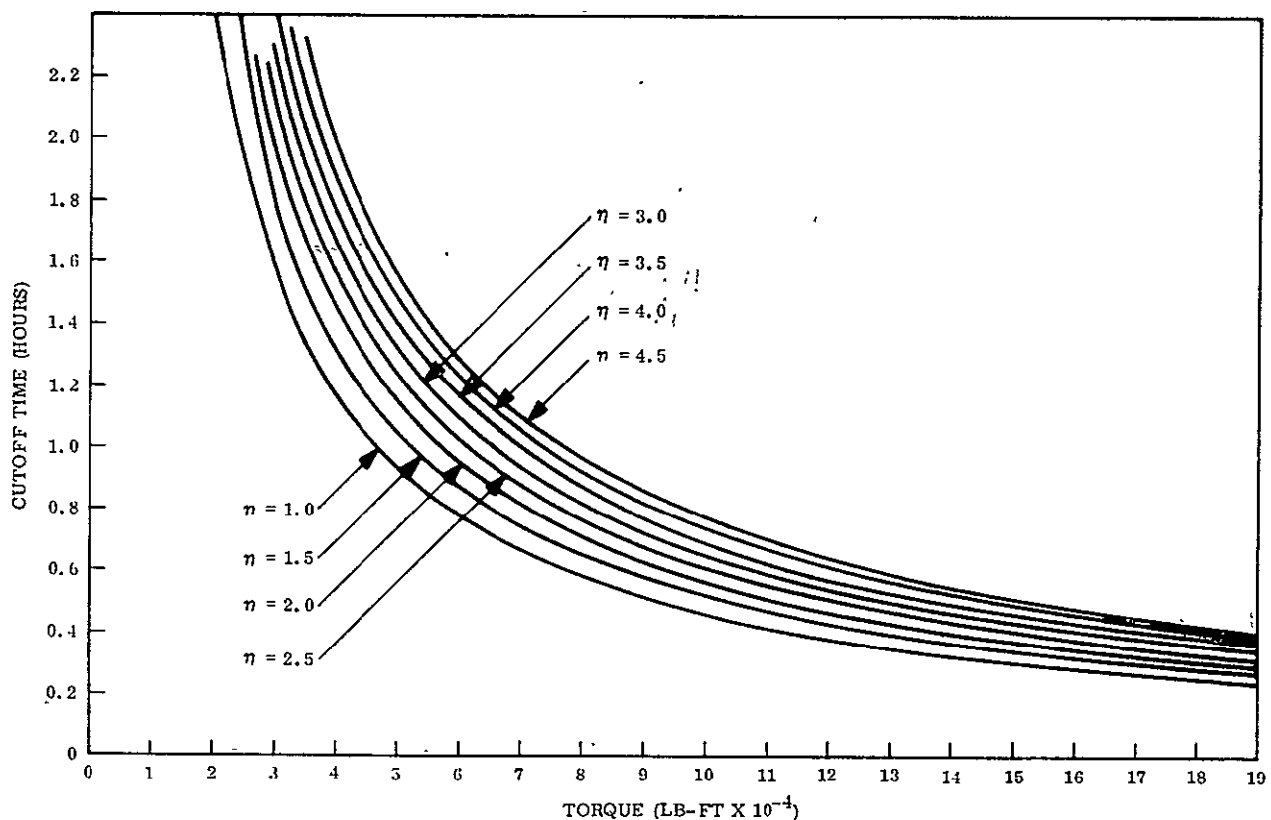
Figure 3. 4-12. Cutoff Time versus Thruster Torque for ATS-D
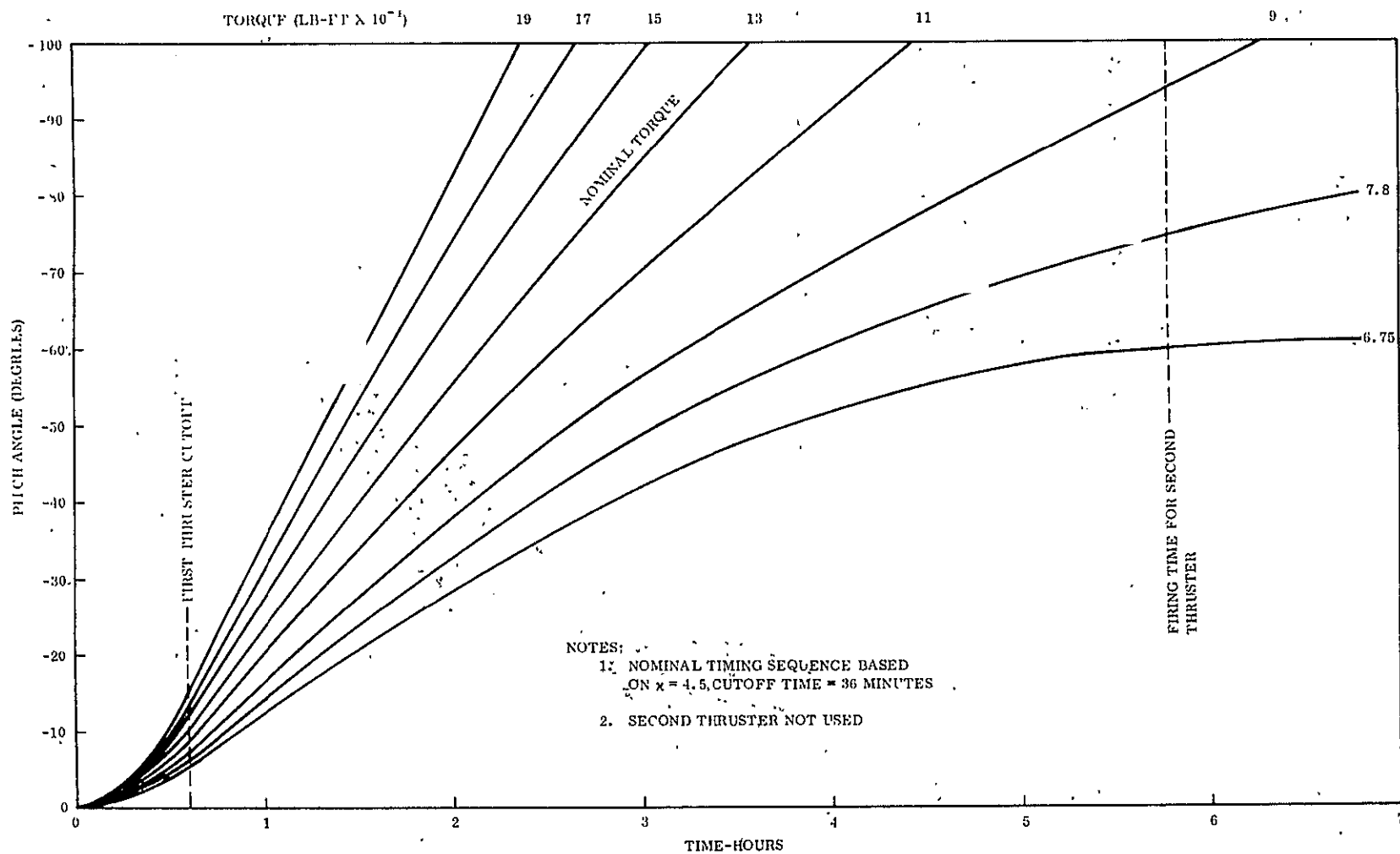
Figure 3.4-13. ATS-D Inversion Maneuver Trajectory
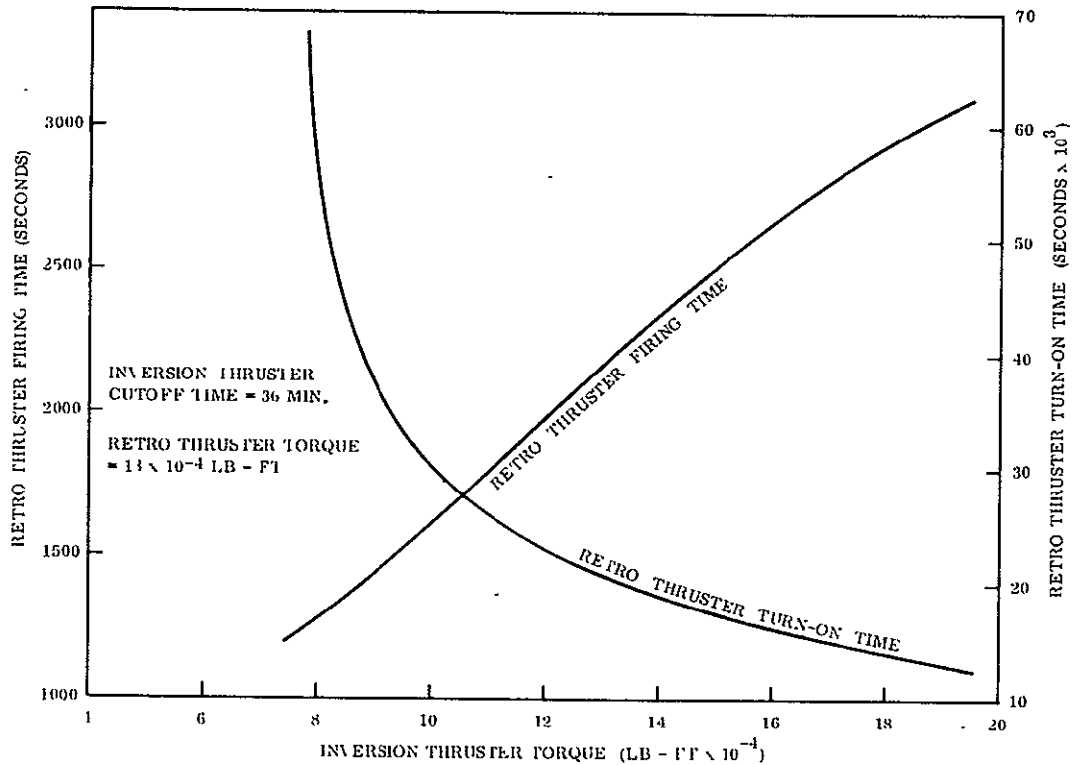
Figure 3.4-14. Retro Thruster Timing Data for ATS-D Inversion

The data presented in Figure 3.4-14 was obtained in two steps. First, the retro thruster firing time was assumed to be proportional to the total vehicle energy as the vehicle crosses a pitch angle of 90 degrees. Then the data was modified on the basis of a series of computer runs. The final data produced inversions with an overshoot of less than 3 degrees.

The case in which the retro thruster torque is not the nominal value has not been considered. One promising method of accomplishing the inversion maneuver with a non-nominal retro thruster is to turn on the retro thruster at the time given in Figure 3.4-14. The retro thruster would be turned off when the pitch rate, with respect to the orbiting reference frame, is zero. The difference between the pitch angle at this time and 180 degrees is the amount of overshoot in the maneuver.

Following completion of this study, the moment arm for ATS-D/E was changed from 29 to 7 inches and a brief study was performed to determine the new timing sequence. The nominal timing sequence for a 7-inch moment arm is 130 minutes on, a coast time of 303 minutes, and a retro of 130 minutes.

3.4.2.1.2   ATS-D/E Microthruster Inversion Using Real Time Data

The inversion maneuver for the ATS-D/E spacecraft, using two subliming solid rocket engines, was analyzed in the preceding section. That study assumed little or no attitude information would be available during the maneuver. As a consequence, a fixed-time sequence of events, consisting of a period of thrusting, a coast period, and a retro-thrust period, was specified. The studies revealed, however, that the success of the inversion maneuver depended upon exact knowledge of thrust, moments of inertia, etc. As the hardware was developed, it became evident that the thrust value could easily fall outside the acceptable thrust envelope. In addition, rod length uncertainties, initial condition variations and thruster misalignments alter the inversion. As a consequence, an inversion approach had to be formulated which was not sensitive to these minor variations. When arrangements were made to obtain attitude information on a real time basis, it became feasible to develop such an approach. .

The first requirement of the new approach is that real time attitude data be available during the maneuver. This was to be satisfied through real time transmission of data from the ATS ground stations to GE, Valley Forge via the NASCOM teletype network. The second requirement of the approach is an inversion evaluation technique, which in conjunction with the attitude data, indicates a course of action. Figure 3.4-15 is an "Inversion Map" which was designed to specify the "inversion state" of the spacecraft based upon the pitch attitude and pitch rate, and is used to make decisions. The map was generated from the analysis presented in Section 3.4.1 and consists essentially of lines of constant energy (η) plotted on a grid of pitch attitude (degrees) versus pitch rate (degrees/second). A single data point consisting of pitch attitude and rate uniquely defines the energy level. If the energy level of the spacecraft is less than one, the spacecraft does not have sufficient energy to invert, and will remain at less than 90 degrees (or more than 90 degrees depending upon initial
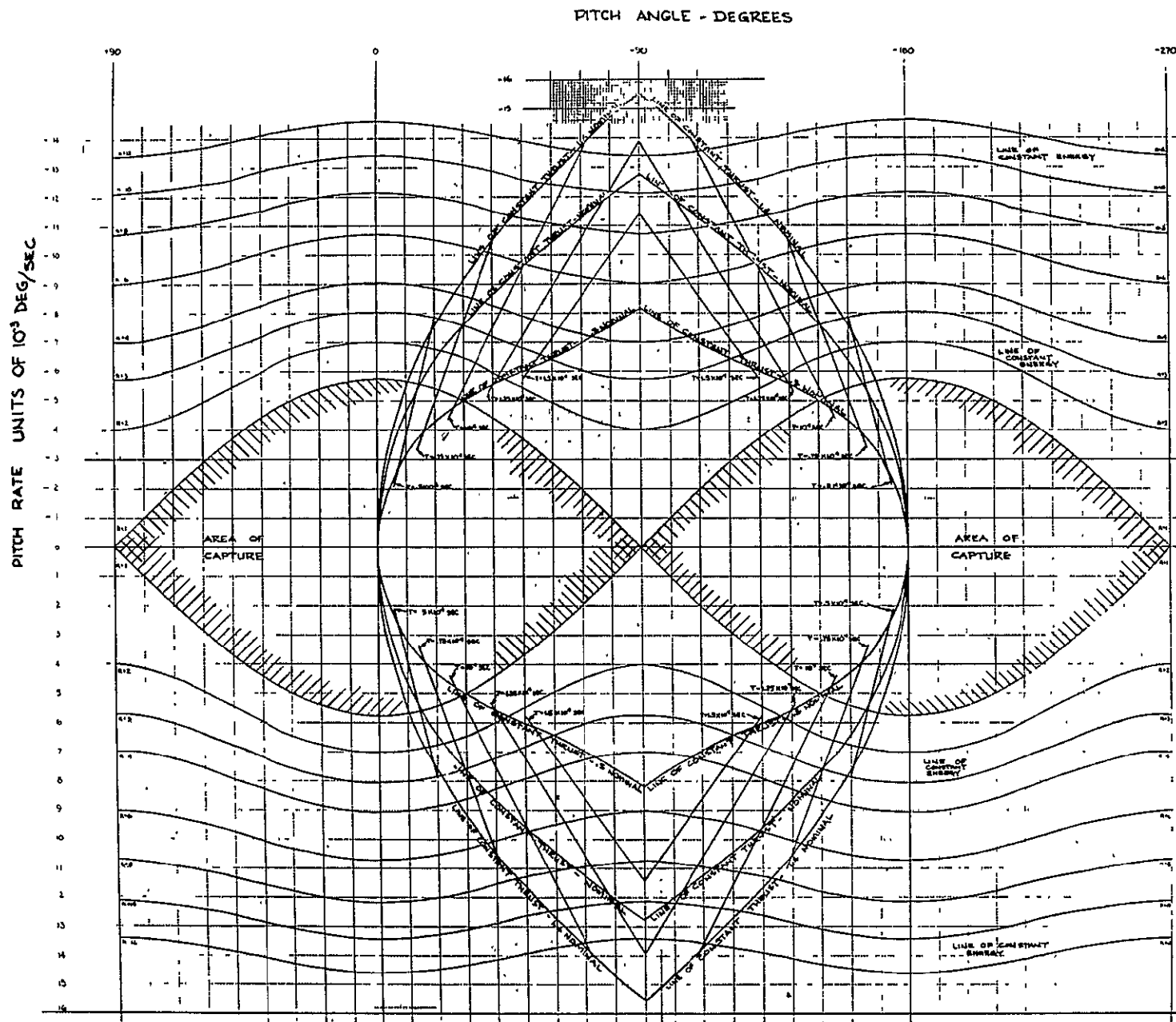
Figure 3.4-15. Inversion Map

orientation) indefinitely. For this reason, energy levels less than one have not been plotted. The area where the energy level is less than one has been shaded on Figure 3.4-15 and labeled "Area of Capture."

It should be noted that it is assumed that the roll and yaw oscillations at the beginning of the inversion are small enough to produce only second order effects, and that the inversion is largely in pitch. It is for this reason only pitch attitude is plotted. Note also, that the effects of the damper and external disturbances have not been included. The map is essentially for a rigid body, an assumption made at the initiation of the study since it greatly simplifies the analysis. Preliminary results indicated that the assumption was good.

To invert the spacecraft (after it has reached steady state and achieved small amplitude oscillations) it is necessary to increase its energy level to a value greater than one. As mentioned earlier, three has been selected as a nominal value. Any combination of pitch and pitch rate which produces this energy level will cause the spacecraft to invert. Once inverted, it is necessary to slow the spacecraft to reduce its energy level to less than one, and prevent it from reinverting. Any combination of pitch and pitch rate which results in this energy level (or less) is satisfactory. The best inversion is obtained, however, when the pitch rate is reduced to zero at the same time the pitch error is reduced to zero (or 180) degrees. Because of thruster misalignments, rod length uncertainities, etc., it is not possible to achieve the ideal inversion; hence, the recommended approach (which yields the best results with the greatest margin of safety) is to retro thrust until the pitch rate is zero.

To assist in interpreting the motions of the spacecraft during thrusting, lines of constant thrust have been plotted on the grid. These lines are essentially the integration of Equation 3.4-7 in Section 3.4.1. and portray the manner in which the pitch and pitch rate change while undergoing thrust. Three lines have been plotted, nominal thrust, 0.5 nominal thrust, and 1.4 nominal thrust. Four reference lines of constant thrusting time have also been plotted. These lines apply to the spacecraft only while undergoing thrust.

Figures 3.4-16 and 3.4-17 provide additional information about the thrusting maneuver. Figure 3.4-16 shows the pitch angle at which the thruster should be cut off, starting from ideal initial conditions, and Figure 3.4-17 shows the time corresponding to this pitch angle. These charts are useful if the thrust levels are known accurately in advance.

To verify the inversion map, and indicate what type of performance can be expected, several inversion runs were made on the Mathematical Model. Figure 3.4-18 is the nominal case wherein both thrusters had nominal thrust and were aligned perfectly, with the timing sequence as specified earlier. There were no external disturbances, and the spacecraft largely followed the nominal pitch curves on the plot. The damper boom had a negligible effect as noted earlier.

Figure 3.4-19 has the same sequence and thrust levels, but the initial pitch error was 5 degrees and the initial roll error was 15 degrees. The performance deviates slightly from Figure 3.4-18 but the inversion was successful.
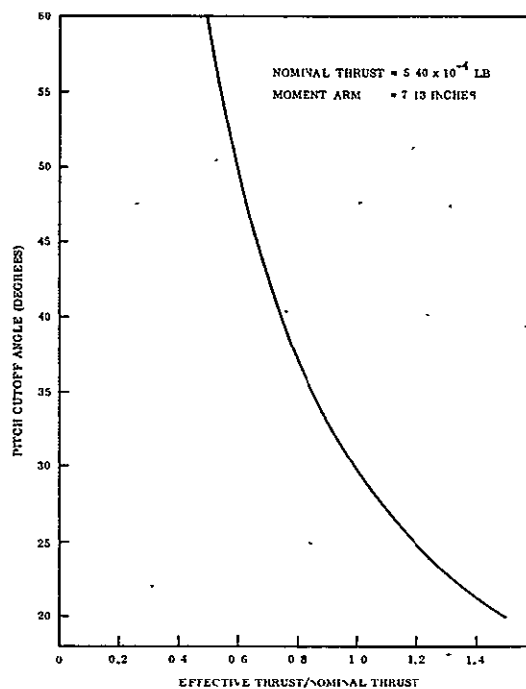
Figure 3.4-16. Thruster Cutoff Angle as a Function of Thrust Level
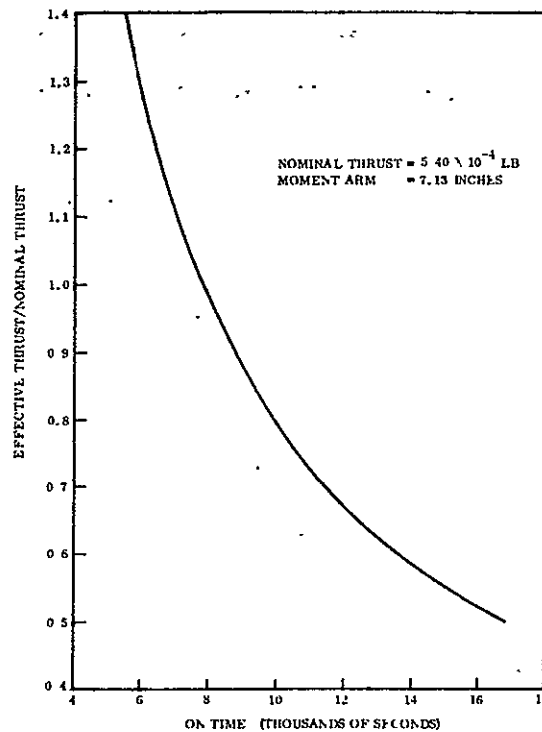
Figure 3.4-17. Burn Time as a Function of Thrust Level

Figure 3.4-20 is similar to Figure 3.4-19, except a yaw error of 10 degrees replaced the roll error. Again the inversion was successful.

Figure 3.4-21 has the initial pitch, roll, and yaw errors, and again the inversion was successful. The approach does not appear to be significantly influenced by initial conditions.

To determine the usefulness of the maps in actual flight, a non-nominal case was processed. The timing sequence was not known in advance. It was assumed that at the instant of inverter turn-on (t = 0 hours), the spacecraft had a pitch attitude of six degrees with a small pitch rate (Figure 3.4-22). The inversion was planned to be backward (negative pitch rate) and the thrust level was unknown (presumably). After one hour of thrusting, the new pitch and pitch rate were determined from attitude data and plotted (t = 1 hour, Figure 3.4-21). From the position of this point, it was obvious that the thruster was working. A third point was obtained at 1.9 hours and was also plotted. Neither of these points is outside the area of capture, and if the thrust were terminated, the spacecraft would probably not invert, and would damp out its initial orientation.

3-196
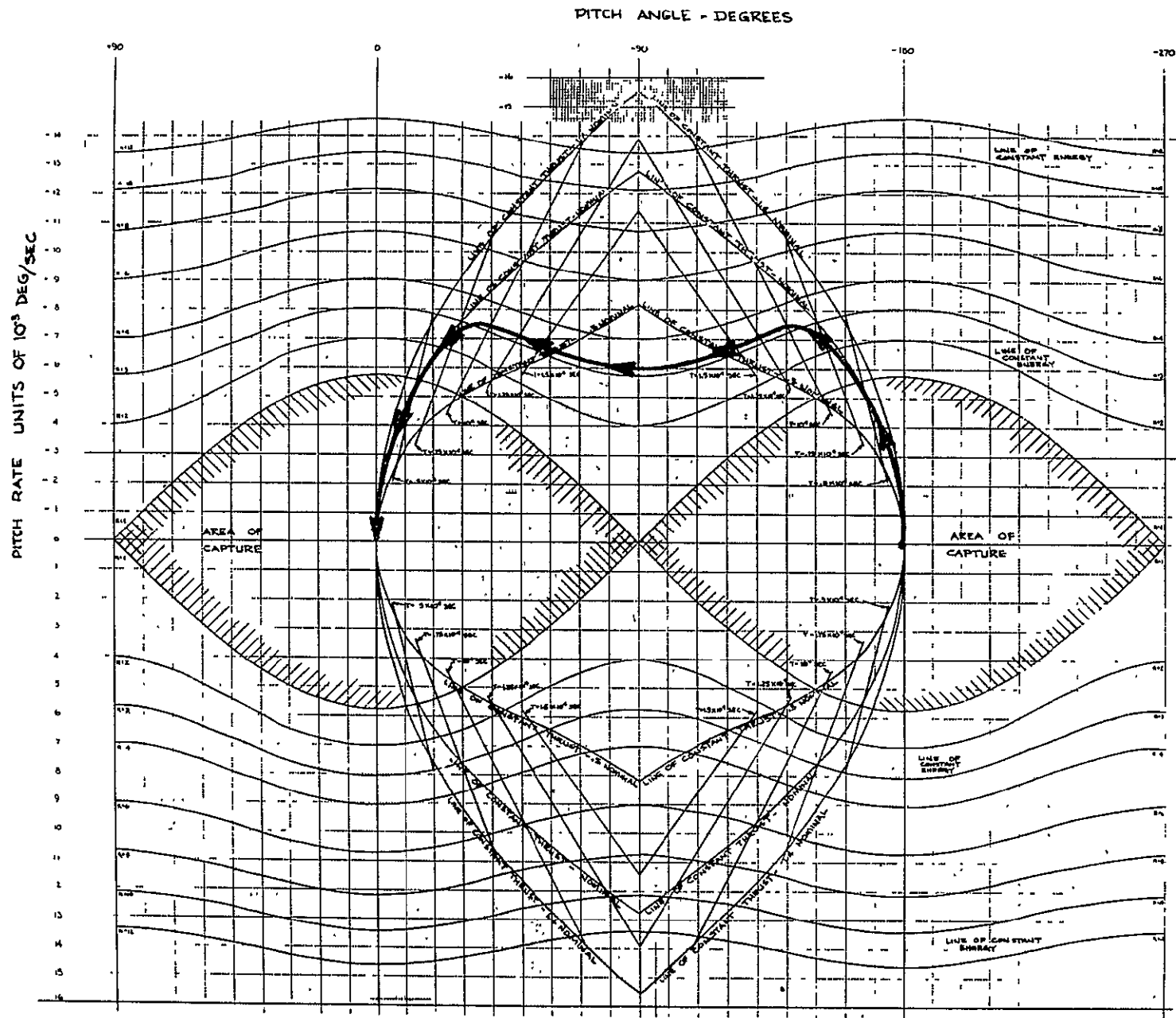
Figure 3.4-18. Nominal Inversion Sequence, Case I
(Pitch = 0 deg, Roll = 0 deg, Yaw = 0 deg)
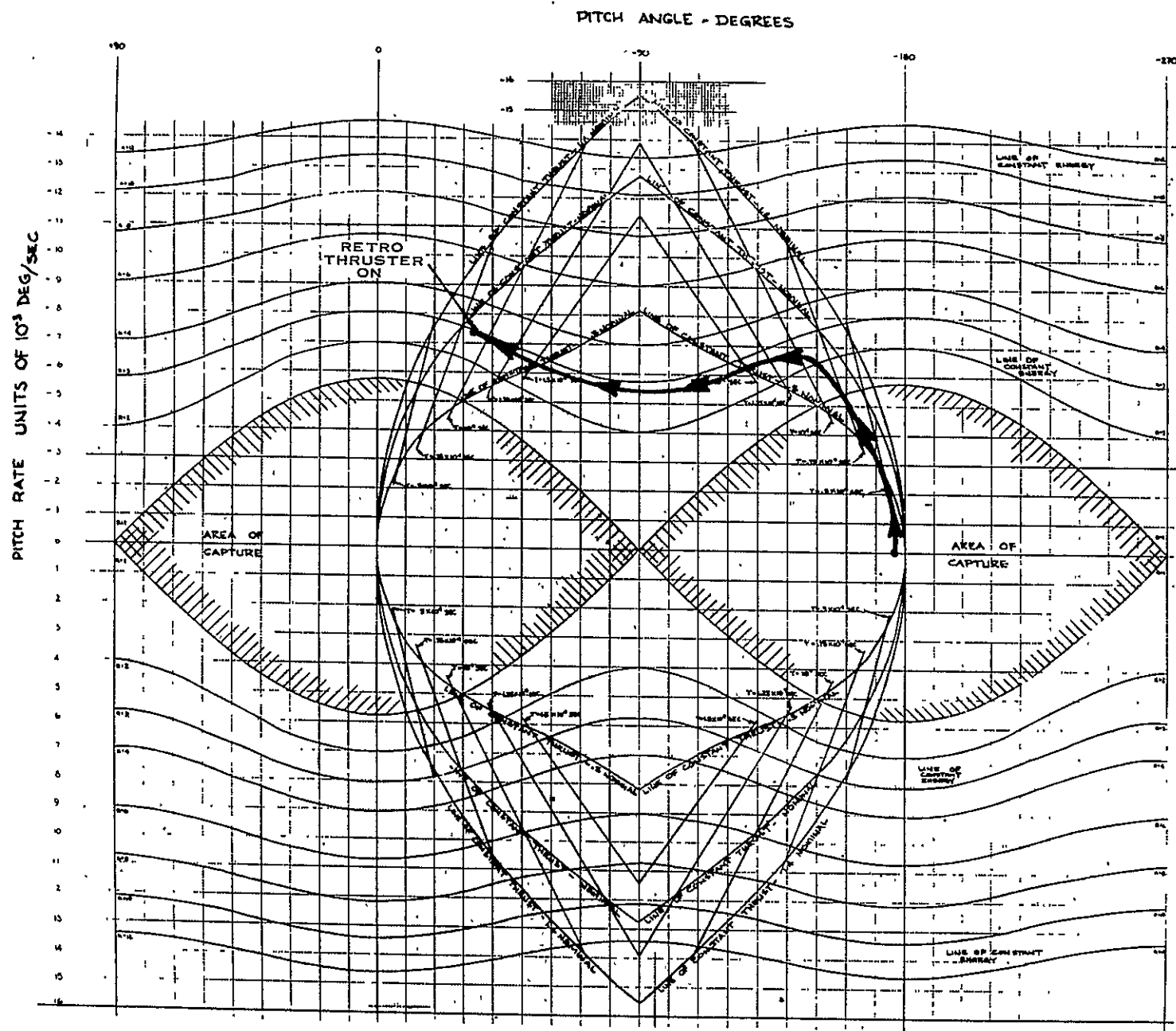
Figure 3.4-19. Nominal Inversion Sequence, Case II
(Pitch = 5 deg, Roll = 15 deg, Yaw = 0 deg)
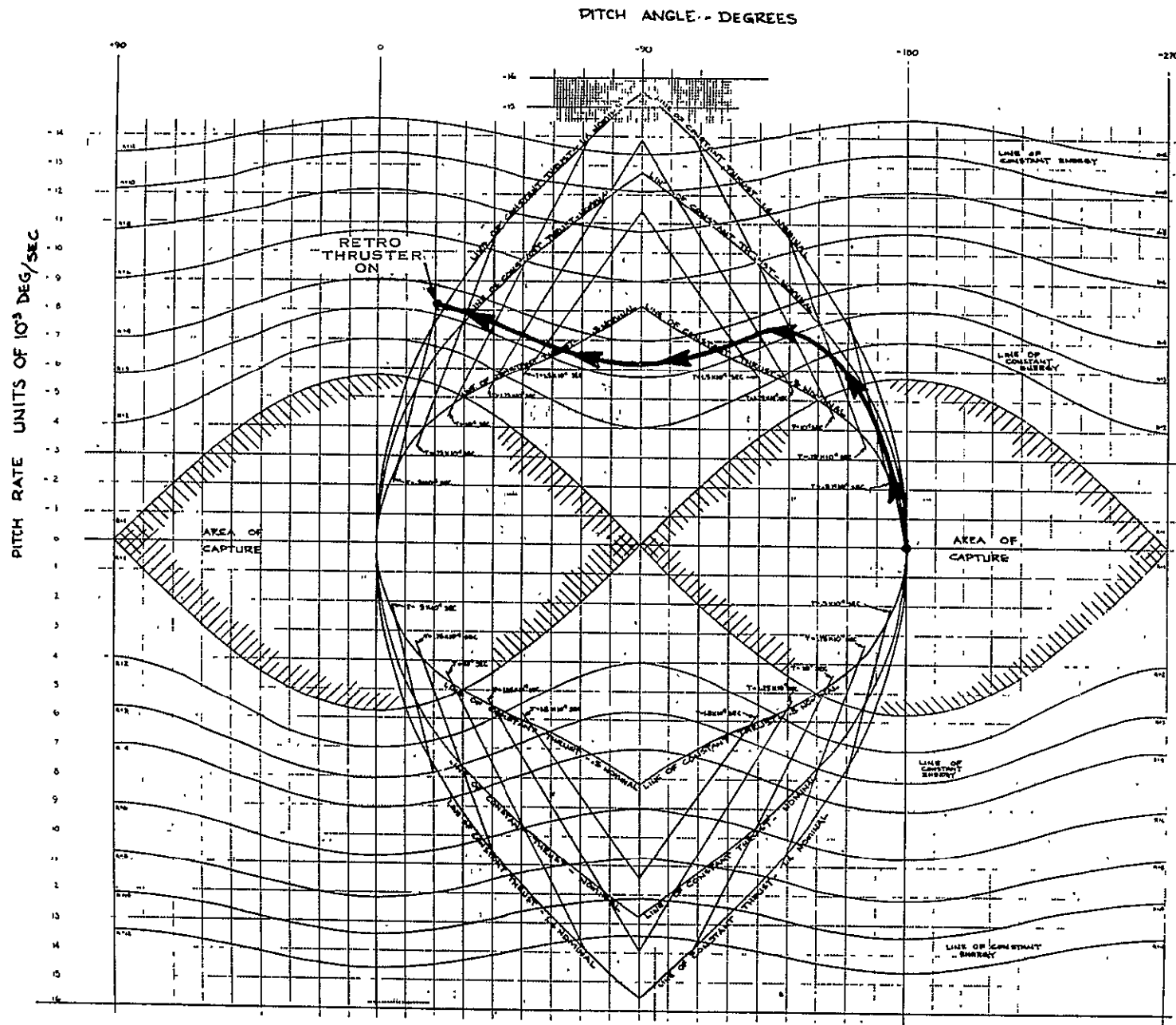
Figure 3.4-20. Nominal Inversion Sequence, Case III (Pitch = 5 deg, Roll = 0 deg, Yaw = 10 deg)
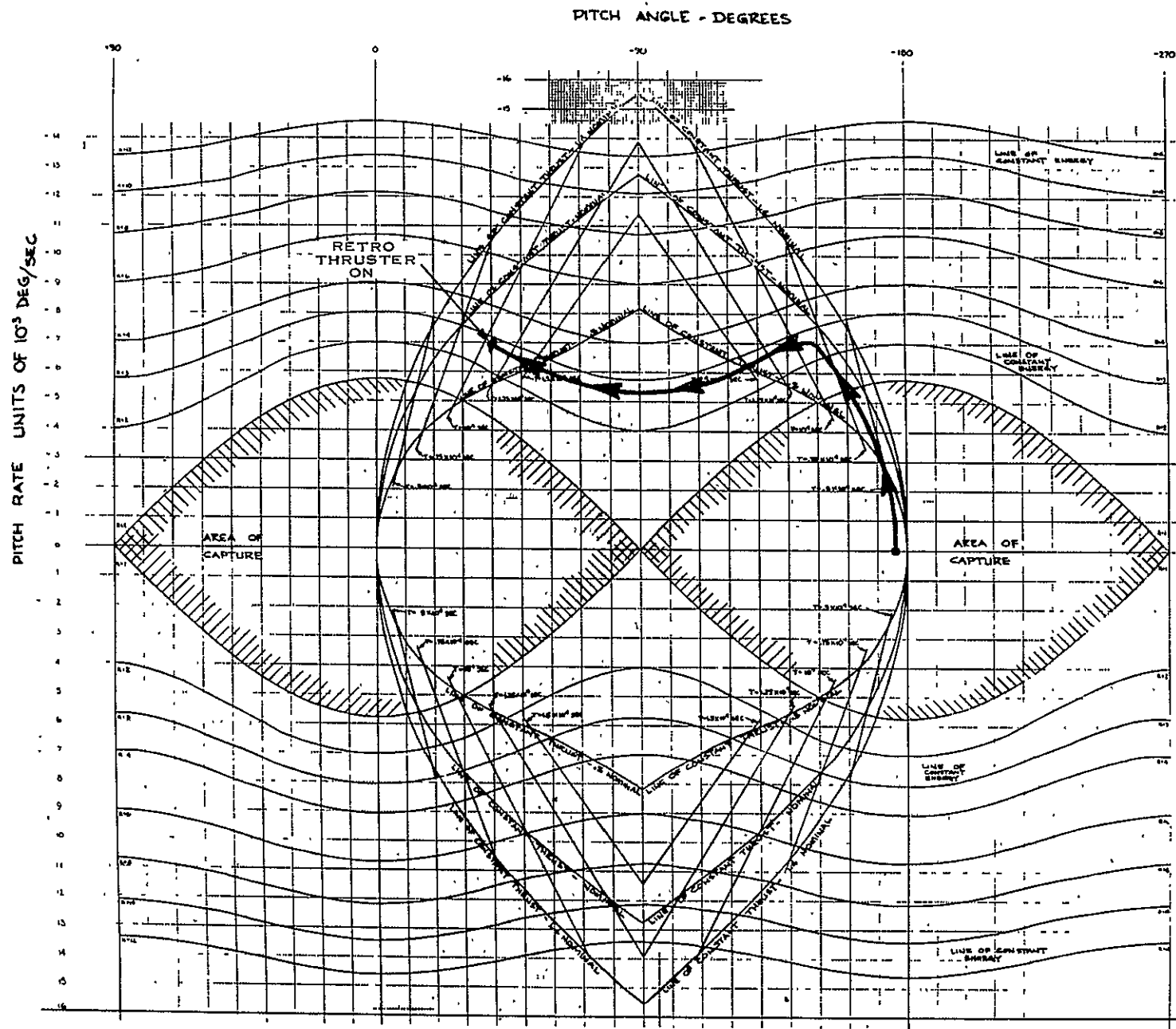
Figure 3.4-21. Nominal Inversion Sequence, Case IV (Pitch = 5 deg, Roll = 15 deg, Yaw = 10 deg)
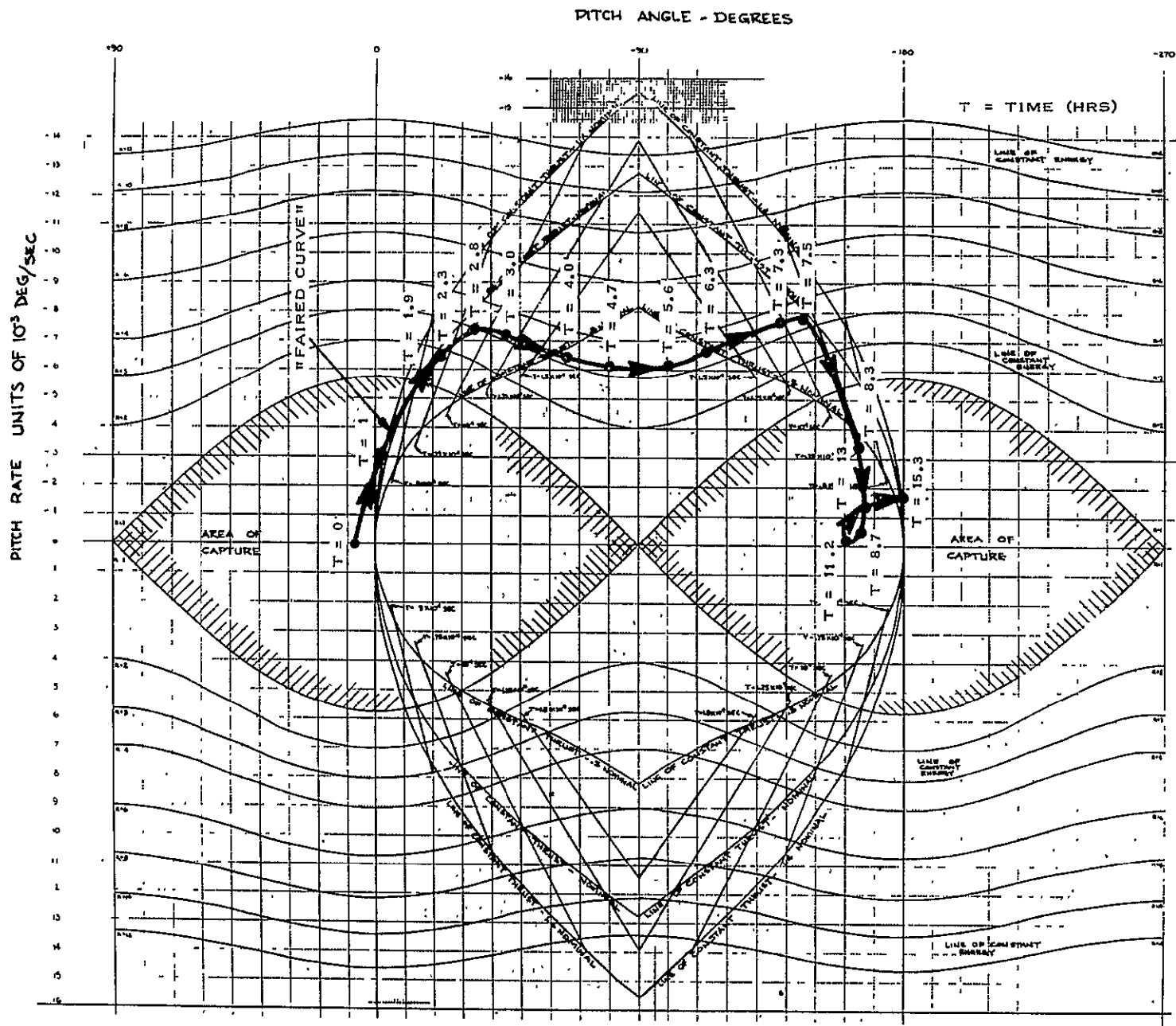
Figure 3.4-22. Operational Sample Case

Table 3.4-5. Events Summary

Time (Hours)	Time From Inverter On (Hours)	Pitch Attitude (Deg)	Pitch Rate (Deg/Sec)	Projected Maneuver Time (Hr)	Remarks
	0	6.0	-0.08×10^{-3}	–	Thruster Turn On
	1.0	0.3	-3.1×10^{-3}	–	Thruster On
	1.9	-13.9	-5.54×10^{-3}	–	Thruster On
	2.3	-23.0	-6.48×10^{-3}	2.44	Thruster On (Projected Turn Off)
	2.8	-33.5	-7.35×10^{-3}	–	Thruster Turn Off
	3.2	-45.5	-7.18×10^{-3}	–	Coast
	4.0	-65.0	-6.46×10^{-3}	–	Coast
	4.7	-80.3	-6.08×10^{-3}	–	Coast
	5.6	-100.0	-6.13×10^{-3}	–	Coast
	6.3	-115.6	-6.6×10^{-3}	–	Coast
	7.2	-138.7	7.56×10^{-3}	7.5	Coast (Projected Turn On)
	7.5	-147.0	-7.8×10^{-3}	–	Retro Thruster Turn On
	8.3	-162.9	-3.21×10^{-3}	8.7	Retro On (Projected Turn Off)
	8.7	-166.0	-0.50×10^{-3}	–	Retro Thruster Off
	11.2	-166.0	-0.283×10^{-3}	–	–
	13.0	-167.6	-1.4×10^{-3}	–	–
	15.3	+178.4	-1.83×10^{-3}	–	–

The same initial conditions as Figure 3.4-22 were tried again with an assumed thruster misalignment. As a reference, the torque in the z axis was unaltered, but additional torques were added to roll and yaw. The inverter thruster has an effective thrust of $1.95.10^{-3}$ pounds with a misalignment of approximately 5 degrees. The retro thruster has an effective thrust of $3.82.10^{-3}$ pounds with a misalignment of approximately 10 degrees. The result of the simulation, assuming the proper timing sequence of Figure 3.4-22, is shown in Figure 3.4-23. The spacecraft did not invert with the inversion thruster. Because it did not invert, the retro thruster increased the energy content beyond the order of capture and the spacecraft will undoubtedly go through an uncontrolled inversion.

A timing sequence can be generated for this thruster arrangement in much the same manner as in Figure 3.4-22. The result of developing a new sequence is shown in Figure 3.4-24, and indicated a successful inversion.

To ensure that the spacecraft did not re-invert, the simulation was carried out for 30 hours. The roll error reached a peak of 24 degrees during the maneuver, and the yaw error reached a peak of 18 degrees. Yaw reached a peak of 60 degrees after the maneuver, however, and could possibly invert. For reference, the "adjusted" timing sequence is 278 minutes of inversion thrust, a coast of 212 minutes, and a retro thrust of 63.3 minutes. There is obviously a considerable difference between the timing sequence of Figure 3.4-22 and that of Figure 3.4-24. However, the "Inversion Map" approach appears feasible if accurate attitude data (position and rate) can be obtained. It should be noted that the approach was successful in Figure 3.4-24 in spite of the roll error of 25 degrees.
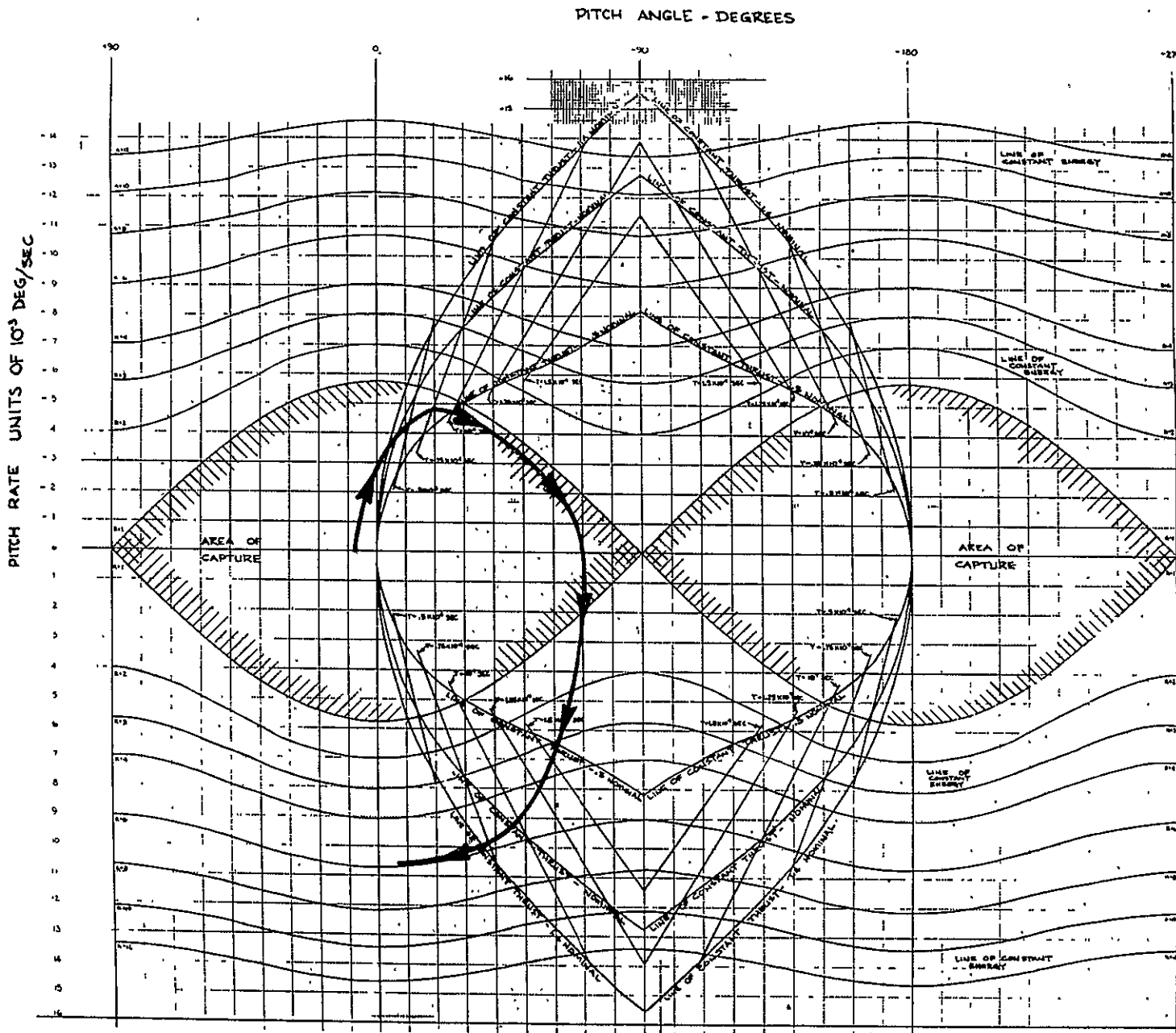
Figure 3.4-23. Operational Sample Case with Misaligned Thruster Nominal Timing Sequence
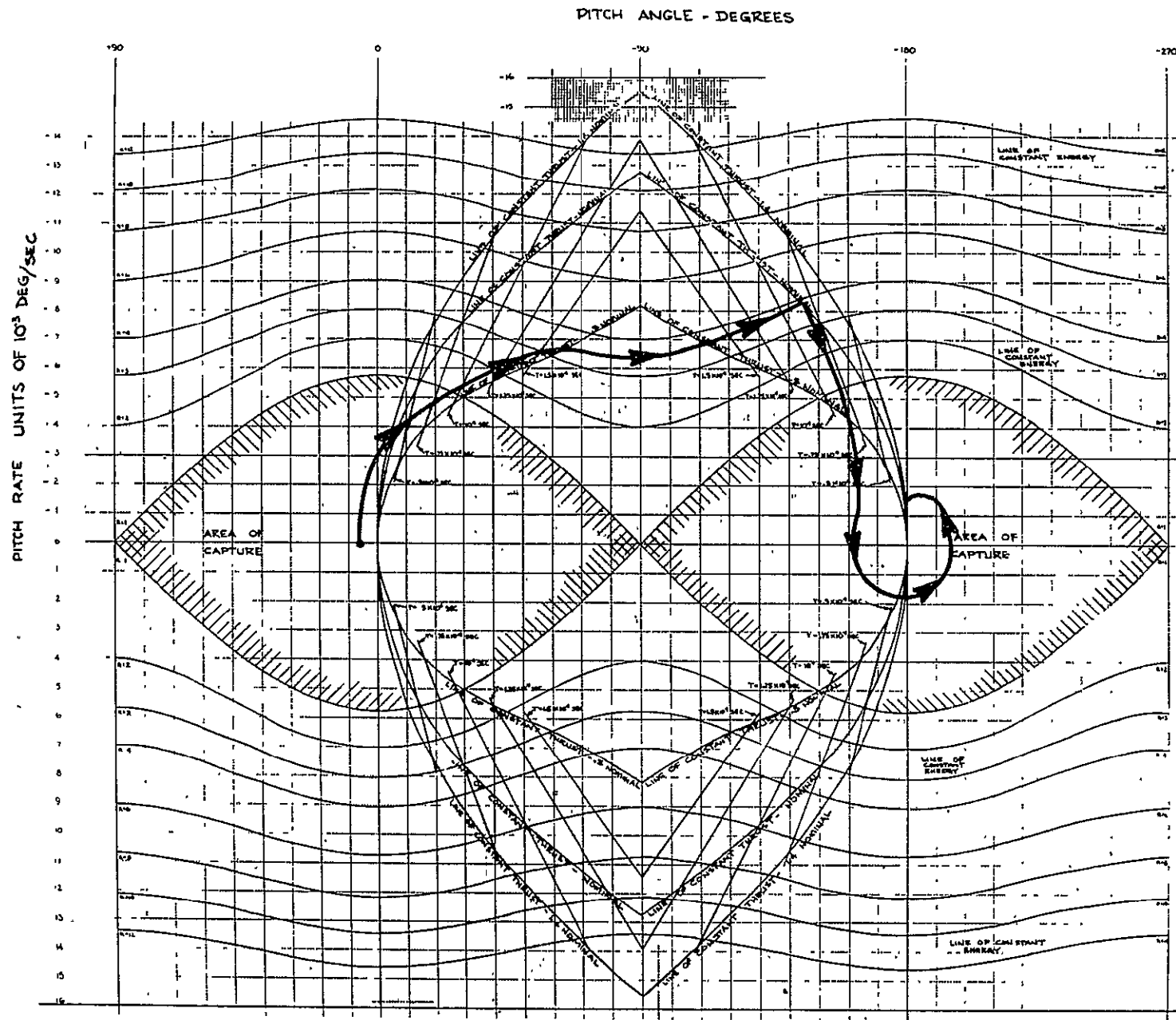
Figure 3.4-24. Operational Sample Case with Misaligned Thrusters – Corrected Timing Sequence

3.4.3 ROD RETRACTION/EXTENSION ANALYSIS

The second method of causing a gravity gradient spacecraft to invert is to retract the gravity gradient rods and then re-extend them with an appropriate timing sequence. Before rod retraction, the nominal spacecraft initial rate is nearly equal to orbital rate, and is about the spacecraft pitch (z) axis. Retracting the rods decreases the spacecraft moment of inertia, and by the principle of conservation of angular momentum, there will be a corresponding increase in inertial rate. The increase in inertial rate can be made large enough (with most current spacecraft) to cause the spacecraft to invert. After the inversion is completed, the rods are extended to their original length, and the spacecraft will be slowed to orbital rate (or nearly so). The spacecraft will then be captured in the inverted position.

The study of inversion is performed primarily by computer because of the nonlinearities involved. The studies for ATS-A, D and E are given as follows:

3.4.3.1 ATS-A Rod Retraction/Extension Analysis

Specific requirements were placed on the ATS-A rod retraction/extension maneuver, and the maneuver was designed specifically to meet these requirements. The requirements were:

1. The time required to complete inversion should not exceed 2.5 hours.

2. Spacecraft oscillations should be held to a minimum.

3. It is desirable to perform the maneuver on the basis of time only.

Several pertinent vehicle parameters used in this study are listed as follows:

1. Nominal Rod Length = 132.34 feet

2. X-Boom Half Angle = 25 degrees

3. Rod Extension and Retraction Rate = 1 ft/sec

The effects of solar pressure torques or thermal bending of the rods on the maneuver was assumed to be insignificant.

Four sets of initial conditions, listed in Table 3.4 6, were used during the study. The nominal set consists of an undisturbed spacecraft rotating at orbital rate about its pitch axis. The other three sets were taken from computer simulations after the spacecraft reached steady state conditions (see Section 3.5). These simulations included a 0.015 orbit eccentricity, solar pressure and rod thermal bending with the sun in the orbit plane, and a 1000 pole-cm magnetic dipole moment along the pitch axis. The columns labeled "ω_z min" and "ω_z max" are those for which ω_z reached its minimum and maximum values, respectively. The set labeled "average" was chosen to include near-maximum values for both ω_z and ω_x.

Table 3.4-6. Initial Conditions

	Nominal	ω_z Min	ω_z Max	Average
θ_p (deg)	0	0.1	0.3	1.9
θ_R (deg)	0	-0.2	0	0.2
θ_Y (deg)	0	-3.0	2.9	2.2
γ (deg)	0	2.2	-1.6	-1.6
ω_x (deg/sec)	0	-0.000166	-0.000896	-0.000606
ω_y (deg/sec)	0	-0.000750	-0.000893	0.000639
ω_z (deg/sec)	0.01565	0.01453	0.01689	0.01656
γ^o (deg/sec)	0	-0.000419	0.000173	0.000225

The first task in this study was to determine to what length the rod should be retracted. Under nominal initial conditions, the maximum value of retracted rod length for which inversion occurs is 88 feet. For this case the spacecraft inertial rate is increased to 2.4 times orbital rate. In the most severe case, using the ω_z Min initial conditions, the maximum value of retracted rod length for which inversion occurs is 85 feet. The complete maneuver at this retracted rod length requires 2.85 hours.

There was some uncertainty as to how accurately the rods can be retracted to a specified length when the spacecraft is in orbit. The accuracy of the rod extension read-out sensor is ±3 inches. However, there are other factors that can markedly reduce this accuracy. These included variations in the manner in which the rod tape is tored on the drum, power supply variations and telemetry errors. The latest estimate on rod length accuracy is ± 2 feet. These measurements are received at 3 second intervals.

To accomodate these errors and to decrease the time required to complete the inversion, a nominal value of 75 feet was chosen for the retracted rod length.

The mechanics of rod retraction provide that the nominal length rod is retracted to the specified length. One rod in each rod pair can be as much as 2 feet short at its nominal length, and the shorter rod is always shorter, even in the retracted position. Therefore, the effect of short rods is to reduce the spacecraft moment of inertia in both the extended and retracted positions. The ratio of these moments of inertia for the case of one rod in each pair 2 feet short is almost identical to the moment of inertia ratio where all the rods are the nominal length. Therefore, the increase in inertial rate is almost identical. The net result is that short rods have no significant effect on the inversion maneuver. This con-clusion has been verified by computer runs.

Figures 3.4-25 through 3.4-28 show four complete inversion maneuvers, starting with the average initial conditions. In each case, rod extension was commanded when the spacecraft pitch attitude reached 180 degrees. This results in minimum spacecraft oscillations. The case shown in Figure 3.4-25 uses the nominal retracted rod length of 75 feet and the eddy current damper. Figure 3.4-26 is the identical case, except that the hysteresis damper is used. There is virtually no difference between the spacecraft attitude of Figure 3.4-25 and Figure 3.4-26 during the period of the inversion maneuver. The choice of dampers has no significant effect on the inversion maneuver. All other computer runs in this study employec the eddy current damper.
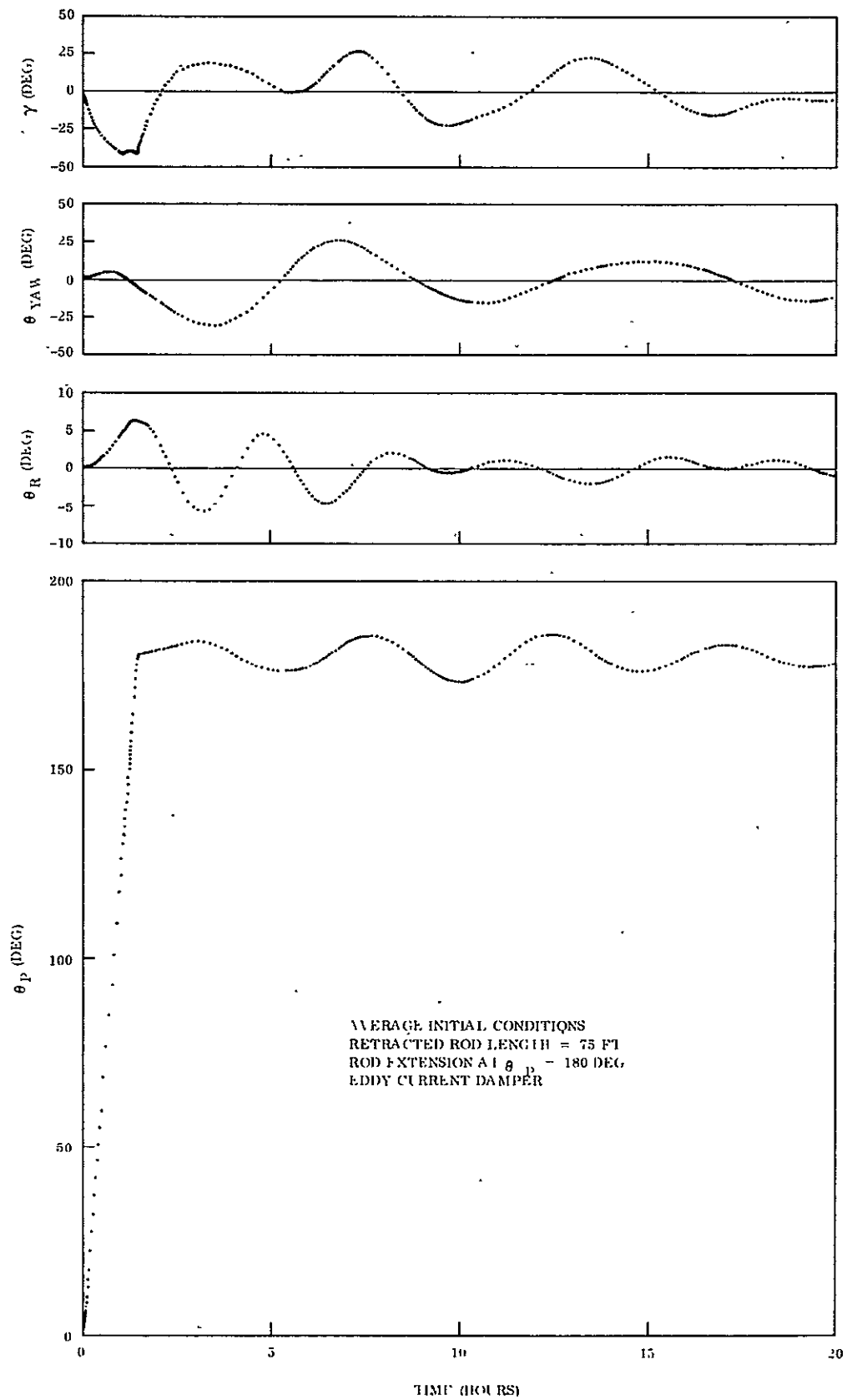
Figure 3.4-25. ATS-A Inversion Maneuver, Eddy Current Damper
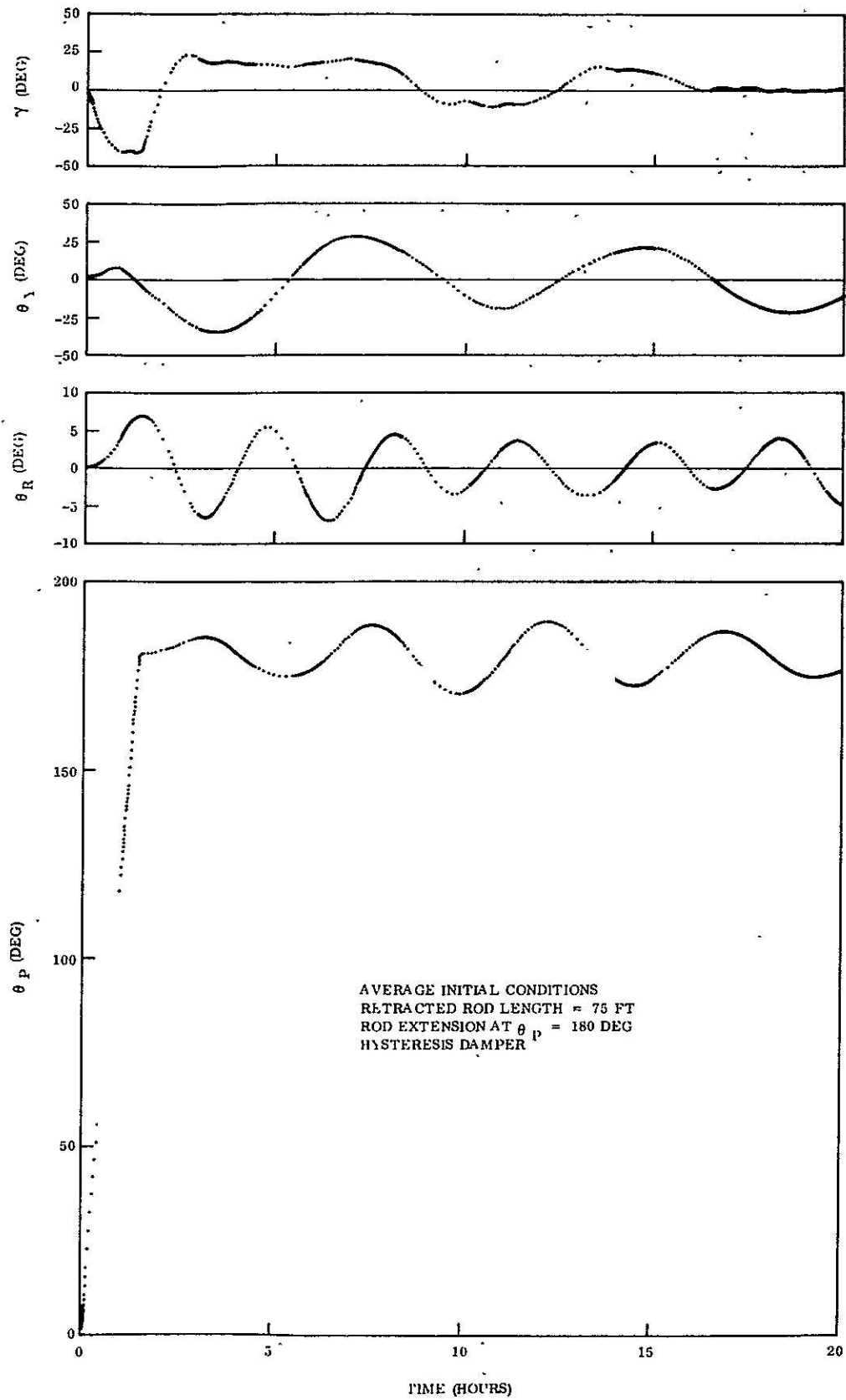
Figure 3.4-26. ATS-A Inversion Maneuver, Hysteresis Damper
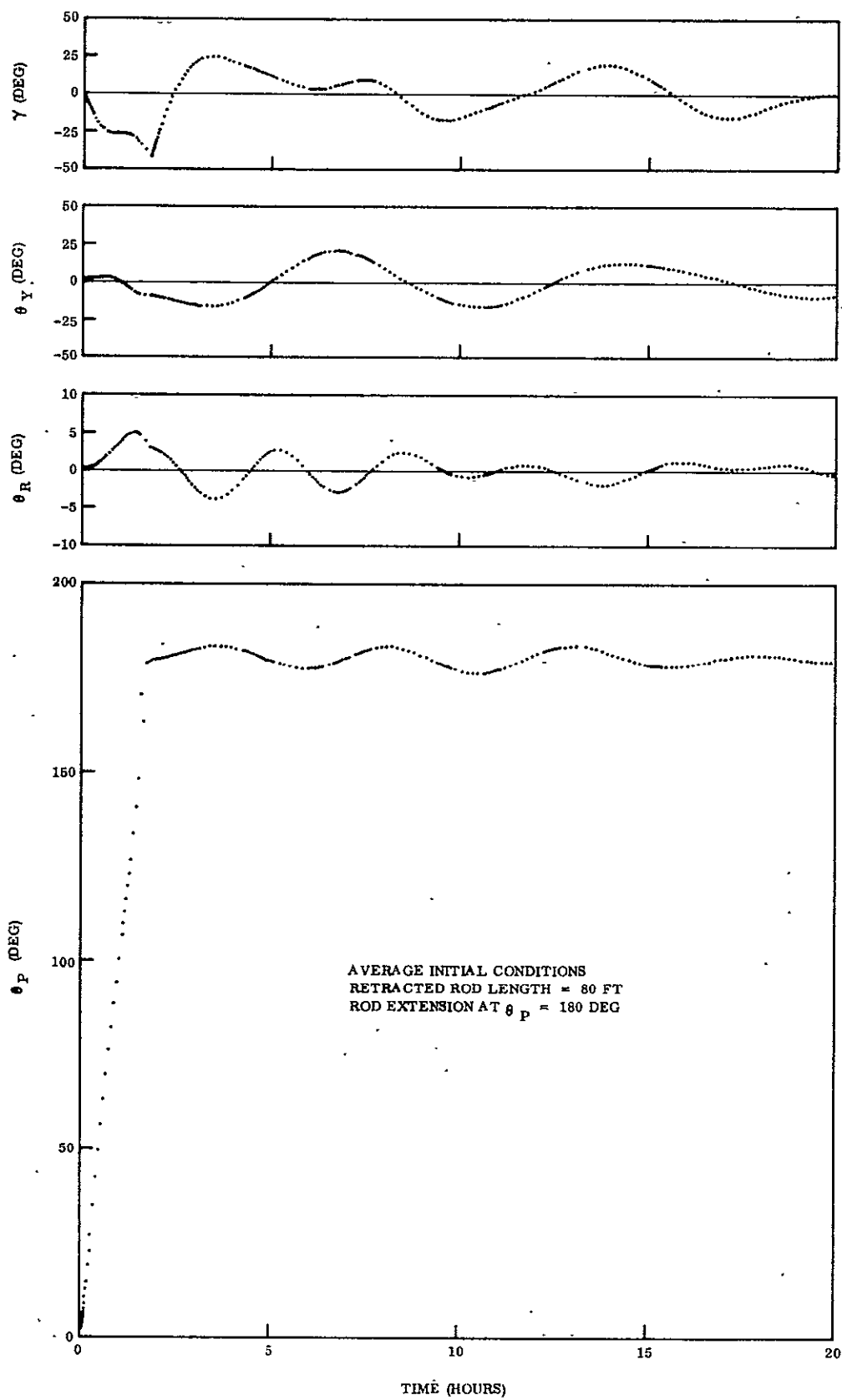
Figure 3.4-27.   ATS-A Inversion Maneuver

AVERAGE INITIAL CONDITIONS
RETRACTED ROD LENGTH = 70 FT
ROD EXTENSION AT θ_P = 180 DEG

TIME (HOURS)
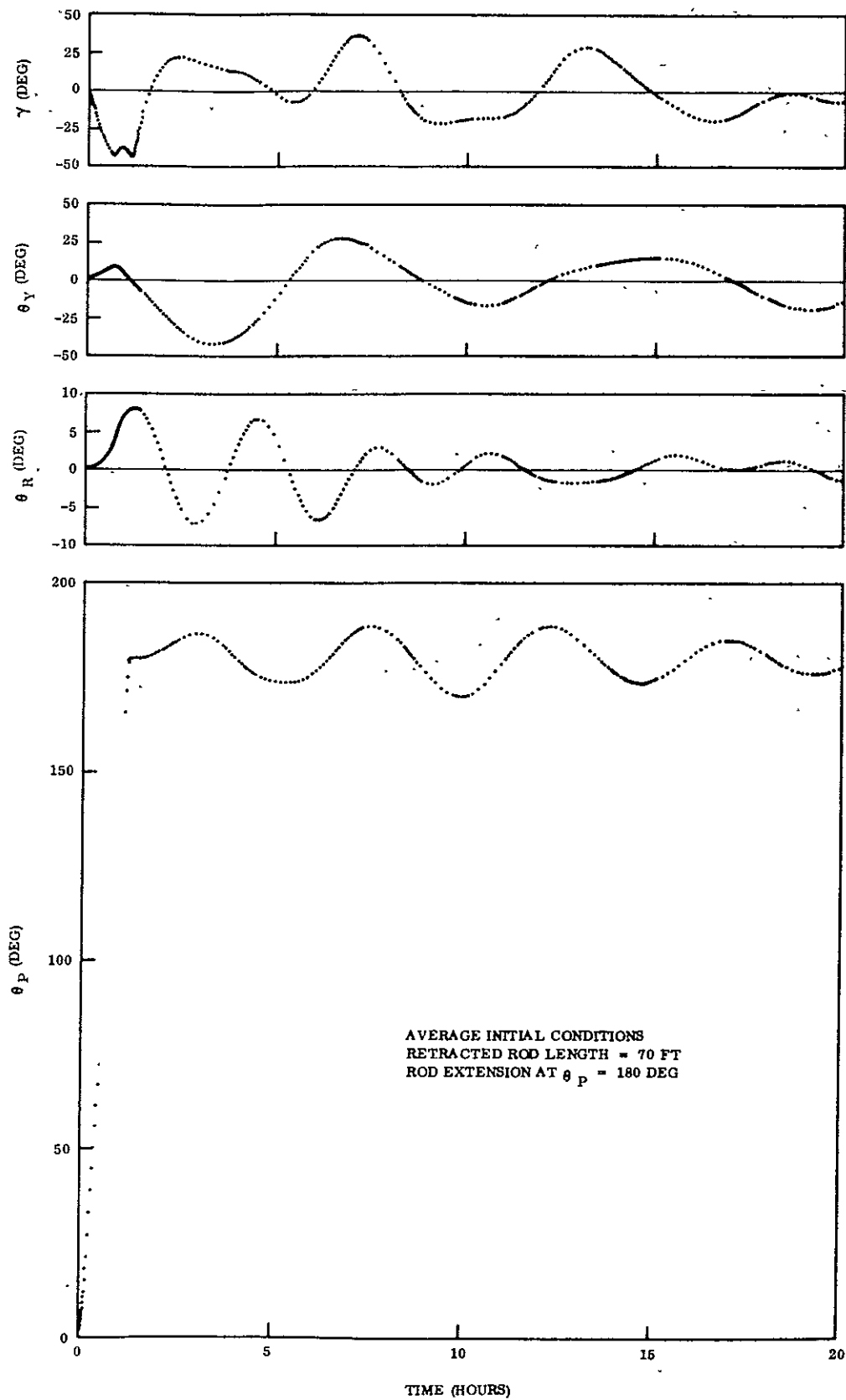
Figure 3.4-28. ATS-A Inversion Maneuver

Figures 3.4-27 and 3.4-28 show inversion maneuvers in which the retracted rod lengths vary +5 feet and -5 feet, respectively, from the nominal value of 75 feet and rod extension is commanded when pitch attitude reaches 180 degrees. Spacecraft oscillations are relatively low and the damper boom does not hit its stops. It is apparent that the maneuver is insensitive to retracted rod length provided that:

1. The rod is retracted sufficiently to cause inversion.

2. Rod extension occurs when pitch attitude reaches 180 degrees.

The times required to complete the inversion maneuver for the cases shown in Figures 3.4-25, 3.4-27, and 3.4-28 are listed below.

Retracted Rod Length (Feet)	Time to Complete Inversion Maneuver (Hours)
70	1.166
75	1.589
80	1.798

It is desirable to be able to accomplish the inversion maneuver without being completely dependent upon spacecraft pitch attitude information. Four computer runs were made for inversion maneuvers in which rod extension is commanded at 93.45 minutes after reaching the retracted rod length. Retracted rod lengths of 70, 72, 78 and 80 feet were used which represent errors of ± 3 and ± 5 feet. Initial conditions were chosen to provide the worst case. The "ω_z max" initial conditions were used for retracted rod lengths above nominal. All four inversion maneuvers were successful. However, as expected, large spacecraft oscillations occurred. For the cases in which the error in retracted rod length was ± 5 feet, pitch oscillations of ± 70 degrees occurred which in turn led to yaw inversion. The damper rod traveled 3.7 degrees into the snubber spring. These four cases are plotted in Figures 3.4-29 through 3.4-32 inclusive.

After 2.3 hours (from initial thruster turn-on) a fourth point was obtained and plotted. This point has an energy level only slightly greater than one. Since an energy level of three is preferred, the thrust was maintained. To determine the thrust cutoff time, a time curve was faired in (using a French curve), and from this curve it was estimated that the $\eta = 3$ constant energy line (the nominal line) would be reached in 8800 seconds (2.44 hours). However, because of the operational time lag associated with obtaining the data point at 2.3 hours, it was assumed that the turnoff time had already been passed. As a consequence, the thruster was turned off immediately and a data point taken (t = 2.8 hours). Data points were then taken continuously during the coast phase at approximately regular interfals. The spacecraft follows the constant energy line fairly well and crosses 90 degrees at approximately 5.1 hours. Three more data points are taken at 5.6 hours, 6.3 hours, and 7.2 hours. At 7.2 hours, the line of nominal constant thrust was being approached and, projecting ahead, the nominal thrust line should be crossed at 7.5 hours. The time estimate was made assuming that equal distances are "traveled" in equal times on lines of constant energy. Since the distance from t = 7.2 hours to the nominal thrusting line is approximately 1/3 the distance between the points at 6.3 hours and 7.2 hours, an additional 0.3 hours is required. At this time (7.5 hours), the retro thruster was turned on. The nominal burn time for the retro thruster is 7500 seconds at this poisition. At 8.3 hours (3960 seconds of On-time), a data point was taken, and indicated that the retro thruster was stronger than the nominal. At t = 8.3 hours, the thruster could be turned off, since the energy level was less than one, but because of uncertainties of roll and yaw attitudes, it was felt that it was better to reduce the pitch rate to zero (as closely as possible. A quick estimate of the time to cross 180 degrees, based onthe amount of rate change in 0.8 hour (8.3 hours – 7.5 hours) is 8.7 hours. At 8.7 hours the thruster was turned off, and as indicated by the subsequent data points in Figure 3.4-21, the spacecraft captured in the inverted position. Table 3.4-5 shows the steps in the procedure in tabulated form. (A table of this sort is recommended for keeping track of times and events). The timing sequence for this inversion is inversion thruster for 165 minutes, a coast of 285 minutes, and a retro thruster On-time of 71 minutes.
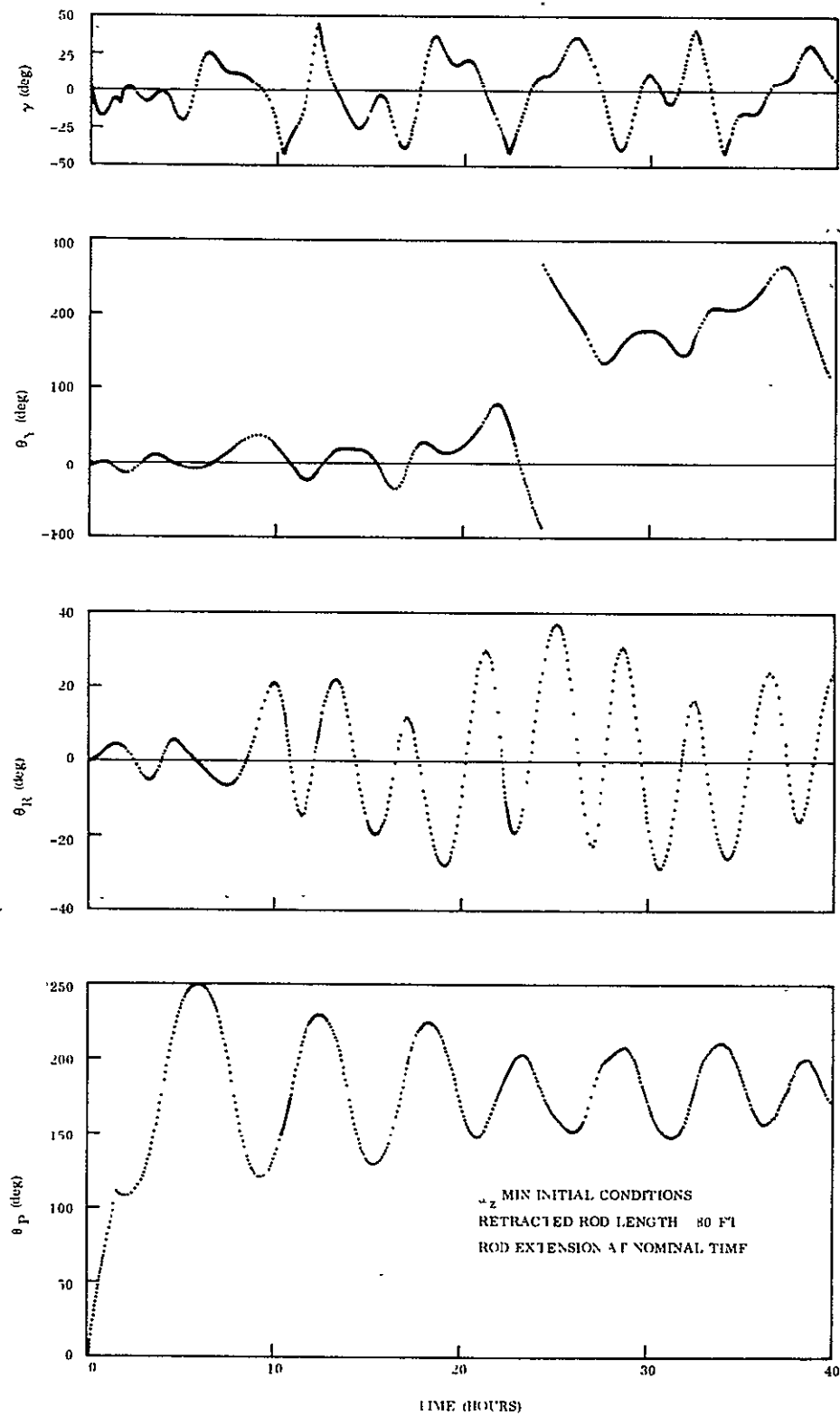
Figure 3. 4-29. ATS-A Inversion Maneuver
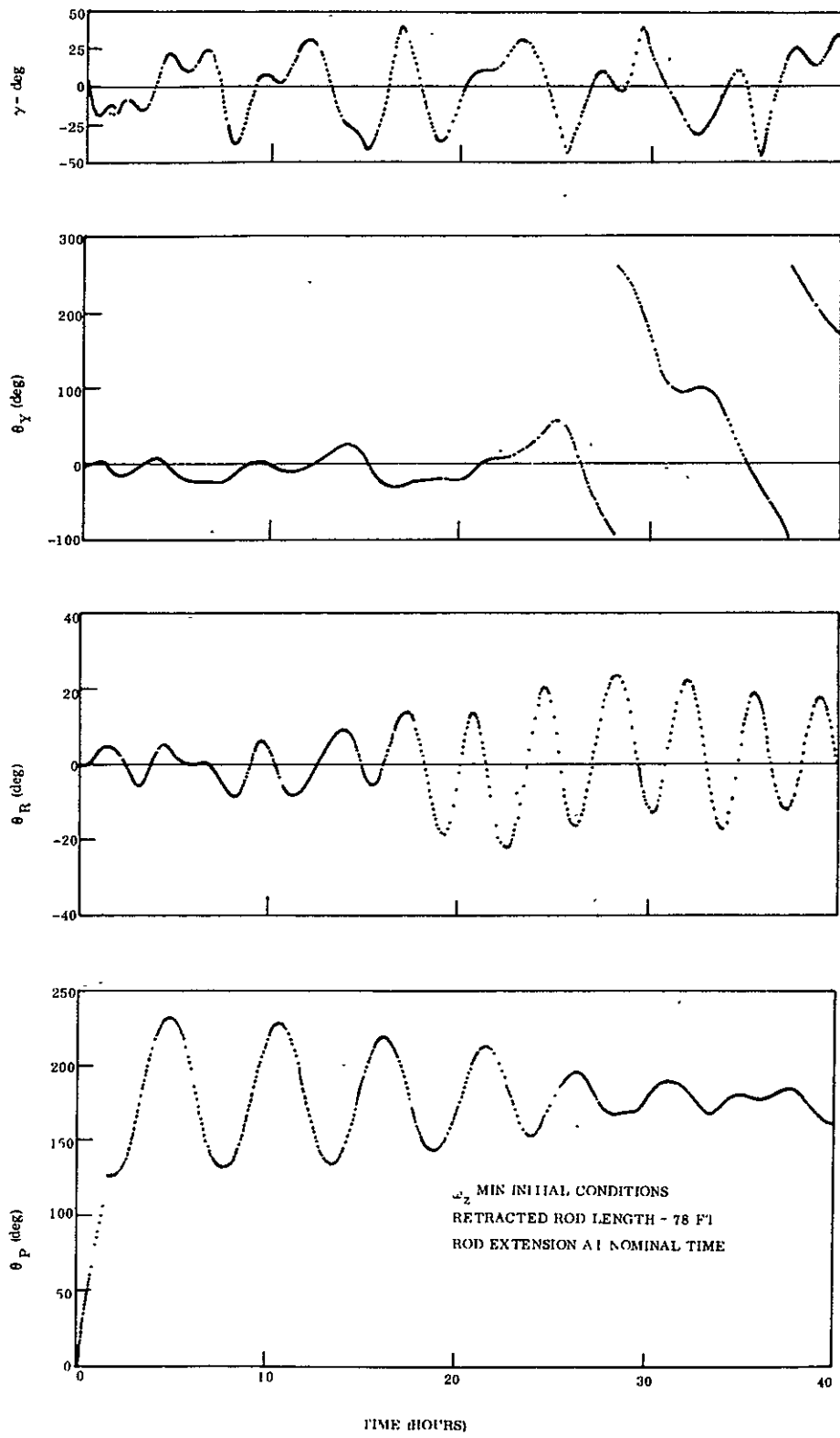
Figure 3.4-30.   ATS-A Inversion Maneuver
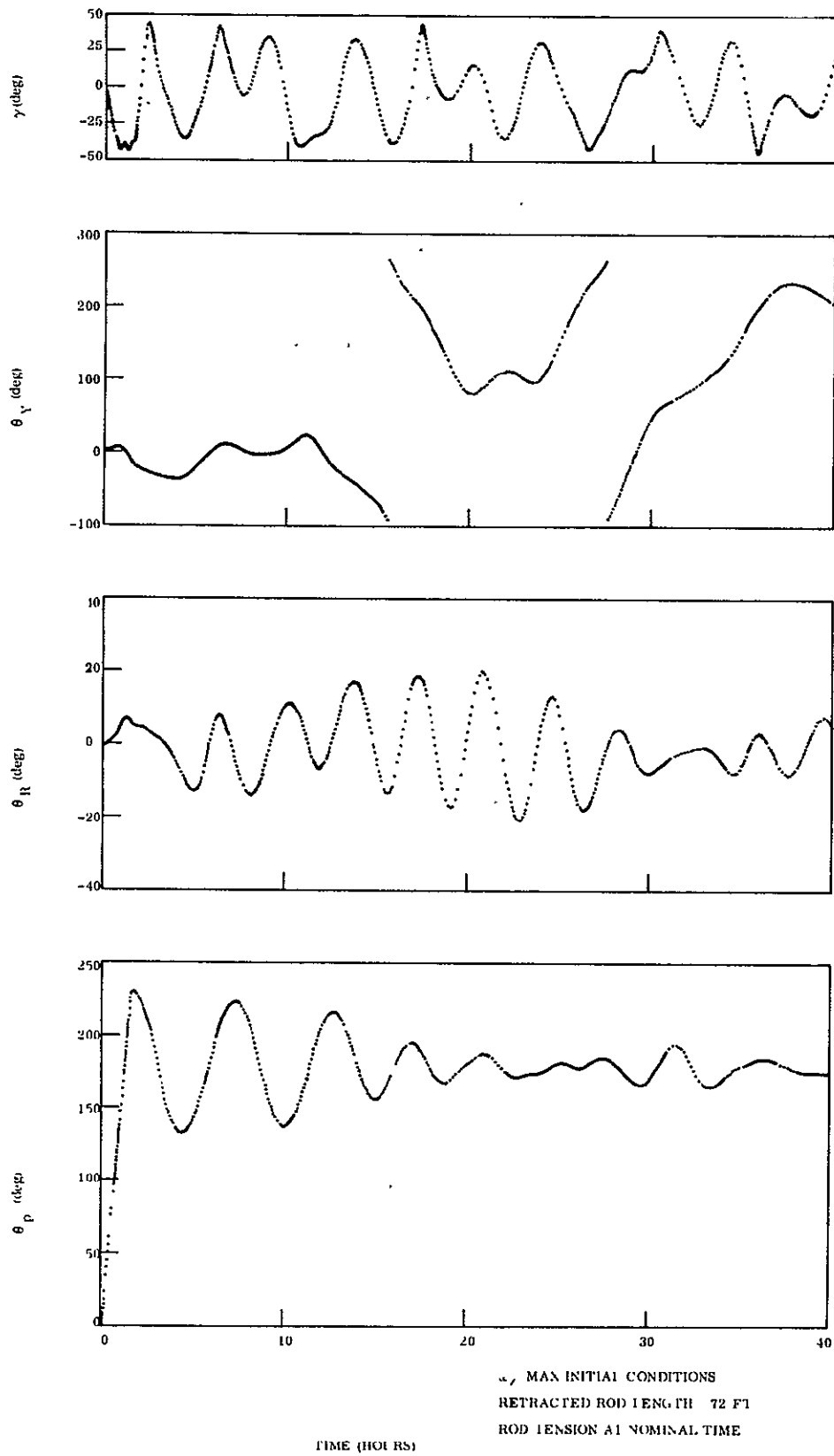
Figure 3.4-31. ATS-A Inversion Maneuver
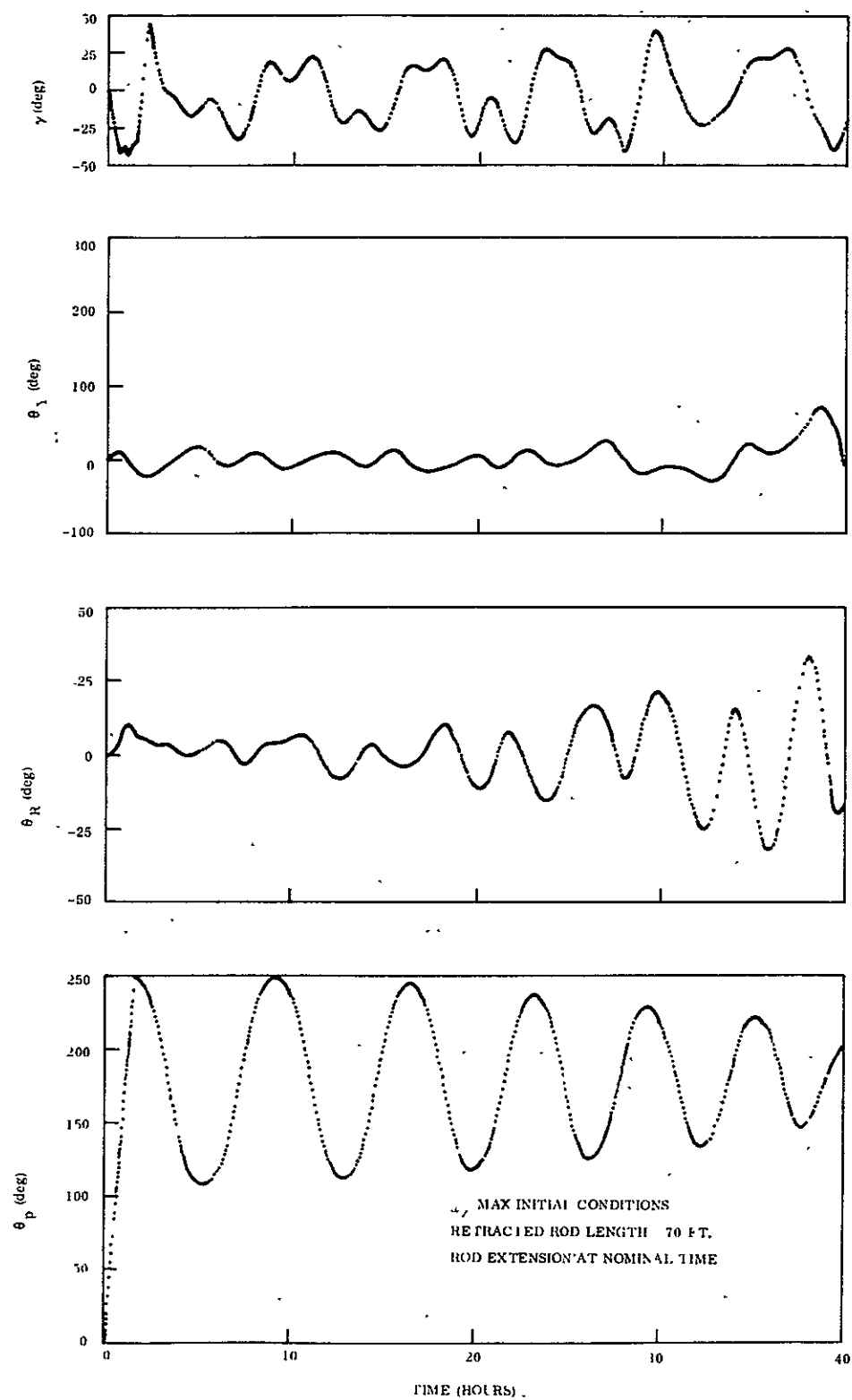
Figure 3.4-32. ATS-A Inversion Maneuver

It should be noted that rod retraction and extension results in large damper cocking torques. The maximum value observed during this study was 48,320 dyne-cm. This torque will cause the eddy current damper to bottom, resulting in loss of damping for the duration of rod extension or retraction. This loss of damping has no significant effect on the maneuver because it occurs for a very short period, approximately 50 seconds. However, the damper must be able to withstand this large torque without being damaged.

3.4.3.2 ATS-D ROD Retraction/Extension Analysis

This section describes a study performed to determine a specific inversion maneuver for ATS-D employing rod retraction and extension. This work closely parallels the ATS-A inversion study described in Section 3.4.2.1. The maneuver was designed to:

1. Minimize vehicle oscillations

2. Be performed on a time basis only in the event pitch attitude data is not available

The pertinent vehicle parameters used in this study are:

1. Nominal Rod Length = 123 feet

2. X-Boom Half Angle = 25.0 degrees

3. Rod Extension and Retraction Rate = 1 ft/sec

As with the ATS-A study, the effects of solar pressure torques or thermal bending of the rods was assumed to be insignificant.

Three sets of initial conditions were used during the study and are listed in Table 3.4-7. The nominal set consists of an undisturbed spacecraft rotating at orbital rate about its pitch axis. The other two sets are taken from a steady state computer simulation after the spacecraft reached steady state conditions. This simulation included the following effects:

1. Sun in the orbit plane .

2. 1000 pole-cm magnetic dipole moment along the roll axis

3. CP-CM displacement of 1 inch along both the yaw and pitch axes

The sets labeled "ω_z min" and "ω_z max" are those for which ω_z reached its minimum and maximum values, respectively.

Table 3.4-7. Initial Conditions

	Nominal	ω_z min	ω_z max
θ_P (deg)	0	-0.2	-0.1
θ_R (deg)	0	-0.4	-0.3
θ_Y (deg)	0	2.8	2.8
γ (deg)	0	4.8	2.0
ω_x (deg/sec)	0	1.662 E-4	-1.278 E-4
ω_y (deg/sec)	0	7.440 E-5	3.724 E-4
ω_z (deg/sec)	0.004178	4.038 E-3	4.307 E-3
$\dot{\gamma}$ (deg/sec)	0	1.290 E-4	-2.566 E-4

The first task in this study was to determine to what length the rod should be retracted. Under nominal initial conditions the maximum value of retracted rod length for which inversion occurs is 80 feet. For this case the spacecraft inertial rate is increased to 2.4 times orbital rate. In the most severe case, using the ω_z minimum initial conditions, the maximum value of retracted rod length for which inversion occurs is also 80 feet.

To accomodate the uncertainty in rod length point out in Section 3.4.3.1, a nominal value of 70 feet was chosen for the retracted length. The effect of rod shortness is considered to be neglible for ATS-D as it was for ATS-A.

3-220

Two computer runs were made for inversion maneuvers in which rod extension is commanded at 390.68 minutes after reaching the retracted rod length. Retracted rod lengths of 65 and 75 feet were used which represent errors of ±5 feet. Initial conditions were chosen to provide the worst case. The "ω_z max" initial conditions were used for retracted rod lengths below nominal and "ω_z minimum" initial conditions were used for retracted rod lengths above nominal. Both inversion maneuvers were successful. However, as expected, large spacecraft pitch oscillations occurred. The maximum amplitude was 64 degrees.

The maximum value of damper cocking torque observed in the ATS-D inversion study was 16070 dyne-cm.

3.4.3.3 ATS-E Rod Retraction/Extension Analysis

The ATS-E spacecraft differs from the ATS-D spacecraft in several ways. From the rod retraction/extension analysis standpoint, the most significant difference is the rate at which the Westinghouse rods extend: 0.5 ft/sec for the Westinghouse rods compared to 1 ft/sec for the nominal ATS-D. The first step in the analysis of ATS-E was to apply the ATS-D timing sequence. Results are presented in Figure 3.4-33. Obviously, the sequence is unsuccessful for the Westinghouse extension rates and a new timing sequence is required. A computer study similar to that performed in Section 3.4.2.2 was planned but was delayed until it was certain that the Westinghouse rods would be available for the flight. By the time the study was reinitiated, the spacecraft had been launched and it became obvious that the study was no longer required. As a result, the analysis was terminated.
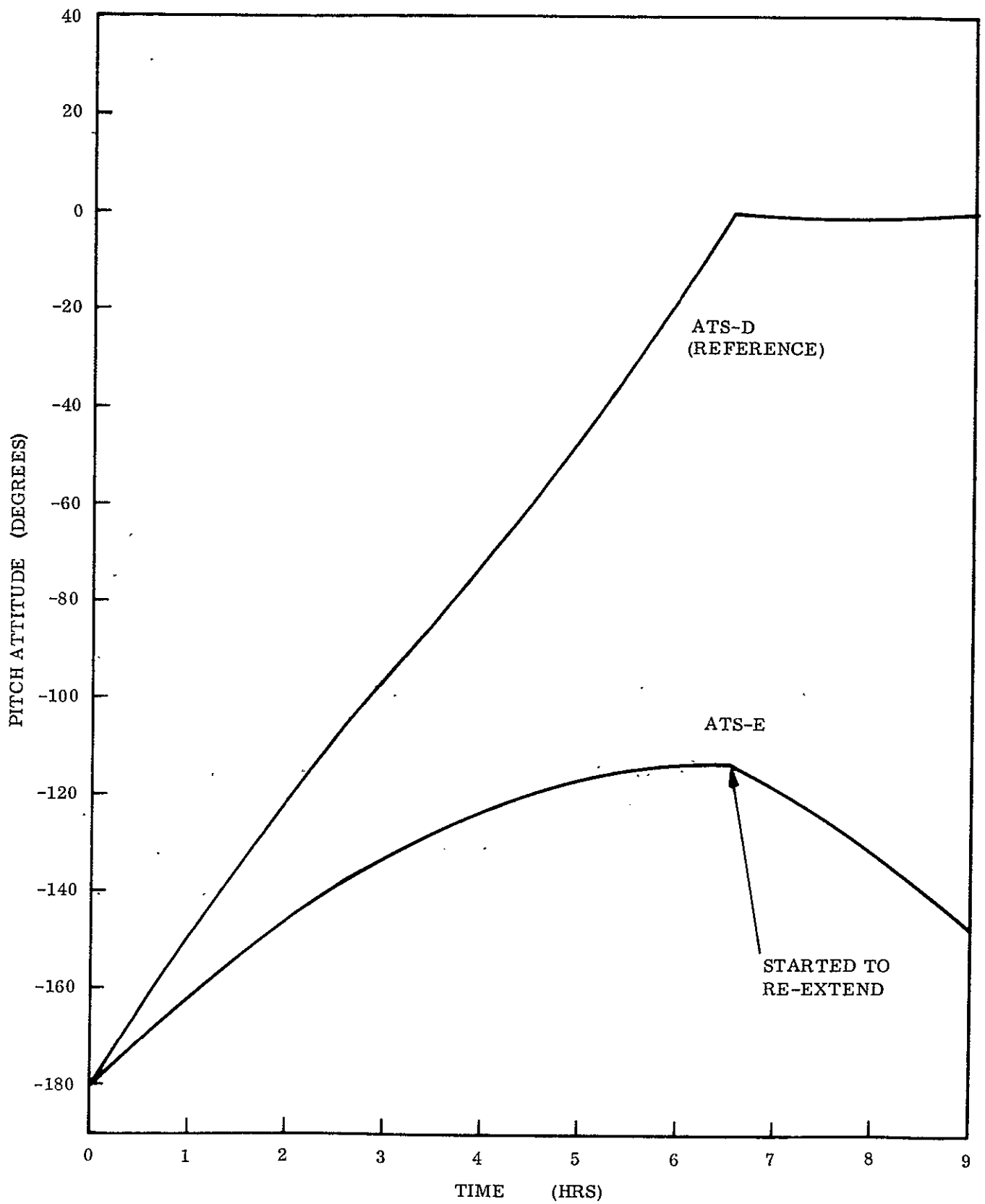
Figure 3.4-33. Unsuccessful ATS-E Inversion Using ATS-D Timing
Sequence

3.5 PERFORMANCE ANALYSIS

The purpose of the ATS series of gravity gradient experiments was to evaluate the performance capability of gravity gradient stabilization subsystems. Part of this evaluation was directed towards comparing the actual flight performance with the performance predicted by analysis during the design and development phase. A performance analysis of the spacecraft was therefore performed which included a performance prediction. Both steady state and transient damping performances were included in the prediction, and all configurations, both nominal and experimental, were evaluated. The experimental configurations are those obtained by "scissoring" the rods to half angles other than the nominal of 25 degrees. The steady state performance was obtained using the procedure originally employed for the second optimization (Section 3.2.2), and identifies and evaluates each error source. For convenience in the performance prediction phase, however, the external torques were assumed to operate on an ideal spacecraft, which had no center of pressure/center of mass offset, no thruster misalignment, perfectly straight rods, etc. The effects of manufacturing tolerances were evaluated separately, combined, and included in the error budgets (Section 3.5.3) as a separate error source. Because error sources due to tolerances are random, their contribution to the performance prediction was approximated by root sum squaring all the individual error sources. This result was then added directly to the error estimates from the external torques. The resulting error budgets include all the known error sources.

Manufacturing tolerances not only affect steady state, but damping and settling time, and this effect was determined analytically. Typically, the effect on damping is determined linearly, in conjunction with the rest of the characteristic equation. The approach, is, of course restricted to small motions, but the results may be considered as representative of the damping, at all spacecraft attitudes.

The following sections contain a brief description of the error sources, their effect on the ATS spacecraft, and an estimate (error budget) of the steady state performance capabilities of the spacecraft.

3.5.1 EXTERNAL DISTURBANCE TORQUES

The majority of the disturbance torques have been discussed in Section 3.2.2 and the definition and description of the torques will not be repeated here. The effect on the optimized spacecraft will be noted in this section, however, as well as the effect of two disturbances (tip targets and internal disturbances) not previously considered. The "ground rules" for the performance prediction are shown in Table 3.5-1. They consist primarily of a standard set of spacecraft and orbit parameters. The original studies assumed ATS-D and ATS-E to be identical. Therefore, results for ATS-D were also considered applicable to ATS-E.

Table 3.5-1. Performance Estimate Assumptions

- Orbit Eccentricity = 0.005 (ATS-A)
                     = 0.000 (ATS-D)

- Magnetic Dipole = 1000 Pole-CM, Z-Axis (ATS-A)
                  = 1000 Pole-CM, Y-Axis (ATS-D)

- Internal Disturbances = 0.2 Deg, All Axes

- Stationkeeping (ATS-D Only)
    - Thrust Level = 10^{-5} Pounds
    - 30 Days On/60 Days Off (Subsystem Errors)
    - 1 - Degree Thrust Vector Misalignment

- Damper Spring Null Shift = 1 Degree

- Surface Properties
    - Boom Reflectivity = 0.85 (Specular)
    - Cylindrical Surface = 0.30 (Specular)
    - Solar Pressure Ring = 0.30 (Specular)
    - Boom Tip Targets = 0.50 (Diffuse) 9-Inch Diameter

- Solar Pressure = 9.65 x 10^{-8} Lb/Ft^2

- Boom Geometry Assumptions (Worst Case, Each Axis)
    - Alignment Error = 1.0 Degree
    - Initial Straightness = 0.5 Ft Env. Rad. at 100 Ft
    - Boom Shortness = 1.80 Ft (ATS-A) - One of Each Pair
                     = 1.64 Ft (ATS-D) - One of Each Pair

- Surface Property Unbalance (Worst Case, Each Axis)
    - Central Body Absorptivity Unbalance = 0.10
    - Boom System Absorptivity Unbalance = 0.10

3.5.1.1 Magnetic Torque

The magnetic dipole of the ATS spacecraft was assumed to be 1000 pole-cm (1 ampere turn-meter^2) oriented on the $\vec{Y}$ Axis (roll) of ATS-A, and the $\vec{Z}$ Axis (pitch) of ATS-D. This magnetic moment was not arbitrary, but was estimated based on the construction of the spacecraft. There was concern, however, that the magnetic moment of the spacecraft would be higher than 1000 pole-cm, and a brief study was undertaken to determine the effect of large magnetic dipoles oriented arbitrarily. The results for ATS-A and ATS-D/E are shown in Table 3.5-2. For ATS-A, the errors are both sinusoidal and constant (bias), and increase with increasing dipole (as would be expected from the discussion of Section 3.2.2.1.1 The magnet orientation which produces the largest pitch error is along the $\vec{Y}$ axis, but the orientation which produces the largest yaw error is along the $\vec{Z}$ Axis. As a worst case, the maximum error in each axis is quoted in the ATS-A error budget (Table 3.5-10) for a 1000 pole-cm dipole.

For ATS-D, due to its synchronized orbit, only the stationary earth's magnetic field was considered. Hence the attitude errors are biases only. The dipole orientation with the largest error is along the Y axis, and the error quoted in the ATS-D error budget (see Table 3.5-11) is for a 1000 pole-cm magnetic dipole located on that axis. ATS-E has the same error (see Table 3.5-12).

During the course of the study, the question of the effect of magnetic dipole on the tip masses arose. The dipoles on the tip masses were 15 pole-cm each for ATS-A, and at 6000 nm and 28 degree orbital inclination, the maximum possible torque about the damping axis due to these magnets is 3.13×10^{-8} lb-ft. The torque may be either sinusoidal (once orbital) or constant, depending upon the orientation of the dipole.

The torques about the other axes are transmitted directly to the spacecraft since the damper boom is constrained in those axes and the magnets produce the same effect as a spacecraft fixed dipole. The maximum pitch and yaw errors occur if the torque is sinusoidal, and the maximum roll error occurs if the torque is constant. The response functions for these cases are (from Figure 3.2-8):

Table 3.5-2.   ATS-A and ATS-D Magnetic Errors

ATS-A Magnetic Errors								
Magnetic Dipole Moment	Dipole Orientation	Pitch		Roll		Yaw	
		Bias	Osc	Bias	Osc	Bias	Osc
(pole-cm)	(Axis)	(Deg)		(Deg)		(Deg)	
1000	X_1	0	0.1	0	0	0	0
5000	X_1	-0.05	0.45	-0.2	0	-0.05	0.55
10,000	X_1	-0.05	0.85	-0.4	0.1	-0.05	1.05
1000	Y_1	0	0.2	0	0	0.55	0.25
5000	Y_1	0	0.8	0	0.1	2.65	1.45
10,000	Y_1	-0.15	1.45	0	0.2	5.25	2.85
1000	Z_1	0	0.1	0	0	0	1.1
5000	Z_1	-0.05	0.55	0	0.2	-0.25	5.25
10,000	Z_1	-0.1	1.1	0	0.4	-0.6	10.0

ATS-D Magnetic Errors				
Magnetic Dipole Moment (Pole-cm)	Dipole Orientation (Axis)	Pitch (Deg)	Roll (Deg)	Yaw (Deg)
1000	X_1	0	0	0
5000	X_1	0	-0.1	0
10,000	X_1	0	-0.2	0
1000	Y_1	0	0	0.3
5000	Y_1	0	0	1.5
10,000	Y_1	-0.1	0	2.9
1000	Z_1	0	0	0
5000	Z_1	0	0	-0.2
10,000	Z_1	0	0.1	-0.3

$$\theta_P / (T_D/I_D\omega_o^2) = 0.064$$

$$\theta_R/(T_D/I_D\omega_o^2) = 0.035$$

$$\theta_Y/(T_D/I_D\omega_o^2) = 0.57$$

where

$\theta_{P,R,Y}$ = pitch, roll and yaw attitude error (rad)

T_d = damper torque (lb-ft)

I_d = damper moment of inertia (slug-ft^2)

ω_o = orbital rate (rad/sec)

The errors (with a damper moment of inertia of 231 slug-ft^2) are 0.006 degree in pitch, 0.0035 degree in roll, and 0.05 degree in yaw.

If the torques are normal to the damping axis, the effect is to increase the effective dipole of the spacecraft from 1000 pole-cm to 1030 pole-cm resulting in an increase in the magnetic error of 3 percent. The pitch error would increase 0.006 degree, and the yaw error would increase 0.03 degree. As a consequence, the worst errors are those when the torques are about the damping axis. In neither case were the errors large enough to record on the ATS-A error budget.

The physical effect of these torques on the damper was also checked and is negligible. The torque of 3.13×10^{-8} lb-ft is 0.425 dyne-cm. This would result in a damper boom offset (for a constant torque) of 0.02 degree based upon a damper spring capability of 21 dyne-cm/deg. The cocking torque capability of the damper is 2500 dyne-cm at an angular offset of approximately 20 minutes. This provides an average spring constant of 2500 dyne-cm/deg. The magnetic torque will cause an angular displacement of 5.6×10^{-5} degrees. The magnetic forces are negligible.

An additional magnetic study was performed for ATS-E, assuming a 1000 pole-cm dipole located on the damper boom. The large dipole would have been the result of using a motorized deployment mechanism in place of the currently employed self-extending rod on the ATS-D damper boom. The large magnetic dipole is created by the use of nickel cadmium batteries for the deployment mechanism. It was felt that the torque created by the dipole could significantly alter the damping and steady state characteristics of the gravity gradient stabilization subsystem.

To accurately evaluate the effect of this large dipole, the magnetic field at synchronous altitude had to be more accurately modeled. The magnitude of the field (150 gamma) is not significantly different from that calculated based on a pure dipole model of the earth, but the direction of the field is changed drastically by the magnetic effects of the sun. For the purposes of analysis, the direction was assumed to be arbitrary.

As a conservative estimate, the magnetic field strength was assumed to be 300 gamma $(300 \times 10^{-5}$ oersted). The torque on the damper boom due to the 1000 pole-cm magnetic dipole is 3 dyne-cm. If the unit vector is normal to the damping axis torque, the torque appears as a cocking torque on the combination passive damper. The maximum value of the torque is 3 dyne-cm compared to the cocking torque capability of 1200 dyne-cm. There should be no structural difficulty, therefore, and the only other effect of the dipole in this orientation would be an attitude error on the spacecraft. From previous work, the maximum error would be on the order of 0.3 to 1.3 degrees, depending upon the frequency of the field variation and its strength.

If the 3 dyne-cm torque is along the damping axis, it may add or subtract from the spring constant built into the damper. The linear spring constant associated with 1000 pole-cm is approximately 0.05 dyne-cm/deg which is slightly less than 2 percent of the nominal spring constant of 3.5 dyne-cm/deg. The actual spring constant on ATS-E is 3.99 dyne-cm/deg and adding or subtracting 0.05 dyne-cm/deg keeps it within the desired table tolerance of $3.5 \begin{smallmatrix} -0 \\ +20\% \end{smallmatrix}$, although somewhat on the high side. No difficulty is anticipated from this effect.

The other effect of the dipole in this orientation is to excite the damper boom as the magnetic field fluctuates. Assuming the maximum torque (3 dyne-cm) occurs at the frequency with the highest sensitivity (0.75 orbital), the peak error is 4.4 degrees in yaw. Pitch and roll errors would be 1.7 degrees (if excited at 1.3 orbital) and 0.75 degree (if excited at 2.0 orbital), respectively. The most likely disturbance torque frequency is orbital, however, and at this frequency the yaw error would be 2.5 degrees and the pitch error would be 0.26 degree. If the torque is constant, the pitch and roll errors would be on the order of 0.1 degree.

These error values have been obtained assuming a magnetic field of 300 gamma, arbitrarily located, and varying sinusoidally at arbitrary frequencies. While there is a certain amount of randomness to the field, this represents an extreme case, and the actual errors would probably be much less. An order of magnitude decrease may be conceivable.

The errors resulting from this source are not included in the ATS-E error budget since the deployer for the damper booms on ATS-E was not changed.

3.5.1.2 Solar Torque and Thermal Bending

The estimates of the errors induced by solar torque and thermal bending were obtained by computer simulation, assuming the spacecraft to be perfect. Perfection requires all rods to be the same, the spacecraft body to be perfectly balanced (no CP/CM misalignment), straight rods, etc. The error estimates obtained from this simulation will be less than the errors obtained for the optimization (Section 3.2.2.1.3) since the CP/CM misalignment is not included. The center of mass does "wander" as a result of thermal bending however, and this effect is included in the results. As indicated in Tables 3.5-10, 3.5-11 and 3.5-12, the errors resulting from solar torque and thermal bending are primarily oscillatory. The errors are shown for two sun positions.

3.5.1.3 Tip Target Solar Torque

One of the experiments performed on the ATS spacecraft was to use a television camera to determine the motion of the gravity gradient rod under the influence of thermal bending.

To determine the motion of the tip of the rod, a 9-inch diameter target (of very small thickness) was attached to the end of each rod with the target facing the spacecraft. The solar torques on these tip targets were calculated for ATS-D assuming the sun was at the winter solstice, and the absorptivity and diffuse reflectivity of the targets were both 0.5. The torques on each axis, the frequency of the torques, and resulting attitude errors are shown in Table 3.5-3. The result of combining the torques (with attention to phasing of the individual torques and the responses) is shown in the ATS-D error budget (Table 3.5-11).

Table 3.5-3. Errors Due to Tip Targets

Torque (Dyne-cm)	Axis	Frequency (X Orbital)	Pitch Error (Deg)	Roll Error (Deg)	Yaw Error (Deg)
2.11	X (Yaw)	1	0.1	0.1	1.0
6.60	Y (Roll)	1	0.1	0.1	0.3
7.75	Z (Pitch)	1	0.2	0.1	0

The effect of solar pressure on ATS-A was determined by scaling the results obtained for ATS-D.

3.5.1.4 Orbit Eccentricity

It is pointed out in Section 3.2.2.1.4 that the response to orbit eccentricity is dependent only upon the non-dimensional parameters and the orbit eccentricity. Since ATS-A and ATS-D have essentially the same non-dimensional parameters, their response to orbit eccentricity is identical. Only ATS-A has an orbit eccentricity error, however, because ATS-D is synchronous, and the orbit is trimmed to remove any eccentricity. The maximum eccentricity for ATS-A was estimated to be 0.005 based upon updated booster characteristics. The resulting errors are shown in the ATS-A error budget, Table 3.5-10. The errors are lower than those obtained for the optimization since the updated eccentricity estimate was less than the eccentricity value used for the optimization.

3.5.1.5 Internal Disturbances

Several experiments placed aboard the ATS spacecraft were known to have rotating or scanning parts. Movements of components within the spacecraft can significantly affect the performance of a gravity gradient spacecraft since the angular momentum caused by the motion will interact with the angular momentum of the spacecraft. Consequently, the effect of these components should be evaluated. The components were not adequately defined for analysis, however, and an upper limit was placed on the allowable error. The maximum was 0.2 degree on all axes.

3.5.1.6 Stationkeeping Errors

ATS-D/E has two stationkeeping thrusters nominally located on the roll axes of the spacecraft. For perfect alignment of the thruster and no center of mass/center of geometry offset, the attitude error due to stationkeeping is the result only of center of mass wander due to thermal bending. The magnitude of the resultant error is a function of the distance the center of mass moves and the pulsing frequency of the stationkeeping thruster. The original optimization studies (see Section 3.2.2.1.5) assumed a constant thrust of 0.5×10^{-5} pounds, half the maximum value. The constant thrust approach was an ideal case, but provided a basis of comparison for evaluating configurations. Subsequent to the optimization, it was determined that a constant thruster could not be employed for this mission, and a pulsing mode of operation would be necessary. To reduce the errors associated with pulsing, it was necessary to select a pulsing frequency more compatible with gravity gradient stabilized vehicles. To determine the optimum frequency, use was made of the frequency response diagrams (Section 3.2.2). The "square wave" pulse train of the thruster was approximated by a constant torque equal to one-half the peak thruster torque and a sinusoidal torque of one-half the peak torque. The peak torque was obtained from the analysis contained in Section 3.2.2.1.5, and includes thruster errors resulting from thermal bending, rod misalignments, etc. With this simplification, the principle of linear superposition can be applied in conjunction with the frequency response characteristics, and an estimate of the pitch, roll and yaw errors obtained.

Figure 3. 5-1 represents the estimated attitude errors as a function of pulsing frequency. This is the response of the system due only to yaw torques. There will be pitch and roll thruster torques, but they should result in small errors, particularly at high frequencies. The curves have been smoothed in the range of zero to twice orbital forcing frequency, because higher frequencies would normally be selected, and the local hills and valleys are of no concern. It is evident from Figure 3. 5-1, that frequencies higher than twice orbital produce small errors. In the limit, the yaw error would be approximately 5. 5 degrees, and the pitch and roll errors would be zero. The approach to this limit is quite rapid and negligible pitch and roll errors occur beyond forcing frequencies four times orbital. At this point, the estimated yaw error is 5. 7 degrees, only 0. 2 degree higher than the minimum. In view of the difficulties associated with high frequency pulsing (per telephone discussions with NASA/Goddard), and the limited improvement in pointing accuracy, a pulsing frequency of four times orbital was recommended as a minimum. The relative insensitivity of spacecraft performance to this frequency eases the tolerance requirement on the pulsing.

The analysis from which the frequency response characteristics were obtained is a linearize small angle approximation and is the response to a sinusoidal disturbance. As mentioned previously, the thruster more closely approximates a square wave, and the conclusions draw from the analyses were verified by simulation. Figure 3. 5-2 shows the performance as determined by simulation for the selected pulsing frequency and a 50 percent duty cycle. The peak yaw error is 6. 3 degrees, slightly higher than estimated. Yaw shows two characteristi frequencies. The first one is approximately four times orbital with an amplitude of 0. 3 degree agreeing closely with that predicted. It also, however, has a beat of approximately 0. 3 degree amplitude, at orbital frequency, which may be due to the pitch excitation.

As further verification of the approximation, two additional runs were made: one at twice orbital frequency (6 hours on, 6 hours off) which is the roll natural frequency, and one at 0. 76 orbital (the yaw natural frequency). Figures 3. 5-3 and 3. 5-4 show the results.
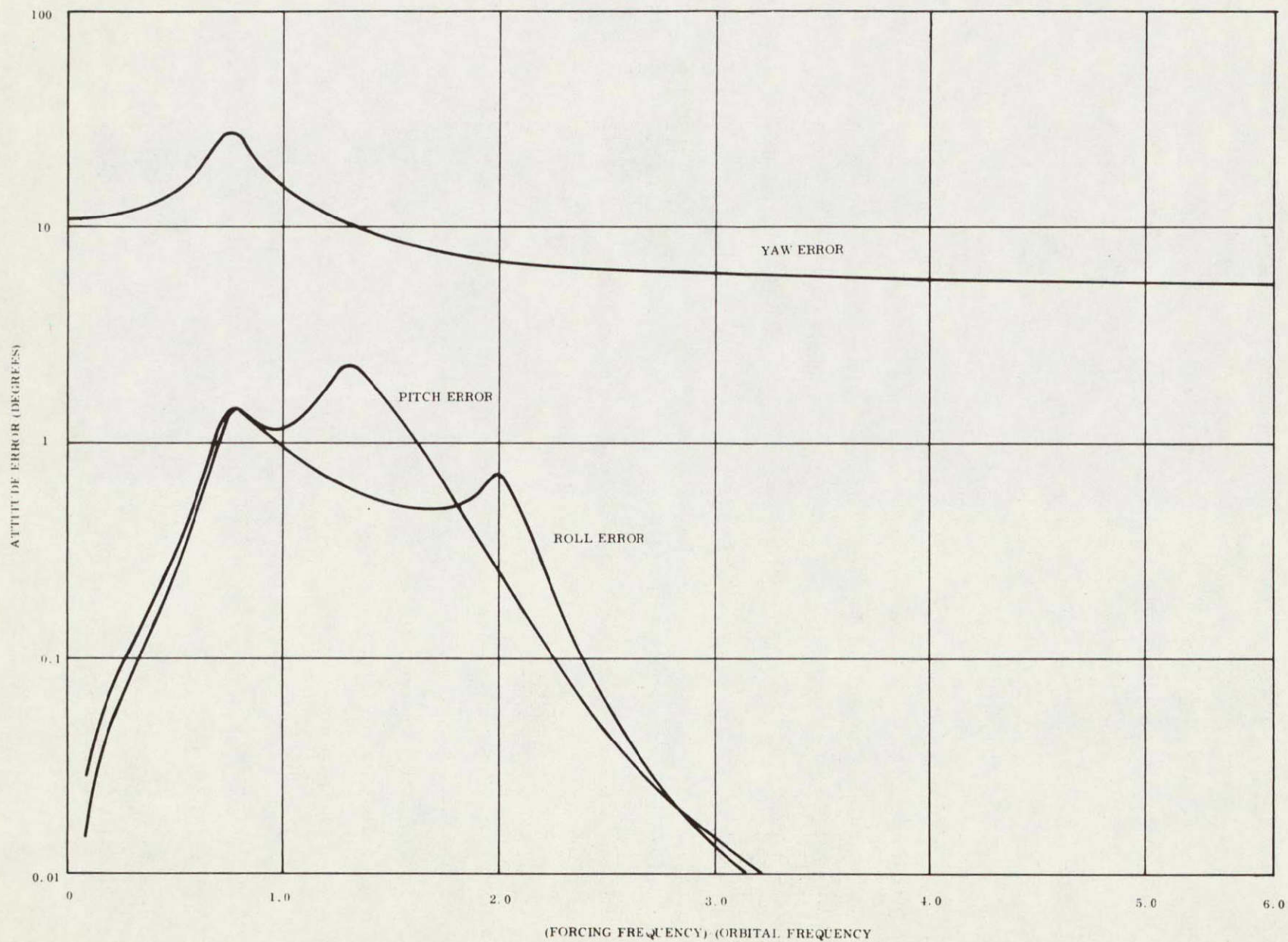
Figure 3.5-1.   ATS-D Attitude Errors for Stationkeeping Thruster

Figure 3.5-2. Effect of Thruster on ATS-D

PULSING MODE 6 HRS ON – 6 HRS OFF (2 x ORBITAL)
NO DISTURBANCES EXCEPT THRUSTER
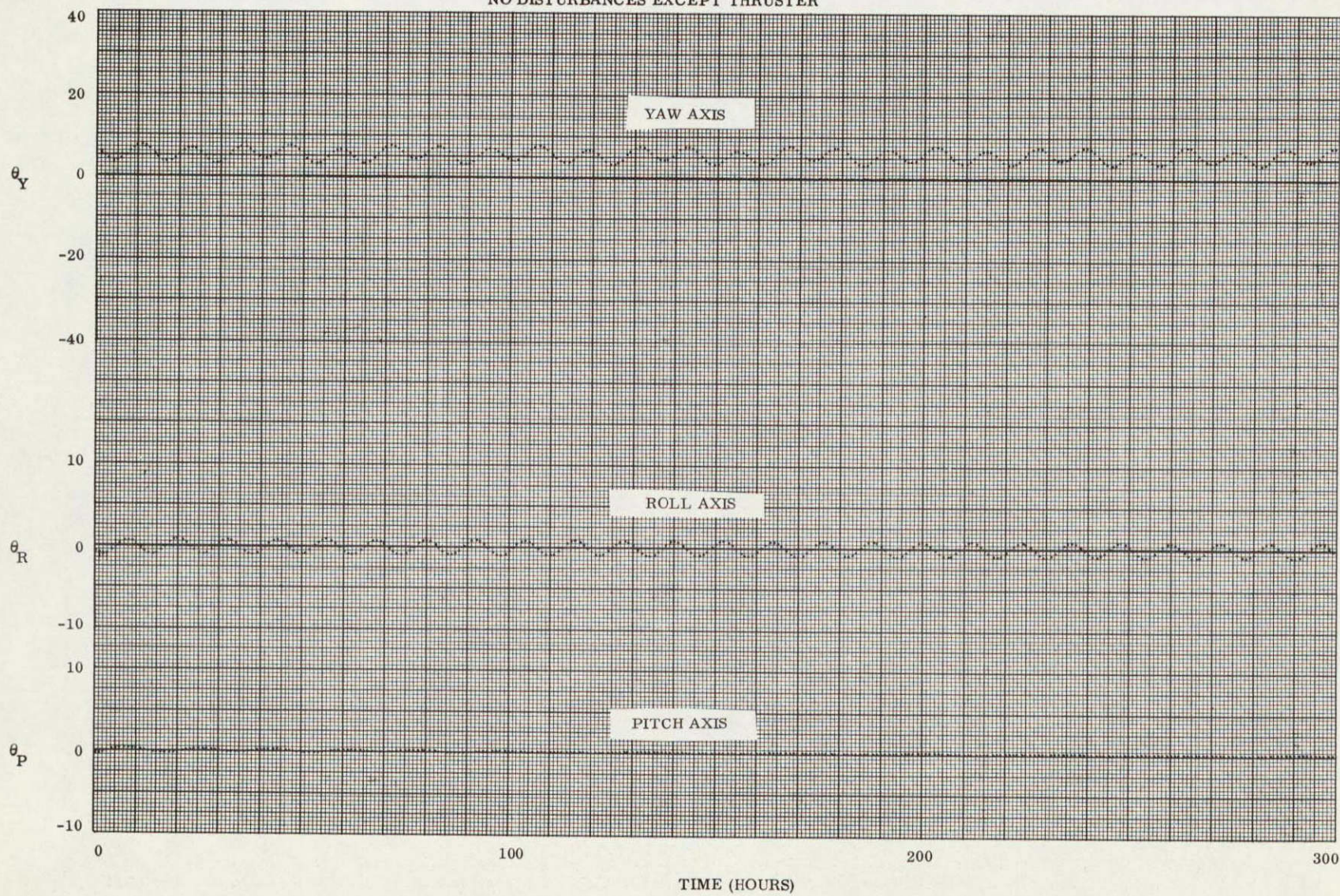
Figure 3.5-3. Effect of Thruster on ATS-D

PULSING MODE 4.87 HRS ON - 4.87 HRS OFF
NO DISTURBANCES EXCEPT THRUSTER
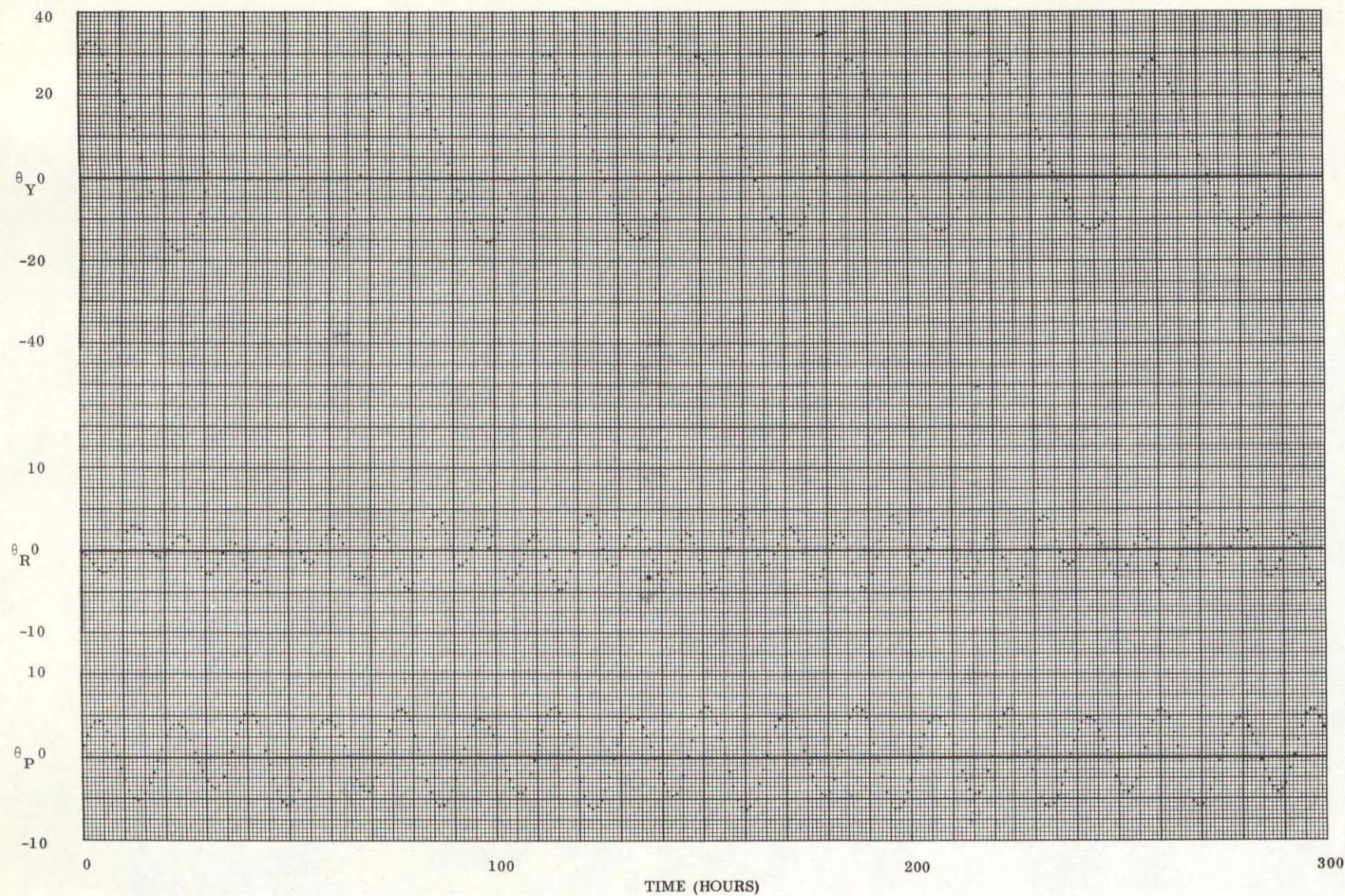
Figure 3.5-4. Effect of Thruster on ATS-D

Table 3. 5-4 shows the estimated values from the frequency response, and the values obtained from simulation. These agree reasonably well in spite of the approximation and linearization. The 3-hour on, 3 hour off cycle was therefore recommended.

Table 3. 5-4. Error Comparison

Frequency (X Orbital)	Pitch Error		Roll Error		Yaw Error	
	Estimated	Actual	Estimated	Actual	Estimated	Actual
0. 76	1. 4	6..0	1. 4	4. 5	27. 5	29
2	0. 25	≈ 0	0. 72	1	7	8
4	≈ 0	0. 1	≈ 0	0. 3	5. 7	6. 3

As the stationkeeping thruster neared completion, it became evident that even a 3-hour on, 3-hour off, cycle could not be employed. After reviewing the capabilities of the thruster, and the stationkeeping requirements, a duty cycle of 36 days on, 60 days off, was selected. The errors shown in the ATS-D error budget (see Table 3. 5-11) were determined by computer simulation and represent the steady state errors with no tolerance effects. Peak errors when the thruster is first turned on, will be approximately twice as high as those shown.

3. 5. 2 TOLERANCES, UNCERTAINTIES, AND VARIATIONS
The preceding section evaluated the effects of external and internal disturbances as though the spacecraft were perfect. Manufacturing limitations, however, prevent a perfect spacecraft from being constructed, and there will be departures from the ideal in many areas. The effect of these tolerances and uncertainties on the spacecraft performance were evaluated in terms of the maximum possible attitude error they can induce, and their influence on transient damping.

3.5.2.1 <u>Transient Performance Effects</u>

Manufacturing tolerances affect not only steady state performance, but transient damping as well. The optimization presented in Section 3.2.2.2 defined five parameters which affect damping performance:

1. Damping coefficient

2. Spring constant

3. Moment of inertia of the secondary boom (I_d)

4. Moment of inertia of the spacecraft (I_p)

5. Angle (ϕ) between the X rod plane and damper.

The primary effect of manufacturing tolerances is to alter these parameters indirectly. It is convenient to ignore evaluation of each individual tolerance, however, and consider only general variations of the five parameters. This can be accomplished by using the solution of the characteristic operation as discussed in Section 3.2.2.2. These solutions provide natural frequencies, and damping time constants for the system for small amplitude motion. The damping time constant quoted here and in Section 3.2.2.2 is the time constant of the least-damped mode. In performing the analysis, the effect of spring constant, damping coefficient, spacecraft moment of inertia and orientation angle were determined directly by individually adjusting the specific non-dimensional parameter. However, the damper moment of inertia (I_d) appears in three of the non-dimensional parameters, and they were all adjusted simultaneously.

Figures 3.5-5, 3.5-6, 3.5-7, 3.5-8 and 3.5-9 present the percentage variation in system damping as a function of percentage variation in parameter. As mentioned previously, the analysis applied only to small amplitudes, but experience has shown that the values are good indicators of the relative damping performance of the system during large amplitude oscillations. The fact that the optimization is of a "spike type" (Section 3.2.2.2) is readily apparent from the pointed nature of the curves at the origin. The change in slope is real and is not the result of the method of plotting.

3-238
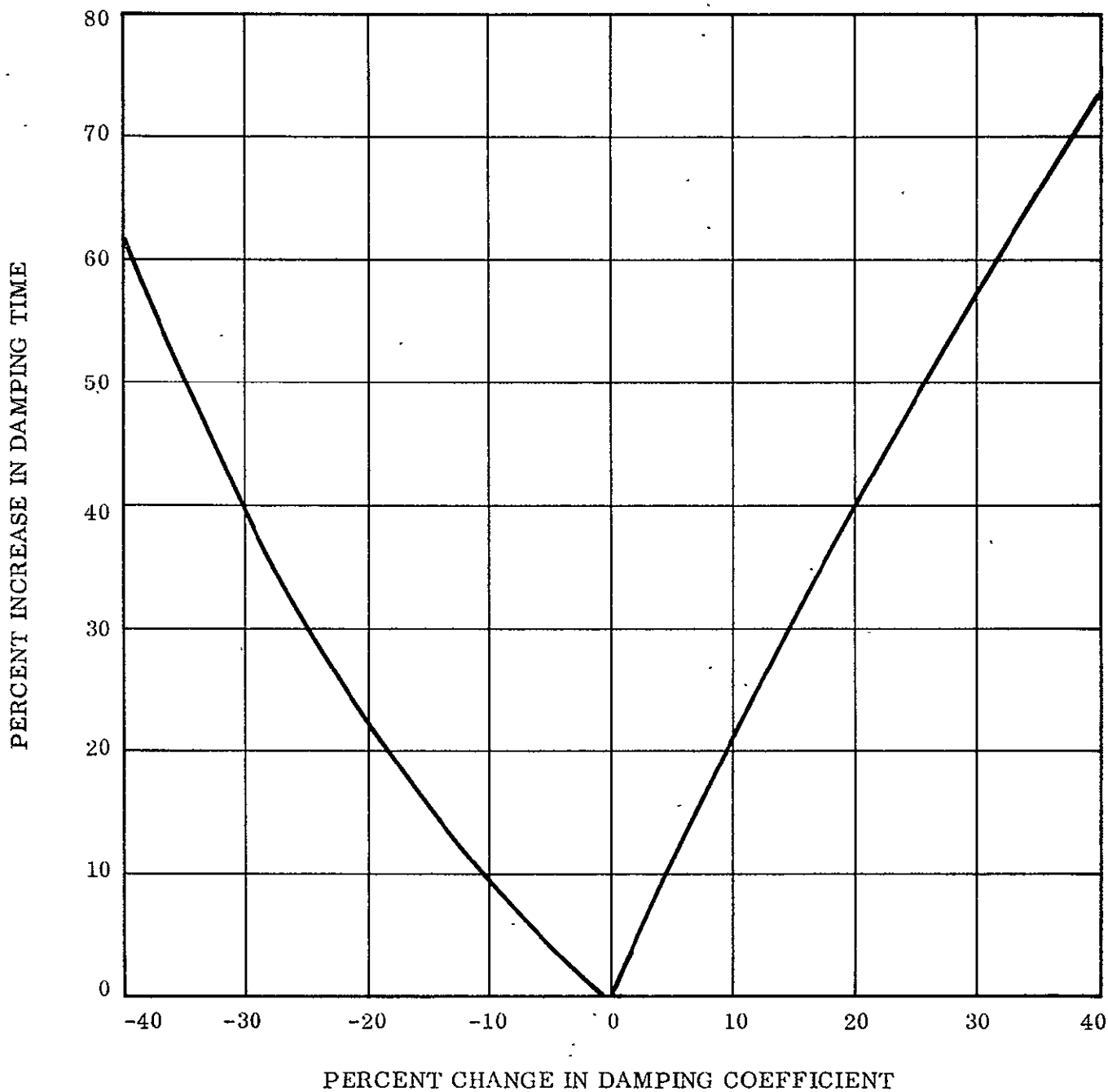
Figure 3. 5-5. Effect of Damping Coefficient on System Damping for Least-Damped
Mode of ATS-A and D
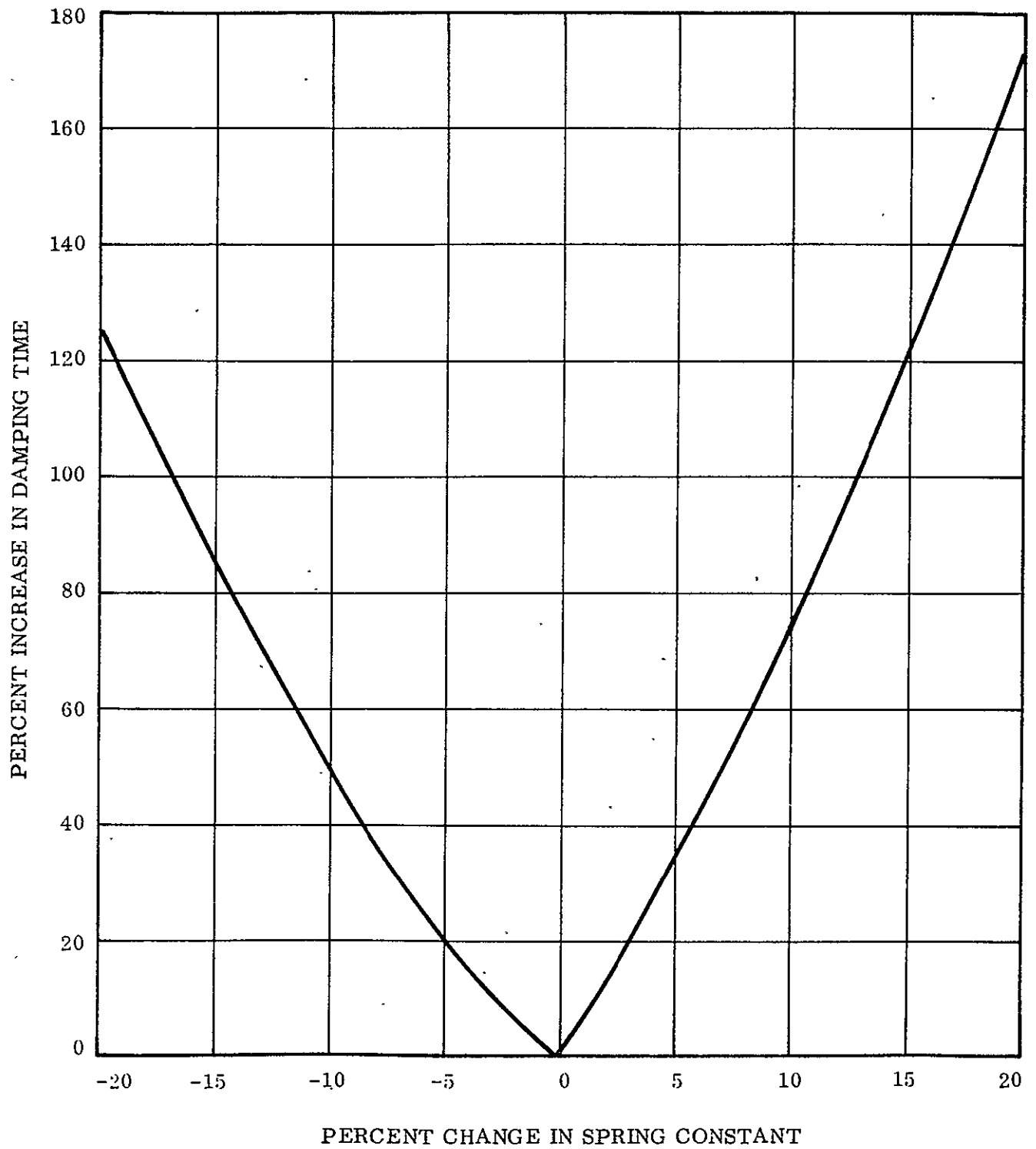
Figure 3.5-6. Effect of Spring Constant on System Damping for Least-Damped
Mode of ATS-A and D
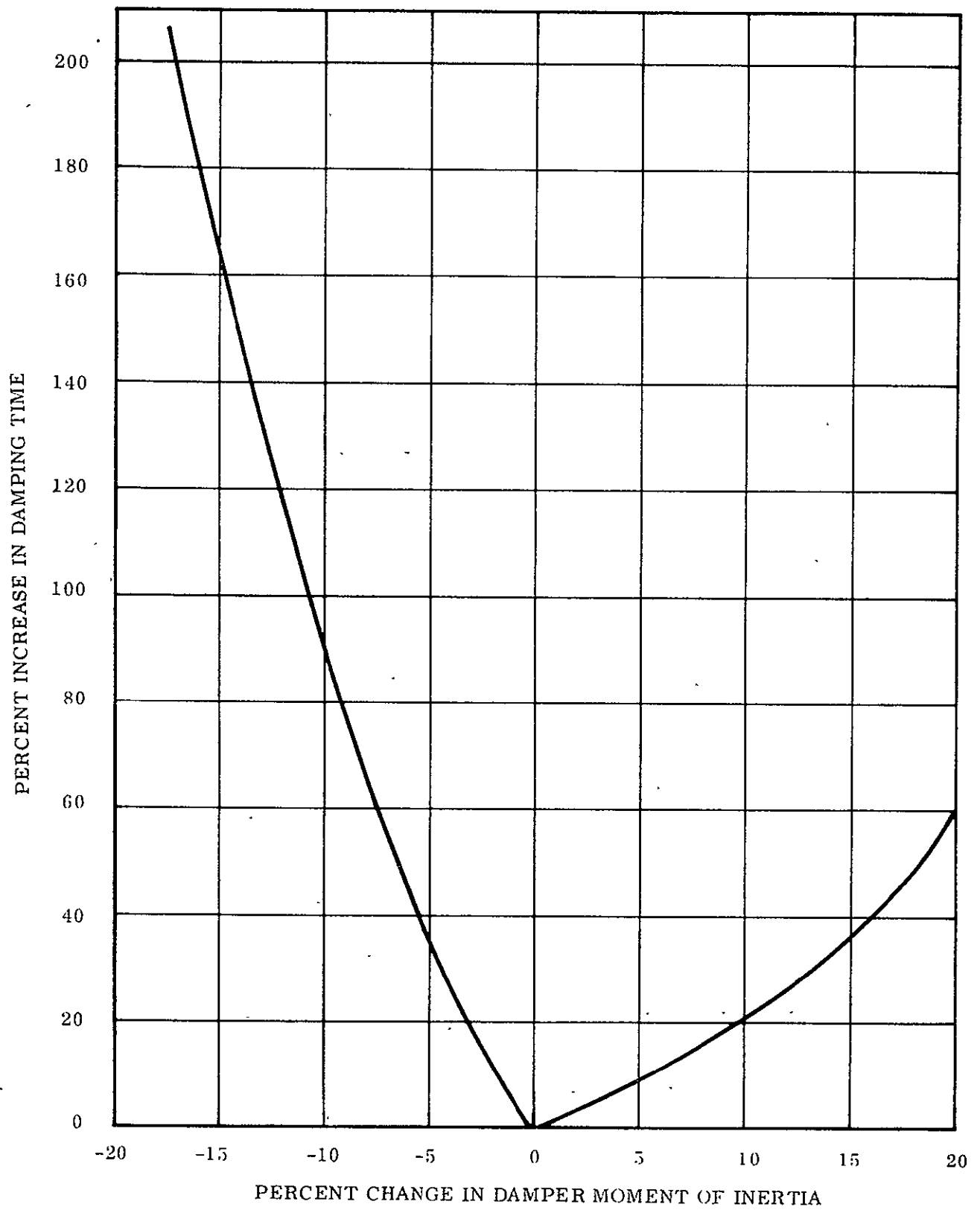
Figure 3. 5-7.   Effect of Damper Moment of Inertia on System Damping for Least-Damped
Mode of ATS-A and D
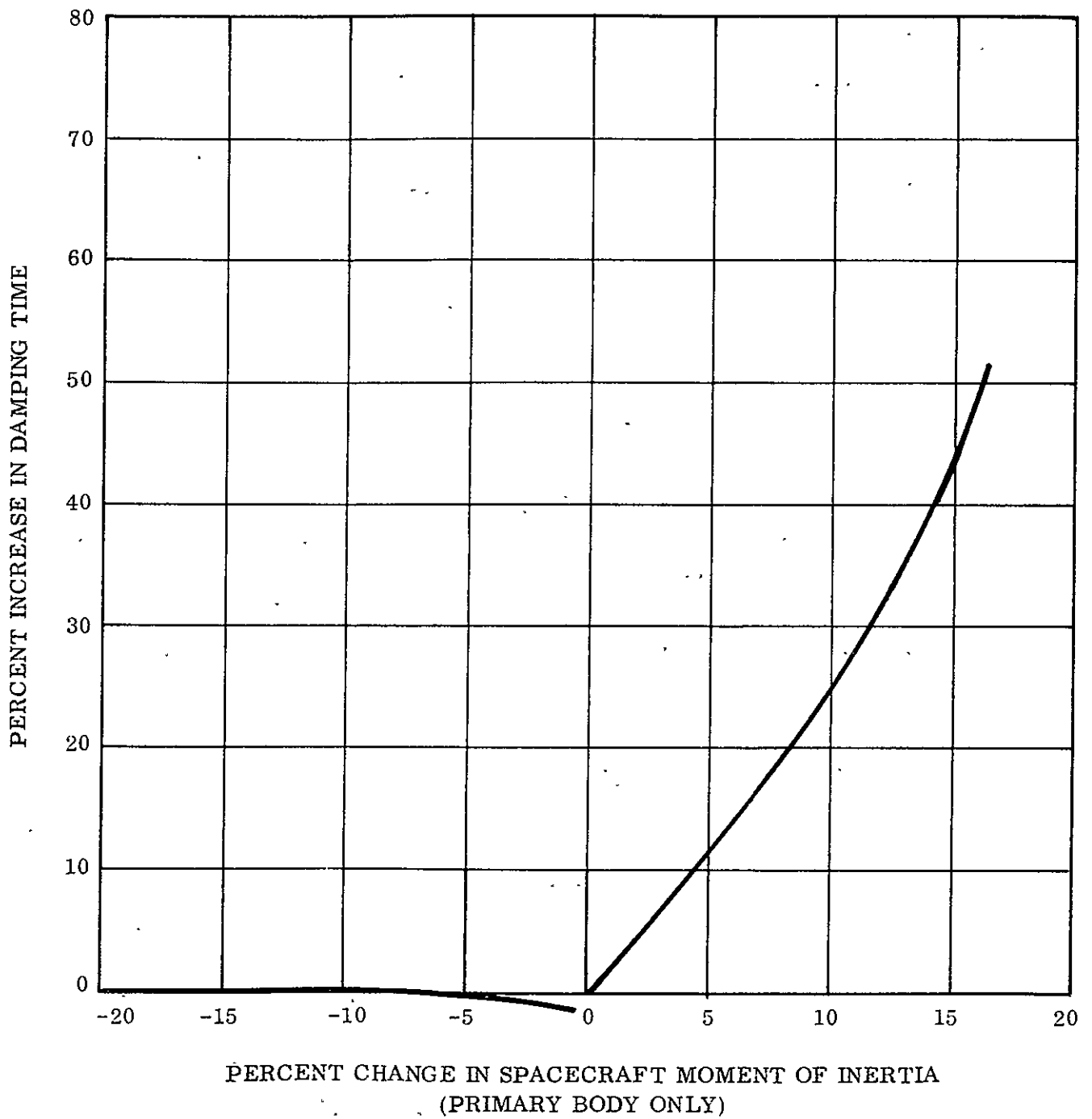
Figure 3. 5-8. Effect of Spacecraft Moment of Inertia on System Damping for
Least-Damped Mode of ATS-A and D
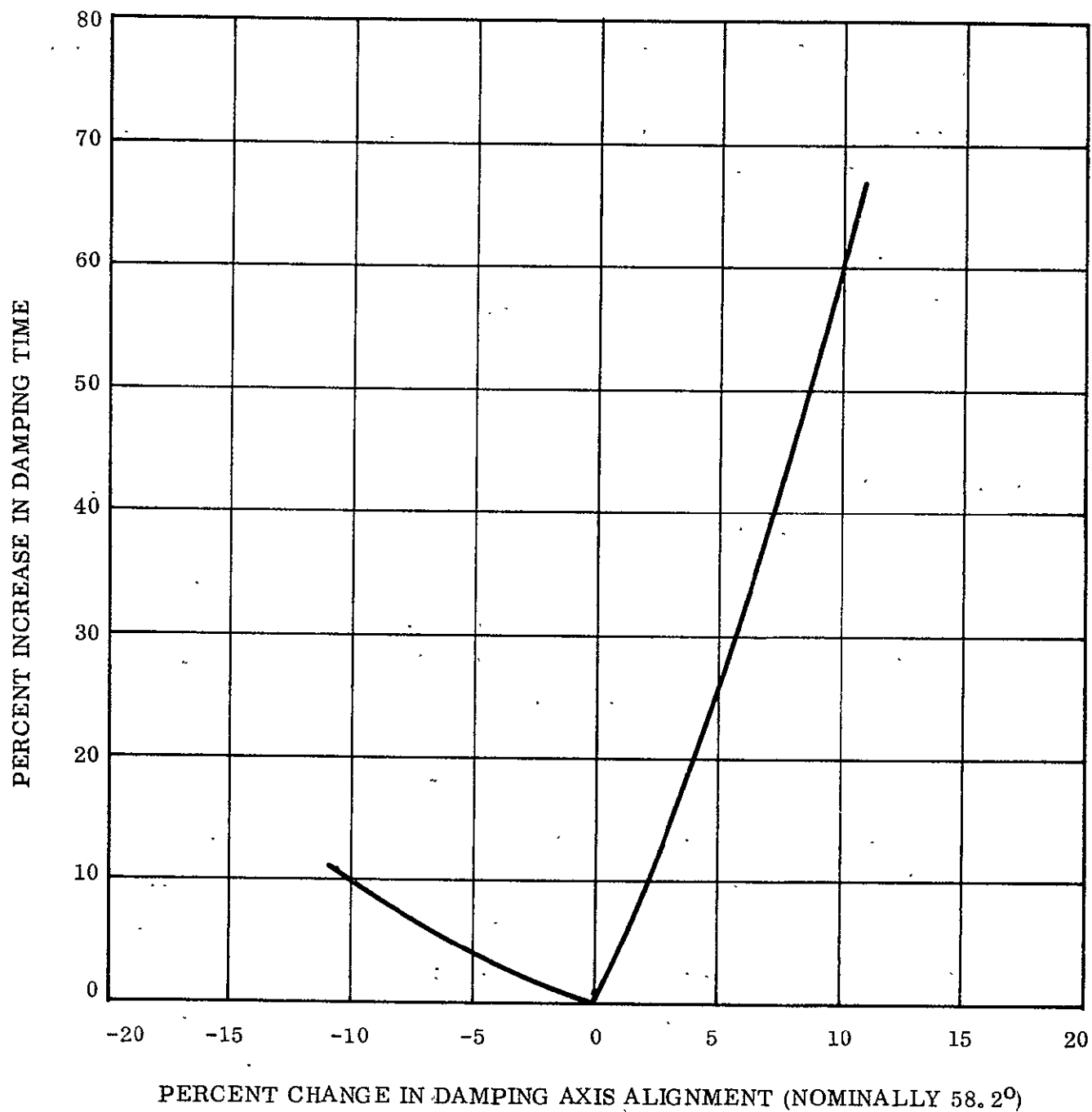
Figure 3.5-9.   Effect of Damping Axis Alignment on System Damping for
Least-Damped Mode of ATS-A and D

For the nominal system, only the variations allowed by specification are of concern. The variation in the damping coefficient is by specification, ± 40 percent (15 percent manufacturing tolerance, and 25 percent temperature effects). The effect on system damping is a 74 percent increase in damping time (at worst) as shown in Figure 3.5-5. The allowable spring constant variation is also by specification, -0, $+20$ percent. The effect of ± 20 percent has been evaluated and the results as shown in Figure 3.5-6, indicate a 175 percent increase in damping time.

There is no specific allowance on the damper boom moment of inertia, but a tip mass tolerance of ± 0.05 pound, and the rod length tolerance of $\pm 1/8$ feet allowed by specification would result in a worst case damper boom moment of inertia variation of 0.3 percent. The plot shown in Figure 3.5-7 indicates a negligible effect.

Variations in the moments of inertia of the primary system (i.e., the X rods) will also cause variations in damping performance. With a ± 0.05 pound tolerance on the tip weights, and a ± 2 feet uncertainty in the length of two of the four rods, the moment of inertia of the primary system will vary 1.6 percent producing a 3 percent increase in damping time (Figure 3.5-8). The tolerance on the alignment of the damping axis (Figure 3.5-9) is ± 15 minutes, and produces a negligible effect.

3.5.2.2 Steady State Effects

The primary effect of manufacturing tolerances and uncertainties on the steady state performance is to induce external torques and shift the principal axes. The principal axis shift causes the spacecraft to "fly" in a biased position, with its principal axes along the orbiting reference frame. Because the attitude of the spacecraft is measured with respect to the reference axes (which are no longer the principal axes), an attitude error appears.

The torques created by manufacturing tolerances are largely "solar" for ATS-A and D/E and "thruster" for ATS-D/E. The gravity gradient rods are the largest sources of error in this respect and the rod tolerances are put into four categories for convenience:

1.   Rod length variations

2.   Rod envelope variations

3.   Rod alignment variations

4.   Solar Absorptivity variations.

Two of these tolerances, rod envelope variations and rod alignment were felt to be impor
ant enough to be included in the stationkeeping Section (3. 2. 2. 1. 5) of the optimization
(3. 2. 2. 2).   Much of the work on these two sources was performed for the analysis con-
tained in that section, and is utilized in the following sections.   The work has been ex-
panded to include solar torque on the toleranced rods.

The misalignment of the stationkeeper is another major source of torque which was incluc
in the optimization.   A more general study than that previously performed is included in
Section 3. 5. 2. 2. 7.

3. 5. 2. 2. 1 Gravity Gradient Rod Length Variations

The gravity gradient rod specification requires that when one rod of the primary pair
reaches its fully extended length (150 feet) the other rod of the pair must be within 2 feet
of it.   Because there are two pair of rods on the spacecraft, the specification permits two
rods to be shorter than the other two.   Depending upon which rods are short, the principa
axes can shift, the center of mass can shift (with respect to the spacecraft), or both.
Figure 3. 5-10 illustrates all three possibilities.   Configuration (a) of Figure 3. 5-10 has r
principal axis shift, but the center of mass of the spacecraft, as well as the center of sol;
pressure are shifted downwards.   Consequently, a pitch solar torque and a pitch thruster
torque (ATS-D/E) are created.   Configuration (b) has a large principal axis shift, but no
appreciable center of mass shift.   There is a yaw induced solar torque.   Configuration (c)
has both a center of mass shift and a principal axis shift, although both are of less
magnitude than those of previous configurations.

CM SHIFT NO PA SHIFT	PA SHIFT NO CM SHIFT	PA AND CM SHIFTS
(a)	(b)	(c)

KEY   PA = PRINCIPAL AXIS
CM = CENTER OF MASS
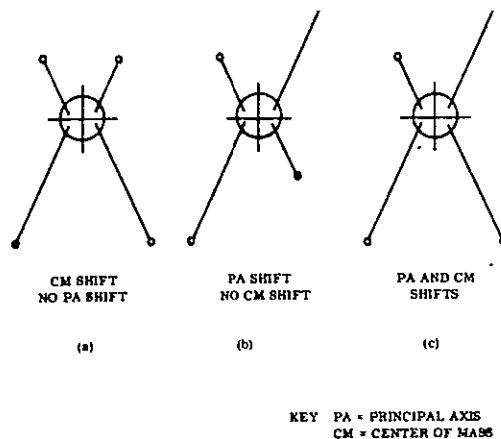
Figure 3. 5-10.   Gravity Gradient Rod Length Variations

Figures 3. 5-11 and 3. 5-12 show the yaw and pitch errors resulting from principal axes shifts. No roll errors were caused. The most significant error is the pitch error. Assuming that the variation in rod length is linear with length, the maximum variation for a 124. 33 foot rod is 1. 66 feet. If two rods are short by 1. 66 feet, one up and one down as shown in Figure 3. 5-10b, a 0. 5 degree pitch error results. A computer run was made to verify the pitch error, as well as the yaw error, and both errors were verified.

Figure 3. 5-13 and 3. 5-14 show the yaw and pitch errors resulting from CM shifts. No roll errors are caused. Thruster forces of 0. 5 and 1. 0 x 10^{-5} pounds were assumed.

The maximum pitch errors caused by principal axis shift and CM shift cannot exist simultaneously. However, both yaw errors can exist simultaneously. The yaw error caused by principal axis shift is always negative. Therefore, whether the two yaw errors add or subtract depends upon the directions of the thruster force vector and the CM displacement. The principal axis shift and the thruster errors for the short rods are:

3-246
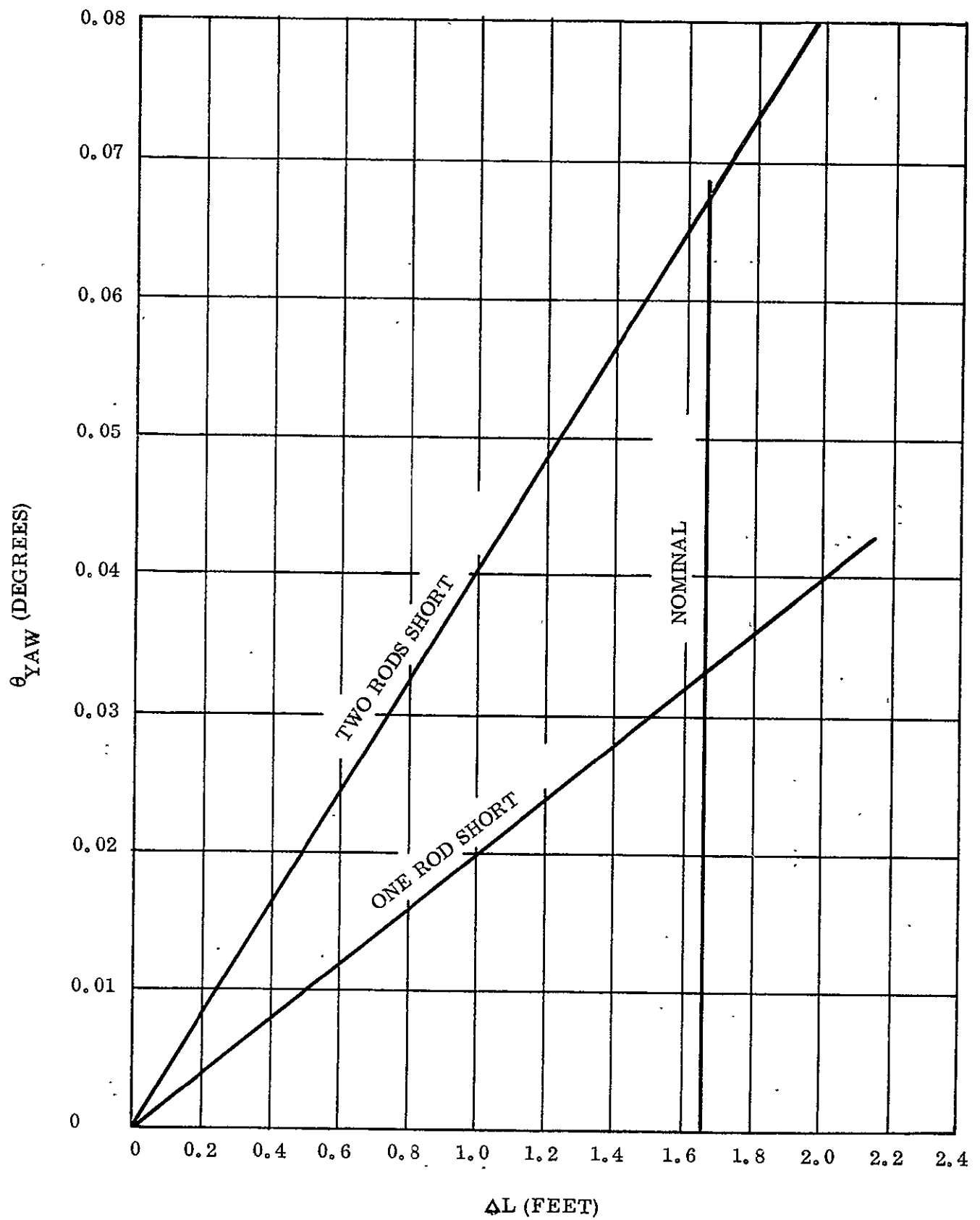
Figure 3.5-11. Yaw Error Caused by Principal Axes Shift Resulting from
Short Primary Rods
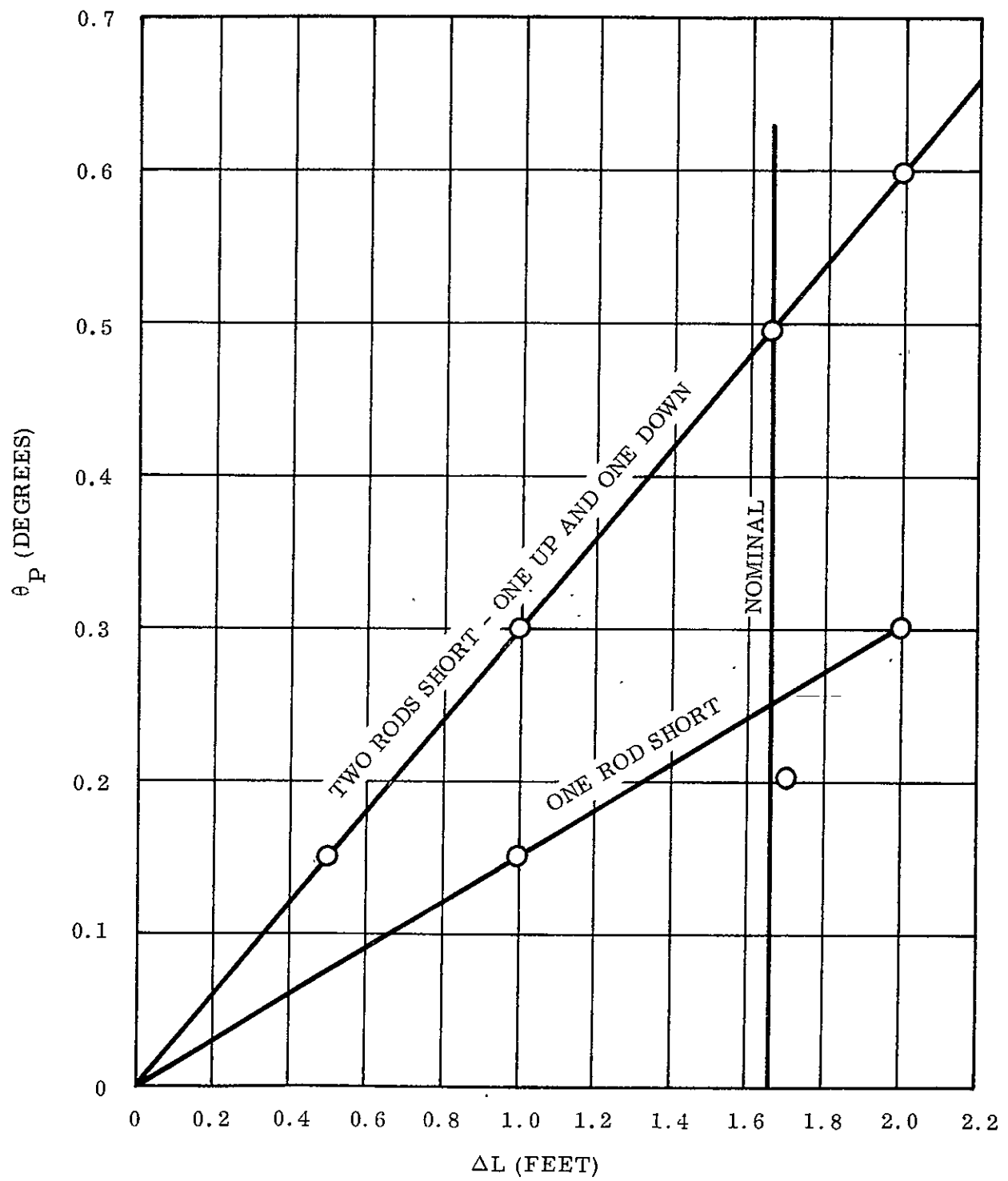
Figure 3.5-12.   Pitch Error Caused by Prinicpal Axes Shift Resulting from
Short Primary Rods
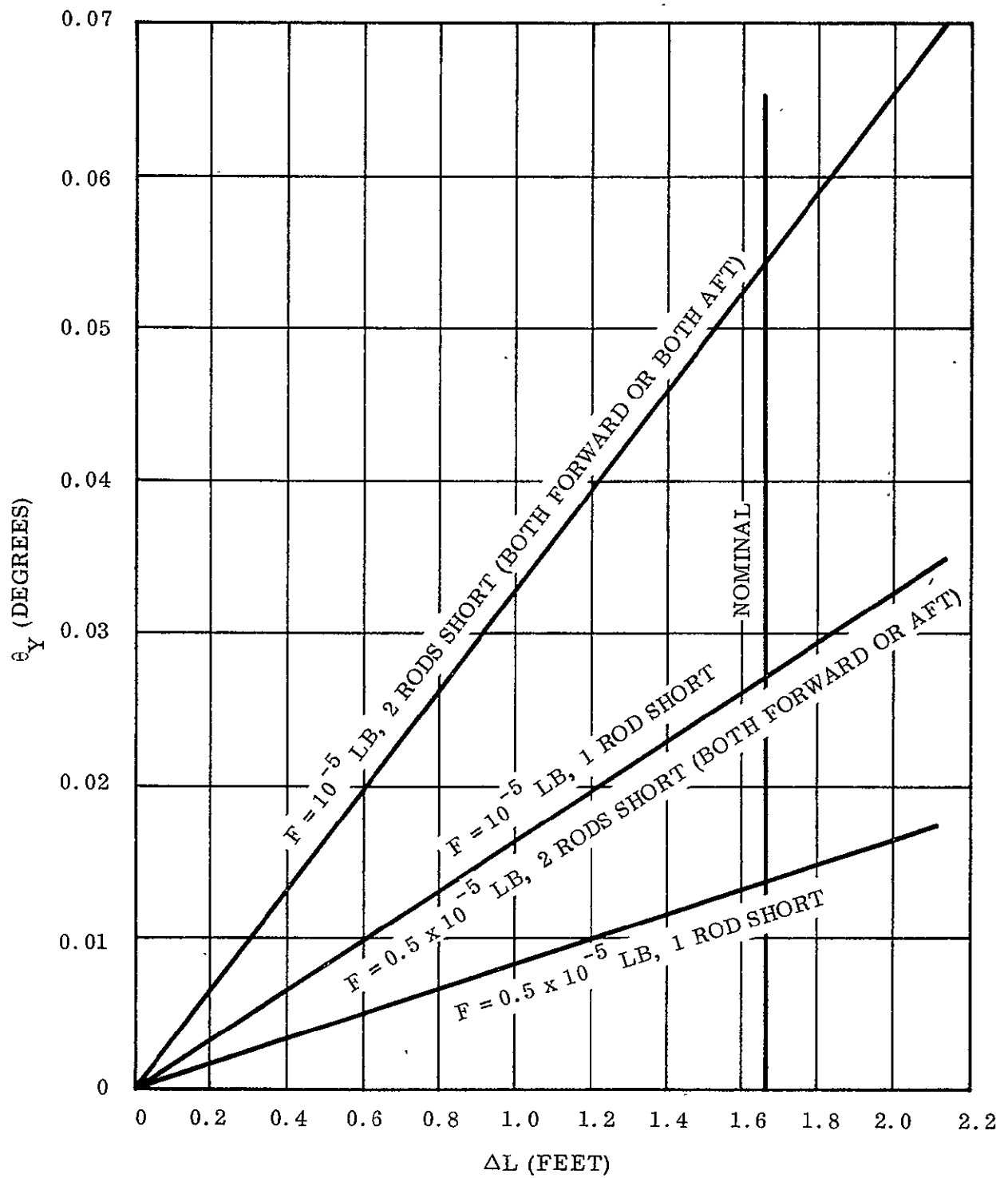
Figure 3.5-13. Yaw Error Caused by Center of Mass Shift Resulting from Short Primary Rods
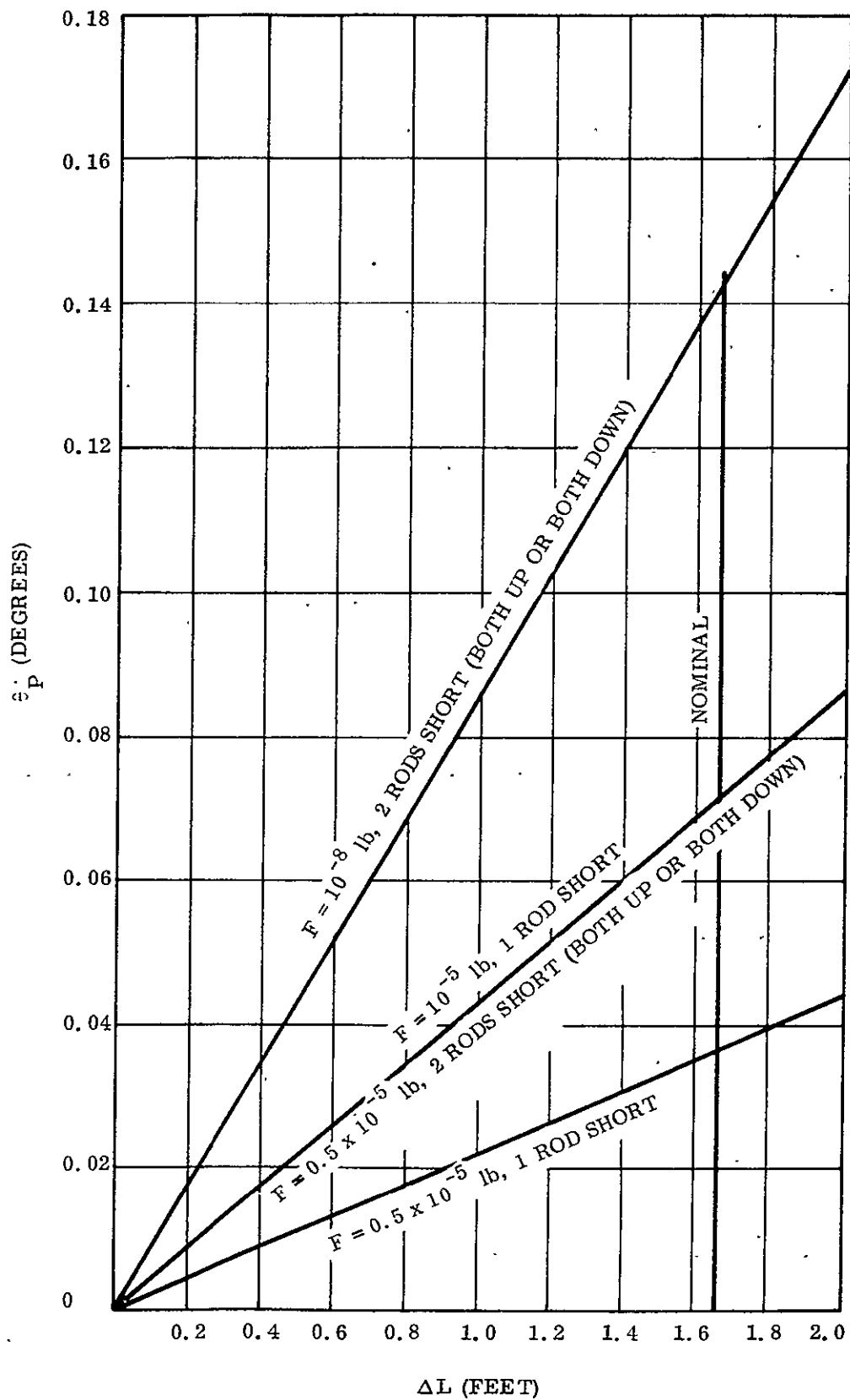
Figure 3.5-14. Pitch Error Caused by Center of Mass Shift Resulting from
Short Primary Rods

1. Pitch – Principal Axis Shift Error   0. 5 degree

2. Yaw – Principal Axis Shift Error   0. 068 degree

3. Pitch – Thruster Error   0. 14 degree

4. Yaw – Thruster Error   0. 055 degree

Then errors are recorded in the ATS-D and E error budgets of Section 3. 5. 3.

The solar torque error estimates for rod length variations contained in the error budgets were made by assuming the worst case solar condition for each axis. The torques were calculated for the "extra" rod lengths, and the errors calculated using the frequency response characteristics of Section 3. 2. 2. The worst case pitch errors occur when the sun is in the orbit plane, and the rod configuration is similar to that of Configuration (a) in Figure 3. 5-10. The maximum pitch error is 0. 7 degrees, with a 0. 7 degrees yaw error resulting from coupling.

The largest yaw error occurs for the sun at 23. 45 degrees to the orbit plane with the rod configuration similar to that of Configuration (b) of Figure 3. 5-10. The direct yaw torque produces a yaw error of 2. 6 degrees with the pitch error (produced by coupling) approximately 0. 3 degree. The pitch error produced by solar torque at this sun orientation cannot exceed 0. 3 degree even with Configuration (a); hence, the pitch error recorded in the ATS-D error budget is 0. 3 degree. The errors were scaled from ATS-D to obtain the estimates for ATS-A.

3. 5. 2. 2. 2 Gravity Gradient Rod Envelope Variations
The gravity gradient rods are not straight when manufactured, but have a distinct curvature. At the start of the ATS program, specifications were placed to restrict the curvature, and this specification was used in the analysis. However, the rods for the ATS spacecraft were measured for straightness, prior to mounting in the spacecraft and indicated significant deviations from the specified value. For the ATS-A spacecraft, the deviations were so great that a special study was made using the Mathematical Model Digital Computer

Program to simulate the curvature. The study was expanded to include placement of the rods on ATS-D in order to minimize the attitude error. The two studies are as follows.

3.5.2.2.2.1 ATS-A Rod Envelope Study. Straightness measurements taken on the ATS-A gravity gradient rods indicated that the rods were significantly curved and the question immediately arose as to the effect on spacecraft performance of the curved rods. The ATS Mathematical Model computer program was not designed to accommodate initially curved rods, but the measured curvature was large enough (see Figures 3.5-15 and 3.5-16) to warrent changing the model. To avoid extensive changes in the Mathematical Model, it was conventient to use a parabolic approximation of the initial curvature of the rod, and the appropriate additions were made to the model.

To determine the effect of initial rod curvature on the spacecraft performance, three computer runs were made:

1. Nominal straight rod case

2. Straight rod approximation to the initially curved rod

3. The parabolic approximation to the initially curved rod

The only disturbances considered in the runs were those due to the sun, and the orbit eccentricity.

The effects, on the spacecraft attitude errors, of the curved rods (see Figures 3.5-18 and 3.5-19) are significant when compared to the attitude errors of the initially straight rods (see Figure 3.5-17). The difference between the straight rod approximation to the initially curved rod and the parabolic approximation are negligible (Figure 3.5-20). As a consequence the simpler straight rod approximation to the curved rods was adopted and the error estimates were based upon that model.
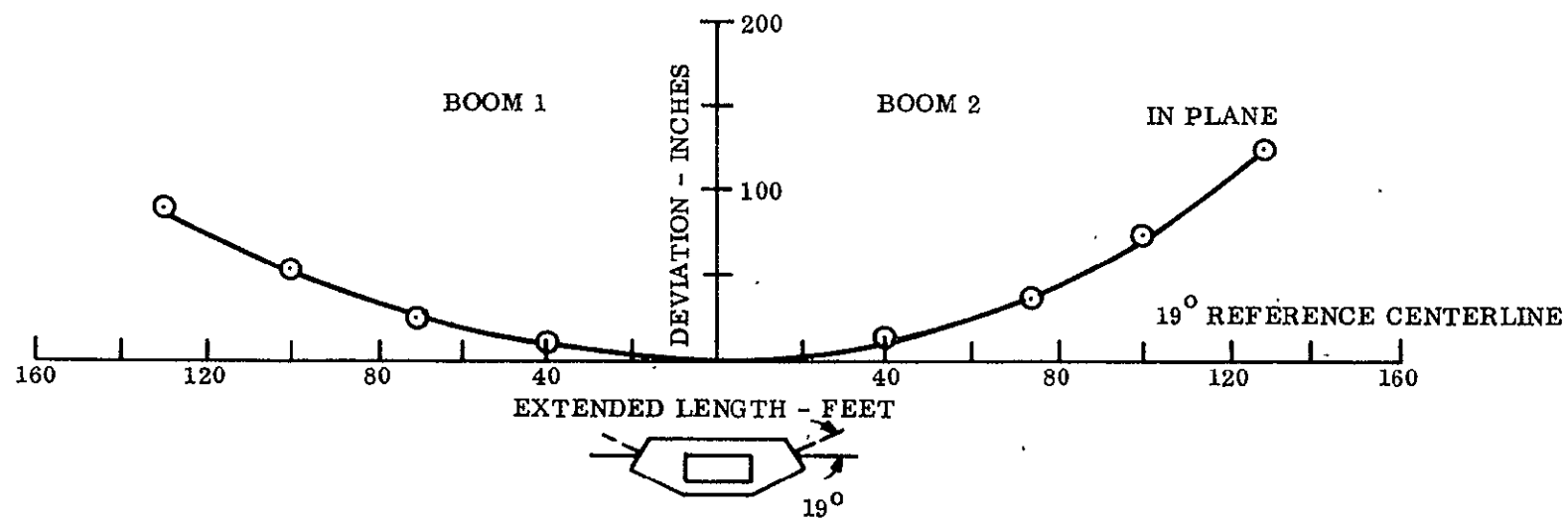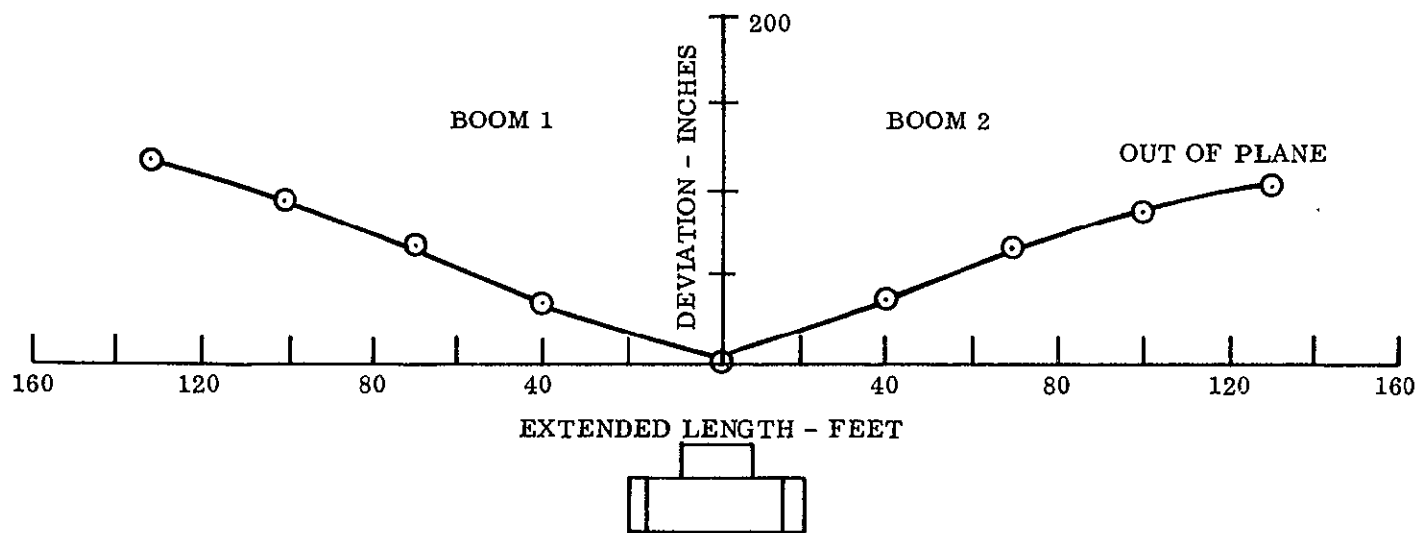
Figure 3.5-15. Serial Number 101 Primary Boom Profile

BOOM 1   DEVIATION - INCHES   BOOM 2   OUT OF PLANE

100

50

160   120   80   40   40   80   120   160

EXTENDED LENGTH - FT

BOOM 1   DEVIATION - INCHES   BOOM 2   IN PLANE

100

50

160   120   80   40   40   80   120   160

EXTENDED LENGTH - FT

19°
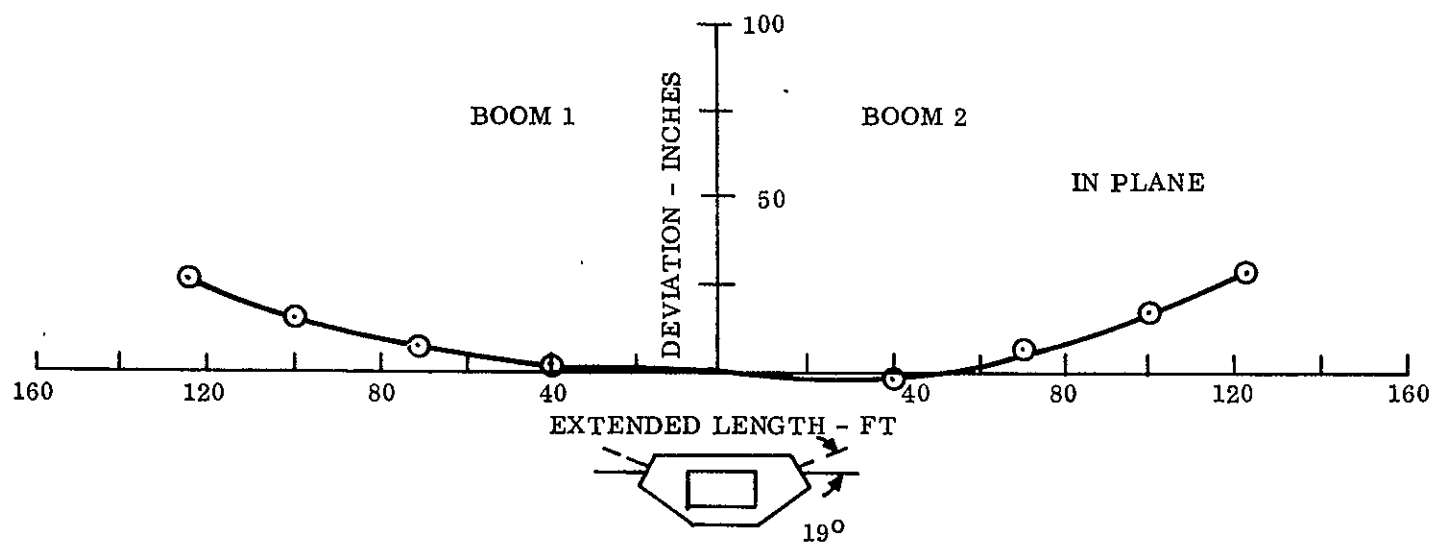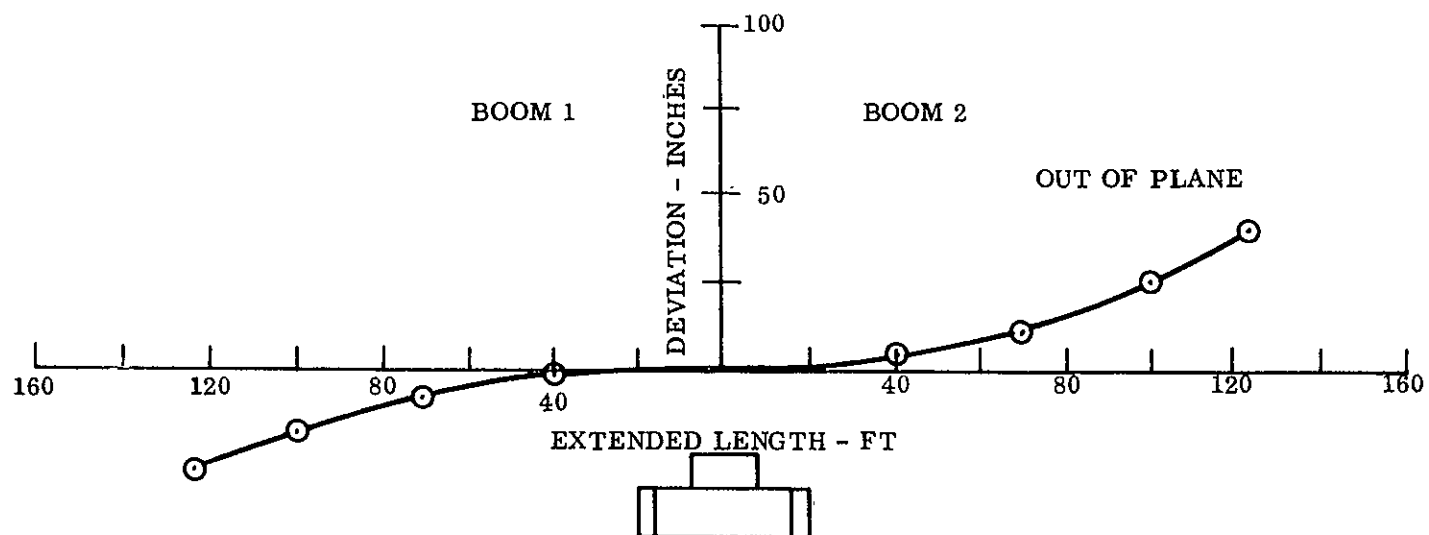
Figure 3.5-16.   Serial Number 102 Primary Boom Profile
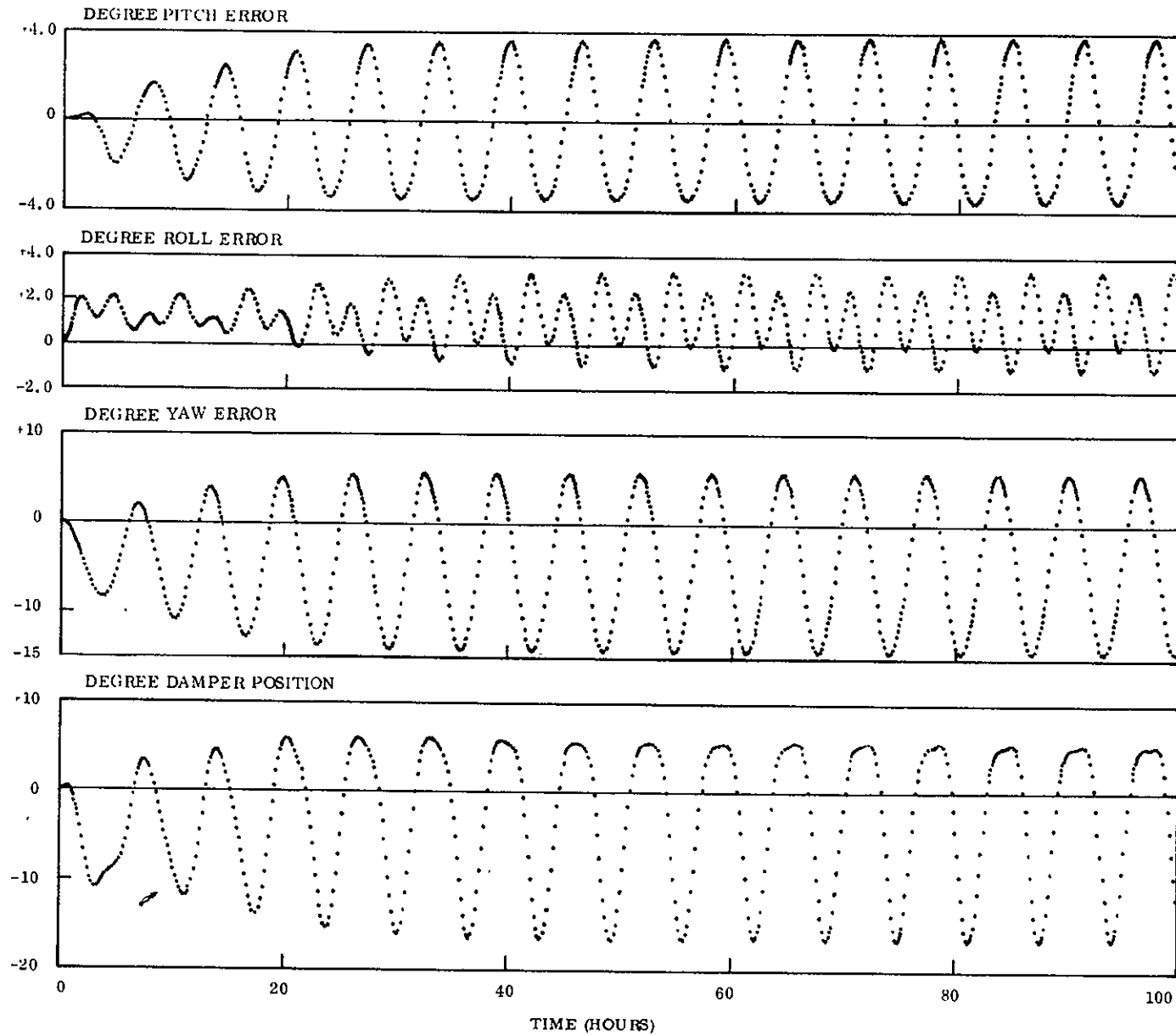
Figure 3.5-17. Steady State Performance of ATS-A Straight Rod Simulation

NOMINAL CASE ROD ANGLE ~ 28.4°
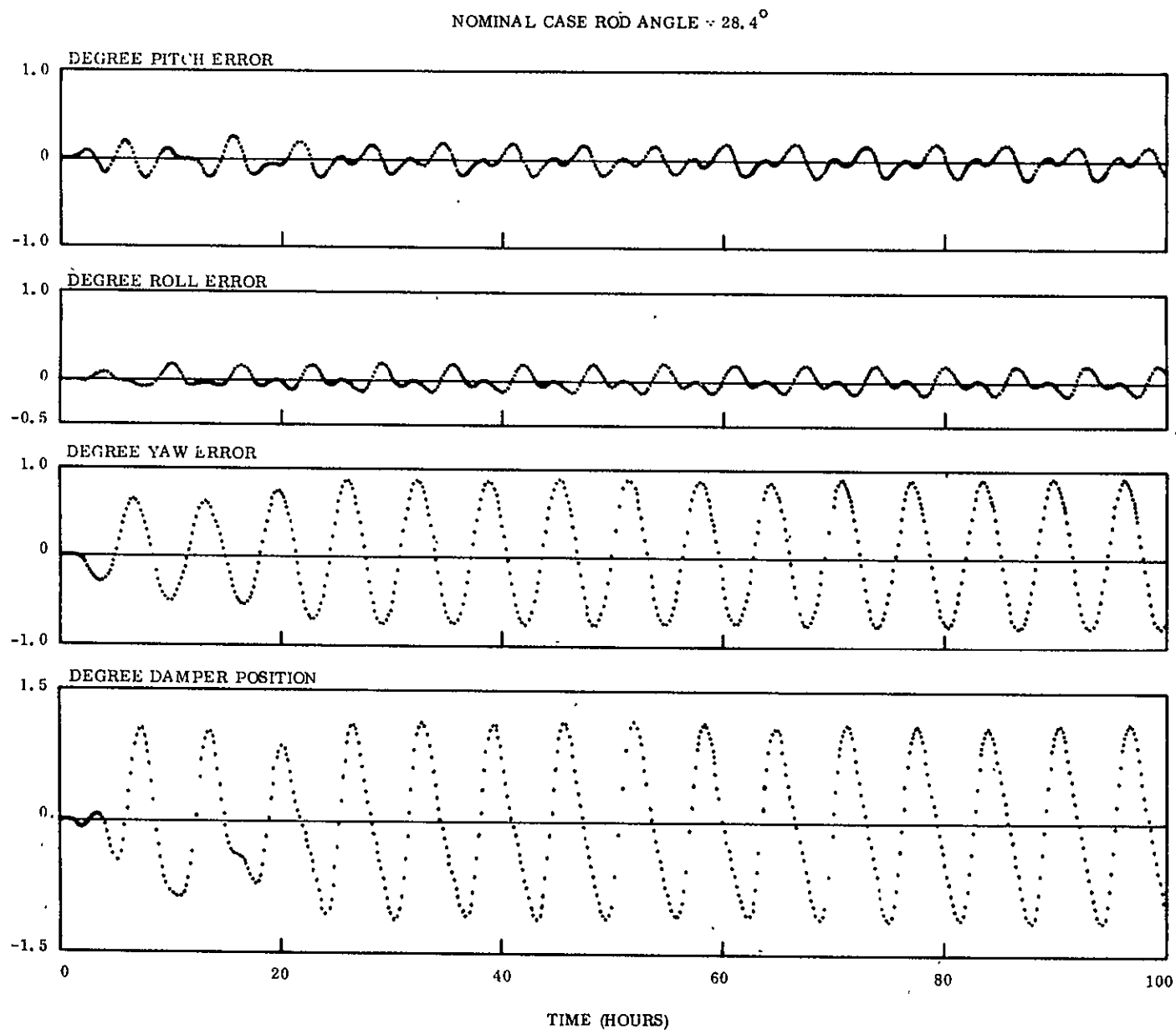
Figure 3.5-18. Steady State Performance of ATS-A for Nominal Case Rod Angle = 28.4 Degrees
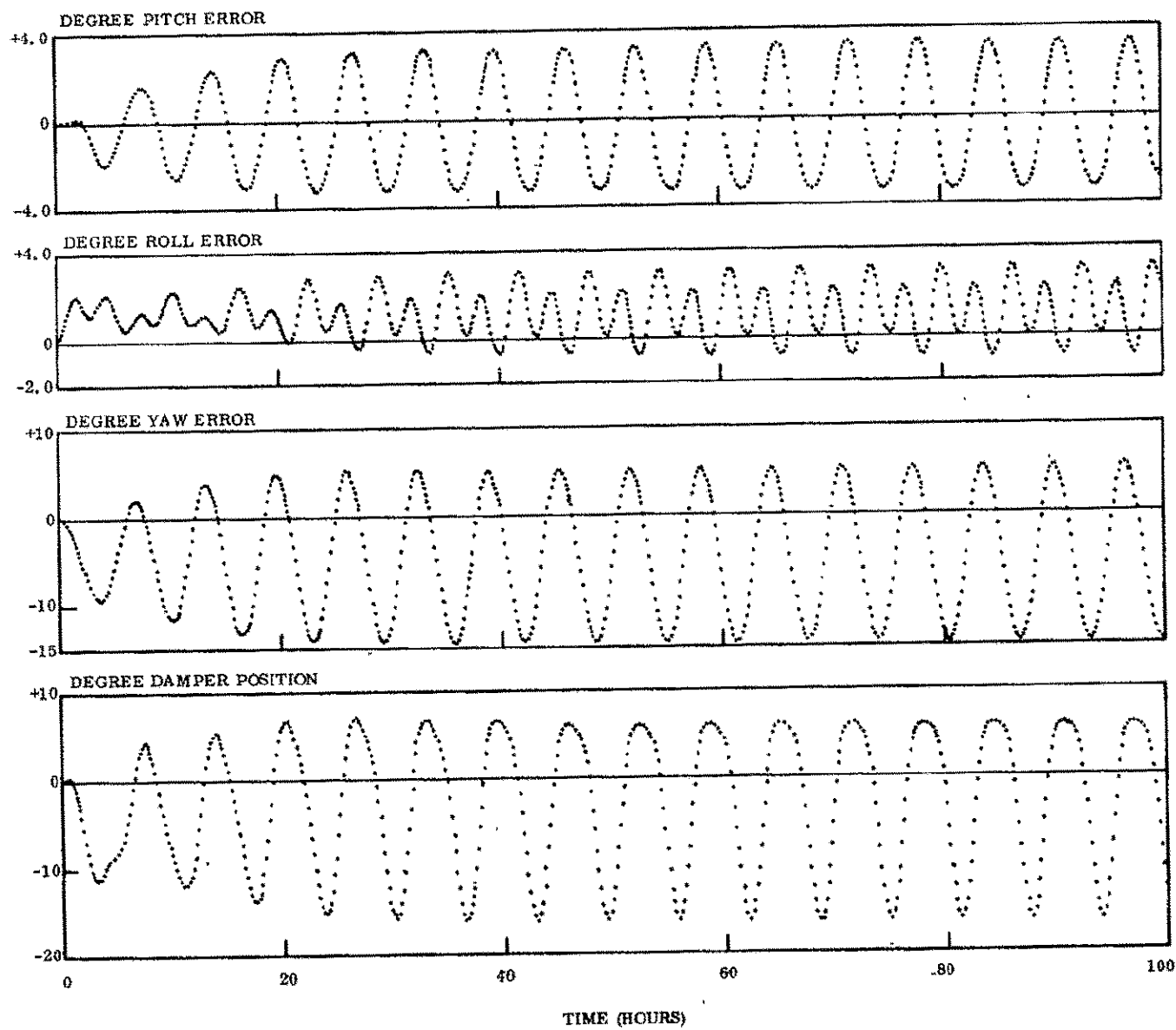
Figure 3.5-19. Steady State Performance of ATS-A Curved Rod Simulation
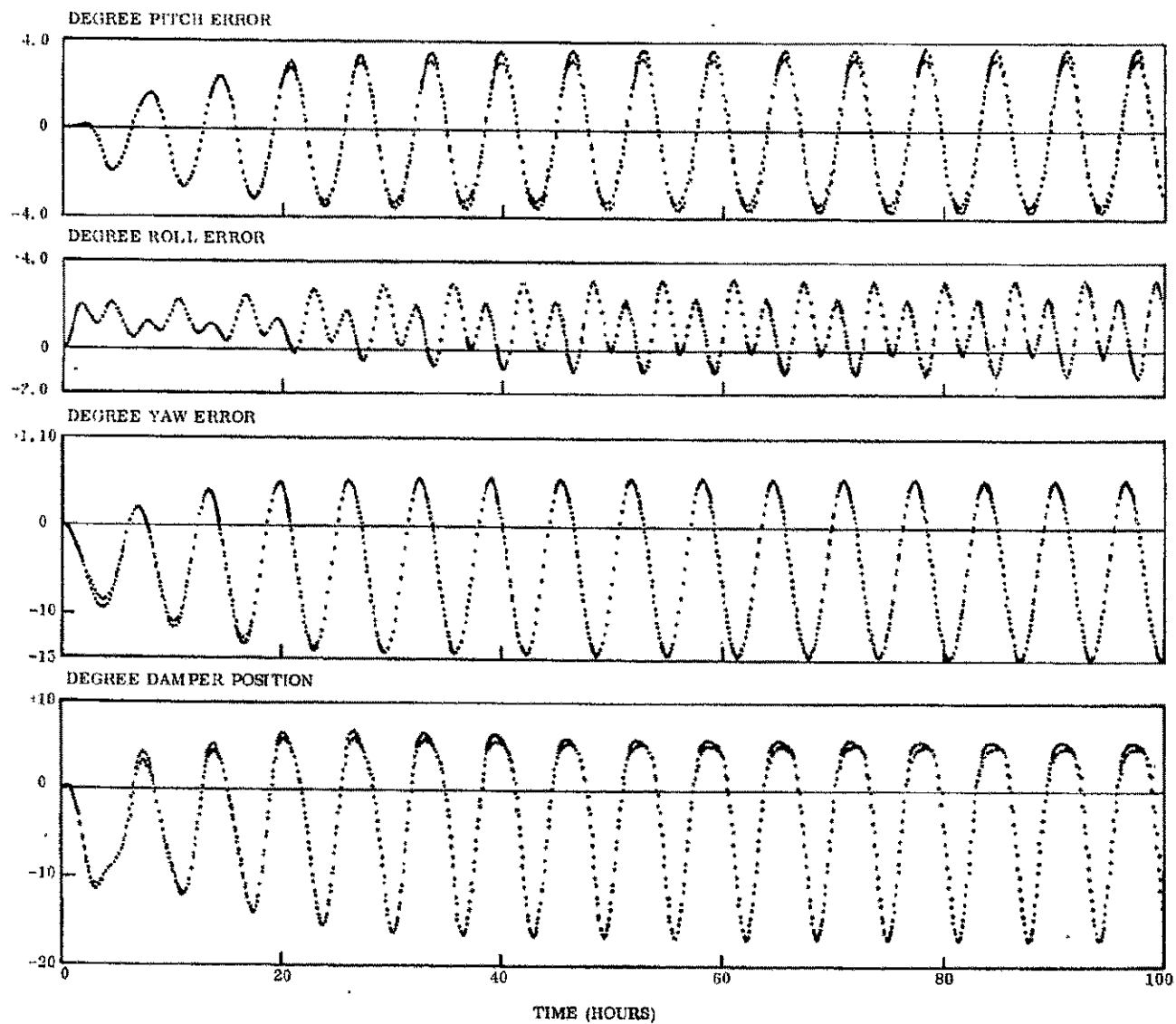
Figure 3.5-20. Steady State Performance for ATS-A Comparison of Rod Simulations

The error contributions of the rods were broken into biases which were assumed to be the result of solar pressure. The errors indicate a pitch error growth of 3.4 degrees in oscillation, a roll axis bias error of 1.1 degrees, with an oscillatory error increase of 2.0 degrees, and a yaw bias of -4.5 degrees with an oscillatory increase of 9.1 degrees. These errors, however, were felt to be too much of an extreme. The in-plane bending shown in Figures 3.5-15 and 3.5-16 can be partially corrected by scissoring the rod deployment units in orbit, and bringing the products of inertia down. This significantly reduces the pitch and yaw bias, and brings the configuration more towards the nominal. As a result, the solar torque on the configuration is also reduced. The estimated attitude errors for ATS-A with the rod half angles trimmed are shown in the ATS-A error budget of Section 3.5.3. The biases cannot be completely removed, however, since scissoring is symmetrical and the rod offsets are not. Note that the roll bias error is not significantly reduced by scissoring, because it is largely the result of the out-of-plane bending of the rods of Serial No. 102 rod deployment mechanism. The "positive" bending of one rod, and the "negative" bending of the other is particularly severe.

Subsequent to these studies, structural analyses performed on the rods indicated that much of the curvature measured on the rods was a result of the manner in which the rods were measured (see Section 3.5.2.2.2.2). Subsequent measurements, in conjunction with structural analyses, revealed that in a zero G field the rods would bend considerably less in most cases by a factor of at least three. Consequently, the attitude errors would be much less than those recorded in the error budgets.

3.5.2.2.2.2 ATS-D Rod Envelope Study. The effect of the initially curved rods in ATS-A was quite severe as noted in the ATS-A error budget. The effect on ATS-D would be even more severe because the reduction in gravity gradient torque at synchronous altitude increases the solar torque effects. As a consequence, every rod planned for use on ATS-D was measured for straightness. As anticipated, the rods were not straight, and the curvature varied from rod to rod in both magnitude and direction. The actual value of the curvature obtained by ground test was felt to be pessimistic, however, because the rods were constrained in one axis, the effect of gravity was not removed, and the overlap seam

was artificially forced to repeat the contour observed in vertical suspension tests. To correct for this, a structural analysis was performed which removed all test constraints and projected the results into a zero G field. Six gravity gradient rods were evaluated in this manner for two primary boom units: Serial No. 100 and Serial No. 105.

To minimize the spacecraft attitude errors resulting from these rods, it was decided to evaluate spacecraft performance for all possible rod combinations and permutations. To determine the best rods to use on ATS-D, studies were performed to determine the solar pressure errors, and the principal axis rotations caused by the curved rods. A preliminary study immediately eliminated two of the rods, Rod 2 of Serial No. 105 primary rod erection unit, and Rod 1 of Serial No. 100 primary unit. The curvature of these two rods was excessive, and significantly impaired spacecraft performance.

To determine the best location for each of the remaining four rods, it was necessary to calculate the effect of solar pressure, center of mass shift, and principal axis rotation. Since there are four rods and four rod locations, the number of permutations is 24. The use of the mathematical model for evaluation of the performance was felt to be unwarranted, as well as expensive, and a small linearized program was utilized. This program performs all calculations assuming the rods are straight, and it is necessary to make a straight rod approximation to the curved rods. The most accurate approach is to calculate the tip mass location of the curved rod, and determine the orientation a straight rod must have in order to have the same tip mass location. This calculation was performed (see Appendix F) for the ATS-D configuration. The tip deflections for all the rods are shown in Table 3.5-5. The rod lengths were assumed to be 121 feet rather than the normal 123 feet to reflect the latest change in rod length (for ATS-D). All other parameters were nominal.

Since the rods were considered independently, a number designation was given to each rod corresponding to the primary boom unit on which it was originally installed, and the number the boom had on that unit (i.e., 1041 is Boom Number 1 on Serial No. 104 primary boom unit). There are four locations on the spacecraft, and these were given letter

Table 3.5-5.   Rod Tip Deflections

Boom No.	Parallel to X Rod Plane (ft)	Perpendicular to X Rod Plane (ft)
104-1	3.0	1.0
104-2	0.9	1.1
105-1	0.3	2.4
105-2	4.9	4.6
100-1	4.2	2.6
100-2	0.1	0.2

The sign of the deflection was adjusted at each boom location (A, B, C, and D).

designations A, B, C and D as shown in Figure 3.5-21. With the original boom placement plan, the booms have the designations: 1041A, 1051B, 1052C and 1042D. Rod 1052 was subsequently replaced by 1002, and the new configuration was considered the "standard."

Because all possible combinations of rods were considered, "mirror images" appear. Mirror images are the configurations which require only an interchange of the primary boom units, not relocation of the booms. The mirror image of the standard configuration is 1051A, 1042B, 1041C, and 1002D.

The results of the computer runs are shown in Table 3.5-6. All the errors shown, with the exception of the yaw oscillation error, are those of a rigid body (i.e., fixed damper boom). The difference in the pitch and roll performance between a rigid body and an ATS-type spacecraft is not very large (approximately 10 percent at orbital frequency), and no adjustment was required. The yaw error had to be adjusted for the ATS-type configuration because of a significant difference in performance. Coupling between the axes was not considered.
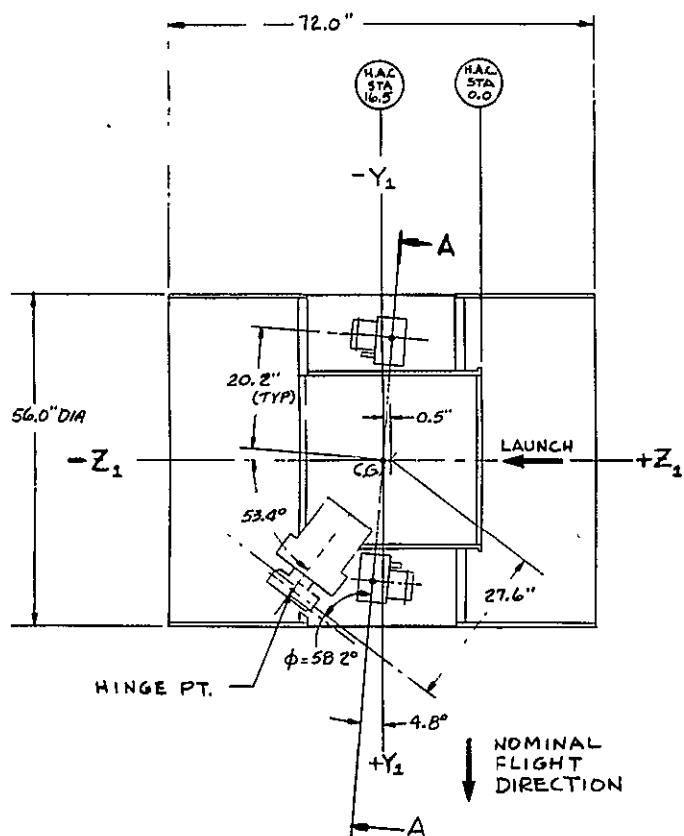
PARAMETER	ATS-A	ATS-D&E
X-BOOM LENGTH (PIVOT PT TO TIP)	132.3 FT	123.3 FT
X-BOOM TIP MASS	2.50 LBS	8.00 LBS
X-BOOM HALF ANGLE (S)	25.0°	24.9°
DAMPER BOOM LENGTH (HINGE PT TO TIP)	45.0 FT	45.0 FT
DAMPER BOOM TIP MASS	1.60 LBS	4.06 LBS
ANGLE BETWEEN X-BOOM PLANE AND X,Y, PLANE	-4.8°	-4.8°

* [ ] Designations in interface documents.
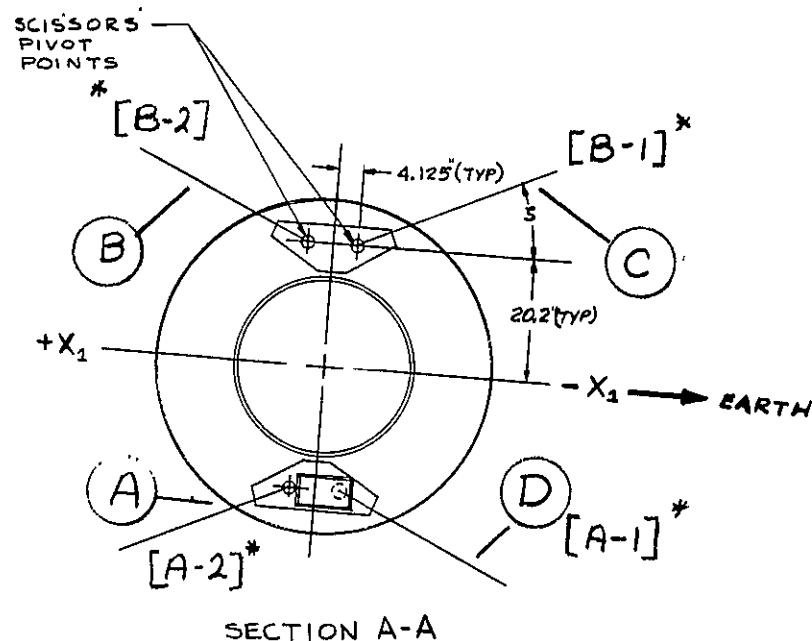
PARAMETER*	ATS-A	ATS-D&E
MOMENT OF INERTIA ABOUT Z,	7082 SLUG FT²	16625 SLUG FT²
MOMENT OF INERTIA ABOUT Y,	5770 SLUG FT²	13545 SLUG FT²
MOMENT OF INERTIA ABOUT X,	1326 SLUG FT²	3117 SLUG FT²
DAMPER MOMENT OF INERTIA	231 SLUG FT²	540 SLUG FT²
SPRING CONSTANT	21 DYNE CM/DEG	3.5 DYNE CM/DEG
E.C. DAMPING CONSTANT	15800 DYNE CM/DEG/SEC	9870 DYNE CM/DEG/SEC
P.H.D. SATURATION TORQUE	173 DYNE-CM	50 DYNE-CM

* MOMENTS OF INERTIA DO NOT INCLUDE CONTRIBUTIONS OF CENTRAL BODY OR DAMPER BOOMS

Figure 3.5-21. ATS Standardized Configuration

Table 3.5-6. Results of Computer Runs

Location				Attitude Error					
				Pitch		Roll		Yaw	
A	B	C	D	Bias	Osc	Bias	Osc	Bias	Osc
* Straight				0.0	0.7	0.0	0.4	0.2	0.5
1042	1051	1002	1041	0.4	1.5	0.2	0.6	1.2	1.1
**MI 1051	1042	1041	1002	0.4	0.2	0.2	0.3	1.2	0.4
1051	1002	1041	1042	0.4	0.4	0.6	0.4	0.6	0.4
MI 1002	1051	1042	1041	0.4	1.2	0.6	0.5	0.6	0.9
1051	1002	1042	1041	0.3	1.4	0.1	0.2	0.6	2.2
MI 1002	1051	1041	1042	0.3	0.3	0.1	1.0	0.6	3.1
1041	1051	1002	1042	0.2	1.4	0.4	1.1	0.0	3.1
MI 1051	1041	1042	1002	0.2	0.3	0.3	0.3	0.1	2.5
1002	1041	1051	1042	0.5	0.3	0.0	0.3	1.3	1.0
MI 1041	1002	1042	1051	0.5	1.2	0.0	0.8	1.3	1.8
1002	1042	1041	1051	0.3	0.3	0.3	1.0	0.2	3.0
MI 1042	1002	1051	1041	0.3	1.5	0.3	0.3	0.2	2.2
1002	1042	1051	1041	0.6	1.2	0.6	0.3	0.2	0.8
MI 1042	1002	1041	1051	0.6	0.4	0.6	0.7	0.2	1.6
1042	1051	1041	1002	0.5	0.2	0.1	0.7	1.2	1.6
MI 1051	1042	1002	1041	0.5	1.3	0.1	0.3	1.2	0.8
1041	1042	1051	1002	0.3	1.2	0.7	0.4	0.6	0.3
MI 1042	1041	1002	1051	0.3	0.4	0.7	0.4	0.6	0.6
1042	1041	1051	1002	0.3	0.4	0.0	0.3	0.6	2.4
MI 1041	1042	1002	1051	0.3	1.3	0.0	1.1	0.6	3.3
1051	1041	1002	1042	0.4	0.4	0.7	0.3	0.1	1.0
MI 1041	1051	1042	1002	0.5	1.2	0.0	0.3	1.2	1.1
1041	1002	1051	1042	0.3	1.4	0.3	0.4	1.3	0.4
MI 1002	1041	1042	1051	0.3	0.2	0.3	0.4	1.3	0.6

* Reference Case   ** Selected Case
  MI Mirror Image of Preceding Case

The error values on Table 3.5-6 indicate that effect of the curved rods is not major, but is too large to be ignored. The standard case is not a good arrangement when compared to many of the other cases because of the large pitch error (1.4 degree oscillation). Its mirror image is quite good, however, and was tentatively recommended.

To check the recommendation, two computer runs were made on the Mathematical Model, simulating the standard case, and its mirror image. The results are peak errors (bias plus oscillation) of 1.4 degrees in pitch, 0.8 degree in roll, and 4.0 degrees in yaw for the standard case, and 0.8 degree in pitch, 0.6 degree in roll, and 1.7 degrees in yaw for the mirror image. These runs agree with the conclusions drawn from the linearized program. As a result, the rod units were interchanged.

The attitude errors for the selected rod configuration are included in the ATS-D error budg of Section 3.5.3. The errors represent the absolute difference between the nominal configuration and the reference configuration. The biases were assumed to be due to principal axis shift entirely, and the oscillations were attributed to solar pressure. The solar torque errors were corrected for sun out of the orbit plane.

The attitude error created by the stationkeeper is also influenced by the rod envelope, because the spacecraft center of mass shifts due to the non-straight rods. The amount of shift is not large for the selected rods, however, being less than 0.6 inch along the pitch axis. The steady state yaw error (constant torque) is approximately 1.8 degrees for this amount of shift. The pitch error is negligible because the direct pitch torque is much less than the yaw torque and the pitch axis is considerably stronger. The roll error is negligible since there is no direct roll torque.

3.5.2.2.3 Rod Alignment Variations

Misalignment of the gravity gradient rods will produce attitude errors in a manner similar to the rod curvature. It was in fact, pointed out in Section 3.5.2.2.2.1 that the effect of curved rods could be simulated by appropriately oriented straight rods. Rod alignment causes a change in the geometry which, as with the other rod tolerance effects, produces solar torque errors, thruster errors, and principal axis alignment errors.

The worst case principal axis alignment is when all the rods are misaligned in such a way as to add. This results in either a pitch or roll error of 1 degree. The pitch error can be partially overcome by appropriate rod scissoring. The yaw error does not relate directly to the rod alignment, but must be calculated considering the geometry of the spacecraft. This results in a yaw error which is beyond the misalignment of one degree. The worst case error is 1.9 degrees and is shown in the error budget in Section 3.5.3.

The solar torque error produced by rod misalignment is maximized when the rods are oriented such as to produce a large center of pressure shift. The two positions of greatest solar torque are with rods all misaligned forward (or backward) so as to move the center of pressure along the z axis. The latter arrangement provides both roll and yaw torques when the sun is in the orbit plane, and the former prevents roll and yaw torques when the sun is out of the orbit plane. The solar torques, as determined by simulation, are shown in the error budgets.

The yaw attitude error caused by the stationkeeping thruster for ATS-D/E as a function of out of plane rod misalignment is shown in Figure 3.5-22. This error is the static error, and coupling to the other axes is negligible. A direct pitch torque can be obtained with appropriate rod position, but the center of mass shift is in the X-Y plane, and is much smaller than the actual plane shift. The pitch error from this small CM offset is negligible. The roll torque is essentially zero, producing no attitude error.

3.5.2.2.4 Solar Absorptivity Variations

The nominal coefficient of absorptivity for the gravity gradient rods is required to be 0.15 and the rods have been silver-plated to achieve this absorption. However, variations in silver plate, silver corrosion while stored on the ground, and variations in surface condition will alter the actual absorptivity. The absolute absorptivity is of importance to thermal bending, but the difference among the rods is of importance to solar torque. The pitch, roll and yaw torques for ATS-A and D have been calculated assuming the worst arrangement of absorptivites on each axis, and the "worst" time in orbit. For pitch and
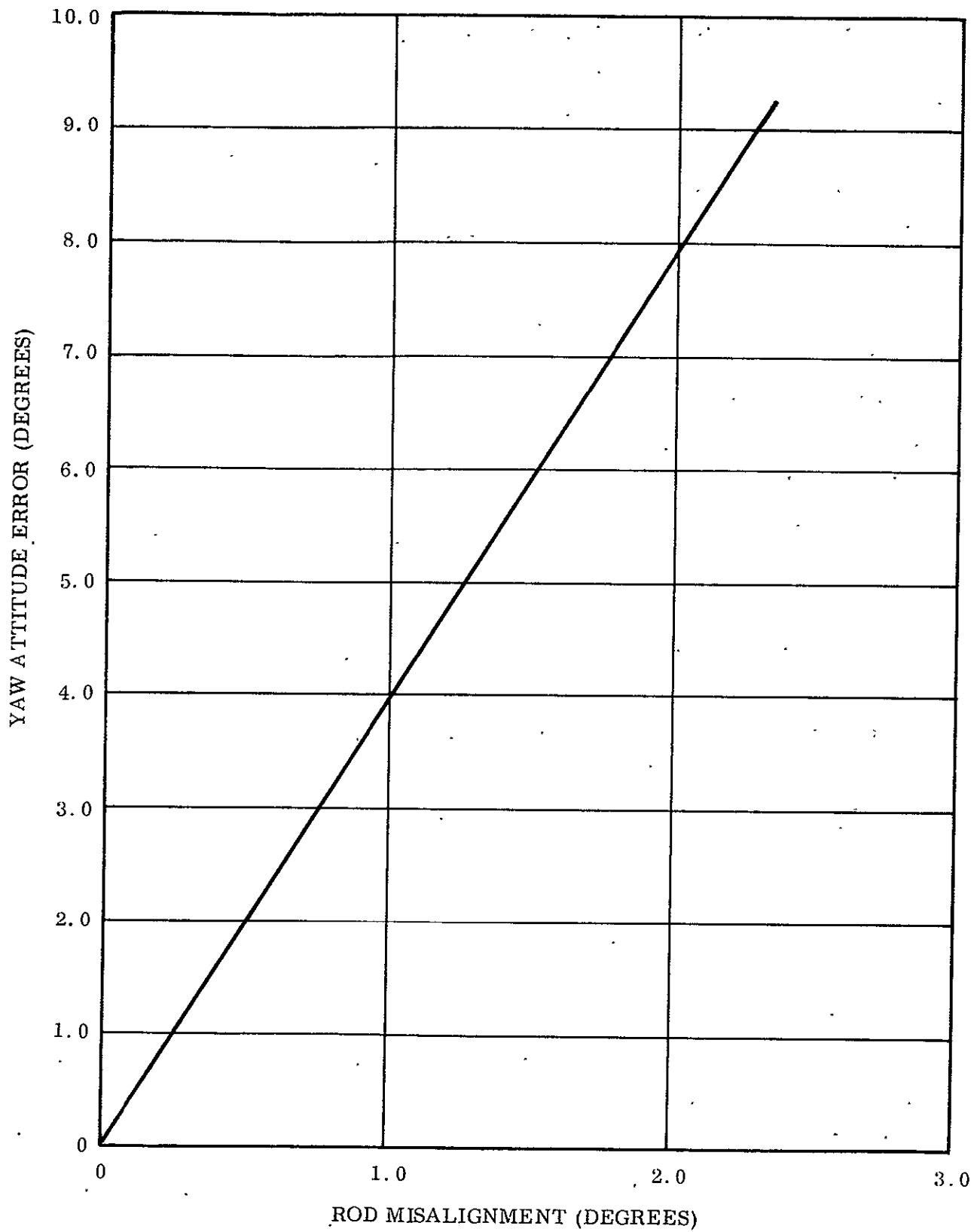
Figure 3.5-22. Yaw Attitude Error Due to Stationkeeping Torques Caused by Rod Misalignment

roll, the worst rod arrangement is when the two up rods have reflectivities different from the down rods (or vice versa). The worst case for yaw is when the two leading rods have reflectivities different from the two trailing rods (or vice versa).

The errors shown for a rod absorptivity difference of 1.0 are shown in Table 3.5-7 for ATS-A and Table 3.5-8 for ATS-D, and the analysis is contained in Appendix G. Such a difference in reflectivities is virtually impossible because one rod would have to be purely absorptive and one purely reflective. A difference of 0.1 is more likely, and the error budgets of Section 3.5.3 reflect this value.

3.5.2.2.5 Spring Null Shift

In Section 3.1, it was pointed out that the principal of operation of the spacecraft requires that the damper boom be placed in unstable gravity gradient equilibrium, and stabilized with a spring. For this reason, the damper boom is in the horizontal plane, and the spring is adjusted to have zero torque when the boom is perpendicular to the spacecraft yaw axis. Nominally, therefore, the spring null is coincident with the gravity gradient null.

The actual position of the spring null with respect to the yaw axis is determined by the alignment procedures on the ground. Preliminary indications were that the spring in the passive hysteresis damper could not be controlled to accuracy any better than approximately 1.5 degrees. The effect of this spring null shift is to cause the damper boom to be in unstable equilibrium when horizontal, and it will "droop." The new equilibrium position for the boom is where the spring torque equals the gravity gradient torque. With the damper in the new position, the principal moments of inertia of the spacecraft are no longer along the reference axes, and bias errors develop. The errors were determined by computer simulation (the simplest approach) for ATS-A and ATS-D. The results are shown in Table 3.5-9. A value of 1.5 degrees was selected as the spring null shift for the error budgets of Section 5.3.3.

Table 3.5-7. ATS-A Errors Due to Solar Torques (Δ Absorbtivity = 1)

	Sun 26.0 Degrees out of the Orbit Plane						Sun in Orbit Plane					
	Pitch		Roll		Yaw		Pitch		Roll		Yaw	
	Bias	Osc	Bias	Osc	Bias	Osc	Bias	Osc	Bias	Osc	Bias	Osc
Axis of Max Torque												
Yaw	-0.05	1.25	0.22	1.82	-0.49	1.42						
Roll-Sun-Plane-52°	0.24	1.77	0.76	0.01	1.85	1.85						
Pitch							0	2.70	0	0.04	0	2.91
Damper							0	0.24	0	0.10	0	2.14
Slug - feet^2												

$\dfrac{1XX1}{1378}$	$\dfrac{1YY1}{5802}$	$\dfrac{1ZZ1}{7118}$	$\dfrac{1YY2}{231}$	$\dfrac{\phi^{\circ}}{58.2^{\circ}}$	$\dfrac{\alpha^{\circ}}{53.4^{\circ}}$	$\dfrac{\delta^{\circ}}{-4.8^{\circ}}$	$\dfrac{\xi^{\circ}}{25^{\circ}}$
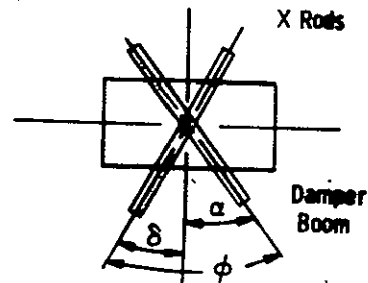
Table 3.5-8. ATS-D Errors Due to Solar Torques (ΔAbsorbtivity = 1)

	Sun 23.45 Degrees Out of Orbit Plane						Sun in Orbit Plane					
	Pitch		Roll		Yaw		Pitch		Roll		Yaw	
	Bias	Osc	Bias	Osc	Bias	Osc	Bias	Osc	Bias	Osc	Bias	Osc
Axis of Max Torque												
Yaw	0.14°	6.62°	1.43°	0.08°	7.05°	2.59°						
Roll	0.87°	13.42°	0.05°	1.95°	4.42°	14.08°						
Pitch							0	14.05	0	0.19	0	15.12
Damper							0	1.46	0	0.58	0	13.87

Slug - feet^2

$\dfrac{1_{\lambda x1}}{3157}$	$\dfrac{1_{yy1}}{13,587}$	$\dfrac{1_{zz1}}{16,656}$	$\dfrac{1_{yy2}}{540}$	$\dfrac{\phi^{\circ}}{58.2^{\circ}}$	$\dfrac{\alpha^{\circ}}{53.4^{\circ}}$	$\dfrac{\delta^{\circ}}{4.8^{\circ}}$	$\dfrac{\xi^{\circ}}{24.9^{\circ}}$
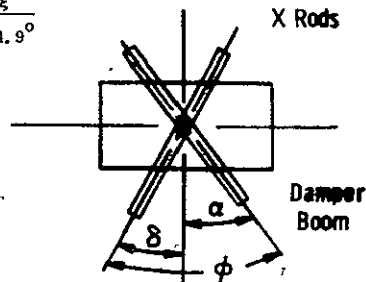
Table 3.5-9. Error Budget for Steady-State Conditions

ATS-A						
Spring Null	θ_p		θ_r		θ_y	
	Bias	Amp	Bias	Amp	Bias	Amp
$\Delta\gamma_\eta = 0.5^o$	0.1	0	-0.1	0	0	0
$\Delta\gamma_\eta = 1^o$	0.1	0	-0.1	0	0	0
$\Delta\gamma_\eta = 1.5^o$	0.2	0	-0.1	0	0.05	0.05

ATS-D						
Spring Null	θ_p		θ_r		θ_y	
	Bias	Amp	Bias	Amp	Bias	Amp
$\Delta\gamma_\eta = 0.5^o$	0.1	0	-0.1	0	0	0
$\Delta\gamma_\eta = 1.0^o$	0.1	0	-0.1 / -0.2	0	0	0
$\Delta\gamma_\eta = 1.5^o$	0.2	0		0	0.1	<0.05

3.5.2.2.6 Spacecraft Solar Torque

The ATS spacecraft is a cylindrical vehicle, 72 inches long by 56 inches in diameter (see Figure 3.5-23). Externally it is divided into three bands; two outer bands consisting primarily of solar cells, and a center band (the primary structure) whose surface is coated for thermal control.

For the spacecraft to have zero solar torque, the center of solar pressure must be at the center of mass for all sun angles. This can be accomplished only if the center of mass is at the center of geometry, and only if the ends of the spacecraft have the same specular reflectivity as the cylindrical portion of the spacecraft. The first criterion was met by making the spacecraft mass distribution symmetrical with respect to the center of geometry.
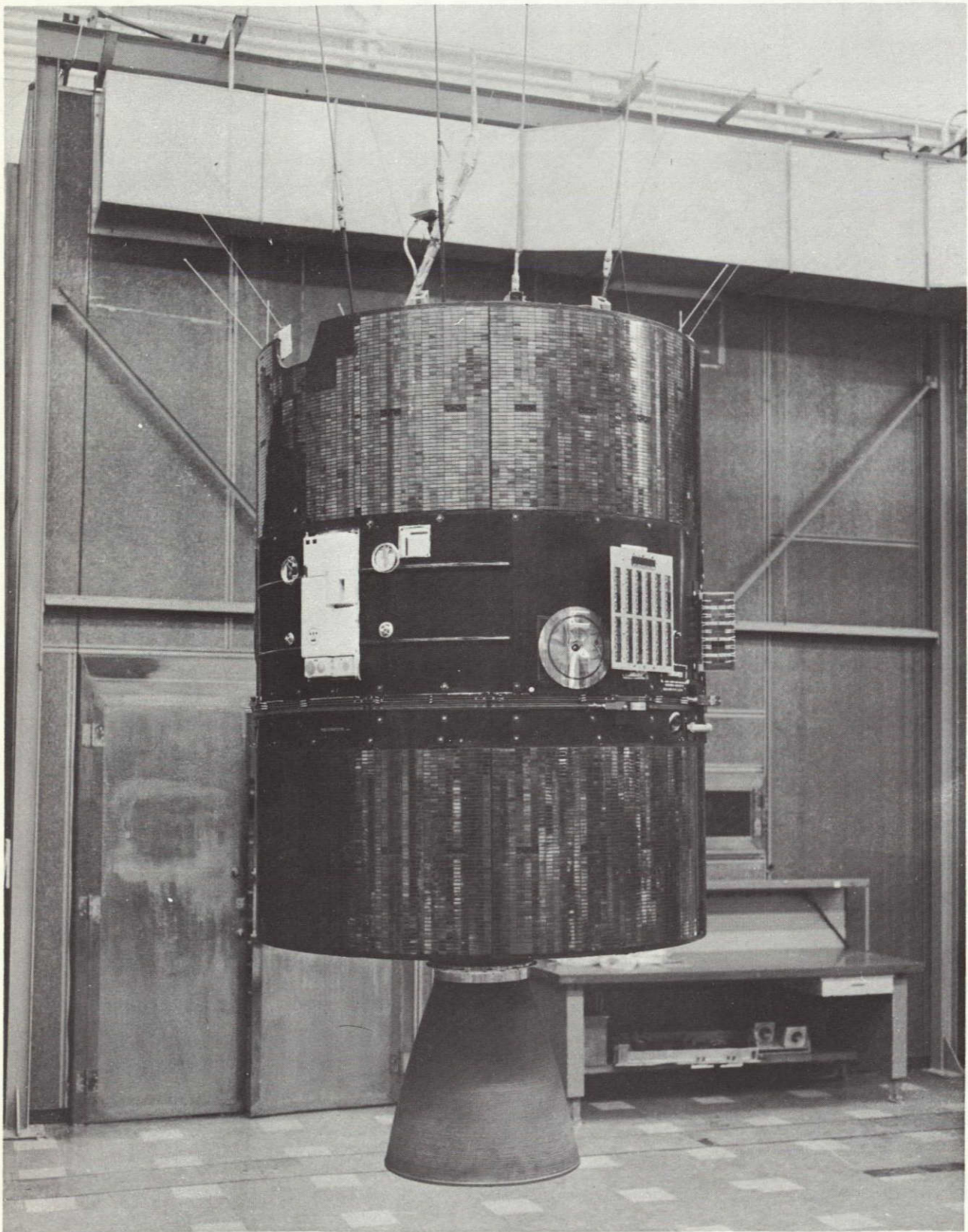
Figure 3.5-23. ATS-E Configuration

The second criterion was met by the introduction of solar pressure rings on the ends of the spacecraft. The rings are high reflectivity annuluses which correct for the dark end section.

3.5.2.2.6.1 ATS-A and ATS-D. The nominal solar torque is zero, but solar torque will appear on the spacecraft whenever the solar reflectivities deviate from the nominal. Two cases are considered: variations in reflectivity of the cylindrical section and variations between the cylindrical portion and the end section. The cylindrical reflectivities produce the greatest torque when the sun is in the orbital plane. The torque is a function of the reflectivity variations of the surface. Assuming a variation of 0.1, the errors are as shown in the error budget.

The end effect is most severe when the sun is out of the orbit plane, and the errors shown in the error budget are for a reflectivity variation of 0.1 between the end and the cylindrical surface.

3.5.2.2.6.2 ATS-E. The ATS-E spacecraft preserved the basic solar symmetry of ATS-D, but a large number of experiments were added which upset the solar pressure balance. The experiments include a solar cell experiment and an L-band experiment, as well as the magnetometer and boom associated with the magnetic sample and hold damping system. These experiments (shown in Figure 3.5-23), produce a significant solar torque which must be included in the error budget.

To obtain the appropriate solar torque profile, a small computer program simulating solar torques was used. The complexity of the configuration prevented a meaningful three-axis simulation, and the errors caused by the central body were calculated on a linear basis. The errors are shown in the ATS-E error budget (see Table 3.5-12), which has not been divided into end effects and surface effects since only the attitude error (total) is known.

3.5.2.2.7 Stationkeeping Tolerances

The stationkeeper produces the largest force on the ATS-D/E spacecraft, and to keep the level of applied torque low, the force vector must pass through the center of mass of the spacecraft. Two tolerances identifiable with the thruster can prevent that from occurring: misalignment of the thruster and mounting location tolerances. The latter effect is small compared to the misalignment effect and is not considered. The torque caused by the misaligned thruster is given by Equation 3.2-29 and with the thruster thrusting along the roll axis, will produce a yaw or pitch torque. For a one degree misalignment, a thrust of 10^{-5} pounds, and the thruster located at the periphery of the spacecraft (29 inches), the torque is 4.2×10^{-7} ft-lb, which produces a yaw error of 1.4 degrees or a pitch error of 0.1 degree. There is no roll error because there is no roll torque.

3.5.2.2.8 Center of Mass Uncertainty

The position of the center of mass is nominally coincident with the center of geometry. However, the center of mass is not known exactly, and to allow for variations and unknowns, it is assumed that the center of mass is not known to within 0.5 inch. This uncertainty will produce only solar torque errors, and thruster errors because it is assumed that there is no principal axis shift associated with the uncertainty.

The center of mass uncertainty can produce either a pitch or yaw stationkeeper torque. Coincidentally, the errors induced by the center of mass uncertainty are virtually identical to those created by the rod misalignment errors. These errors for ATS-D/E are 0.1 degree in pitch and 1.4 degrees in yaw, and they are shown in the error budget in Section 3.5.3.

The solar torque error is largest on yaw, especially with the sun in the orbit plane. Nominally, the center of pressure (CP) is at the geometric center of the spacecraft; hence, the CP/CM misalignment is due only to the CM uncertainty, and is therefore one-half inch. The yaw error produced by this offset is 1.6 degrees with a pitch error of 0.2 degree, and a roll error of 0.1 degree for ATS-D/E. These were calculated using the total area of the spacecraft, and the frequency response functions of Section 3.2.2. The errors are somewhat smaller with the sun out of the orbit plane. The results were scaled down for ATS-A.

3.5.3 ERROR BUDGETS

The error budgets for ATS-A, D, and E are shown in Tables 3.5-10, 3.5-11, and 3.5-12 respectively. Each table is divided into two main charts, one containing the overall performance estimates, including the effect of disturbance torques, and one detailing the effects of individual manufacturing tolerances. Several sun position are considered since the sun position changes with time. The extreme cases for ATS-D/E are equinox (sun in the orbit plane) and solstices (sun 23.5 degrees to the orbit plane). Both cases are shown. The highest sun position relative to the orbit plane for ATS-A is approximately 51.5 degrees but this position is not reached in the first year of operation. Consequently, a position of 26 degrees was used.

The attitude errors are broken into bias errors and oscillation errors for convenience in evaluating flight performance. As a total error estimate, the effect of the external disturbance torques were added directly without regard to phasing. This total is then added to the root sum square of the tolerance effects for a total error estimate. For ATS-D, the stationkeeper is a significant error source, but is not on at all times. The ATS-D error budgets therefore contain error estimates with and without stationkeeper. The transient caused by turning the thruster on or off has not been included.

3.5.4 SPECIAL DAMPING STUDIES

In conjunction with the spacecraft performance estimates discussed in the preceeding section, several special studies were performed. These were related to the effects of actual damper parameters on spacecraft capture and damping. The actual damper characteristics were obtained from test and used to initialize the computer simulation. One modification had to be made, however. Previous computer studies (to determine the optimum hysteresis contour) used an ideal approximation to the Variable Torque Hystereses Damper. To correctly simulate the actual VTHD damper, a curve fitting routine was added to the Mathematical Model. This routine accepted input test data and constructed a hysteresis contour to fit the data.

Table 3.5-10A. ATS-A Error Budget

Error Source	Sun 26° To Orbit Plane						Sun in Orbit Plane					
	Pitch		Roll		Yaw		Pitch		Roll		Yaw	
	Bias	Osc	Bias	Osc	Bias	Osc	Bias	Osc	Bias	Osc	Bias	Osc
Magnetic Errors	0	0.2	0	0	0	1.1	0	0.2	0	0	0	1.1
Solar Torque and Thermal Bending	0	0.4	0	0.5	0	0.9	0	0.3	0	0.3	0	0.2
Eccentricity = 0.005	0	0.8	0	0.1	0.1	1.0	0	0.8	0	0.1	0.1	1.0
Tip Targets	0	<0.1	0	<0.1	0	<0.2	0	0.1	0	0	0	0.2
Internal Disturbance (Limit)	0	0.2	0	0.2	0	0.2	0	0.2	0	0	0	0.2
RSS Errors (See Table 3.5-10B)	0.8	0.2	0.7	0.2	1.4	0.2	0.8	0.3	0.7	1.4	1.4	0.4
Total Sum of Errors	0.8	1.9	0.7	1.1	1.5	3.6	0.8	1.9	0.7	1.5	1.5	3.1

Moments of Inertia

Pitch	Roll	Yaw	Damper	ϕ	α	δ	ξ
1378.4	5804.3	1378.4	231	58.2°	53.4°	-4.8°	25.02°
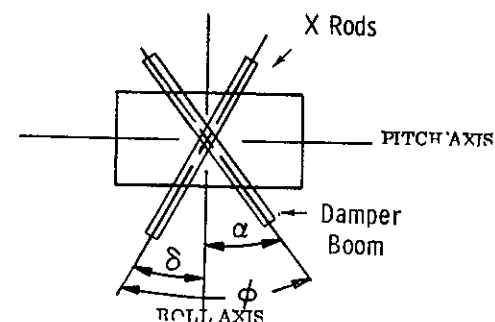
Table 3.5-10B. ATS-A Design Tolerance Effects

ATS-A Tolerance Effects	Sun 26° To Orbit Plane						Sun in Orbit Plane					
	Pitch		Roll		Yaw		Pitch		Roll		Yaw	
	Bias	Osc	Bias	Osc	Bias	Osc	Bias	Osc	Bias	Osc	Bias	Osc
Cylinder Reflectivity												
End Effect	0	0	0	0	0	0	0	0	0	0	0	0
Surface Effect	0	0	0	0	0	0	0	0	0	0	0	0.1
Unequal Rod Absorptivity	0	0.2	0	0.2	0.2	0.2	0	0.3	0	0	0	0.3
Spring Null Shift	0.2	0	0.2	0	0.1	0	0.2	0	0.2	0	0.1	0
Rod Shortness												
Principal Axis Shift	0.5	0	0	0	0.1	0	0.5	0	0	0	0.1	0
Solar Torque	0	0.1	0	0	0	0.1	0	0	0	0	0	0
Rod Non-Straightness												
Principal Axis Shift	0.3	0	0.3	0	0.6	0	0.3	0	0.3	0	0.6	0
Solar Torque												
Rod Misalignment Angle = 1.0 Degree												
Principal Axis	0.5	0	0.6	0	1.2	0	0.5	0	0.6	0	1.2	0
Solar Torque	0	0	0	0	0	0	0	0	0	0	0	0
Center of Mass Shift (Solar Torque)	0	0.1	0	0	0	0.1	0	0	0	0	0	0.2
RSS Errors	0.8	0.2	0.7	0.2	1.4	0.2	0.8	0.3	0.7	0	1.4	0.4

Moments of Inertia

Pitch	Roll	Yaw	Damper	ϕ	α	δ	ξ
1378.4	5804.3	1378.4	231	58.2°	53.4°	-4.8°	25.02°

X Rods

PITCH AXIS

Damper Boom

ROLL AXIS
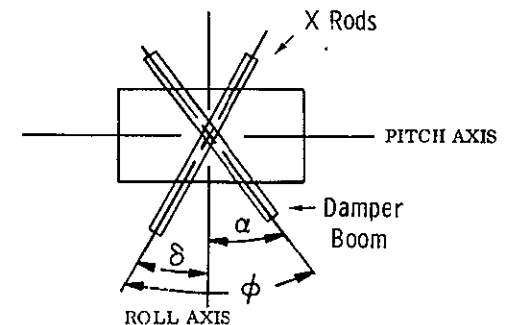
Table 3.5-11A. ATS-D Error Budget

Error Source	Sun 23.5° To Orbit Plane						Sun In Orbit Plane					
	Pitch		Roll		Yaw		Pitch		Roll		Yaw	
	Bias	Osc	Bias	Osc	Bias	Osc	Bias	Osc	Bias	Osc	Bias	Osc
With Station-Keeping:												
Magnetic Errors (Fixed Field)	0	0	0	0	0.3	0	0	0	0	0	0.3	0
Solar Torque and Thermal Bending	0.2	1.4	0.1	1.7	0.2	2.0	0	1.3	0	1.2	0	1.1
Tip Targets	0	0.2	0	0.2	0	1.1	0	0.1	0	0.1	0	0.7
Internal Disturbances (Limit)	0	0.2	0	0.2	0	0.2	0	0.2	0	0.2	0	0.2
Thruster Errors (30 Days On)	0.1	0.6	0.2	0.1	1.0	2.3	0.1	0.4	0.1	0.4	1.6	2.2
RSS Errors (See Table 3.5-11B)	1.2	1.7	1.0	0.2	5.3	3.0	1.2	1.5	1.0	0.2	5.3	4.9
Total Sum of Errors	1.5	4.1	1.3	2.4	6.8	8.6	1.3	3.5	1.1	2.1	7.2	9.1
Without Station-Keeping:												
Magnetic Errors (Fixed Field)	0	0	0	0	0.3	0	0	0	0	0	0.3	0
Solar Torque and Thermal Bending	0.2	1.4	0.1	1.7	0.2	2.0	0	1.3	0	1.2	0	1.1
Tip Targets	0	0.2	0	0.2	0	1.1	0	0.1	0	0.1	0	0.7
Internal Disturbances (Limit)	0	0.2	0	0.2	0	0.2	0	0.2	0	0.2	0	0.2
RSS Errors (See Table 3.5-11B)	1.2	1.7	1.0	0.2	2.3	3.0	1.2	1.5	1.0	0.2	2.2	4.9
Total Sum of Errors	1.4	3.5	1.1	2.3	2.8	6.3	1.2	3.1	1.0	1.7	2.5	6.9

Moments of Inertia

Pitch	Roll	Yaw	Damper	ϕ	α	δ	ξ
16.662	13.591	3158	540.0	58.2	53.4	-4.8	24.94
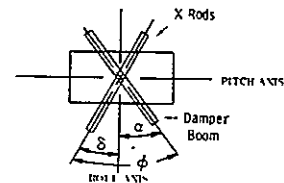
Table 3.5-11B. ATS-D Tolerance Effects

ATS-D Tolerance Effects	Sun 23.5° To Orbit Plane						Sun In Orbit Plane					
	Pitch		Roll		Yaw		Pitch		Roll		Yaw	
	Bias	Osc	Bias	Osc	Bias	Osc	Bias	Osc	Bias	Osc	Bias	Osc
Cylinder Reflectivity												
End Effect	0	0	0	0	0	0.1	0	0	0	0	0	0.1
Surface Effect	0	0	0	0	0	0.1	0	0	0	0	0	0.2
Unequal Rod Absorptivity	0.1	1.4	0	0.2	0.7	1.5	0	1.4	0	0	0	1.5
Spring Null Shift	0.2	0	0.2	0	0.1	0	0.2	0	0.2	0	0.1	0
Rod Shortness												
Principal Axis Shift	0.5	0	0	0	0.1	0	0.5	0	0	0	0.1	0
Thruster	0.1	0	0	0	0.1	0	0.1	0	0	0	0.1	0
Solar Torque	0	0.7	0	0	0	0.7	0	0.3	0	0.1	0	2.6
Rod Envelope												
Principal Axis	0.4	0	0.2	0	1.0	0	0.4	0	0.1	0	1.0	0
Thruster	0.0	0	0	0	1.8	0	0.0	0	0	0	1.8	0
Solar Torque	0	0.5	0	0.1	0	0.1	0	0.4	0	0.1	0	0.1
Rod Misalignment -1°												
Principal Axis Shift	1.0	0	1.0	0	1.9	0	1.0	0	1.0	0	1.9	0
Thruster	0.0	0	0	0	4.0	0	0	0	0	0	4.0	0
Solar Torque	0	0.3	0	0	0	2.0	0	0.2	0	0	0	3.5
Thruster -1° Misalignment	0.1	0	0	0	1.4		0.1	0	0		1.4	0
CM Uncertainty												
Thruster	0.1	0	0	0	1.4	0	0.1	0	0	0	1.4	0
Solar Torque	0	0.1	0	0.1	0	1.4	0	0.2	0	0.1	0	1.6
RSS Errors												
No Thruster	1.2	1.7	1.0	0.2	2.3	3.0	1.2	1.5	1.0	0.2	2.2	4.9
With Thruster	0	0.1	0	0.1	0	1.4	0	0.2	0	0.1	0	1.6

Moments of Inertia

Pitch	Roll	Yaw	Damper	ϕ	α	δ	ξ
16,662	13,591	3158	540.0	58.2	53.4	-4.8	24.94
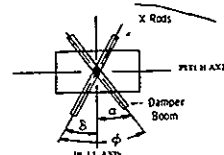
Table 3.5-12A. ATS-D Error Budget

Error Source	Sun 23.5° To Orbit Plane						Sun in Orbit Plane					
	Pitch		Roll		Yaw		Pitch		Roll		Yaw	
	Bias	Osc	Bias	Osc	Bias	Osc	Bias	Osc	Bias	Osc	Bias	Osc
With Station-Keeping:												
Magnetic Errors (Fixed Field)	0	0	0	0	0.3	0	0	0	0	0	0.3	0
Solar Torque and Thermal Bending	0.0	0.1	0	0.2	0	0.2	0	0.1	0	0.1	0	0.1
Tip Targets	0	0.2	0	0.2	0	1.1	0	0.1	0	0.1	0	0.7
Internal Disturbances (Limit)	0	0.2	0	0.2	0	0.2	0	0.2	0	0.2	0	0.2
Thrusters errors (30 days on)	0.0	0.1	0.0	0.0	0.1	0.1	0	0	0	0	0.2	0.2
RSS Errors (See Table 3.5-12B)	1.0	1.6	0.7	0.4	6.3	4.8	1.0	1.6	0.7	0.3	6.3	4.3
Total Sum of Errors	1.0	2.2	0.7	1.0	6.7	6.5	1.0	2.0	0.7	0.7	6.7	5.5
Without Station-Keeping:												
Magnetic Errors (Fixed Field)	0	0	0	0	0.3	0	0	0	0	0	0.3	0
Solar Torque and Thermal Bending	0.2	0.1	0	0.2	0	0.2	0	0.1	0	0.1	0	0.1
Tip Targets	0	0.2	0	0.2	0	1.1	0	0.1	0	0.1	0	0.7
Internal Disturbances (Limit)	0	0.2	0	0.2	0	0.2	0	0.2	0	0.2	0	0.2
RSS Errors (See Table 3.5-12B)	0.8	1.6	0.7	0.4	1.7	4.8	0.8	1.6	0.7	0.3	1.6	4.3
Total Sum of Errors	1.0	2.1	0.7	1.0	2.0	6.3	0.8	2.0	0.7	1.7	1.9	5.3

Moments of Inertia

Pitch	Roll	Yaw	Damper	ϕ	α	δ	ξ
16.662	13.591	3158	540.0	58.2	53.4	-4.8	24.94
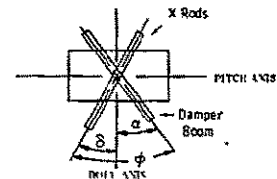
Table 3.5-12B. ATS-D Tolerance Effects

ATS-D Tolerance Effects	Sun 23.5° To Orbit Plane						Sun In Orbit Plane					
	Pitch		Roll		Yaw		Pitch		Roll		Yaw	
	Bias	Osc	Bias	Osc	Bias	Osc	Bias	Osc	Bias	Osc	Bias	Osc
Cylinder Reflectivity	0	0.4	0	0.4	0	3.7	0	0.1	0	0.2	0	0.4
Unequal Rod Absorptivity	0 1	1 4	0	0.2	0.7	1 5	0	1.8	0	0	0	1.8
Spring Null Shift	0.2	0	0 2	0	0.1	0	0.2	0	0.2	0	0.1	0
Rod Shortness												
Principal Axis Shift	0.5	0	0	0	0.1	0	0.5	0	0	0	0.1	0
Thruster	0.4	0	0	0	3 7	0	0.4	0	0	0	3.7	0
Solar Torque	0	0.3	0	0	0	2.0	0	0.5	0	0.1	0	3 5
Rod Envelope												
Principal Axis	0.4	0	0.2	0	1.0	0	0.4	0	0.2	0	1.0	0
Thruster	0	0	0	0	1.8	0		0	0	0	1.8	0
Solar Torque	0	0.5	0	0.1	0	0.1	0	9 4	0	0.1	0	0.1
Rod Misalignment -1°												
Principal Axis Shift	0.5	0	0 6	0	1.2	0	0.5	0	0.6	0	1.2	0
Thruster	0.2	0	0	0	4.0	0	0.2	0	0	0	4.0	0
Solar Torque	0	0.1	0	0	0	0.6	0	0.1	0	0	0	0.9
Thruster -1° Misalignment	0.1	0	0	0	1.4	0	0 1	0	0	0	1.4	0
CM Uncertainty												
Thruster	0.1	0	0	0	1.4	0	0.1	0	0	0	1.4	0
Solar Torque	0	0.1	0	0.1	0	1.4	0	0.2	0	0.1	0	1 6
RSS Errors												
No Thruster	0.8	1.6	0.7	0.4	1.7	4.8	0.8	1.6	0.7	0.3	1.6	4.3
With Thruster	1.0	1.6	0.7	0.4	6.3	4.8	1.0	1 6	0.7	0.3	6 3	4.3

Moments of Inertia

Pitch	Roll	Yaw	Damper	ζ	α	δ	ξ
16.662	13.591	3158	540 0	58.2	53.4	-4.8	24.94
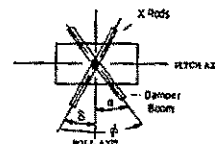
3.5.4.1 Performance of ATS-D with Actual VTHD Damper

After completion of the curve fitting modification to the ATS Mathematical Model, a simulation of the ATS-D capture performance was made. The curve fitting routine fits hysteresis torque data points with an nth order (12th order maximum) polynomial. Figure 3.5-24 is the data obtained from test for the VTHD used on ATS-D. Superimposed over the data points are points calculated by the Mathematical Model curve fitting routine. In general, the fit is excellent, the most significant difference being at -45 degrees damper angle and at -0.75 dyne-cm hysteresis torque. The error is approximately 7 percent. For convenience in the simulation, the spring torque was included in the hysteresis torque. The venience in the simulation, the spring torque was included in the hysteresis torque. The results of the computer run are shown in Figure 3.5-25 and Figure 3.5-26. The initial conditions for this run, as well as the spacecraft parameters, are identical to those used in simulating the constant torque hysteresis damper in Section 3.2.3. A direct comparison between Figure 3.5-25 of this Section and Figure 3.2-53 of Section 3.2.3.2 indicates the VTHD has damping nearly equivalent to the constant torque hysteresis damper at high oscillations. Comparing Figure 3.5-26 with Figure 3.2-54 of Section 3.2.3.2, however, indicates that the VTHD damps the spacecraft much more rapidly than the constant torque hysteresis damper at intermediate and low amplitude oscillations. At the end of 400 hours, the constant torque hysteresis damper has reduced the pitch, roll, and yaw errors to 10.7 degrees, 7.0 degrees, and 8.4 degrees, respectively. In the same time, the VTHD damper has reduced the pitch, roll, and yaw errors to 1.5 degrees, 1.3 degrees and 11.2 degrees, respectively. These results confirmed that the VTHD manufactured for ATS-D would result in a significant improvement in damping time over the constant torque hysteresis damper.

3.5.4.2 Performance of ATS-E with Actual Damper

The measured values of the spring and damper constant for the ATS-E damper were found to be high (3.99 dyne-cm/deg and 11,500 dyne-cm/deg/sec, respectively) compared to the nominal (3.5 dyne-cm/deg and 9860 dyne-cm/deg/sec, respectively). In addition, there was a small amount of hysteresis (5.5 dyne-cm) present in the damper.
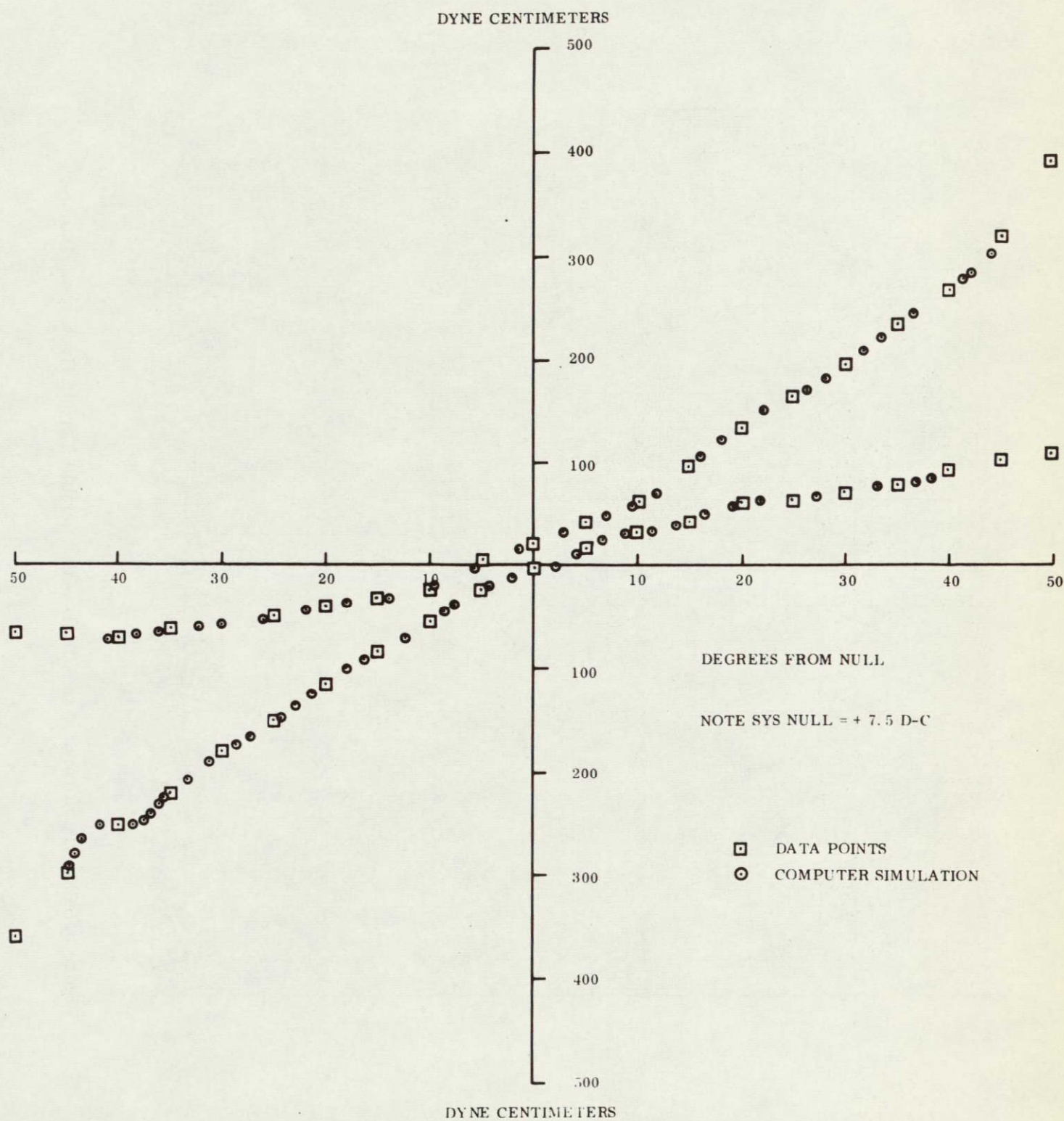
Figure 3.5-24.   VTHD No. 007 Post-Vibration Static Test Data
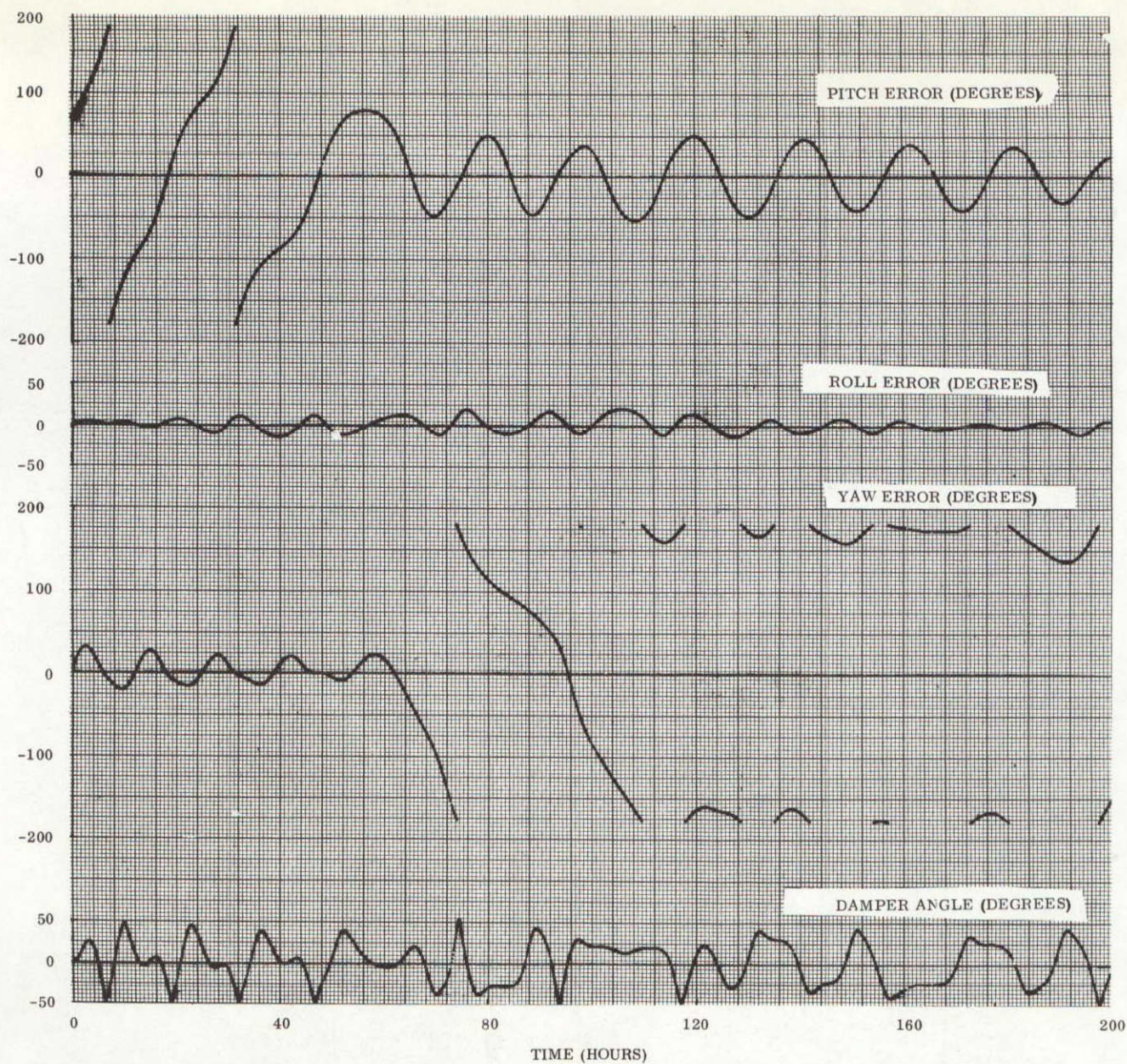
Figure 3.5-25.   Performance of ATS-D with Variable Torque Hysteresis Damper
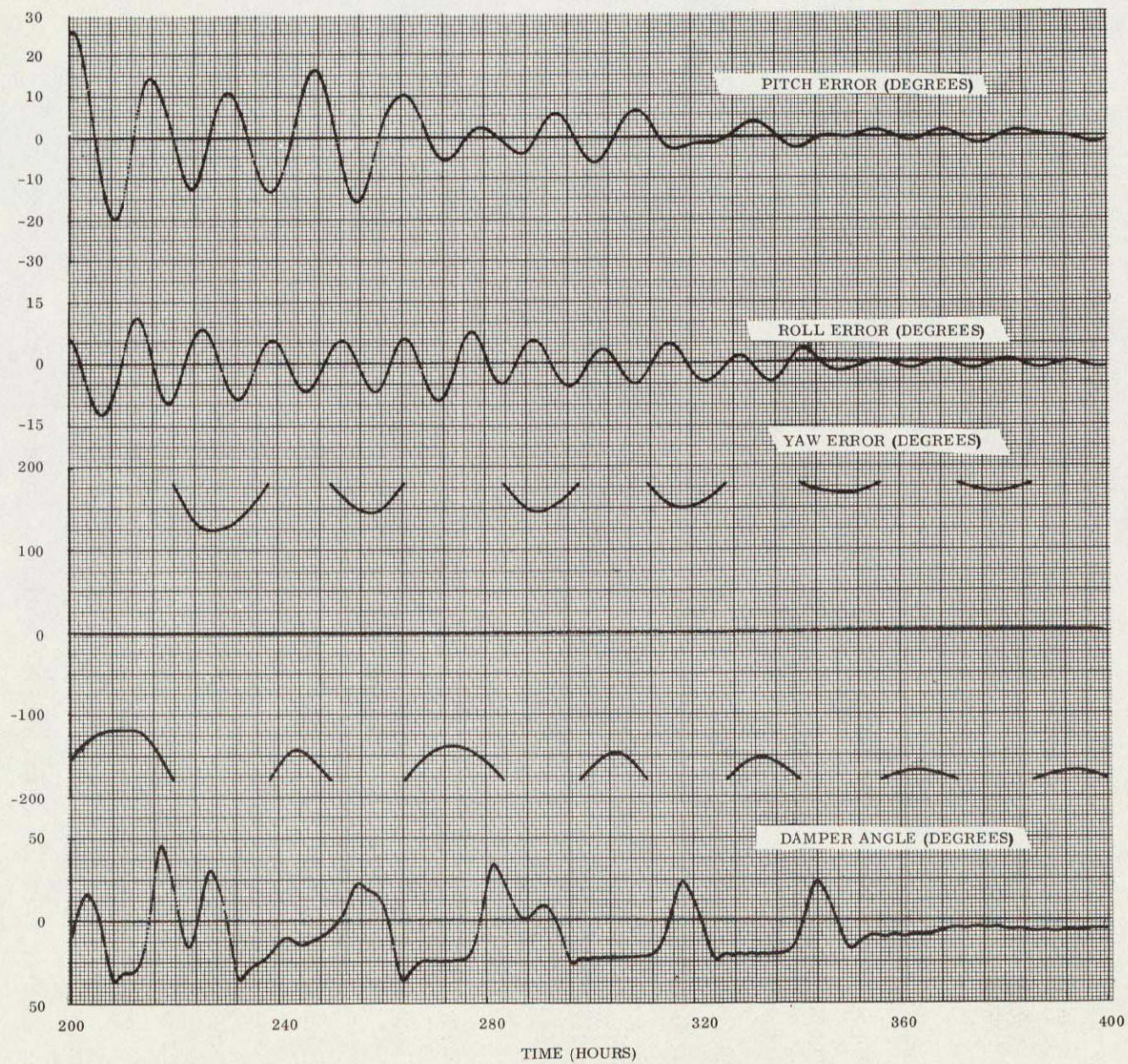
Figure 3.5-26.   Performance of ATS-D with Variable Torque Hysteresis Damper

Because the time and effort involved in physically adjusting these coefficients is extensive, the question was raised as to the effect of these actual values on the performance of ATS-E.

To determine the effect on the capture performance, a computer run was made using the "standard" capture conditions and the actual damper parameters. In addition, a reference run was made simulating the nominal case. The results are shown in Figures 3.5-27, 3.5-28, 3.5-29 and 3.5-30 and indicate that there is little effect on damping of the "out of spec" values.

On the surface, this appears to be contrary to the linearized damping estimates presented in Section 3.5.2.1 which would have indicated an increase in damping time of approximately 156 percent. Remember, however, that these estimates assume small angle motion. For small angles, the damper boom motion is controlled by gravity gradient, the spring and damping constant, and the motion of the spacecraft. For large amplitude motions, however, the damper is driven by the spacecraft motion; gravity gradient and the spring constant are secondary effects (for reasonable values of spring constant). Hence, for large amplitude motions, the damping time is determined largely by the damping constant (within limits). This is higher for the actual ATS-E than the nominal. As a consequence, the actual ATS-E damps slightly faster than the nominal ATS-E for the period of performance covered by these runs. It is expected that if the runs had been extended, the nominal ATS-E would have achieved steady state sooner than the actual ATS-E.

To verify this conclusion, two damping runs were made. These runs were transient runs, but did not start from capture conditions and were intended to show relative damping and steady state performances. The initial conditions were zero roll and yaw rate, with pitch at 50 degrees with an angular rate (inertial) of one-half orbital.

The results of the simulations are shown in Figures 3.5-31 and 3.5-32. The performances are very similar, with the actual damper settling to steady state slightly faster than the nominal. The performance of the spacecraft with the actual combination passive damper is quite satisfactory from the stabilization standpoint even in the slightly "out-of-spec" condition.

3-282
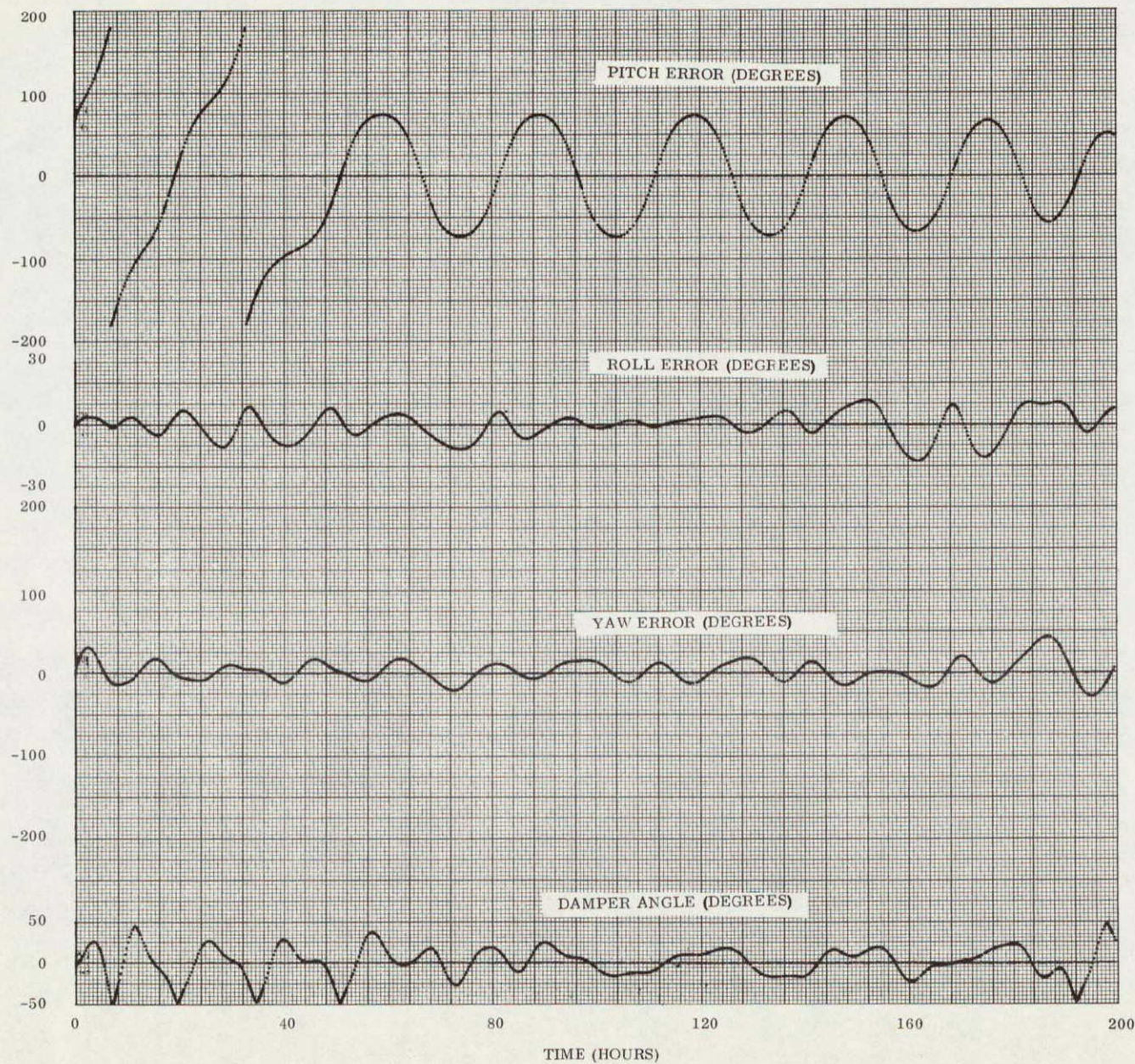
Figure 3.5-27. Performance of ATS-E with Nominal Spring and Eddy Current Damper,
First 200 Hours
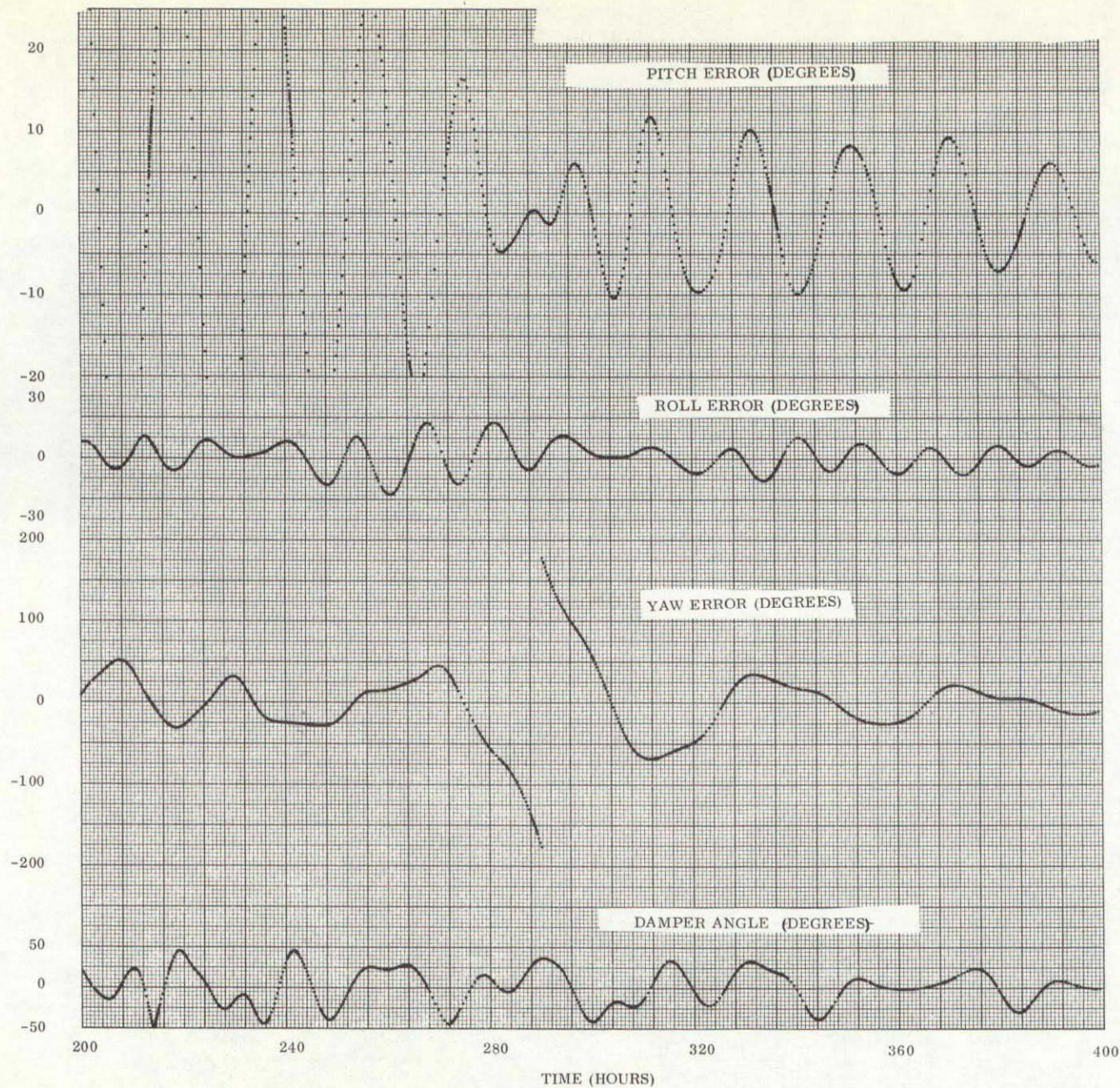
Figure 3.5-28. Performance of ATS-E with Nominal Eddy Current Damper Characteristics, Second 200 Hours
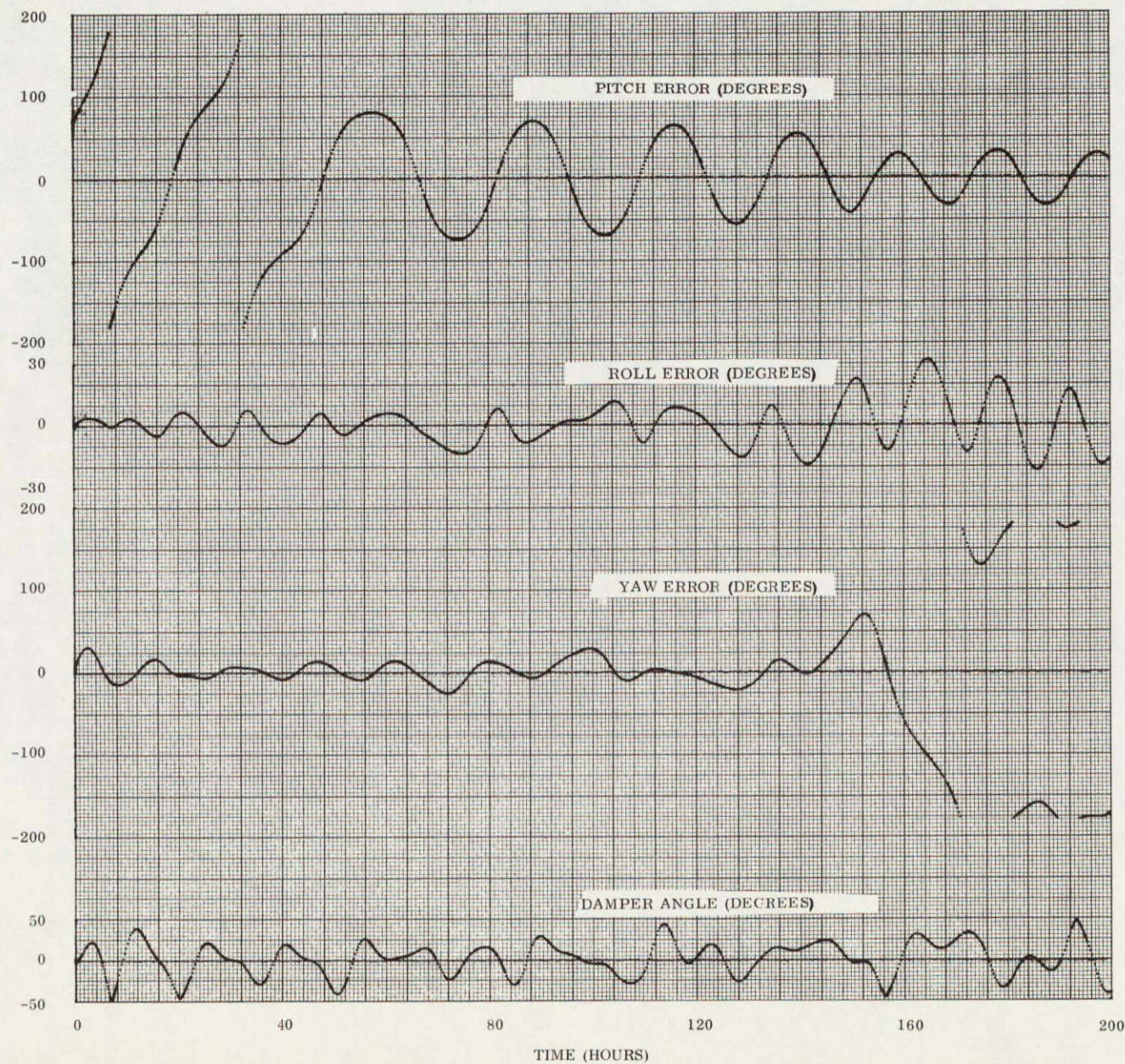
Figure 3.5-29. Performance of ATS-E with Actual Spring and Eddy Current Damper,
First 200 Hours

3-285
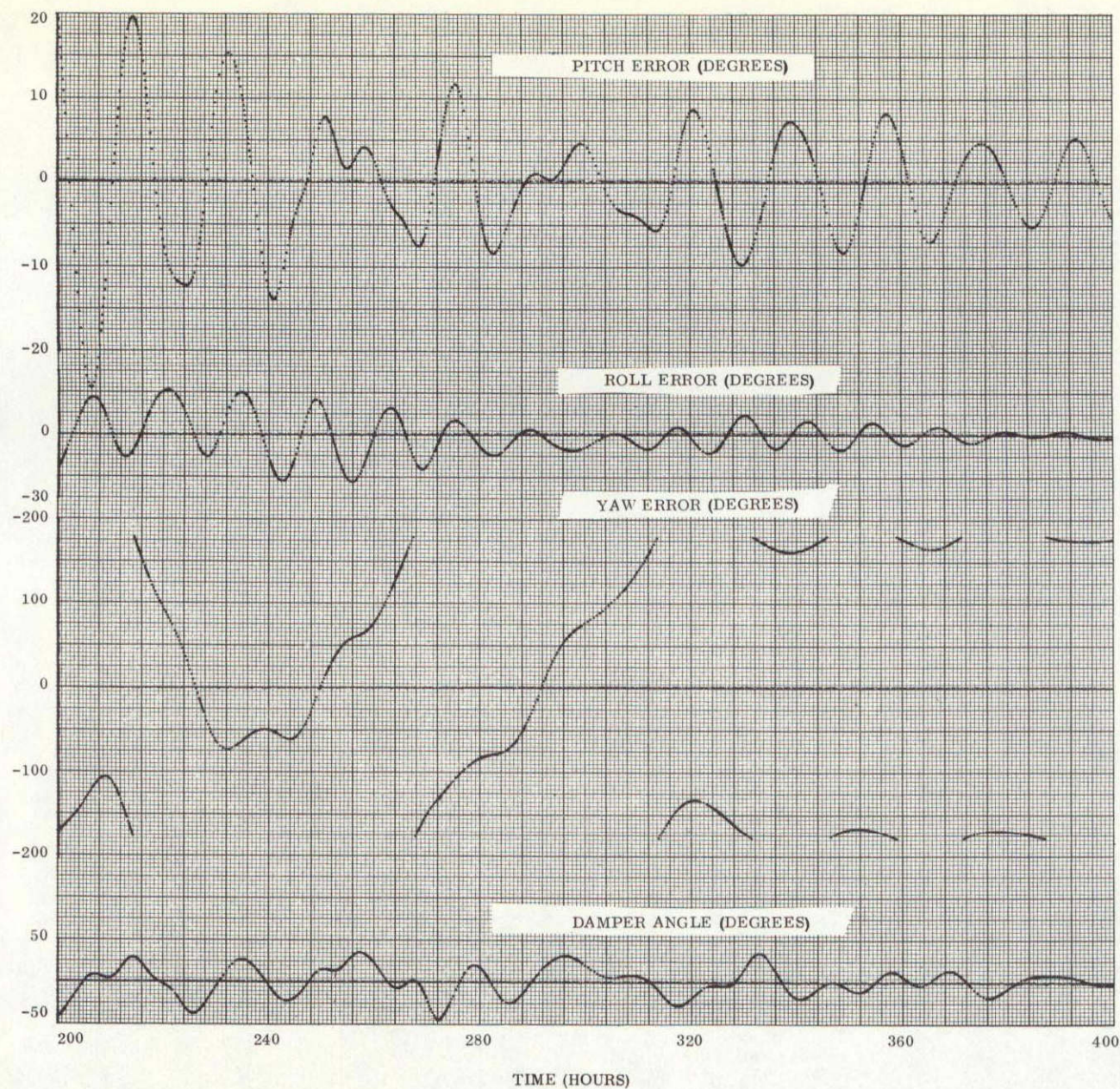
Figure 3.5-30. Performance of ATS-E with Actual Eddy Current Damper Characteristics, Second 200 Hours
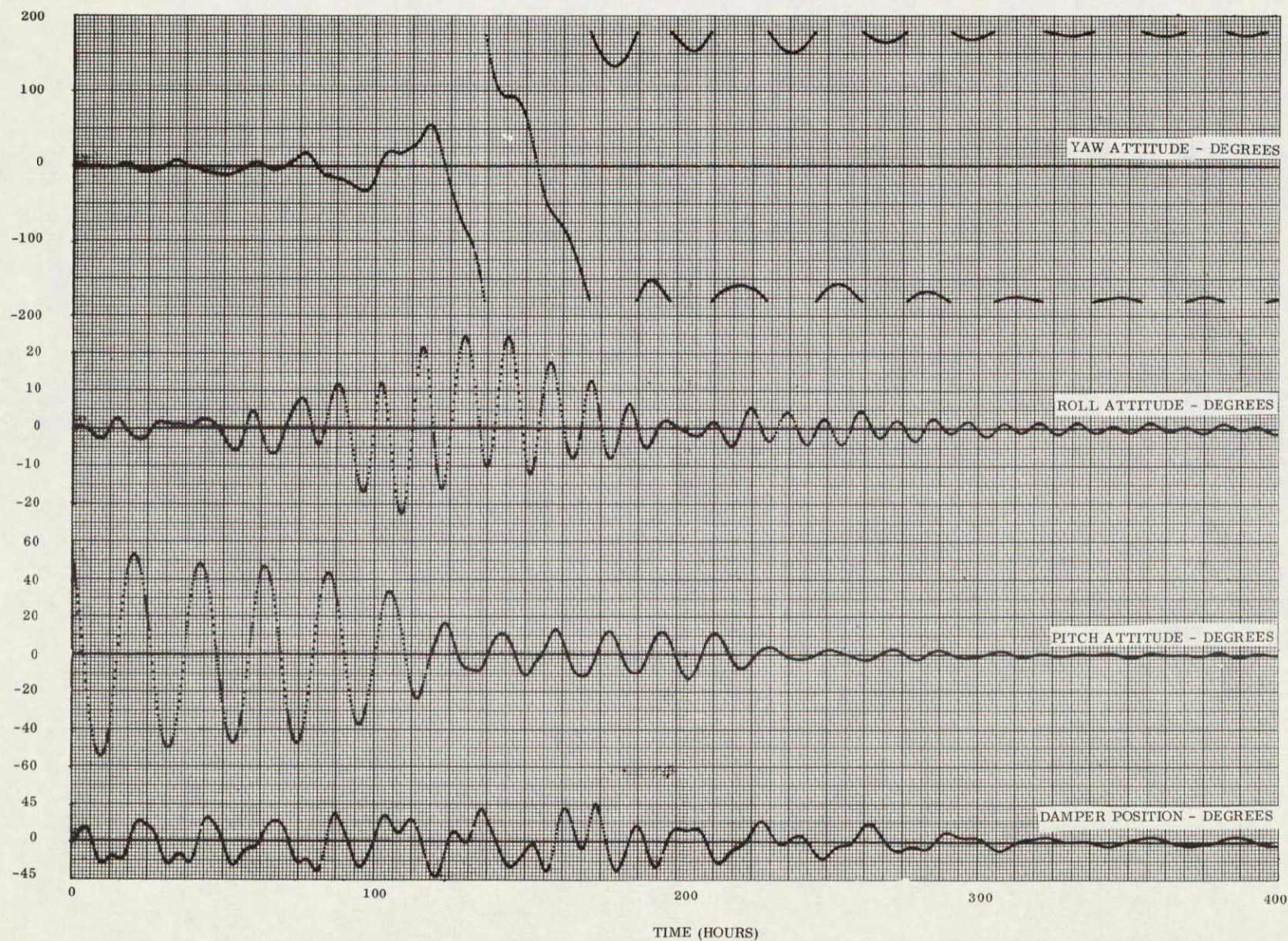
Figure 3.5-31. Performance of Actual ATS-E Damper
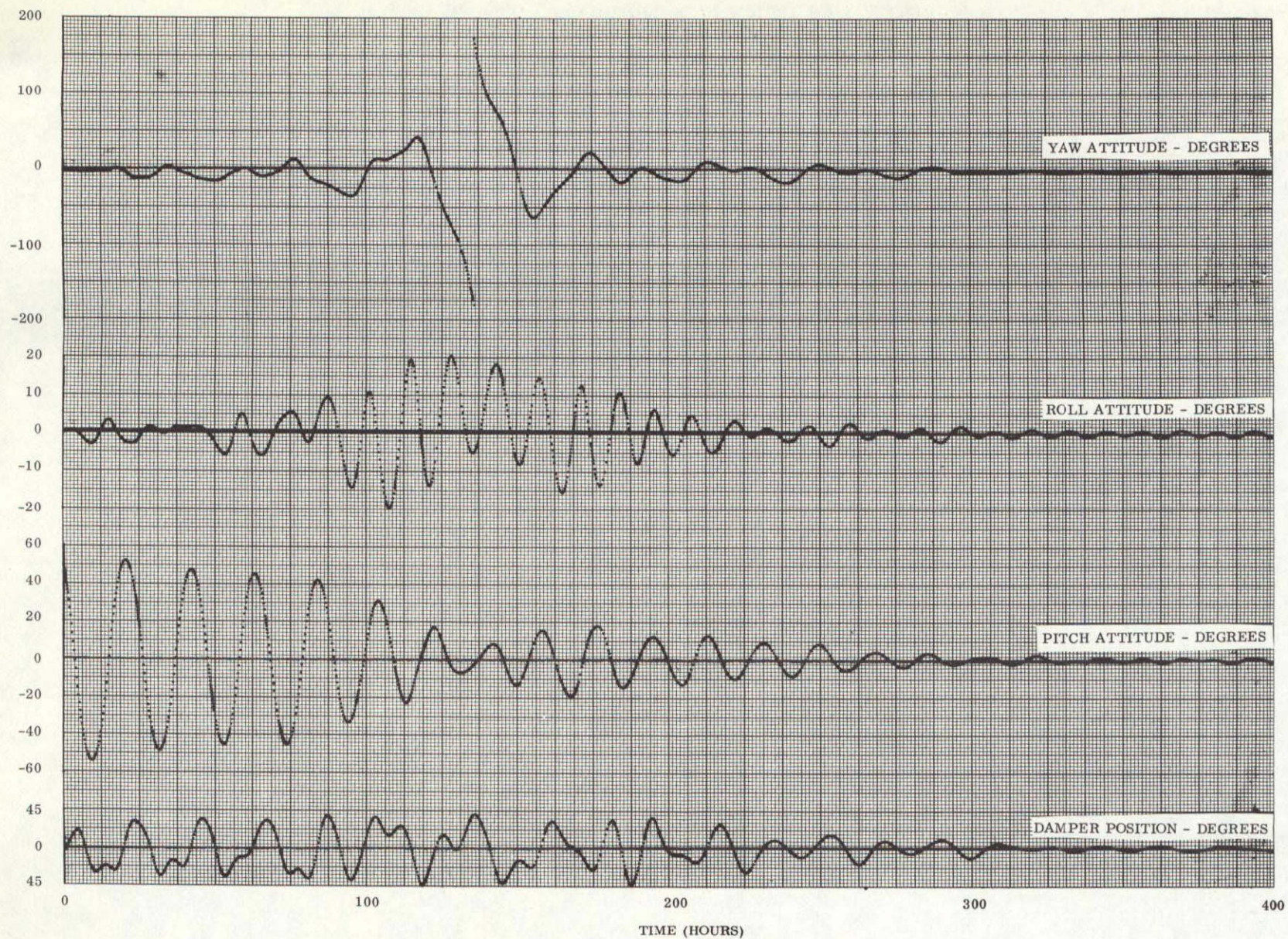
Figure 3.5-32.   Performance of Nominal ATS-E Damper

The fact that this damper damped faster than the nominal raised questions regarding the validity of the optimization studies. It should be pointed out again that the optimization studies are developed from linearized (and small angle) equations where external disturbances are not considered. For these studies, the spacecraft is defined exactly (from the standpoint of numerical inputs). External disturbances, damper offsets, actual rod orientations, etc., are all included in the full simulations. All these factors affect both the damping and steady state performance of the spacecraft. To avoid the requirement for re-optimization studies after every small hardware change, the linearized studies were used to provide a basis for estimating the relative importance of each parameter. It was expected that this would represent a worst case and it is not surprising that the performance of ATS-E with the actual damper is somewhat different than predicted. Fortunately (but not predictably), the real damping is better than the nominal damping.

3.5.5 EXPERIMENTAL CONFIGURATIONS

The primary purpose of the ATS-A, D/E spacecraft was to perform attitude stabilization experiments on the gravity gradient stabilization subsystem. To this end, the rod deployment mechanisms on the primary spacecraft were equipped with scissor mechanisms which permitted the rod angles to be changed while the spacecraft was in orbit. In addition, two types of dampers were included on the spacecraft, a magnetic hysteresis damper and an eddy current rate damper. Part of the mission profile was to determine the performance of the spacecraft with several rod half angles, both dampers, and several rod lengths.

3.5.5.1 ATS-A

To estimate the performance of the experimental configurations, a series of computer simulations was made which included a combination of error sources. Included in the errors were a magnetic dipole along the pitch axis, an eccentric orbit, and solar pressure and thermal bending, with initial position angles in pitch and roll. Three parameters were varied among the runs to obtain various conditions. These are:

1. Type of Damping - eddy current or hysteresis

2. Rod Half Angle (Zeta) - 11, 15, 19, 25.02 and 31 degrees

3. Sun Vector to Orbit Plane Angle -- 0 and 28 degrees

A complete set of twenty runs was made to cover all combinations of the variables. Each run was plotted and both the plot and the tabular data were examined to determine approximate damping time and the final oscillation and bias of each axis. These data are tabulated on the attached error budgets (see Table 3.5-13). The damping times listed are, for the eddy current runs, approximations taken from the plots. For the hysteresis damping runs, the damping times are the ends of the major portion of decay. Previous experience indicates that hysteresis damping continues for a longer time than the eddy current does, but eventually matches the biases and amplitudes at steady state. The amplitude and bias values were extracted from the last 15 hours of the tabulated data. As such, they represent steady state values for eddy current damping and interim values for hysteresis damping.

For purposes of comparison, the runs are grouped by type of damping, then by sun in or out of orbit plane, and finally by the main rod half angle. From these lists it is seen that, while local points of quicker damping occur randomly, all four runs show minimum damping time at the design main rod half angle of 25.02 degrees. Lower values of oscillations and biases occur at different points throughout the runs. As an example, the pitch axis shows an increase in oscillation amplitude with increase in zeta. The exception is at zeta equals 25.02 degrees, hysteresis damping, sun out of plane. A very sharp drop in value was noted here. Roll axis oscillations are lowest in the 15 to 25.02 degree range for zeta. No special comment can be made concerning this range. The point, or points, of minimum amplitude depends on sun relationship and type of damping. Oscillations about the yaw axis are generally lowest at the 19 degree point. Here again, an exception occurred for eddy current damping, sun out of plane, zeta equals 25.02 degrees.

As a means of illustrating the relative damping of the two types of dampers, the times for the eddy current damper envelope to decay to the final values for the hysteresis damper are given in Table 3.5-14. The bias and amplitude values are listed for convenience of comparison.

Table 3.5-13. Results of Runs

Hysteresis Damping

Sun in Orbit Plane

Zeta	Pitch Amp	Pitch Bias	Roll Amp	Roll Bias	Yaw Amp	Yaw Bias
11°	3.3	0.3	6.7	0.1	9.3	-18.6
Damping Time Hours	44		68		64	
15°	4.6	0.3	3.2	0.1	8.1	- 7.3
Damping Time Hours	48		48		38	
19°	3.7	0.4	3.5	0.5	9.0	- 3.2
Damping Time Hours	40		64		56	
25.02°	3.9	0.2	2.4	0.2	15.8	180.3
Damping Time Hours	36		56		50	
31°	10.3	0.8	3	0.2	3	1.9
Damping Time Hours	88		88		76	

Sun 28° Out of Orbit Plane

Zeta	Pitch Amp	Pitch Bias	Roll Amp	Roll Bias	Yaw Amp	Yaw Bias
11°	2.3	0.3	4.0	-0.1	11.8	-17.9
Damping Time Hours	56		68		76	
15°	5.1	0.2	3.8	0	8.7	171.3
Damping Time Hours	50		62		60	
19°	5.1	0	0.5	0	6.8	177.8
Damping Time Hours	58		54		56	
25.02°	1.5	-0.2	3.4	0	15.9	0.9
DampingTime Hours	44		50		50	
31°	7.1	0.8	2.8	0.2	6.2	2.3
Damping Time Hours	88		94		100	

Table 3.5-13. Results of Runs (cont'd)

Eddy Current Damping

Sun in Orbit Plane

Zeta	Pitch Amp	Pitch Bias	Roll Amp	Roll Bias	Yaw Amp	Yaw Bias
11°	1.3	0.2	0.5	0	2.8	-17.8
Damping Time Hours	76		76		84	
15°	1.4	0.3	0.5	0.1	2.8	171.5
Damping Time Hours	70		80		100	
19°	1.6	0.2	0.2	0	2.9	- 3.5
Damping Time Hours	80		88		96	
25.02°	2.4	0.2	0.1	0	3.4	- 0.3
Damping Time Hours	48		60		76	
31°	7.5	0.3	1.7	-0.1	7.2	180.9
Damping Time Hours	96		88		108	

Sun 28° Out of Orbit Plane

Zeta	Pitch Amp	Pitch Bias	Roll Amp	Roll Bias	Yaw Amp	Yaw Bias
11°	1.3	0.2	0.7	0.1	3	-18
Damping Time Hours	56		70		80	
15°	1.4	0.3	0.7	0	1.9	171.1
Damping Time Hours	62		72		76	
19°	1.6	0.2	0.4	0	3.1	- 3.4
Damping Time Hours	74		96		86	
25.02°	2.4	0.2	0.5	0	2.3	180
Damping Time Hours	54		72		62	
31°	7.9	0.3	1.7	-0.2	6.0	181.0
Damping Time Hours	88		88		84	

Table. 3.5-14. Sun In and Out of Orbit Plane

| Zeta (degree) | Amplitude (degree) | Sun In Orbit Plane | | | |
| | | Hysteresis | | Eddy | |
		Time (hour)	Bias (degree)	Time (hour)	Bias (degree)
11	9.3	150	-18.6	98	-19.8
15	8.1	150	-7.3	90	-6.3
19	9.0	150	-3.2	78	-3.0
25.02	15.8	150	0.3	49	0.2
31	3	150	1.9	*	3.0

*Did not damp to this level.

| Zeta (degree) | Amplitude (degree) | Sun Out of Orbit Plane | | | |
| | | Hysteresis | | Eddy | |
		Time (hour)	Bias (degree)	Time (hour)	Bias (degree)
11	11.8	150	-17.9	78	-18
15	8.7	150	171.3	52	-6
19	6.8	150	177.8	88	-3
25.02	15.9	150	0.9	43	1
31	6.2	150	2.3	136	2

As the rod half angle is increased from 11 degrees toward 25.02 degrees, the eddy current damper shows a corresponding improvement in damping times. Between 25.02 and 31 degrees a sharp worsening occurs such that for "Sun in Plane," the hysteresis damper is the better. The sharp increase which occurs for "Sun Out of Plane" shows the approaching of an equal time point. Probably, if the rod angle were opened to 35 degrees, the hysteresis damper would be the more effective.

The results seem to indicate that hysteresis damping is the more efficient at rod half angles above 25.02 degrees and eddy current damping is more effective at rod half angles below 25.02 degrees.

Most of the tabulations and graphs show the range of 19 to 25 degrees for rod half angle to offer the best combination of low residual bias and oscillation. In this range, using the eddy current damper, the damping times were minimized.

3.5.5.2 ATS D/E

A study identical to that performed for the ATS-A experiment configurations was performed for ATS-D. The results agree, in general with those obtained for ATS-A, and are shown in Tables 3.5-15 and 3.5-16.

Table 3.5-15. Results of Runs

	Pitch		Roll		Yaw	
Eddy Current Damping - levels at 400 hours Sun in the Orbit Plane						
Half Angle	Amp	Bias	Amp	Bias	Amp	Bias
11	1.7	-0.1	3.4	0.1	6.4	-19
15	1.5	0.2	2.0	0.3	1.8	-7.2
19	1.4	0	1.7	0	0.8	-3.5
24.94	1.9	0.5	1.1	0	0.5	-0.1
31	3.4	0.2	0.8	0	3.0	+1.3
Sun Out of Orbit Plane						
11	1.6	0	3.7	0.2	2.5	-20.3
15	1.5	-0.2	2.3	+0.2	3.7	-8.0
19	1.2	0.1	1.5	0.3	3.8	-2.8
24.94	1.3	-0.1	1.6	0.1	2.0	0.4
31	2.8	-0.2	1.8	-0.1	3.8	1.6
Hysteresis Damping - Levels at 400 hours.						
Sun in the Orbit Plane						
11	6.8	0.3	5.3	0.2	42.0	-22.2
15	10.9	0.5	5.9	0.1	35.0	-8.8
19	4.7	-0.4	2.1	-0.6	*	*
24.94	6.2	0.8	8.6	-0.3	18	-0.8
31	15.5	-0.3	5.3	-0.6	9.1	1.0
Sun Out of the Orbit Plane						
11	8.2	0.3	6.5	-0.1	19.1	-17.3
15	5.8	0.2	7.0	-0.6	29.3	-10
19	8.5	-1.0	7.0	0.6	21.5	-6
24.94	8.9	-0.1	3.1	0	26.2	-3.2
31	5.6	0.1	6.1	-0.1	23.6	-0.2

*Did not damp within 400 hours.

Table 3.5-16. Sun In and Out of Orbit Plane

Zeta (degree)	Amplitude (degree)	Sun In Orbit Plane			
		Hysteresis		Eddy	
		Time (hour)	Bias (degree)	Time (hour)	Bias (degree)
11	42	400	-22.2	218	-24
15	35	400	-8.8	169	-6
19	*	400	*	**	**
24.94	18	400	-8.2	165	-3
31	9.1	400	1.0	208	+4

*Did not damp within 400 hours.
**No comparison was drawn.

Zeta (degree)	Amplitude (degree)	Sun Out of Orbit Plane			
		Hysteresis		Eddy	
		Time (hour)	Bias (degree)	Time (hour)	Bias (degree)
11	19.1	400	-17.3	193	-21
15	29.3	400	-8.5	241	-6
19	21.5	400	-6.8	291	-4
24.94	26.2	400	-3.2	174	+2
31	23.6	400	-0.16	135	+5

3.6 ADDITIONAL STUDIES

3.6.1 RESPONSE OF ATS TO SOLITARY IMPULSE

The response of the ATS gravity gradient vehicle to a solitary impulse can be determined by a simplified analysis. The pulse is assumed to be solitary in that it is not preceded or followed a pulse of similar nature.

The simplified analysis used to estimate the performance (Appendix H) assumes each axis is individual and decoupled from the other axes. The results obtained from this analysis were checked in the simulation, and good agreement was obtained for pitch and roll. The yaw agreement was not as good however, and additional computer runs were made. The results indicate the performance is linear with impulse, but because of the large oscillations of the damper boom, the performance of the yaw axis cannot be determined without regard to the other axes (primarily the damper).

The results of the simplified analysis were combined with the results of the simulation, and plotted as shown in Figures 3.6-1 through 3.6-6. The errors are linear with impulse for impulses which do not cause large errors or those which are not applied for a time exceeding the natural period of oscillation. If this is not the case, the amplitude of oscillation (or tumble) is not a direct function of the impulse.

3.6.2 ATS PITCH-UP MANEUVER

As part of the ATS experiment plan, the spacecraft was to be pitched up to evaluate its damping characteristics. The approach taken was to use the inversion thrusters to disturb the spacecraft, but not to invert it. To do this, the inversion thrusters must be cutoff earlier than for inversion. Figures 3.6-7 and 3.6-8 give the inversion thruster cutoff time required to reach a given pitch attitude for ATS-A and ATS-D, respectively. These data are based upon computer runs, assuming nominal initial conditions and no disturbances.

Note that for a given value of thruster torque, the maximum pitch angle attained is approximately proportional to thruster cutoff time. Also, for a given value of thruster cut
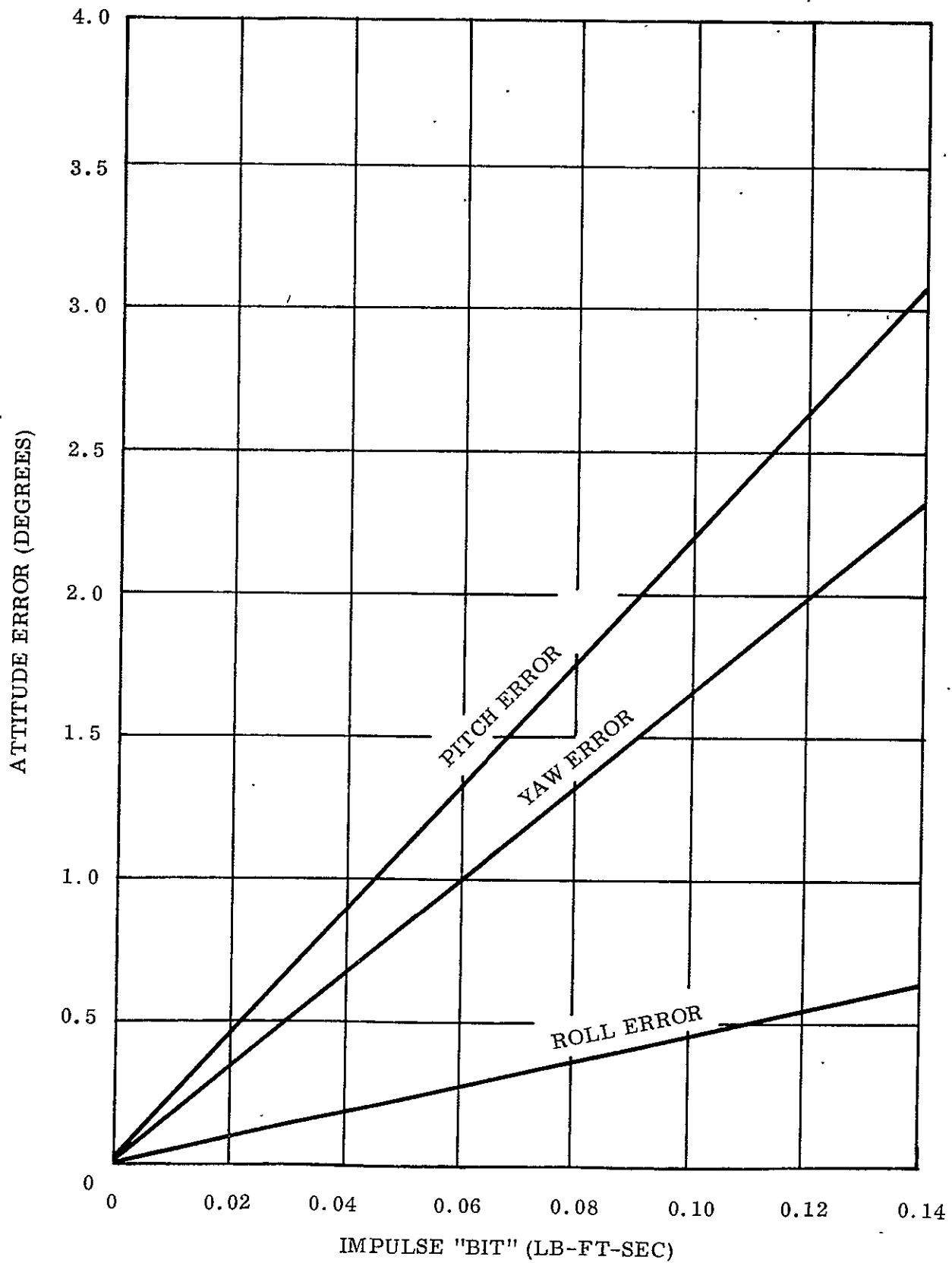
Figure 3.6-1 ATS-A Response To Pitch Impulse
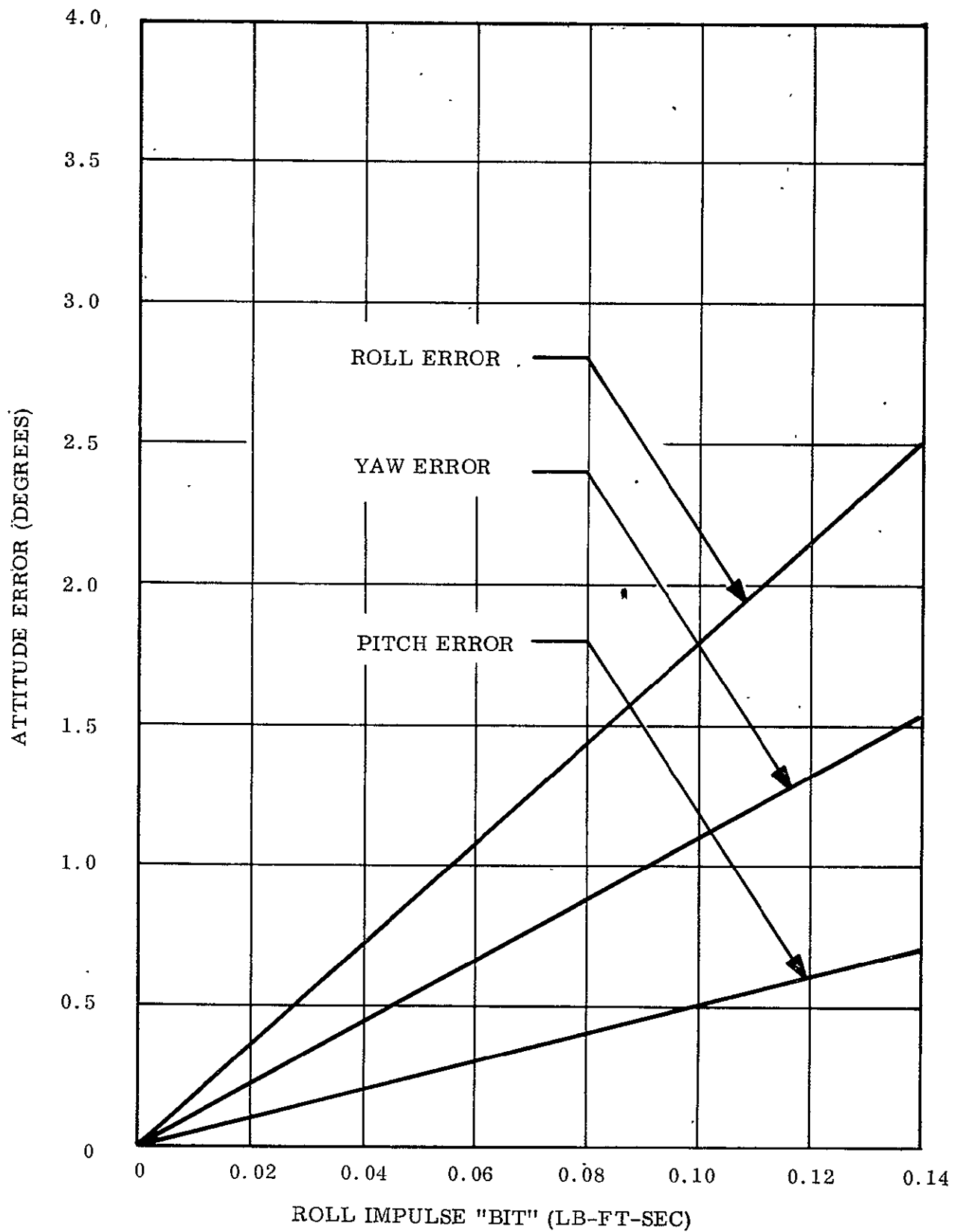
Figure 3.6-2 ATS-A Response To Roll Impulse
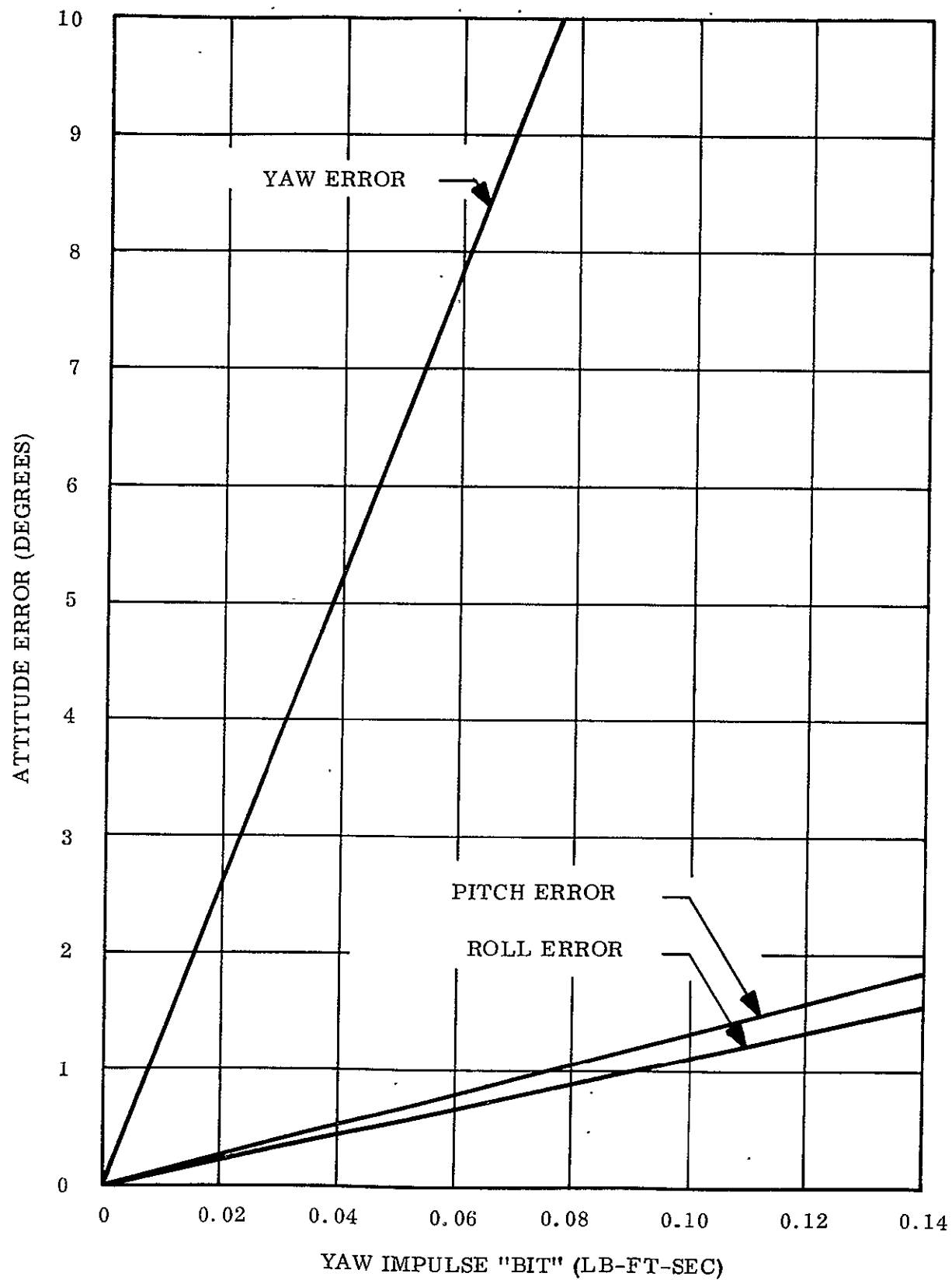
Figure 3.6-3 ATS-A Response to Yaw Impulse
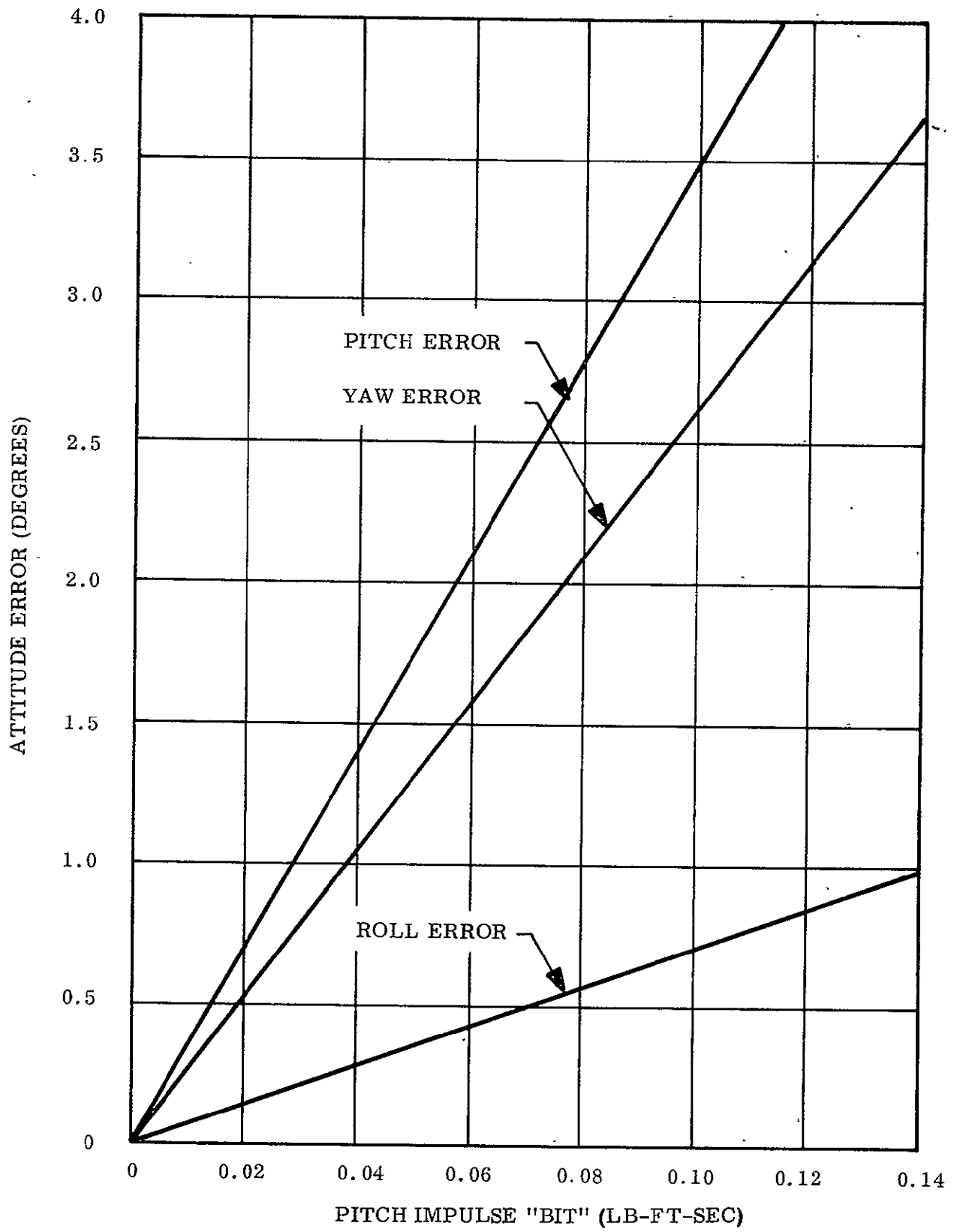
Figure 3.6-4 ATS-D Response to Pitch Impulse
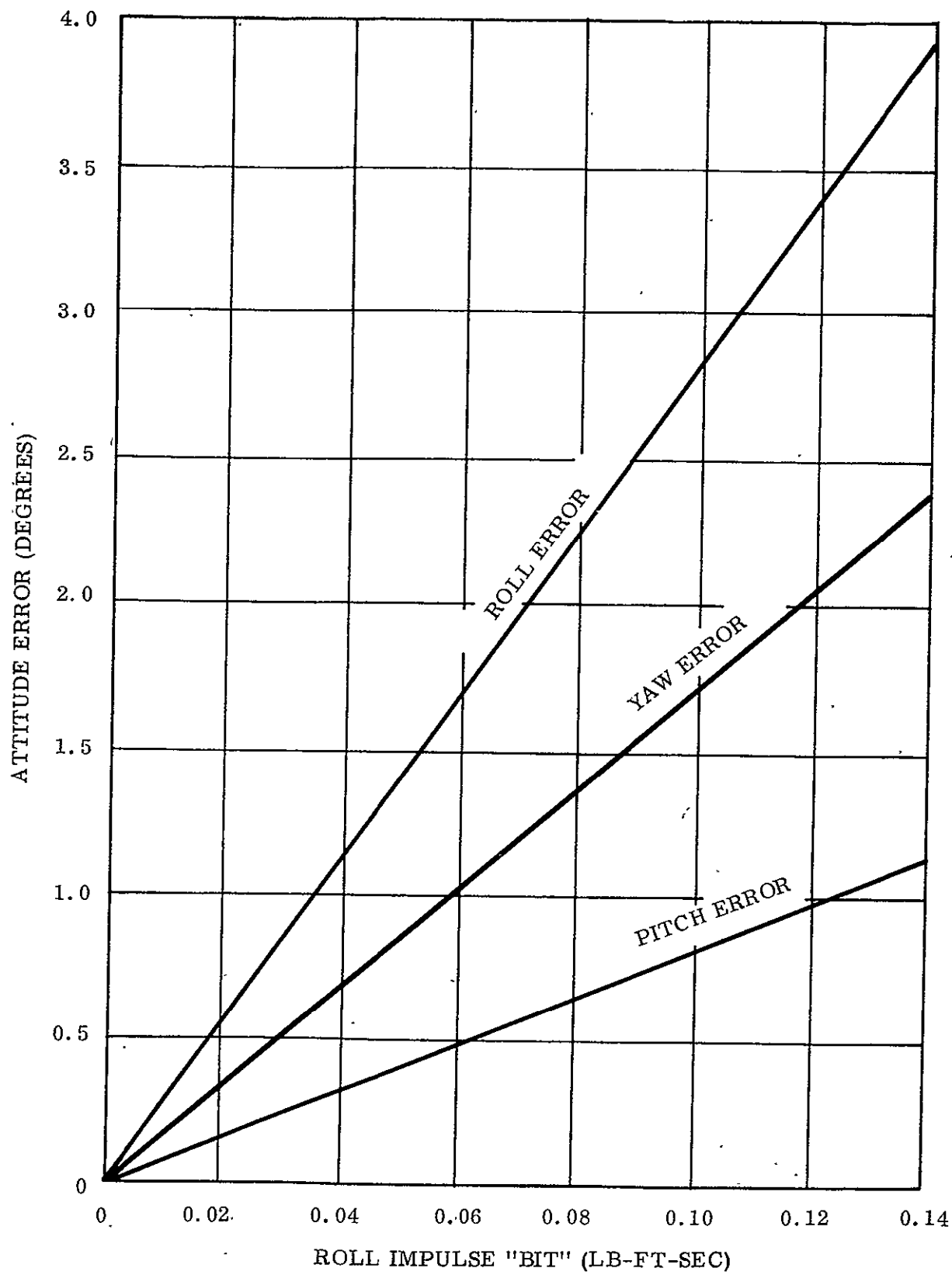
Figure 3.6-5 ATS-D Response to Roll Impulse
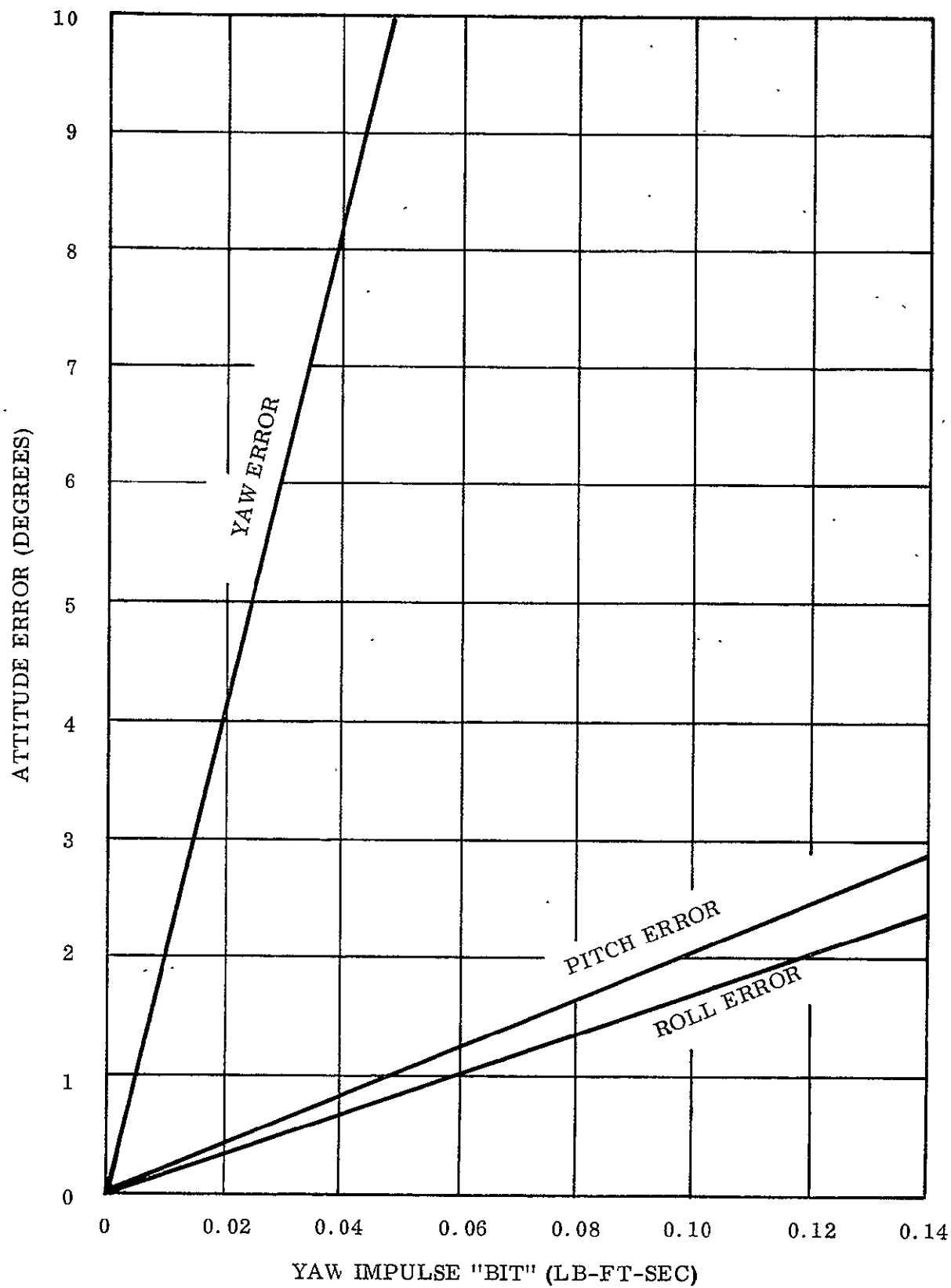
Figure 3.6-6 ATS-D Response to Yaw Impulse

off time, the maximum pitch angle is approximately proportional to thruster torque. These relationships hold for pitch angles up to 40 degrees.

Figure 3.6-9 shows the total time required to reach the maximum pitch angle. These times include the thruster cutoff time and a coast time.

Negative values of thruster torque were used in these computer runs. However, when positive torques are used, the results are identical.

3.6.3 EFFECT OF DAMPER DEPLOYMENT SQUIBS ON ATTITUDE PERFORMANCE

Deployment of the damper booms on both ATS-A and ATS-D requires firing several squib actuated pistons (ref: Sixth Quarterly Progress Report). Leakage of the combustion products to ambient could disturb the spacecraft. To calculate the attitude error resulting from this disturbance, it is necessary to determine the angular impulse imparted by the squib and to evaluate the response of the vehicle. The response of the vehicle is dependen upon the manner in which the impulse is expended. Two modes of expenditure are consit ered in this section: instantaneous and "trickle". Peak errors are calculated for each mode.

To calculate the angular impulse, several assumptions must be made. The source of the impulse is the squib mechanism used to deploy the damper. The total quantity of explosiv per valve is 75 milligrams, approximately $1.65 \cdot 10^{-4}$ lb. If the combustion products leak a thrust will be produced for a short period of time. The impulse produced by this thrust is directly dependent upon the specific impulse of the combustion products. The leakage is not through a carefully designed nozzle and the specific impulse will not be large. As an estimate, a specific impulse of 100 sec was assumed. The total impulse per squib is

$$I = 1.65 \cdot 10^{-4} \text{ lb} \times 100 \text{ sec} = 0.0165 \text{ lb-sec}$$

To convert this to angular momentum, the moment arm to the center of mass is required.
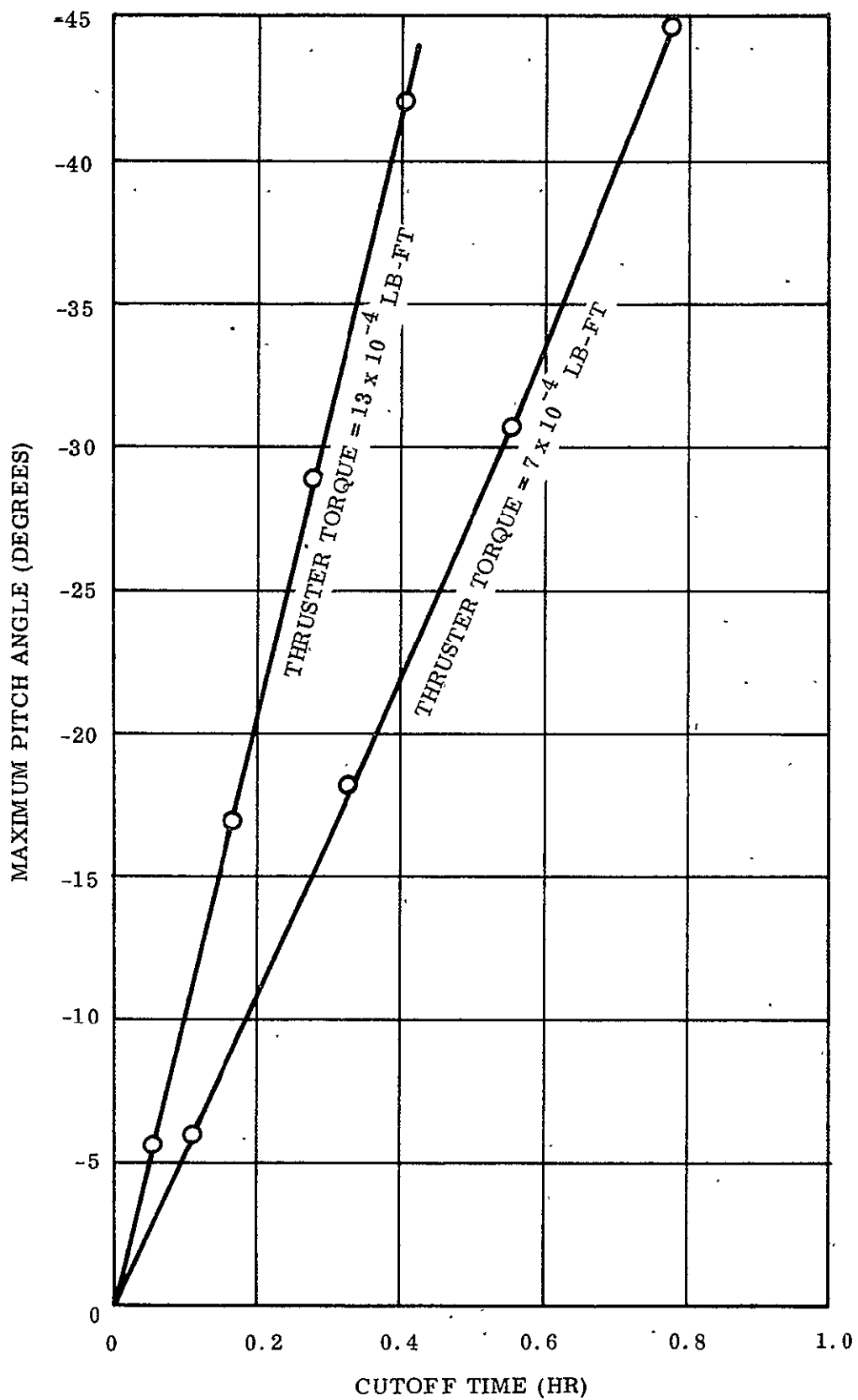
Figure 3.6-7 Maximum Pitch Angle versus Thruster
Cutoff Time for ATS-A Pitch-up Maneuver
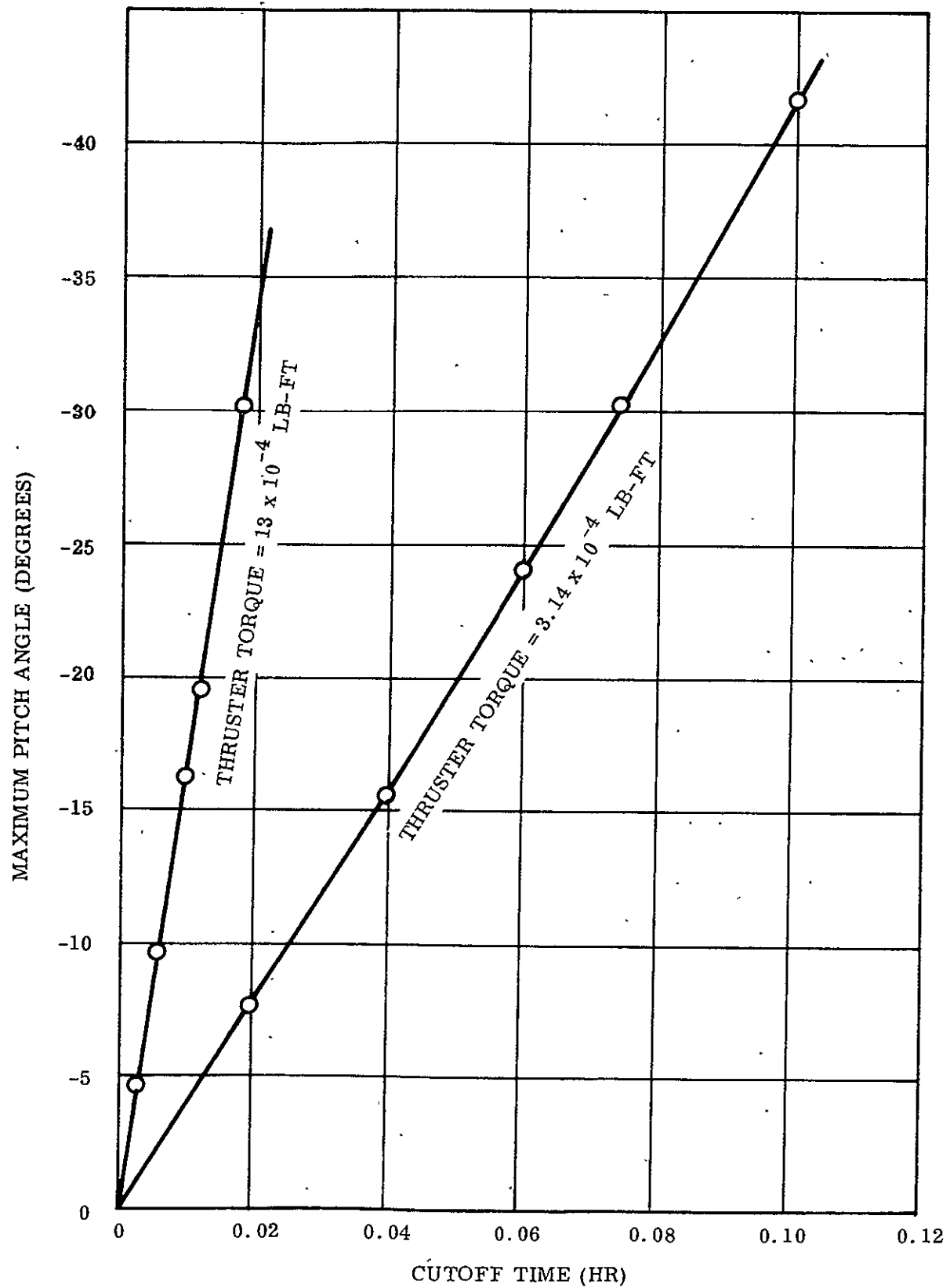
Figure 3.6-8 Maximum Pitch Angle versus Thruster
Cutoff Time for ATS-D Pitch-up Maneuver
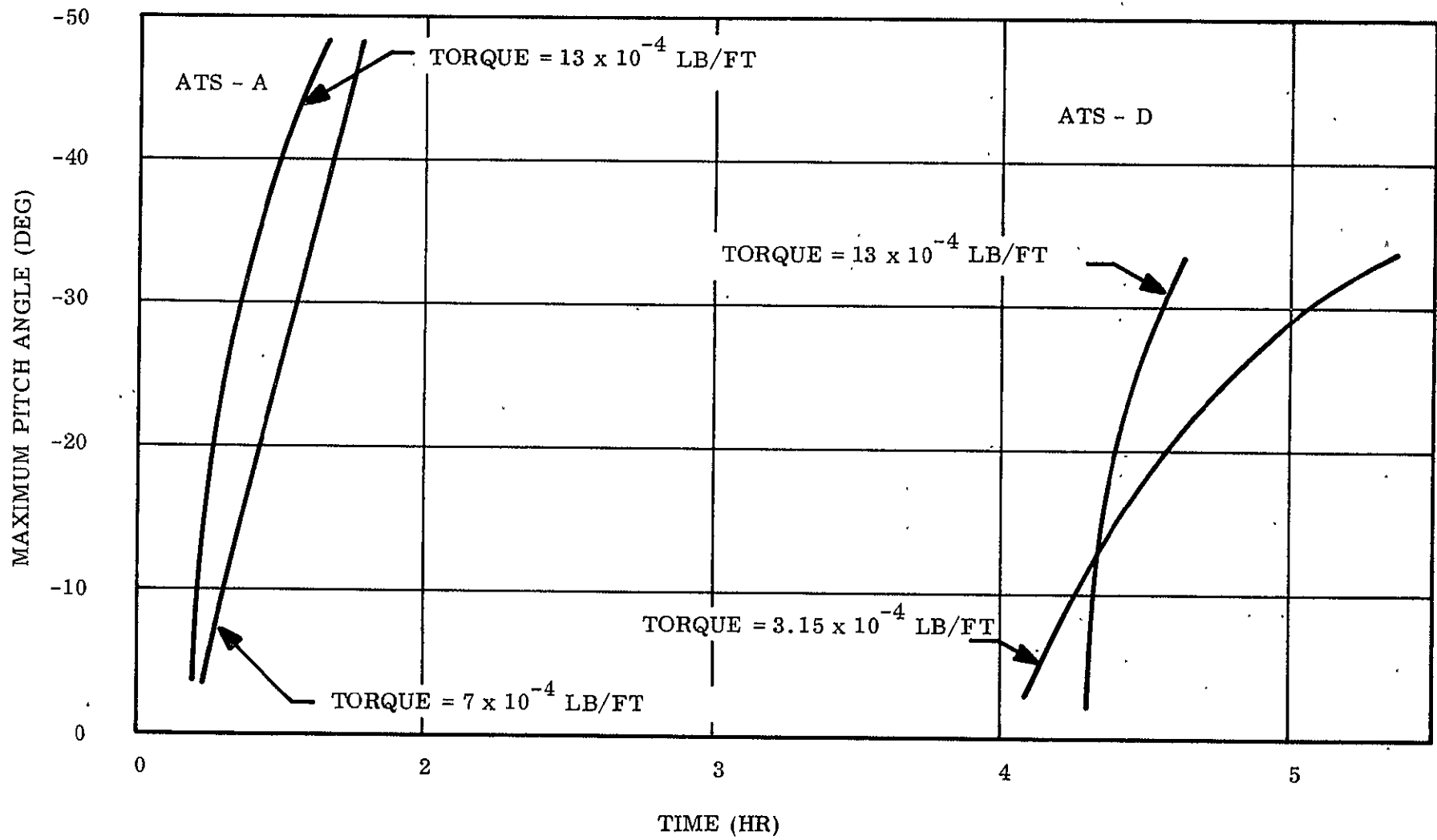
Figure 3.6-9 Time Required to Reach Maximum Pitch Angle for ATS Pitch-up Maneuvers

The squib valves are located 22.3 in. from the center of mass (CM) along the y axis and 16.2 in. from the CM along the z axis. The maximum moment arms are therefore 1.86 feet fo pitch torque, 1.35 feet for roll torque, and 2.30 feet for yaw torque. The corresponding angular impulse bit for each squib is 0.0307 lb-ft-sec for pitch, 0.0223 lb-ft-sec for roll, and 0.0369 lb-ft-sec for yaw.

If the impulse bits were expended instantaneously, the amplitude of oscillation would be 0.7 degree in pitch; 0.4 degree in roll and 4.8 degrees in yaw (per squib) for ATS-A, and 1 degree in pitch, 0.6 degree in roll, and 7.5 degrees in yaw for ATS-D. These errors are the maximum which could be realized irrespective of the manner in which the gas leaked.

If the leakage occurs during the capture phase of operation, its effect on attitude dynamics will probably be unrecognizable because of the large amplitude motions the vehicle is already undergoing. To affect steady state motion, the leakage must occur either after the capture and transient phase of operation, or "trickle out" slowly following squib firing. Since approximately three days are required for ATS-A to reach steady state, the impulse must be "stretched out" over that time period if leakage starts immediately after firing. This would produce a maximum yaw error (the largest error) of 0.1 degree (per squib). For ATS-D, the steady state will not be reached for approximately 15 days. The resulting yaw error is 0.1 degree. Pitch and roll attitude errors are less than 0.01 degree. If the trickle is even slower, the attitude errors will be less.

3.6.4 COMPENSATION FOR SHORTENED DAMPER BOOMS AND INCREASED STIFFNESS OF DAMPER SPRING FOR ATS-A

The combination of manufacturing tolerances encountered during ATS-A boom fabrication resulted in the damper booms for the ATS-A being 43.3 feet long. Since the nominal design value was 45 feet, the damper boom moment of inertia was reduced from 231 slug ft^2 to about 213 slug ft^2.

At the time of measurement, the damper spring constant for the combination passive damper was on the high end of the tolerance range (1.0184 x 10^{-4} ft-lb per radian instead of the nominal 0.8874 ft-lb per radian) and the damping coefficient was

6.342×10^{-2} ft-lb-sec per radian, which is below its nominal value of 6.680×10^{-2} ft-lb-sec per radian. Since each of these parameters is used in the specification of system performance, the effects of each, and the total effect was reexamined for this vehicle. The non-dimensional parameters arrected are:

$$b/I_D \omega_o, \quad K/I_D \omega_o 2, \quad \text{and} \quad I_D/Ip.$$

The values of ϕ, I_Y/I_P, were unaffected.

The most serious effect of these changes is the degradation of damping performance. The combined effects increase the system damping time constant by 227 percent. This was considered to be intolerable and corrections were necessary. Moment of inertia compensation for damper rod shortness required the addition of 0.1528 pound to each secondary tip weight. This however, while helpful, does not adequately compensate for the increased spring constant; the system damping time constant will still be 120 percent over nominal value. Bringing the damper time constant back to normal required that the nondimensional parameter value of $K/I_D \omega_o 2 = 5.1504$ be maintained. In turn, this requirement increased each damper boom tip mass by 0.443 lb (i.e., from 1.60 lb to 2.043 lb). As a consequence, the damper boom moment of inertia, increased from 230.88 slug ft^2 to 264.96 slug ft^2 about the hinge point and its product of inertia increased from 110.11 slug ft^2 to 126.72 slug ft^2 about the vehicle yaw axis. The increased product of inertia (16.6 slug ft^2) introduced a yaw error of approximately 0.6 degree.

Correction of the yaw error could be accomplished in either of two ways. The first method required the addition of 0.47 pound to each primary tip mass (i.e., a weight increase from 2.5 to 2.97 lb each tip weight). This method adds 1.88 lb in addition to the 0.89 pound required by the damper booms, for a total of 2.77 pounds. Scissoring the primary booms to a half angle of 26.4 degrees instead of the nominal value of 25 degrees will also effect the yaw correction. Since the scissoring capability already existed, and since it added no weight, this method was recommended.

With the adjusted damper moment of inertia, the nondimensional damping time constant is low (i.e., 0.8818 vs. 1.0588). As a consequence, the damping performance of the system will be degraded by approximately 17.7 percent; this was considered acceptable.

3.6.5 SIMULATION OF ATS-A FAILURE MODE

Two computer runs were made simulating ATS-A failure modes. One assumed that a scissor unit had malfunctioned, while the second assumed that one damper boom unit had malfunctioned (i.e., failed to deploy). In each of these runs, the eccentricity was 0.01, the magnetic dipole was 1000 pole-cm oriented along the positive roll axis, and the sun was in the orbit plane. The steady state results are shown in Table 3.6-1. The nominal errors for the normal configurations are also shown.

The effect on damping time was not evaluated in this study, but a significant increase in time to steady state could be expected with only one camper boom deployed. A 400 to 500 percent increase is not unreasonable. The reduced spacecraft moment of inertia associated with the malfunctioned scissor unit should not significantly affect damping time.

Table 3.6-1. Steady State Results

	Malfunctioned Scissor Unit		Malfunctioned Damper Unit		Nominal	
	Bias	Osc.	Bias	Osc.	Bias	Osc.
Pitch	0.3	6.8	0.1	2.9	0	1.7
Roll	0.2	2.0	0.2	2.0	0	0.3
Yaw	0.3	6.8	2.7	13.8	0.6	1.7
Damper	2.6	7.6	1	9.0	0	2.3

3.6.6 PERFORMANCE OF ATS-A IN AN ORBIT WITH A 0.2 ECCENTRICITY

The ATS-A spacecraft, designated ATS-2 after launch, was injected into a highly eccentric orbit (e = 0.4) and was unable to stabilize. The primary causes of nonstabilization were the high eccentricity and the influence of aerodynamics at low altitude (perigee). Because of aerodynamic drag, the apogee began to decay and the eccentricity grew smaller.

This began to prompt questions concerning the performance of gravity gradient spacecraft in highly eccentric orbits.

To more accurately simulate the effect of orbit eccentricity in the Mathematical Model, the power series used to determine the true anomaly of the spacecraft as a function of time was expanded to represent orbits of high eccentricity. The secular effects (motion of the right ascension of the ascending node, and rotation of the line of apsides) were not altered since their effect on attitude stability is small.

A computer run was made using the ATS-A spacecraft parameters(Figure 3.6-10) and an orbit eccentricity of 0.2. The results are shown in Figure 3.6-11. After an initial transient (due to the inputs not exactly simulating steady state), the spacecraft settles out to a "steady state" oscillation. The pitch axis is oscillating at 30 degrees with no clear pattern. The roll axis has settled to an amplitude of approximately nine degrees, although a "beat" may be present. Yaw is not under control and is unlikely to achieve control at this orbit eccentricity.

3.6.7   EFFECT OF THERMAL FLUTTER ON ATS-D AND ATS-E
Prior to the launch of ATS-D and ATS-E there was concern about thermal flutter of gravity gradient rods and the effect on spacecraft performance. The concern centered on the damper boom, since, according to the then current theory, this is the boom most likely to flutter.

Figure 3.6-10 ATS-A Configuration

1.2728° Kg

18°

18°

1.2737 Kg

37.3807 m

1.2737 Kg

13.2143 m

39.3455 m

(0.1048 m, 0.5113 m, −0.0429 m)
TYPICAL FOUR PLACES

0.711 m

13.2143 m

0.9444 Kg

39.3455 m

1.2791 Kg

FLIGHT DIRECTION

18°

18°

37.3807 m

1.2783 Kg

TO EARTH
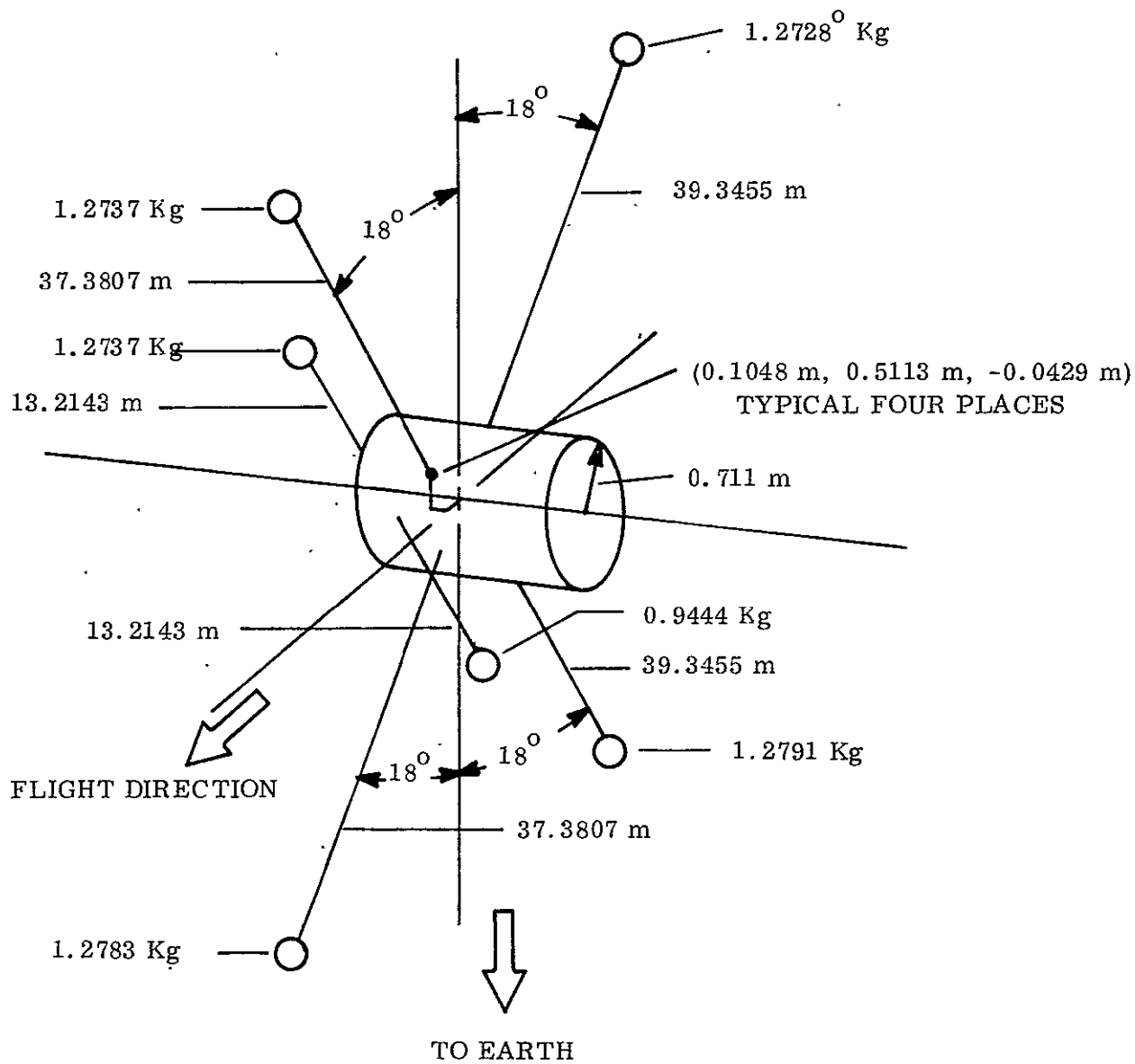
SPACECRAFT WEIGHT = 304.7658 kg
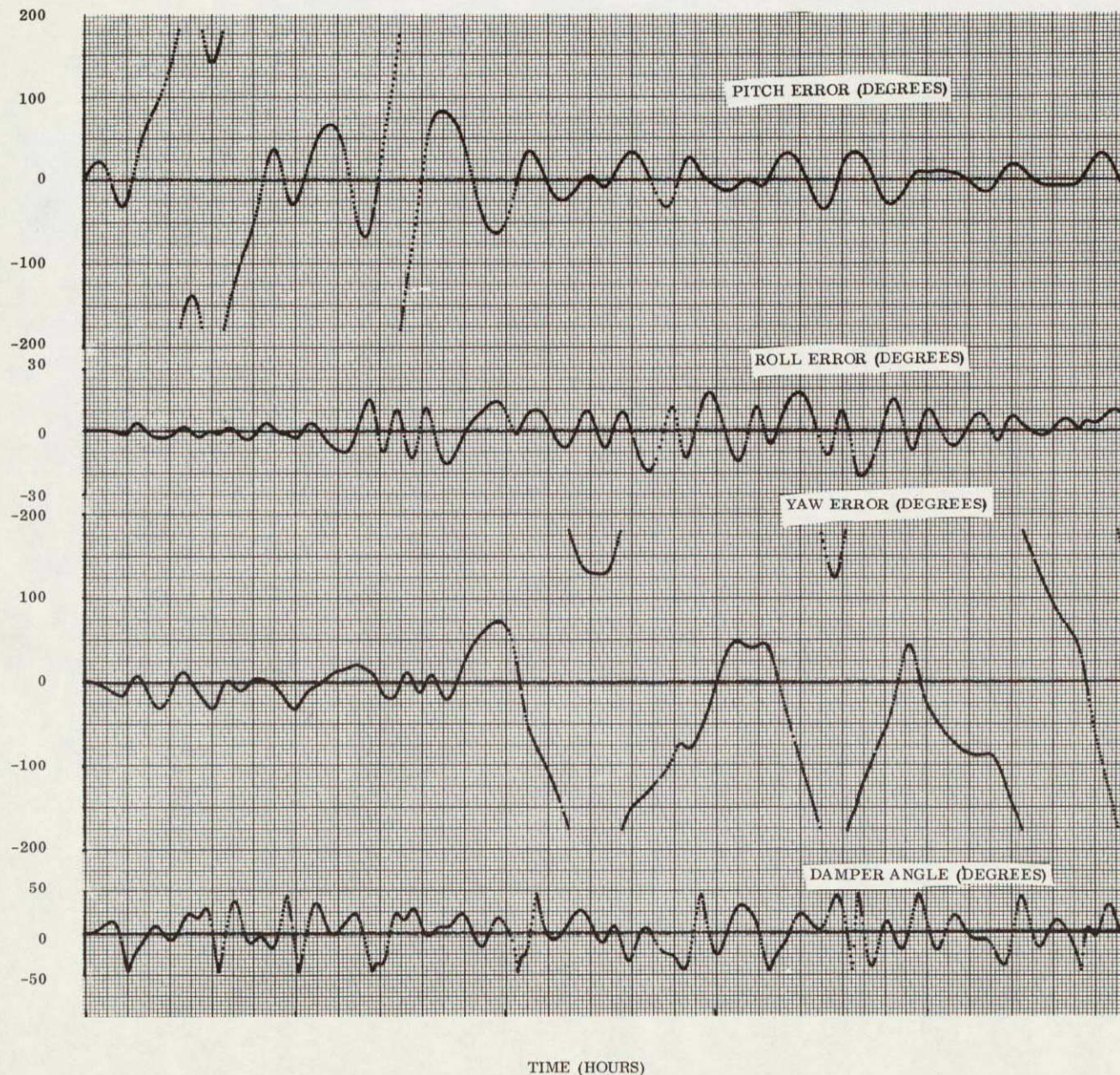
Figure 3.6-11 Performance of ATS-A in an Orbit of 0.2 Eccentricity (No Aerodynamics and No Solar Effects)
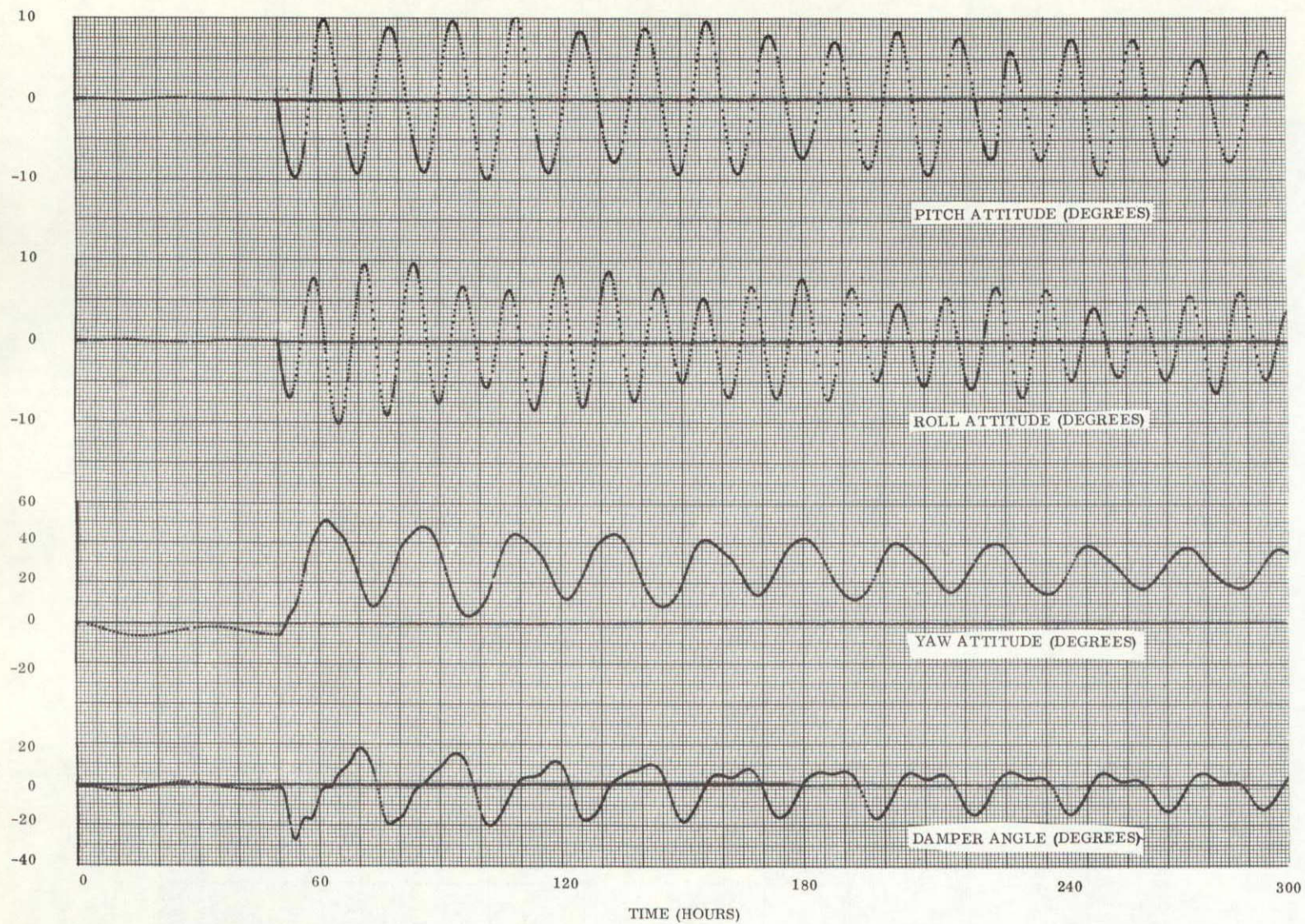
Figure 3.6-12 Effect on ATS-D of Thermal Flutter of the Damper Boom

A computer simulation was made using a modified ATS Mathematical Model. It was assumed that only the damper boom fluttered. The characteristics of the flutter were estimated and an equivalent momentum wheel determined (Table 3.6-2). The simulation was made with the nominal ATS-D spacecraft, but with no external disturbances other than the momentum wheel. The pitch and roll errors were zero, and the yaw error was approximately three degrees when thermal flutter was assumed to start at 50 hours.

The result of the simulation is shown in Figure 3.6-12. Pitch attained a peak error of 10 degrees, roll reached a peak error of 10 degrees, and yaw reached a peak of 50 degrees. Neither pitch nor roll achieved a large bias, but yaw is biased approximately 26 degrees. Steady state was not reached at the end of 300 hours, although damping was obviously taking place. The effectiveness of the damper was impaired because of the yaw bias position assumed by the spacecraft, and the resistance to motion of the "momentum wheel" on the damper boom. Basically, however, the configuration is stable.

The results of this run are in good agreement with linearized estimates of 11 degree pitch error, 7 degree roll error, and 25 degree yaw bias.

Table 3.6-2. Thermal Flutter Parameters

Radius of Tip Mass Revolution	–	5 ft
Period of Tip Mass Revolution	–	100 sec
Time to Reach Peak Radius	–	1200 sec
Equivalent Momentum Content	–	0.236 lb-ft-sec
Equivalent Momemtum Wheel Time Constant	–	310 sec

The performance of the ATS-E spacecraft was also evaluated by means of the GE Math Model under various conditions of applied angular momentum. The momentum wheel subroutine of the Math Model was used to simulate angular motion of tip masses on the ends of all the booms, rather than just the damper booms. Specifically, twelve computer runs were made. The results are shown in Figures 3.6-13 through 3.6-24 in terms of spacecraft attitude and damper boom angle relative to the orbiting reference frame as a function of time. Most of the runs represent one orbit (24 hr); however, for the cases in which the momentum was held for 24 hours, the runs were extended to 30 hours.

Table 3.6-3 lists the computer runs made. For convenience, the magnitude of the momentum for each run is referenced to that of run no. 1 (Figure 3.6-13). The primary booms have been referred to as No. 1 and No. 2. In reality, No. 1 represents a "co-linear pair". one of which extends forward and upward from the spacecraft body. Primary No. 2 is the other co-linear pair. On run No. 1 through 6, the applied momentum is positive in the direction of the upper and forward rod. On run No. 7 through 10, the positive momentum vector is parallel to the forward pointing damper rod. Run No. 11 is identical to run No. 6, except that the same momentum is placed on both sets of co-linear pairs. The direction of the momentum vectors are such that the vertical components add. (Horizontal components cancel.) Run No. 12 has angular momentum applied to both primary pairs and to the damper boom in such a manner that all horizontal components add in the forward direction.

H_1 ON PRIMARY BOOM (+ UP & FWD) $\Delta t_1 = 0.15$ HOUR

$H_1 = 0.1475 \dfrac{\text{kg m}^2}{\text{sec}}$ (0.1085 LB FT SEC) $\Delta t_2 = 8$ HOURS
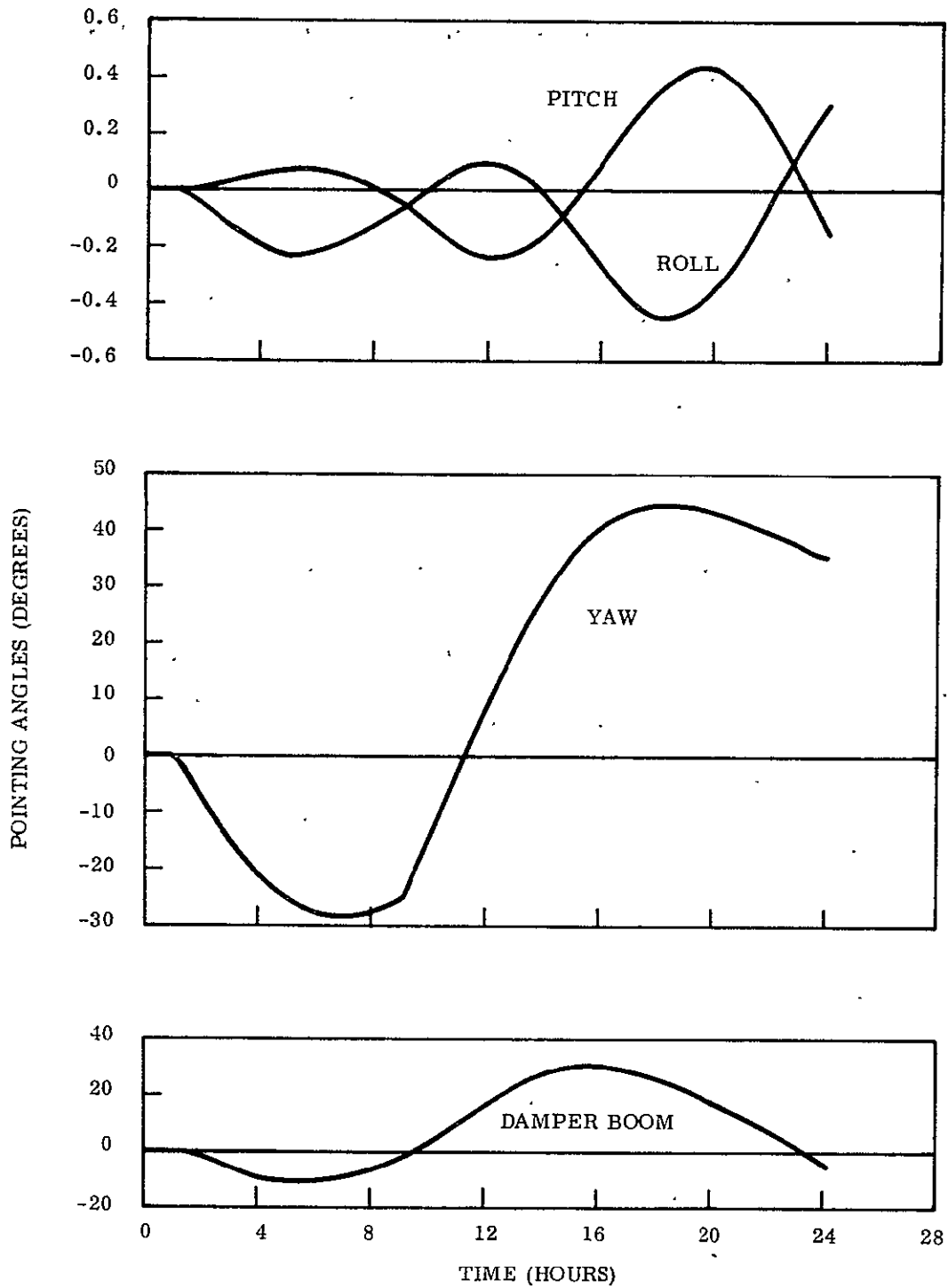
Figure 3.6-13. ATS Thermal Flutter
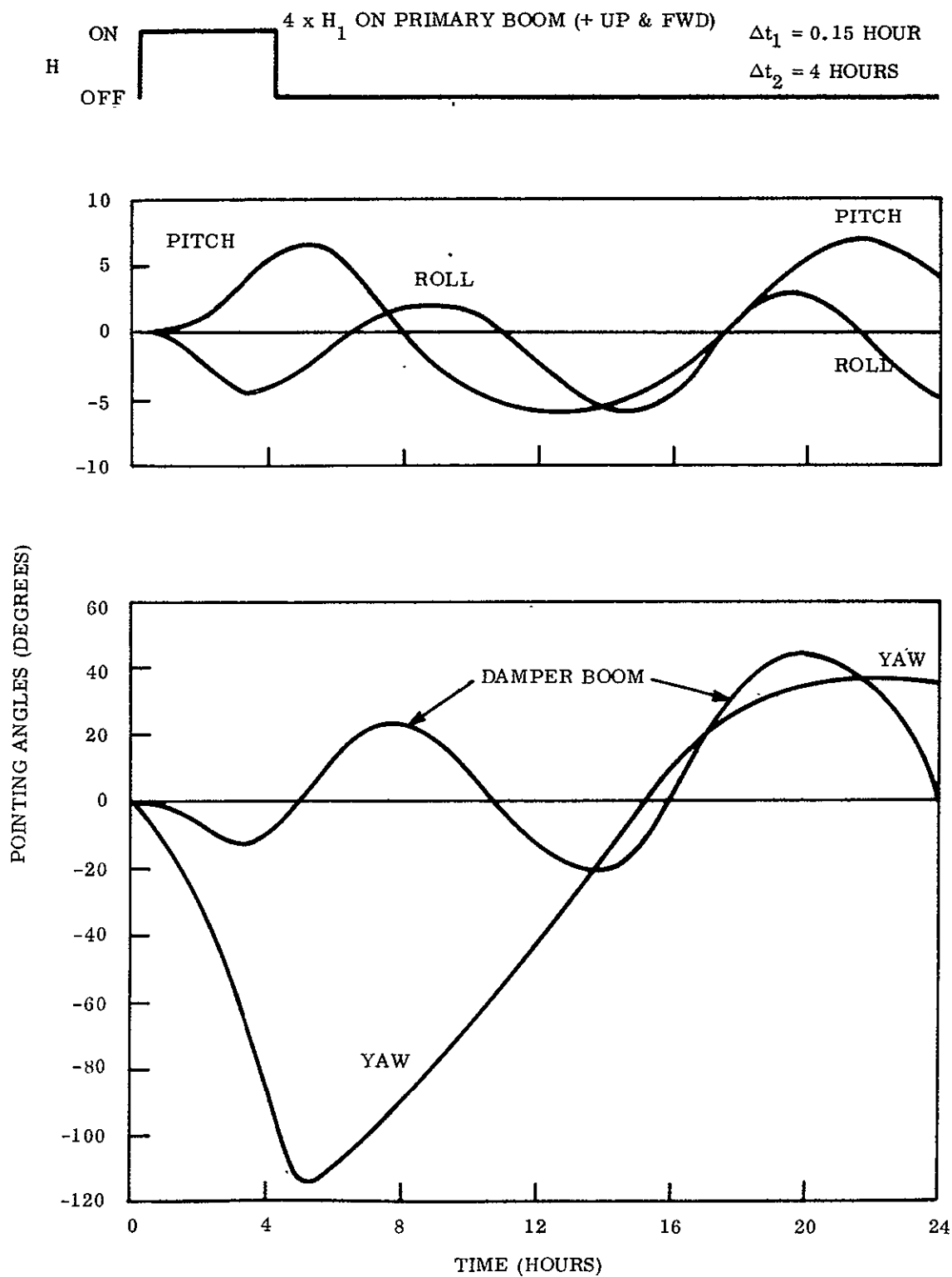
Figure 3.6-14. ATS Thermal Flutter

4 x H_1 ON PRIMARY BOOM (+ UP & FWD)

$\Delta t_1 = 0.15$ HOUR

$\Delta t_2 = 8$ HOURS
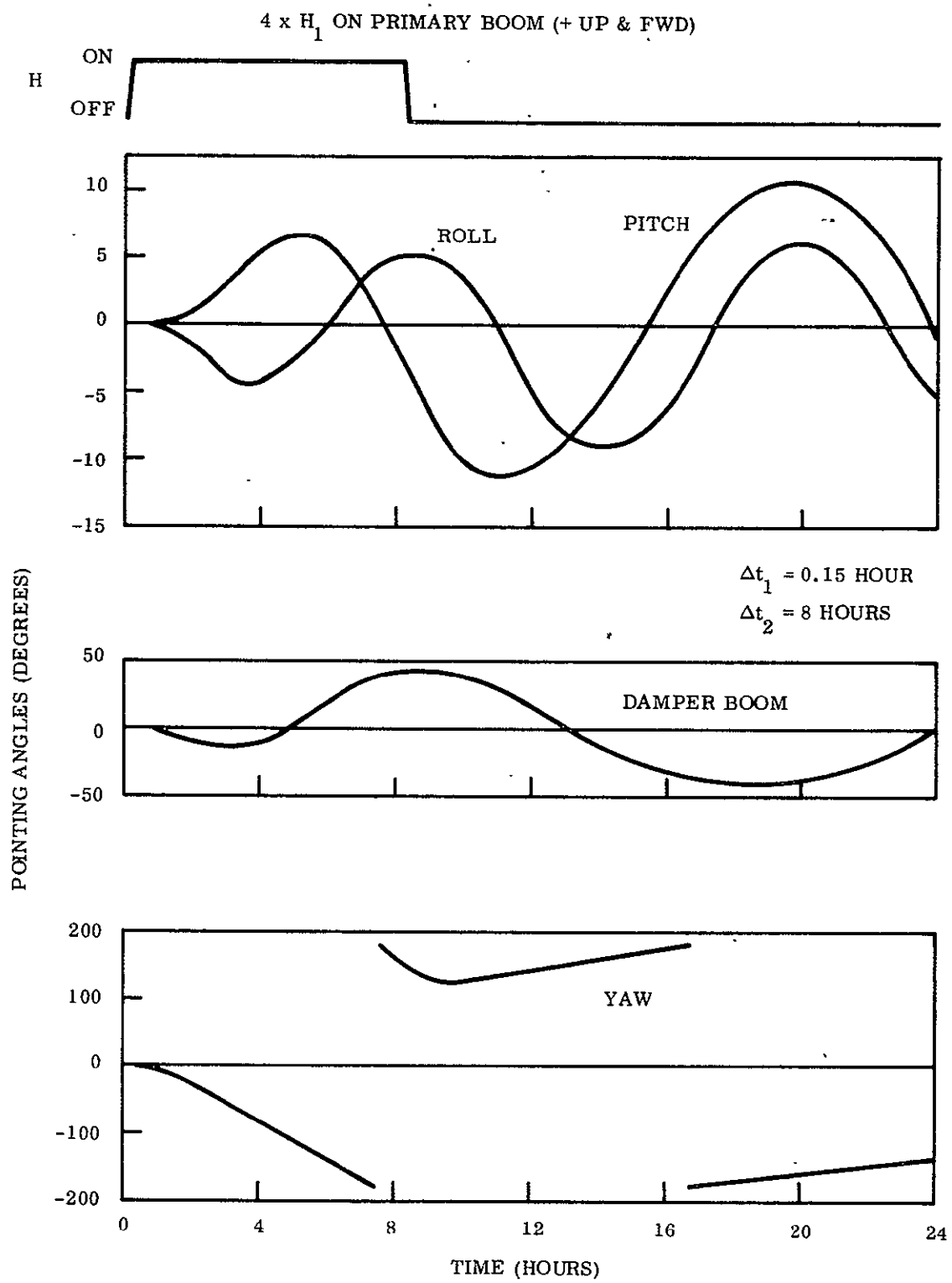
Figure 3.6-15. ATS Thermal Flutter
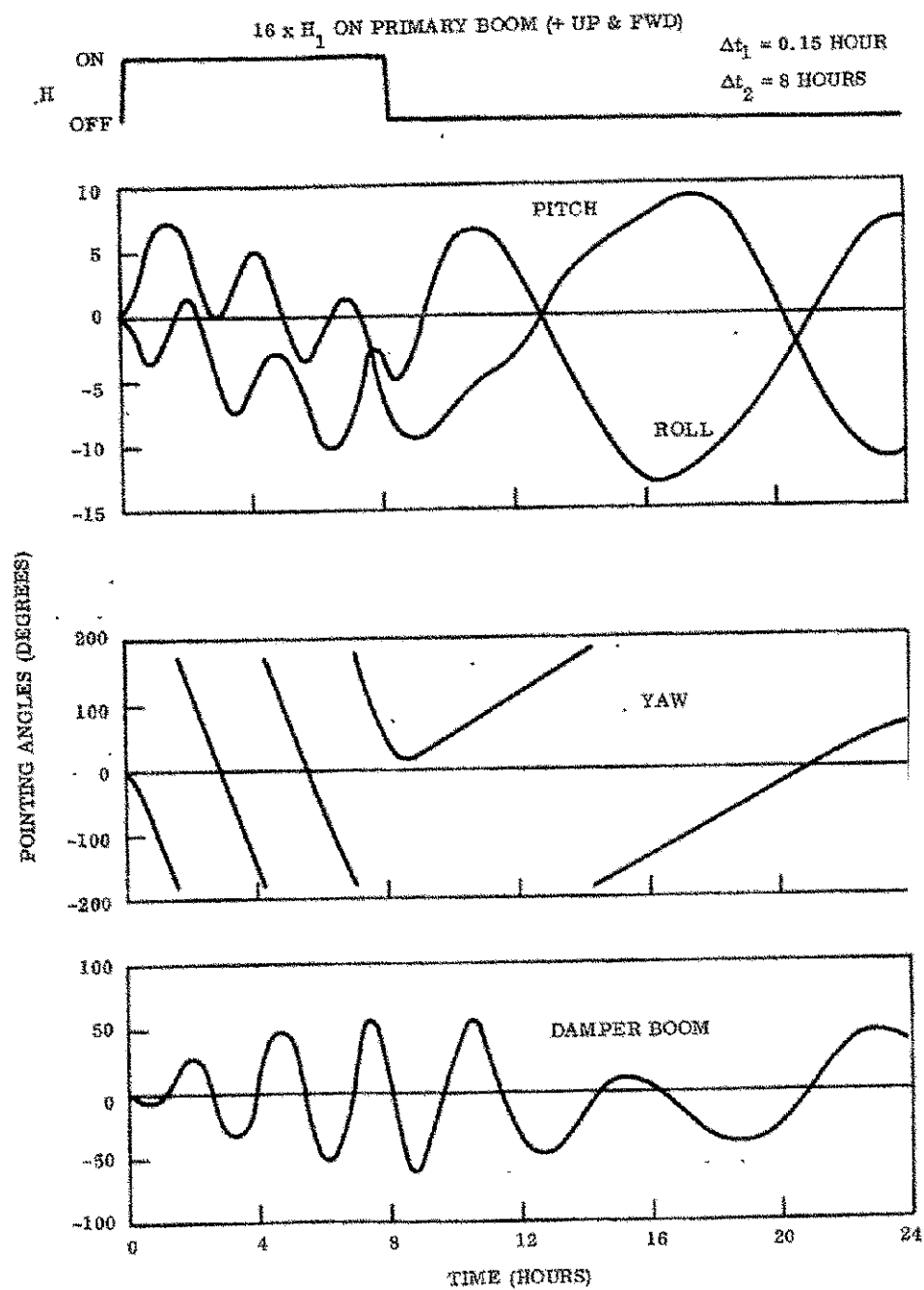
Figure 3.6-16. ATS Thermal Flutter
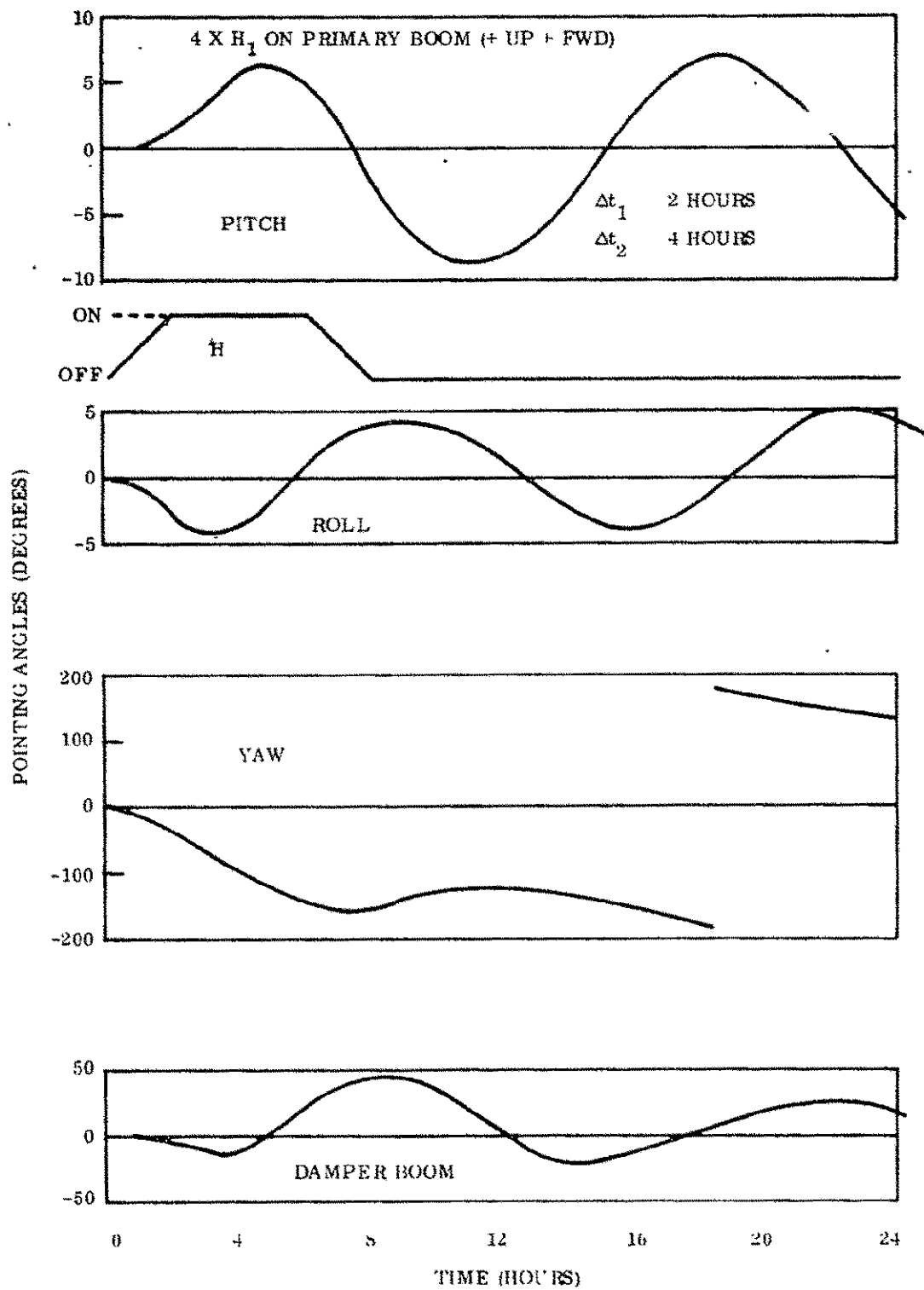
Figure 3.6-17. ATS Thermal Flutter
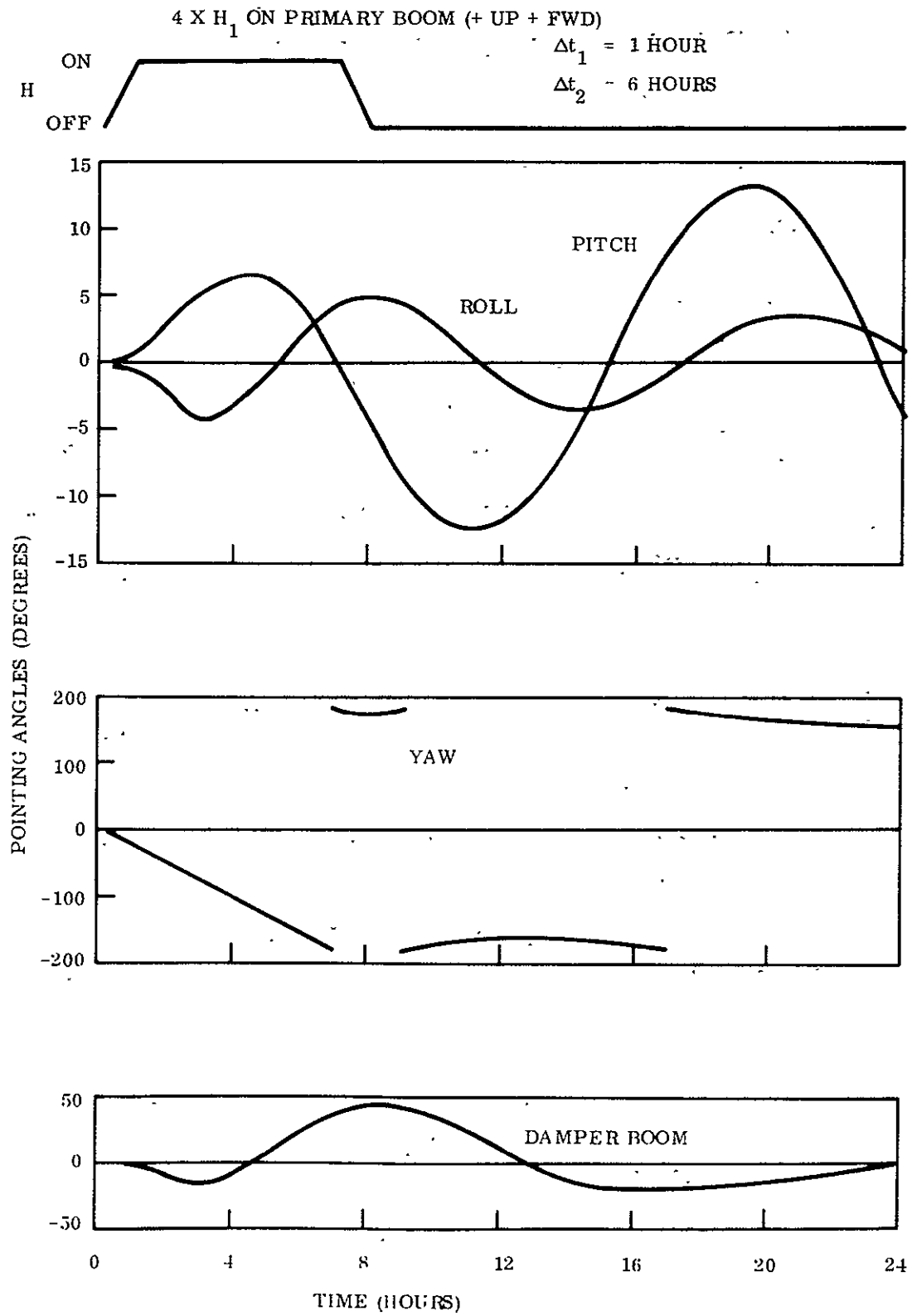
Figure 3.6-18. ATS Thermal Flutter
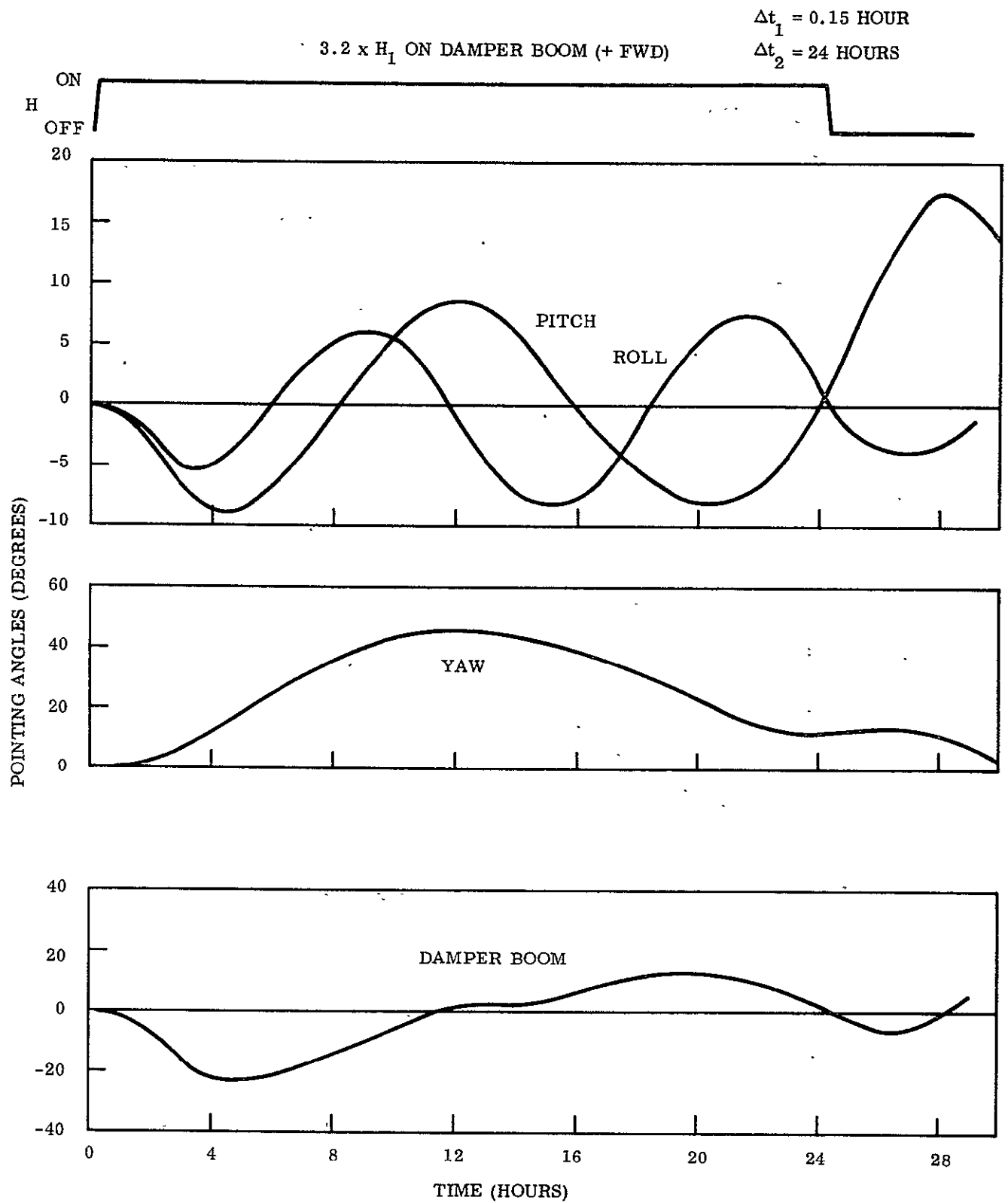
Figure 3.6-19. ATS Thermal Flutter
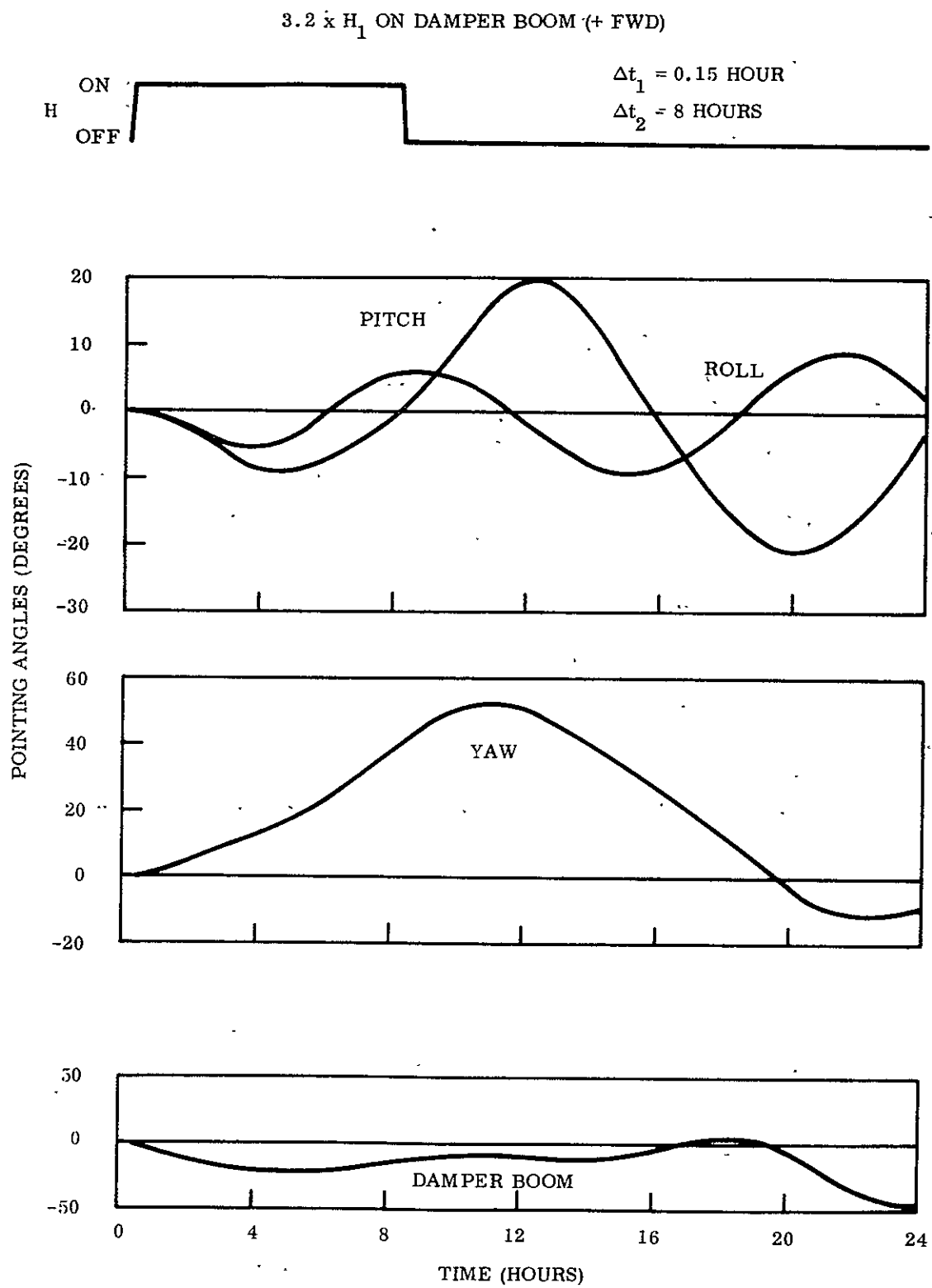
Figure 3.6-20. ATS Thermal Flutter
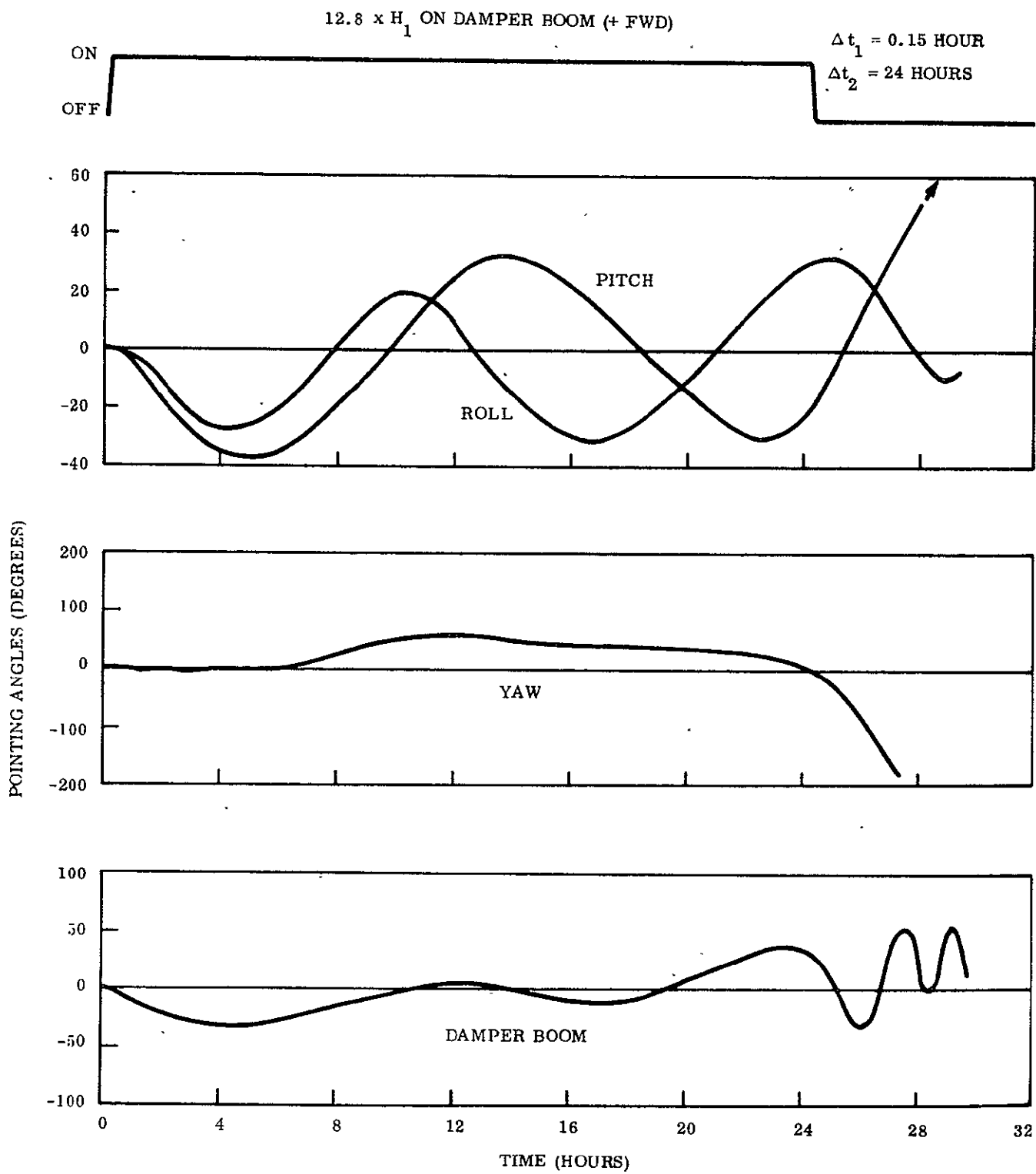
Figure 3. 6-21.   ATS Thermal Flutter
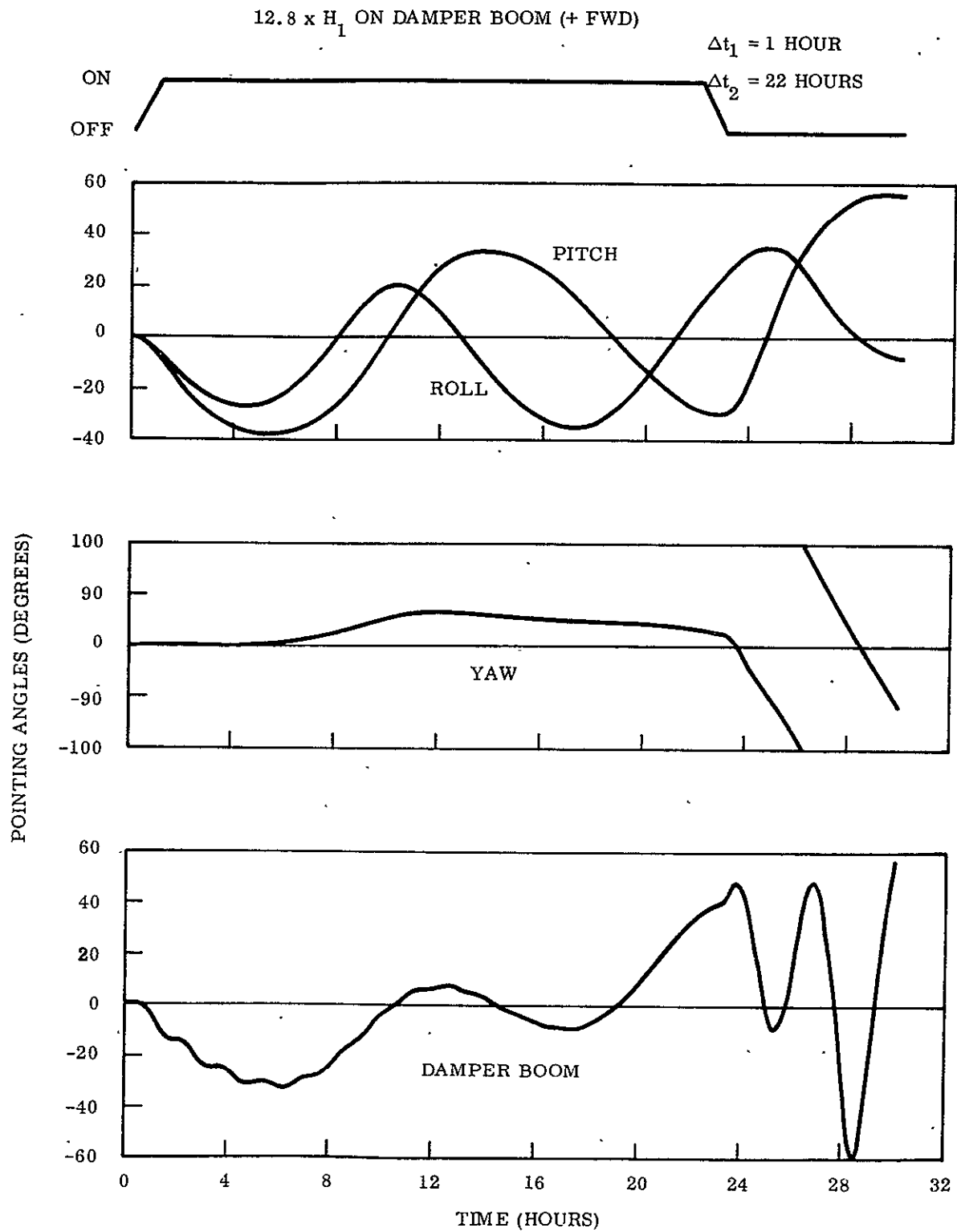
Figure 3. 6-22. ATS Thermal Flutter
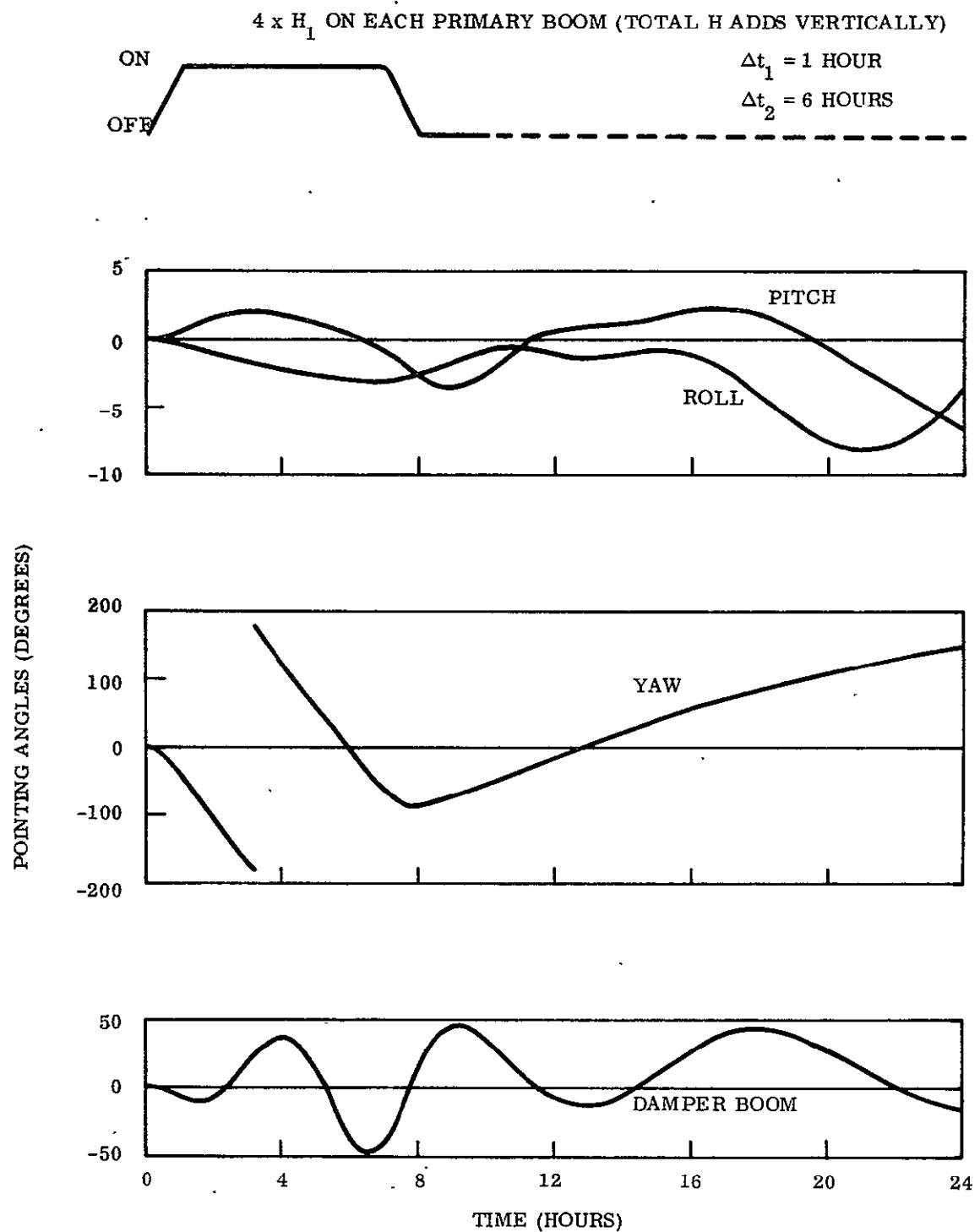
Figure 3.6-23. ATS Thermal Flutter
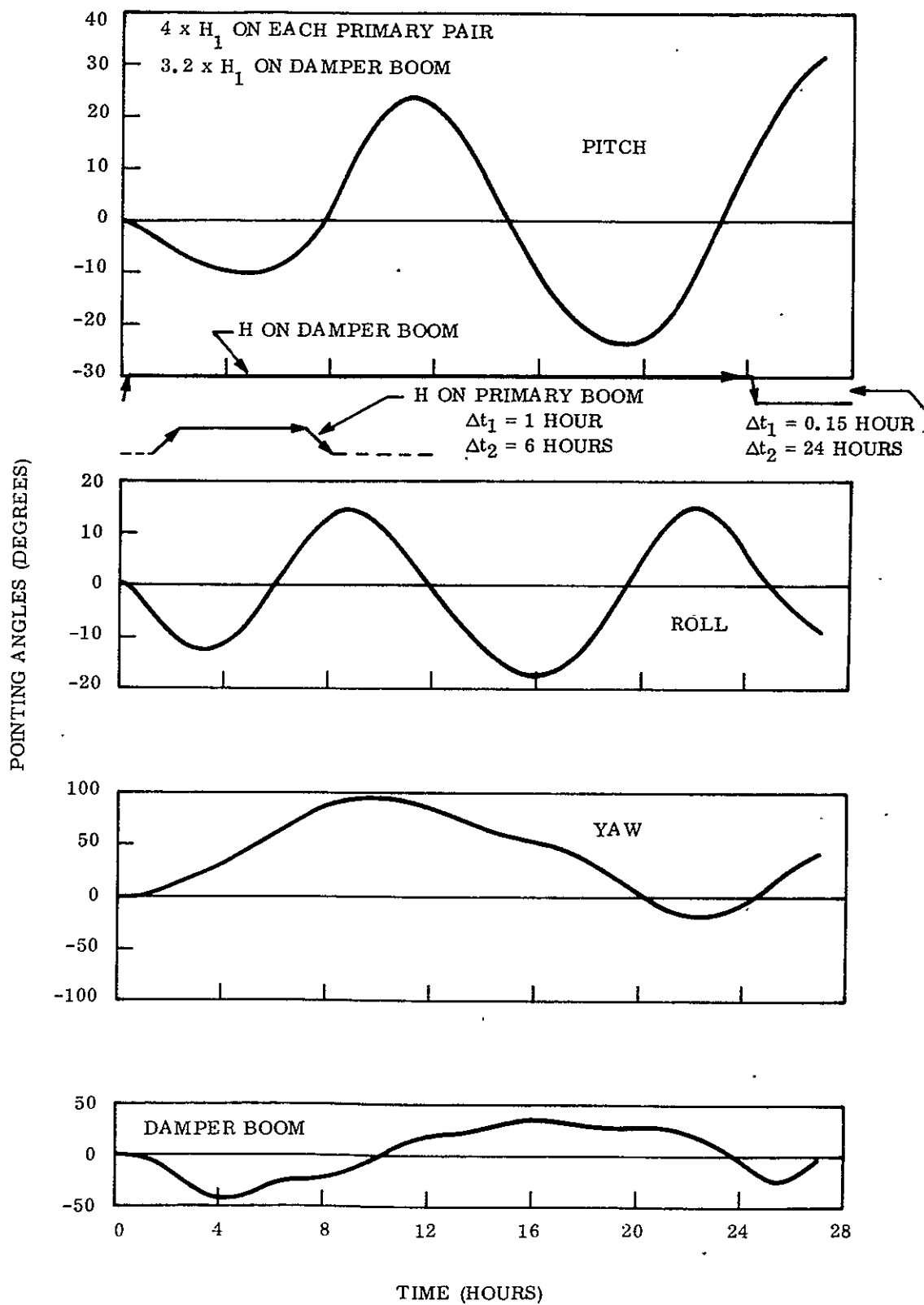
Figure 3.6-24. ATS Thermal Flutter

Table 3.6-3. Computer Runs

Run No. and Figure No.		H Angular Momentum	H Location	γmax (ft)	Δt_1 (hr)	Δt_2 (hr)
1	3.6-13	H_1*	Primary Boom No. 1	5	0.15	8.0
2	3.6-14	$4H_1$	Primary Boom No. 1	10	0.15	4.0
3	3.6-15	$4H_1$	Primary Boom No. 1	10	0.15	8.0
4	3.6-16	$16H_1$	Primary Boom No. 1	20	0.15	8.0
5	3.6-17	$4H_1$	Primary Boom No. 1	10	2.0	4.0
6	3.6-18	$4H_1$	Primary Boom No. 1	10	1.0	6.0
7	3.6-19	$3.2H_1$	Damper Boom	5	0.15	24.0
8	3.6-20	$3.2H_1$	Damper Boom	5	0.15	8.0
9	3.6-21	$12.8H_1$	Damper Boom	10	0.15	24.0
10	3.6-22	$12.8H_1$	Damper Boom	10	1.0	22.0
11	3.6-23	$4H_1$	Primary No. 1	10	1.0	6.0
		$4H_1$	Primary No. 2	10	1.0	6.0
12	3.6-24	$4H_1$	Primary No. 1	10	1.0	6.0
		$4H_1$	Primary No. 2	10	1.0	6.0
		$3.2H_1$	Damper Room	5	0.15	24.0

* $H_1 = 0.1475 \dfrac{Kg\text{-}m^2}{sec}$ (0.1085 lb-ft-sec)

γmax = simulated radius of circular motion of tip mass.

Δt_1 = Rise time and decay time of angular momentum.

Δt_2 = Time for which constant momentum maintained.

3.6.8 PERFORMANCE OF ATS-E WITH A YAW STABILIZING FLYWHEEL

The use of a yaw stabilizing momentum wheel for gravity gradient spacecraft has been suggested for several spacecraft. Yaw stabilization is obtained by the gyrocompassing action of the momentum sheel, which tends to align itself with the orbit normal. The yaw performance obtained with this device is typically an order of magnitude better than can be obtained by pure gravity gradient.

With an ATS-type system, there is a drawback associated with the use of a yaw stabilizing flywheel. Damping of the spacecraft oscillations (resulting from deployment, etc.) in all axes is accomplished by a single-axis damper oriented such that all three spacecraft axes are coupled. Placing a yaw stabilizing flywheel on the spacecraft pitch axis will increase the coupling between roll and yaw, but will tend to "decouple" pitch. As a consequence, pitch damping may be decreased, requiring longer to reach steady state with the momentum wheel than without it.

A rapid qualitative determination of the effect was obtained by simulating the flywheel in the Mathematical Model. The momentum wheel selected was the OAO fine momentum wheel with a no load momentum capability of 2 lb-ft-sec. This wheel was selected based upon previous studies with "rigid body" type configurations. The wheel was assumed to be operating at 75 percent of the no-load momentum in order to be compatible with a tentative control system. The initial conditions were similar to those of a capture run after initial capture had been achieved. For this run, it was assumed that the yaw position was correct to within ten degrees, since it is expected that during initial deployment, the spacecraft will be aligned reasonably well.

Table 3.6-4 shows the initial conditions and Figure 3.6-25 shows the results of the run. At the end of 400 hours, the roll and yaw errors are 0.6 and 0.5 degrees, respectively. Typically, these errors would be 1.6 degrees in roll and 7.4 degrees in yaw at the same time. However, pitch is higher than normal after 400 hours, being 5.6 degrees with the flywheel, as compared to 2.1 degrees without. This tends to confirm the increase in the time to reach steady state.
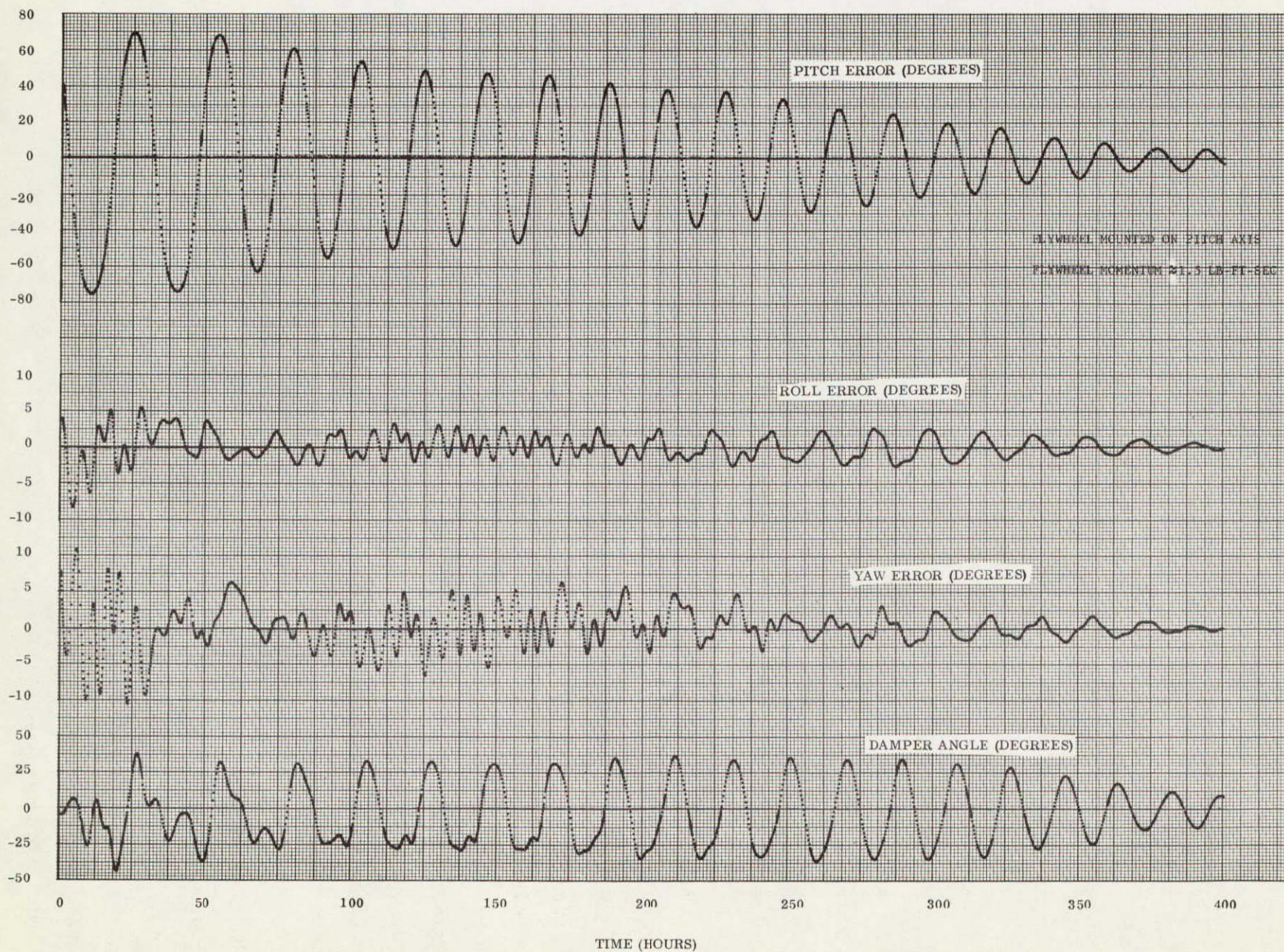
Figure 3.6-25. Performance of ATS-E with OAO Flywheel

The increase in damping time, however, is not large, and in view of the large improvement in yaw, may be an acceptable penalty. Of course, optimization can improve the "tradeoff" between yaw pointing and pitch damping.

Table 3.6-4 Initial Conditions for ATS-E/Flywheel Run

Pitch Error	=	42.6 deg
Roll Error	=	3.8 deg
Yaw Error	=	8.9 deg
Damper Angle	=	-4.7 deg
Pitch Rate (Inertial)	=	7.591×10^{-5} deg/sec
Roll Rate (Inertial)	=	5.69×10^{-5} deg/sec
Yaw Rate (Inertial)	=	-2.542×10^{-3} deg/sec
Damper Rate (Relative)	=	-3.324×10^{-4} deg/sec

3.6.9 DETERMINATION OF SPIN RATE DIRECTION ON ATS-E

For a period of time following the orbit circularization at synchronous altitude, the ATS-E spacecraft was spinning about an axis normal to the cylinder axis.

To make the spacecraft operational, the empty case of the spent apogee motor was to be jettisoned. After its release, the spacecraft would reach a stable spin about the z axis, which is the proper axis. Because of the initial conditions, however, the direction of spin was uncertain, and since the ATS-E spacecraft uses a yo-yo despin mechanism which only works one way, the possibility of not being able to despin arose. This section presents the results of a brief study to determine if the proper final direction of spin could be achieved by controlling the initial conditions.

At the time of the study, ATS-E was spinning about its x axis at approximately 90 rpm. The x axis was the axis of maximum moment of inertia with the spent apogee motor case attached. Because of the large amount of passive damping on the spacecraft, the motion was quite stable. Unfortunately, successful completion of the mission required

that the spacecraft be spinning aobut the z axis (the cylinder axis) and in the proper direction. The limitation is imposed by the yo-yo which only works on one axis, and only in one direction

When the apogee motor case is jettisoned, the x axis becomes the intermediate axis of inertia, and has a moment of inertia greater than that of the y axis and less than that of the z axis. The intermediate axis of inertia is the only dynamically unstable axis of the three axes. Spin about the axis of maximum moment of inertia is completely stable, and spin about the axis of minimum moment of inertia is unstable only in the presence of damping. The axis of intermediate moment of inertia, however, is totally unstable and rates will almost immediately appear on the other axes. Qualitatively, the direction of these rates is arbitrary depending on the initial rate conditions. A study was therefore undertaken to determine the effect of initial conditions on the final conditions (Appendix I). Qualitative evaluation of the dynamical equations indicated that the rates on the y and z axes were related to each other, but that they would continue in whatever direction they were started. The analysis was continued and the equations were linearized. The results of the linearization indicated that the rate of rate buildup was exponential with the exponent being proportional (and close to) the spin rate. Hence, following the jettison of the circularizing engine, the spacecraft would almost certainly go into wild oscillations.

The results of the linear analysis were checked by use of an analog simulation which included the total equations of motion for a rigid body. The exponential increase in rates was observed, but the nonlinearities associated with large motions of rigid bodies appeared, and the spacecraft went into a cyclic motion (the general nature of which is predictable on theoretical grounds). If an initial rate was put on one axis, the rate on that axis never fell

below (in absolute terms) that initial rate during any part of the motion. The motion, however, was cyclic, and the indications were that once an initial rate was added, that rate controlled the direction of the final rate.

An observation from these runs was, that the dynamic coupling terms were on the order of hundreds of pound-feet of equivalent torque. Consequently, after the motion had started, short bursts from the available thrusters (in the pound-feet category) would probably be useless. Therefore, the proper initial conditions would have to be set up prior to apogee motor-case jettison.

Damping was not included in the simulations and, as a preliminary estimate of the damping effect, rate proportional damping was added to all axes. The results were that all axes were damped with no transfer of momentum. The changeover of spin rate from the minimum to the maximum moment of inertia applies only if momentum is conserved for the system, and apparently, not even a rough approximation can be made using direct rate proportional damping.

To simulate a spin nutation damper, the equations for a passive spring mass damper (developed for a dual spin spacecraft) were implemented. The results were less than satisfactory, however, since the damper could not be tuned to damp the observed nutation. The nutation frequency of a dual spin spacecraft, when the damper is on the de-spun section, is approximately the spin frequency. The nutation frequency is slightly higher or slightly lower than the spin frequency depending upon the ratio of the transverse moment of inertia to the spin moment of inertia.

For the damper located on the spinning section, however, the nutation frequency is much lower than the spin frequency for this case by nearly an order of magnitude. In the simulation, if the natural frequency of the nutating damper were dropped to the nutation frequency, the damper went unstable due to the spin rate, and produced no system damping. If the natural frequency of the damper were high enough to be stable, it was too stiff to damp effectively. As a consequence, the approach was abandoned.

To simulate the damping present in the real spacecraft, the source of the damping had to be identified. The conclusions drawn from the orbit transfer phase of ATS-E were that the heat pipes located on the spacecraft were responsible for the majority of the passive damping. It was decided, therefore, to simulate one of the heat pipes. The analysis is in Appendix J.

The heat pipes were considered to be continuous loops around the periphery of the space-craft containing a "slug" of fluid. The equations are in complete form, but require digital integration for an exact answer. A simplified set of equations was programmed on the analog computer and simulations attempted. Unfortunately, scaling and sine function generator difficulties prevented a meaningful simulation. Hand calculations, however, indicated that the motion of the fluid within the tube was dominated by the spacecraft dynamics, and a heavily damped fluid could easily provide considerable system damping. The results, on a qualitative basis, appear to agree with independent conclusions regarding the heat pipe as the probable source of excess damping. A side effect, not contained within the simulation but calculated by hand, was the movement of the fluid from one side of the spacecraft to the other. This could cause a principal axis shift of approximately 10 degrees and interfere with the action of the active nutation damper.

Within the limitations of this study, therefore, it appears that the initial conditions control the final spin direction. It also appears that short bursts of thrust from the available thrusters can be effective only initially, since the dynamics of the spacecraft dominate the motion immediately after apogee motor ejection. The final spin direction, therefore, can be controlled only to the extent that the initial conditions immediately preceding apogee motor ejection can be controlled.

SECTION 4

DATA PROCESSING SYSTEM

SECTION 4

DATA PROCESSING SYSTEM

4.1 DATA SYSTEM REQUIREMENTS

A brief description of the ATS "Long-Term" Gravity Gradient Data Processing System was presented in Section 2.3.2. The requirements for the system were based primarily on the multiple needs for an in-depth analysis of spacecraft attitude data and a correlation of that data with the system status of the gravity gradient hardware. The data and analysis were required at GE to satisfy the mission requirements of the gravity gradient experiment an were required at NASA/GSFC for redistribution, along with other payload data, to other ATS experimenters.

Command, control and data acquisition for all ATS flights was handled by three tracking stations located at Rosman, North Carolina, Mojave, California and Toowoomba, Australia. Operations control was centered at the ATS Operations Control Center (ATSOCC) at the Goddard Space Flight Center in Greenbelt, Maryland.

During satellite operations, each tracking station in view of the satellite recorded data in accordance with a master schedule generated by ATSOCC. The data was delivered weekly to GSFC's Information Processing Division for formatting to user requirements. The GSFC data reduction essentially entailed the conversion from serial PCM data to parallel binary data, and stripping and formatting the telemetry words required by each experimenter. In GE's case, the formatted telemetry words were those required to compute spacecraft attitude and to analyze gravity gradient subsystem performance. The resultant magnetic tape was provided GE on a weekly basis and was designated the Raw Telemetry Data Tape (RTDT). Along with the RTDT, GSFC was to prepare and deliver to GE a magnetic tape containing tracking station measurements of the spacecraft antenna polari- zation angle (POLANG). Due to the unfortunate circumstances surrounding each flight, the system for provision of POLANG tapes was given only minimal implementation. In addition to the digital magnetic tapes, GE was to receive 35 mm film negatives, developed and processed at GSFC after photographic recording of TV monitors at the tracking stations.

This film data was to be manually read on a Gerber Scientific Film Viewer and the resultant data processed through a TV Data Reduction Program (TVDRP, see Appendix K). The end result would have been data on gravity gradient boom tip deflections for analysis of boom dynamics and thermal bending, as well as data on the earth disk for use in evaluating the gravity-gradient system TV as a potential attitude sensor.

GE data requirements and a specification of GE/NASA data system interfaces and formats were consolidated in the following documents:

1. SVS-7429, ATS DATA FORMATS, 27 April 1966 (ATS-A) (Revision A, 17 November 1966; Revision B, 15 March 1967)

2. SVS-7556, ATS-D DATA SYSTEM INTERFACES, 14 June 1968

3. ATS-7723, ATS-E DATA SYSTEM INTERFACES, July 1969

The volume (or quantity) of data for GE processing was established by mutual agreement between the GE and GSFC Project Offices and was based on the type of orbit (subsynchronous or synchronous), the operation plan schedules, and a series of studies which attempted to optimize the desired-versus-required data coverage for satisfaction of gravity experiment attitude requirements. For the ATS-A subsynchronous orbit, the data volume was established on the basis of average tracking station coverage for weekly periods. For the synchronous ATS-D and E orbits, the quantity of data to be processed weekly was established at a nominal 56 hours of real-time transmission to a tracking station. This was primarily dictated by overall program economics. A turnaround time of 24 hours (after receipt of data by GE) was established as a goal for the production and delivery of computed attitude data to NASA/GSFC. The format of data to be supplied NASA was also specified in the data system interface documents and the deliverable NASA Attitude Data Tape was referred to as the NADT. The remaining data processing requirements were scheduled on a weekly basis for specified periods after each launch.

4.2 PROGRAM DEVELOPMENT

The original system design and software development for ATS was performed with the IBM-7094 computer which was the large-scale batch processing EDP machine in use at GE/VFSTC in 1967 for engineering and scientific computations. The data processing for ATS-A was performed on this machine. The machine configuration consisted of 32,000 words of core (36 bits per word) and 2 banks of 10 digital tape transports each. It became evident in the early design and specification stages that the total ATS Data Processing System would exceed the computer storage capacity. The system was therefore segmented into three functional packages:

1. Preliminary Processing (using the Data Reduction Module or DRM)

2. Attitude Determination (using the Data Analysis Module or DAM)

3. Diagnostic Data Processing (using the Line Image Sort and Listing Program or LISLP)

Computer processing to generate the NASA Attitude Data Tape (NADT) required the Preliminary Processing and Attitude Determination Programs. These were processed within the required 24-hour period, including the intermediate time for evaluation of the raw attitude data. The Diagnostic Data Processing was usually performed during the 24-hour period immediately following delivery of the NADT. A single processing run through the IBM-7094 was timed using 20 hours of telemetry data recorded on an RTDT. The computer running time per hour of data was calculated as follows:

1. Preliminary Processing: 0.03 hr per hr of data

2. Attitude Determination: 0.004 hr per hr of data

3. Diagnsotic Data Processing: 0.0092 hr per hr of data

The Attitude Determination timing, however, is low by at least a factor of two because the data quality was very poor and the logic of the program deleted poor quality data rather than continue the computations. Neither is the time for processing of merged POLANG data included.

With the changeover from the IBM-7094 computer to the GE-635 computer at VF STC in 1968, the ATS Data Processing System was converted to the newer computer before the launch of ATS-D. The GE-635 computer is a large scale processor with 128,000 words of core (36 bits per word), 12 digital tape transports and two 24 million character disks. The use of this computer allowed almost complete processing to be performed in a single pass; however it was felt necessary to incorporate an intervention for the determination of data quality before the computation of attitude and the concept of a three-pass system was retained. This new system utilized 52,000 words of core, 7 digital tape transports and portions of both disks. The changeover from the IBM-7094 to the GE-635 also entailed a change in peripheral printers from the IBM-1401 to the GE-415. As a subsequent cost improvement for ATS-E, preparations had been made to accomplish all output data printing on an SDS-910 computer (GFE) in the Data Systems Laboratory at VF-STC. This would have eliminated all leased printer costs on the ATS contract. Use of the system was severely curtailed, however, by the anomalous operational conditions on ATS-E. Plotted data (for intermediate and final evaluation at GE and presentation of selected functions to NASA/ GSFC) was generated on the Stromberg-Carlson SC-4020 Plotter. All plot formats were generated on the computers (IBM-7094 or GE-635) and outputted on digital tapes. These tapes were in turn processed through the SC-4020 system to produce 35 mm film strips. Associated film processing equipment then produced hard copy plots on 11-inch paper rolls.

4.3 DATA DESCRIPTION

4.3.1 TELEMETRY DESCRIPTION

4.3.1.1 Normal Mode

The spacecraft telemeter configuration is a PCM (pulse code modulation) design. The bit stream is generated at the rate of 194.18 bits per second. Each word or channel of the format consists of 9 bits. The telemetry word is then generated at a rate of 21.58 words per second. The bit numbering method for the word is shown below with Bit 1 being the most significant (MS) and Bit 9 the lease significant (LS).

bit	1	2	3	4	5	6	7	8	9
bit weight	2^8	2^7	2^6	2^5	2^4	2^3	2^2	2^1	2^0

MS (top left) ... LS (top right)

The bit weight of Bit 1 is therefore $2^8 = 256$ and the bit weight of Bit 9 is $2^0 = 1$. A telemetr word contains a PCM count varying from zero to 511. A Main Frame of the telemeter defines 64 words with the first three words containing a fixed and unique bit pattern known as sync words. A sequence of 64 Main Frames is known as a Master Frame. Two words of a Main Frame are subcommutated as shown in Figure 4.3-1. Main Frame Word 62 is subcommutated by 64 words and Word 63 by 32 words.

Main Frame = 64 words transmitted in 2.9664 seconds
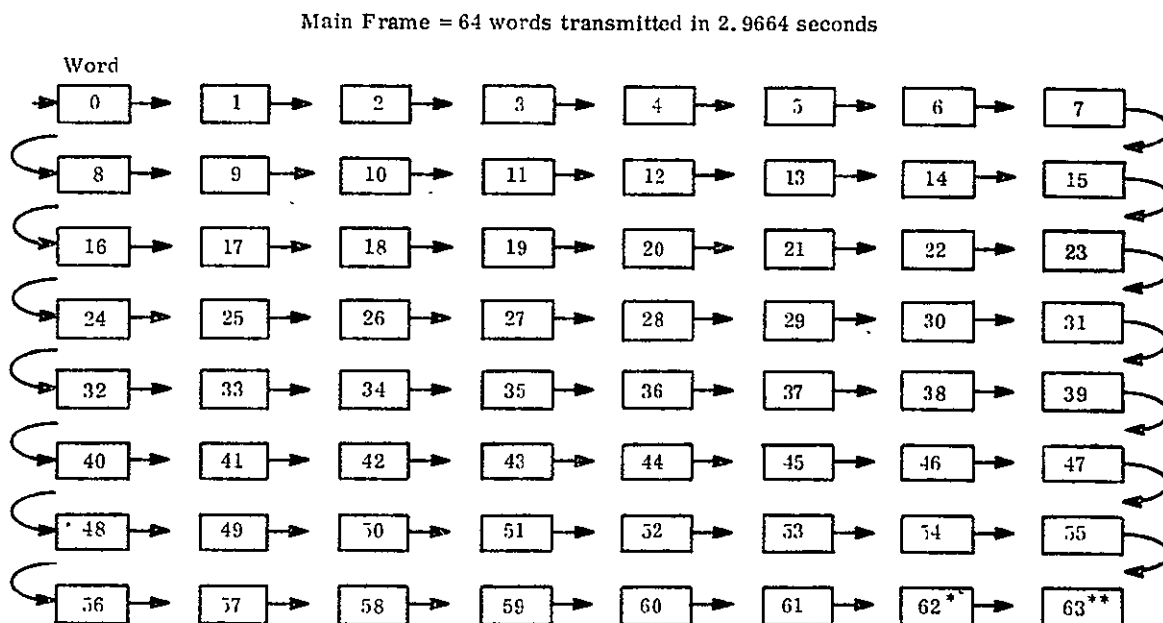
Words 0, 1, 2 are sync words of nonvarying format.
*Word 62 is subcommutated by 64 words (1/192 word rate).
**Word 63 is subcommutated by 32 words (1/96 word rate).

All words (channels) are 9 bits each.

Figure 4.3-1. ATS Telemetry Configuration

Therefore, any single subcommutated word in Word 62 is sampled once per Master Frame and a single word in Word 63 is sampled twice per Master Frame. All telemetry functions are classified as analog, Gray code, or event. The analog voltage fed to the telemetry processor varies from zero to -5.11 volts corresponding to the PCM count from zero to 511. Gray code data and event data are fed to the processor bit-for-bit such that the telemeter reads out the data in the 9-bit word patterns as inputted.

4.3.1.2 Dwell Mode

The spacecraft telemeter is commandable from ground stations into a dwell mode in which the telemeter, instead of sequentially outputting all words, repeatedly outputs the value from a single word of a Main Frame. This can be performed on any Main Frame word except Words 0, 1, 2, or 3. A dwelled Main Frame then consists of the normal mode's first four telemetry words followed by 60 channels of the dwell word. This mode will continue until a command for a new dwell word or for a return to the normal mode is sent to the vehicle. In either mode, Channel 3 will indicate the last commanded mode of the telemeter. If the telemeter is made to dwell on the subcommutated channels 62 or 63, the telemeter Main Frame is filled with the subcommutated word sequence of that particular word. Since there can be 64 subcommutated words (Channel 62) and only space for 60 words, the first 4 subcommutated words are lost when the telemeter is dwelled on Channel 62.

4.3.2 ANTENNA POLARIZATION DATA

Antenna Polarization Data is used, in complement with Infrared (IR) and Solar Aspect Sensor (SAS) data, to determine spacecraft attitude. An RF antenna, coaxial with the satellite pitch axis, transmits a polarized RF signal to the tracking station where the orientation of the electric vector (as determined by maximum signal strength) is measured normal to the line of sight. Thus, except for Faraday rotation and atmospheric refraction, the measured electric vector lies in a plane defined by the spacecraft's pitch axis and the line of sight from the station to the satellite. The orientation of the electric vector is defined relative to a reference plane which is defined by the local vertical of the station and the line of sight to the satellite. Positive sense is defined by the right-hand

rule with the thumb pointed along the line of sight from satellite to ground station. Hence, as viewed from the ground station, counterclockwise angles are positive.

The POLANG data was to be subjected to data reduction at GSFC before transmittal to GE. This consisted of digitization, filtration, interpolation and corrections due to Faraday rotation and earth's magnetic filed. After these procedures, the sampling period of the POLANG output could vary from a minimum of about 3 seconds to a maximum of about 5 minutes. The period for any given batch of data was to be established through ATSOCC, based on actual needs at the time of data acquisition. Data, in all cases, was to coincide with whole units of time. The data processing programs at GE could handle the POLANG at these different rates; however, at too large a time interval between samples, the data would have lost its usefulness in combination with sun and earth attitude sensor data.

4.3.3 ATS SYSTEM TIME

A timing system is utilized by ATSOCC such that the tracking stations and the control center can communicate on a common time base. Each tracking station uses a time generator to maintain this base during an orbital mission. All data received by the tracking stations from the satellite are recorded with this time code. The time code in use is the NASA 36-bit Time Code, a 100 pps pulse-width-modulated (PWM) time code which modulates a 1000-cycle sine wave carrier. The code is composed of a Reference Marker and nine subcode words which describe time of year in seconds, minutes, hours, and days. Each subcode is weighted in BCD format. The leading edges of all pulses are precisely spaced at 10-millisecond intervals. The Time Frame is completed by 100 pps index markers and by index markers occurring every 100 to 900 milliseconds. The frame Reference Marker is described by five binary one's followed by a binary zero. The leading edge of the binary zero is the reference time. The Time Frame provides for the insertion of control functions for identifying the recording stations (four bits). The time code is formatted with the telemetry data by GSFC's Information Processing Division when the individual experimenter tapes are prepared.

4.3.4 ORBIT PARAMETERS

Orbit parameters are those mathematical quantities which describe the initial conditions and confinements of the elliptic orbital path of the spacecraft. These quantities must be inputted to the Lyddane-Brouwer orbit model program, a subroutine of the Attitude Determination Processor, before the calculations of attitude can be performed. The orbit parameters were to be received weekly from NASA/GSFC along with the RTDT and POLANG tapes. In the event no new parameters were received, and in the absence of any other information, parameters from the previous week were to be used. The parameters to be supplied were as follows:

1. Epoch Time: Year, day of year, hour, minute, and second (GMT)

2. Semimajor Axis: Mean semimajor axis of the elliptical orbit at epoch (kilometers)

3. Eccentricity: Mean eccentricity of the elliptical orbit at epoch (dimensionless ratio)

4. Inclination: Mean inclination of the elliptical orbit at epoch (degrees)

5. Right Ascension Ascending Node: Mean right ascension of ascending node at epoch (degrees)

6. Argument of Perigee: Mean argument of the perigee at epoch (degrees)

7. Mean Anomaly: Mean "mean anomaly" of the satellite point at epoch (dimensionless)

4.3.5 TV DATA

TV data was to be received at GE in rolls of time-annotated 35 mm negative transparent film. The presentation format was carefully defined in the Data System Interface specs. ATS-A TV data was transmitted from two TV subsystem cameras mounted on opposite sides of the spacecraft: one pointing toward earth and the other pointing toward space. ATS-D had only a space-oriented camera and ATS-E had only an earth-oriented camera. The TV signal was displayed on monitors located at each of the tracking sites. There, periodically, in response to direction from ATSOCC, the TV monitors were to be photographed by 35 mm cameras along with the system time clock. These film strips were then to be shipped to NASA/GSFC for development before shipment to GE. The TV data was then to be manually read on the Gerber Scientific Film Viewer to obtain the data input for the TV Data Program (TVDP). TV camera data processing techniques and procedures are discussed in detail in Appendix K.

4.4 <u>GENERAL SYSTEM DESCRIPTION</u> (Reference Figure 4.4-1)

The requirement for a 24-hour turnaround on the production of a NASA Attitude Data Tape (NADT) was a major factor in the development of a three-phase operational approach to the processing of gravity gradient experiment data. The first phase of operations (Pre-Processing Phase) utilized the Telemetry Configuration and Calibration Tape Generation Program (TCCTGP) to prepare the Telemetry Configuration and Calibration Tape (TCCTP). The TCCTP was prepared in advance of receipt of the RTDT and POLANG tapes from NASA so that processing of the NASA tapes could begin immediately upon receipt. (The TCCTP contained all fixed information essential to the processing and merging of data from the RTDT and POLANG tapes.) The second phase of operations (Normal Processing Phase) required three computer passes. The first pass utilized the Data Reduction Module (DRM) to merge data from the RTDT and POLANG tapes, convert the data to useful engineering units and produce a summary listing of spacecraft status, a Data Analysis Module Tape (DAMTP), a Data List Tape (DLT), a Telemetry Data Tape (TDT) and a plot tape for the SC4020 plotter. The second pass utilized the Data Analysis Module, Version 2 (DAM 2) to compute spacecraft attitude performance as a function of time. Before commitment to Pass Number 2, data plots and reports from Pass Number 1 were closely examined to ensure a quality of data commensurate with requirements for a reliable computation of spacecraft attitude. Any required changes resulting from this examination were introduced by DAM 2 parameter card modifications. The DAMTP, produced during Pass Number 1, provided the DAM 2 input data and three tapes were produced as output:

1. <u>NASA Attitude Data Tape (NADT)</u>

    The requirements for this tape took precedence over all other requirements. The NADT was required by NASA/GSFC within 24 hours after GE receipt of the RTDT and POLANG tapes. The NADT was to be utilized by GSFC in the production of a world map for distribution to all ATS experimenters. The world map was to contain the time history of spacecraft orbital position and attitude relative to the earth and sun.

2. <u>GE Attitude Data Tape (GEADT)</u>

    This tape was produced for subsequent use by GE in an in-depth analysis of spacecraft attitude performance. It was therefore of prime importance to the gravity gradient evaluation team.
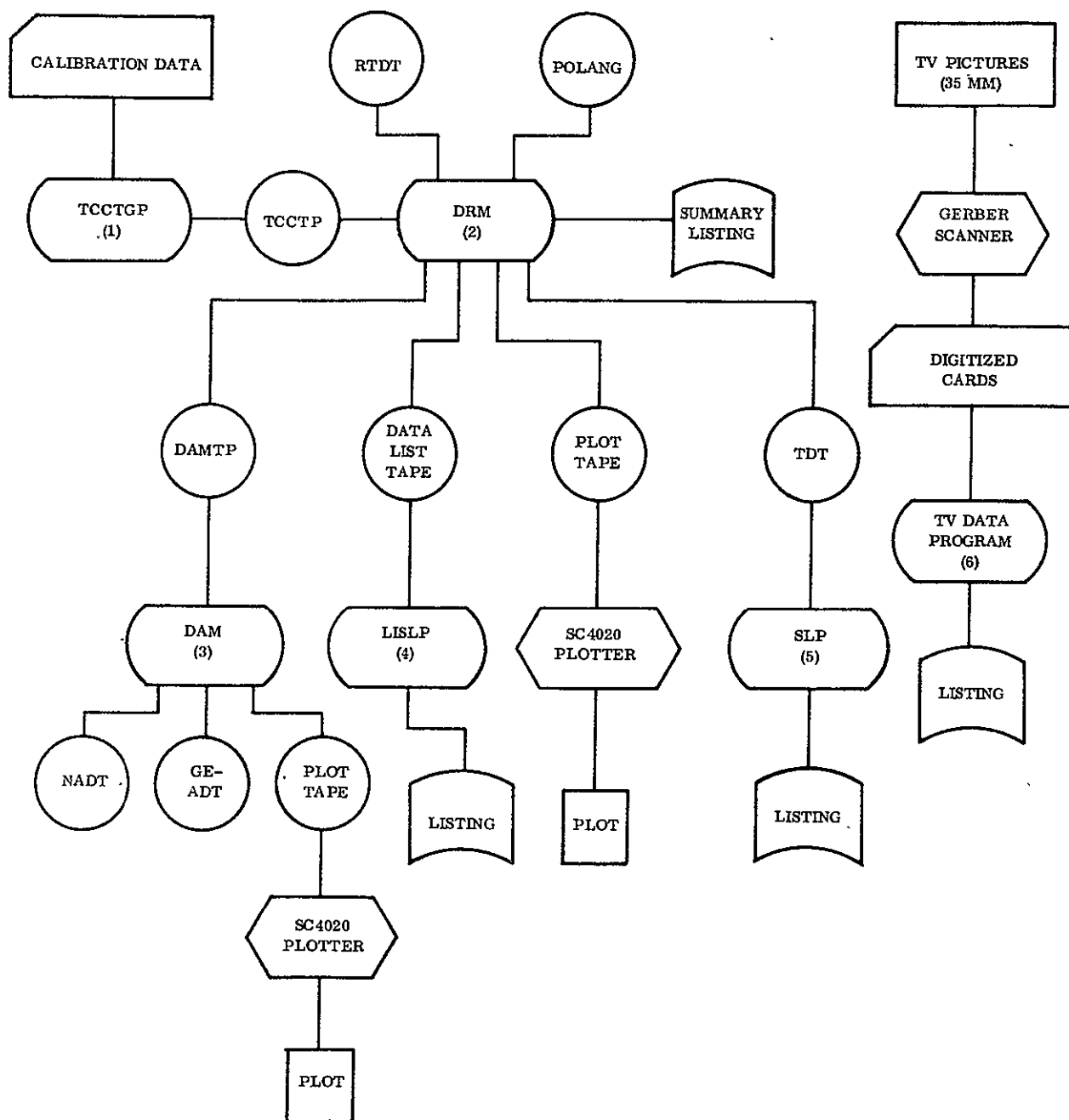
Figure 4.4-1. ATS Data Processing System

3. SC-4020 Plot Tape

This tape provided for the automatic production of attitude plots (pitch, roll, yaw and damper boom angle as a function of time) on the SC-4020 plotter. Two sets of plots were to be produced: one for NASA/GSFC and the other for the GE evaluation team.

The third pass of the Normal Processing Phase was accomplished after delivery of the NADT - usually during the second 24-hour period following receipt of the RTDT and POLANG tapes. The third pass utilized the Line Image Sort and Listing Program (LISLP) to output the reports required by the gravity gradient experiment evaluation team. This included means and standard deviations, event levels, event conditions, and point-by-point listings of selected sensors. The input to the LISLP was the Data List Tape (DLT) produced during Pass Number 1. The Telemetry Data Tape (TDT) was used for this purpose on ATS-A (see Figure 2.3-2), but by the time of the ATS-D and E launches, enough additional report requirements and output format options existed that a separate tape (the DLT) was created for processing of normal report requirements. The TDT was then reserved for use during the Post-Processing Phase. The TDT contained all scaled telemetry values and was used as input to the Selective Listing Program (SLP). The SLP was an analysis tool which was used to provide listings of selected parameters over time intervals of special interest. The SLP could output a listing of up to 15 parameters, each pass, in a time ordered column format. In addition to SLP operation, the Post-Processing Phase included processing of filmed TV data on the Gerber Film Scanner and processing of the punched card output through the TV Data Program (TVDP). The TVDP was designed to provide an output listing of data on boom tip deflections and earth orientation. The essentials of the TVDP are outlined in Appendix K.

4.5 PROGRAM FUNCTIONAL DESCRIPTIONS

The ATS Data Processing System is actually composed of six separate and distinct programs which are interrelated through their input and output. Table 4.5-1 summarizes the input and output for each program. Reference to Figure 4.4-1 will provide an overview. The following paragraphs describe the specific functions of each program.

Table 4.5-1. Input/Output For ATS Data Processing Programs

Program	Input	Output
TCCTGP	a) Control Cards b) Telemetry Configuration and Parameter Description Cards c) Calibration and Event Level Assignment Cards	a) Telemetry Configuration and Calibration Tape (TCCTP) b) A summary listing of the setup, organized by parameter
DRM (Pass No. 1)	a) Control Cards b) Telemetry Configuration and Calibration Tape (TCCTP) c) Raw Telemetry Data Tape (RTDT) d) POLANG Data Tape	a) Data Analysis Module Tape (DAMTP) b) Telemetry Data Tape (TDT) c) Data List Tape (DLT) d) Time history plots of Solar Aspect Sensor, Earth IR Sensor, Angle Indicator, POLANG and Magnetometer "raw" data outputs and related status items such as SAS ID, Earth Sensor Sun-in-View, etc.
DAM 2 (Pass No. 2)	a) Control Cards b) Data Analysis Module Tape (DAMTP)	a) NASA Attitude Data Tape (NADT) b) GE Attitude Data Tape (GEADT) c) Summary Listing d) SC 4020 Plot Tape (Pitch, Roll, Yaw, Pointing Angle and Damper Boom Angle as a function of time)
LISLP (Pass No. 3)	a) Control Cards b) Data List Tape (DLT)	One or more printed data list reports by pre-established report format (Mean and SD, High/Low Limits, etc.)
SLP	a) Control Cards b) Telemetry Data Tape (TDT)	Parameter listings in a column format (time controlled with editing options)
TVDP	a) Control Cards b) Digitized Cards from scanner film processing	a) Listing of coordinate deflections of boom tips in field of view b) Listing of earth center and terminator coordinates

4.5.1 TELEMETRY CONFIGURATION AND CALIBRATION TAPE GENERATION PROGRAM (TCCTGP)

The primary function of the TCCTGP is to translate and convert function-oriented parameter input specifying the frame position, sampling rate, conversion requirements, calibration/ gray codes, titles and other basically fixed information into matrices and tables which are utilized by the DRM for normal processing. This program is run only a few times for a normal launch. This program is the first program required in the data reduction system. It's primary output is the telemetry configuration and calibration tape (TCCTP). This program is run during the pre-processing phase before receipt of RTDT and POLANG tapes from NASA. The ATS Calibration Book and flight evaluation requirements are the source for much of the input information. Tables are created in a systematic order with appropriate linking to allow functional separation of each. These tables provide a complete condensed source of setup information to the DRM:

1. A table is built to define each function as to telemetry word, bit, and order required to form the word (including normal and subcommutated positions).

2. A table of reduction type of each parameter is formed. In addition, scaling tables are built in PCM levels versus engineering units when required. Options provided are scaling (funtionalizing), gray code, event level (on/off), or bit configuration (no reduction). Section 4.6.2 details the scaling procedure.

3. Normalization tables, indicating channels to be corrected for analog-to-digital converter drift and instrumentation voltage variations, are built.

4. Arrays providing parameter titles, output accuracy, presentations, and indications of checks to be performed are organized.

5. All inputs are checked for errors and inconsistencies.

4.5.2 DATA REDUCTION MODULE (DRM)

The heart of the ATS Data Processing System is the Data Reduction Module (DRM). The DRM is composed of two essential subprograms, the Master Control Data Reduction Program (MCDRP) and the input module referred to as INPATS. The MCDRP is a small FORTRAN program which directs the flow and processing of data during Preliminary Processing (Pass No. No. 1) by transferring control to predeveloped task-oriented modules. The first module called is

the input module (INPATS). This module, by MCDRP direction, unpacks one complete
frame of data at a time from the RTDT and, according to instructions previously taken from
the TCCTP (Section 4.5.1) evaluates, normalizes, converts to meaningful units and stores
in the data base with respect to time, all data from that particular data frame. The POLANG
data for the corresponding time period is also unpacked and stored during this operation.
INPATS returns to the MCDRP after each complete frame of telemetry. The MCDRP then
calls the modules which need this data to produce the Data Evaluation Reports specified by
the input parameters. Each module generates one type of Data Evaluation Report, and has
its own input parameter set so that any combination of telemetry functions can be processed
by each. The modules are designed to retrieve all data, parameters, linkage directives and
communications from the data base. The following Data Evaluation Report Modules are avail-
able to the MCDRP:

1.   Mean and Standard Deviation Reports

2.   Out of Limits Summary

3.   Event Status Summary

4.   Data List Reports

After all the Modules have utilized the stored data for the particular data frame, the MCDRP
transfers back to the INPATS Module to continue processing. This procedure is continued
until preliminary processing has been completed for all RTDT and POLANG data. If require-
ments change, this procedure gives the user the capability of simply adding or deleting a
CALL statement or input parameters at time of execution.

The following submodules are included in and executed specifically by the INPATS Module.
The Data Analysis Tape Generator Module (DMTGEN) collects the RTDT and POLANG data
needed by the DAM 2 Attitude Determination Program. Selected telemetry function data and
(if available) Polarization Angle Data is merged at a pre-selected rate. The selected data
is written on a magnetic tape (referred to in this document as the Data Analysis Module Tape,
DAMTP) and stored in the Data Base as input to the ATS SC-4020 Display Module, which

generates a time history display of the telemetry function data used in the computation of spacecraft attitude. For historic (and possible post processing purposes) all the processed RTDT and POLANG data is written on a magnetic tape (referred to herein as the Telemetry Data Tape, TDT) by the INPATS Module. Production of the DAMTP and TDT complete the essentials of Pass No. 1. As a part of Pass No. 1, the operating technician was supplied with a summary list of the files on the tape. This was done for record keeping and to establish data quality that might have affected the insertion of parameter cards for subsequent computer processing.

This summary initially shows the label record information of the data file. It then presents the time period of the data (i.e., the times of the first and last data frames and the number of main frames contained in that period). If the commutator was dwelled during the time period, the dwell channel number, either in the main frame words or subcom words is indicated. The time interval and the repetition rate of the POLANG data from the POLANG tape, if it exists, is shown on the Summary report. The report presents a list of the frames omitted from further processing due to a time discrepancy. This was designed to alleviate any problem in the fixed-rate merging of the telemetry and POLANG data. Finally, the Summary list provides information on filled data frames. Some filled frames are by design and are called out in the Data System Interface Specifications; others are due to data dropout.

One of the prime functions of Pass No. 1 is the merging, by flight time, of the PCM telemetry data and POLANG data. Some difficulty was experienced in obtaining general agreement on the data sampling rate for POLANG and an internal requirement was established to provide the capability for merger of the two sets of data at almost any POLANG sampling rate.

The applicability of POLANG for attitude determination decreases as its sampling rate drops below that of the PCM data. As an example, the sun sensor data is sampled at intervals of approximately 3 seconds. The sampling of POLANG at a rate of one sample per minute would require that either 19 of the 20 values of sun sensor data not be used or that 20 samples of sun data be used in combination with one value of POLANG data for one attitude calculation. Since POLANG data for this particular application was not considered to be as reliable as

the sun data, the quality value of either of these means of determining attitude was considered quite low for "high frequency" attitude components. Accordingly, GE has always requested that POLANG exhibit a sampling rate at least equal to that of the sun sensor data, since the "high frequency" data is quite fundamental to studies of thermal twang or thermal flutter. The merging procedure uses logic to locate the data time on the POLANG tape that most closely coincides with data time on the telemetry tape. The POLANG words are then added to that respective telemetry frame of data. For telemetry frames with no associated POLANG data, the added POLANG data is inserted as all zeros. POLANG data from as many as four tracking stations is provided for. The output of this merge module is two tapes, one (labelled TDT) contains all telemetry and POLANG data and the other (labelled DAMTP) contains only that telemetry data and POLANG data required for computation of attitude. Incomplete frames of data, questionable data, and dwell mode data are not included. The TDT and DAMTP are retained in the GE tape library and the RTDT's and POLANG tapes are returned to GSFC.

The preliminary processing pass also outputs SC-4020 plots of the sun and IR earth sensor data (as well as magnetometer and POLANG data) as a function of time. These plots are reviewed by data evaluation personnel before proceeding to Pass No. 2. This is primarily to ensure good data quality before committing to attitude determination. This intermediate plotting and evaluation proved to be quite valuable due to the anomalous conditions experienced in orbit. Data for complete attitude computation was very meager, but the "raw" sensor data plots were quite valuable in terms of visualizing general dynamic behavior.

Along with two-axis readings of the sun and IR earth sensors, the plots also displayed the identification number of the sun sensor in use (No. 1 through 5), and the sun-in-view indicator for the IR sensors. The two-axis readings from both IR sensors (ATS-2) were displayed simultaneously. The plot symbols differentiated between sensors, and the sensor not in view of the earth exhibited data riding the plot zero reference.

For the tumbling spacecraft, these plots allowed for an analysis which determined the axis of tumbling and the rate to a relatively good accuracy. Typical plots were included in all final flight reports.

4-16

In summary, the following operations can be performed in the DRM. Control cards specify what operations are required and what data is to be reduced. (Control is normally in terms of data files or acquisition times.) Section 4.6.5 details the hardware requirements of the DRM. The operations are not necessarily performed in the order listed and some need not be included for some reduction cycles.

1. TCCTP Tables and control information is stored with appropriate linkage. Limited updating of this information from card input at run time is permitted.

2. Raw telemetry data is read from the raw telemetry data tape (RTDT). It is checked for content and processed accordingly. Complete logic is provided for handling:

   a. Time start and stop control

   b. Encoder change

   c. Data drop out

   d. Mixed dwell and normal data with independent processing requirements

   e. Time discontinuity

   f. Unexpected end of data

3. Individual channels are unpacked from the normal and subcom frames as required to form PCM words ranging from 1 to 36 bits. These values are stored versus the current time.

4. The values are then normalized, if required. Section 4.6.1 explains the methods used.

5. Individual functions are unpacked and if required scaled or converted through one of four procedures.

   a. Gray Codes are processed through a point per level table lookup. (Each PCM level has an exact engineering units equivalence in the table.)

   b. Event Levels use step-type table lookups (ranges of PCM levels correspond to finite status of one or more functions) which yield true (1) and false (0) indications.

4-17

c. Scaling uses functionalizing table lookups with linear interpolation and extrapolation. This provides a smooth range of PCM levels versus engineering units. Section 4.6.2 contains a more detailed explanation.

d. Bit Configuration provides PCM level outputs as received.

6. Means and standard deviation values of selected parameters are computed. Two different schemes are used as specified in the controlling input. These summaries are output as a single integrated report or as separate reports. The summaries are controlled by time intervals. Two intervals are used. In addition, each parameter in each report can accumulate two means and two deviations as directed by any event function which may be associated. Section 4.6.4 presents the equations used.

7. An out-of-limits check is performed on all parameters specified. The limits may be constant or change with the state of any related event-type parameter. A time-ordered report is created, noting the state (in or out of limits) of each parameter being checked and restating the new status with appropriate time notation each time a parameter crosses a limit.

8. An event status summary notes the change of state of all requested event type parameters. The output is an independent report which notes the initial state and subsequent changes (and time of each) of the parameters being monitored.

9. Three special ATS plots are created while processing normal data. Section 4.6.3 details the plots and plotting procedure.

10. Data listings are created as requested. One or more time ordered data listings with up to ten parameters in each list may be processed. Main frame and sub-com functions may be mixed as desired.

11. POLANG data may be merged with telemetry data at any selected rate or at the rate of POLANG availability. The selected RTD and available POLANG will appear on the special time history plots as well as the DAMTP.

12. A special record select output function is incorporated to control output. This routine tags each line of each report with an identification character to allow reconstruction of the interlaced reports.

13. A reduction summary report is output to provide a permanent record of what data is reduced, its quality, and the outputs produced.

4.5.3 DATA ANALYSIS MODULE, VERSION 2 (DAM 2)

The exclusive function of DAM 2 is to compute spacecraft attitude. The DAMTP (generated by the DRM in Pass No. 1) is the primary source of input. Calculations are based on solar

aspect sensor, earth sensor, POLANG and magnetometer data in that order. Primary outputs from DAM 2 are the NASA Attitude Data Tape (NADT) and the GE Attitude Data Tape (GEADT). The NADT was generated to a NASA-prescribed format and contained computed attitude data and related information at 5-minute intervals. The GEADT contained computed data at 1-minute intervals as well as intermediate computations for an in-depth analysis of the attitude determination system and spacecraft performance by the GE experiment evaluation team. Attitude plots and detailed listings were also produced with data shown at its maximum rate. The complete equations for DAM 2 are contained in "ATS-D Data Analysis Module (DAM 2) Equations and Basic Logic," Program Information Release 1K05-006, 24 July 1968 by M. A. Martin. The DAM 2 differs from the original DAM in the techniques used to arrive at a single optimum solution for attitude in a situation in which there are typically multiple and/or ambiguous solutions to the attitude determination problem. Consideration of more attitude-related measurements than are minimally required to determine attitude allows a computational optimization to improve the accuracy of determination. The original DAM attempted to compute one optimum solution to the attitude problem by using (in a weighted fashion) all available attitude sensor data. DAM 2 computes attitude by all available means and then attempts to pick the optimum of the multiple resultant solutions.

4.5.4 LINE IMAGE SORT AND LISTING PROGRAM (LISLP)

All MCDRP-controlled modules use a Record Select Output subroutine to produce their listing output. This subroutine assigns each report (or printout) a unique character and includes it in the line image output. All report output is simultaneously written on one tape, referred to as the Data List Tape (DLT). The Line Image Sort and Listing Program (LISLP) produces the respective printouts by sorting the tape once for every character. Each sort prints all the line images assigned to that specific character and thereby forms the report.

4.5.5 SELECTIVE LISTING PROGRAM (SLP)

This program selects any combination of up to 15 parameters and forms a time ordered column listing of their levels. The listing is time-controlled with editing options. The SLP is an analysis tool designed for use when an in-depth analysis is indicated by conditions identified in the initial reduction summaries. It is not required for normal data reduction.

4.5.6 TV DATA PROGRAM (TVDP)

The TV Data Program produces boom bending and earth orientation data from the digitized data output (punched cards) of the Gerber Scanner. The Gerber Scanner is used to digitize data from strips of 35 mm film provided by NASA/GSFC and produced by photographing TV monitors at the ground stations. Appendix K provides a detailed description of TVDP techniques.

4.6 PROGRAM OPERATIONS

4.6.1 NORMALIZATION

Normalization is the adjustment applied to PCM data to correct errors introduced by drifting of the on-board analog-to-digital conversion unit and changes in the instrumentation power supply. The performance of the A to D unit is measured by monitoring the indicated output of a precision voltage supply incorporated for that purpose. The instrumentation power supplies are measured as independent parameters. Functions to be adjusted and corresponding references are indicated as part of the calibration setup procedure. The correction takes the form:

$$PV_c = PV_u \times K_{REF}$$

or $$PV_c = PV_u \times K_{INS}$$

Where

PV_u = uncorrected PCM level of the parameter

PV_c = corrected PCM level of the parameter

K_{REF} = ratio of predicted reference voltage level to the actual

K_{INS} = ratio of predicted instrumentation voltage supply to the actual

Scaling is completed in the normal manner using the corrected values. Note that both corrections need not be applied as the actual instrumentation voltage reading and the parameters requiring this correction are subject to identical A-to-D errors which cancel.

4.6.2 SCALING

Calibrations for functionalized parameters are input as X versus Y tables of from 2 to 14 points. They are expanded to X versus Y and M tables in the TCCTGP. The actual scaling logic uses a linear slope intercept form of

$$Y' = (X' - X) M + Y$$

Where

$Y' =$ Engineering units value

$X' =$ PCM level of the point being scaled

And

$X =$ Calibration reference point PCM level

$Y =$ Engineerinal units corresponding to X

$M =$ Slope (Eng'r units/count) consistent with Y and the next higher point

(The next lower value of X and Y are used except for off table values when the adjacent end points are applied in the equation.)

The DRM cuts reduction time and core requirements by sharing tables, where functions have duplicate calibrations, and by storing the last entry level for each function and using it as the most probable label in the subsequent entry.

4.6.3 DRM PLOTS

All plots in the ATS data system are formed on the GE-635. They are output on magnetic tape which is in turn processed by the SC 4020 CRT plotter. The 4020 output is 35. mm film which is processed by associated equipment to produce useful hard copy plots. The DRM plots are produced on continuous grids except for intervals when data is interrupted. The plots created are (as a function of time):

1. SAS Angle A + B
    SAS Detector ID
    Earth Sensor
    ESI (on/off)
    Sun in view (on/off)
    I. O. (camera mirrors) in view (ATS-D only)

2. Angle Indicator
    POLANG

3. Magnetometer "X" axis – Insensitive
    Magnetometer "Y" axis – Insensitive
    Magnetometer "Z" axis – Insensitive
    Magnetometer "X" axis – Sensitive
    Magnetometer "Y" axis – Sensitive
    Magnetometer "Z" axis – Sensitive

4.6.4 MEANS AND STANDARD DEVIATIONS

The means and standard-deviations are computed over specified intervals. One and four hours are normally used.

The mean is computed as

$$\bar{X} = \sum_{i=1}^{N} X_i/N$$

The standard deviation uses the equation

$$Y = \sqrt{\frac{\sum\limits_{i=1}^{N} X_i^2}{N} - \overline{X}^2}$$

4.6.5 DRM OPERATIONS

The data reduction module normally requires nine tape drives and 52,000 words of memory on the GE-635. The GE-635 has only 12 tape units available; consequently, the 9-tape requirement restricts access to the machine.

To ease the requirements, two of the tapes are replaced by permanent disk files. One disk is used as the program library and the other for telemetry configuration and calibration inputs. These disk files are created by utility programs which transfer information from tape to disk.

This transfer function is a separate entry of the system and is not a normal step in the reduction procedure. The resulting DRM requires 7 tape units and 52,000 words of memory with input cards for control.

The processing time is about 0.1 computer hour per hour of data. This figure is reduced as rate options are used and outputs are deleted.

SECTION 5

FLIGHT SUPPORT SUMMARY

SECTION 5

FLIGHT SUPPORT SUMMARY

General Electric's support of the ATS flights took two basic forms: on-line data review and in-depth flight evaluation. The on-line support served an operational function, enabling conditions to be recognized and decisions to be made quickly on the basis of attitude and diagnostic data samplings. In-depth evaluation provided detailed analyses of component performance and spacecraft motions. Each of the three flights required a different relative emphasis be given the two kinds of support. A more detailed summary of flight support activities is provided in the Final Flight Report for each spacecraft. Section 6.9 provides the specific references.

5.1 ON-LINE SUPPORT

5.1.1 ATS-2

On the ATS-2 flight, complete three-axis attitude performance determination was precluded for most of the flight, and minimal on-line computation of attitude was performed. On-line analysis of spacecraft system and health status was suspended after verification of several command executions. Considerable in-depth analysis was performed, however. This is discussed in Section 5.2.1.

5.1.2 ATS-4

General Electric became an active participant in ATS-4 spacecraft operations. Activities were aimed primarily at controlling and reducing the total angular momentum content of the tumbling ATS-4/Centaur space vehicle system. Because complete three-axis attitude determination could not be accomplished with the one on-board sensor able to provide meaningful attitude information (Solar Aspect Sensor), an alternative scheme was implemented to compute spin rate and spin axis orientation in support of ATSOCC operations.

The scheme was first used on 12 August 1968 and verified that the ATS-4/Centaur combination was in a flat spin with a tumble rate of 8 degrees per second. The spin axis was calculated

to be in the X-Y plane of the spacecraft, oscillating between the +X and +Y axes with a 192-second period. On 14 August 1968, the same technique was used to initiate a despin maneuver which required a particular orientation of the spin vector for thruster firing. On 16 August, the scheme was used again to monitor the spin-up and denutation maneuvers. It was observed, at that time, that the computer program was able to indirectly yield such spin dynamics information as precession angle, precession rate, and orientation of the angular momentum vector relative to the sun line. This information was of value to ATSOCC personnel in verifying various reorientation maneuvers and steps were taken to mechanize the scheme. By 17 August, all three ATS ground stations were able to transmit Solar Aspect Sensor data to the GE Valley Forge facility by teletype. At Valley Forge, GE engineers expanded the capability of the computer program to receive "bulk" data by teletype and to generate teletype answer messages for transmittal to ATSOCC personnel. The improved scheme enabled solutions to be computed at 3-second intervals rather than at 30-second intervals. One of the computed parameters (SSA) was hand-plotted at GE and ATSOCC for most "daylight" station passes and became the primary indicator of spacecraft motion.

General Electric personnel continued to support ATSOCC operations in this manner for the duration of ATS-4 orbital life. After reentry, similar computations were performed for the period 11 August 1968 to 16 August 1968 by extracting Solar Aspect Sensor data from the gravity gradient experimenter magnetic data tapes. Under the circumstances, GE-computed spin parameters probably offered the most complete description of the dynamic aspects of the ATS-4/Centaur flight.

5.1.3 ATS-5

General Electric provided similar support for the ATS-5 flight. Spin parameters were again computed throughout the flight. Solar Aspect Sensor data was used to give spin axis and sun position parameters in a spacecraft-based reference frame. Inertial spin-axis orientation also became available when the spacecraft spun-up about the -Z axis because valid polarization angle data could then be acquired.

The Solar Aspect Sensor spin axis calculations were first put to use on 12 August 1969 in support of an ATS-5/Centaur yaw maneuver performed by ATSOCC. Several different quantities were computed and manual methods were employed in anticipation of the possible spacecraft motions during this maneuver. The computed results were sent to ATSOCC in near real time via the NASCOM teletype loop; in addition, a preliminary estimate of the spacecraft motion was given by telephone. This preliminary estimate confirmed the success of the maneuver as a rotation of approximately 120 degrees about an axis near the Y axis. A later detailed analysis confirmed these results.

At 17:10:21 GMT of the same day (12 August), the apogee motor was fired. However, the motor case was not released from the spacecraft, because of the presence of uncontrolled nutations. The resulting dynamic state appeared as an unusual series of patterns in the quantities computed from Solar Aspect Sensor data. These patterns were analyzed, and the spacecraft was found to have gone into a flat spin about an axis near the X axis. Because of a coincidence between telemetry sampling rate and spin rate, the direction of spin about this axis was ambiguous. Further analysis by GE personnel revealed that the spacecraft was spinning about an axis near the negative X axis. This spin direction was later confirmed by magnetometer data.

Preparations were then made to compute the spin axis which would result from releasing the apogee motor case on 5 September 1969. Manual and computational methods were devised with the object of determining the spin axis as quickly as possible after the case was released. Analyses were also performed to determine the extent of the damage which would result from a collision between the spacecraft and the apogee motor case.

The apogee motor case was released at 5:30:07 GMT on 5 September. The raw Solar Aspect Sensor data indicated that the spacecraft immediately tended toward a spin about the -Z axis. Later computations from this data showed that the spacecraft was unmistakably spinning about the -Z axis by 5:36:49 GMT. Magnetometer and accelerometer data independently confirmed the -Z axis spin direction. In this -Z axis spin mode, valid polarization angle data was available. This data was used in conjunction with Solar Aspect Sensor data to

provide ATSOCC with Z-axis attitude information as computed by the GE Quick-Look System. Because of the low turnaround time possible with this system, the information was useful for the operational support of the spacecraft maneuvers which were performed from 8 to 11 September 1969.

General Electric personnel continued to support ATSOCC, throughout the flight interval, in determination of spacecraft spin-axis orientation by providing aspect angle computations via the NASCOM teletype loop. Support was also provided to the magnetometer experiment which was inoperative up this point because of the high rate of spin. Preliminary results indicate that a successful method was devised for eliminating the effects of the spin conditio

5.2 IN-DEPTH EVALUATION

5.2.1 ATS-2

An in-depth attitude analysis of the ATS-2 flight was performed at GE. Except for two short time periods during the first day of flight, the attitude information was estimated solely by examination of raw attitude sensor data. The ATS Mathematical Model was also used in an attempt to estimate attitude through a period of no data. The ATS Boom Dynamic computer program was exercised to investigate observed high frequency components of primary boom motion.

On 6 April 1967, the ATS-2 spacecraft was separated from the Agena launch vehicle. The spacecraft attitude information for this period was based on data obtained from the IR Earth Sensors since all other attitude sensors were turned off during this time interval. The spacecraft was separated from the Agena with a pointing attitude rate of 0.33 degree per second, based on the motion of the earth immediately following separation. The exact motion of the spacecraft (pitch versus roll) could not be determined on the basis of one attitude sensor because the yaw attitude at separation was not known. The earth left the field of view of IR Earth Sensor No. 1 at 5:25:00 GMT. At 5:27:18 GMT, the Solar Aspect Sensor was turned on for the first time. Based on the Solar Aspect Sensor data, the space-craft pointing angle (with respect to the local vertical) continued to increase at the tip-off

angular velocity until the primary booms were extended. At this time (5:28:44 GMT), a significant decrease in pointing angle rate was observed. The earth returned to the field of view of IR Earth Sensor No. 1 at 6:05:00 GMT on 6 April and a two-sensor (earth and sun) solution of spacecraft attitude was possible for the first time.

Based on the pointing angle and Solar Aspect Sensor data discussed previously, it was apparent that the spacecraft did not invert on its initial swing. This was consistant with results of a post-launch mathematical simulation in the vicinity of the first apogee based on a "best" approximation to the initial conditions.

No spacecraft data was obtained between the first perigee and third apogee. Solar Aspect Sensor data in the vicinity of the third apogee clearly indicated that the spacecraft was in a tumble mode. This was evident from the cyclic switching of the three sun detectors physically located around the spacecraft belly band. The order in which the three detectors viewed the sun was 2, 4, 3, 2, 4, etc., which identified the spacecraft to be rotating about its Z axis in the negative direction, with small oscillations about the spacecraft Y axis. The rate of tumble was 18.5 degrees per minute.

Because of the absence of flight data between the first perigee and the third apogee, it is impossible to estimate when the spacecraft tumbling actually began. A large angle computer simulation was made using the ATS Mathematical Model to investigate the possible space-craft motion resulting from the effects of the highly eccentric (0.455) orbit. The results of the simulation indicated that the tumbling began approximately 5 hours after separation. It should be pointed out, however, that the ATS Mathematical Model did not have the capability to simulate aerodynamic drag, and approximations for orbit eccentricity beyond 0.1 introduced slight errors. The simulation also indicated the spacecraft to be tumbling and oscillating heavily in all axes for the first 60 hours. At approximately 60 hours, a tumble pattern was established in pitch and an oscillation pattern in roll. The presence of this pattern implied that a "steady-state" condition was reached (or nearly reached). Both yaw and roll stabilized near the end of the simulation in spite of the pitch tumble. This apparent stabilization was probably the result of the large rate of tumble which tended to

spin-stabilize the spacecraft. The roll gravity gradient torques (which are effective in spite of the orbit eccentricity) prevented the spin axis from wandering and created a "gyrocompassing" situation. As a consequence, yaw was also partially stabilized.

It should be emphasized that this pattern of motion could be achieved only in the presence of damping. The mathematical model indicated that, in spite of the high rates of the spacecraft, the damper was functionally operative.

Raw attitude sensor data obtained from 11:11:40 GMT of 6 April 1967 through spacecraft shutdown at 19:45:20 GMT of 23 October 1967 showed the spacecraft to be continually tumbling. Since complete attitude determination was impossible under these flight conditions, spacecraft attitude performance was estimated on the basis of raw attitude sensor data whenever possible.

The observed spacecraft tumbling rates for the period 6 April 1967 through 14 May 1967 were consistently under 28 degrees per minute. At the end of 15 May 1967, the spacecraft tumbling rate started to increase, and rates as high as 51 degrees per minute were observed on 16, 18, 19, and 20 May 1967. The increase in tumble rate occurred at approximately the time the sky-pointing boom of Assembly A disappeared from the field of view of the sky-pointing TV camera.

The observed tumble rates fluctuated considerably during the period 16 May 1967 through 2 September 1967, but remained consistently under 51 degrees per minute. On 3 September 1967, the tumble rate increased to 80 degrees per minute. Although very little flight data was collected (and reduced) during the period 3 September 1967 through 23 October 1967, high tumble rates were observed on 3 October 1967 (72 degrees per minute) and 23 October 1967 (84 degrees per minute). The increase in tumble rate observed on 3 September 1967 may have been caused by the loss of the sky-pointing boom of Assembly B. The time at which the boom broke off is not known, but television data obtained on 7 September 1967 showed the boom to be missing.

Raw attitude sensor data acquired just before spacecraft shut down shows the highest spacecraft tumble rate (84 degrees per minute) observed throughout the active flight period.

The ATS Boom Dynamics program was utilized to study the effects of orbital eccentricity on the dynamics of motion of the ATS Primary Boom System. Two computations were performed. The first was for an orbit with a perigee of 115.8 miles, and an apogee of 6947.6 miles corresponding approximately to the orbit achieved by ATS-2. The computation was started with the vehicle at perigee, in an upright position with body rates and acceleration equal to zero. Motions at 100-, 45-, and 20-second periods were seen. No additional excitations were applied and the observed motions occurred at a time only 1300 seconds from a completely still condition.

The second computation was made for a circular orbit of 115.8 miles. No high frequency oscillations were observed. Primary boom tip motion was negligible compared with tip motions of the elliptical orbit. The conclusion was that the dynamics of the ATS-2 eccentric orbit were the prime forcing functions in the excitation of observed components of high frequency motion.

The ATS-2 flight data was also analyzed to evaluate the performance of each gravity gradient system component. A summary of each component's in-flight performance was compiled, and all anomalous behavior was investigated. With the exception of several erroneous Solar Aspect Sensor data samplings and a continual angular output from the IR Earth Sensors, all components of the gravity gradient system performed as expected.

The deployment of the gravity gradient booms provided the highlights of the component performance investigation. The highly eccentric orbit of ATS-2 imposed severe bending and torsional loads on the gravity gradient booms. Boom data obtained by photographing the TV monitors at the ATS tracking stations showed that, although the apparent boom motions were extremely wild, the primary booms were withstanding the punishing environment. All four primary booms were clearly visible and showed no apparent damage in TV data acquired from 6 April 1967 through 15 May 1967.

On 16 May 1967, ground station personnel reported that one of the sky-pointing primary boom was missing from the field of view of TV Camera 2 and was later identified as Rod 2 of Primary Boom Assembly B. On the same day, a significant increase in tumble rate was observed. The boom did not appear in any TV data acquired from 16 May 1967 through 19 June 1967.

On 1 June 1967, the Toowoomba tracking station reported that the visible sky-pointing boom (Rod 2 of Primary Boom Assembly A) had a sharp bend in it. Data recorded on 35 mm film during several subsequent days verified that the boom was crippled and indicated that the point of crippling was located approximately 20 feet from the scissor pivot point of that boom.

On 20 June 1967, the 35 mm TV data recorded by the Rosman tracking station revealed that, for the first time since 16 May 1967, two boom tips were present in several picture sequences taken by the sky-pointing TV camera. In addition, a sequence of pictures taken by the earth-pointing TV camera clearly showed three boom tips. A detailed analysis of 136 photographs determined that the "new" boom tips were those of the previously "missing" booms and not of the damper boom.

On 7 September 1967, the Toowoomba tracking station reported that the crippled boom (Rod 2 of Primary Boom Assembly A) had broken off at the crippling point, having a rigid stub approximately 20 feet long. Assembly A was scissored from 30.2 degrees to 11.0 degrees on 4 September 1967; however, poor TV reception precluded observation of the response of the crippled boom to the scissoring maneuver. The first time TV data was acquired subsequent to the scissoring maneuver was on 7 September 1967. Because of the absence of TV data during and immediately after the scissoring maneuver, it is impossible to determine whether or not the cirppled boom broke off during the scissoring operation. TV data, acquired from 7 September 1967 through 23 October 1967, verified that Rod 2 of Assembly A was broken off at the crippling point. Rod 2 of Assembly B did not appear in the field of view of the camera (since 20 June) and presumably broke away from the spacecraft. The fact that no part of the boom was visible with the assembly scissored to 11 degrees

suggested that the point of breakage was located within 5 feet of the spacecraft center body. On the other hand, both earth-pointing primary booms (Rod 1 of Assembly A and Rod 1 of Assembly B) consistently appeared within the field of view of TV Camera No. 1, throughout the active flight period, and showed no apparent structural damage.

5.2.2 ATS-4

No detailed in-depth evaluation was performed on ATS-4. Efforts were primarily applied to on-line data review.

5.2.3 ATS-5

No in-depth ATS-5 attitude analysis was performed, but component performance was investigated. All hardware operated during the ATS-5 flight performed satisfactorily. The major component malfunction of the flight occurred when Solar Aspect Sensor Detection No. 1 was open-circuited by its collision with the ejected apogee motor case on 5 September 1969. The remaining detectors continued to function nominally. No instances were discovered of component operating characteristics approaching critical levels.

SECTION 6

BIBLIOGRAPHY

SECTION 6

BIBLIOGRAPHY

This section contains a selected list of references which, when placed in context, provide a brief history and summary of developments in ATS gravity gradient software and analysis. References are categorized according to significant areas of development and study.

6.1 ATS MATHEMATICAL MODEL

The ATS Mathematical Model is a digital computer program designed to simulate the two-body, four-degree-of-freedom, gravity gradient configuration used for Applications Technology Satellites A, D and E. Gravity gradient orienting torques, damping torques (both eddy current and magnetic hysteresis) and disturbance torques are simulated in the Mathematical Model and, by integration of Euler's dynamical equations, the time history of both large and small angle performances can be depicted.

Document No.	Date	Title	Author(s)
PIR 4730-005	11/2/64	ATS Mathematical Model Coordinate Frames	Hinrichs, Foulke,
PIR 4730-008	11/4/64	ATS Math Model Requirements	Hinrichs
PIR 4424-007	11/12/64	Notes on Euler Parameters	Martin
PIR 4730-014	11/13/64	ATS Math Model-Orbit Equations	Hinrichs
PIR 4730-055	2/25/65	Responsibility for ATS Math Model	Clayton
PIR 4174-007	3/25/65	Preliminary Flow Diagram of ATS Mathematical Model	Foulke, Holthenrichs
PIR 4424-028	4/21/65	Remarks on a Proposed Numerical Integration Technique	Green
PIR 4174-017	5/11/65	Inclusion of Out-of-Plane Rod Bending in the ATS Mathematical Model	Siegel
PIR 2290-028	6/30/65	Provisional Model of the Geomagnetic Field Near Synchronous Satellite Altitude	Frost, Wouch
PIR 4174-026	8/27/65	Octic-Written in Fortran II	Evans

Document No.	Date	Title	Author(s)
PIR 4174-039	11/15/65	Input Definitions for the GAPS-IV Program	Evans
PIR 4174-049	2/28/66	Variation of Reflectance with Angle of Incidence	Hinrichs
PIR 4174-054	4/12/66	FAFRB-Four Axis Frequency Response - Version B	Evans
PIR 4174-057	4/25/66	Output Conversion Equations for ATS Digital Simulation	Hinrichs
66SD4214	6/1/66	Attitude Equations for the Applications Technology Satellite	Hinrichs
ATS Systems Memo No. 91	6/7/66	General Capability Requirements for the ATS Mathematical Model	Clayton, Foulke
66SD4214	7/15/66	Abridged Attitude Equations for the Applications Technology Satellite	Hinrichs
66SD4214	9/15/66	Errors in Attitude Equations of the ATS Satellite	Hinrichs
PIR 41MI-321	11/28/66	Corrections to NASA/Goddard's Mathematical Model	Foulke
66SD4569	12/22/66	Mathematical Model User's Manual	Foulke, Holthenrichs
PIR 41MI-396	–	Corrections to NASA/Goddard's Mathematical Model	Foulke
ATS Systems Memo No. 111	3/6/67	Analytical Justification of ATS Math Model Assumptions	Clayton
66SD4567	3/15/67	Geomagnetic Field Simulation for the ATS	Evans, Foulke
PIR 4T22-017	3/15/67	"Excess" Kinetic Energy of a Rigid Body	Hinrichs
PIR 41M9-003	3/16/67	Corrections to NASA/Goddard's Mathematical Model	Foulke
PIR 4T22-020	3/21/67	Incorporating Initial Curvature of Rods into ATS Mathematical Model	Hinrichs
PIR 41M9-007	5/17/67	Revision of NASA/Goddard's Mathematical Model	Foulke
PIR 41M9-008	5/17/67	Simulation of High Eccentricity Orbits in the Mathematical Model	Foulke

Document No.	Date	Title	Author(s)
PIR 41M9-015	7/6/67	"Excess" Potential Energy of a Rigid Body	Foulke
PIR 41M9-018	7/31/67	Revision of Mathematical Model to Include Variable Torque Hystaresis Damper	Holthanrichs, Foulke
PIR 41M5-083	12/8/67	Corrections to ATS Math Model Program	Evans
PIR 41M5-086	12/21/67	Vehicle Performance Comparison Using Different Models for the Main Boom	Evans
PIR 41M9-037	1/11/68	Computer Runs to Check Out Mathematical Model at NASA/GSFC	Foulke
PIR 1JM1-641	5/23/68	Euler's Dynamical Equations	Foulke

6.2 BOOM DYNAMICS

The primary objective of the ATS Mathematical Model is the simulation of spacecraft central body attitude performance. Both large and small angle performance simulation is a basic requirement. The total ATS gravity gradient configuration, including the fully deployed boom system, tends to take on many of the characteristics of a large, flexible body. For practical reasons, the simulation of rod dynamics was excluded from the Math Model development; this was due, primarily, to limitations on IBM 7094 computer capacity. The ATS Mathematical Model, then, is essentially a rigid body approximation to a large flexible body configuration. For the rod lengths utilized on ATS, however, this approximation is considered a valid one and the errors introduced by the approximation are assumed as small, if not smaller, than errors due to other uncertainties. To substantiate this assumption (as well as develop the capability for simulating separately the anticipated dynamic response of the rods to scissoring maneuvers, boom retraction and extension, thermal "twang" and thruster inversion),a separate boom dynamics simulation program was developed. The completed program allows the substantiation of Math Model assumptions in addition to a validation of the structural integrity of the deployed boom system when subjected to the range of dynamic forcing functions expected in the course of ATS gravity gradient experimentation.

Document No.	Date	Title	Author (s)
PIR 9731-163	9/29/64	Response of GG Rods to Impulsive Load	Josloff
PIR 9732-149	10/13/64	Dynamic Response of Booms	Roach
PIR 9732-148	10/13/64	Boom Damping Studies	Freelin
PIR 4145e-049	2/22/65	Investigation of Effect of GG Rod Retraction Rate on Structural Integrity of ATS Primary Booms	Josloff
PIR 4145d-143	6/14/65	Coupling of Structural Flexibility with a Control System Feeback Loop	Roach
PIR 4145-223 Revision A	10/21/65 11/29/65	Motion of Rod End Mass Relative to Center Body Rotation	Roach
PIR 4145d-371	5/9/66	Gravity Gradient Rod Retraction	Kazares
PIR 4145d-343 Revision A	4/27/66 7/27/66	Equations of Motion for a Flexible Body in Space	Roach
PIR 4TK2-55	11/14/66	Stopping Load on the deHavilland Boom (SAGGE 8 lb Mass)	Josloff
PIR 4T45-23	11/28/66	ATS Attitude and Boom Dynamics	Kazares
PIR 4T73-42	3/7/67	Structural Integrity of Primary Booms During Retraction Sequences	Josloff
67SD4292, Section 2.4	5/20/67	Boom Dynamics Investigations	Roach
PIR 4T75-24	6/27/67	ATS-2 Booms Dynamics in Elliptical Orbit	Roach, Kazares
PIR 4T75-30	10/2/67	Comments Regarding the Thermo-Structural Dynamic Response of Thin Rods	Freelin
Trip Report	2/28/68	Possibility of Thermally Driven Oscillation of ATS-D Booms	Freelin
PIR 4T75-42	2/29/68	Period of Fundamental Cantilever Frequency for Beam with End Mass	Gaitens, Freelin

Document No.	Date	Title	Author(s)
PIR 41M1-589	3/7/68	Damping Rod Oscillations of ATS-D by Magnetic Dampers	Foulke
PIR 1K75-001	3/13/68	Preliminary Estimate of Required Damping for ATS-D Rods	Freelin
PIR 1K75-002	3/18/68	Vibration Analysis of ATS-D Spacecraft	Gaitens
PIR 1K74-026	5/2/68	Temperature Distributions Across Gravity Gradient Rods Under a Specialized Transient Condition	Florio
PIR 1K75-014	6/25/68	Mode Shapes and Frequencies of NRL Spacecraft	Gaitens
PIR 1K75-016	7/22/68	Natural Frequencies and Mode Shapes of ATS-D Spacecraft	Gaitens
PIR 1K75-017	8/7/68	Natural Frequencies and Mode Shapes of DODGE Spacecraft	Gaitens
PIR 1JM1-675	8/7/68	Effect of Thermal Flutter of the Damper Boom on ATS-D	Foulke
69SD4215	10/25/68	Gravity Gradient Rod Thermal Flutter Study Report	Moyer
PIR 1450-001	1/10/69	The Feasibility of Simulating the Possible Thermal Flutter Effects on ATS-E Attitude Performance	Moyer
PIR 1450-004	2/12/69	Report on Thermal Flutter Investigations	Freelin
PIR 1450-001	2/27/69	Results of Simulated "Thermal Flutter " on the ATS-E Spacecraft	Schaffer
PIR 1450-005	3/3/69	Conclusions Regarding Thermal Flutter Effects on the ATS-E Spacecraft	Moyer
PIR 1K33-116	4/10/69	Results of Structural Tests on GE Interdigitated 1/2 inch Diameter deHavilland Damper Boom	Josloff
PIR 1450-006	5/16/69	Review at APL of Latest DODGE Tumble	Moyer

6.3 BOOM THERMAL BENDING

The biggest uncertainty in the development of the ATS Mathematical Model was the pheno-
menon of boom thermal bending. Since thermal bending is one of the more significant
sources of disturbance in gravity stabilized systems (especially at synchronous altitudes),

a substantial effort, including both analysis and test, was undertaken in an attempt to reduce the uncertainties to a minimum. Thermal bending produces a simultaneous shift in spacecraft center of pressure, center of mass and moment of inertia distribution. These effects, in turn, introduce solar pressure torque disturbances and a shift in the preferred orientation to the gravity gradient field. Since center of mass "wander" is a consequence, disturbances are introduced by stationkeeping thrusters which by design intent are required to thrust through the spacecraft center of mass. The equations for thermal bending were established in a semiempirical form so that data derived from orbit could be utilized to improve on the modeling when possible. Out-of-plane (relative to the plane containing the boom centerline and sun vector) effects were included in the model after system studies established the significance of these components.

Document No.	Date	Title	Author(s)
PIR 9750-009	8/2/64	A Proposed Mathematical Model for the Thermal Bending of Gravity Gradient Rods	Hinrichs
PIR 9732-142	8/3/64	Gravity Gradient Rod-Thermal Deflection Analysis	Berkowitz
PIR 9732-147	10/13/64	Thermal Rod Bending	Freelin
PIR 9732-150	10/14/64	Thermal Deflection of an 8-foot long, 1/2-inch BeCu Rod	Freelin
PIR 4142-355	11/12/64	Thermal Gradient Testing for Gravity Gradient Rods	Florio
PIR 4145d-005	12/4/64	Remarks and Questions about the Recent Thermal Tests of Gravity Gradient Rods	Freelin
PIR 4142-386	12/30/64	Thermal Testing of Gravity Gradient Rods	Florio
PIR 4145d-032	1/25/65	Requirements for Thermal Bending Tests of Gravity Gradient Rods	Freelin
PIR 4174-002	1/26/65	The Effects of Thermal Bending of the Gravity Gradient Rods on SAGGE	Siegel
PIR 4326-510	4/2/65	Rod Thermal Bending Test	Cooper
PIR 4142-476	4/10/65	Temperature Gradients in Silver Plated Gravity Gradient Rods	Florio

Document No.	Date	Title	Author(s)
PIR 4326-510	4/14/65	Requirements for Thermal Bending Tests of Gravity Gradient Rods	Florio
PIR 4142-486	4/15/65	Evaluation of Incident Solar Flux During Penumbra	Florio
PIR 4374-033	6/1/65	Thermal Bending Test--Gravity Gradient Rods	Boebel
PIR 4375-036	6/1/65	Temperature Distribution of GG Rod with Line Heat Source	Bretts
PIR 4375-043	6/11/65	Temperature Distribution in BeCu GG Rods	Bretts
PIR 4145d-142	6/11/65	Planning for Structural Thermal Bending Tests	Freelin
PIR 4145d-165	7/21/65	Status of Thermal Bending of Gravity Gradient Rod Studies	Freelin
TIS 65SD294	8/6/65	An Analytical Representation of Temperature Distribution in Gravity Gradient Rods	Florio, Jasper
PIR 4142-578	8/17/65	Temperature Distributions in Gravity Gradient Rods	Florio
Memo No. 4732-18	11/2/65	Thermal Bending Test Equipment	Bretts
Memo No. 4732-19	11/2/65	Gravity Gradient Thermal Deflection Tests	Mazur
PIR 4730-169	11/9/65	Thermal Bending Tests of ATS Rods	Oxenreider
PIR 4141-10	11/17/65	Plan for Tests in the NASA/Goddard Vacuum-Solar Simulation Facility to Measure Temperature Distributions and Deflections of Gravity Gradient Rods	Hieser
Trip Report, Nasa/GSFC	11/19/65	Discussion with H. P. Frisch Regarding His Work on the Bending of Gravity Gradient Rods	Freelin
PIR 4145d-304	2/3/66	Least Squares - Best Fit for Gravity Gradient Rod Temperature Distribution Equations	Kazares
PIR 4145d-305	2/3/66	DSCS Program for Solution of the Least Squares - Best Fit Matrix for Gravity Gradient Rod Temperature Distribution Equations	Kazares

Document No.	Date	Title	Author(s)
PIR 4145d-306	2/4/66	DSCS Program for Solution of Gravity Gradient Rod Temperature Distribution Equations	Kazares
PIR 8156-1912	2/17/66	Control Rod Thermocouple Installation	Hill
PIR 4141-01	2/21/66	Thermocouple Calibrations - ATS Stainless Steel Rod	Hobbs
PIR 4145d-332	3/16/66	Thermal Bending of a Beam of Overlapped Tubular Cross Section	Freelin
PIR 4142-805	3/23/66	Temperature Gradients in Gravity Gradient Rods	Florio
PIR 4145d-337	3/24/66	Comparison of Curvatures in deHavilland Type Rods Produced by Temperature Distributions as Predicted by GE and GSFC Analyses	Kazares, Freelin
PIR 4145d-338	3/28/66	The Effect of Including Section Warping on the Bending Predicted by Gravity Gradient Rod Thermal Bending Analysis	Kazares, Freelin
PIR 4145d-345	4/1/66	Reevaluation of Gravity Gradient Rod Thermal Test	Freelin, Kazares
PIR 4142-823	4/15/66	Predicted Temperature Distributions for Rod Samples to be Used in the Gravity Gradient Rod Bending Tests	Florio
PIR 4145d-361	4/27/66	Predicted Deflections for BeCu Overlapped Rod and Stainless Steel Control Rod	Kazares
Trip Report, NASA/GSFC	5/66	Trip to NASA/Goddard to Perform Gravity Gradient Rod Thermal Bending Tests	Hieser, Kelley
Tech. Rpt. F-B2370-1 (Franklin Inst.)	5/66	Gravity Gradient Rod Stiffness Matrix	Berkowitz
PIR 4T42-004	6/1/66	Temperature Distributions for Gravity Gradient Rods	Florio

Document No.	Date	Title	Author(s)
Exp. Tech. Data Rpt. 2-66	9/20/66	Experimental Verification Studies of Thermal Bending Theory for deHavilland Type Gravity Gradient Rods	Hobbs, Hieser
PIR 4T74-016	12/23/66	Users Manual for Gravity Gradient Rod Temperature Distribution Program	Florio, Carpitella
67SD4239	3/3/67	Thermal Bending of deHavilland Type Rods	Freelin

6.4 SYSTEM REQUIREMENTS AND ANALYSIS, TVCS

The gravity gradient television system was designed, primarily, to provide an opportunity for viewing orbital performance of the gravity gradient boom system. Data on boom thermal bending and boom dynamics was desired for confirmation and/or modification of boom system analytical models discussed in Sections 6.2 and 6.3. Activities summarized in the following references were aimed at ensuring compatibility between TVCS hardware characteristics and required data on boom bending.

Document No.	Date	Title	Author(s)
Tech Memo 9744-64-006	8/28/64	Resolution and Accuracy of TV Camera System for ATS	Woestman
PIR 9744-059	9/28/64	Limitations of TVCS	Woestman
PIR 4176-001	10/22/64	TV Camera Subsystem Scan Rate	Woestman
PIR 4127-002	11/3/64	Summary Data Reduction Methods ATS TVCS Sensor Slow Scan	Hewton
PIR 4176-004	11/3/64	Slow Scan Version of TVCS	Woestman
Sys. Memo No. 017	11/4/64	System Requirements for TV	Clayton
PIR 4176-053	12/4/64	Performance of TV Camera Subsystem	Woestman
PIR 4176-108	1/8/65	Available Readout Accuracy of TV Camera Subsystem	Woestman
Sys. Memo No. 027	1/28/65	TV Camera Subsystem and Boom Tip Targets	Clemson

Document No.	Date	Title	Author(s)
Sys. Memo No. 031	2/12/65	TV Data Resolution Requirements	Clayton
PIR 4126-012	2/16/65	TV Data Reduction Equipment Justification	Schmitt
PIR 4126-024	3/3/65	Measurement Techniques Test for ATS TV Data	Schaller, Hallett, Schmitt
PIR 4176-198	—	Measurement of Angular Displacement of Boom Targets	Woestman
Tech. Memo No. 65-2 (ISO)	3/17/65	TV Sensor Analysis	Wilson
PIR 4176-286	4/22/65	Apparent Brightness of Earth Features Seen from Space	Woestman
PIR 4760-029	4/27/65	Technical Requirements for TV Camera Subsystem for ATS	Charp
PIR 4145d-117	4/29/65	Accuracy of Measurement of Boom End Position	Roach
Sys. Memo No. 044	5/11/65	Review of ATS System TV Data Requirements	Clayton
Sys. Memo No. 050	6/16/65	Justification for TVCS System Requirements	Clayton
PIR 4176-559	11/5/65	TV Camera Subsystem Field of View Orientation	Woestman
PIR 4390-020	12/6/65	Investigation of ATS-TVCS Camera Requirements	Zaputowycz
PIR 4176-620	12/10/65	TVCS Parameters to be Defined and Their Effects on Accuracy of Boom Displacement Analysis	Woestman
—	1/11/66	Status Report - TVCS-ATS	Clemson
PIR 4A23-044	1/24/66	TVCS-Derived Data for Flight Analysis/Evaluation	Horn
Sys. Memo No. 070	2/3/66	Revised System Requirements for TVCS	Clayton
PIR 4176-691	2/17/66	Sensitivity of TVCS to Earth Albedo	Woestman
Sys. Memo No. 082	4/12/66	TV Camera Component Axes	Frey, Clayton

Document No.	Date	Title	Author(s)
PIR 41M2-037, Revision A	8/31/66 10/7/66	TVCS Sun Shutter Operation	Kitinoja
PIR 41M2-065	10/13/66	Detecting Position of ATS Boom Target	Malizia
PIR 4411-024, Revision A	1/31/67	Equations for Determining Boom Deflections from ATS Camera Measurements	Martin
TWX to ATSOCC	4/17/67	Inadequacies in TV Film Data Supplied GE	Clayton
PIR 41M2-170	5/10/67	Method to Improve Quality of ATS-A TVCS Photographs	Kitinoja
PIR 41M2-212	7/13/67	Flight ATS-D TVCS Thermal Configuration	Kitinoja
PIR 1JM7-070	8/27/68	TVCS Sun Shutter Operation on ATS-E	Kitinoja

6.5 ATTITUDE SENSOR REQUIREMENTS AND ANALYSIS

One of the primary objectives of the ATS gravity gradient mission is verification of the
ATS Mathematical Model. The accomplishment of this objective requires a comparison of
flight data with Math Model performance predictions. To achieve this end with any degree
of sophistication, a spacecraft attitude sensing system is required with a total accuracy
commensurate with the verification requirements. The first task, therefore, in the definition
of the ATS attitude sensing system was the selection of an array of attitude sensors which
would satisfy the requirements of accurate 3-axis attitude determination without introducing
unproven sensors with excessive development costs.

A variety of sensors were considered including use of the gravity gradient television cameras,
two different earth IR sensors, an RF sensor, an earth albedo sensor, the solar aspect
sensor and utilization of antenna polarization measurements. Analyses of all sensors, taken
two at a time and finally three at a time, were conducted to establish sensor system accu-
racies as a function of the various parameters affecting accuracy. Final recommendations
were made and accepted with the resultant system currently in use on ATS. Analysis of
the selected system was then centered on a final assessment of measurement errors and

development of mathematical models of the individual sensors for use in the GE Attitude Determination Program and Quick-Look Attitude Program.

Document No.	Date	Title	Author (s)
Tech Memo 9744-64-008	8/31/64	Determination of ATS Vehicle Pitch, Roll and Yaw Angles from Solar Aspect Sensor Information	Schott
4143-FDDM-007	11/3/64	Satellite Attitude Determination via On-Board Earth Detector and Radio Sensor Information	Levinson
Tech Memo 4176-001	11/20/64	Analysis of the ADCOLE Sun Sensor	Schott
FDDM-007	11/24/64	Satellite Attitude Determination via On-Board Radio Sensor Measurements, Two Ground Transmitter Stations	Levinson
Tech Memo 4176-004	12/23/64	The Influence of Earthshine on ATS Sun Sensor Operation	Schott
PIR 4123-008	3/16/65	ATS Vehicle Attitude Sensor Selection	Hallett, Horn
Tech Memo No. 65-2 (ISO)	3/17/65	TV Sensor Analysis	Wilson
4143-FDDM-010	3/22/65	Satellite Attitude Determination via On-Board RF Measurements and Radar POLANG Measurements	Levinson
Interim Report (ISO)	3/26/65	TV Attitude Sensor Analysis	Wilson
Tech Rpt. No. 65-3 (ISO)	3/26/65	The Effect of Errors in Estimating Orbital Elements on the Determination of Attitude	McCabe
4143-FDDM-011	4/6/65	Satellite Attitude Determination via On-Board Earth IR Sensor Measurements and Ground-Based Polarization Angle Measurements	Levinson
Letter Report (ISO)	4/19/65	Utilization of Visual Data from the Ground Station Monitor for Real-time On-site Estimates of Spacecraft Attitude and Rate	Wilson

Document No.	Date	Title	Author(s)
4143-FDDM-012	4/23/65	Solar Aspect Sensor: Sun-Line Orientation; Detector Error Coefficients	Levinson
4143-FDDM-013	5/13/65	Satellite Attitude Determination via Earth Albedo Sensor and Solar Aspect Sensor Measurements	Levinson
Tech Memo No. 65-5 (ISO)	5/21/65	A Convenient Method to Determine Attitude Given Solar Aspect Sensor Measurements and Ground-Based Polarization Angle Measurements	McCabe
4143-FDDM-014	6/7/65	Satellite Attitude Determination via On-Board Earth IR and Solar Aspect Measurements	Levinson
4143-FDDM-015	6/21/65	Pitch Determination During Inversion Maneuver via Solar Aspect Sensor Measurements	Levinson
4143-FDDM-016	7/28/65	Satellite Attitude Determination via Radar Polarization Angle and Solar Aspect Sensor Measurements	Levinson
Sys Memo No. 057	7/30/65	Reliable Earth Sensor	Frey
4143-FDDM-017	8/13/65	Triple Line of Sight Techniques for Attitude Determination	Levinson
PIR 4424-056	11/22/65	Remarks on Calculation of Rates and Faraday Rotation	Green
Trip Report	12/15/65	ATD IR Sensor Design Review	Frey, Horn
PIR 4424-065	2/3/66	Basic Equations for ATS New Earth Sensor	Martin
PIR 4424-066	2/7/66	Sensitivity Coefficients Using Adcole Sun Sensor Counts	Martin
Sys Memo No. 075	2/11/66	World Map Attitude Errors	Clayton
Sys Memo No. 078	3/4/66	SAS Compound Angle Measurements	Clayton
PIR 5540-23	3/8/66	Faraday Rotation	Green

Document No.	Date	Title	Author(s)
PIR 5540-24	3/17/66	Remarks on the Brouwer Orbit Model	Green
PIR 5540-26	4/4/66	A Brief Error Analysis of the Brouwer Orbit Model	Green
PIR 4730-218	4/13/66	IR Earth Sensor Data Reduction	Frey
PIR 4424-077	5/20/66	Orbit Position Error Study for ATS	Martin
PIR 4411-007	8/19/66	ATS Sun Sensors: Measurement Errors and Weights	Martin
PIR 4411-008	9/6/66	Equations for ATS IR Earth Sensor Data Processing	Martin
PIR 4411-009	9/14/66	ATS Attitude Determination with Two Reference Vectors	Martin
Sys Memo No. 103	11/30/66	Record of Telecon with A. Sabelhaus, 23 November 1966	Clayton
PIR 4A23-103	12/21/66	Analysis of GGTS Solar Aspect Sensor Anomaly	Kraus
PIR 4411-018	12/21/66	Analysis of Calibration Data for Two ATS IR Earth Sensors	Martin
TIS 67SD207	1/16/67	Geophysical Ephemeris Calculations on the GE-DSCS at MSD	Green, Davis
Sys Memo No. 109	3/6/67	Quick-Look POLANG Corrections	Clayton
PIR 4T23-034	5/12/67	North-South Station Keeping Considerations of Synchronous Equatorial Orbits	Laudermilch
PIR 4T53-128	12/26/67	POLANG and Faraday Rotation	Mielke
PIR 1K05-009	9/11/68	Recent Attempts to Determine Attitude of ATS-2 Satellite	Martin

6.6 ATS ATTITUDE DETERMINATION PROGRAM

The ATS Attitude Determination Program is a generic title used to reference a group of
large scale digital computer programs developed for ATS attitude computations and used
for smoothing preliminary processing of "raw" PCM telemetry data; merger with data
relative to spacecraft antenna polarization; reduction and computation of statistical para-
meters associated with diagnostic data; reduction and processing of data extracted from

filmed television pictures; production of data lists for selected gravity gradient telemetry functions; production of summary data reports; and finally, the production of attitude and raw data plots.

Document No.	Date	Title	Author (s)
PIR 4126-011	2/15/65	Required Inputs for ATS Software Design and Development	Schmitt, Schaller
–	5/7/65	Preliminary Remarks on the ATS Attitude Determination Program	Green
Tech Rpt No. 65-12 (ISO)	6/24/65	Techniques and Philosophy of Data Smoothing for ATS	Collins, Frangione, McCabe
PIR 4424-035	6/29/65	Investigation of Data Processing Techniques for ATS Attitude Determination	Martin
–	7/9/65	ATS Data Processing System Preliminary Design Specification	Schmitt
PIR 4424-037	7/13/65	Computer Modules for ATS Attitude Determination	Martin
PIR 4424-039	8/18/65	Specifications for ATS Attitude Determination Investigation Program (ADIP)	Martin
PIR 4424-051	10/8/65	A Note on the ATS Attitude Determination Program Requirements	Green
PIR 4424-055	11/1/65	Attitude Determination During a Pitch Maneuver	Green
PIR 4424-061	12/20/65	Sensitivity Coefficients and Estimates of ATS Attitude Angles	Martin
PIR 4424-068	2/10/66	Proposed Printed Output for ATS Attitude Determination Program	Martin
PIR 4A26-037	3/31/66	ATS-A Data Reduction and Computer Programs Specifications	Schmitt
SVS-7429	4/27/66	ATS Data Format Specification	Schmitt
PIR 4424-076	5/3/66	ADIP-III, Fundamental Equations and General Description of the Computer Program	Martin

Document No.	Date	Title	Author(s)
PIR 4A26-061	6/9/66	ADIP-III, Computer Program Writeup (7094)	Paparella
PIR 4411-003	7/8/66	ADIP-III, Influence of the Weights on the Calculated Attitude Angles	Martin
PIR 4A26-096	10/10/66	ATS Data Reduction Computer Software System Description	Shebby, Kohler
SVS-7429 Revision A	11/17/66	ATS Data Formats Specifications	Schmitt
PIR 4411-015	12/18/66	ATS Data Analysis Module (DAM) Fundamental Equations and General Description of the Computer Program	Martin
PIR 4B80-011	2/20/67	Final Format of POLANG Tape	Shebby
SVS-7429, Revision B	3/15/67	ATS Data Formats Specification	Schmitt, Clayton
PIR 4TAO-001 Revision A	3/20/67	Recent Modifications to the ATS Data Analysis Module (DAM)	Martin
67SD4322	6/30/67	ATS-A Data Processing System, Vol I	Kohler, Shebby, Candor, McCully, Schmitt
67SD4395	11/15/67	ATS-A Data Processing System, Vol II	
67SD4345	12/1/67	ATS-A Data Processing System, Vol III	
SVS-7556	6/14/68	ATS-D Data System Interfaces	Montgomery
PIR 1K05-005	7/1/68	Equations for Processing IR Earth Sensor Data in DAM2 Program	Martin
PIR 1K05-006	7/24/68	ATS-D Data Analysis Module (DAM2) Equations and Basic Logic	Martin
PIR 1P32-112	9/12/68	ATS-D Long Term Data System, General Description of	Montgomery
SVS-7723	July 1969	ATS-E Data System Interfaces	Bielefeld

6.7 DATA SYSTEM CHECKOUT

To ensure a state of operational readiness for first data following launch of ATS-A, a plan was generated for checkout of the prime modules of the Attitude Determination Program using simulated attitude performance generated by the ATS Math Model. This required the development of a Data Simulation Program which accepted, as input, an attitude tape produced by the Math Model and provided, as output, a simulated GE-POLANG and RTDT in accordance with tape formats specified in SVS-7429. These two tapes simulated operational tapes to be received by GE from NASA/GSFC. The diagnostics were added as a separate input to the Data Simulation Program and provided a range which included anticipated excursions of all diagnostics. The resultant output, when processed through the Attitude Determination Program, was compared with original Math Model outputs and diagnostic inputs for confirmation of proper programs operation.

Document No.	Date	Title	Author(s)
PIR 4424-040	8/20/65	ATS Simulation Program	Green
PIR 4126-087	9/1/65	ATS Simulation Program	Vischak
PIR 4126-128	11/29/65	Modification to ATS Data Simulation Program	Schmitt
PIR 4174-057	4/25/66	Output Conversion Equations for ATS Digital Simulation	Hinrichs
PIR 4A26-112	11/23/66	Modification II to ATS Data Simulation Program	Schmitt
PIR 4A23-106	12/16/66	ATS Data System Checkout Phase I Schedule	Horn
–	12/18/66	ATS Data System Checkout Plan	Horn
PIR 4A23-108	12/19/66	Data System Checkout, Simulation Orbit Definition – Phase I	Horn
PIR 4A23-120	–	Data System Checkout, Simulation Orbit Definition – Phase II	Horn
PIR 4B80-014	3/14/67	ATS Simulation Program	Richter
PIR 4BD2-024	5/19/67	Data System Checkout Report	Schmitt

6.8 QUICK-LOOK DATA SYSTEM

The ATS Quick-Look Data System was developed to provide a near-to-real-time data link between GE/VFSTC and the ATS ground stations at Rosman, North Carolina; Mojave, California; Toowoomba, Australia; and Kashima, Japan. The system utilizes the existing NASCOM teletype communications network and interfaces with the GE Desk Side Computer Service (DSCS) at GE/Penn Park.

Document No.	Date	Title	Author(s)
Memo No. 4732-67	2/14/66	Quick-Look Data System Proposal	Clayton
PIR 5540-38	8/18/66	GGTS Quick-Look Attitude Determination Program	Green, Royer
Sys. Memo No. 100	11/16/66	ATS Quick-Look Data System	Clayton
Sys. Memo No. 103	11/30/66	Record of Telecon with A. Sabelhaus 11/23/66 (Re:ATS Quick-Look System)	Clayton
Sys. Memo No. 104	12/2/66	ATS Quick-Look System Installation	Clayton
PIR 5540-45	1/11/67	Progress Report on the ATS Quick-Look Math Model Program	Powell, Green
Sys. Memo No. 109	3/6/67	Quick Look POLANG Corrections	Clayton
PIR 5540-48	3/20/67	DSCS Quick-Look Math Model	Green
PIR 5540-70	1/8/68	A Package of DSCS Programs that May Be Used for ATS Type Calculations	Green
68SD4219	2/19/68	ATS-2 Quick Look System Computer Programs	Kraus
69SD4376	12/31/69	ATS-5 Quick-Look System	Latona

6.9 ATS GRAVITY GRADIENT ORBIT TEST AND FLIGHT EVALUATION

At program inception, mission guidelines were defined in only the most general of terms. Beginning in July 1964, a continuing effort was inaugurated to definitize the specific objectives and philosophy of the ATS gravity gradient mission, as well as formalize plans for the accomplishment of the mission. This included generation of data requirements and data

processing and analysis requirements and culminated in a five-volume ATS-A Orbit Test Plan which encompassed post-launch flight analysis and gravity gradient experiment plans, specifics of the mission and orbit test philosophy and objectives, a gravity gradient experiment operational contingency plan, a description of system capabilities, and a collection of operational aids referred to separately as the Orbit Test Handbook. The Orbit Test Plan and Orbit Test Handbook were then updated prior to the subsequent flights of ATS-D and ATS-E. Flight Reports were prepared after each flight.

Document No.	Date	Title	Author(s)
Sys. Memo No. 003	7/22/64	Preliminary ATS Orbit Test Plan	Clayton
PIR 9733-30	10/8/64	Shadow History Studies – Gravity Gradient System Experiment for ATS	Weinstein
Sys. Memo No. 040	4/22/65	Trip Report, ATS Trajectory Meeting at Lewis Research Center, 21 April 1965	Clayton
Sys. Memo No. 041	4/23/65	Launch Constraints Associated with Achieving an Initial Period of Continuous Sunlight	Clayton
–	7/9/65	ATS Preliminary Flight Evaluation Plan	Horn
Sys. Memo No. 056	7/22/65	Results of NASA/GE Working Session on Data Processing and Flight Evaluation Plans	Clayton
Sys. Memo No. 061	8/27/65	Action Items Established at 19 July Data Processing Meeting at NASA/GSFC	Clayton
Sys. Memo No. 066	11/4/65	NASA Response to GE's Request for non-GE Telemetry Data	Clayton
PIR 4123-032	12/10/65	ATS/A Long Term Data Quantity Estimates	Horn
PIR 4123-035	12/13/65	Weekly Scan of Telemetry Data	Horn
Sys. Memo No. 068	12/30/65	ATS Gravity Gradient Orbit Test Philosophy	Clayton
PIR 4A23-040	1/17/66	Proposed ATS/A ADP Input Data Survey	Horn
PIR 4A23- 041	1/18/66	Preliminary ATS-A Orbit Test Plan "Test Packages"	Kait

Document No.	Date	Title	Author(s)
PIR 4A23-042	1/24/66	Proposed ATS/A Input Data Survey	Horn
PIR 4A23-043	1/24/66	Detailed Data Format Capability	Horn
PIR 4A23-044	1/24/66	TVCS-Derived Data for Flight Analysis/Evaluation	Horn
PIR 4A23-047	2/15/66	ADP/Flight Analysis Requirements – Data Analysis Module	Horn
PIR 4E10-012	2/28/66	Flight Malfunction Analysis/Corrective Action Plan (Preliminary)	DeSantis, Sturgeon
Sys. Memo No. 081	4/8/66	NASA/GE Working Session on Operations Interfaces	Clayton
Sys. Memo No. 084	4/20/66	Trip Report – NASA/GE Working Session on Operations Interfaces, 15 April 1966	Clayton
PIR 4A23-060	5/2/66	Orbital Data Program	Horn
PIR 4E10-025	5/13/66	Flight Malfunction Analysis/ Corrective Action Plan	Sturgeon, DeSantis
Sys. Memo No. 089	5/16/66	Notes on ADP Working Session at GE, 6 May 1966	Clayton
PIR 4341-001	5/26/66	ATS Gravity Gradient Orbit Test Sequencing Method	Zanetti
Sys. Memo No. 093	6/16/66	Earth Constants	Clayton
Sys. Memo No. 095	7/15/66	GSFC Orbital Operations Plan Interfaces	Clayton
66SD4525	11/15/66	Telemetry Calibration Book (Nominal Data)	Hill, Horn
Sys. Memo No. 101	11/23/66	GE/NASA Data System Interface Meeting	Clayton
Sys. Memo No. 102	11/30/66	ATS Ground Station GG Command Interlocks	Clayton
PIR 4A23-101	12/6/66	Primary Boom Length Telemetry Accuracy Estimates	Kraus
Sys. Memo No. 105	12/12/66	GE Responsibility in Flight Evaluation of the ATS Earth Sensors	Clayton

Document No.	Date	Title	Author(s)
Sys. Memo No. 106	12/19/66	Record of Telecon with A. Sabelhaus and G. Banks NASA/GSFC, 12 December 1966 (Re: Earth Sensors, Cal Data, SAS, Inversion Thrusters)	Horn
67SD4232	2/12/67	Orbit Test Plan, Volume II Recommended ATS-A Orbit Operational Procedures	Kraus, Horn
Sys. Memo No. 107	2/17/67	ATS-A Experimenters Meeting, Trip Report	Clayton
Sys. Memo No. 108	2/22/67	STADAN Data Coverage, ATS	Clayton
67SD4244	3/6/67	Orbit Test Plan, Volume III ATS-A Flight Evaluation Plan	Horn
Sys. Memo No. 110	3/6/67	Record of Telecon with A. Sabelhaus, 3/3/67 (Re: Data System Interfaces)	Clayton
Sys. Memo No. 112	3/9/67	Comments on NASA Plans for ATS-A Launch Sequence	Clayton
67SD4254	3/15/67	Orbit Test Plan, Volume V, Appendix B, ATS-A Orbit Test Handbook	Kraus, Horn
Sys. Memo No 114	3/22/67	Comments on ATS-A Launch Rehearsal Conducted 21 March 1967	Clayton
67SD4305	3/27/67	Orbit Test Plan, Volume I, Test Philosophy and Objectives	Clayton
67SD4276	4/10/67	Four-Day Flight Report for the ATS Gravity Gradient Stability System	Horn, Kraus
67SD4264	5/22/67	Orbit Test Plan, Volume V, Appendix A, ATS Supplementary Material	Horn
Sys. Memo No. 115	6/12/67	Trip Report: ATS-2 Boom Scissor and Damper Clutch Operations	Clayton
Sys. Memo No. 117	7/21/67	ATS-2 Flight Analysis Termination	Clayton
Sys. Memo No. 119	7/31/67	Preliminary Info on ATS-D Ion Engine	Clayton
Sys. Memo No. 122	9/7/67	Teleon with M. Geller (ATSOCC) Re: Recent GG Tests on ATS-2	Clayton

Document No.	Date	Title	Author(s)
68SD4276	12/29/67	ATS-2 Final Flight Report for the Applications Technology Satellite	Horn, Kraus, Mielke
68SD4282	6/14/68	ATS-D Gravity Gradient Orbit Test Plan	Kraus, Mielke
68SD4287	7/1/68	ATS-D Gravity Gradient Orbit Test Handbook	Kraus, Mielke, Wallace
68SD4321	9/15/68	Interim Flight Report for the Applications Technology Satellite (ATS-D)	Kraus Mielke
	10/25/68	ATS-4 Flight Summary	Kraus
68SD4364	12/31/68	ATS-4 Final Flight Report for the Applications Technology Satellite Gravity Gradient Stabilization System	Kraus
68SD4283	5/19/69	ATS-E Gravity Gradient Orbit Test Plan	Kraus
69SD4335	7/3/69	ATS-E Gravity Gradient Orbit Test Handbook	Kraus, Coyne
	8/8/69	ATS-E Calibration Curves for Telemetry Received by GE	Mueller
	10/1/69	Evaluation of ATS-E Mission Recovery through Gravity Gradient Boom Deployment	Clayton, Foulke, Moyer
69SD4377	12/31/69	ATS-5 Final Flight Report for the Applications Technology Satellite Gravity Gradient Stabilization System	Mueller

6.10 SYSTEM DESIGN ANALYSIS

The design of a gravity gradient stabilization system is so intimately associated with the configurational parameters of the total spacecraft that the first and primary area of concern in the design of ATS was an analytical optimization of system parameters governing performance. This required the simultaneous consideration of factors affecting initial capture, transient damping and steady-state performance. Once the basic system parameters were specified, tolerance studies on those parameters were necessitated to provide a framework for the generation of a realistic set of gravity gradient system hardware and spacecraft interface specifications. Once this was accomplished, a final assessment of expected performance was required to allow the specification of a realistic orbit test plan and demonstrate the projected ability to satisfy basic mission objectives. To these ends, an extensive system design analysis activity was initiated at program inception and continued through launch of ATS-E.

6.10.1 INITIAL CAPTURE

Document No.	Date	Title	Author(s)
PIR 9750-025	9/64	Capture of MAGGE	Moyer, Foulke
PIR 4730-059	3/2/65	Capture of MAGGE with 12-Second Time Delay	Foulke
Sys. Memo No. 040	4/22/65	Trip Report, ATS Trajectory Meeting at Lewis Research Center, 21 April 1965	Clayton
PIR 4174-018	6/4/65	Initial Capture of the ATS-A Vehicle	Siegel
Sys. Memo No. 058	8/13/65	ATS Capture Studies	Clayton
PIR 4174-030	10/14/65	Initial Capture of the ATS-A and ATS-D Vehicles	Siegel
Memo 4732-81	3/8/66	Inertia and Rate Restraints for the ATS Spacecraft	Frey

Document No.	Date	Title	Author(s)
PIR 4174-052	3/14/66	Pitch Axis Momentum Limits for ATS-D Capture Maneuver	Siegel
Memo 4732-111	4/13/66	Record of Telecon with G. Banks on 4/12/66	Clayton
Sys. Memo No. 092	6/14/66	Additional Capture Runs, ATS-D	Clayton
PIR 41MI-342	12/16/66	Maximum Allowable Rate for ATS Vehicles	Foulke, Evans
PIR 41MI-366	1/18/67	Capture Runs for ATS-D/E	Foulke, Evans
PIR 41M9-010	5/19/67	Upright Capture of ATS-A	Foulke
PIR 1JMI-657	6/27/68	Two Stage Capture Deployment Sequence	Foulke
PIR 1J72-1015	11/19/69	Summary of ATS-E Capture Studies	Schaffer

6.10.2   INVERSION STUDIES

Document No.	Date	Title	Author(s)
PIR 9750-035	9/18/64	Inversion Maneuver of the MAGGE Configuration	Foulke
Sys. Memo No. 010	9/24/64	ATS Thruster Characteristics	Clayton
PIR 9750-053	10/21/64	Nominal Thrust and Tolerance for MAGGE Inversion Maneuver	Foulke
PIR 4174-012	4/22/65	Inversion of ATS-A with 100-Foot Rods	Foulke
Sys. Memo No. 046	5/17/65	Ground Rules for ATS Inversion Maneuver	Clayton
4143-FDDM-15	6/21/65	Pitch Determination During Inversion Maneuver via Solar Aspect Sensor Measurements	Levinson

Document No.	Date	Title	Author(s)
PIR 4174-041	12/6/65	Comparison of the Effects of 7-inch and 29-inch Inversion Thruster Moment Arms in ATS-D	Siegel
PIR 4174-042	12/15/65	ATS-A Inversion Maneuver Based Upon a Specified Timing Sequence	Siegel
PIR 4174-043	1/6/66	ATS Pitch-Up Maneuver	Siegel
PIR 4174-044	1/21/66	ATS-D Inversion Maneuver Using Thrusters	Siegel
PIR 4174-045	2/3/66	Inversion of ATS-A and ATS-D	Foulke
PIR 4174-053	3/31/66	ATS-A Inversion Using Rod Retraction and Extension	Siegel
PIR 4174-056	4/22/66	ATS-D Inversion Using Rod Retraction and Extension	Siegel
PIR 41MI-378, Revision A	2/9/67	Allowable Leakage Rates on the Inversion Thrusters	Foulke
PIR 1JMI-667	7/19/68	Inversion of ATS-D Using Real Time Data	Foulke

6.10.3 STATIONKEEPING

Document No.	Date	Title	Author(s)
PIR 4174-028	9/28/65	Pulsing Frequency of Station-keeping Thruster for ATS-D	Foulke
PIR 4174-031	10/18/65	Effect of a Stationkeeping Thruster on ATS-D with TM2A Parameters	Siegel
PIR 4174-048	2/15/66	Conversation with L. Grasshoff (Re: change in stationkeeping thruster duty cycle)	Foulke
PIR 4174-047	2/15/66	ATS-D Yaw Attitude Errors Caused by the Stationkeeping Thruster	Evans
PIR 4T23-034	5/12/67	North-South Stationkeeping Considerations of Synchronous Equatorial Orbits	Laudermilch

6.10.4 SYSTEM PERFORMANCE STUDIES

Document No.	Date	Title	(Author(s)
PIR 9750-012	8/11/64	Effect of a Magnetic Dipole on MAGGE	Foulke
PIR 9750-023	9/1/64	Transient Performance of MAGGE	Moyer, Foulke
PIR 9750-024	9/8/64	Effect of a Magnetic Dipole on SAGGE	Foulke
PIR 9750-034	9/18/64	Crab Angles of the MAGGE Configuration	Foulke
PIR 4422-315	11/16/64	ATS Solar Torque	Sellers
PIR 4174-004	2/11/65	ATS Configuration Using GSFC-Specified Parameters	Siegel
PIR 41MI-253	9/27/66	Revision of ATS-D Error Budgets	Evans
PIR 41MI-254	9/27/66	Revision of ATS-A Error Budgets	Evans
PIR 41MI-318	11/14/66	Effect of Hardware Tolerances on ATS-A and D	Foulke
PIR 41MI-342	12/16/66	Maximum Allowable Rate for ATS Vehicles	Foulke
PIR 41MI-349	12/23/66	Second Revision of ATS-D Error Budgets	Evans
PIR 41MI-365	1/17/67	Results of Computer Runs Evaluating Failure Modes	Foulke
PIR 41MI-385 Revision A	2/13/67	Effect of Magnetic Dipole of Tip Masses on ATS-A Performance	Foulke
PIR 41M9-006	5/12/67	Performance of ATS-A in an Orbit with 0.2 Eccentricity	Foulke
PIR 41M9-011	6/1/67	Performance of ATS-E with a Yaw Stabilizing Flywheel	Foulke
PIR 41MI-586	3/6/68	Simulation of DODGE Spacecraft	Foulke
PIR 1JMI-601	4/3/68	Simulation of DODGE-Pass 3	Foulke

Document No.	Date	Title	Author(s)
PIR 4174-002	3/10/65	Response to Internal Disturbance Torques	Evans
Sys. Memo No. 036	3/12/65	Optimization Study Standard Disturbance Parameters	Mazur
65SD4266 Section 2.1.6.1	4/20/65	ATS Optimization Studies	Foulke, Evans, Siegel
PIR 4174-015	5/3/65	Nominal System Parameters for the ATS-A and ATS-D Vehicles	Siegel
PIR 4174-016	5/5/65	Performance Studies of the ATS-D Vehicle	Siegel
Sys. Memo No. 047	6/1/65	ATS Standardized Configuration	Clayton
PIR 4174-019	7/8/65	Solar Pressure Torques due to TV Targets on Rod Tips	Evans
PIR 4174-027	9/3/65	Frequency Response of ATS	Foulke
PIR 4174-029	9/23/65	Attitude Errors Caused by Vehicle Magnetic Dipole Moment	Siegel
PIR 4174-032	10/28/65	Response of ATS to Solitary Impulse	Foulke
PIR 4174-035	11/1/65	Attitude Errors Caused by Solar Pressure on the TV Targets	Evans
PIR 4174-046	2/4/66	Effect of Damper Deployment Squibs on Attitude Performance	Foulke
PIR 4174-051	3/2/66	Primary Body Moments and Products of Inertia Depending on Rod Half Angle	Evans
PIR 4174-055	4/13/66	ATS-A Error Budgets	Evans
PIR 4174-063	5/16/66	Comparison Graphs for Main Rod Half Angle of 11°, 15°, 19°, 25.02° and 31° (ATS-A)	Evans
PIR 41MI-147	6/23/66	ATS-D Error Budgets	Evans
Sys. Memo No. 094	7/11/66	Spacecraft Surface Optical Properties	Clayton
PIR 41MI-191	7/22/66	Comparison Graphs for Main Rod Half Angle of 11°, 15°, 19°, 24.94°, and 31° (ATS-D)	Evans

PIR 1JMI-612	4/11/68	Use of Controlled Dipole as Damping Mechanism (ATS Sample and Hold Technique)	Schaffer
PIR 1JMI-620	4/24/68	ATS Detumble Time Using Magnetic Damping	Schaffer
PIR 1JMI-666	7/18/68	ATS-D Sample and Hold Timing Specifications for Magnetic Torquing	Schaffer

6.10.5   BOOM SYSTEM TOLERANCE STUDIES

Document No.	Date	Title	Author(s)
PIR 4174-001	12/8/64	Yaw Error Caused by Primary Rod Bending for MAGGE	Siegel
PIR 4141-048	4/20/65	ATS Gravity Gradient Rods-Solar Torque-Reflectivity Sensitivity Coefficients	Wilcox
PIR 4174-013	4/22/65	Attitude Errors Caused by Short Primary Gravity Gradient Rods on ATS-D	Siegel
PIR 4174-014	5/3/65	Attitude Errors Caused by Short Primary Gravity Gradient Rods on ATS-A	Siegel
PIR 4141-058	7/22/65	Determination of Sensitivity of Coefficients for Gravity Gradient Rods	Pucher
PIR 4174-023 Revision A	10/29/65	Solar Torques on Rods of Unequal Absorptivity	Foulke
PIR 4174-034	10/29/65	Yaw Error Versus Rod Envelope Radius	Evans
PIR 4174-036	11/1/65	Variations in Damping Time and in Vehicle Yaw Angle Versus Damper Angle	Evans
PIR 4174-037	11/5/65	Variations in Vehicle Attitude Versus Variations in Rod Alignments	Evans

Document No.	Date	Title	Author(s)
PIR 4174-038	11/8/65	Pitch and Roll Attitude Errors Caused by Rod Envelope Criteria	Evans
PIR 4494-028	11/19/65	The Rate of Evaporation of Silver Sulfide from a Silver Surface in Space	Tweedie, Babjak
Sys. Memo No. 079	3/28/66	Variation of Solar Absorptivity with Solar Incidence Angle for Silver-Plated, Be-Cu Boom Samples	Clayton
PIR 4T94-020	6/29/66	Reflectance of Boom Samples	Young
PIR 41M1-162	7/7/66	Rod Error Tradeoff Curves	Evans
PIR 4T94-048	8/23/66	Micrometeorite Tests of BeCu Gravity Gradient Rods	Bretts
Sys. Memo No. 098	10/27/66	Installation of ATS-A Primary Boom Flight Tapes	Clayton
Sys. Memo No. 099	11/14/66	Replacement Tape for Boom No. 226-1	Clayton
PIR 41M1-336	12/12/66	Compensation for Shortened Damper Booms and Increased Stiffness of Damper Spring	Evans
PIR 41M2-122	2/20/67	Effect of Twist on Straightness Profiles of Molybdenum GG Booms of ATS Configuration	Matteo
Sys. Memo No. 120	8/15/67	Installation of ATS-D Primary Boom Flight Tapes	Clayton
PIR 4T73-104	8/25/67	Analytical Study of Boom Deflection and Twist Profiles	Ferguson, Josloff
PIR 41M9-025	9/25/67	Placement of Gravity Gradient Rods on ATS-D	Foulke
PIR 41M5-086	12/21/67	Vehicle Performance Comparisons Using Different Models for the Main Booms	Evans
PIR 1K73-039	8/27/68	Zero-G Tip Deflections for ATS Booms S/N 10 and 103	Ferguson
PIR 1K73-052	10/4/68	Revised Tip Deflections for ATS Booms S/N 10-2 and 103-2	Ferguson

6.10.6 DAMPER SYSTEM STUDIES

Document No.	Date	Title	Author(s)
PIR 9750-033	9/18/64	Evaluation of Magnetic Damper Clearance	Burtoff
Sys. Memo No. 009	9/18/64	Design Criteria for CPD	Rosenberg
Sys. Memo No. 011	10/6/64	Damping Constant for CPD	Rosenberg
Sys. Memo No. 013	10/14/64	"In-Orbit" Damper Boom Tolerances	Rosenberg
PIR 9461-165	10/16/64	Reasons for Limiting Damper Boom Rotation to $\pm$ 45 Degrees	Siegel
PIR 4730-017	11/30/64	Effect of Spring Constant on Damping Performance of MAGGE	Foulke, Moyer
PIR 4730-023	12/18/64	Variation of Damping with Boom Position	Foulke
Sys. Memo No. 038	4/13/65	Eddy Current Damper Design Parameters	Mazur
PIR 4174-020	7/21/65	ATS-A Damper Performance with One Damper Rod Extended	Siegel
PIR 4174-040 Revision A	11/30/65	Effect of Centrifugal Force Acting Upon the Damper Rod Tip Masses	Siegel
PIR 4T45-1	6/8/66	Response of Damper Boom with Soft Stop Removed from the CPD	Freelin
PIR 41M1-126	6/14/66	Soft Stops on CPD	Foulke
PIR 41M2-805	6/16/66	CPD Soft Stop	Buerger

6.10.7 HYSTERESIS DAMPER STUDIES

Document No.	Date	Title	Author(s)
PIR 4174-009	3/25/65	Estimate of the Effect of Hysteresis Saturation Torque on System Transient Response (Amplitude Decrement)	Kait
PIR 4174-010	4/9/65	Simplified Math Model of Hysteresis Damper Characteristics for Preliminary GAPS-III Studies	Kait
Tech. Rpt. No. 65-8 (ISO)	4/20/65	A Theory of Hysteresis Damping in Thin Annular Disks	Collins
Sys. Memo No. 048	6/14/65	System Requirements for Hysteresis Damper	Clayton
PIR 4174-021	8/16/65	Selection of Hysteresis Damper Saturation Torque for the ATS-A and ATS-D Vehicles	Siegel
PIR 4174-022	8/16/65	Improved Performance Hysteresis Damper	Siegel
PIR 4174-033	10/28/65	Hysteresis Curve Fitting	Foulke
PIR 41M1-380	2/9/67	Nominal Hysteresis Contour for the Varying Torque Hysteresis Damper	Foulke
PIR 41M1-387	2/16/67	Passive Hysteresis Damper Null Offset	Foulke
PIR 41M2-169	5/8/67	VTHD Engineering Unit Test Results	Kitinoja
PIR 41M9-017	7/6/67	Simulation of Variable Torque Hysteresis Damper	Foulke
PIR 41M9-020	7/11/67	Results of the Computer Simulation of the ATS-D Variable Torque Hysteresis Damper	Foulke

6.11 SYSTEMS INTEGRATION

The general task of systems integration included the periodic publication of system requirements and analysis task summaries, memos related to general interface problems with GSFC and HAC, system test procedures and participation in interface meetings, design reviews and presentations to management. This activity continued through delivery of the ATS-E hardware.

Document No.	Date	Title	Author(s)
Sys. Memo No. 001	7/10/64	ATS Environmental Specification	Clayton
Sys. Memo No. 002	7/13/64	ATS Program Engineering Personnel	Mazur
Sys. Memo No. 004	7/24/64	Tentative Agenda for HAC Interface Meeting on 7/29/64	Clayton
Sys. Memo No. 005	8/26/64	Radiation Environment	Mazur
Sys. Memo No. 006	9/9/64	ATS Coordinate Systems	Clayton
Sys. Memo No. 007	9/10/64	Thermal Information	Smith
Sys. Memo No. 008	9/16/64	NASA Requirements for Component Qualification and Acceptance Tests	Smith
Sys. Memo No. 012	10/14/64	Test Document Responsibility	Smith
Sys. Memo No. 014	10/27/64	Test Dates and Responsibilities	Smith
Sys. Memo No. 015	10/30/64	General Electric Component Test Requirements for the HAC System Thermal Test	Smith
Sys. Memo No. 016	11/2/64	GGSS (ATS) Ordnance Devices	Berges
Sys. Memo No. 018	11/17/64	GE Component Test Requirements for the HAC System Vibration Test	Smith
Sys. Memo No. 019	11/30/64	Acceleration Test Requirements for SAGGE Qualification	Smith
Sys. Memo No. 020	12/16/64	Solar Vacuum Component Evaluation Tests	Smith
Sys. Memo No. 021	1/4/65	Component Acceleration Requirements	Smith
Sys. Memo No. 022	1/4/65	Proposed Plan for Parts Power Aging and Assembled Component Testing of TV Camera	Smith
Sys. Memo No. 023	1/14/65	NASA Environmental Qualification and Acceptance Test Spec (S2-0102, 9-1-64)	Smith

Document No.	Date	Title	Author(s)
Sys. Memo No. 024	1/14/65	ATS Program Requirements for Temperature Sensors	Smith
Sys. Memo No. 025	1/19/65	Revised Boom System Parameters	Matteo
Sys. Memo No. 026	1/21/65	System Requirements and Analysis Task Priorities	Clayton
Sys. Memo No. 028	1/28/65	PCU Design for 150-foot Booms	Clemson
Sys. Memo No. 029	1/28/65	ATS Integrated Test Program Dates	Smith
Sys. Memo No. 030	2/11/65	HAC Test Plans for Measuring Spacecraft Magnetic Dipole	Smith
Sys. Memo No. 032	2/23/65	ATS Temperature Sensor Requirements	Smith
Sys. Memo No. 033	3/3/65	Action Item No. 65-ATS Program Meeting (Re: Squib Requirements for Damper and Damper Boom Assembly)	Mazur
Sys. Memo No. 034	3/9/65	Systems Design Review	Clayton
Sys. Memo No. 035	3/11/65	Magnetic Dipole Acceptance Test Requirements	Smith
Sys. Memo No. 039	4/1/65	System Requirements and Analysis Task Summary	Clayton
Sys. Memo No. 042	4/29/65	RF Experiment Information	Smith
Sys. Memo No. 043	5/5/65	Weight Bogies for ATS Components	Mazur
Sys. Memo No. 045	5/7/65	Revisions to S2-0102	Smith
Sys. Memo No. 049	6/16/65	ATS Component Location and Nomenclature	Clayton
Sys. Memo No. 051	6/22/65	CPD Angle Indicator Design Review	Mazur
Sys. Memo No. 054	7/15/65	Installation and Alignment Procedure for CPD (Preliminary)	Rosenberg
Sys. Memo No. 055	7/16/65	Waivers to Component Qualification Spec S2-0102	Smith

Document No.	Date	Title	Author(s)
Sys. Memo No. 059	8/16/65	Requirements for the Dynamic Models to be Used in the HAC System Vibration Test	Smith
Sys. Memo No. 062	10/4/65	Gravity Gradient Components Interface Information – Alignment and Handling	Frey
SVS-7312	10/8/65	ATS Gravity Gradient System Requirements Specification	Clayton
PIR 4730-159	10/15/65	ATS System Evaluation Requirements and Test Plan	Smith
Sys. Memo No. 064	10/19/65	Facility Requirements for System Test	Smith
Sys. Memo No. 065	10/29/65	Component Magnetic Dipole Requirements	Smith
Sys. Memo No. 067	11/23/65	Revised Component Qualification Test Cycles	Smith
Sys. Memo No. 071	1/17/66	ATS Component Qualification Standing Instructions Review	Smith
Sys. Memo No. 072	1/18/66	Boom System Acceptance Testing Sequence	Smith
Sys. Memo No. 076	2/21/66	Humidity Testing of SAS	Mazur
Sys. Memo No. 077	3/2/66	System Requirements and Analysis Task Summary	Clayton
Sys. Memo No. 079	3/28/66	Variation of Solar Absorptivity with Solar Incidence Angle for Silver-Plated, BeCu Boom Samples	Clayton
Sys. Memo No. 080	4/4/66	ITPB Meeting on Damper Boom Qualification Test Procedure DHC-SP-ST 11017, Issue B	Smith
Sys. Memo No. 083	4/13/66	GE System Requirements for HAC System Tests	Clayton
65SD4499-B Revision B Parts I and II	4/18/66	GE Gravity Gradient System Prototype Field Test Plan	Smith, et al
Sys. Memo No. 085	4/27/66	Qualification of CPD on the Damper Boom	Smith

Document No.	Date	Title	Author(s)
SVS-7312, Revision A	4/29/66	ATS Gravity Gradient System Requirements Specification	Clayton
Sys. Memo No. 087	5/9/66	Special Safety Requirements for ATS Damper Boom	Englund
Sys. Memo No. 088	5/11/66	GE/HAC Interface Meeting, 10-11 May 1966	Smith
Sys. Memo No. 090	6/6/66	Qualification Testing of the CPD and Damper Boom	Smith
Sys. Memo No. 096	7/20/66	Damper Boom Qualification Status	Smith
66SD4222	8/1/66	Installation and Alignment Instructions	Frey
Sys. Memo No. 097	9/1/66	Revisions to Component SI's	Smith
66SD2032	9/1/66	ATS Gravity Gradient Stabilization System (Lectures presented NASA/GSFC on 1-2 September, 1966)	Clayton, Foulke, Mazur, Kraus, Horn
66SD4495	1/23/67	Design and Test Audit	(Various)
Sys. Memo No. 113 (1st)	3/15/67	Telecons with G. Banks and E. Metzger on 14 March 1967 (Re: Momentum Vector in ATS-A Met Package)	Clayton
Sys. Memo No. 113	3/21/67	Telecons with G. Banks, 3/20/67, and J. Lotta (HAC), 3/17/67 (Re: Final Spacecraft Moments of Inertia and Magnetic Dipole)	Clayton
67SD4268	3/27/67	ATS-A Mission Description	Frey, Clayton
Sys. Memo No. 116	7/7/67	Pre-launch (ATS-D) System Requirements and Analysis Task Summary (W. P. 2100)	Clayton
Sys. Memo No. 118	7/21/67	Decreased Damper Boom Tip Mass (ATS-D)	Clayton
Sys. Memo No. 118B	7/31/67	Trip Report, ATS Interface Meeting at GSFC on 24-25 July, 1967	Clayton
68SD4342	10/31/68	Report of the Audit Team on Flight Readiness of the ATS-E Gravity Gradient Stabilization Subsystem Components	Drabek, Gudikunst, Taylor

APPENDIXES

APPENDIX A

LINEARIZED EQUATIONS OF MOTION

LINEARIZED EQUATIONS OF MOTION

A coordinate system $xy3$ will be assumed located within an orbiting vehicle, and attached to it. The rpq coordinate system is an orbital coordinate system which rotates at orbital rate about the $\vec{q}$ axis. The relationship between $xy3$ and rpq is given by the $[E]$ matrix which is illustrated in Figure 1, and defined in equation 1

Θ_P = FIRST ROTATION (ABOUT $\vec{q}$)

Θ_R = SECOND ROTATION

Θ_Y = THIRD ROTATION (ABOUT $\vec{z}$)

COORDINATE SYSTEM RELATIONSHIP - FIGURE 1

$$\begin{bmatrix} x \\ y \\ 3 \end{bmatrix} = [E] \begin{bmatrix} r \\ p \\ q \end{bmatrix}$$

$$c_{11} = \cos\Theta_P \cos\Theta_R$$

$$c_{12} = \sin\Theta_P \cos\Theta_R$$

$$c_{13} = -\sin\Theta_R$$

(1)

A-1

$$c_{21} = \cos\theta_P \sin\theta_R \sin\theta_Y - \sin\theta_P \cos\theta_Y$$

$$c_{22} = \cos\theta_P \cos\theta_Y + \sin\theta_P \sin\theta_R \sin\theta_Y$$

$$c_{23} = \cos\theta_R \sin\theta_Y$$

$$c_{31} = \sin\theta_P \sin\theta_Y + \cos\theta_P \sin\theta_R \cos\theta_Y$$

$$c_{32} = \sin\theta_P \sin\theta_R \cos\theta_Y - \cos\theta_P \sin\theta_Y$$

$$c_{33} = \cos\theta_R \cos\theta_Y$$

$\}$ (1.

SINCE THE LINEARIZED EQUATIONS OF MOTION ARE OF INTEREST, THE xyz COORDINATE SYSTEM WILL BE ASSUMED COINCIDENT WITH THE AXES OF PRINCIPAL MOMENTS OF INERTIA. THE GRAVITY GRADIENT TORQUES IN THIS COORDINATE SYSTEM BECOME

$$T_{gx} = \frac{3K}{r^3}\left[c_{21}c_{31}\left(I_{zz} - I_{yy}\right)\right.$$

$$T_{gy} = \frac{3K}{r^3}\left[c_{11}c_{31}\left(I_{xx} - I_{zz}\right)\right.$$

$$T_{gz} = \frac{3K}{r^3}\left[c_{11}c_{21}\left(I_{yy} - I_{xx}\right)\right.$$

$\}$ (2)

WHERE

T_g = GRAVITY GRADIENT TORQUE

K = UNIVERSAL GRAVITATIONAL CONSTANT MULTIPLIED BY THE MASS OF THE EARTH

r = GEOCENTRIC DISTANCE

I = MOMENT OF INERTIA

SUBSCRIPTS xyz REFER TO THE APPROPRIATE AXES

EULER'S DYNAMICAL EQUATIONS OF MOTION FOR A RIGID BODY WITH NO PRODUCTS OF INERTIA ARE

$$\sum T_x = I_{xx}\dot{\omega}_x + \omega_y \omega_3 (I_{33} - I_{yy})$$

$$\sum T_y = I_{yy}\dot{\omega}_y + \omega_x \omega_3 (I_{xx} - I_{33})$$

$$\sum T_3 = I_{33}\dot{\omega}_3 + \omega_x \omega_y (I_{yy} - I_{xx})$$

$$(3)$$

WHERE

$$\omega = \text{BODY ANGULAR RATES}$$
$$\dot{\omega} = \text{BODY ANGULAR ACCELERATION}$$
$$\sum T = \text{SUM OF THE TORQUES}$$

IN TERMS OF THE EULER ANGLE RATES, THE BODY RATES CAN BE WRITTEN

$$\omega_x = \dot{\Theta}_Y - (\dot{\Theta}_P + \dot{\gamma}) \sin \Theta_R$$

$$\omega_y = \dot{\Theta}_R \cos \Theta_Y + (\dot{\Theta}_P + \dot{\gamma}) \sin \Theta_Y \cos \Theta_R$$

$$\omega_3 = -\dot{\Theta}_R \sin \Theta_Y + (\dot{\Theta}_P + \dot{\gamma}) \cos \Theta_Y \cos \Theta_R$$

$$4$$

WHERE

$$\dot{\gamma} = \text{ORBITAL RATE} = \text{RATE ABOUT } \gamma \text{ AXIS}$$

FOR SIMPLICITY, A CIRCULAR ORBIT WILL BE ASSUMED. HENCE

$$\dot{\gamma} = \text{CONSTANT} = \sqrt{\frac{K}{r^3}} \qquad (5)$$

WITH THIS RESTRICTION, THE BODY ANGULAR ACCELERATIONS BECOME

$$\dot{\omega}_x = \ddot{\Theta}_Y - \ddot{\Theta}_P \sin \Theta_R - \dot{\Theta}_R (\dot{\Theta}_P + \dot{\gamma}) \cos \Theta_R \qquad (6)$$

$$\dot{\omega_y} = \ddot{\theta}_R \cos\theta_Y - \dot{\theta}_R \dot{\theta}_Y \sin\theta_Y + \ddot{\theta}_P \sin\theta_Y \cos\theta_R$$

$$+ \dot{\theta}_Y (\dot{\theta}_P + \dot{\eta}) \cos\theta_Y \cos\theta_R - \dot{\theta}_R (\dot{\theta}_P + \dot{\eta}) \sin\theta_Y \sin\theta_R$$

$$\dot{\omega_3} = -\ddot{\theta}_R \sin\theta_Y - \dot{\theta}_R \dot{\theta}_Y \cos\theta_Y + \ddot{\theta}_P \cos\theta_Y \cos\theta_R$$

$$- \dot{\theta}_Y (\dot{\theta}_P + \dot{\eta}) \sin\theta_Y \cos\theta_R - \dot{\theta}_R (\dot{\theta}_P + \dot{\eta}) \cos\theta_Y \sin\theta_R$$

To obtain the linearized equations of motion, it is necessary to assume small amplitude motion and discard second order terms. Equations 4 and 6 become

$$\omega_x = \dot{\theta}_Y - \dot{\eta}\,\theta_R$$

$$\omega_y = \dot{\theta}_R + \dot{\eta}\,\theta_Y$$

$$\omega_3 = \dot{\theta}_P + \dot{\eta}$$

$$\dot{\omega_x} = \ddot{\theta}_Y - \dot{\theta}_R \dot{\eta}$$

$$\dot{\omega_y} = \ddot{\theta}_R + \dot{\theta}_Y \dot{\eta}$$

$$\dot{\omega_3} = \ddot{\theta}_P$$

(7)

(8)

The matrix elements of equation 1, and the gravity gradient torques of equation 2 become

$$e_{11} = 1$$

$$e_{12} = \theta_P$$

$$e_{13} = -\theta_R$$

$$e_{21} = -\theta_P$$

(9)

A-4

$$c_{22} = 1$$

$$c_{23} = \theta_Y$$

$$c_{31} = \theta_R$$

$$c_{32} = -\theta_Y$$

$$c_{33} = 1$$

$$T_{gx} = 0$$

$$T_{gy} = 3\dot{z}^2 \theta_R (I_{xx} - I_{33})$$

$$T_{g3} = -3\dot{z}^2 \theta_P (I_{yy} - I_{xx})$$

COMBINING EQUATIONS 3, 7, 8, AND 10, AND SIMPLIFYING

$$\sum T_x = I_{xx}\ddot{\theta}_Y + \dot{\theta}_R\dot{z}(I_{33} - I_{yy} - I_{xx}) + \theta_Y\dot{z}^2(I_{33} - I_{yy})$$

$$\sum T_y = I_{yy}\ddot{\theta}_R + \dot{\theta}_Y\dot{z}(I_{xx} + I_{yy} - I_{33}) + 4\dot{z}^2\theta_R(I_{33} - I_{xx})$$

$$\sum T_3 = I_{33}\ddot{\theta}_P + 3\dot{z}^2\theta_P(I_{yy} - I_{xx})$$

WHERE

$$\sum T = \text{ALL EXTERNAL TORQUES EXCEPT GRAVITY GRADIE.}$$

o NATURAL FREQUENCY

IT IS CONVENIENT TO CALCULATE THE NATURAL FREQUENCY IN TERMS OF ORBITAL. TO CHANGE THE TIME SCALE TO ORBITAL

$$\tau = \dot{z}t$$

HENCE

$$\frac{d}{dt} = \overset{\circ}{\gamma}\,\frac{d}{d\gamma} \qquad\qquad \frac{d^2}{dt^2} = \overset{\circ}{\gamma}^2\,\frac{d^2}{d\gamma^2} \tag{13}$$

SUBSTITUTING INTO EQUATION 11, RETAINING THE "DOT" NOTATION TO DENOTE DIFFERENTIATION WITH RESPECT TO γ, AND SIMPLIFYING

$$\frac{I_{xx}}{I_{33}}\overset{\circ\circ}{\Theta}_Y + \overset{\circ}{\Theta}_R\left(1 - \frac{I_{yy}}{I_{33}} - \frac{I_{xx}}{I_{33}}\right) + \Theta_Y\left(1 - \frac{I_{yy}}{I_{33}}\right) = \frac{\sum T_x}{I_{33}\overset{\circ}{\gamma}^2} \tag{14}$$

$$\frac{I_{yy}}{I_{33}}\overset{\circ\circ}{\Theta}_R + \overset{\circ}{\Theta}_Y\left(\frac{I_{yy}}{I_{33}} + \frac{I_{xx}}{I_{33}} - 1\right) + 4\Theta_R\left(1 - \frac{I_{xx}}{I_{33}}\right) = \frac{\sum T_y}{I_{33}\overset{\circ}{\gamma}^2} \tag{15}$$

$$\overset{\circ\circ}{\Theta}_P + 3\Theta_P\left(\frac{I_{yy}}{I_{33}} - \frac{I_{xx}}{I_{33}}\right) = \frac{\sum T_3}{I_{33}\overset{\circ}{\gamma}^2} \tag{16}$$

APPENDIX B

LINEARIZED DYNAMIC EQUATIONS OF A
TWO-BODY COUPLED SYSTEM

APPENDIX B

LINEARIZED DYNAMIC EQUATIONS OF A TWO-BODY COUPLED SYSTEM

SUMMARY

The dynamic equations of motion are derived for a two-body coupled system in orbit, influenced only by the gravity gradient, in which the secondary body has one degree of freedom with respect to the primary body, which has three degrees of attitude freedom. These equations are then linearized first with respect to any arbitrary initial conditions, and then with respect to particular simplifying initial conditions. The resulting four equations lead to an eighth-degree polynomial in the differentiation operator D, whose roots are accessible.

In the fashion and notation of reference [1], the following coordinate frames and transformations are employed:

$$\begin{bmatrix} r \\ p \\ q \end{bmatrix} = \begin{bmatrix} c_\eta & s_\eta & 0 \\ -s_\eta & c_\eta & 0 \\ 0 & 0 & 1 \end{bmatrix} \begin{bmatrix} 1 & 0 & 0 \\ 0 & c_\nu & s_\nu \\ 0 & -s_\nu & c_\nu \end{bmatrix} \begin{bmatrix} c_\Omega & s_\Omega & 0 \\ -s_\Omega & c_\Omega & 0 \\ 0 & 0 & 1 \end{bmatrix} \begin{bmatrix} u \\ v \\ w \end{bmatrix} \qquad (1)$$

relates the local frame (r p q) with the inertial frame (u v w), where (r p q) is fixed in the orbit plane and rotates with the satellite, r being a unit vector in the direction of the radius vector from the earth to the center of mass of the satellite, p being a unit vector in the orbit plane $\perp$ r and positive in the direction of the velocity vector of the satellite, and q being a unit vector in the direction of the pole of the orbit. The Euler angles are: Ω ; the right ascension of the ascending node, measured from u about w; ν, the orbital inclination; η, the orbital angular position, measured from the ascending node. (r p q) is dextral in the named order. The notation c_η denotes cos η and s_Ω denotes sin Ω. Eq. (1) will be abbreviated: (r) = [A] (u), where the orthogonal matrix [A] denotes the product of the three square matrices.

If $\Omega = \nu = \eta = 0$, $\begin{bmatrix} r \\ p \\ q \end{bmatrix} \equiv \begin{bmatrix} u \\ v \\ w \end{bmatrix}$.

$$\begin{bmatrix} x_1 \\ y_1 \\ z_1 \end{bmatrix} = \begin{bmatrix} 1 & 0 & 0 \\ 0 & c_y & s_y \\ 0 & -s_y & c_y \end{bmatrix} \begin{bmatrix} c_r & 0 & -s_r \\ 0 & 1 & 0 \\ s_r & 0 & c_r \end{bmatrix} \begin{bmatrix} c_p & s_p & 0 \\ -s_p & c_p & 0 \\ 0 & 0 & 1 \end{bmatrix} \begin{bmatrix} r \\ p \\ q \end{bmatrix} \qquad (2)$$

1. Hinrichs, R., "Attitude Dynamics of a Two-Body Coupled System," TIS #62SD821, G. E. Co., MSD, Valley Forge, Pa, December, 1962.

relates the main body axes $(x_1\ y_1\ z_1)$ with the local axes (r p q) via the three Euler angles: θ_p, a rotation of the x_1-, y_1- axes about the q-axis; θ_r, a rotation of the x_1-, z_1- axes about the intermediate y_1- axis; θ_y, a rotation of the y_1-, z_1-axes about the final x_1- axis. $(x_1\ y_1\ z_1)$ is dextral in the named order. The notation c_y denotes $\cos \theta_y$; S_r denotes $\sin \theta_r$; c_p denotes

$\cos \theta_p$. If $\theta_p = \theta_r = \theta_y = 0$, $\begin{bmatrix} x_1 \\ y_1 \\ z_1 \end{bmatrix} \equiv \begin{bmatrix} r \\ p \\ q \end{bmatrix}$. If θ_p, θ_r and θ_y are 'small,' they may be con-

sidered as pitch, roll and yaw deviations of the main body, respectively. Eq. (2) will be abbreviated: $(x_1) = \begin{bmatrix} E \end{bmatrix}$ (r), where the orthogonal matrix $\begin{bmatrix} E \end{bmatrix}$ denotes the product of the three square matrices.

$$
\begin{bmatrix} x_2 \\ y_2 \\ z_2 \end{bmatrix} = \begin{bmatrix} c_\theta & 0 & -s_\theta \\ 0 & 1 & 0 \\ s_\theta & 0 & c_\theta \end{bmatrix} \begin{bmatrix} 1 & 0 & 0 \\ 0 & c_\phi & s_\phi \\ 0 & -s_\phi & c_\phi \end{bmatrix} \begin{bmatrix} x_1 \\ y_1 \\ z_1 \end{bmatrix}
\tag{3}
$$

relates the secondary body axes $(x_2\ y_2\ z_2)$ with the main body axes $(x_1\ y_1\ z_1)$ via: ϕ, a rotation of the y_2- z_2- axes about the x_1- axis; θ, a rotation of the x_2-, z_2- axes about the final y_2- axis. $(x_2\ y_2\ z_2)$ is dextral in the named order. c_θ and s_ϕ denote $\cos \theta$ and $\sin \phi$ respectively.

If $\phi = \theta = 0$, $\begin{bmatrix} x_2 \\ y_2 \\ z_2 \end{bmatrix} \equiv \begin{bmatrix} x_1 \\ y_1 \\ z_1 \end{bmatrix}$. Eq. (3) will be abbreviated: $(x_2) = \begin{bmatrix} \Gamma \end{bmatrix} (x_1)$, where the orthogonal

matrix $\begin{bmatrix} \Gamma \end{bmatrix}$ denotes the product of the two square matrices.

The main and secondary bodies of this analysis are joined so that ϕ is fixed, and the x_1- and x_2- axes are connected by a spring and damper so that the torque transmitted from the secondary body to the main body in the direction of the y_2- axis, denoted Q_{y_2}, is $b\dot{\theta} + k\theta$.

These transformations are depicted in Figs. 1-4.

Figure 1
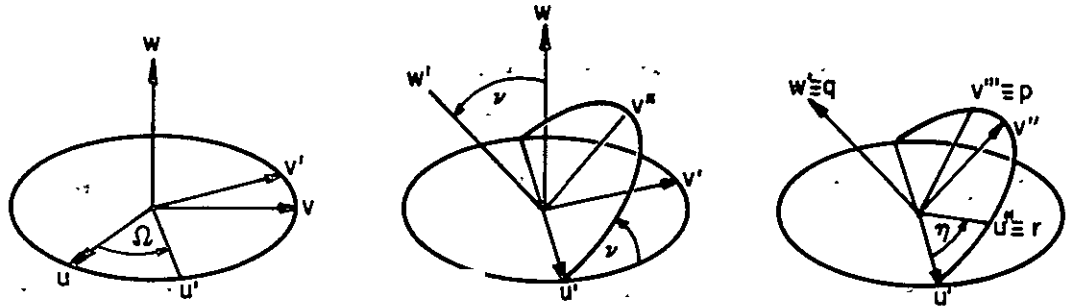
Figure 2
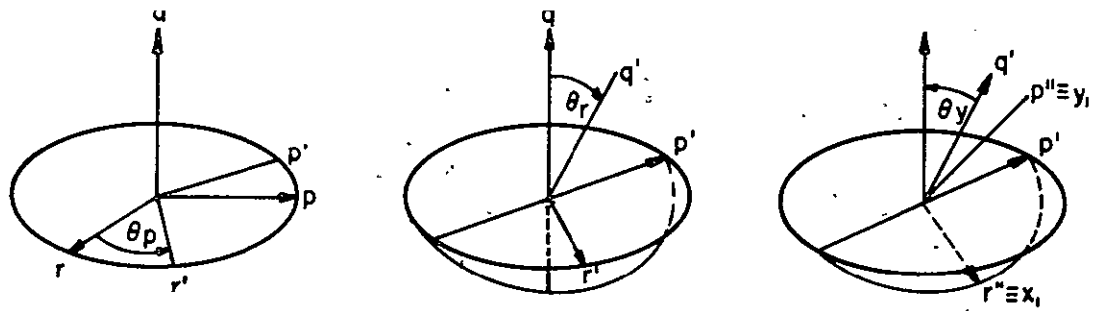
Figure 3
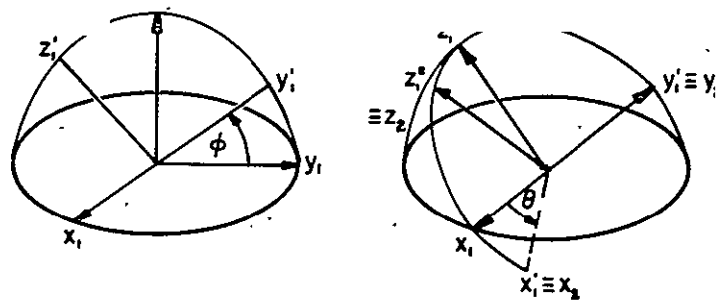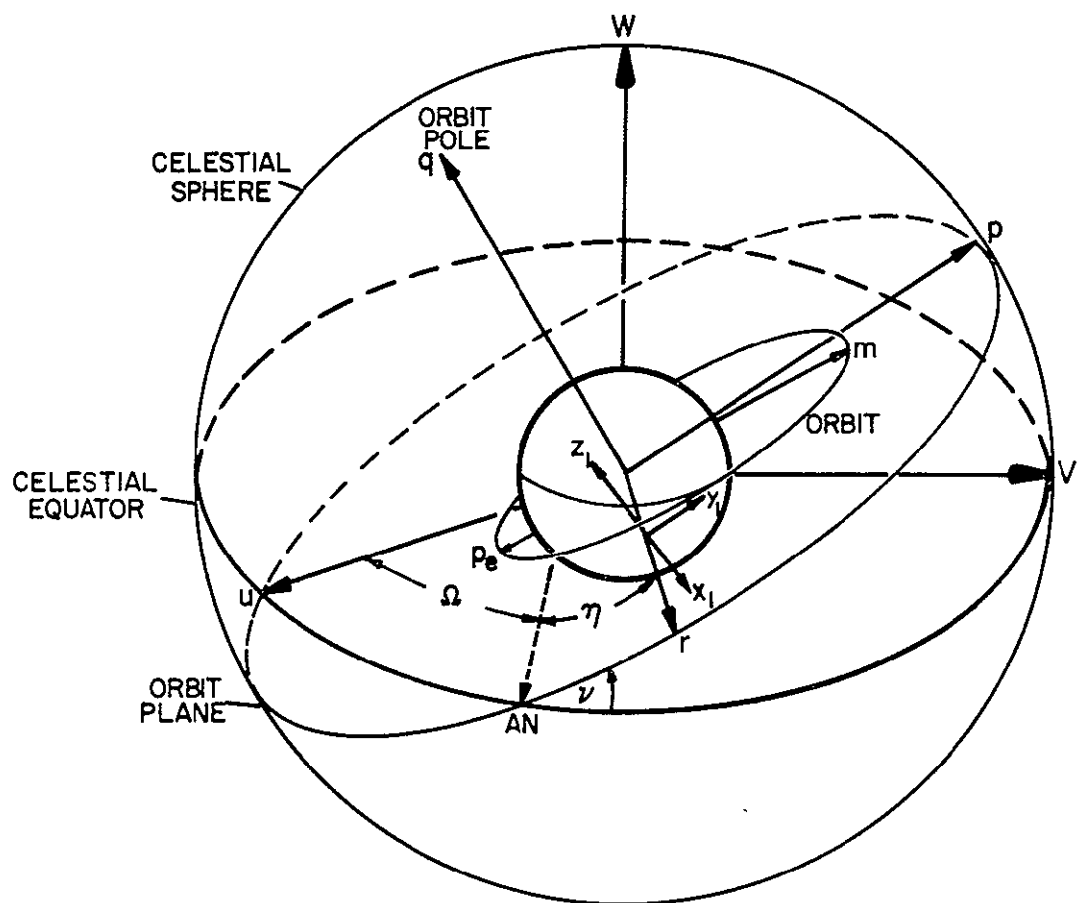
Figure 4

Euler's dynamical equations of motion for the main body are:

$$(T_1 + Q_1) = \begin{bmatrix} I_1 \end{bmatrix} (\dot{\omega}_1) + \begin{bmatrix} W_1 \end{bmatrix} \begin{bmatrix} I_1 \end{bmatrix} (\omega_1) \qquad (4)$$

where $(T_1 + Q_1) \equiv \begin{bmatrix} T_{x_1} + Q_{x_1} \\ T_{y_1} + Q_{y_1} \\ T_{z_1} + Q_{z_1} \end{bmatrix}$; $\begin{bmatrix} I_1 \end{bmatrix} = \begin{bmatrix} I_{xx_1} & 0 & 0 \\ 0 & I_{yy_1} & 0 \\ 0 & 0 & I_{zz_1} \end{bmatrix}$, where it has been assumed

that the main body axes are principal axes, so all products of inertia vanish; $(\omega_1) \equiv \begin{bmatrix} \omega_{x_1} \\ \omega_{y_1} \\ \omega_{z_1} \end{bmatrix}$;

$$\begin{bmatrix} W_1 \end{bmatrix} \equiv \begin{bmatrix} 0 & -\omega_{z_1} & \omega_{y_1} \\ \omega_{z_1} & 0 & -\omega_{x_1} \\ -\omega_{y_1} & \omega_{x_1} & 0 \end{bmatrix}$$; $(Q_1) = \begin{bmatrix} Q_{x_1} \\ Q_{y_1} \\ Q_{z_1} \end{bmatrix}$ are the components of the transmitted torque Q

from the secondary body to the main body, resolved along the main body axes; $(T_1) \equiv \begin{bmatrix} T_{x_1} \\ T_{y_1} \\ T_{z_1} \end{bmatrix}$

are the components resolved along the main body axes of the torque on the main body due to the gravity gradient.

Expanding eq. (4) yields

$$\begin{matrix} a) \\ b) \\ c) \end{matrix} \begin{bmatrix} T_{x_1} + Q_{x_1} \\ T_{y_1} + Q_{y_1} \\ T_{z_1} + Q_{z_1} \end{bmatrix} = \begin{bmatrix} I_{xx_1} \dot{\omega}_{x_1} \\ I_{yy_1} \dot{\omega}_{y_1} \\ I_{zz_1} \dot{\omega}_{z_1} \end{bmatrix} + \begin{bmatrix} (I_{zz_1} - I_{yy_1}) \omega_{z_1} \omega_{y_1} \\ (I_{xx_1} - I_{zz_1}) \omega_{x_1} \omega_{z_1} \\ (I_{yy_1} - I_{xx_1}) \omega_{y_1} \omega_{x_1} \end{bmatrix} \qquad (5)$$

Linearizing eq. (5),

$$
\begin{bmatrix}
\Delta T_{x_1} + \Delta Q_{x_1} \\[4pt]
\Delta T_{y_1} + \Delta Q_{y_1} \\[4pt]
\Delta T_{z_1} + \Delta Q_{z_1}
\end{bmatrix}
=
\begin{bmatrix}
I_{xx_1} \; \Delta \dot\omega_{x_1} \\[4pt]
I_{yy_1} \; \Delta \dot\omega_{y_1} \\[4pt]
I_{zz_1} \; \Delta \dot\omega_{z_1}
\end{bmatrix}
+
\begin{bmatrix}
(I_{zz_1} - I_{yy_1})\,(\hat\omega_{y_1} \Delta\omega_{z_1} + \hat\omega_{z_1} \Delta\omega_{y_1}) \\[4pt]
(I_{xx_1} - I_{zz_1})\,(\hat\omega_{z_1} \Delta\omega_{x_1} + \hat\omega_{x_1} \Delta\omega_{z_1}) \\[4pt]
(I_{yy_1} - I_{xx_1})\,(\hat\omega_{x_1} \Delta\omega_{y_1} + \hat\omega_{y_1} \Delta\omega_{x_1})
\end{bmatrix}
\tag{5}
$$

where the hat over a variable signifies its initial or nominal value.

Euler's dynamical equations of motion for the secondary body are:

$$
(T_2 - Q_2) = \begin{bmatrix} I_2 \end{bmatrix} (\dot\omega_2) + \begin{bmatrix} W_2 \end{bmatrix} \begin{bmatrix} I_2 \end{bmatrix} (\omega_2),
\tag{6}
$$

where $(Q_2) \equiv \begin{bmatrix} Q_{x_2} \\ Q_{y_2} \\ Q_{z_2} \end{bmatrix}$ are the components of Q resolved along the secondary body axes;

$$
\begin{bmatrix} I_2 \end{bmatrix} \equiv
\begin{bmatrix}
I_{xx_2} & 0 & 0 \\
0 & I_{yy_2} & 0 \\
0 & 0 & I_{zz_2}
\end{bmatrix},
$$
where it has been assumed that the secondary body axes are prin-

cipal axes; $(T_2) \equiv \begin{bmatrix} T_{x_2} \\ T_{y_2} \\ T_{z_2} \end{bmatrix}$ are the components resolved along the secondary body axes of the

torque on the secondary body due to the gravity gradient; $\begin{bmatrix} W_2 \end{bmatrix}$ and (ω_2) are similar to $\begin{bmatrix} W_1 \end{bmatrix}$ and (ω_1), with appropriate subscripts.

Assuming that $I_{xx_2} = 0$ and $I_{yy_2} = I_{zz_2}$, since the secondary body is a rod, eq. (6) may be expanded to yield:

$$
\begin{bmatrix} T_{x_2} - Q_{x_2} \\ T_{y_2} - Q_{y_2} \\ T_{z_2} - \dot{Q}_{z_2} \end{bmatrix} = I_{yy_2} \begin{bmatrix} 0 \\ \dot{\omega}_{y_2} - \omega_{x_2}\,\omega_{z_2} \\ \dot{\omega}_{z_2} + \omega_{x_2}\,\omega_{y_2} \end{bmatrix}
\qquad (7)
$$

Linearizing eq. (7),

$$
\begin{bmatrix} \Delta T_{x_2} - \Delta Q_{x_2} \\ \Delta T_{y_2} - \Delta Q_{y_2} \\ \Delta T_{z_2} - \Delta Q_{z_2} \end{bmatrix} = I_{yy_2} \begin{bmatrix} 0 \\ \Delta\dot{\omega}_{y_2} - \hat{\omega}_{x_2}\,\Delta\omega_{z_2} - \hat{\omega}_{z_2}\,\Delta\omega_{x_2} \\ \Delta\dot{\omega}_{z_2} + \hat{\omega}_{x_2}\,\Delta\omega_{y_2} + \hat{\omega}_{y_2}\,\Delta\omega_{x_2} \end{bmatrix}
\qquad (7L)
$$

The gravity gradient torques (T_1) on the main body are adapted from reference $[1]$, p. 7-1, by setting the products of inertia to zero, and replacing $\dfrac{K}{R^3}$ with $\omega_0^{\,2}$, the square of the mean angular velocity of the satellite mass center (orbital velocity):

$$
\begin{bmatrix} T_{x_1} \\ T_{y_1} \\ T_{z_1} \end{bmatrix} = 3\omega_0^{\,2} \begin{bmatrix} e_{21} & e_{31} & (I_{zz_1} - I_{yy_1}) \\ e_{11} & e_{31} & (I_{xx_1} - I_{zz_1}) \\ e_{11} & e_{21} & (I_{yy_1} - I_{xx_1}) \end{bmatrix} = 3\omega_0^{\,2} \begin{bmatrix} (c_p\,s_r\,s_y - s_p\,c_y)\,(s_p\,s_y + c_p\,s_r\,c_y) \\ c_p\,c_r\,(s_p\,s_y + c_p\,s_r\,c_y) \\ c_p\,c_r\,(c_p\,s_r\,s_y - s_p\,c_y) \end{bmatrix}
\qquad (8)
$$

$$
\begin{bmatrix} (I_{zz_1} - I_{yy_1}) \\ (I_{xx_1} - I_{zz_1}) \\ (I_{yy_1} - I_{xx_1}) \end{bmatrix}
$$

where the e_{i1} are the direction cosines of the local vertical unit vector r with respect to the main body axes, and are elements of the matrix $[E]$.

Linearizing eq. (8),

$$\Delta T_{x_1} = 3\omega_0^2 (I_{zz_1} - I_{yy_1}) \left[\Delta\theta_p \left\{ s_r(c_p^2 - s_p^2)(s_y^2 - c_y^2) - 2 s_p c_p s_y c_y (1+s_r^2) \right\}_0 \right.$$

$$+ \Delta\theta_r \left\{ c_p c_r \left[s_p(s_y^2 - c_y^2) + 2c_p s_r s_y c_y \right] \right\}_0 + \Delta\theta_y \left. \left\{ (c_y^2 - s_y^2)(c_p^2 s_r^2 - s_p^2) + 4 s_p c_p s_r s_y c_y \right\}_0 \right] \tag{8Lx}$$

$$\Delta T_{y_1} = 3\omega_0^2 (I_{xx_1} - I_{zz_1}) \left[\Delta\theta_p \left\{ c_r s_y(c_p^2 - s_p^2) - 2 s_p c_p s_r c_r c_y \right\}_0 + \Delta\theta_r \left\{ c_p^2 c_y(c_r^2 - s_r^2) - s_p c_p s_r s_y \right\}_0 \right.$$

$$\left. + \Delta\theta_y \left\{ c_p c_r(s_p c_y - c_p s_r s_y) \right\}_0 \right] \tag{8Ly}$$

$$\Delta T_{z_1} = 3\omega_0^2 (I_{yy_1} - I_{xx_1}) \left[\Delta\theta_p \left\{ c_r c_y(s_p^2 - c_p^2) - 2 s_p c_p s_r c_r s_y \right\}_0 \right.$$

$$\left. + \Delta\theta_r \left\{ c_p^2 s_y(c_r^2 - s_r^2) + s_p c_p s_r c_y \right\}_0 + \Delta\theta_y \left\{ c_p c_r(c_p s_r c_y + s_p s_y) \right\}_0 \right], \tag{8Lz}$$

where brace sub-zero denotes evaluation at initial value (same as hat notation).

Note that if $\left\{ \begin{matrix} \theta_p = \theta_r = \theta_y \end{matrix} \right\}_0 \equiv \hat\theta_p = \hat\theta_r = \hat\theta_y = 0$, these reduce to: $\Delta T_{x_1} = 0$, ΔT_{y_1}

$= 3\omega_0^2 (I_{xx_1} - I_{zz_1}) \Delta\theta_r$, $\Delta T_{z_1} = -3\omega_0^2 (I_{yy_1} - I_{xx_1}) \Delta\theta_p$, which agrees with Roberson's

equation (our pitch axis is directed opposite to Roberson's).

The gravity gradient torques on the secondary body (T_2) are obtained analogously.
Since $(x_2) = [\Gamma](x_1)$ and $(x_1) = [E](r)$, then $(x_2) = [\Gamma][E](r)$.

$$\begin{bmatrix} T_{x_2} \\ T_{y_2} \\ T_{z_2} \end{bmatrix} = 3\omega_0^2 \begin{bmatrix} h_{21} & h_{31} & (I_{zz_2} - I_{yy_2}) \\ h_{11} & h_{31} & (I_{xx_2} - I_{zz_2}) \\ h_{11} & h_{21} & (I_{yy_2} - I_{xx_2}) \end{bmatrix} = 3\omega_0^2 I_{yy_2} \begin{bmatrix} 0 \\ -h_{11} & h_{31} \\ h_{11} & h_{21} \end{bmatrix}, \tag{9}$$

where it is assumed that $I_{xx_2} = 0$ and $I_{yy_2} = I_{zz_2}$, and where h_{i1} are elements of the product $\begin{bmatrix} \Gamma \end{bmatrix} \begin{bmatrix} E \end{bmatrix}$. Thus

$$\begin{bmatrix} T_{x_2} \\ T_{y_2} \\ T_{z_2} \end{bmatrix} = 3\omega_0^2\, I_{yy_2} \begin{bmatrix} 0 \\ -s_\phi c_\theta \left[(c_p c_r)^2 - F^2 \right] - c_p c_r\, (s_\theta^2 - c_\theta^2)\, F \\ \left[c_\phi e_{21} + s_\phi e_{31} \right] \left[c_\theta c_p c_r + s_\theta F \right] \end{bmatrix} \tag{10}$$

where $F = s_\phi e_{21} - c_\phi e_{31}$

and $\quad e_{21} = c_p s_r s_y - s_p c_y; \quad e_{31} = s_p s_y + c_p s_r c_y$

Linearizing eq. (10),

$$\Delta T_{x_2} = 0 \tag{10Lx}$$

$$\frac{\Delta T_{y_2}}{3\omega_0^2 I_{yy_2}} = \Delta\theta_p \left[2s_\theta c_\theta s_p c_p c_r^2 + s_p c_r (s_\theta^2 - c_\theta^2) F + \left\{ c_p c_r (s_\theta^2 - c_\theta^2) - 2 s_\theta c_\theta F \right\} \left\{ s_p s_r A + c_p B \right\} \right]_0$$

$$+ \Delta\theta_r \left[2s_\theta c_\theta c_p c_r \left\{ c_p s_r + AF \right\} + c_p (s_\theta^2 - c_\theta^2) \left\{ -c_p c_r^2 A + s_r F \right\} \right]_0 \tag{10Ly}$$

$$+ \Delta\theta_y \left[\left\{ s_p A + c_p s_r B \right\} \left\{ 2 s_\theta c_\theta F - c_p c_r (s_\theta^2 - c_\theta^2) \right\} \right]_0$$

$$+ \Delta\theta \left[(c_p^2 c_r^2 - F^2)(s_\theta^2 - c_\theta^2) - 4 s_\theta c_\theta c_p c_r F \right]_0$$

$$\frac{\Delta T_{z_2}}{3\omega_0^2 I_{yy_2}} = \Delta\theta_p \left[-(c_\phi e_{21} + s_\phi e_{31})\left\{ c_\theta s_p c_r + s_\theta c_p B + s_\theta s_p s_r A \right\} + (c_\theta c_p c_r + s_\theta F)(c_p A - s_p s_r B) \right]$$

$$+ \Delta\theta_r \left[(c_\phi e_{21} + s_\phi e_{31})\left\{ -c_\theta c_p s_r + s_\theta c_p c_r A \right\} + (c_\theta c_p c_r + s_\theta F)\left\{ c_p c_r B \right\} \right]_0$$

$$+ \Delta\theta_y \left[(c_\phi e_{21} + s_\phi e_{31})\left\{ s_\theta (s_p A + c_p s_r B) \right\} + \left\{ c_\theta c_p c_r + s_\theta F \right\}\left\{ -c_p s_r A + s_p B \right\} \right]_0 \tag{10Lz}$$

$$+ \Delta\theta \left[(c_\phi e_{21} + s_\phi e_{31})\left\{ -s_\theta c_p c_r + c_\theta F \right\} \right]_0$$

where $A = s_\phi s_y - c_\phi c_y = -c_{\phi+y}$

$\qquad B = c_\phi s_y + s_\phi c_y = S_{\phi+y}$; $e_{21} = c_p s_r s_y - s_p c_y$

$\qquad F = s_\phi e_{21} - c_\phi e_{31}$ $\qquad e_{31} = s_p s_y + c_p s_r c_y$

The components of Q along the $(x_2\ y_2\ z_2)$ - axes are

$$(Q) = \begin{bmatrix} Q_{x_2} \\ Q_{y_2} \\ Q_{z_2} \end{bmatrix} = \begin{bmatrix} \dot{Q}_{x_2} \\ b\dot{\theta} + k\bar{\theta} \\ Q_{z_2} \end{bmatrix} \text{, where } \bar{\theta} = \theta - \theta_0 \text{, where } \theta_0 \text{ represents that value of } \theta \text{ for} \tag{11}$$

which no tension or compression exists in the spring, due to θ alone. Linearizing,

$$\begin{bmatrix} \Delta Q_{x_2} \\ \Delta Q_{y_2} \\ \Delta Q_{z_2} \end{bmatrix} = \begin{bmatrix} \Delta \dot{Q}_{x_2} \\ b\Delta\dot{\theta} + k\Delta\theta \\ \Delta Q_{z_2} \end{bmatrix} \tag{11L}$$

Since $(x_2) = [\Gamma](x_1)$, $(x_1) = [\Gamma]^{-1}(x_2) = [\Gamma]^T(x_2)$, since $[\Gamma]$ is orthogonal. Thus Q may be resolved along the $x_1\, y_1\, z_1$ axes.

$$
\begin{bmatrix} Q_{x_1} \\ Q_{y_1} \\ Q_{z_1} \end{bmatrix} = [\Gamma]^T \begin{bmatrix} Q_{x_2} \\ Q_{y_2} \\ Q_{z_2} \end{bmatrix} = \begin{bmatrix} Q_{x_2}c_\theta + Q_{z_2}s_\theta \\ Q_{x_2}s_\theta s_\phi + (b\dot\theta + k\overline\theta)c_\phi - Q_{z_2}c_\theta s_\phi \\ -Q_{x_2}s_\theta c_\phi + (b\dot\theta + k\overline\theta)s_\phi + Q_{z_2}c_\theta c_\phi \end{bmatrix} \tag{12}
$$

Linearizing,

$$
\begin{bmatrix} \Delta Q_{x_1} \\ \Delta Q_{y_1} \\ \Delta Q_{z_1} \end{bmatrix} = \begin{bmatrix} \hat c_\theta \Delta Q_{x_2} + \hat s_\theta \Delta Q_{z_2} + \left\{ Q_{z_2}c_\theta - Q_{x_2}s_\theta \right\}_0 \Delta\theta \\ \hat s_\theta \hat s_\phi \Delta Q_{x_2} + b\hat c_\phi \Delta\dot\theta - \hat c_\theta \hat s_\phi \Delta Q_{z_2} + \left\{ Q_{x_2}c_\theta s_\phi + Q_{z_2}s_\theta s_\phi + kc_\phi \right\}_0 \Delta\theta \\ -\hat s_\theta \hat c_\phi \Delta Q_{x_2} + b\hat s_\phi \Delta\dot\theta + \hat c_\theta \hat c_\phi \Delta Q_{z_2} + \left\{ -Q_{x_2}c_\theta c_\phi - Q_{z_2}s_\theta c_\phi + ks_\phi \right\}_0 \Delta\theta \end{bmatrix} \tag{12L}
$$

The angular velocity vector of the main body (ω_1) consists of the sum of several infinitesimal rotations, each in some specified direction. One contribution to (ω_1) is from $\dot\theta_p + \dot\eta$, which is in the direction of the q-axis, and which can be transformed into body axis components via matrix $[E]$: since $(x_1) = [E](r)$,

$$
\begin{bmatrix} \omega_{x_1} \\ \omega_{y_1} \\ \omega_{z_1} \end{bmatrix} = [E] \begin{bmatrix} 0 \\ 0 \\ \dot\theta_p + \dot\eta \end{bmatrix} = \begin{bmatrix} -s_r(\dot\theta_p + \dot\eta) \\ c_r s_y(\dot\theta_p + \dot\eta) \\ c_r c_y(\dot\theta_p + \dot\eta) \end{bmatrix}
$$

The next contribution to (ω_1) is due to $\dot\theta_r$, which is in the direction of the intermediate y_1 - axis, and which can be transformed into body axis components via matrix $[C]$: since $(x_1) = [C](r')$,

$$
\begin{bmatrix} \omega_{x_1} \\ \omega_{y_1} \\ \omega_{z_1} \end{bmatrix} = [C] \begin{bmatrix} 0 \\ \dot\theta_r \\ 0 \end{bmatrix} = \begin{bmatrix} 0 \\ c_y\dot\theta_r \\ -s_y\dot\theta_r \end{bmatrix}, \text{ where } [C] \equiv \begin{bmatrix} 1 & 0 & 0 \\ 0 & c_y & s_y \\ 0 & -s_y & c_y \end{bmatrix}
$$

Since the final contribution to ω_1 (from $\dot{\theta}_y$) is already in the x_1- direction,

$$\begin{bmatrix} \omega_{x_1} \\ \omega_{y_1} \\ \omega_{z_1} \end{bmatrix} = \begin{bmatrix} \dot{\theta}_y \\ 0 \\ 0 \end{bmatrix} \quad . \quad \text{Adding like contributions,}$$

$$\begin{bmatrix} \omega_{x_1} \\ \omega_{y_1} \\ \omega_{z_1} \end{bmatrix} = \begin{bmatrix} -s_r (\dot{\theta}_p + \dot{\eta}) + \dot{\theta}_y \\ c_r s_y (\dot{\theta}_p + \dot{\eta}) + c_y \dot{\theta}_r \\ c_r c_y (\dot{\theta}_p + \dot{\eta}) - s_y \dot{\theta}_r \end{bmatrix} \quad . \tag{13}$$

Linearizing, under the assumption that $\dot{\eta}$ is constant,

$$\begin{bmatrix} \Delta\omega_{x_1} \\ \Delta\omega_{y_1} \\ \Delta\omega_{z_1} \end{bmatrix} = \begin{bmatrix} -\hat{s}_r \Delta\dot{\theta}_p - \hat{c}_r(\hat{\dot{\theta}}_p + \hat{\dot{\eta}}) \Delta\theta_r + \Delta\dot{\theta}_y \\ \hat{c}_r\hat{s}_y \Delta\dot{\theta}_p + \hat{c}_y \Delta\dot{\theta}_r - \hat{s}_r \hat{s}_y(\hat{\dot{\theta}}_p + \hat{\dot{\eta}}) \Delta\theta_r + \left\{ c_r c_y (\dot{\theta}_p + \dot{\eta}) - s_y \dot{\theta}_r \right\}_0 \Delta\theta_y \\ \hat{c}_r\hat{c}_y \Delta\dot{\theta}_p - \hat{s}_y \Delta\dot{\theta}_r - \hat{s}_r\hat{c}_y (\hat{\dot{\theta}}_p + \hat{\dot{\eta}}) \Delta\theta_r + \left\{ -c_r s_y (\dot{\theta}_p + \dot{\eta}) - c_y \dot{\theta}_r \right\}_0 \Delta\theta_y \end{bmatrix} \tag{13L}$$

Differentiating eq. (13),

$$\begin{bmatrix} \dot{\omega}_{x_1} \\ \dot{\omega}_{y_1} \\ \dot{\omega}_{z_1} \end{bmatrix} = \begin{bmatrix} -s_r(\ddot{\theta}_p + \ddot{\eta}) - c_r(\dot{\theta}_p + \dot{\eta}) \dot{\theta}_r + \ddot{\theta}_y \\ c_r s_y(\ddot{\theta}_p + \ddot{\eta}) + (c_r c_y \dot{\theta}_y - s_r s_y \dot{\theta}_r) (\dot{\theta}_p + \dot{\eta}) + c_y \ddot{\theta}_r - s_y \dot{\theta}_r \dot{\theta}_y \\ c_r c_y (\ddot{\theta}_p + \ddot{\eta}) + (-c_y s_r \dot{\theta}_r - c_r s_y \dot{\theta}_y) (\dot{\theta}_p + \dot{\eta}) - s_y \ddot{\theta}_r - c_y \dot{\theta}_r \dot{\theta}_y \end{bmatrix} \tag{14}$$

Linearizing,

$$\Delta\dot{\omega}_{x_1} = \Delta\ddot{\theta}_p \left\{ -s_r \right\}_0 + \Delta\dot{\theta}_p \left\{ -c_r \dot{\theta}_r \right\}_0 + \Delta\ddot{\theta}_r \left\{ -c_r(\dot{\theta}_p + \dot{\eta}) \right\}_0 + \Delta\theta_r \left\{ -c_r(\ddot{\theta}_p + \ddot{\eta}) + s_r(\dot{\theta}_p + \dot{\eta})\dot{\theta}_r \right\}_0$$

$$+ \Delta\ddot{\theta}_y \tag{14Lx}$$

$$\Delta\dot\omega_{y_1} = \Delta\ddot\theta_p \left\{ c_r s_y \right\}_0 + \Delta\dot\theta_p \left\{ c_r c_y \dot\theta_y - s_r s_y \dot\theta_r \right\}_0 + \Delta\ddot\theta_r \left\{ c_y \right\}_0 + \Delta\dot\theta_r \left\{ -s_r s_y (\dot\theta_p + \dot\eta) - s_y \dot\theta_y \right\}_0$$

$$+ \Delta\theta_r \left\{ -s_r s_y (\ddot\theta_p + \ddot\eta) + (-s_r c_y \dot\theta_y - c_r s_y \dot\theta_r)(\dot\theta_p + \dot\eta) \right\}_0 + \Delta\dot\theta_y \left\{ c_r c_y (\dot\theta_p + \dot\eta) - s_y \dot\theta_r \right\}_0 \tag{14Ly}$$

$$+ \Delta\theta_y \left\{ c_r c_y (\ddot\theta_p + \ddot\eta) + (-c_r s_y \dot\theta_y - s_r c_y \dot\theta_r)(\dot\theta_p + \dot\eta) - s_y \ddot\theta_r - c_y \dot\theta_r \dot\theta_y \right\}_0 \;.$$

$$\Delta\dot\omega_{z_1} = \Delta\ddot\theta_p \left\{ c_r c_y \right\}_0 + \Delta\dot\theta_p \left\{ -c_y s_r \dot\theta_r - c_r s_y \dot\theta_y \right\}_0 \tag{14Lz}$$

$$+ \Delta\ddot\theta_r \left\{ -s_y \right\}_0 + \Delta\dot\theta_r \left\{ -c_y s_r (\dot\theta_p + \dot\eta) - c_y \dot\theta_y \right\}_0 + \Delta\theta_r \left\{ -s_r c_y (\ddot\theta_p + \ddot\eta) + (-c_y c_r \dot\theta_r + s_r s_y \dot\theta_y)(\dot\theta_p + \dot\eta) \right\}_0$$

$$+ \Delta\dot\theta_y \left\{ -c_r s_y (\dot\theta_p + \dot\eta) - c_y \dot\theta_r \right\}_0 + \Delta\theta_y \left\{ -c_r s_y (\ddot\theta_p + \ddot\eta) + (s_r s_y \dot\theta_r - c_r c_y \dot\theta_y)(\dot\theta_p + \dot\eta) - c_y \ddot\theta_r + s_y \dot\theta_r \dot\theta_y \right\}_0$$

The vector rotation ω_i of the $(x_i\, y_i\, z_i)$ frame with respect to inertial space has the components $(\omega_{x_i},\, \omega_{y_i},\, \omega_{z_i})$ in the $(x_i\, y_i\, z_i)$ frame, $i = 1, 2$.

$(\dot x_2)$ may be derived in two ways. Firstly,

$$\begin{bmatrix} \dot x_2 \\ \dot y_2 \\ \dot z_2 \end{bmatrix} = \begin{bmatrix} \omega_2 \times x_2 \\ \omega_2 \times y_2 \\ \omega_2 \times z_2 \end{bmatrix} = \begin{bmatrix} y_2\, \omega_{z_2} - z_2\, \omega_{y_2} \\ z_2\, \omega_{x_2} - x_2\, \omega_{z_2} \\ x_2\, \omega_{y_2} - y_2\, \omega_{x_2} \end{bmatrix}, \text{ and then using eq. (3)}: \begin{bmatrix} x_2 \\ \dot y_2 \\ z_2 \end{bmatrix} = [\Gamma] \begin{bmatrix} x_1 \\ y_1 \\ z_1 \end{bmatrix} \tag{15}$$

$\;$ express $(\dot x_2\, \dot y_2\, \dot z_2)$ in terms of $(x_1\, y_1\, z_1)$, yielding:

B-14

$$\begin{bmatrix} \dot{x}_2 \\ \dot{y}_2 \\ \dot{z}_2 \end{bmatrix} = \begin{bmatrix} x_1(-\omega_{y_2} s_\theta) + y_1(\omega_{z_2} c_\phi + \omega_{y_2} c_\theta s_\phi) + z_1(\omega_{z_2} s_\phi - \omega_{y_2} c_\theta c_\phi) \\[4pt] x_1(\omega_{x_2} s_\theta - \omega_{z_2} c_\theta) + y_1(-\omega_{x_2} c_\theta s_\phi - \omega_{z_2} s_\theta s_\phi) + z_1(\omega_{x_2} c_\theta c_\phi + \omega_{z_2} s_\theta c_\phi) \\[4pt] x_1(\omega_{y_2} c_\theta) + y_1(\omega_{y_2} s_\theta s_\phi - \omega_{x_2} c_\phi) + z_1(-\omega_{y_2} s_\theta c_\phi - \omega_{x_2} s_\phi) \end{bmatrix} \qquad (16)$$

Secondly, differentiate eq. (3) and use $\begin{bmatrix} \dot{x}_1 \\ \dot{y}_1 \\ \dot{z}_1 \end{bmatrix} = \begin{bmatrix} \omega_1 \times x_1 \\ \omega_1 \times y_1 \\ \omega_1 \times z_1 \end{bmatrix}$ and $\dot{\phi} = 0$ to obtain:

$$\begin{bmatrix} \dot{x}_2 \\[6pt] \dot{y}_2 \\ \dot{z}_2 \end{bmatrix} = \begin{bmatrix} x_1(-\omega_{z_1} s_\theta s_\phi - \omega_{y_1} s_\theta c_\phi - \dot{\theta} s_\theta) + y_1(\omega_{z_1} c_\theta + \omega_{x_1} s_\theta c_\phi + \dot{\theta} c_\theta s_\phi) \\ \qquad\qquad\qquad + z_1(-\omega_{y_1} c_\theta + \omega_{x_1} s_\theta s_\phi - \dot{\theta} c_\theta c_\phi) \\[8pt] x_1(-\omega_{z_1} c_\phi + \omega_{y_1} s_\phi) + y_1(-\omega_{x_1} s_\phi) + z_1(\omega_{x_1} c_\phi) \\[8pt] x_1(\omega_{z_1} c_\theta s_\phi + \omega_{y_1} c_\theta c_\phi + \dot{\theta} c_\theta) + y_1(\omega_{z_1} s_\theta - \omega_{x_1} c_\theta c_\phi + \dot{\theta} s_\theta s_\phi) \\ \qquad\qquad\qquad + z_1(-\omega_{y_1} s_\theta - \omega_{x_1} c_\theta s_\phi - \dot{\theta} s_\theta c_\phi) \end{bmatrix} \qquad (17)$$

Equating like coefficients from eqs. (16) and (17), nine equations result, only three of which are independent, yielding:

$$\dot{\theta} = \omega_{y_2} - \omega_{z_1} s_\phi - \omega_{y_1} c_\phi \qquad (18)$$

$$\omega_{x_2} = -\omega_{z_1} s_\theta c_\phi + \omega_{x_1} c_\theta + \omega_{y_1} s_\theta s_\phi \qquad (19)$$

$$\omega_{z_2} = \omega_{z_1} c_\theta c_\phi + \omega_{x_1} s_\theta - \omega_{y_1} c_\theta s_\phi \qquad (20)$$

Since only one degree of freedom exists for the secondary body, it is to be expected that two of the three secondary body angular rates would be dependent; ω_{x_2} and ω_{z_2} are taken to be the dependent rates, while ω_{y_2} is independent.

From eq. (18), solving for ω_{y_2},

$$\omega_{y_2} = \dot{\theta} + \omega_{y_1} c_\phi + \omega_{z_1} s_\phi \tag{21}$$

Linearizing eqs. (19), (20) and (21),

$$\Delta\omega_{x_2} = \hat{c}_\theta \Delta\omega_{x_1} + \hat{s}_\theta \hat{s}_\phi \Delta\omega_{y_1} - \hat{s}_\theta \hat{c}_\phi \Delta\omega_{z_1} + \Delta\theta\left[-\hat{\omega}_{x_1} \hat{s}_\theta + \hat{\omega}_{y_1} \hat{c}_\theta \hat{s}_\phi - \hat{\omega}_{z_1} \hat{c}_\theta \hat{c}_\phi\right] \tag{19L}$$

$$\Delta\omega_{z_2} = \hat{s}_\theta \Delta\omega_{x_1} - \hat{c}_\theta \hat{s}_\phi \Delta\omega_{y_1} + \hat{c}_\theta \hat{c}_\phi \Delta\omega_{z_1} + \Delta\theta\left[\hat{\omega}_{x_1} \hat{c}_\theta + \hat{\omega}_{y_1} \hat{s}_\theta \hat{s}_\phi - \hat{\omega}_{z_1} \hat{s}_\theta \hat{c}_\phi\right] \tag{20L}$$

$$\Delta\omega_{y_2} = \Delta\dot{\theta} + \hat{c}_\phi \Delta\omega_{y_1} + \hat{s}_\phi \Delta\omega_{z_1} \tag{21L}$$

Differentiating eqs. (19), (20) and (21),

$$\dot{\omega}_{x_2} = c_\theta \dot{\omega}_{x_1} + s_\theta s_\phi \dot{\omega}_{y_1} - s_\theta c_\phi \dot{\omega}_{z_1} + \dot{\theta}\left[-\omega_{x_1} s_\theta + \omega_{y_1} c_\theta s_\phi - \omega_{z_1} c_\theta c_\phi\right] \tag{22}$$

$$\dot{\omega}_{y_2} = \ddot{\theta} + c_\phi \dot{\omega}_{y_1} + s_\phi \dot{\omega}_{z_1} \tag{23}$$

$$\dot{\omega}_{z_2} = s_\theta \dot{\omega}_{x_1} - c_\theta s_\phi \dot{\omega}_{y_1} + c_\theta c_\phi \dot{\omega}_{z_1} + \dot{\theta}\left[\omega_{x_1} c_\theta + \omega_{y_1} s_\theta s_\phi - \omega_{z_1} s_\theta c_\phi\right] \tag{24}$$

Linearizing eqs. (23) and (24),

$$\Delta\dot{\omega}_{y_2} = \Delta\ddot{\theta} + \hat{c}_\phi \Delta\dot{\omega}_{y_1} + \hat{s}_\phi \Delta\dot{\omega}_{z_1} \tag{23L}$$

$$\Delta\dot{\omega}_{z_2} = \Delta\dot{\omega}_{x_1}\left[\hat{s}_\theta\right] + \Delta\omega_{x_1}\left[\hat{\dot{\theta}}\hat{c}_\theta\right] + \Delta\dot{\omega}_{y_1}\left[-\hat{c}_\theta\hat{s}_\phi\right] + \Delta\omega_{y_1}\left[\hat{\dot{\theta}}\hat{s}_\theta\hat{s}_\phi\right] + \Delta\dot{\omega}_{z_1}\left[\hat{c}_\theta\hat{c}_\phi\right] \quad (24L)$$

$$+ \Delta\omega_{z_1}\left[-\hat{\dot{\theta}}\hat{s}_\theta\hat{c}_\phi\right] + \Delta\dot{\theta}\left[\hat{\omega}_{x_1}\hat{c}_\theta + \hat{\omega}_{y_1}\hat{s}_\theta\hat{s}_\phi - \hat{\omega}_{z_1}\hat{s}_\theta\hat{c}_\phi\right]$$

$$+ \Delta\theta\left[\hat{c}_\theta\hat{\omega}_{x_1} + \hat{s}_\theta\hat{s}_\phi\hat{\omega}_{y_1} - \hat{s}_\theta\hat{c}_\phi\hat{\omega}_{z_1} - \hat{\dot{\theta}}\hat{s}_\theta\hat{\omega}_{x_1} + \hat{\dot{\theta}}\hat{c}_\theta\hat{s}_\phi\hat{\omega}_{y_1} - \hat{\dot{\theta}}\hat{c}_\theta\hat{c}_\phi\hat{\omega}_{z_1}\right]$$

* * * * * * * * * * * * * *

The following simplifying assumptions will now be made, providing the initial or nominal configuration about which the linearization occurs:

$$\hat{\theta}_p = \hat{\theta}_r = 0 \qquad \left\{\theta_y\right\}_0 = \hat{\theta}_y, \qquad \left\{\theta\right\}_0 = \hat{\theta}, \qquad \left\{\phi\right\}_0 = \hat{\phi},$$

$$\hat{\dot{\theta}}_p = \hat{\dot{\theta}}_r = \hat{\dot{\theta}}_y = \hat{\dot{\theta}} = \dot{\phi} = 0 \qquad \hat{\eta} = \omega_0$$

$$\hat{\ddot{\theta}}_p = \hat{\ddot{\eta}} = \hat{\ddot{\theta}}_r = \hat{\ddot{\theta}}_y = \hat{\ddot{\theta}} = 0$$

Under these assumptions, the following reductions occur:

$$\begin{bmatrix} \Delta T_{x_1} \\ \Delta T_{y_1} \\ \Delta T_{z_1} \end{bmatrix} = 3\omega_0^2 \begin{bmatrix} 0 \\ (I_{xx_1} - I_{zz_1})(\hat{s}_y\,\Delta\theta_p + \hat{c}_y\,\Delta\theta_r) \\ (I_{yy_1} - I_{xx_1})(-\hat{c}_y\,\Delta\theta_p + \hat{s}_y\,\Delta\theta_r) \end{bmatrix} \qquad (8L)'$$

$$\begin{bmatrix} \Delta T_{x_2} \\ \Delta T_{y_2} \\ \Delta T_{z_2} \end{bmatrix} = 3\omega_0^2 I_{yy_2} \begin{bmatrix} 0 \\ (\hat{s}_\theta^2 - \hat{c}_\theta^2)\left[\Delta\theta + (\hat{s}_\phi\hat{c}_y + \hat{c}_\phi\hat{s}_y)\,\Delta\theta_p + (\hat{c}_\phi\hat{c}_y - \hat{s}_\phi\hat{s}_y)\,\Delta\theta_r\right] \\ \hat{c}_\theta\left[(\hat{s}_\phi\hat{s}_y - \hat{c}_\phi\hat{c}_y)\,\Delta\theta_p + (\hat{c}_\phi\hat{s}_y + \hat{s}_\phi\hat{c}_y)\,\Delta\theta_r\right] \end{bmatrix} = \qquad (10L)'$$

$$3\omega_0^2 I_{yy_2} \begin{bmatrix} 0 \\ (\hat{s}_\theta^2 - \hat{c}_\theta^2)\left[\Delta\theta + \hat{B}\,\Delta\theta_p - \hat{A}\,\Delta\theta_r\right] \\ \hat{c}_\theta\left[\hat{A}\,\Delta\theta_p + \hat{B}\,\Delta\theta_r\right] \end{bmatrix}, \qquad \text{where } \hat{A} = (\hat{s}_\phi\hat{s}_y - \hat{c}_\phi\hat{c}_y)$$

$$\hat{B} = (\hat{c}_\phi\hat{s}_y + \hat{s}_\phi\hat{c}_y)$$

$$\begin{bmatrix} \hat{\omega}_{x_1} \\ \hat{\omega}_{y_1} \\ \hat{\omega}_{z_1} \end{bmatrix} = \omega_0 \begin{bmatrix} 0 \\ \hat{s}_y \\ \hat{c}_y \end{bmatrix}$$

$$\begin{bmatrix} \Delta\omega_{x_1} \\ \Delta\omega_{y_1} \\ \Delta\omega_{z_1} \end{bmatrix} = \begin{bmatrix} -\omega_0 \Delta\theta_r + \Delta\dot{\theta}_y \\ \hat{s}_y \Delta\dot{\theta}_p + \hat{c}_y \Delta\dot{\theta}_r + \omega_0 \hat{c}_y \Delta\theta_y \\ \hat{c}_y \Delta\dot{\theta}_p - \hat{s}_y \Delta\dot{\theta}_r - \omega_0 \hat{s}_y \Delta\theta_y \end{bmatrix}$$

$$\begin{bmatrix} \dot{\hat{\omega}}_{x_1} \\ \dot{\hat{\omega}}_{y_1} \\ \dot{\hat{\omega}}_{z_1} \end{bmatrix} = \begin{bmatrix} 0 \\ 0 \\ 0 \end{bmatrix}$$

$$\begin{bmatrix} \Delta\dot{\omega}_{x_1} \\ \Delta\dot{\omega}_{y_1} \\ \Delta\dot{\omega}_{z_1} \end{bmatrix} = \begin{bmatrix} -\omega_0 \Delta\dot{\theta}_r + \Delta\ddot{\theta}_y \\ \hat{s}_y \Delta\ddot{\theta}_p + \hat{c}_y \Delta\ddot{\theta}_r + \dot{\omega}_0 \hat{c}_y \Delta\dot{\theta}_y \\ \hat{c}_y \Delta\ddot{\theta}_p - \hat{s}_y \Delta\ddot{\theta}_r - \omega_0 \hat{s}_y \Delta\dot{\theta}_y \end{bmatrix}$$

$$\begin{bmatrix} \hat{\omega}_{x_2} \\ \hat{\omega}_{y_2} \\ \hat{\omega}_{z_2} \end{bmatrix} = \omega_0 \begin{bmatrix} \hat{s}_\theta (\hat{s}_\phi \hat{s}_y - \hat{c}_\phi \hat{c}_y) \\ (\hat{c}_\phi \hat{s}_y + \hat{s}_\phi \hat{c}_y) \\ -\hat{c}_\theta (\hat{s}_\phi \hat{s}_y - \hat{c}_\phi \hat{c}_y) \end{bmatrix} = \omega_0 \begin{bmatrix} \hat{s}_\theta \hat{A} \\ \hat{B} \\ -\hat{c}_\theta \hat{A} \end{bmatrix}$$

$$\Delta\dot{\omega}_{z_2} = \hat{s}_\theta \Delta\dot{\omega}_{x_1} - \hat{c}_\theta \hat{s}_\phi \Delta\dot{\omega}_{y_1} + \hat{c}_\theta \hat{c}_\phi \Delta\dot{\omega}_{z_1} + \Delta\dot{\theta} \left[\hat{\omega}_{x_1} \hat{c}_\theta + \hat{\omega}_{y_1} \hat{s}_\theta \hat{s}_\phi - \hat{\omega}_{z_1} \hat{s}_\theta \hat{c}_\phi \right]$$

$$= \hat{s}_\theta \Delta\dot{\omega}_{x_1} - \hat{c}_\theta \hat{s}_\phi \Delta\dot{\omega}_{y_1} + \hat{c}_\theta \hat{c}_\phi \Delta\dot{\omega}_{z_1} + \Delta\dot{\theta} \left[\omega_0 \hat{s}_\theta \hat{A} \right]$$

$$(24L)'$$

From eqs. (7x) and (10x), $Q_{x_2} = T_{x_2} = 0$, $\therefore$

$$\hat{Q}_{x_2} = 0 \tag{7x}'$$

From eq. (7z), $Q_{z_2} = T_{z_2} - I_{yy_2} (\dot{\omega}_{z_2} + \omega_{x_2} \omega_{y_2})$.

But from eq. (10z),

$$\hat{T}_{z_2} = 0 \text{ and from eqs. (24) and (14)',} \tag{10z}'$$

$$\hat{\omega}_{z_2} = 0. \text{ Finally, using eqs. (19)' and (21)',} \tag{24}'$$

$$\hat{Q}_{z_2} = -I_{yy_2} \omega_0^2 \hat{s}_\theta AB \tag{7z}'$$

From eqs. (7Lx) and (10L);

$$\Delta Q_{x_2} = 0 \tag{7Lx}'$$

From eq. (7Lz), $\Delta Q_{z_2} = \Delta T_{z_2} - I_{yy_2} (\Delta \dot{\omega}_{z_2} + \hat{\omega}_{x_2} \Delta \omega_{y_2} + \hat{\omega}_{y_2} \Delta \omega_{x_2})$, or,

$$
\begin{aligned}
\frac{\Delta Q_{z_2}}{I_{yy_2}} = &\ \Delta\theta_p \left[D^2 \left\{ \hat{c}_\theta \hat{A} \right\} + D \left\{ -2\omega_0 \hat{s}_\theta \hat{A}\hat{B} \right\} + \left\{ 3\omega_0^2 \hat{c}_\theta \hat{A} \right\} \right] \\
&+ \Delta\theta_r \left[D^2 \left\{ \hat{c}_\theta \hat{B} \right\} + D \left\{ \omega_0 \hat{s}_\theta (\hat{A}^2 - \hat{B}^2 + 1) \right\} + \left\{ 4\omega_0^2 \hat{c}_\theta \hat{B} \right\} \right] \\
&+ \Delta\theta_y \left[D^2 \left\{ -s\hat{\theta} \right\} + \left\{ \omega_0^2 \hat{s}_\theta (\hat{A}^2 - \hat{B}^2) \right\} \right] \\
&+ \Delta\theta \left[D \left\{ -2\omega_0 \hat{s}_\theta \hat{A} \right\} + \left\{ -\omega_0^2 \hat{c}_\theta \hat{A}\hat{B} \right\} \right]
\end{aligned}
\tag{7Lz}'
$$

$$\frac{\Delta Q_{x_1}}{I_{yy_2}} = \Delta\theta_p \left[D^2\left\{\hat{s}_\theta \hat{c}_\theta \hat{A}\right\} + D\left\{-2\omega_0 \hat{s}_\theta^2 \hat{A}\hat{B}\right\} + \left\{3\omega_0^2 \hat{s}_\theta \hat{c}_\theta \hat{A}\right\} \right]$$

$$+ \Delta\theta_r \left[D^2\left\{\hat{s}_\theta \hat{c}_\theta \hat{B}\right\} + D\left\{\omega_0 \hat{s}_\theta^2 (\hat{A}^2 - \hat{B}^2 + 1)\right\} + \left\{4\omega_0^2 \hat{s}_\theta \hat{c}_\theta \hat{B}\right\} \right]$$

$$+ \Delta\theta_y \left[D^2\left\{-\hat{s}_\theta^2\right\} + D\left\{0\right\} + \left\{\omega_0^2 \hat{s}_\theta^2 (\hat{A}^2 - \hat{B}^2)\right\} \right] \qquad (12Lx)'$$

$$+ \Delta\theta \left[D\left\{-2\omega_0 \hat{s}_\theta^2 \hat{A}\right\} + \left\{-2\omega_0^2 \hat{s}_\theta \hat{c}_\theta \hat{A}\hat{B}\right\} \right]$$

$$\frac{\Delta Q_{y_1}}{I_{yy_2}} = \Delta\theta_p \left[D^2\left\{-\hat{c}_\theta^2 \hat{s}_\phi \hat{A}\right\} + D\left\{2\omega_0 \hat{s}_\theta \hat{c}_\theta \hat{s}_\phi \hat{A}\hat{B}\right\} + \left\{-3\omega_0^2 \hat{c}_\theta^2 \hat{s}_\phi \hat{A}\right\} \right]$$

$$+ \Delta\theta_r \left[D^2\left\{-\hat{c}_\theta^2 \hat{s}_\phi \hat{B}\right\} + D\left\{-\omega_0 \hat{s}_\theta \hat{c}_\theta \hat{s}_\phi (\hat{A}^2 - \hat{B}^2 + 1)\right\} + \left\{-4\omega_0^2 \hat{c}_\theta^2 \hat{s}_\phi \hat{B}\right\} \right]$$

$$+ \Delta\theta_y \left[D^2\left\{\hat{s}_\theta \hat{c}_\theta \hat{s}_\phi\right\} + \left\{-\omega_0^2 \hat{s}_\theta \hat{c}_\theta \hat{s}_\phi (\hat{A}^2 - \hat{B}^2)\right\} \right] \qquad (12Ly)'$$

$$+ \Delta\theta \left[D\left\{2\omega_0 \hat{s}_\theta \hat{c}_\theta \hat{s}_\phi \hat{A} + \frac{b\hat{c}_\phi}{I_{yy_2}}\right\} + \left\{-\omega_0^2 \hat{s}_\phi \hat{A}\hat{B}(\hat{s}_\theta^2 - \hat{c}_\theta^2) + \frac{k\hat{c}_\phi}{I_{yy_2}}\right\} \right]$$

$$\frac{\Delta Q_{z_1}}{I_{yy_2}} = \Delta\theta_p \left[D^2\left\{\hat{c}_\theta^2 \hat{c}_\phi \hat{A}\right\} + D\left\{-2\omega_0 \hat{s}_\theta \hat{c}_\theta \hat{c}_\phi \hat{A}\hat{B}\right\} + \left\{3\omega_0^2 \hat{c}_\theta^2 \hat{c}_\phi \hat{A}\right\} \right]$$

$$+ \Delta\theta_r \left[D^2\left\{\hat{c}_\theta^2 \hat{c}_\phi \hat{B}\right\} + D\left\{\omega_0 \hat{s}_\theta \hat{c}_\theta \hat{c}_\phi (\hat{A}^2 - \hat{B}^2 + 1)\right\} + \left\{4\omega_0^2 \hat{c}_\theta^2 \hat{c}_\phi \hat{B}\right\} \right]$$

$$+ \Delta\theta_y \left[D^2\left\{-\hat{s}_\theta \hat{c}_\theta \hat{c}_\phi\right\} + \left\{\omega_0^2 \hat{s}_\theta \hat{c}_\theta \hat{c}_\phi (\hat{A}^2 - \hat{B}^2)\right\} \right] \qquad (12Lz)'$$

$$+ \Delta\theta \left[D\left\{-2\omega_0 \hat{s}_\theta \hat{c}_\theta \hat{c}_\phi \hat{A} + \frac{b\hat{s}_\phi}{I_{yy_2}}\right\} + \left\{\omega_0^2 \hat{c}_\phi \hat{A}\hat{B}(\hat{s}_\theta^2 - \hat{c}_\theta^2) + \frac{k\hat{s}_\phi}{I_{yy_2}}\right\} \right]$$

where D is the Differentiation operator.

Let $\tau = \omega_0 t,\ \dfrac{d}{d\tau} = \dfrac{1}{\omega_0}\ \dfrac{d}{dt}\ ;\ \dfrac{d^2}{d\tau^2} = \dfrac{1}{\omega_0^2}\ \dfrac{d^2}{dt^2}\ .$

Denote $(\Delta\theta_p,\ \Delta\theta_r,\ \Delta\theta_y,\ \Delta\theta)$ by $(x_1,\ x_2,\ x_3,\ x_4)$ respectively; divide by I_{yy_2}. Substitution in eqs. (5L) and (7Ly) yields the four eqs. :

$$x_1 \left[D^2 \left\{ s_\theta c_\theta A \right\} + D \left\{ -2 s_\theta^2 AB - s_{2y} \frac{(I_{zz_1} - I_{yy_1})}{I_{yy_2}} \right\} + \left\{ 3 s_\theta c_\theta A \right\} \right]$$

$$+ x_2 \left[D^2 \left\{ s_\theta c_\theta B \right\} + D \left\{ s_\theta^2 (A^2 - B^2 + 1) + \frac{I_{xx_1}}{I_{yy_2}} + \frac{(I_{zz_1} - I_{yy_1})}{I_{yy_2}} (s_y^2 - c_y^2) \right\} + \left\{ 4 s_\theta c_\theta B \right\} \right]$$

$$\text{(5Lx)}{-}(1)$$

$$+ x_3 \left[D^2 \left\{ -s_\theta^2 - \frac{I_{xx_1}}{I_{yy_2}} \right\} + D \left\{ 0 \right\} + \left\{ s_\theta^2 (A^2 - B^2) + \frac{(I_{zz_1} - I_{yy_1})}{I_{yy_2}} (s_y^2 - c_y^2) \right\} \right]$$

$$+ x_4 \left[D^2 \left\{ 0 \right\} + D \left\{ -2 s_\theta^2 A \right\} + \left\{ -s_{2\theta} AB \right\} \right] = 0$$

$$x_1 \left[D^2 \left\{ -c_\theta^2 s_\phi A - \frac{I_{yy_1}}{I_{yy_2}} s_y \right\} + D \left\{ s_{2\theta} s_\phi AB \right\} + \left\{ 3 s_y \frac{(I_{xx_1} - I_{zz_1})}{I_{yy_2}} - 3 c_\theta^2 s_\phi A \right\} \right]$$

$$+ x_2 \left[D^2 \left\{ -c_\theta^2 s_\phi B - \frac{I_{yy_1}}{I_{yy_2}} c_y \right\} + D \left\{ -s_\theta c_\theta s_\phi (A^2 - B^2 + 1) \right\} + \right.$$

$$\left. \left\{ 4 c_y \frac{(I_{xx_1} - I_{zz_1})}{I_{yy_2}} - 4 c_\theta^2 s_\phi B \right\} \right]$$

$$\text{(5Ly)}{-}(2)$$

$$+ x_3 \left[D^2 \left\{ s_\theta c_\theta s_\phi \right\} + D \left\{ -c_y \left(\frac{I_{xx_1} + I_{yy_1} - I_{zz_1}}{I_{yy_2}} \right) \right\} + \left\{ -s_\theta c_\theta s_\phi (A^2 - B^2) \right\} \right]$$

$$+ x_4 \left[D^2 \left\{ 0 \right\} + D \left\{ s_{2\theta} s_\phi A + \frac{bc_\phi}{\omega_0 I_{yy_2}} \right\} + \left\{ -s_\phi (s_\theta^2 - c_\theta^2) AB + \frac{kc_\phi}{\omega_0^2 I_{yy_2}} \right\} \right] = 0$$

$$x_1 \left[D^2 \left\{ c_\theta^2 c_\phi A - \frac{I_{zz_1}}{I_{yy_2}} c_y \right\} + D \left\{ -s_{2\theta} c_\phi AB \right\} + \left\{ 3c_\theta^2 c_\phi A - 3c_y \left(\frac{I_{yy_1} - I_{xx_1}}{I_{yy_2}} \right) \right\} \right]$$

$$+x_2 \left[D^2 \left\{ c_\theta^2 c_\phi B + \frac{I_{zz_1}}{I_{yy_2}} s_y \right\} + D \left\{ s_\theta c_\theta c_\phi (A^2 - B^2 + 1) \right\} + \left\{ 4c_\theta^2 c_\phi B + 4s_y \left(\frac{I_{yy_1} - I_{xx_1}}{I_{yy_2}} \right) \right\} \right]$$

$$\text{(5Lz)}\!\!\text{(3)}$$

$$+x_3 \left[D^2 \left\{ -s_\theta c_\theta c_\phi \right\} + D \left\{ s_y \left(\frac{I_{xx_1} - I_{yy_1} + I_{zz_1}}{I_{yy_2}} \right) \right\} + \left\{ s_\theta c_\theta c_\phi (A^2 - B^2) \right\} \right]$$

$$+x_4 \left[D^2 \{0\} + D \left\{ -s_{2\theta} c_\phi A + \frac{b s_\phi}{I_{yy_2} \omega_0} \right\} + \left\{ c_\phi (s_\theta^2 - c_\theta^2) AB + \frac{k s_\phi}{I_{yy_2} \omega_0^2} \right\} \right] = 0$$

$$x_1 \left[D^2 \{-B\} + D \left\{ -s_{2\theta} A^2 \right\} + \left\{ 3(s_\theta^2 - c_\theta^2) B \right\} \right]$$

$$+x_2 \left[D^2 \{A\} + D \left\{ -s_{2\theta} AB \right\} + \left\{ -4(s_\theta^2 - c_\theta^2) A \right\} \right]$$

$$\text{(7Ly)}\!\!\text{(4)}$$

$$+x_3 \left[D^2 \{0\} + D \left\{ 2s_\theta^2 A \right\} + \left\{ -s_{2\theta} AB \right\} \right]$$

$$+x_4 \left[D^2 \{-1\} + D \left\{ -\frac{b}{I_{yy_2} \omega_0} \right\} + \left\{ (s_\theta^2 - c_\theta^2)(A^2 + 3) - \frac{k}{I_{yy_2} \omega_0^2} \right\} \right] = 0$$

Let $d_{ij} \equiv a_{ij} D^2 + b_{ij} D + c_{ij}$, where a_{ij} denotes the coefficient of D^2 in eq. i,

variable x_j. Then a non-trivial solution exists if f the determinant $\left| d_{ij} \right| = 0$, which con-

dition yields an eighth-degree polynomial equation in D, the characteristic equation which

was sought.

APPENDIX C

MAXIMUM ALLOWABLE ANGULAR RATE

APPENDIX C

MAXIMUM ALLOWABLE ANGULAR RATE

The coordinate systems utilized in the analysis are shown in Figure 1. The $\overrightarrow{xyz}$ coordinate system is the main body coordinate system and the $\overrightarrow{x_s y_s z_s}$ coordinate system is the secondary body coordinate system. The two coordinate systems are related by a fixed rotation α_s about x axis, and a time dependent angle γ_s about the displaced z axis (the z_s axis).
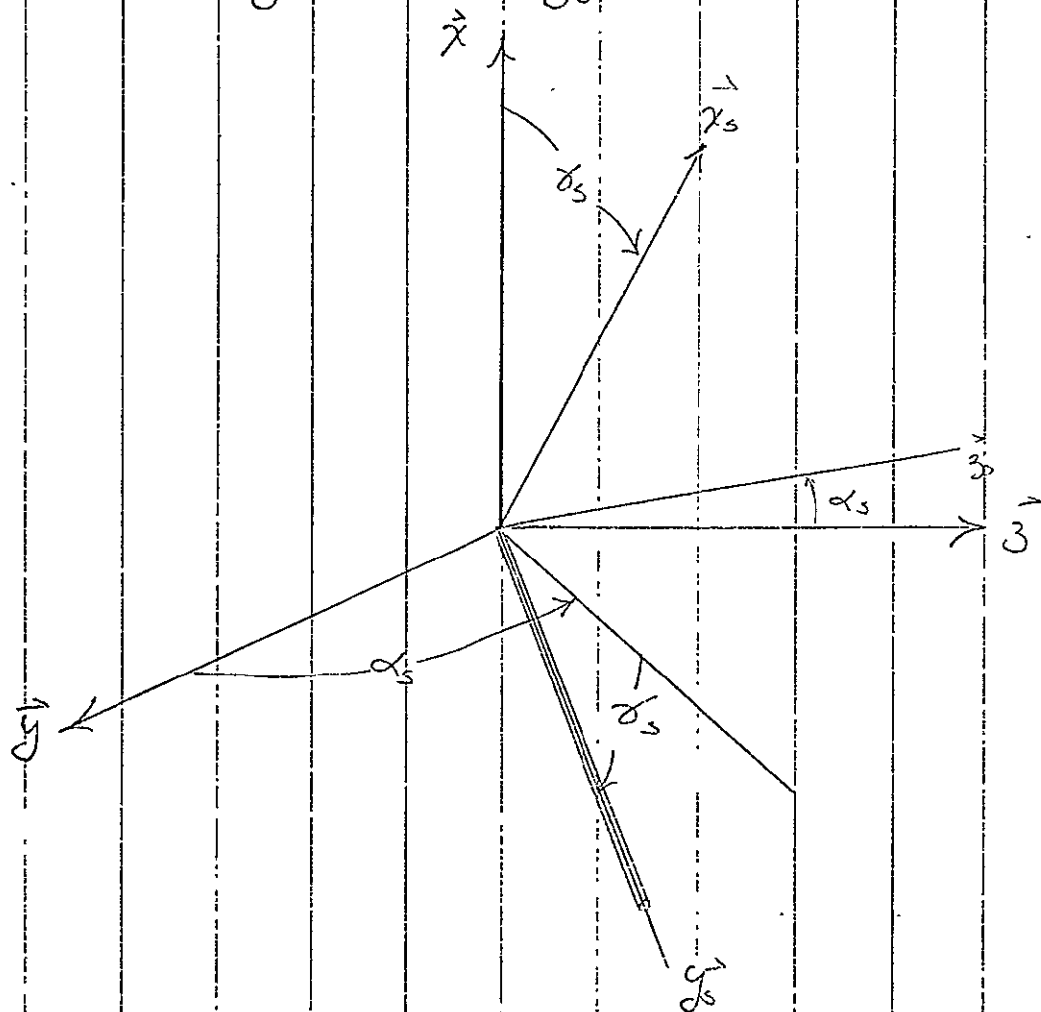
Figure 1 Primary Coordinate System

The rate of rotation of the $\overrightarrow{xyz}$ coordinate system is

$$\vec{\omega} = \omega_x \vec{x} + \omega_y \vec{y} + \omega_z \vec{z}$$

C-1

THE RATE OF ROTATION OF THE $\overrightarrow{x_s y_s z_s}$ COORDINATE SYSTEM IS

$$\vec{\omega}_s = [A][\vec{\omega}] + \dot{\gamma}\,\vec{z}_s \qquad (2)$$

WHERE

$$\begin{aligned}
a_{11} &= \cos\gamma \\
a_{12} &= \sin\gamma\,\cos\alpha \\
a_{13} &= \sin\alpha\,\sin\gamma \\
a_{21} &= -\sin\gamma \\
a_{22} &= \cos\gamma\,\cos\alpha \\
a_{23} &= \sin\alpha\,\cos\gamma \\
a_{31} &= 0 \\
a_{32} &= -\sin\alpha \\
a_{33} &= \cos\alpha
\end{aligned} \qquad (3)$$

EULER'S DYNAMICAL EQUATIONS OF MOTION FOR THE SECONDARY BODY (WITH NO PRODUCTS OF INERTIA) ARE

$$\begin{aligned}
T_{xs} &= I_{xxs}\,\dot{\omega}_{xs} + \omega_{ys}\omega_{zs}\left(I_{zzs} - I_{yys}\right) \\
T_{ys} &= I_{yys}\,\dot{\omega}_{ys} + \omega_{xs}\omega_{zs}\left(I_{xxs} - I_{zzs}\right) \\
T_{zs} &= I_{zzs}\,\dot{\omega}_{zs} + \omega_{ys}\omega_{xs}\left(I_{yys} - I_{xxs}\right)
\end{aligned} \qquad (4)$$

WHERE I = MOMENT OF INERTIA (SLUG-FT^2)

THE SECONDARY BODY IS CONSTRAINED ABOUT x_s AND y_s BY THE HINGE, AND ONLY MOTION ABOUT $\vec{z}_s$ IS IMPORTANT. NOTING THAT $I_{yys} \approx 0$ AND $I_{xxs} = I_{zzs}$

$$T_{zs} = I_{zz}\,\dot{\omega}_{zs} - \omega_{ys}\omega_{xs}\,I_{xxs} \qquad (5)$$

IT WILL BE ASSUMED THAT $\omega_x,\ \omega_y,$ AND ω_z ARE CONSTANTS.

EXPANDING EQUATION (2)

$$\omega_{XS} = \omega_x \cos\gamma + \omega_y \sin\gamma \cos\alpha + \omega_3 \sin\alpha \sin\gamma$$

$$\omega_{YS} = -\omega_y \sin\gamma + \omega_y \cos\alpha \cos\gamma + \omega_3 \sin\alpha \cos\gamma$$

$$\omega_{3S} = -\omega_y \sin\alpha + \omega_3 \cos\alpha + \dot{\gamma}$$

(6)

DIFFERENTIATING $\dot{\omega}_{3S}$

$$\dot{\omega}_{3S} = \ddot{\gamma}$$

(7)

SUBSTITUTING INTO EQUATION (5)

$$T_{3S} = I_{033}\ddot{\gamma} - (-\omega_x \sin\gamma + \omega_y \cos\alpha\cos\gamma + \omega_3 \sin\alpha\cos\gamma) \times$$

$$(\omega_x \cos\gamma + \omega_y \sin\gamma\cos\alpha + \omega_3 \sin\alpha\sin\gamma)I_{033}$$

(8)

THE TORQUES ACTING ON $\vec{3S}$ AXIS ARE

$$T_{3S} = -k\gamma - b\dot{\gamma} + T_D$$

(9)

WHERE K = SPRING CONSTANT OF DAMPER SPRING

b = DAMPING COEFFICIENT OF DAMPER

T_D = DISTURBANCE TORQUE

SINCE THE SPRING TORQUE IS RESTORING, AND THE "DYNAMICAL TORQUE" IS UPSETTING, THERE IS LIKELY TO BE A STABLE POSITION γ_S. LINEARIZING ABOUT γ_S

$$\sin\gamma = \sin(\gamma_S + \gamma_R) = \sin\gamma_S + \gamma_R \cos\gamma_S$$

(10)

$$\cos\gamma = \cos(\gamma_S + \gamma_R) = \cos\gamma_S - \gamma_R \sin\gamma_S$$

(11)

C-3

SUBSTITUTING INTO EQUATIONS (8) AND (9)

$$-k\gamma_R - k\gamma_S - b\dot{\gamma} + T_D = I_{33}\ddot{\gamma} - (-\omega_x \sin\gamma_S - \omega_x \gamma_R \cos\gamma_S$$

$$+ \omega_y \cos\alpha \cos\gamma_S - \gamma_R \omega_y \cos\alpha \sin\gamma_S + \omega_z \sin\alpha \cos\gamma_S$$

$$- \gamma_R \omega_z \sin\alpha \sin\gamma_S)(\omega_x \cos\gamma_S - \gamma_R \omega_x \sin\gamma_S + \omega_y \cos\alpha \sin\gamma_S$$

$$+ \omega_y \gamma_R \cos\alpha \cos\gamma_S + \omega_z \sin\alpha \sin\gamma_S + \omega_z \gamma_R \sin\alpha \cos\gamma_S)I_{33} \quad (\cdots)$$

COLLECTING TERMS AND SETTING $\dot{\gamma} = \ddot{\gamma} = \gamma_R = 0$ TO FIND STATIC EQUILIBRIUM (ASSUMING $T_D = 0$).

$$-k\gamma_S = -(-\omega_x \sin\gamma_S + \omega_y \cos\alpha \cos\gamma_S + \omega_z \sin\alpha \cos\gamma_S) \times$$

$$(\omega_x \cos\gamma_S + \omega_y \cos\alpha \sin\gamma_S + \omega_z \sin\alpha \sin\gamma_S)I_{33} \quad (13)$$

ASSUMING EACH RATE IS APPLIED INDEPENDENTLY

$$-k\gamma_{S_1} = \frac{1}{2}\omega_x^2 \sin 2\gamma_S \quad (14)$$

$$+k\gamma_{S_2} = +\frac{1}{2}\omega_y^2 \cos^2\alpha \sin 2\gamma_S \quad (15)$$

$$+k\gamma_{S_3} = +\frac{1}{2}\omega_z^2 \sin^2\alpha \sin 2\gamma_S \quad (16)$$

EQUATION 14 HAS $\gamma_S = 0$ AS ITS ONLY SOLUTION (OF INTEREST) AFTER LINEARIZING, THE DYNAMIC EQUATIONS OF MOTION BECOME

$$-k\gamma_R - b\dot{\gamma}_R + T_D = I_{33}\ddot{\gamma}_R - \gamma_R I_{33}\left[(-\omega_x \sin\gamma_S + \omega_y \cos\alpha \cos\gamma_S\right.$$

$$+ \omega_z \sin\alpha \cos\gamma_S)^2 - (\omega_x \cos\gamma_S + \omega_y \cos\alpha \sin\gamma_S + \omega_z \sin\gamma_S \sin\alpha)^2 \quad (\cdots)$$

NON DIMENSIONALIZING ON ORBITAL RATE, $\dot{\theta}$, AND ASSUMING EACH
RATE IS APPLIED INDEPENDENTLY

$$\frac{T_D}{I_{33S}\dot{\theta}^2} = \ddot{\gamma}_{R_x} + \frac{b}{I_{33S}\dot{\theta}}\dot{\gamma}_{R_x} + \gamma_{R_x}\left[\frac{k}{I_{33S}\dot{\theta}^2} + \frac{\omega_x^2}{2\dot{\theta}^2}\cos 2\gamma_s\right] \qquad (18)$$

$$\frac{T_D}{I_{33S}\dot{\theta}^2} = \ddot{\gamma}_{R_y} + \frac{b}{I_{33S}\dot{\theta}}\ddot{\gamma}_{R_y} + \gamma_{R_y}\left[\frac{k}{I_{33S}\dot{\theta}^2} - \frac{\omega_y^2}{\dot{\theta}^2}\cos^2\alpha\,\cos 2\gamma_s\right] \qquad (19)$$

$$\frac{T_D}{I_{33S}\dot{\theta}^2} = \ddot{\gamma}_{R_3} + \frac{b}{I_{33S}\dot{\theta}}\dot{\gamma}_{R_3} + \gamma_{R_3}\left[\frac{k}{I_{33S}\dot{\theta}^2} - \frac{\omega_3^2}{\dot{\theta}^2}\sin^2\alpha\,\cos 2\gamma_s\right] \qquad (20)$$

THE EXPRESSIONS IN BRACKETS ARE EQUIVALENT SPRING
CONSTANTS.

THE ACTUAL DAMPER TO BE USED ON ATS, IS LIMITED IN TRAVEL
TO 45°. HENCE RATES WHICH WOULD CAUSE γ_s TO EXCEED
45° MERELY "PIN" THE DAMPER. AT THIS POINT, THE TORQUES
WHICH PIN THE DAMPER ARE (FROM EQUATIONS (2) AND (3))

$$\frac{T_{Dy}}{I_{33S}\dot{\theta}^2} = \frac{1}{2}\frac{\omega_y^2}{\dot{\theta}^2}\cos^2\alpha - \frac{k(.785)}{I_{33S}\dot{\theta}^2}$$

$$\frac{T_{D3}}{I_{33S}\dot{\theta}^2} = \frac{1}{2}\frac{\omega_3^2}{\dot{\theta}^2}\sin^2\alpha - \frac{k(.785)}{I_{33S}\dot{\theta}^2}$$

NOTE FROM EQUATIONS (14) AND (18), ω_x MERELY INCREASES THE
SPRING CONSTANT.

APPENDIX D

GRAVITY GRADIENT POTENTIAL ENERGY

THE GRAVITY GRADIENT POTENTIAL ENERGY WILL BE DERIVED USING THE APPROACH GIVEN IN REFERENCE 1, BUT INCLUDING PRODUCTS OF INERTIA.

THE $\overrightarrow{xyz}$ COORDINATE SYSTEM (FIGURE 1.) IS ASSUMED LOCATED AT THE CENTER OF MASS OF THE BODY AND RIGIDLY ATTACHED TO IT. THE ORBITAL COORDINATE SYSTEM IS THE $\overrightarrow{rpq}$ COORDINATE SYSTEM. THE $\vec{r}$ VECTOR IS ALONG THE LOCAL VERTICAL AND IS POSITIVE DIRECTED OUTWARDS. THE $\vec{q}$ UNIT VECTOR IS NORMAL TO THE ORBIT PLANE AND ORIENTED SUCH THAT IT IS POSITIVE IN THE DIRECTION OF THE ORBITAL ANGULAR VELOCITY. THE $\vec{P}$ UNIT VECTOR FORMS A RIGHT HANDED COORDINATE SYSTEM.
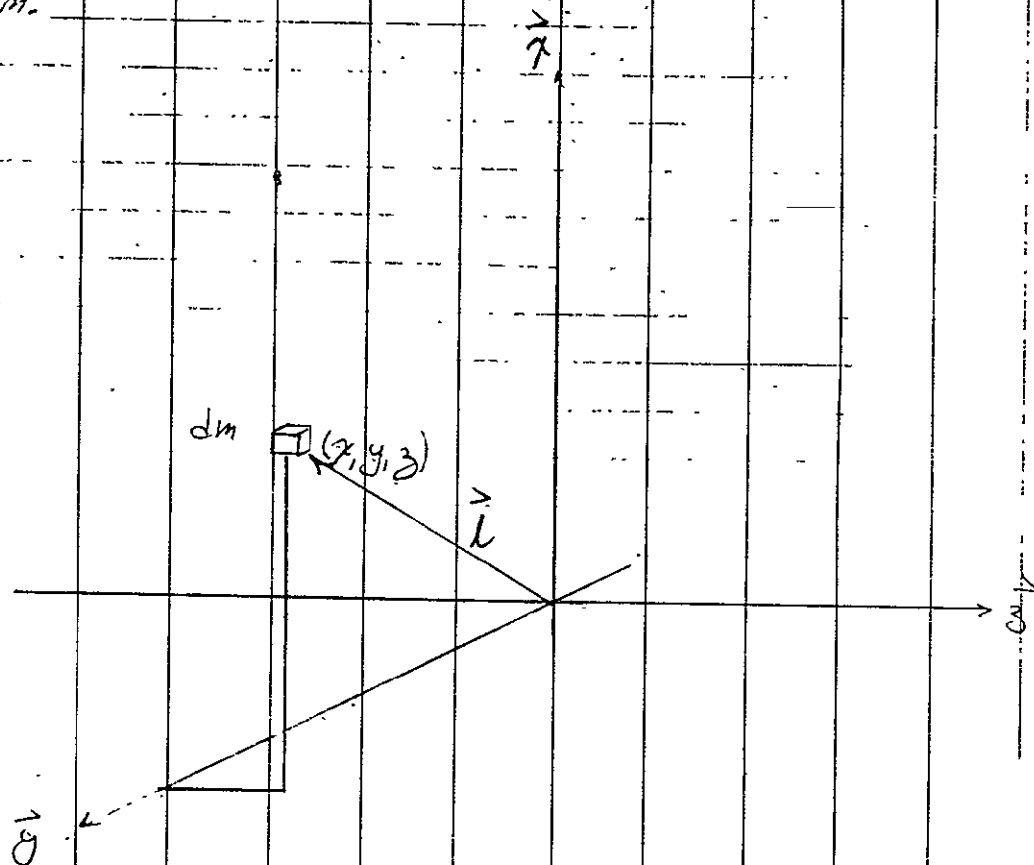
FIGURE 1. BODY COORDINATE SYSTEM

THE RELATIONSHIP BETWEEN $\vec{x}\vec{y}\vec{3}$ AND $\vec{r}\vec{p}\vec{q}$ IS

$$\begin{bmatrix} \vec{x} \\ \vec{y} \\ \vec{3} \end{bmatrix} = [E] \begin{bmatrix} \vec{r} \\ \vec{p} \\ \vec{q} \end{bmatrix} \qquad (1)$$

WHERE

$$e_{11} = \cos\Theta_P \cos\Theta_R$$
$$e_{12} = \sin\Theta_P \cos\Theta_R$$
$$e_{13} = -\sin\Theta_R$$
$$e_{21} = \cos\Theta_P \sin\Theta_R \sin\Theta_Y - \sin\Theta_P \cos\Theta_Y$$
$$e_{22} = \cos\Theta_P \cos\Theta_Y + \sin\Theta_P \sin\Theta_R \sin\Theta_Y$$
$$e_{23} = \cos\Theta_R \sin\Theta_Y$$
$$e_{31} = \sin\Theta_P \sin\Theta_Y + \cos\Theta_P \sin\Theta_R \cos\Theta_Y$$
$$e_{32} = \sin\Theta_P \sin\Theta_R \cos\Theta_Y - \cos\Theta_P \sin\Theta_Y$$
$$e_{33} = \cos\Theta_R \cos\Theta_Y$$

$\qquad (2)$

Θ_P = 1ST EULER ROTATION WHICH IS ABOUT THE $\vec{q}$ AXIS

Θ_R = 2ND EULER ROTATION WHICH IS ABOUT THE DISPLACED $\vec{p}$ AXIS

Θ_Y = 3RD EULER ROTATION ABOUT THE DISPLACED $\vec{r}$ AXIS

THE RELATIONSHIP BETWEEN THE COORDINATE SYSTEM IS SHOWN IN FIGURE 2. NOTE THAT WHEN $\Theta_P = \Theta_R = \Theta_Y$, $\vec{x}$ COINCIDES WITH $\vec{r}$, $\vec{y}$ COINCIDES WITH $\vec{p}$, AND $\vec{3}$ COINCIDES WITH $\vec{q}$.

CONSIDER A POINT MASS , dm, LOCATED AT A DISTANCE $\vec{\ell}$ FROM THE CENTER OF MASS OF THE BODY (FIGURE 1). THE LENGTH, ℓ IS DEFINED BY

$$\vec{\ell} = x\vec{x} + y\vec{y} + 3\vec{3} \qquad (3)$$

THE TOTAL DISTANCE ℓ_R OF THIS POINT MASS FROM THE CENTER OF THE EARTH IS
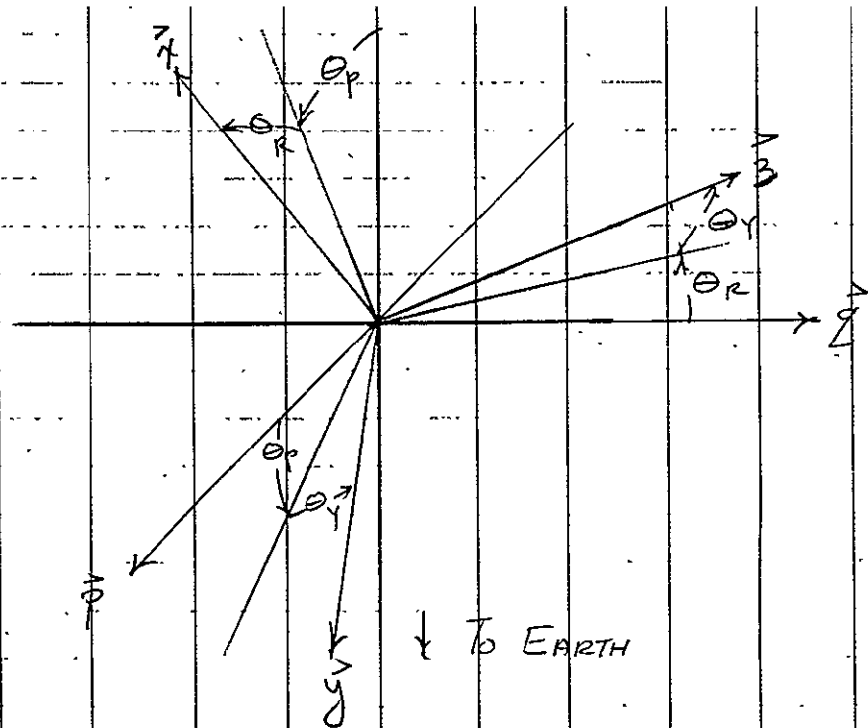
FIGURE 2   COORDINATE SYSTEM RELATIONSHIPS.

$$\vec{l}_R = r\vec{r} + [x, y, z] [E] \begin{bmatrix} \vec{r} \\ \vec{p} \\ \vec{q} \end{bmatrix} \qquad (4)$$

WHERE r = DISTANCE FROM THE CENTER OF THE EARTH
TO THE CENTER OF MASS OF THE SPACECRAFT

EXPANDING,

$$\vec{l}_R = (e_{11}x + e_{21}y + e_{31}z + r)\vec{r}$$

$$+ (e_{12}x + e_{22}y + e_{32}z)\vec{p} \qquad (5)$$

$$+ (e_{13}x + e_{23}y + e_{33}z)\vec{q}$$

THE MAGNITUDE OF $\vec{l}_R$ IS

$$|\vec{l}_R| = l = [x^2 + y^2 + z^2 + r^2 + 2e_{11}xr + 2e_{21}yr + 2e_{31}zr]^{1/2} \qquad (6)$$

AND

$$\frac{1}{r_i} = \frac{1}{r}\left[1 + \frac{x^2+y^2+3^2}{r^2} + 2e_{11}\frac{x}{r} + 2e_{21}\frac{y}{r} + 2e_{31}\frac{3}{r}\right]^{-\frac{1}{2}} \quad (7)$$

SINCE $\frac{x}{r}$ IS SMALL, EQUATION (7) IS OF THE FORM $(1+a)^{-\frac{1}{2}}$, WHERE a IS SMALL. USING THE BINOMIAL THEOREM

$$(1+a)^{-\frac{1}{2}} = 1 - \frac{1}{2}a + \frac{3}{8}a^2 - \dashv \quad (8)$$

SUBSTITUTING

$$\frac{1}{r_i} = \frac{1}{r}\left[1 - \frac{x^2+y^2+3^2}{2r^2} - e_{11}\frac{x}{r} - e_{21}\frac{y}{r} - e_{31}\frac{3}{r} + \frac{3}{2}e_{11}^2\frac{x^2}{r^2}\right.$$
$$\left. + \frac{3}{2}e_{21}^2\frac{y^2}{r^2} + \frac{3}{2}e_{31}^2\frac{3^2}{r^2} + 3e_{11}e_{21}\frac{xy}{r^2} + 3e_{11}e_{31}\frac{x3}{r^2}\right.$$
$$\left. + 3e_{21}e_{31}\frac{y3}{r^2} + \dashv\mathrel{} \dashv\mathrel{}\right] \quad (9)$$

TERMS ON THE ORDER OF $\frac{x^3}{r^3}$ HAVE BEEN NEGLECTED.

THE GRAVITATIONAL POTENTIAL ENERGY CAN BE CALCULATED FROM

$$V = \int -\frac{M}{r_i}\,dm \quad (10)$$

WHERE M = UNIVERSAL CONSTANT MULTIPLIED BY THE MASS OF THE EARTH.

COMBINING EQUATIONS (9) AND (10)

$$V = -\frac{M}{r}\left[\int dm - \frac{e_{11}}{r}\int x\,dm - \frac{e_{21}}{r}\int y\,dm - \frac{e_{31}}{r}\int 3\,dm\right.$$
$$\left. + \frac{3e_{11}^2-1}{2r^2}\int x^2\,dm + \frac{3e_{21}^2-1}{2r^2}\int y^2\,dm\right.$$

$$+ \frac{3e_{31}^2 - 1}{2r^2} \int \mathfrak{z}^2 dm + 3\frac{e_{11}e_{21}}{r^2} \int xy \, dm + 3\frac{e_{11}e_{31}}{r^2} \int xy \, dm$$

$$+ \left. \frac{3e_{21}e_{31}}{r^2} \int y\mathfrak{z} \, dm \right]$$

THE FOLLOWING SIMPLIFICATIONS CAN BE MADE

$$\int x \, dm = \int y \, dm = \int \mathfrak{z} \, dm = 0$$

BY CHOICE OF ORIGIN.

$$\int x^2 dm = \frac{I_{yy} + I_{\mathfrak{z}\mathfrak{z}} - I_{xx}}{2}$$

$$\int y^2 dm = \frac{I_{xx} + I_{\mathfrak{z}\mathfrak{z}} - I_{yy}}{2}$$

$$\int \mathfrak{z}^2 dm = \frac{I_{xx} + I_{yy} - I_{\mathfrak{z}\mathfrak{z}}}{2}$$

$$\int xy \, dm = I_{xy}$$

$$\int x\mathfrak{z} \, dm = I_{x\mathfrak{z}}$$

$$\int y\mathfrak{z} \, dm = I_{y\mathfrak{z}}$$

WHERE I = MOMENTS OR PRODUCTS OF INERTIA AS DENOTED BY THE SUBSCRIPTS.

SUBSTITUTING THESE RELATIONSHIPS INTO EQUATION (1)

$$V = -\frac{Mm}{r} - \frac{M}{r^3} \left\{ \frac{I_{xx}}{4} \left[3\left(e_{21}^2 + e_{31}^2 - e_{11}^2\right) - 1 \right] \right.$$

$$+ \frac{I_{yy}}{4}\left[3\left(e_{11}^2 + e_{31}^2 - e_{21}^2\right) - 1\right]$$

$$+ \frac{I_{33}}{4}\left[3\left(e_{11}^2 + e_{21}^2 - e_{31}^2\right) - 1\right]$$

$$+ 3\left(e_{11} e_{21} I_{xy} + e_{11} e_{31} I_{xg} + e_{21} e_{31}' I_{yz}\right)\Big\}$$

THE FIRST TERM, $-\frac{Mm}{r}$, IS THE POTENTIAL ASSOCIATED WITH THE GRAVITY TERM, AND IS IGNORED FOR GRAVITY GRADIENT CONSIDERATIONS.

THE POTENTIAL ENERGY AT $\Theta_P = \Theta_R = \Theta_Y = 0$ IS NOT ZERO AS CAN BE READILY DETERMINED FROM THE EQUATIONS. TO PROVIDE A STANDARD BASE OF REFERENCE, THE POTENTIAL ENERGY AT ZERO ATTITUDE ERROR WILL BE SUBTRACTED FROM THE INSTANTANEOUS POTENTIAL ENER. FOR THE SPACECRAFT WITH $\Theta_P = \Theta_R = \Theta_Y = 0$

$$V = -\frac{M}{r^3}\left\{ -I_{xx} + \frac{I_{yy}}{2} + \frac{I_{33}}{2}\right\}$$

THE DAMPER BOOM WOULD NORMALLY BE HORIZONTAL, WHICH, FOR THE COORDINATE SYSTEM CHOSEN, REQUIRES $\Theta_P = 9$ SINCE $I_{yy} = I_{33}$, Θ_Y IS IRRELEVANT, AND WILL BE SET EQUAL TO ZERO. THE ELEMENTS OF THE e MATRIX WHICH ARE OF INTEREST ARE.

$$e_{11} = 0$$
$$e_{21} = -1$$
$$e_{31} = 0$$

HENCE

$$V_2 = -\frac{M}{r^3}\left\{\frac{I_{xx_2}}{2} - I_{yy_2} + \frac{I_{33_2}}{2}\right\} \tag{16}$$

WHERE SUBSCRIPT 2 DENOTES THE DAMPER

TWO ADDITIONAL TERMS MUST BE ADDED TO THE REFERENCE POTENTIAL ENERGY. THESE TERMS ARE THOSE DUE TO THE KINETIC ENERGY TERM WHICH HAVE BEEN ADDED TO POTENTIAL ENERGY TO OBTAIN A "RELATIVE POTENTIAL ENERGY." FROM PIR 4T22-017, THE TERM FOR THE SPACECRAFT IS

$$V_s = \frac{1}{2} I_{33} \dot{r}^2 \tag{17}$$

FOR THE DAMPER BOOM

$$V_{s_2} = \frac{1}{2} I_{xx_2} \dot{r}^2 \sin^2(\alpha_s) + \frac{1}{2} I_{33_2} \dot{r}^2 \cos^2(\alpha_s) \tag{18}$$

WHERE α_s IS IS DEFINED IN THE MATHEMATICAL MODEL

THE REFERENCE POTENTIAL ENERGY IS OBTAINED BY ADDING EQUATIONS (14), (15), (16,) AND (17). THE SPACECRAFT WILL STABILIZE TO A POSITION OF ZERO POTENTIAL ENERGY IF THIS VALUE IS SUBTRACTED FROM THE POTENTIAL ENERGY CALCULATED BY EQUATIONS (13) AND (27) OF PIR 4T22-017. NOTE THAT IF, BECAUSE OF NONSYMMETRIES, THE STEADY STATE ERRORS HAVE CONSTANT COMPONENTS, THE FINAL VALUE OF THE POTENTIAL ENERGY WILL NOT BE ZERO.

REFERENCE.

GOODMAN, T.P., AND MERCHANT, B.W., "PROBLEMS IN PASSIVE ATTITUDE CONTROL OF COMMUNICATION SATELLITES," G.E DOCUMENT 62GL68, 1962

APPENDIX E

"EXCESS" KINETIC ENERGY OF A RIGID BODY

APPENDIX E

"EXCESS" KINETIC ENERGY OF

A RIGID BODY

The "excess" kinetic energy of a rigid body satellite is defined as the total kinetic energy minus that due to the orbital motion. It is assumed that the geocenter is fixed in inertial space. The analysis is first performed for a rigid body satellite in general, and then the results are expressed in ATS nomenclature. The ATS satellite is assumed to consist of two rigid bodies, connected by a single-axis gimbal. The energy of the system is the sum of the energies of the parts. The energy is of interest only in the early part of the orbit, when the rods are not undergoing extension, retraction, or scissoring. It is assumed that the time rates of change of rod thermal bending are so small as to have negligible effect on the kinetic energy. Therefore, the assumption of rigid bodies is valid for the time of interest.

The vector relations for a general mass element of a body are shown in Figure 1. The vector from the geocenter to the general mass element, dm_i, is conveniently expressed as the sum,

$$\vec{R}_{Ei} = \vec{R}_c + \vec{R}_i, \tag{1}$$

where

$$\vec{R}_c = \bar{R} R_c, \tag{2}$$

and

$$\vec{R_i} = \bar{X}X_i + \bar{Y}Y_i + \bar{Z}Z_i . \tag{3}$$

Here $\bar{X}$, $\bar{Y}$, and $\bar{Z}$ are any orthonormal triad fixed in the body. For any particular mass element, $\vec{R_i}$ is fixed in length, and its time derivative is due only to its rotation. The angular velocity of the satellite, relative to an inertial frame, i

$$\vec{\omega}_s = \bar{X}\omega_{sx} + \bar{Y}\omega_{sy} + \bar{Z}\omega_{sz} . \tag{4}$$

Then

$$\dot{\vec{R_i}} = \vec{\omega}_s \times \vec{R_i} = - \vec{R_i} \times \vec{\omega}_s . \tag{5}$$

In matrix form,

$$\begin{bmatrix} \dot{R}_{ix} \\ \dot{R}_{iy} \\ \dot{R}_{iz} \end{bmatrix} = \begin{bmatrix} \omega_{sc} \end{bmatrix} \begin{bmatrix} X_i \\ Y_i \\ Z_i \end{bmatrix} = - \begin{bmatrix} R_{ic} \end{bmatrix} \begin{bmatrix} \omega_{sx} \\ \omega_{sy} \\ \omega_{sz} \end{bmatrix} \tag{6}$$

where

$$\begin{bmatrix} \omega_{sc} \end{bmatrix} = \begin{bmatrix} 0 & -\omega_{sz} & \omega_{sy} \\ \omega_{sz} & 0 & -\omega_{sx} \\ -\omega_{sy} & \omega_{sx} & 0 \end{bmatrix} \tag{7}$$

and

$$\left[R_{ic}\right] = \begin{bmatrix} 0 & -Z_i & Y_i \\ Z_i & 0 & -X_i \\ -Y_i & X_i & 0 \end{bmatrix} \qquad (8)$$

The column vector on the left side of equation (6) consists of the components of the time derivative, $\overset{\circ}{\overrightarrow{R}}_i$, and are not the time derivatives of the components, X_i, Y_i, Z_i, which are zero.

$\overrightarrow{R}_c$ rotates and also changes in magnitude, if the orbit is elliptical, and so its time derivative is

$$\overset{\bullet}{\overrightarrow{R}}_c = \bar{R}\,\overset{\circ}{R}_c + R_c\,\overrightarrow{\omega}_R \times \bar{R} \qquad (9)$$

where $\overrightarrow{\omega}_R$ is the angular rate of the unit vector $\bar{R}$, and is given by equation (5.3-25) of Reference A. In matrix form,

$$\begin{bmatrix} \overset{\bullet}{R}_{cR} \\ \overset{\bullet}{R}_{cp} \\ \overset{\bullet}{R}_{cQ} \end{bmatrix} = \overset{\circ}{R}_c \begin{bmatrix} 1 \\ 0 \\ 0 \end{bmatrix} + R_c \left[\omega_{RC}\right] \begin{bmatrix} 1 \\ 0 \\ 0 \end{bmatrix} \qquad (10)$$

where $\left[\omega_{RC}\right]$ is defined by an equation similar to equation (7). The ele_____ the left member of equation (10) are the components of the time derivative, $\overrightarrow{R}_c$, i the local vertical reference frame $\bar{R}\ \bar{P}\ \bar{Q}$. This frame is described in Reference A.

The kinetic energy of the general mass element is

$$dE_i = 1/2 \, \dot{\vec{R}}_{Ei}^2 \, dm_i \tag{11}$$

$$\dot{\vec{R}}_{Ei} = \dot{\vec{R}}_c + \dot{\vec{R}}_i$$

$$= \bar{R} \, \dot{R}_c + R_c \, \vec{\omega}_R \times \bar{R} + \vec{\omega}_s \times (\bar{X} \, X_i + \bar{Y} \, Y_i + \bar{Z} \, Z_i) \tag{12}$$

$$\dot{\vec{R}}_{Ei}^2 = \dot{R}_c^2 + R_c^2 \, (\vec{\omega}_R \times \bar{R})^2 + \left[\vec{\omega}_s \times (\bar{X} \, X_i + \bar{Y} \, Y_i + \bar{Z} \, Z_i) \right]^2$$

$$+ \, 2 \, \dot{R}_c \, \bar{R} \cdot \left[R_c \, \vec{\omega}_R \times \bar{R} + \vec{\omega}_s \times (\bar{X} \, X_i + \bar{Y} \, Y_i + \bar{Z} \, Z_i) \right]$$

$$+ \, 2 \, R_c \, (\vec{\omega}_R \times \bar{R}) \cdot \left[\vec{\omega}_s \times (X \, X_i + Y \, Y_i + Z \, Z_i) \right]. \tag{13}$$

This is integrated over the mass of the body, and simplified. The total mass is M. Then

$$2 \, E = \int \dot{\vec{R}}_{Ei}^2 \, dm_i$$

$$= M \left[\dot{R}_c^2 + R_c^2 \, (\vec{\omega}_R \times \bar{R})^2 \right] + \int \left[\vec{\omega}_s \times (\bar{X} \, X_i + \bar{Y} \, Y_i + \bar{Z} \, Z_i) \right]^2 \, dm_i \, . \tag{14}$$

Note that $\int X_i dm_i = 0$, etc., $\hspace{6cm}$ (15)

and that

$$\bar{R} \cdot \vec{\omega}_R \times \bar{R} = 0. \hspace{4cm} (16)$$

The first term on the right side of equation (14) is (twice) the kinetic energy due to translational motion along the orbital path, and is dropped. The remainder, consisting of the integral in equation (14) is (twice) the total rotational kinetic energy, and is designated $2 E_R$. The integrand is, in matrix form,

$$\left(\left[\omega_{sc} \right] \left[R_i \right] \right)^2 = \left(\left[R_{ic} \right] \left[\omega_s \right] \right)^2$$

$$= \left(\left[R_{ic} \right] \left[\omega_s \right] \right)^T \left[R_{ic} \right] \left[\omega_s \right]$$

$$= \left[\omega_s \right]^T \left[R_{ic} \right]^T \left[R_{ic} \right] \left[\omega_s \right]$$

$$= - \left[\omega_s \right]^T \left[R_{ic} \right]^2 \left[\omega_s \right],$$

$$\hspace{8cm} (17)$$

because

$$\left[R_{ic} \right]^T = - \left[R_{ic} \right] . \hspace{4cm} (18)$$

The integral,

$$\int - \left[R_{1c} \right]^2 \ dm_1 \ = \ \left[I \right],$$

(19)

the familiar inertia matrix (in which the negatives of the products of inertia app
as the off-diagonal elements) Then

$$2 \ E_R \ = \ \left[\omega_s \right]^T \ \left[I \right] \ \left[\omega_s \right].$$

(20)

In vector form,

$$2 \ E_R \ = \ \vec{\omega}_s \ \cdot \ \vec{H}_R,$$

(21)

where $\vec{H}_R$ is the angular momentum of the satellite minus that due to translation in
orbit. When the matrix or vector operations are performed, the result is

$$E_R \ = \ \frac{1}{2} \ I_{xx} \ \omega_{sx}^2 + \frac{1}{2} \ I_{yy} \ \omega_{sy}^2 + \frac{1}{2} \ I_{zz} \ \omega_{sz}^2$$

$$- I_{xy} \ \omega_{sx} \ \omega_{sy} - I_{xz} \ \omega_{sx} \ \omega_{sz} - I_{yz} \ \omega_{sy} \ \omega_{sz} \ .$$

(22)

The angular velocity of the main body of the ATS satellite is

$$\vec{\omega}_1 \ = \ \bar{X}_1 \ \omega_{x1} + \bar{Y}_1 \ \omega_{y1} - \bar{Z}_1 \ \omega_{z1} \ ,$$

(23)

where the $\bar{X}_1 \, \bar{Y}_1 \, \bar{Z}_1$ orthonormal triad is fixed in the body and oriented as described in Reference A. It is desired to express E_R in terms of the orbital angular rate, $\overset{\circ}{\gamma}$, and the Euler angle rates $\overset{\circ}{\theta}_P$, $\overset{\circ}{\theta}_R$, and $\overset{\circ}{\theta}_Y$. The Euler angles relate the body frame to the local vertical frame. The absolute angular velocity components are related to the orbital angular rate and the Euler angle rates by equations (5.3-33) through (5.3-35) of Reference A. The relations are given in terms of the sines and cosines of the Euler angles, but for this analysis, it is more convenient to use the elements of the $\left[E_1\right]$ matrix, which relates the body frame to the local vertical frame.

$$\omega_{x1} = E_{113} \, (\, \overset{\circ}{\gamma} + \overset{\circ}{\theta}_P) + \overset{\circ}{\theta}_Y \, , \tag{24}$$

$$\omega_{y1} = E_{123} \, (\, \overset{\circ}{\gamma} + \overset{\circ}{\theta}_P) + \frac{E_{133} \, \overset{\circ}{\theta}_R}{\sqrt{1 - E_{113}{}^2}} \tag{25}$$

$$\omega_{z1} = E_{133} \, (\, \overset{\circ}{\gamma} + \overset{\circ}{\theta}_P) - \frac{E_{123} \, \overset{\circ}{\theta}_R}{\sqrt{1 - E_{113}{}^2}} \tag{26}$$

These relations are substituted into equation (22), and the result is sorted by powers of $\overset{\circ}{\gamma}$.

$$
\begin{aligned}
E_R = \ &\dot{\gamma}^2 \left[\tfrac{1}{2} (I_{XX1} E_{113}{}^2 + I_{YY1} E_{123}{}^2 + I_{ZZ1} E_{133}{}^2) \right.\\
&\left. - (I_{XY1} E_{113} E_{123} + I_{XZ1} E_{113} E_{133} + I_{YZ1} E_{123} E_{133}) \right]\\[4pt]
&+ \dot{\gamma} \left\{ \dot{\theta}_P \left[I_{XX1} E_{113}{}^2 + I_{YY1} E_{123}{}^2 + I_{ZZ1} E_{113}{}^2 \right.\right.\\
&\left. - 2(I_{XY1} E_{113} E_{123} + I_{XZ1} E_{113} E_{133} + I_{YZ1} E_{123} E_{133}) \right]\\[4pt]
&+ \frac{\dot{\theta}_R}{\sqrt{1 - E_{113}{}^2}} \left[I_{YY1} E_{123} E_{133} - I_{ZZ1} E_{123} E_{133} - I_{XY1} E_{113} E_{133} + I_{XZ1} E_{113} E_{1\ldots} \right.\\
&\left. + I_{YZ1} (E_{123}{}^2 - E_{133}{}^2) \right]\\[4pt]
&\left. + \dot{\theta}_Y (I_{XX1} E_{113} - I_{XY1} E_{123} - I_{XZ1} E_{133}) \right\}\\[4pt]
&+ \dot{\theta}_P{}^2 \left[\tfrac{1}{2}(I_{XX1} E_{113}{}^2 + I_{YY1} E_{123}{}^2 + I_{ZZ1} E_{133}{}^2) \right.\\
&\left. - (I_{XY1} E_{113} E_{123} + I_{XZ1} E_{113} E_{133} + I_{YZ1} E_{123} E_{133}) \right]\\[4pt]
&+ \frac{\dot{\theta}_R{}^2}{1 - E_{113}{}^2} \left(\tfrac{1}{2} I_{YY1} E_{133}{}^2 + \tfrac{1}{2} I_{ZZ1} E_{123}{}^2 + I_{YZ1} E_{123} E_{133} \right)\\[4pt]
&+ \tfrac{1}{2} I_{XX1} \dot{\theta}_Y{}^2 + \frac{\dot{\theta}_R \dot{\theta}_Y}{\sqrt{1 - E_{113}{}^2}} (I_{XZ1} E_{123} - I_{XY1} E_{133})\\[4pt]
&+ \frac{\dot{\theta}_P \dot{\theta}_R}{\sqrt{1 - E_{113}{}^2}} \left[I_{YY1} E_{123} E_{133} - I_{ZZ1} E_{123} E_{133} - I_{XY1} E_{113} E_{133} \right.\\
&\left. + I_{XZ1} E_{113} E_{123} + I_{YZ1} (E_{123}{}^2 - E_{133}{}^2) \right]\\[4pt]
&+ \dot{\theta}_P \dot{\theta}_Y (I_{XX1} E_{113} - I_{XY1} E_{123} - I_{XZ1} E_{133}) \ .
\end{aligned}
\tag{27}
$$

The Euler angle rates appearing in this equation are given by equations (5.3-36) through (5.3-38) of Reference A, in terms of the sines and cosines of the Euler angles, but for this analysis, they are more conveniently expressed in terms of the $\left[E_1 \right]$ matrix elements.

$$\dot{\theta}_R = \frac{\omega_{Y1} E_{133} - \omega_{Z1} E_{123}}{\sqrt{1 - E_{113}^2}} \qquad (28)$$

$$\dot{\theta}_P = -\dot{\gamma} + \frac{1}{\left(\sqrt{1 - E_{113}^2}\right)^2}(\omega_{Y1} E_{123} + \omega_{Z1} E_{133}) \qquad (29)$$

$$\dot{\theta}_Y = \omega_{X1} - E_{113}(\dot{\theta}_P + \dot{\gamma})$$

$$= \omega_{X1} - \frac{E_{113}}{\left(\sqrt{1 - E_{113}^2}\right)^2}(\omega_{Y1} E_{123} + \omega_{Z1} E_{133}) \cdot \qquad (30)$$

- - - - - - -
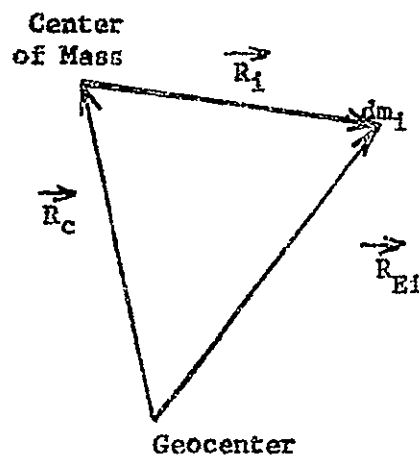
Figure 1. Vector Relations

The equation for the secondary boom is the same, except that the moments of inertia and the angular rates of the secondary boom are used, and the $\left[B_3 \right]$ matrix elements are used in place of the $\left[B_1 \right]$ matrix elements.

Reference A. "Abridged Attitude Equations for the Applications Technology Satellite", GE Spacecraft Dept. Doc. No. 66SD4214, 15 July 1966

APPENDIX F

STRAIGHT ROD SIMULATION OF CURVED RODS

STRAIGHT ROD SIMULATION OF CURVED RODS
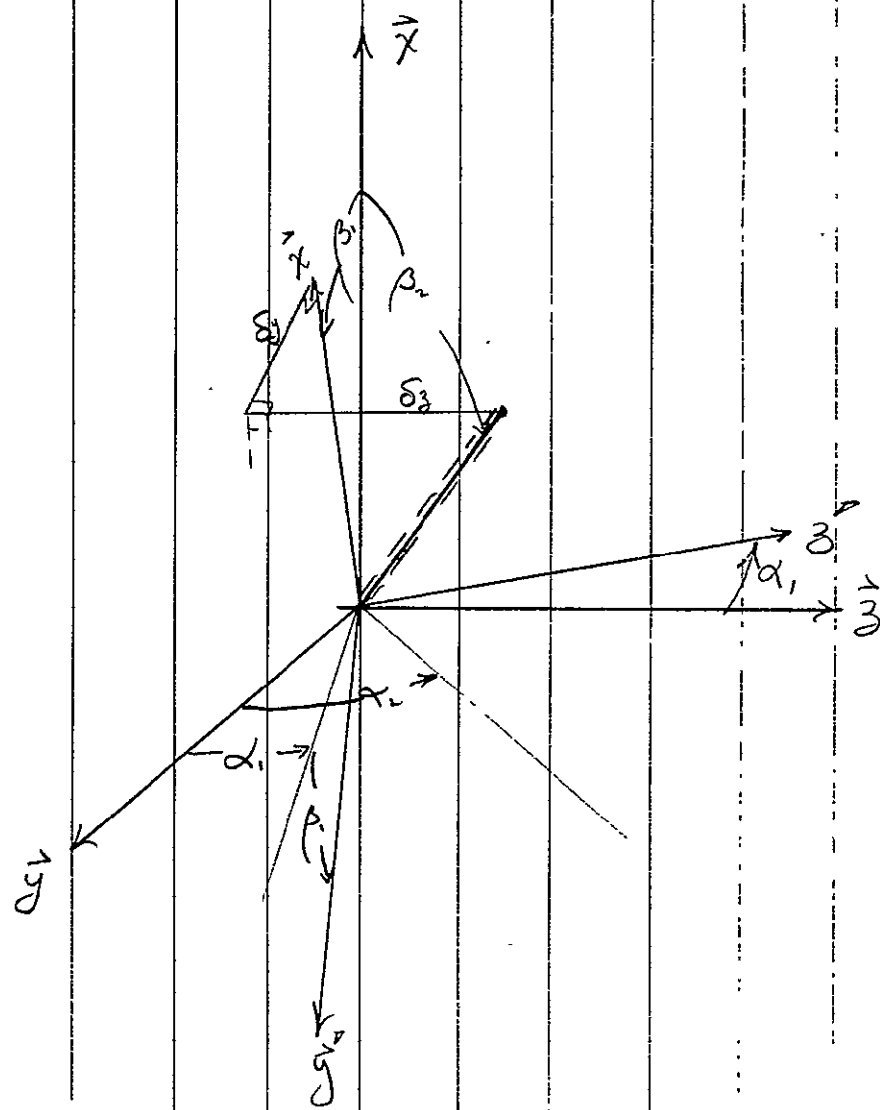
GRAVITY GRADIENT ROD COORDINATE SYSTEM.

THE FINAL POSITION OF THE EQUIVALENT STRAIGHT ROD IS

$$\vec{V}_{T2} = \vec{x}\, \ell \cos\beta_2 + \vec{y}\, \ell \sin\beta_2 \cos\alpha_2 + \vec{z}\, \ell \sin\beta_2 \sin\alpha_2$$

WHERE

ℓ = ROD LENGTH

α_2 / β_2 = ORIENTATION ANGLE FOR EQUIVALENT STRAIGHT ROD (SEE FIGURE)

IF THE ACTUAL GRAVITY GRADIENT ROD WERE STRAIGHT, ITS TIP MASS WOULD BE

$$\vec{V}_{T_1} = \vec{x}\, l\, \cos\beta_1 + \vec{y}\, l\, \sin\beta_1 \cos\alpha_1 + \vec{3}\, l\, \sin\beta_1 \sin\alpha_1 \quad (2)$$

WHERE

$$\alpha_1, \beta_1 = \text{ORIENTATION ANGLE FOR CURVED ROD}$$
$$\text{ASSUMING NO CURVATURE (SEE FIGURE)}$$

THE MEASURED DEFLECTIONS ARE

$$\vec{\delta}_y = \delta_y \vec{y}' \quad (3)$$

$$\vec{\delta}_3 = \delta_3 \vec{3}' \quad (4)$$

IN TERMS OF $xy3$

$$\vec{\delta}_y = -\delta_y \sin\beta_1 \vec{x} + \delta_y \cos\beta_1 \cos\alpha_1 \vec{y} + \delta_y \cos\beta_1 \sin\alpha_1 \vec{3} \quad (5)$$

$$\vec{\delta}_3 = -\delta_3 \sin\alpha_1 \vec{y} + \delta_3 \cos\alpha_1 \vec{3} \quad (6)$$

THE VECTOR TO THE CURVED ROD TIP LOCATION IS THEREFORE

$$\vec{V}_{T_2} = \vec{V}_{T_1} + \vec{\delta}_y + \vec{\delta}_3 \quad (7)$$

EXPANDING

$$\vec{V}_{T_2} = \vec{x} \left[l\, \cos\beta_1 - \delta_y \sin\beta_1 \right]$$

$$+ \vec{y} \left[l\, \sin\beta_1 \cos\alpha_1 - \delta_3 \sin\alpha_1 + \delta_y \cos\beta_1 \cos\alpha_1 \right]$$

$$+ \vec{3} \left[l\, \sin\beta_1 \sin\alpha_1 + \delta_3 \cos\alpha_1 + \delta_y \cos\beta_1 \sin\alpha_1 \right] \quad (8)$$

$\vec{V}_{T_2}$ FROM EQUATION (8) IS THE SAME AS $\vec{V}_{T_2}$ FROM EQUATION (1)
EQUATING TERMS

$$\ell \cos \beta_2 = \ell \cos \beta_1 - \delta_4 \sin \beta_1 \tag{9}$$

$$\ell \sin \beta_2 \sin \alpha_2 = \ell \sin \beta_1 \sin \alpha_1 + \delta_3 \cos \alpha_1 + \delta_4 \cos \beta_1 \sin \alpha_1 \tag{10}$$

$$\ell \sin \beta_2 \cos \alpha_2 = \ell \sin \beta_1 \cos \alpha_1 - \delta_3 \sin \alpha_1 + \delta_4 \cos \beta_1 \cos \alpha_1 \tag{11}$$

ONLY TWO EQUATIONS NEED BE SOLVED, AND (9) AND (10) WERE SELECTED.

$$\cos \beta_2 = \cos \beta_1 - \frac{\delta_4}{\ell} \sin \beta_1 \tag{12}$$

$$\sin \alpha_2 = \frac{1}{\sin \beta_2} \left[\sin \alpha_1 \sin \beta_1 + \frac{\delta_3}{\ell} \cos \alpha_1 + \frac{\delta_4}{\ell} \cos \beta_1 \cos \alpha_1 \right]$$

FOR ALL RODS,

$$\alpha_1 = -4.8° \quad \text{AND} \quad \beta_1 = 25°, -25°, -155°, 155°$$

APPENDIX G

GRAVITY GRADIENT POTENTIAL ENERGY·

APPENDIX G

SOLAR TORQUE ON "X" RODS

THE COORDINATE SYSTEMS USED IN THE ANALYSIS ARE SHOWN IN FIGURE 1. FOR SIMPLICITY, THE "X" RODS ARE ASSUM TO BE IN THE ORBIT PLANE (THE ACTUAL ANGLE IS 4.8°). THE DAMPER IS NOT CONSIDERED.
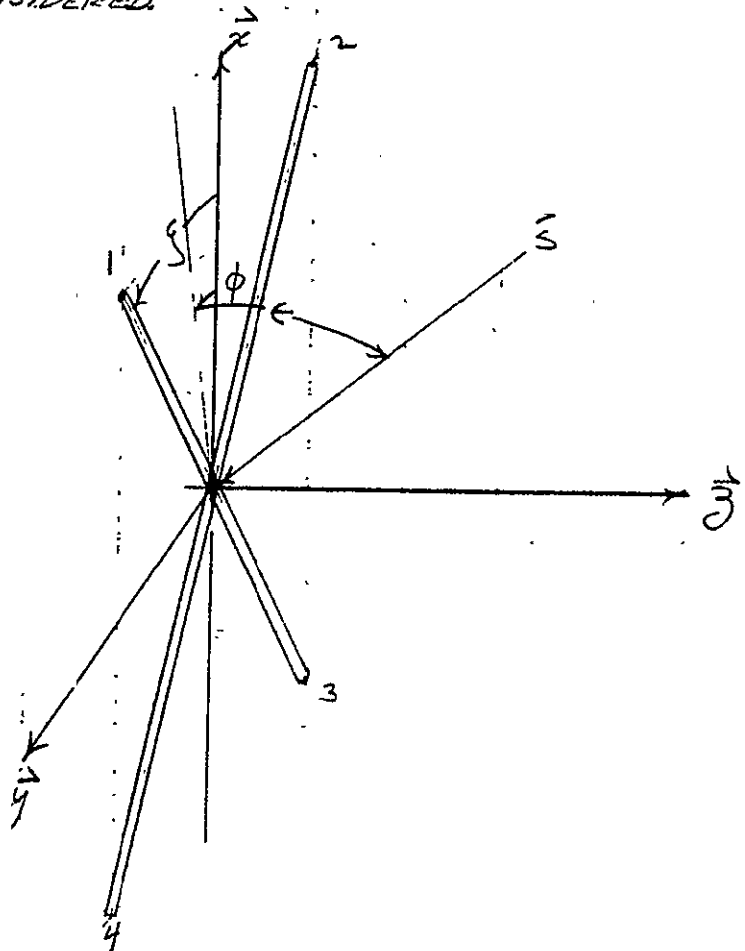
COORDINATE SYSTEMS - FIGURE 1

THE TORQUE EXERTED ON EACH ROD ABOUT THE ORIGIN

$$\vec{T}_i = P_0 \mathcal{L}_i^2 r_p \left(\alpha_i + \frac{4}{3} \rho_i \right) \sin^2 \psi_i \hat{p} \qquad 0 \le \psi \le \pi$$

WHERE

$P_0 =$ LIGHT PRESSURE $= 9.649 \cdot 10^{-8}$ lb/ft^2

$L =$ ROD LENGTH - FT

$r =$ ROD RADIUS - FT

$\alpha =$ ROD ABSORPTIVITY.

$\rho =$ ROD SPECULAR REFLECTIVIT

$\gamma =$ ANGLE BETWEEN SUN VECTOR AND ROD AXIS.

THIS EQUATION IGNORES END EFFECTS AND DIFFUSE REFLECTIVI
A PURELY DIFFUSE REFLECTIVITY HAS A LOWER COEFFICIENT
HAN A PURELY SPECULAR REFLECTION AND IS NOT A MAXIMUN
CONDITION

THE SUN VECTOR $\vec{S}$ IS

$$\vec{S} = -\vec{x}\cos\epsilon\cos\phi - \vec{y}\cos\epsilon\sin\phi - \vec{3}\sin\epsilon$$

THE VECTOR $\vec{j}_o$ CAN BE DETERMINED FROM

$$\vec{j}_o \sin\gamma_o = \vec{V}_o \times \vec{S}$$

WHERE $\vec{V}_o$ IS THE VECTOR DEFINING THE ROD AXIS

FROM FIGURE 1

$$\vec{V}_o \times \vec{S} = \begin{vmatrix} \vec{x} & \vec{y} & \vec{3} \\ \cos\zeta_o & \sin\zeta_o & 0 \\ -\cos\epsilon\cos\phi & -\cos\epsilon\sin\phi & -\sin\epsilon \end{vmatrix}$$

WHERE

$\zeta_o =$ ANGLE BETWEEN ROD i AND $\vec{x}$

$\epsilon =$ ANGLE BETWEEN SUN VECTOR AND ORBIT PLANE

$\phi =$ ORBIT ANGLE $=$ ORBITAL RATE $\times$ TIME

EXPANDING

$$\sin\psi_1 \vec{S} = \vec{x}(-\sin\epsilon \sin\zeta_0) + \vec{y}(\sin\epsilon \cos\zeta_0)$$

$$+\vec{z}(-\cos\epsilon \sin\phi \cos\zeta_0 + \cos\epsilon \cos\phi \sin\zeta_0) \qquad (5)$$

$$\sin\psi_0 \vec{S} = -\vec{x}\sin\epsilon \sin\zeta_0 + \vec{y}\sin\epsilon \cos\zeta_0 + \vec{z}\cos\epsilon \sin(\zeta_0 - \phi) \qquad (6)$$

THE $\sin^2\psi$ CAN BE DETERMINED FROM

$$\sin^2\psi = 1 - \cos^2\psi = 1 - (\vec{V}_0 \cdot \vec{S}) \qquad (7)$$

$$\sin^2\psi = 1 - (-\cos\zeta_0 \cos\epsilon \cos\phi - \cos\epsilon \sin\zeta_0 \sin\phi)^2 \qquad (8)$$

$$|\sin\psi| = \left[1 - \cos^2\epsilon \cos^2(\zeta_0 - \phi)\right]^{1/2} \qquad (9)$$

IT IS MORE CONVENIENT TO WRITE THE TORQUE COEFFICIENT AS

$$\alpha_0 + \frac{4}{3}\rho_0 = \alpha_0 + \frac{4}{3}(1-\alpha_0) = \frac{1}{3}(4-\alpha_0) \qquad (10)$$

COMBINING EQUATIONS (1), (6), (9), AND (10), AND ASSUMING ALL THE RODS HAVE THE SAME RADIUS r

$$\vec{T}_0 = \rho_0 r L_0^2 \frac{(4-\alpha_0)}{3}\left(1 - \cos^2\epsilon \cos^2(\zeta_0 - \phi)\right)^{1/2}\left[-\vec{x}\sin\epsilon \sin\zeta_0\right.$$

$$\left. +\vec{y}\sin\epsilon \cos\zeta_0 + \vec{z}\cos\epsilon \sin(\zeta_0 - \phi)\right] \qquad (11)$$

ASSUMING ALL THE RODS ARE NOMINALLY IN THEIR CORRECT POSITION

$$\zeta_1 = \zeta \qquad \sin\zeta_1 = \sin\zeta \qquad \cos\zeta_1 = \cos\zeta$$

$$\zeta_2 = -\zeta \qquad \sin\zeta_2 = -\sin\zeta \qquad \cos\zeta_2 = \cos\zeta$$

$$\zeta_3 = -(\pi - \zeta) \qquad \sin\zeta_3 = -\sin\zeta \qquad \cos\zeta_3 = -\cos\zeta$$

$$\xi_4 = \pi - \xi \qquad \sin \xi_4 = \sin \xi \qquad \cos \xi_4 = -\cos \xi$$

EQUATION (9) CAN BE BROKEN INTO TWO SETS

$$\left[1 - \cos^2 \epsilon \cos^2(\xi_0 - \phi) \right]^{1/2} = \left[1 - \cos^2 \epsilon \cos^2(\xi - \phi) \right]^{1/2} \text{ RODS 1, 3} \qquad (12)$$

$$\left[1 - \cos^2 \epsilon \cos^2(\xi_0 - \phi) = 1 - \cos^2 \epsilon \cos^2(\xi + \phi) \right] \text{ RODS 2, 4} \qquad (13)$$

EQUATION (11) CAN SIMILARLY BE BROKEN INTO TWO SETS

$$Z \vec{T}_{1,3} = \frac{P_0 r}{3} \left(1 - \cos^2 \epsilon \cos^2(\xi - \phi) \right)^{1/2} \Big\{ -\vec{x} \sin \epsilon \sin \xi \left[L_1^2 (4 - \alpha_1) \right.$$
$$\left. - L_3^2 (4 - \alpha_3) \right] + \vec{y} \sin \epsilon \cos \xi \left[L_1^2 (4 - \alpha_1) - L_3^2 (4 - \alpha_3) \right]$$
$$+ \vec{3} \cos \epsilon \sin(\xi - \phi) \left[L_1^2 (4 - \alpha_1) - L_3^2 (4 - \alpha_3) \right] \Big\} \qquad (14)$$

$$Z \vec{T}_{2,4} = \frac{P_0 r}{3} \left(1 - \cos^2 \epsilon \cos^2(\xi + \phi) \right)^{1/2} \Big\{ -\vec{x} \sin \epsilon \sin \xi \left[L_4^2 (4 - \alpha_4) \right.$$
$$\left. - L_2^2 (4 - \alpha_2) \right] + \vec{y} \sin \epsilon \cos \xi \left[L_2^2 (4 - \alpha_2) - L_4^2 (4 - \alpha_4) \right]$$
$$+ \vec{3} \cos \epsilon \sin(\xi + \phi) \left[L_4^2 (4 - \alpha_4) - L_2^2 (4 - \alpha_2) \right] \Big\} \qquad (15)$$

THE TOTAL TORQUE IS THE SUM OF EQUATIONS (14) AND (15). IN
TERMS OF COMPONENTS

$$T_x = -\frac{P_0 r}{3} \sin \epsilon \sin \xi \Big\{ \left(1 - \cos^2 \epsilon \cos^2(\xi - \phi) \right)^{1/2} \left[L_1^2 (4 - \alpha_1) \right.$$
$$\left. - L_3^2 (4 - \alpha_3) \right] + \left(1 - \cos^2 \epsilon \cos^2(\xi + \phi) \right)^{1/2} \left[L_4^2 (4 - \alpha_4) \right.$$
$$\left. - L_2^2 (4 - \alpha_2) \right] \Big\} \qquad (16)$$

G-

$$T_y = \frac{P_o r}{3} Sin \epsilon Cos \xi \left\{ \left(1 - Cos^2 \epsilon Cos^2 (\xi - \phi)\right)^{1/2} \left[L_1^2 (4 - \alpha_1) - L_3^2 (4 - \alpha_3) \right] \right.$$

$$\left. + \left(1 - Cos^2 \epsilon Cos^2 (\xi + \phi)\right)^{1/2} \left[L_2^2 (4 - \alpha_2) - L_4^2 (4 - \alpha_4) \right] \right] \quad (17)$$

$$T_3 = \frac{P_o r}{3} Cos \epsilon \left\{ Sin (\xi - \phi) \left(1 - Cos^2 \epsilon Cos^2 (\xi - \phi)\right)^{1/2} \left[L_1^2 (4 - \alpha_1) \right. \right.$$

$$\left. - L_3^2 (4 - \alpha_3) \right] + Sin (\xi + \phi) \left(1 - Cos^2 \epsilon Cos^2 (\xi + \phi)\right)^{1/2} \left[L_4^2 (4 - \alpha_4) \right.$$

$$\left. - L_2^2 (4 - \alpha_2) \right] \right\} \quad (18)$$

To STUDY THE EFFECTS ON CHANGES IN α ONLY, IT WILL
BE ASSUMED THAT $L_1 = L_2 = L_3 = L_4 = L$. EQUATIONS (16), (17)
AND (18) BECOME

$$T_x = -\frac{P_o r L^2}{3} Sin \epsilon Sin \xi \left\{ (\alpha_3 - \alpha_1) \left[1 - Cos^2 \epsilon Cos^2 (\xi - \phi) \right]^{1/2} \right.$$

$$\left. + (\alpha_2 - \alpha_4) \left[1 - Cos^2 \epsilon Cos^2 (\xi + \phi) \right]^{1/2} \right\} \quad (19)$$

$$T_y = \frac{P_o r L^2}{3} Sin \epsilon Cos \xi \left\{ (\alpha_3 - \alpha_1) \left[1 - Cos^2 \epsilon Cos^2 (\xi - \phi) \right]^{1/2} \right.$$

$$\left. + (\alpha_4 - \alpha_2) \left[1 - Cos^2 \epsilon Cos (\xi + \phi) \right]^{1/2} \right\} \quad (20)$$

$$T_3 = \frac{P_o r Cos \epsilon L^2}{3} \left\{ (\alpha_3 - \alpha_1) Sin (\xi - \phi) \left(1 - Cos^2 \epsilon Cos^2 (\xi - \phi)\right)^{1/2} \right.$$

$$\left. - (\alpha_4 - \alpha_2) Sin (\xi + \phi) \left(1 - Cos^2 \epsilon Cos^2 (\xi + \phi)\right)^{1/2} \right\} \quad (21)$$

IN THESE EQUATIONS ONLY THE DIFFERENCES IN THE α'S ARE IMPORTANT. FOR CONVENIENCE, IT WILL BE ASSUMED THAT ALL THE $\Delta\alpha$'S ARE IDENTICAL AND WILL BE THE WORST IN EACH AXIS. THIS CANNOT OCCUR FOR ONE VEHICLE, BUT AN INDIVIDUAL "WORST" WHEREIN ONLY ONE AXIS IS BAD CAN. EQUATIONS (19), (20), AND (21) BECOME

$$\frac{T_X}{\Delta\alpha} = -\frac{P_0 r L^2}{3}\sin\epsilon \sin\xi\left[\left(1-\cos^2\epsilon\cos^2(\xi-\phi)\right)^{1/2}+\left(1-\cos^2\epsilon\cos^2(\xi+\phi)\right)^{1/2}\right]$$

$$\frac{T_Y}{\Delta\alpha} = -\frac{P_0 r L^2}{3}\sin\epsilon \cos\xi\left[\left(1-\cos^2\epsilon\cos^2(\xi-\phi)\right)^{1/2}+\left(1-\cos^2\epsilon\cos^2(\xi+\phi)\right)^{1/2}\right]$$

$$\frac{T_3}{\Delta\alpha} = \frac{P_0 r \cos\epsilon L^2}{3}\left\{\sin(\xi-\phi)\left[1-\cos^2\epsilon\cos^2(\xi-\phi)\right]^{1/2}\right.$$

$$\left. -\sin(\xi+\phi)\left[1-\cos^2\epsilon\cos^2(\xi+\phi)\right]^{3/2}\right\} \qquad (24)$$

APPENDIX H

IMPULSE RESPONSE

APPENDIX H

IMPULSE RESPONSE

THE PERFORMANCE OF PITCH, ROLL, AND YAW WILL BE APPROXIMATED BY A SPRING MASS EQUATION. AT $t = 0$, TORQUE IS APPLIED TO THE VEHICLE, THE EQUATION OF MOTION BECOMES

$$\ddot{\Theta}_p + \omega_N^2 \Theta_p = I \qquad (1)$$

T = APPLIED TORQUE

I_p = MOMENT OF INERT

ω_N = NATURAL FREQUE

THE SOLUTION TO THIS WITH $\Theta_p = \dot{\Theta}_p = 0$ AT $t = 0$ IS

$$\Theta_p = \frac{I}{I_p \omega_N^2} \left[1 - \cos \omega_N t \right] \qquad (2)$$

IF THE TORQUE IS REMOVED AT TIME t_f, THE EQUATION OF MOTION BECOMES

$$\ddot{\Theta}_p + \omega_N^2 \Theta_p = C$$

FROM EQUATION (2), THE INITIAL CONDITIONS ARE

$$\Theta_{p_i} = \frac{I}{I_p \omega_N^2} \left[1 - \cos \omega_N t_f \right]$$

$$\dot{\Theta}_{p_i} = \frac{I}{I_p \omega_N} \sin \omega_N t_f$$

THE SOLUTION TO EQUATION (3) IS

$$\Theta_b = A \sin(\omega t + \alpha)$$

$$\dot{\Theta}_P = \omega_N \cdot A \cos(\omega_N t + \phi)$$

Equating equations (4), (5), (6) and (7)

$$A \sin(\omega_N t + \phi) = \frac{T}{I_p \omega_N^2}\left[1 - \cos \omega_N t_f\right]$$

$$A \omega_N \cos(\omega_N t + \phi) = \frac{T}{I_p \omega_N} \sin \omega_N t_f$$

Dividing equation (9) by ω_N, squaring, and adding to the square of equation (8)

$$A^2 = \frac{T^2}{I_p^2 \omega_N^4}\left[\sin^2 \omega_N t_f + 1 - 2\cos \omega_N t_f + \cos^2 \omega_N t_f\right.$$

$$A^2 = \frac{2T^2}{I_p^2 \omega_N^4}\left[1 - \cos \omega_N t_f\right]$$

Finally

$$A = \frac{T}{I_p \omega_N^2}\left[2(1 - \cos \omega_N t_f)\right]^{1/2}$$

t_f small, $\cos \omega_N t_f = 1 - \dfrac{\omega_N^2 t_f^2}{2}$

$$A = \frac{T}{I_p \omega_N^2}\left[2\left(1 - 1 + \frac{\omega_N^2 t_f^2}{2}\right)\right] = \frac{T}{I_p} t_f$$

Calling $T t_f = I$ = impulse

$$A = \frac{I}{I_p \omega_N}$$

SINCE THIS IS THE PEAK AMPLITUDE

$$\Theta_{P_{MAX}} = \frac{I}{I_p \omega_N}$$

FOR PITCH WITH $I = .1$ - ATS-A

$$\Theta_P = \frac{(.1)(57.3)}{(7082)(27.3 \cdot 10^{-5})(1.350)} = 2.2°$$

FOR ROLL WITH $I = .1$

$$\Theta_R = \frac{(.1)(57.3)}{(5770)(27.3 \cdot 10^{-5})(2.05)} \approx 1.8°$$

FOR YAW WITH $I = .1$

$$\Theta_Y = \frac{(.1)(57.3)}{(1326)(27.3 \cdot 10^{-5})(.752)} = 21°$$

FOR ATS-D

PITCH

$$\Theta_P = \frac{(.1)(57.3)}{(6625)(1.350)(7.29 \cdot 10^{-5})} = 3.5°$$

ROLL

$$\Theta_R = \frac{(.1)(57.3)}{(13545)(2.05)(7.29 \cdot 10^{-5})} = 2.8°$$

YAW

$$\Theta_Y = \frac{(.1)(57.3)}{(3117)(.752)(7.29 \cdot 10^{-5})} = 3$$

H-3/4

APPENDIX I

ATS-E SPIN ANALYSIS

EULERS EQUATIONS FOR A RIGID BODY ARE (ASSUMING NO PRODUCTS OF INERTIA) ARE

$$T_x = I_{xx} \dot{\omega}_x + \omega_y \omega_3 (I_{33} - I_{yy})$$ 1

$$T_y = I_{yy} \dot{\omega}_y + \omega_x \omega_3 (I_{xx} - I_{33})$$ 2

$$T_3 = I_{33} \dot{\omega}_3 + \omega_x \omega_y (I_{yy} - I_{xx})$$ 3

WHERE

I = MOMENT OF INERTIA

ω = INERTIAL ANGULAR RATE

$\dot{\omega}$ = INERTIAL ANGULAR ACCELERATION

T = EXTERNALLY APPLIED TORQUE

SUBSCRIPTS $x, y, 3$ REFER TO THE COORDINATE AXES OF ANY RIGHT HANDED COORDINATE SYSTEM.

PRIOR TO APOGEE ENGINE SEPARATION, THE SPACECRAFT, IS SPINNING ABOUT THE x AXIS, WHICH IS THE AXIS OF MAXIMUM MOMENT OF INERTIA. IMMEDIATELY AFTER SEPARATION, HOWEVER, IT IS THE INTERMEDIATE AXIS OF INERTIA. HENCE

$$I_{yy} < I_{xx} < I_{33}$$ 4

ASSUME AT THE INSTANT OF SEPARATION THAT ω_x IS VERY LARGE COMPARED TO ω_y AND ω_3, THEN

$$T_x \approx I_{xx} \dot{\omega}_x$$ 5

$$T_y \doteq I_{yy}\dot{\omega}_y + \omega_x\omega_z\left(I_{xx} - I_{zz}\right)$$

$$T_z \doteq I_{zz}\dot{\omega}_z + \omega_x\omega_y\left(I_{yy} - I_{xx}\right)$$

... WHERE $\omega_x \doteq$ CONSTANT.

CONSIDERING ONLY EQUATIONS 6 AND

$$\dot{\omega}_y = \frac{T_y + \omega_x\omega_z\left(I_{zz} - I_{xx}\right)}{I_{yy}}$$

$$\dot{\omega}_z = \frac{T_z + \omega_x\omega_y\left(I_{xx} - I_{yy}\right)}{I_{zz}}$$

BOTH $I_{zz} - I_{xx}$, AND $I_{xx} - I_{yy}$ ARE POSITIVE, BY EQUATION (5). ASSUME THAT AT THE COMPLETION OF SEPARATION $T_y = T_z = 0$; THEN

$$\dot{\omega}_y = \omega_x\omega_z\left(\frac{1}{I_{yy}}\right)\left(I_{zz} - I_{xx}\right)$$

$$\dot{\omega}_z = \omega_x\omega_y\left(\frac{1}{I_{zz}}\right)\left(I_{xx} - I_{yy}\right)$$

TO ILLUSTRATE WHAT WOULD HAPPEN ASSUME : $\omega_{z\,INITIAL}$ IS SMALL AND POSITIVE. THE $\dot{\omega}_y$ IS POSITIVE, AND A POSITIVE ω_y WILL APPEAR SHORTLY. THEN A POSITIVE $\dot{\omega}_z$ WILL APPEAR WHICH RESULTS IN A POSITIVE ADDITION TO ω_z INITIAL, WHICH CAUSES A LARGER $\dot{\omega}_y$, AND A LARGER ω_y, ETC. THE RESULT IS BOTH ω_y AND ω_z BOTH INCREASE. THE SYSTEM IS UNSTABLE

APPLYING THE SAME PROCEDURE WITH A NEGATIVE $\omega_{3\,INITIAL}$ PRODUCES THE SAME RESULT EXCEPT THAT THE RATES INCREASE IN THE NEGATIVE DIRECTION. HENCE THE INITIAL RATE DETERMINES THE INITIAL DIRECTION OF ROTATION ON THE OTHER AXES. A SIMILAR SITUATION EXISTS WITH $\omega_{y\,INITIAL}$.

TO ILLUSTRATE STABILITY, ASSUME

$$I_{33} < I_{yy} < I_{xx} \qquad 12$$

THEN EQUATIONS 10 AND 11 BECOME

$$\dot{\omega}_y = -\omega_x \omega_3 \left(\frac{1}{I_{yy}} \right) \left(I_{xx} - I_{33} \right) \qquad 13$$

$$\dot{\omega}_3 = \omega_x \omega_3 \left(\frac{1}{I_{33}} \right) \left(I_{xx} - I_{yy} \right) \qquad 14$$

IN THIS SITUATION, A SMALL POSITIVE $\omega_{3\,INITIAL}$ CREATES A NEGATIVE $\dot{\omega}_y$, AND ω_y WHICH PRODUCES A NEGATIVE $\dot{\omega}_3$ AND ω_3, WHICH REDUCES THE $\omega_{3\,INITIAL}$, REDUCING $\dot{\omega}_y$, AND TENDING TO STABILIZE THE SPACECRAFT.

ASSUMING ω_x IS CONSTANT, EQUATIONS 10 AND 11 CAN BE WRITTEN IN LAPLACE FORM

$$[S]\omega_y + \omega_x I_\phi \omega_3 = 0 \qquad 15$$

$$\omega_x [I_\Theta]\omega_y + [S]\omega_3 = 0 \qquad 16$$

I-3

WHERE

$$I_\phi = \frac{1}{I_{yy}} \left(I_{33} - I_{xx} \right)$$

$$I_\theta = \frac{1}{I_{33}} \left(I_{xx} - I_{yy} \right)$$

BOTH I_ϕ AND I_θ ARE POSITIVE. THE CHARACTERISTIC EQUATION RESULTING FROM EQUATIONS 15 AND 16 IS

$$S^2 - \omega_x^2 I_\phi I_\theta = 0 \hspace{4cm} 17$$

THE ROOTS TO EQUATION 17 ARE

$$S = \pm \sqrt{I_\phi I_\theta} \, \omega_x \hspace{4cm} 18$$

WHICH MEANS THAT THE ANGULAR RATES CHANGE AS

$$\omega_y = A e^{\sqrt{I_\phi I_\theta} \, \omega_x t} + B e^{-\sqrt{I_\phi I_\theta} \, \omega_x t} \hspace{2cm} 19$$

$$\omega_z = C e^{\sqrt{I_\phi I_\theta} \, \omega_x t} + D e^{-\sqrt{I_\phi I_\theta} \, \omega_x t} \hspace{2cm} 20$$

HENCE BOTH RATES GROW EXPONENTIALLY. A SIMILAR EXERCISE FOR EQUATIONS 13 AND 14 WOULD PRODUCE A RESULT OF THE FORM

$$\omega_y = A \sin\left(\sqrt{I_\phi I_\theta} \, \omega_x t + \psi \right) \hspace{3cm} 21$$

ETC.

HENCE THE MOTION WOULD BE SINUSOIDAL, RATHER THAN EXPONENTIALLY INCREASING, FOR A STABLE MODE. IF I_{xx} WERE THE MINIMUM MOMENT OF INERTIA, AN EQUATION SIMILAR TO EQUATION 21 WOULD RESULT SINCE THE SITUATION WOULD BE UNSTABLE ONLY IN PRESENCE OF DAMPING.

SINCE THE INITIAL CONDITIONS ARE UNKNOWN, THE PROSPECT OF USING THE APPLIED TORQUES TO OFFSET THE INITIAL CONDITIONS WAS REVIEWED. IF THE INITIAL CONDITIONS ARE FAVORABLE, THERE IS NO PROBLEM. IF THEY ARE UNFAVORABLE, HOWEVER IT IS NECESSARY TO MAKE THEM FAVORABLE. REFERRING TO EQUATION 8 AND 9, IF IT IS DESIREABLE TO MAKE $\dot{\omega}_3$ POSITIVE WHEN ω_y IS NEGATIVE

$$T_3 > \omega_y \omega_{x_{INIT.}} (I_{xx} - I_{yy}) \qquad 22$$

OR

$$T_y > \omega_x \omega_{3_{INIT}} (I_{33} - I_{xx}) \qquad 23$$

THE SITUATION IS MORE COMPLICATED IF $\omega_{y_{INIT}}$, $\omega_{3_{INIT}}$, T_x, AND T_y ALL EXIST SIMULTANEOUSLY. THE BEST APPROACH IS TO SOLVE EQUATIONS 8 AND 9 SIMULTANEOUSLY, AND DETERMINE T_y AND T_3 AS FUNCTIONS OF $\omega_{3_{INIT}}$ AND $\omega_{y_{INIT}}$. REARRANGING EQUATIONS 10 AND 11

$$[s]\omega_y + \omega_x I_\phi \omega_3 = T_y / I_{yy} \qquad 24$$

$$[\omega_x I_\theta]\omega_y + \omega_x [s] = T_3 / I_{33} \qquad 25$$

THE COMPLEMENTARY SOLUTION IS

$$\omega_y = A e^{\sqrt{I_\phi I_\theta}\,\omega_x t} + B e^{-\sqrt{I_\phi I_\theta}\,\omega_x t} \qquad\qquad 26$$

$$\omega_3 = C e^{\sqrt{I_\phi I_\theta}\,\omega_x t} + D e^{-\sqrt{I_\phi I_\theta}\,\omega_x t} \qquad\qquad 27$$

DIFFERENTIATING

$$\dot\omega_y = A\sqrt{I_\phi I_\theta}\,\omega_x e^{\sqrt{I_\phi I_\theta}\,\omega_x t} - B\sqrt{I_\phi I_\theta}\,\omega_x e^{-\sqrt{I_\phi I_\theta}\,\omega_x t} \qquad 28$$

$$\dot\omega_3 = C\sqrt{I_\phi I_\theta}\,\omega_x e^{\sqrt{I_\phi I_\theta}\,\omega_x t} - D\sqrt{I_\phi I_\theta}\,\omega_x e^{-\sqrt{I_\phi I_\theta}\,\omega_x t} \qquad 29$$

SUBSTITUTING INTO EQUATIONS 8 AND 9, (WITH $T_y = T_3 = 0$)

$$A\sqrt{I_\phi I_\theta}\,\omega_x e^{\sqrt{I_\phi I_\theta}\,\omega_x t} - B\sqrt{I_\phi I_\theta}\,\omega_x e^{-\sqrt{I_\phi I_\theta}\,\omega_x t} \qquad\qquad 30$$

$$= \omega_x I_\phi\, C e^{\sqrt{I_\phi I_\theta}\,\omega_x t} + D\omega_x I_\phi e^{-\sqrt{I_\phi I_\theta}\,\omega_x t} \qquad\qquad 31$$

HENCE EQUATING TERMS

$$A = \frac{I_\phi C}{\sqrt{I_\phi I_\theta}} = C\sqrt{\frac{I_\phi}{I_\theta}} \qquad B = -D\sqrt{\frac{I_\phi}{I_\theta}} \qquad 32$$

HENCE

$$\omega_y = C\sqrt{\frac{I_\phi}{I_\theta}}\, e^{\sqrt{I_\phi I_\theta}\,\omega_x t} - D\sqrt{\frac{I_\phi}{I_\theta}}\, e^{-\sqrt{I_\phi I_\theta}\,\omega_x t} \qquad 33$$

$$\omega_3 = C e^{\sqrt{I_\phi I_\theta}\,\omega_x t} + D e^{-\sqrt{I_\phi I_\theta}\,\omega_x t} \qquad\qquad 34$$

At $t = 0$, $\quad \omega_y = \omega_{y,o}, \quad \omega_3 = \omega_{3,o}$.

Finally

$$\omega_{y,o} = C\sqrt{\frac{I_\phi}{I_\Theta}} - D\sqrt{\frac{I_\phi}{I_\Theta}} \qquad 35$$

$$\omega_{3,o} = C + D \qquad 36$$

Solving simultaneously

$$2C\sqrt{\frac{I_\phi}{I_\Theta}} = \omega_{y,o} + \omega_{3,o}\sqrt{\frac{I_\phi}{I_\Theta}} \qquad 37$$

$$C = \frac{1}{2}\left\{\omega_{y,o}\sqrt{\frac{I_\Theta}{I_\phi}} + \omega_{3,o}\right\} \qquad 38$$

$$2D\sqrt{\frac{I_\phi}{I_\Theta}} = \omega_{3,o}\sqrt{\frac{I_\phi}{I_\Theta}} - \omega_{y,o} \qquad 39$$

$$D = \frac{1}{2}\left\{\omega_{3,o} - \omega_{y,o}\sqrt{\frac{I_\Theta}{I_\phi}}\right\} \qquad 40$$

Hence

$$\omega_y = \frac{1}{2}\left(\omega_{y,o} + \omega_{3,o}\sqrt{\frac{I_\phi}{I_\Theta}}\right)e^{\sqrt{I_\phi I_\Theta}\,\omega_x t} - \frac{1}{2}\left(\omega_{3,o}\sqrt{\frac{I_\phi}{I_\Theta}} - \omega_{y,o}\right)e^{-\sqrt{I_\phi I_\Theta}\,\omega_x t} \qquad 41$$

$$\omega_3 = \frac{1}{2}\left(\omega_{3,o} + \omega_{y,o}\sqrt{\frac{I_\Theta}{I_\phi}}\right)e^{\sqrt{I_\phi I_\Theta}\,\omega_x t} + \frac{1}{2}\left(\omega_{3,o} - \omega_{y,o}\sqrt{\frac{I_\Theta}{I_\phi}}\right)e^{-\sqrt{I_\phi I_\Theta}\,\omega_x t} \qquad 42$$

The particular solutions are of the form

$$\omega_y = E + Ft \qquad\qquad 43$$

$$\omega_3 = G + Ht \qquad\qquad 44$$

FROM EQUATIONS 8 AND 9

$$F = \frac{T_y}{I_{yy}} + \omega_x I_\phi G + \omega_x I_\phi H t \qquad\qquad 45$$

$$H = \frac{T_{33}}{I_{33}} + \omega_x I_\theta E + \omega_x I_\theta F t \qquad\qquad 46$$

AND FINALLY

$$\omega_y = -\frac{T_{33}}{I_{33} I_\theta} \omega_x + \frac{1}{2}\left(\omega_{y,0} + \omega_{3,0}\sqrt{\frac{I_\phi}{I_\theta}}\right) e^{\sqrt{I_\phi I_\theta}\,\omega_x t}$$

$$-\frac{1}{2}\left(\omega_{3,0}\sqrt{\frac{I_\phi}{I_\theta}} - \omega_{y,0}\right) e^{-\sqrt{I_\phi I_\theta}\,\omega_x t} \qquad 47$$
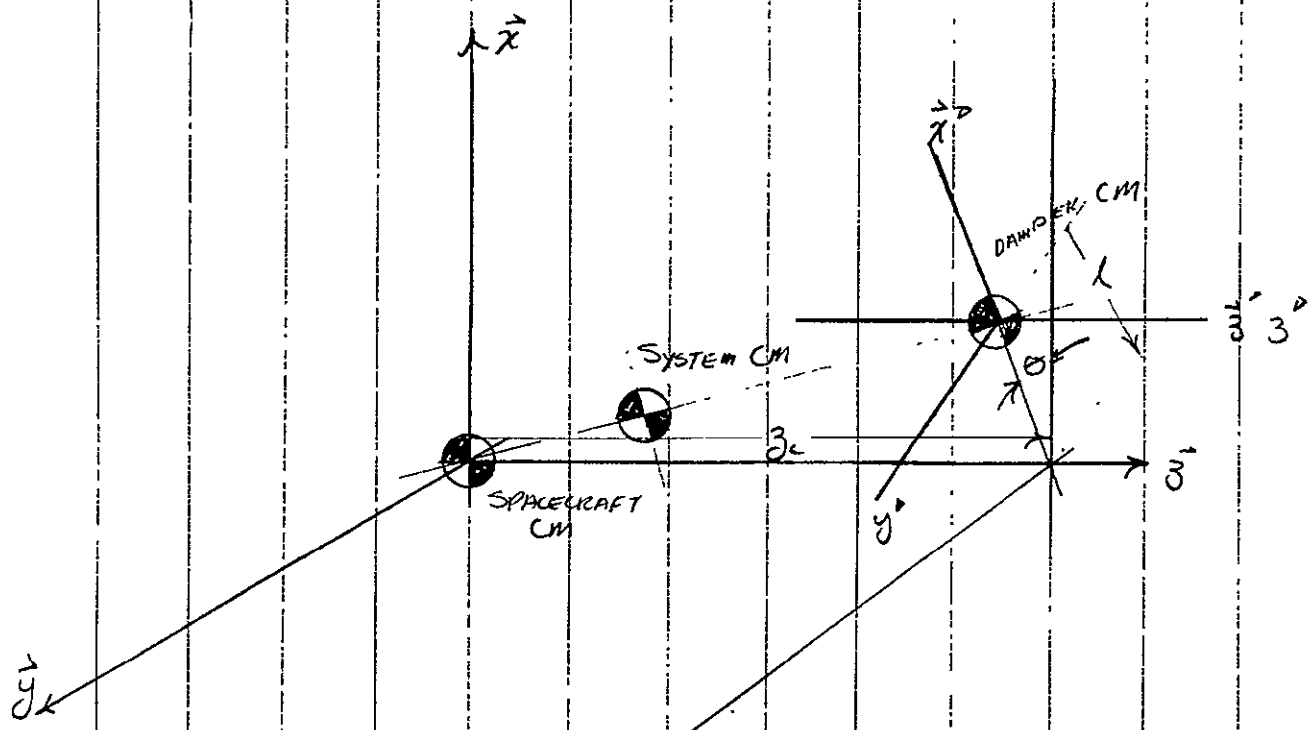
$$\omega_3 = -\frac{T_y}{I_{yy} I_\phi} \omega_x + \frac{1}{2}\left(\omega_{3,0} + \omega_{y,0}\sqrt{\frac{I_\theta}{I_\phi}}\right) e^{\sqrt{I_\phi I_\theta}\,\omega_x t}$$

$$+\frac{1}{2}\left(\omega_{3,0} - \omega_{y,0}\sqrt{\frac{I_\theta}{I_\phi}}\right) e^{-\sqrt{I_\phi I_\theta}\,\omega_x t} \qquad 48$$

APPENDIX J

HEAT PIPE NUTATION DAMPING

HEAT PIPE NUTATION DAMPING

THE SLOSHING OF THE AMMONIA INSIDE THE ATS-E HEAT PIPE WILL BE APPROXIMATED BY A PENDULUM FREE TO PIVOT ON THE 3 AXIS OF THE SPACECRAFT. THE SPACECRAFT PLUS THE DAMPER WILL BE CONSIDERED A TWO BODY PROBLEM AS SHOWN IN FIGURE 1

SPACECRAFT AND DAMPER COORDINATES - FIGURE 1

EULERS DYNAMICAL EQUATIONS WILL BE EMPLOYED FOR BOTH BODIES. FOR THE SPACECRAFT

$$T_x = I_{xx} \dot{\omega}_x + \omega_y \omega_3 (I_{33} - I_{yy}) \tag{1}$$

$$T_y = I_{yy} \dot{\omega}_y + \omega_z \omega_y (I_{xx} - I_{33}) \tag{2}$$

$$T_3 = I_{33} \dot{\omega}_3 + \omega_x \omega_y (I_{yy} - I_{xx}) \tag{3}$$

WHERE

$\omega_x, \omega_y, \omega_3$ = INERTIAL ANGULAR RATES ON $x, y, 3$

$$I_{XX}, I_{yy}, I_{33} = \text{PRINCIPAL MOMENTS OF INERTIA ON } x, y, 3$$

$$T_x, T_y, T_3 = \text{TORQUES ON THE SPACECRAFT.}$$

FOR SIMPLICITY, THE TORQUES WILL BE DIVIDED INTO EXTERNAL AND INTERNAL TORQUES. THE INTERNAL TORQUES ARE THOSE DUE STRICTLY TO THE DAMPER AT THE HINGE. HENCE

$$T_x = T_{E_x} + T_{H_x} \tag{4}$$

$$T_y = T_{EY} + T_{Hy} \tag{5}$$

$$T_3 = T_{E3} + T_{H3} \tag{6.}$$

WHERE THE SCRIPTS E AND H REFER TO EXTERNAL AND HINGE RESPECTIVELY

THE HINGE TORQUES CAN BE RESOLVED INTO TWO SOURCES, DIRECT TORQUES AND TORQUES DUE TO HINGE FORCES.

$$\begin{bmatrix} T_{Hx} \\ T_{Hy} \\ T_{H3} \end{bmatrix} = \begin{bmatrix} T_{HTx} \\ T_{HTy} \\ T_{HT3} \end{bmatrix} + \begin{bmatrix} \vec{r} \times \vec{F_H} \end{bmatrix} \cdot \begin{bmatrix} \hat{x} \\ \hat{y} \\ \hat{3} \end{bmatrix} \tag{7)}$$

FOR THE SPACECRAFT $\vec{r} = 3_c \vec{3}$. HENCE

$$\begin{bmatrix} T_{Hx} \\ T_{Hy} \\ T_{H3} \end{bmatrix} = \begin{bmatrix} T_{HTx} + 3_c F_{Hy} \\ T_{HTy} + 3_c F_{Hx} \\ T_{HT3} \end{bmatrix} \tag{8.}$$

THE HINGE TORQUE T_{HT3} IS THAT DUE ONLY TO DAMPING HENCE,

$$\begin{bmatrix} T_{HX} \\ T_{HY} \\ T_{H3} \end{bmatrix} = \begin{bmatrix} T_{HTX} & + 3_C F_{HY} \\ T_{HTY} & + 3_C F_{HX} \\ b\dot{\theta} & \end{bmatrix} \tag{9}$$

WHERE b = DAMPING COEFFICIENT

FOR THE SECONDARY BODY

$$T_{X_D} = I_{XX_D} \dot{\omega}_{X_D} + \omega_{y_D} \omega_{3_D} (I_{33_D} - I_{yy_D}) \tag{10}$$

$$T_{y_D} = I_{yy_D} \dot{\omega}_{y_D} + \dot{\omega}_{X_D} \omega_{3_D} (I_{XX_D} - I_{33_D}) \tag{11}$$

$$T_{3_D} = I_{33_D} \dot{\omega}_{3_D} + \omega_{X_D} \omega_{y_D} (I_{yy_D} - I_{XX_D}) \tag{12}$$

WHERE $\omega_{X_D}, \omega_{y_D}, \omega_{3_D}$ = INERTIAL ANGULAR RATES ON $x^{\circ} y^{\circ} 3^{\circ}$

$I_{XX_D}, I_{yy_D}, I_{33_D}$ = PRINCIPAL DAMPER MOMENTS OF INERTIA ON $x', y', 3^{\circ}$

$T_{X_D}, T_{y_D}, T_{3_D}$ = TORQUES ON DAMPER.

IT WILL BE ASSUMED THAT THERE WILL BE NO EXTERNAL FORCES OR TORQUES ON THE DAMPER. BY NEWTON'S THIRD LAW

$$\begin{bmatrix} T_{HDX} \\ T_{HDY} \\ T_{HD3} \end{bmatrix} = - \begin{bmatrix} T_{HX} \\ T_{HY} \\ T_{H3} \end{bmatrix}_{x^{\circ} y^{\circ} 3^{\circ}} \tag{13}$$

$$\begin{bmatrix} F_{HDX} \\ F_{HDY} \\ F_{HD3} \end{bmatrix} = - \begin{bmatrix} F_{HX} \\ F_{HY} \\ F_{H3} \end{bmatrix}_{x^{\circ} y^{\circ} 3^{\circ}} \tag{14}$$

J-3

THE RELATIONSHIP BETWEEN $\vec{x}\,\vec{y}\,\vec{3}$ AND $\vec{x}'\vec{y}'\vec{3}'$ IS

$$\begin{bmatrix} \vec{x}' \\ \vec{y}' \\ \vec{3}' \end{bmatrix} = \begin{bmatrix} \cos\theta & \sin\theta & 0 \\ -\sin\theta & \cos\theta & 0 \\ 0 & 0 & 1 \end{bmatrix} \begin{bmatrix} \vec{x} \\ \vec{y} \\ \vec{3} \end{bmatrix} = \begin{bmatrix} H \end{bmatrix} \begin{bmatrix} \vec{x} \\ \vec{y} \\ \vec{3} \end{bmatrix} \tag{13}$$

AS WITH THE SPACECRAFT

$$\begin{bmatrix} T_{HDX} \\ T_{HDY} \\ T_{HD3} \end{bmatrix} = \begin{bmatrix} T_{HDTX} \\ T_{HDTY} \\ T_{HDT3} \end{bmatrix} + \begin{bmatrix} \vec{r}_D \times -\vec{F}_H \end{bmatrix} \cdot \begin{bmatrix} \vec{x}',\vec{y}',\vec{3}' \end{bmatrix} \tag{16}$$

FOR THE DAMPER, $\vec{r}_D = -\ell\,\vec{x}'$, HENCE

$$\begin{bmatrix} T_{HDX} \\ T_{HDY} \\ T_{HD3} \end{bmatrix} = \begin{bmatrix} T_{HDTY} \\ T_{HDTY} + \ell F_{HD3} \\ T_{HDT3} - \ell\, F_{HDY} \end{bmatrix} \tag{17}$$

IN THE ABSENCE OF EXTERNAL FORCES

$$(m_S + m_D)\,\ddot{\vec{r}}_{SS} = 0 \tag{18}$$

WHERE

$m_S =$ SPACECRAFT MASS

$m_D =$ DAMPER MASS

$\vec{r}_{SS} =$ DISTANCE OF SYSTEM CM FROM INERTIALLY FIXED COORDINATE SYSTEM.

FROM FIGURE 2, AND NEWTON'S FIRST LAW

$$(m_D\,\ddot{\vec{r}}_{D_o} + m_S\,\ddot{\vec{r}}_{S_o}) = (m_S + m_D)\,\ddot{\vec{r}}_{SS} = 0 \tag{19}$$

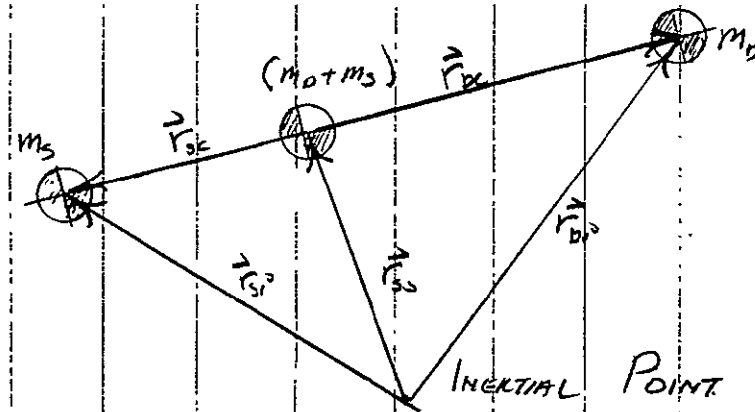$$m_D(\ddot{\vec{r}}_{DC} + \ddot{\vec{r}}_{SG}) + m_S(\ddot{\vec{r}}_{SP} + \ddot{\vec{r}}_{SC}) = 0 \tag{20}$$

FIGURE 2 — CENTER OF MASS COORDINATES

AND

$$m_D \, \vec{\bar{r}}_{DC} + m_S \, \vec{\bar{r}}_{SC} = 0 \tag{21}$$

SINCE ONLY TWO BODIES ARE INVOLVED, THE CENTER OF MASS OF THE SYSTEM MUST LIE ALONG A LINE JOINING THEM. FROM THE DEFINITION OF CENTER OF MASS.

$$m_S \, \vec{r}_{SC} + m_D \, \vec{r}_{DC} = 0 \tag{21}$$

FROM FIGURE 1

$$\vec{r}_{DC} - \vec{r}_{SC} = 3 \epsilon \, \vec{3} + \ell \, \vec{x}^{\prime}. \tag{22}$$

AND

$$\vec{r}_{DC} \left(1 + \frac{m_D}{m_S} \right) = 3 \epsilon \, \vec{3} + \ell \, \vec{x}^{\prime} \tag{23}$$

HENCE

$$\vec{r}_{DC} = \left[\frac{m_S}{m_S + m_D} \right] \left(3 \epsilon \, \vec{3}^{\prime} + \ell \, \vec{x}^{\prime} \right) \tag{24}$$

SIMILARLY

$$\vec{r}_S = \left[\frac{m_D}{m_S + m_D} \right] \left(-3 \epsilon \, \vec{3} - \ell \, \vec{x}^{\prime} \right) \tag{25}$$

$$\vec{r}_s = \left[\frac{m_D}{m_s + m_D}\right]\left[-\ell\cos\theta\,\vec{x} - \ell\sin\theta\,\vec{y} - 3c\,\vec{3}\right] \tag{26}$$

FOR THE SPACECRAFT

$$\begin{bmatrix} F_{HDX} \\ F_{HDY} \\ F_{HDZ} \end{bmatrix} = m_s \begin{bmatrix} \ddot{r}_{sx} \\ \ddot{r}_{sy} \\ \ddot{r}_{s3} \end{bmatrix} \tag{27}$$

DIFFERENTIATING EQUATION (24)

$$\dot{\vec{r}}_D = \left[\frac{m_s}{m_s + m_D}\right]\left(\vec{\omega}_D \times \vec{r}_P\right) \tag{28}$$

$$\dot{\vec{r}} = \left[\frac{m_s}{m_s + m_D}\right]\left[\omega_{yo}3c\,\vec{x}^\circ + \left(\omega_{3o}\ell - \omega_{xo}3c\right)\vec{y}^\circ - \omega_{yo}\ell\,\vec{3}^\circ\right] \tag{29}$$

$$\ddot{\vec{r}} = \left[\frac{m_s}{m_s + m_D}\right]\Bigg\{\dot\omega_{yo}3c\,\vec{x}_o^\circ + \left(\dot\omega_{3o}\ell - \dot\omega_{xo}3c\right)\vec{y}^\circ - \dot\omega_{yo}\ell\,\vec{3}^\circ$$

$$+\left[-\omega_{yo}^2\ell - \omega_{3o}\left(\omega_{3o}\ell - \omega_{xo}3c\right)\right]\vec{x}^\circ$$

$$+\left[\omega_{3o}\omega_{yo}3c - \omega_{yo}\omega_{xo}\ell\right]\vec{y}^\circ$$

$$+\left[\omega_{xo}\left(\omega_{3o}\ell - \omega_{xo}3c\right) - \omega_{yo}^2\,3c\right]\vec{3}^\circ\Bigg\} \tag{30}$$

COMBINING

$$\ddot{\vec{r}}_o = \left[\frac{m_s}{m_s + m_D}\right]\Bigg\{\left[\dot\omega_{yo}3c - \ell\left(\omega_{yo}^2 + \omega_{3o}^2\right) + \omega_{xo}\omega_{3o}3c\right]\vec{x}^\circ$$

$$+\left[\dot\omega_{3o}\ell - \dot\omega_{xo}3c + \omega_{3o}\omega_{yo}3c - \omega_{yo}\omega_{xo}\ell\right]\vec{y}^\circ$$

$$+\left[-\ddot{\omega}_{yo}\ell - 3_c\left(\omega_{xo}^2 + \omega_{yo}^2\right) + \ell\omega_{xo}\omega_{3o}\right]\vec{3}^o\right\} \tag{31}$$

AND

$$F_{HOX} = \frac{m_o m_s}{m_s + m_b}\left[\ddot{\omega}_{yo}3_c - \ell\left(\omega_{yo}^2 + \omega_{3o}^2\right) + \omega_{xo}\omega_{3o}3_c\right] \tag{32}$$

$$F_{HOy} = \frac{m_o m_s}{m_s + m_b}\left[\ddot{\omega}_{3o}\ell - \ddot{\omega}_{xo}3_c + \omega_{3o}\omega_{yo}3_c - \omega_{yo}\omega_{xo}\ell\right] \tag{33}$$

$$F_{HO3} = \frac{m_o m_s}{m_s + m_b}\left[-\ddot{\omega}_{yo}\ell - 3_c\left(\omega_{xo}^2 + \omega_{yo}^2\right) + \ell\omega_{x}\omega_{3o}\right] \tag{34}$$

FROM EQUATION (17)

$$T_{HOX} = T_{HOTX} \tag{35}$$

$$T_{HOY} = T_{HOTY} + \frac{m_o m_s}{m_s + m_b}\left[-\ddot{\omega}_{yo}\ell^2 - 3_c\ell\left(\omega_{xo}^2 + \omega_{yo}^2\right) + \ell^2\omega_{x_o}\omega_{3o}\right]$$

$$T_{HO2} = T_{HOT3} + \frac{m_o m_s}{m_s + m_b}\left[-\ddot{\omega}_{3o}\ell^2 + \ddot{\omega}_{xo}3_c\ell + \omega_{3o}\omega_{yo}3_c\ell + \omega_{yo}\omega_{xo}\ell^2\right] \tag{37}$$

FROM EQUATIONS 9 AND 13

$$T_{HOT3} = -b\ddot{\theta} \tag{39}$$

THE RELATIONSHIP BETWEEN ω_{xo}, ω_{yo}, AND ω_{3o} ARE

$$\begin{bmatrix}\omega_{xo}\\\omega_{yo}\\\omega_{3o}\end{bmatrix} = [\Theta]\begin{bmatrix}\omega_x\\\omega_y\\\omega_3\end{bmatrix} + \begin{bmatrix}0\\0\\\dot{\theta}\end{bmatrix} \tag{39}$$

HENCE

$$
\begin{bmatrix} \omega_{x_0} \\ \omega_{y_0} \\ \omega_{3_0} \end{bmatrix} = \begin{bmatrix} \omega_x \cos\theta + \omega_y \sin\theta \\ -\omega_x \sin\theta + \omega_y \cos\theta \\ \dot\theta + \omega_3 \end{bmatrix} \tag{40}
$$

AND

$$
\begin{bmatrix} \dot\omega_{x_0} \\ \dot\omega_{y_0} \\ \dot\omega_{3_0} \end{bmatrix} = \begin{bmatrix} \dot\omega_x \cos\theta + \dot\omega_y \sin\theta - \dot\theta \omega_x \sin\theta + \dot\theta \omega_y \cos\theta \\ -\dot\omega_x \sin\theta + \dot\omega_y \cos\theta - \dot\theta \omega_x \cos\theta - \dot\theta \omega_y \sin\theta \\ \ddot\theta + \dot\omega_3 \end{bmatrix} \tag{41}
$$

2.0 FUNDAMENTAL SIMPLIFICATION

ASSUME THAT ALL FORCES AND TORQUES ARE CANCELLED EXCEPT THOSE WHICH CAUSE MOTION ABOUT THE 3^{-} AXIS. EQUATIONS (12), (37), (38), (40), AND (41) BECOME

$$
-b\dot\theta + \frac{m_D m_S}{m_S + m_D}\left[-\dot\omega_{3_0} \ell^2 + \dot\omega_{x_0} 3c\ell + \omega_{3_0}\omega_{y_0} 3c\ell + \omega_{y_0}\omega_{y_0}\ell^2 \right]
$$

$$
= I_{33_0}\dot\omega_{3_0} + \omega_{x_0}\omega_{y_0}\left(I_{yy_0} - I_{xx_0} \right) \tag{42}
$$

ASSUME $I_{xx_0} = I_{yy_0} = I_{33_0} \cong 0$. THEN

$$
-b\dot\theta = \frac{m_D m_S}{m_S + m_D}\left[\dot\omega_{3_0}\ell^2 - \dot\omega_{x_0} 3c\ell - \omega_{3_0}\omega_{y_0} 3c\ell - \omega_{y_0}\omega_{y_0}\ell^2 \right] \tag{43}
$$

SUBSTITUTING

$$\frac{m_D m_S l^2}{m_S + m_D}\ddot{\theta} = -b\dot{\theta} - \frac{m_D m_S}{m_S + m_D}\left[\dot{\omega}_z l^2 - \dot{\omega}_{xo} 3_c l - \omega_{3o}\omega_{yo} 3_c l - \omega_{xo}\omega_{yo} l^2\right] \quad (44)$$

$$\ddot{\theta} = -b\frac{(m_D + m_S)}{m_D m_S l^2}\dot{\theta} - \frac{1}{l^2}\left[\dot{\omega}_z l^2 - \dot{\omega}_{xo} 3_c l - \omega_{3o}\omega_{yo} 3_c l - \omega_{xo}\omega_{yo} l^2\right] \quad (45)$$

SUMMARIZING, THE EQUATIONS ARE

$$\ddot{\theta} = -b\frac{(m_D + m_S)}{m_D m_S l^2}\dot{\theta} - \frac{1}{l^2}\left[\dot{\omega}_3 l^2 - \dot{\omega}_{xo} 3_c l - \omega_{3o}\omega_{yo} 3_c l - \omega_{xo}\omega_{yo} l^2\right] \quad (45)$$

$$\begin{bmatrix} \omega_{xo} \\ \omega_{yo} \\ \omega_{3o} \end{bmatrix} = \begin{bmatrix} \omega_x \cos\theta + \omega_y \sin\theta \\ -\omega_x \sin\theta + \omega_y \cos\theta \\ \dot{\theta} + \omega_3 \end{bmatrix} \quad (47)$$

$$\dot{\omega}_{xo} = \dot{\omega}_x \cos\theta + \dot{\omega}_y \sin\theta - \dot{\theta}\omega_x \sin\theta + \dot{\theta}\omega_y \cos\theta$$

TO SIMPLIFY THE ANALOG CALCULATIONS, EQUATION (46) WILL BE EXPANDED.

$$-\omega_{3o}\omega_{yo} = +\dot{\theta}\omega_x \sin\theta - \dot{\theta}\omega_y \cos\theta + \omega_x\omega_3 \sin\theta - \omega_y\omega_3 \cos\theta \quad (47)$$

$$\omega_{xo}\omega_{yo} = -\omega_x^2 \sin\theta\cos\theta + \omega_x\omega_y \cos^2\theta - \omega_x\omega_y \sin^2\theta$$
$$+ \omega_y^2 \sin\theta\cos\theta \quad (48)$$

$$-\omega_{xo}\omega_{yo} = \frac{1}{2}(\omega_x^2 - \omega_y^2)\sin 2\theta - \omega_x\omega_y \cos 2\theta \quad (49)$$

COMBINING

$$\ddot{\theta} = -b\frac{(m_D + m_S)}{m_D m_S l^2}\dot{\theta} - \frac{1}{l^2}\left[\dot{\omega}_3 l^2 - 3_c l \dot{\omega}_x \cos\theta - 3_c l \dot{\omega}_y \sin\theta\right.$$

$$+ 3_c l \dot{\theta} \omega_x \sin\theta - 3_c l \dot{\theta} \omega_y \cos\theta + 3_c l \dot{\theta} \omega_x \sin\theta$$

$$- 3_c l \dot{\theta} \omega_y \cos\theta + 3_c l \omega_y \omega_3 \sin\theta - 3_c l \omega_y \omega_3 \cos\theta$$

$$+ \frac{l^2}{2} (\omega_x^2 - \omega_y^2) \sin 2\theta - \omega_x \omega_y l^2 \cos 2\theta \Big] \qquad (50)$$

$$\ddot{\theta} = \frac{-b(m_D + m_s)}{m_D m_s l^2} \dot{\theta} - \frac{1}{l^2} \Big[\dot{\omega}_3 l^2 + \big(-3_c l \dot{\omega} - 2 3_c l \dot{\theta} \omega_y$$

$$- 3_c l \omega_y \omega_3 \big) \cos\theta + \big(-3_c l \dot{\omega}_y + 2 3_c l \dot{\theta} \omega_x$$

$$+ 3_c l \omega_x \omega_3 \big) \sin\theta + \frac{l^2}{2} (\omega_x^2 - \omega_y^2) \sin 2\theta - \omega_x \omega_y l^2 \cos 2\theta \Big] \qquad (51)$$

$$\ddot{\theta} = - \frac{b(m_D + m_s)}{m_D m_s l^2} \dot{\theta} - \dot{\omega}_3 - \frac{3_c}{l} \big(\dot{\omega}_x + 2\dot{\theta} \omega_y + \omega_y \omega_3 \big) \cos\theta$$

$$+ \frac{3_c}{l} \big(\dot{\omega}_y + 2\dot{\theta} \omega_x + \omega_x \omega_3 \big) \sin\theta$$

$$+ \frac{1}{2} (\omega_x^2 - \omega_y^2) \sin 2\theta - \omega_x \omega_y \cos 2\theta \qquad (52)$$

THE TORQUE APPLIED TO THE $\vec{3}$ AXIS IS

$$T_{m_3} = b\dot{\theta}$$

APPENDIX K

TV CAMERA DATA PROCESSING TECHNIQUES AND PROCEDURES

APPENDIX K

TV CAMERA DATA PROCESSING TECHNIQUES AND PROCEDURES

K.1 INTRODUCTION

TV data reduction in the ATS program entails the digitization of boom and earth data measured from 35mm photographs of a TV monitor and conversion of data into a format for data evaluation.

The TV camera is a subsystem of the ATS gravity stabilized spacecraft and is utilized for the following functions:

a. To monitor the location of the gravity gradient scissor or X-boom disks within the camera field of view for the purpose of determining boom bending

b. To monitor the location of the earth within the downward-facing camera for the purpose of determining spacecraft attitude

K.2 TV DATA FILM FLOW

The ATS tracking stations are equipped with TV monitors to display the TV signal received from the orbiting spacecraft. Periodically, at the stations, the TV monitor is photographed by a 35mm camera positioned at a prescribed distance from the TV screen. Located in the immediate area is a decimal display of the ATS system time code in which the time code is photographed along with the monitor.

The 35mm processed film is transported by NASA to GE-VFSTC in rolls up to 400 feet in length. At GE, each film roll is scrutinized on a film display to determine data quality for boom and earth data. Each frame to be digitized for either piece of data is marked by the film evaluator. Each appropriately marked frame in the roll is then displayed on the Gerber Film Scanner located in the Data Reduction Laboratory at GE-VFSTC. The frame is digitally read with the digital data punched onto hollerith cards along with appropriate

identification information. The film roll is retained in a library in the laboratory area. Selected fields on the hollerith cards are printed for data verification and for a "first look" analysis by the data evaluator.

The digitized boom data is processed through a boom deflection computer program which converts the digital readings into the in-plane and cross-plane deflections of each boom. These data are then plotted for evaluation purposes.

The digitized earth location data is processed through a conversion computer program to translate digital counts into degrees. The earth location data in degrees is listed for analysis and punched onto cards for input to the Data Analysis Module (DAM) for determination of spacecraft attitude. This is the Attitude Determination Processor (Pass 2) of the ATSDPS.

K.3 TVCS COORDINATE SYSTEM

In the first gravity gradient stabilized spacecraft, ATS-A, there are two TV cameras mounted on opposite sides of the vehicle (as shown in Figure K-1) to monitor both extensions of the primary booms (Vehicles ATS-D and E each have only one camera).

Because of mounting restrictions, the vidicon scanning directions are not to be coincident with the Y and Z axes, and are mounted in the $X_1 Y_1$ plane for ATS-A as shown in Figures K-2 and K-3 for the earthward ($-X_1$) and upward ($+X_1$) scanning cameras.

These figures should be viewed as if looking out through the camera system. Adjacent to the face of the vidicon tube is the reticle rectangle which forms the perimeter of each

UPWARD FACING TV CAMERA (NO. 2)

DOWNWARD FACING TV CAMERA (NO. 1)

DOUBLE SCISSOR ANGLE (22° to 62°)

CAMERA FIELD OF VIEW (FOV) 64° x 48°

X-BOOMS

BOOM TIP TARGETS (9-INCH DIAMETER DISK)

ATS-A
SPACECRAFT

EARTH
(6000 NM AWAY)
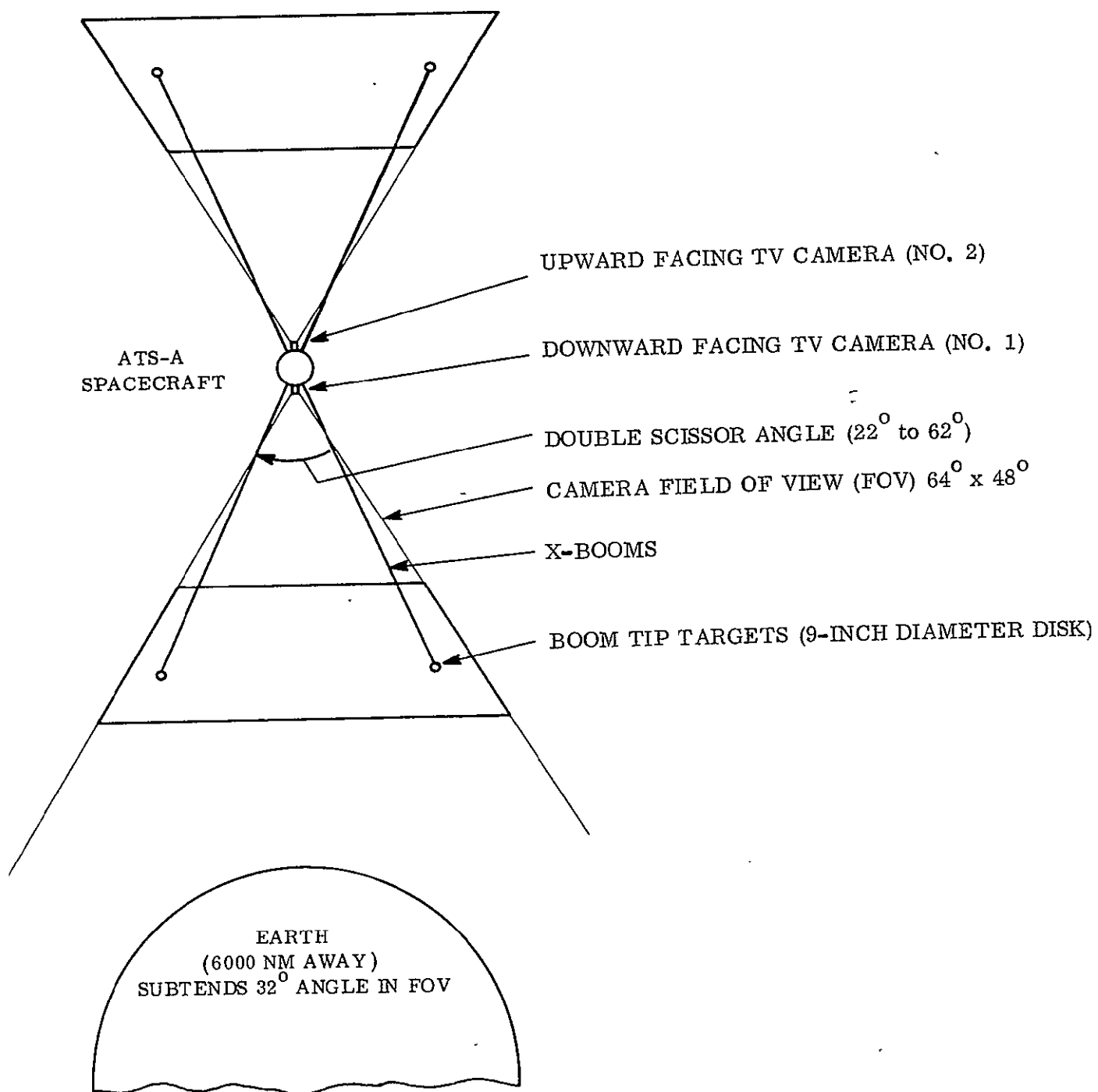SUBTENDS 32° ANGLE IN FOV

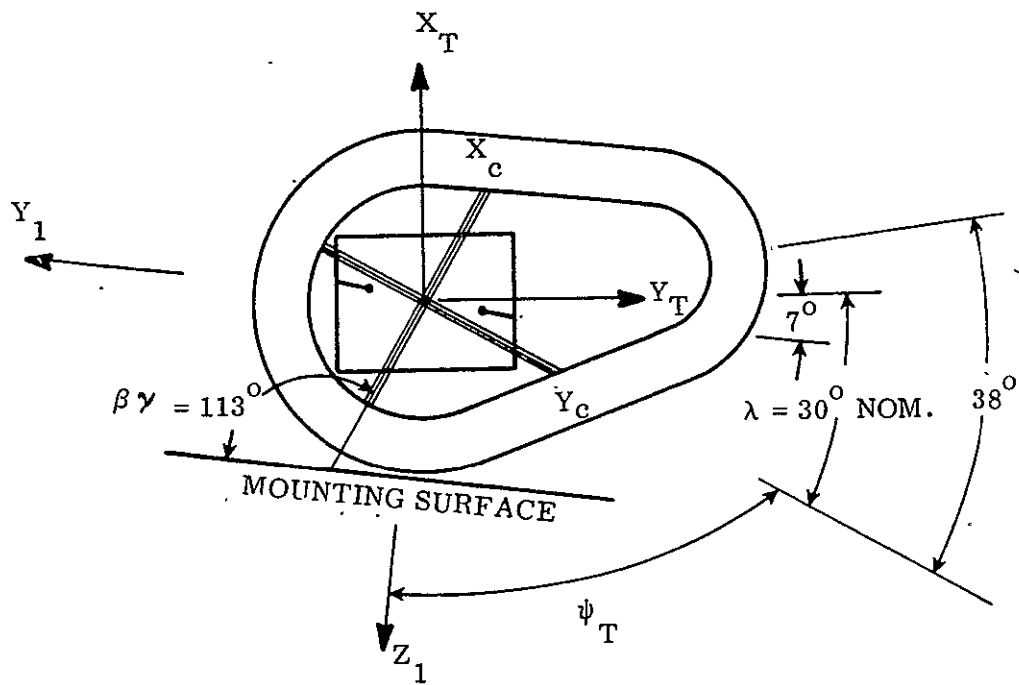Figure K-1. ATS-A TV Camera View Orientations

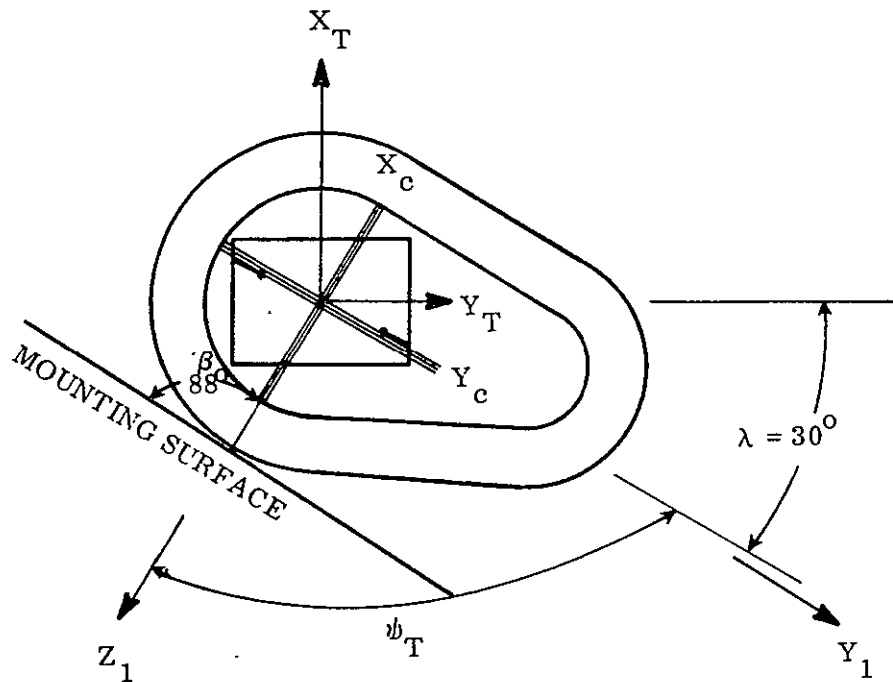Figure K-2. No. 1 Camera-Viewed Coordinates (Earth Oriented)

Figure K-3. No. 2 Camera-Viewed Coordinates (Space Oriented)

picture transmitted. The coordinates defining the reticle are shown in Figures G-2 and K-3 with the subscript T. These figures then show that the Z_T axes in both cases are "into" the paper, i.e., the Z_T axis is positioned out from the spacecraft for both cameras.

Between the face of the vidicon and the exterior quartz window, there is an eight-piece lens system which inverts the image seen by the vidicon. (In transmission and processing, this signal is inverted again such that the pictures received at GE are true images.) The quartz window is coated except for two crosshair lines that are used for TVCS alignment when mounting to the spacecraft.

At GE, the TVCS is assembled while maintaining and measuring the alignment between the camera axes $(X_T\text{-}Y_T\text{-}Z_T)$, the crosshair reference axes $(X_c\text{-}Y_c\text{-}Z_c)$, and the camera mounting surface. Note that the alignment angles of crosshair reference and mounting surface for the two cameras in a spacecraft are different.

The measured alignment angles are recorded (SI 237013 and Dwg. No. 47D209695) and are available for the coordinate transformation required in processing the TV data.

The TVCS, as an assembly, is shipped to Hughes Aircraft Company (HAC) where the cameras (now differentiated as No. 1 and 2) are mounted to the spacecraft. There the measured alignment angles between the vehicle axis (X, -Y, -Z) and the crosshair reference axes (Xc-Yc-Fc) are recorded. These alignments were performed to GE tolerances and were available for alignment transformations required for TV data evaluation.

Figures K-4 and K-5 present the expected film presentations for cameras No. 1 and 2, respectively. The camera axes as shown are true and the transformation angles between the camera, vehicle, and boom plane are nominal. Note that the boom disks (tip masses) are reversed between cameras No. 1 and 2.

Figure K-6 and K-7 define the alignment angles measured at HAC at the time of camera installation in the ATS-A spacecraft. These angles are made available for TV data translation.

In summary, the listing below shows all alignment angles measured in the assembly and installation of the two ATS-A cameras.

Camera No. 1				Camera No. 2			
Angle	Mag. (Deg)	Tol.	Figure Reference	Angle	Mag. (Deg)	Tol.	Figure Reference
β	113	$\pm 30'$	K-2	β	88	$\pm 30'$	K-3
λ	30	$\pm 10^{\circ}$	K-2	λ	30	$\pm 10^{\circ}$	K-3
ψ_T	67		K-2	ψ_T	92		K-3
θ_T	90	$\pm 30'$	K-6	θ_T	90	$\pm 30'$	K-7
ϕ_T	180	$\pm 30'$	K-6	ϕ_T	0	$\pm 30'$	K-7

K. 4 MANUAL DIGITIZING CRITERIA AND FILM SETUP

Figures K-4 and K-5 are representations of the expected 35mm frames of TV data. These magnified views are somewhat smaller than those seen on the Gerber Scanner which are used to digitize the boom and earth data. The scanner presents the frame approximately 14 inches by 10 inches on the screen.

The film frame is located in the center of the viewing surface by rotation of the reel winders at each side of the scanner. The film elevation adjustment may be required (wheel adjustments at top left and right of viewer box) but once set, should not need readjustment for the entire film reel.
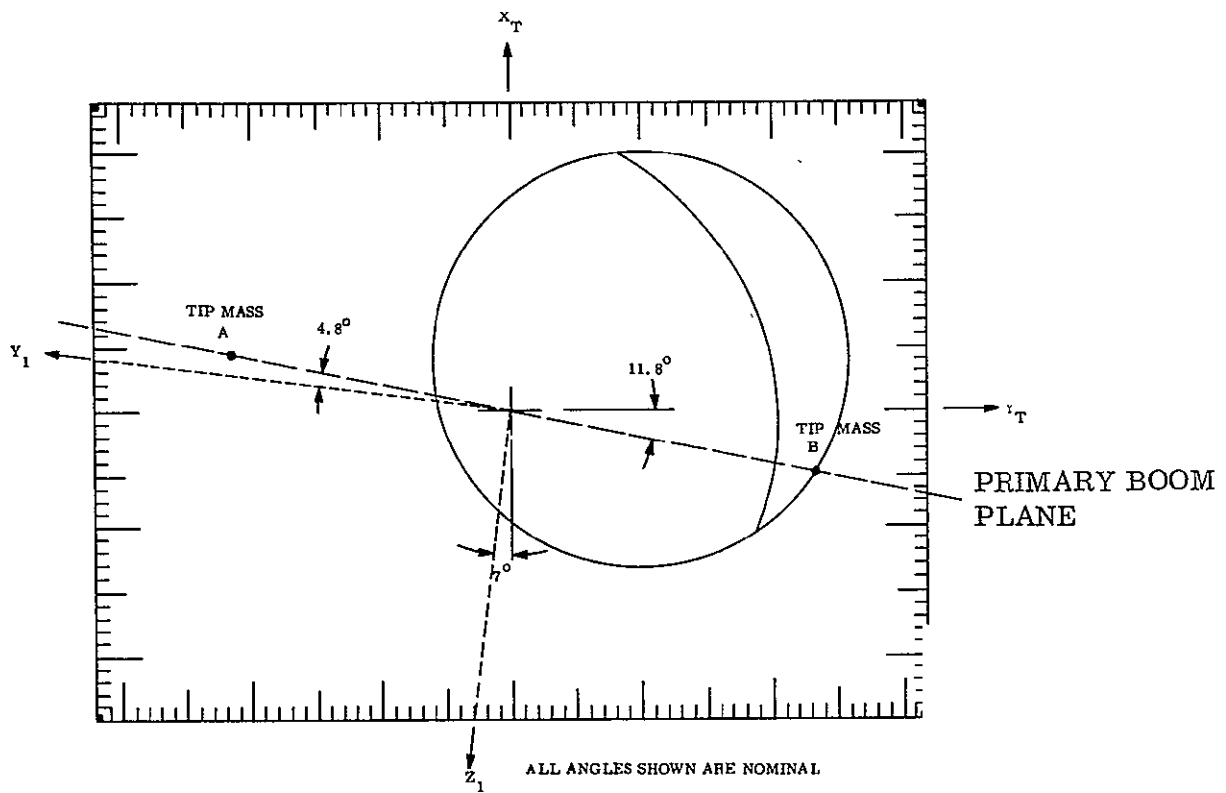
Figure K-4. Camera No. 1 Presentation (Earth Pointing in $-X_1$ Direction)
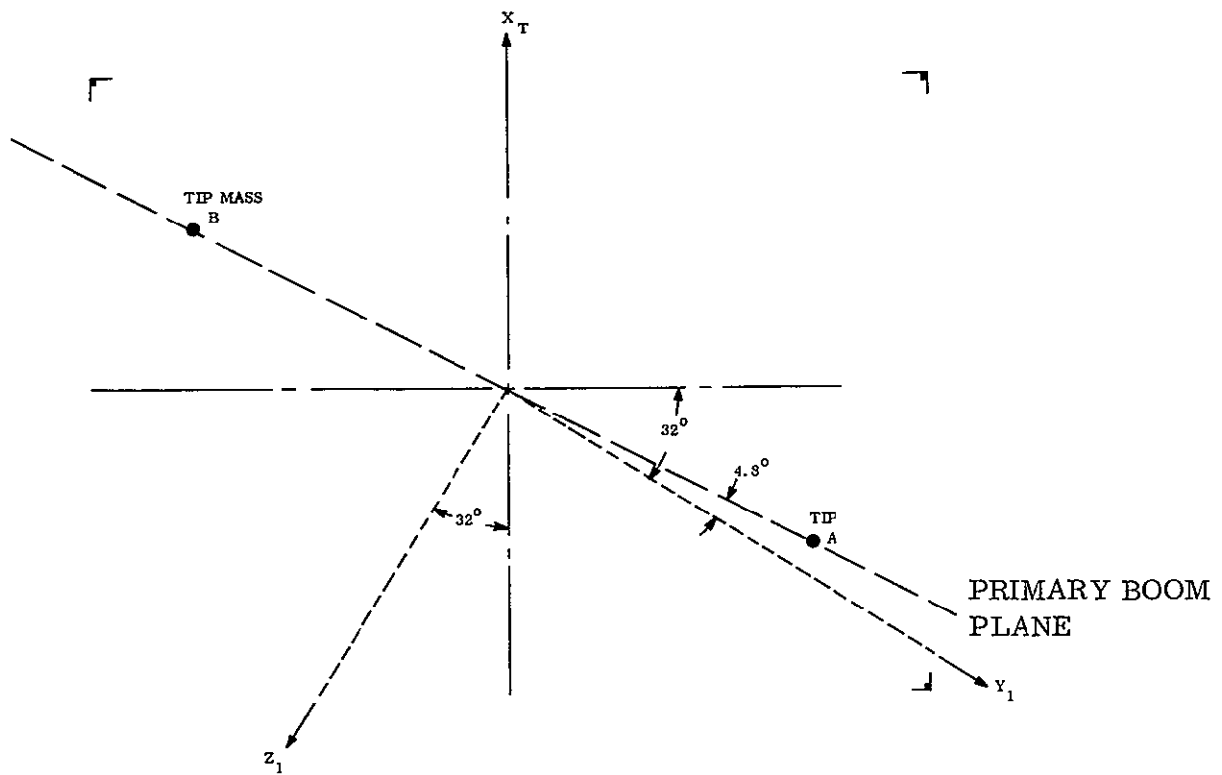

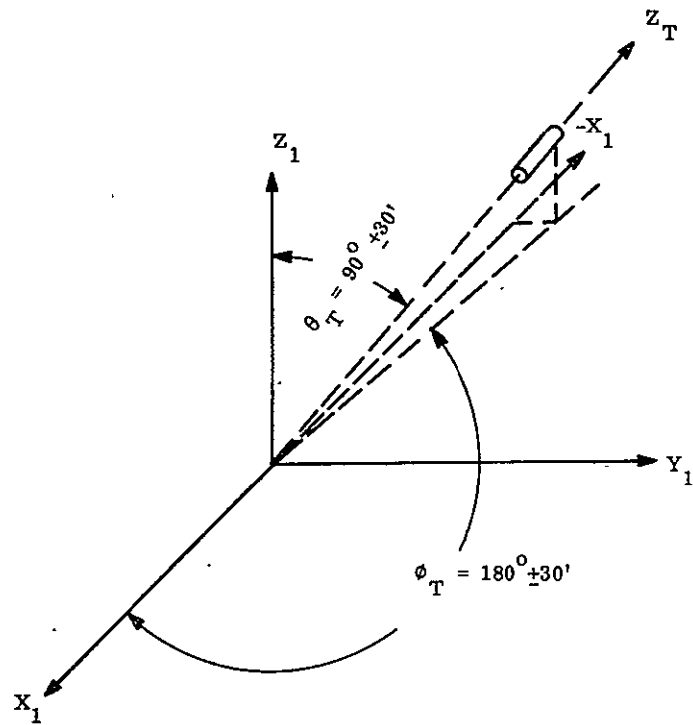Figure K-5. Camera No. 2 Presentation (Skyward Pointing in $+X_1$ Direction)

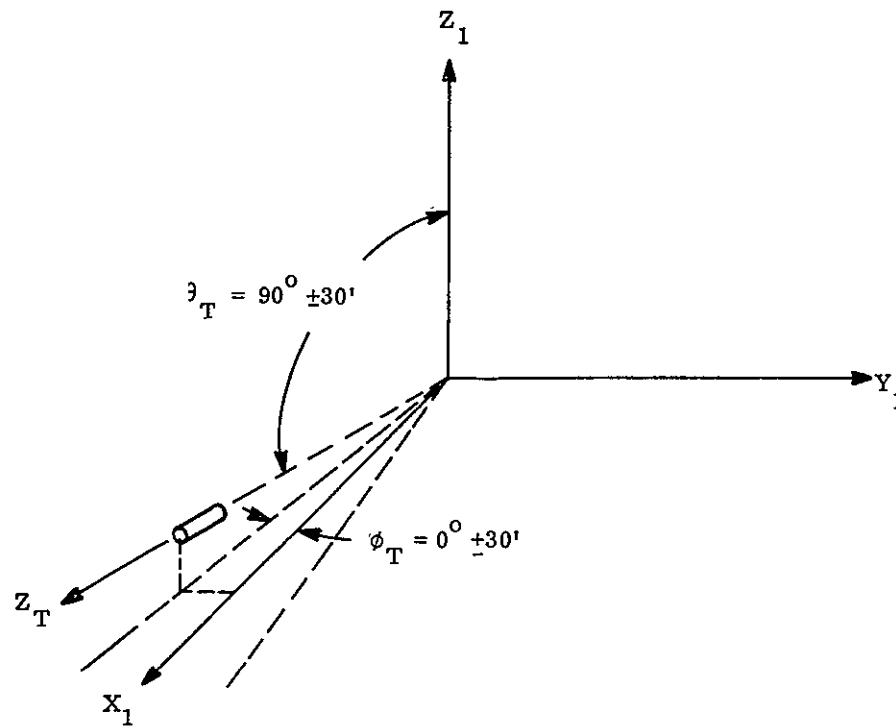Figure K-6. Vehicle Axis and Camera No. 1 Alignment

Figure K-7. Vehicle Axis and Camera No. 2 Alignment

It should be noted that the X and Y scales of the scanner, and axis of the film, are reversed as can be seen in Figures K-4 and K-5. This transform is accounted for in the computer program and all scanner readings conform to the scanner scaling.

The 1000 counts of the X and Y scanner scales are adjusted to read 500 ± 5 counts at the center cross of the film frame. In the X direction then, the 0 to 999 counts cover the film width; in the Y direction, the count spread is approximately 200 to 800 along the film height.

In the X direction of the scanner, the digital counts are increased from left to right, from zero to 999; the reticle markers along this scale are counted from -32 to +32 starting at the left-hand corner. Similarly, in the Y direction of the scanner, the digital counts are increased from bottom to top (0 to 999); the reticle markers along this scale are counted from -24 to +24 starting at the bottom edge.

If it is discovered from examination of the general boom locations that either or both camera pictures are not positioned in the roll of film in this specified manner, the digital count scales on the scanner can be reversed and the film can be, effectively, read upside-down.

K.5 DIGITIZING CRITERIA FOR BOOM DISK

The sketch below shows a typical 35mm display of a boom disk location to be digitized. Since the TV picture is a raster of a TV screen, the contrasting objects in the picture are not continuous and are composed of scan lines. Because of (1) the number of scan lines to the inch, (2) the size of the disk, and (3) the distance of the disk from the camera, each 9-inch disk can be composed of three scan lines as shown in this magnified sketch.
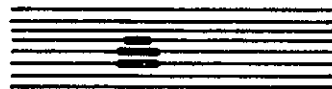

The digitizing techniques require the placing of the crosshairs of the scanner over the disk in such a way that they coincide with a circle visualized around this lighted area. Thus, the

above sketch shows that the true center of the disk does not lie on the middle illuminated line but slightly below it. This requires a certain amount of personal interpretation by the reader and only experience in film reading can determine the effect on accuracy due to this reading variability.

K. 6 DIGITIZING CRITERIA FOR EARTH DATA

Three pieces of earth data are utilized from the TV camera film to determine spacecraft attitude. These three data points define the earth center and the tips of the earth's crescent created by the sun.

The crescent points A_c and B_c are digitized in sequence of first A_c and then B_c. A_c and B_c are always defined with the sunlit portion of the earth on the left and the shadow portion of the earth on the right, as viewed on the film and shown below.

Definition of Crescent Points A_c and B_c
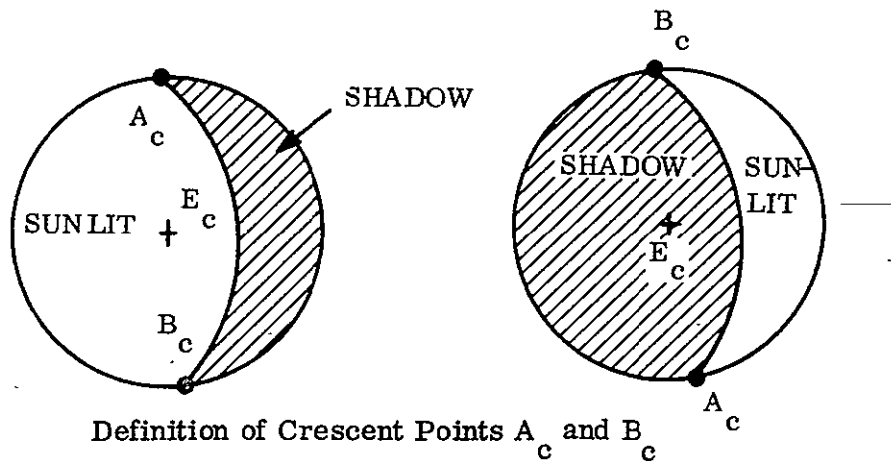
The earth center is the third digital quantity required for attitude determination. The center of the earth circle can best be located by the use of a circle template approximately the same size as the earth figure. Optimum location of the template circle (with center mark) over the earth figure gives the best fit to the true center.

K. 7 HEADER INFORMATION REQUIRED FOR TV PROCESSING

The following information is required to describe each digitized TV picture. This information is made available before picture digitizing is performed.

a. Camera Identification - No. 1 or No. 2

b. Reel Number

c. Station source of TV picture - Rosman, Mojave, etc.

d. Picture number in reel

e. Orbit number during which picture was taken

f. Day of year in which picture was taken

g. Hours-minutes-seconds of time when picture was taken

This information is to be supplied in hard copy form along with the film when delivered to GE-VFSTC. The orbit number is to be shown within the film by a decimal time code display adjacent to the ground station TV monitor.

K. 8 TV DATA DIGITIZING PROCEDURES

The digitization of the film is restricted to a prescribed, fixed procedure in order to comply with the expected continuous work load and maintain reading errors at a minimum. Preliminary editing of the film is accomplished by the data analysis group to enhance the speed of film reading.

The reading and card punching is expedited through the use of a programmed drum card for the IBM 026 keypunch. A significant amount of the identification data is programmed into the keypunch to save the effort required for manual punching.

The following sequence of operations is followed in reading the film. The sequence culminates with data in two card formats as described in Tables K-1 and K-2.

    a.   Locate the individual film frame within the center of the viewing area and align the film, generally, in the horizontal and vertical directions.

    b.   Punch a 1 or 2 to indicate camera No. 1 or 2.

    c.   Punch orbit number. Up to four numeric characters are required for this number.

    d.   Punch day of year. A number from one to 365 is required for this information.

    e.   Punch tracking station source of the film. Three numeric characters will identify each station; 058 is Rosman, 047 is Mojave and 066 is Toowoomba.

    f.   Punch-in time code shown in film active area. This can be in hours-minutes-seconds or in total seconds. The H-M-S characters will total six and the total seconds characters will require five spaces. For either contingency, six characters will be allowed for time code.

    g.   Locate countwise the X and Y encoders such that 500 counts (±5 counts) represents the center crosshair of the film; then zero counts in both axes will be near the lower left corner of the active film area, and 999 counts in both axes will occur near the upper right corner.

    h.   Determine the largest and smallest reticle mark numbers in the X and Y directions which encompass within their boundary the two boom disks and the earth data. The X direction reticles are numbered from -32 (at the left) to +32 (at the right). Likewise, the Y reticles are numbered from -24 (at the bottom) to +24 (at the top).

    i.   Manually punch the smallest X reticle number.

    j.   Manually punch the smallest Y reticle number.

    k.   Manually punch the largest X reticle number.

    l.   Manually punch the largest Y reticle number.

    m.   Digitize (X & Y) the smallest X reticle mark at the bottom of picture.

    n.   Digitize (X & Y) the smallest Y reticle mark at the left of picture.

    o.   Digitize (X & Y) the largest Y reticle mark at the left of picture.

Table K-1. TV Data Digital Card Format (Card 1)

Card	Field	Information	Code	Char.	Accum. Char.
1	1	Card Number		1	1
	2	Camera Identification		1	2
	3	Reel Number of Film		3	5
	4	Station Source of Film		2	8
	5	Picture Number of Reel		4	11
	6	Orbit Number		3	14
	7	Day of Year		3	17
	8	Hours-Minutes-Seconds of Time		6	23
	9	Smaller X Reticle Number	SXRN	2	25
	10	Smaller Y Reticle Number	SYRN	2	27
	11	Larger X Reticle Number	LXRN	2	29
	12	Larger Y Reticle Number	LYRN	2	31
	13	Left X Count at Bottom	LXB	3	34
	14	Left Y Count at Bottom	LYB	3	37
	15	Left X Count at Top	LXT	3	40
	16	Left Y Count at Top	LYT	3	43
	17	Right X Count at Bottom	RXB	3	46
	18	Right Y Count at Bottom	RYB	3	49
	19	Right X Count at Top	RXT	3	52
	20	Right Y Count at Top	RYT	3	55

Table K-2. TV Data Digital Card Format (Card 2)

Card	Field	Information	Code	Char.	Accum. Char.
2	1	Card Number		1	1
	2	Picture Crosshair X Counts	CCX	3	4
	3	Picture Crosshair Y Counts	CCY	3	7
	4	Left Boom X Counts	LBX	3	10
	5	Left Boom Y Counts	LBY	3	13
	6	Right Boom X Counts	RBX	3	16
	7	Right Boom Y Counts	RBY	3	19
	8	Earth Center X Counts	ECX	3	22
	9	Earth Center Y Counts	ECY	3	25
	10	Earth Crescent "A" Point in X Counts	EAX	3	28
	11	Earth Crescent "A" Point in Y Counts	EAY	3	31
	12	Earth Crescent "B" Point in X Counts	EBX	3	34
	13	Earth Crescent "B" Point in Y Counts	EBY	3	37

p. Digitize (X & Y) the smallest X reticle mark at the top of picture.

q. Digitize (X & Y) the largest X reticle mark at the top of picture.

r. Digitize (X & Y) the largest Y reticle mark at the right of picture.

s. Digitize (X & Y) the smallest Y reticle mark at the right of picture.

t. Digitize (X & Y) the largest X reticle mark at the bottom of picture.

K.9 DIGITIZING CRITERIA WITH ABSENCE OF DATA

It is expected that under some circumstances the data to be digitized will not be in view or will not be discernible. An example of the former would be in digitizing earth data from one camera; therefore, no earth data would be present in the other camera. An example of the latter would be when one of the boom disks could not be distinguished against its background. Under these circumstances, the following rules will apply:

a. When one or both booms are not distinguishable, the number 000,000 is manually punched into the hollerith card for each boom not visible. This will represent the X and Y counts.

b. When the earth is in field of view but the earth center is outside the count range, 999,999 is punched in the card.

c. When the earth is not in the field of view, nothing will be punched on the card, i.e., the card is left blank in those three card fields which normally carry that data.

d. When one terminator point is outside the field of view, 999,999 is punched in the card in the appropriate fields.

e. When no terminator points are present, i.e., fully illuminated or fully darkened earth, the two terminator points are punched identically and at the same value as the earth center.

K.10 BOOM DISK LOCATION DETERMINATION BY RETICLE CALIBRATION (COMPUTER SOFTWARE REQUIREMENTS)

This section contains the equations and relationships used by the computer program to determine the boom disk location for each TV camera frame. All input for these calculations is described in Section K-8.

K-14

Boom disks in the following calculations must be identified as tip mass A and tip mass B.
Tip mass A is the left-hand boom disk in camera No. 1 and the right-hand boom disk in
camera No. 2. Tip mass B is the right-hand disk in camera No. 1 and the left-hand
disk in camera No. 2.

The translation of the disk data from Gerber Scanner counts to reticle numbers is performed
by linear interpolation of straight line equations describing constant reticle numbers. In
the following equations, the variable notations are shown in Tables K-1 and K-2 in the
column entitled "CODE".

The calibration between Gerber Scanner machine counts and the reticle number for a
frame is performed once for each frame, and then this calibration is used for the
data for both disks and all the earth data. First, the straight line equation ($y = a x + b$)
is determined for the two X reticle numbers and then for the two Y reticle numbers. These
equations are then interpolated in X and Y to determine the disk and earth data quantities
in terms of reticle counts.

For the X reticles (vertical lines) :

$$X_{(RN)} = a \cdot y_{(RN)} + b$$

for SXRN

$$\left[LYB = (a)_{SXRN} \cdot LXB + B \right] \text{ and } \left[LYT = (a)_{SXRN} \cdot LXT + (b)_{SXRN} \right]$$

then,
$$(a)_{SXRN} = \frac{LXT - LXB}{LYT - LYB}$$

$$(b)_{SXRN} = LXT - (a)_{SXRN} \cdot LYT$$

for LXRN $\quad$ (a)$_{LXRN}$ $= \dfrac{RXT - RXB}{RYT - RYB}$

(b)$_{LXRN}$ $= RXT - $ (a)$_{LXRN}$ $\cdot$ RYT

The horizontal line equations for the constant Y reticle numbers are formed in the same way:

for SYRN $\quad$ (a)$_{SYRN}$ $= \dfrac{LYB - RYB}{LXB - RXB}$

(b)$_{SYRN}$ $= LYB - $ (a)$_{SYRN}$ $\cdot$ LXB

for LYRN $\quad$ (a)$_{LYRN}$ $= \dfrac{LYT - RYT}{LXT - RXT}$

(b)$_{LYRN}$ $= LYT - $ (a)$_{LYRN}$ $\cdot$ LXT

The four calibration equations formed above are now available for transforming the boom disk and earth data from machine counts into reticle numbers.

The four equations which show the Gerber counts and reticle number relationships are (see Figure K-8):

SYRN $\quad$ Y $=$ (a)$_{SYRN}$ $\cdot$ X $+$ (b)$_{SYRN}$

LYRN $\quad$ Y $=$ (a)$_{LYRN}$ $\cdot$ X $+$ (b)$_{LYRN}$

SXRN $\quad$ X $=$ (a)$_{SXRN}$ $\cdot$ Y $+$ (b)$_{SXRN}$

LXRN $\quad$ X $=$ (a)$_{LXRN}$ $\cdot$ Y $+$ (b)$_{LXRN}$

For the left boom disk, the paired X and Y counts are LBX and LBY, respectively.

K-16
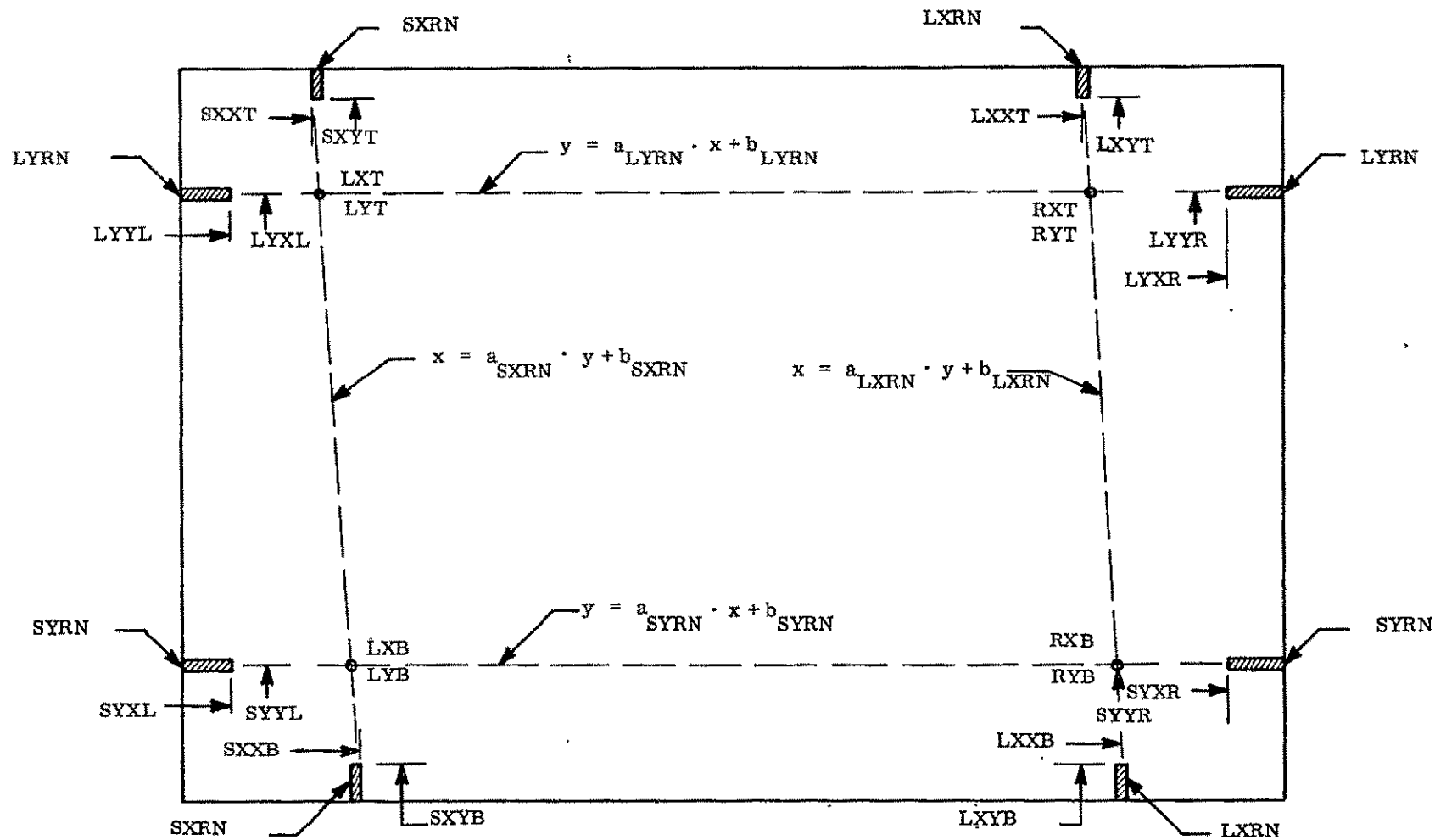
Figure K-8. TV Film Reticle Calibration

Into the equations for SXRN and LXRN, insert LBY

$$X_{SXRN} = (a)_{SXRN} \cdot LBY + (b)_{SXRN}$$

$$X_{LXRN} = (a)_{LXRN} \cdot LBY + (b)_{LXRN}$$

and compute difference $\quad \Delta X = X_{LXRN} - X_{SXRN}$

$$LXRN - SXRN = DXRN$$

$$\frac{\Delta X}{DXRN} = DXX$$

then, the answer for LBXRN will be

$$LBXRN = SXRN + \frac{LBX - LXB}{DXX} - 33.$$

To determine the Y location of the left boom disk in reticle counts, the use of the equations for LYRN and SYRN are used with LBX and LBY

$$Y_{(LYRN)} = (a)_{(LYRN)} \cdot LBX + (b)_{LYRN}$$

$$Y_{(SYRN)} = (a)_{(SYRN)} \cdot LBX + (b)_{SYRN}$$

$$\Delta Y = Y_{(LYRN)} - Y_{(SYRN)}$$

$$DYRN = LYRN - SYRN$$

$$DYY = \frac{\Delta Y}{DYRN}$$

$$LBYRN = SYRN + \frac{LBY - LYB}{DYY} - 25.$$

Similar relationships are calculated for the right boom disk, the earth center, and the A and B terminator points on the earth.

For the right boom

1. $X_{(SXRN)} = (a)_{(SXRN)} \cdot RBY + (b)_{(SXRN)}$

2. $X_{(LXRN)} = (a)_{(LXRN)} \cdot RBY + (b)_{(LXRN)}$

3. $\Delta X = (X)_{LXRN} - (X)_{(SXRN)}$

4. $DXRN = LXRN - SXRN$

5. $\dfrac{\Delta X}{DXRN} = DXX$

6. $RBXRN = SXRN + \dfrac{RBX - LXB}{DXX} - 33.$

7. $Y_{(LYRN)} = (a)_{(LYRN)} \cdot RBX + (b)_{(LYRN)}$

8. $Y_{(SYRN)} = (a)_{(SYRN)} \cdot RBX + (b)_{(SYRN)}$

9. $\Delta Y = Y_{(LYRN)} - Y_{(SYRN)}$

10. $DYRN = LYRN - SYRN$

11. $DYY = \dfrac{\Delta Y}{DYRN}$

12. $RBYRN = SYRN + \dfrac{RBY - LYB}{DYY} - 25.$

For the earth center

1. $X_{(SXRN)} = (a)_{(SXRN)} \cdot ECY + (b)_{(SXRN)}$

2. $X_{(LXRN)} = (a)_{(LXRN)} \cdot ECY + (b)_{(LXRN)}$

3. $\Delta X = (X)_{(LXRN)} - (X)_{(SXRN)}$

4. $DXRN = LXRN - SXRN$

5. $DXX = \dfrac{\Delta X}{DXRN}$

6. $ECXRN = SXRN + \dfrac{ECX - LXB}{DXX} - 33.$

7. $Y_{(LYRN)} = (a)_{(LYRN)} \cdot ECX + (b)_{(LYRN)}$

8. $Y_{(SYRN)} = (a)_{(SYRN)} \cdot ECX + (b)_{(SYRN)}$

9. $\Delta Y = Y_{(LYRN)} - Y_{(SYRN)}$

10. $DYRN = LYRN - SYRN$

11. $DYY = \dfrac{\Delta Y}{DYRN}$

12. $ECYRN = SYRN + \dfrac{ECX - LYB}{DYY} - 25.$

For earth crescent point A

1. $X_{(SXRN)} = a_{(SXRN)} \cdot EAY + b_{(SXRN)}$

2. $X_{(LXRN)} = a_{(LXRN)} \cdot EAY + b_{(LXRN)}$

3. $\Delta X = X_{(LXRN)} - X_{(SXRN)}$

4. $DXRN = LXRN - SXRN$

5. $DXX = \dfrac{\Delta X}{DXRN}$

6. $EAXRN = SXRN + \dfrac{EAX - LXB}{DXX} - 33.$

7. $Y_{(SYRN)} = a_{(SYRN)} \cdot EAX + b_{(SYRN)}$

8. $Y_{(LYRN)} = a_{(LYRN)} \cdot EAX + b_{(SYRN)}$

9. $\Delta Y = Y_{(LYRN)} - Y_{(SYRN)}$

10. $DYRN = LYRN - SYRN$

11. $DYY = \dfrac{\Delta Y}{DYRN}$

12. $EAYRN = SYRN + \dfrac{EAY - LYB}{DYY} - 25.$

For earth crescent point B

1. $X_{(SXRN)} = a_{(SXRN)} \cdot EBY + b_{(SXRN)}$

2. $X_{(LXRN)} = a_{(LXRN)} \cdot EBY + b_{(LXRN)}$

3. $\Delta X = X_{(LXRN)} - X_{(SXRN)}$

4. $DXRN = LXRN - SXRN$

5. $DXX = \dfrac{\Delta X}{DXRN}$

6. $EBXRN = SXRN + \dfrac{EBX - LXB}{DXX} - 33.$

7. $Y_{(SYRN)} = a_{(SYRN)} \cdot EBX + b_{(SYRN)}$

8. $\Delta Y = Y_{(LYRN)} - Y_{(SYRN)}$

9. $DYRN = LYRN - SYRN$

10. $Y_{(LYRN)} = a_{(LYRN)} \cdot EBX + b_{(LYRN)}$

11. $DYY = \dfrac{\Delta Y}{DYRN}$

12. $EBYRN = SYRN + \dfrac{EBY - LYB}{DYY} - 25.$

GENERAL ⟨ge⟩ ELECTRIC

SPACE DIVISION

SPACE SYSTEMS ORGANIZATION